Passive and Active Vibration Control of Renewable Energy Structures

Zhang, Zili

DOI (link to publication from Publisher):
10.5278/vbn.phd.engsci.00024

Publication date:
2015

Document Version
Publisher's PDF, also known as Version of record

PASSIVE AND ACTIVE VIBRATION CONTROL OF RENEWABLE ENERGY STRUCTURES

BY
ZILI ZHANG

DISSERTATION SUBMITTED 2015

AALBORG UNIVERSITY
DENMARK

Passive and Active Vibration Control of Renewable Energy Structures

Ph.D. Dissertation

Zili Zhang

Dissertation submitted September 7, 2015

Thesis submitted: September 7, 2015

PhD supervisor: Prof. Dr.Techn. Søren R.K. Nielsen
Aalborg University

PhD Co-Supervisor: Prof. Jie Li
Tongji University

PhD committee: Professor John Dalsgaard (chairman)
Aalborg University

Professor Steen Krenk
Technical University of Denmark

Professor David J. Wagg
University of Sheffield

PhD Series: Faculty of Engineering and Science, Aalborg University

ISSN (online): 2246-1248
ISBN (online): 978-87-7112-361-6

Published by:
Aalborg University Press
Skjernvej 4A, 2nd floor
DK – 9220 Aalborg Ø
Phone: +45 99407140
aauf@forlag.aau.dk
forlag.aau.dk

Printed in Denmark by Rosendahls, 2015

Thesis Details

Mandatory page in PhD theses:
For any PhD thesis where one or more submitted or published papers are used in the thesis the PhD student should pay close attention to proper citation of the work. If the paper(s) are co-authored the student cannot normally use the papers as if the student was the sole author. To protect the student while still proving some freedom in using material developed during the PhD study a mandatory page including the following must be included:

1. Title:
Passive and active vibration control of renewable energy structures

2. PhD student:
Zili Zhang

3. Supervisors:
Professor Søren R.K. Nielsen
Professor Jie Li

4. List of published papers:

- Nielsen, S.R.K., Zhou, Q., Kramer, M.M., Basu, B., Zhang, Z. (2013). Optimal control of nonlinear wave energy point converters. *Ocean Engineering* 72, 176-187.
- Zhang, Z., Li, J., Nielsen, S.R.K., Basu, B. (2014). Mitigation of edgewise vibrations in wind turbine blades by means of roller dampers. *Journal of Sound and Vibration* 333(21), 5283-5298.
- Zhang, Z., Nielsen, S.R.K., Blaabjerg, F., Zhou, D. (2014). Dynamics and control of lateral tower vibrations in offshore wind turbines by means of active generator torque. *Energies* 7(11): 7746-7772.

- Zhang, Z., Nielsen, S.R.K.. (2014). Edgewise vibration control of wind turbine blades using roller and liquid dampers. In *The Science of Making Torque From Wind Conference, 2014*, Copenhagen, Denmark. Published in *Journal of Physics: Conference Series* 524 (1), 012037. (Not included in thesis)

- Zhang, Z., Nielsen, S.R.K.. (2014). The influence of turbulence on the aeroelastic instability of wind turbines. In *The 9th International Conference on Structural Dynamics (EURODYN 2014)*, Porto, Portugal, 3691-3697. (Not included in thesis)

- Zhang, Z., Basu, B., Nielsen, S.R.K. (2015). Tuned liquid column dampers for mitigation of edgewise vibrations in rotating wind turbine blades. *Structural Control and Health Monitoring* 22(3), 500-517.

- Basu, B., Zhang, Z., Nielsen, S.R.K. (2015). Damping of edgewise vibration in wind turbine blades by means of circular liquid dampers. *Wind energy*. DOI: 10.1002/we.1827.

- Zhang, Z., Nielsen, S.R.K., Basu, B., Li, J. (2015). Nonlinear modeling of tuned liquid dampers (TLDs) in rotating wind turbine blades for damping edgewise vibrations. *Journal of Fluids and Structures*. In review.

- Zhang, Z., Staino, A., Basu, B., Nielsen, S.R.K. (2015). Full-scale real-time hybrid testing of tuned liquid dampers (TLDs) for vibration control of wind turbine towers. *Engineering Structures*. In review.

- Nielsen, S.R.K., Zhang, Z., Kramer, M.M., Olsen, J. (2015). Stability analysis of the Gyroscopic Power Take-Off wave energy point absorber. *Journal of Sound and Vibration* 355, 418-433.

5.

This thesis has been submitted for assessment in partial fulfillment of the PhD degree. The thesis is based on the submitted or published scientific papers which are listed above. Parts of the papers are used directly or indirectly in the extended summary of the thesis. As part of the assessment, co-author statements have been made available to the assessment committee and are also available at the Faculty. The thesis is not in its present form acceptable for open publication but only in limited and closed circulation as copyright may not be ensured.

Curriculum Vitae

Zili Zhang

E-mail: zzl_1116@126.com; zlz@civil.aau.dk
Date of birth: November 16^{th}, 1986
Place of birth: Zhejiang, China

Education Background

06/2012	Master of Engineering in Structural Engineering Tongji University, Shanghai, China
06/2009	Bachelor of Engineering in Civil Engineering Tongji University, Shanghai, China
07/2008	Minor in Engineering Management Tongji University, Shanghai, China

Professional Experience

11/2012- 09/2015	Ph.D. student at the Department of Civil Engineering, Aalborg University, Denmark.
02/2015- 05/2015	Visiting Ph. D. researcher at Department of Civil, Structural and Environmental Engineering, Trinity College Dublin, Ireland.
09/2014- 12/2014	Visiting Ph. D. researcher at Faculty of Aerospace Engineering, Delft University of Technology, the Netherlands.
01/2013- 04/2014	Part-time research assistant, Department of Civil Engineering, Aalborg University, Denmark.

Honors and Awards

2014	Excellent master dissertation in Shanghai for the year 2013, Education Commission of Shanghai.
2011	Prof. Zhaomin Wang Scholarship, Tongji University.
2008	Tongji Architectural Design Co., Ltd Scholarship, Tongji University.
2006,2007,2008	First-Class bachelor student of Tongji University.

Research Interests

Structural dynamics, Vibration control, Wind engineering, Wind turbine aerodynamics and structural dynamics, Aeroelastic stability of structures, Modeling and control of wave energy convertors, Real-time hybrid testing

Academic Memberships and Services

- Member of Danish Center for Applied Mathematics and Mechanics (DCAMM).
- Reviewer for: Journal of Structural Engineering (ASCE), Journal of Vibration and Control, Structure and Infrastructure Engineering, IEEE Transactions on Sustainable Energy.

Preface

The present thesis "Passive and Active Vibration Control of Renewable Energy Structures" is the outcome of a Ph.D. study within the period November 2010 to September 2015 at the Department of Civil Engineering, Aalborg University, Aalborg, Denmark. The thesis is presented as a collection of peer-reviewed articles published (or submitted) within this period in a number of journals.

I would like to show grateful thanks to Prof. Dr.Techn. Søren R.K. Nielsen for the impressive and fruitful supervision in this PhD project. I sincerely appreciate his persistent support and guidance throughout my study, which enable me to overcome all obstacles and keep on progressing. The constructive ideas, invaluable discussions and patient corrections for each paper not only contribute to this work, but also greatly improve my ability of researching, time management and networking.

I would like to thank my co-supervisor at Tongji University, Prof. Jie Li, for his continuous support and encouragement during all these years. I will never forget the inspiring discussions we had, both technically and spiritually. Thanks to him I start to realize the importance of innovative thinking and pursuit of excellence, and he is indeed a major influence on my career.

Further, I would like to greatly thank Prof. Biswajit Basu of Trinity College Dublin (TCD), Ireland, for his important contributions and constructive suggestions for a number of joint papers. I really appreciate him for giving me the opportunity to visit his group for three months and to carry out the full-scale real-time hybrid testing in their lab. The contributions of the technical staffs in the Structures Laboratory at TCD are also acknowledged.

I would like to acknowledge Prof. Gijs Van Kuik of DUWIND group in Delft University of Technology, Netherland, for hosting me in their group for three months. During this period I was introduced to the field of aeroelasticity with the emphasis of flutter of wind turbines. Thanks should be directed to Prof. Van Kuik for being so open and friendly in sharing their research works and ideas with me during my visit to their group.

Moreover, I wish to thank Prof. Frede Blaabjerg at Department of Energy Technology, Aalborg University, for his important contributions to our joint paper, and for an always positive attitude.

I appreciate the funding support provided by the China Scholarship Council and the Department of Civil Engineering, Aalborg University. My thanks also go to all

colleagues I have worked with, in Aalborg, Delft and Dublin, for all help that they have provided. Special thanks are given to all my friends around for pleasant discussions, moral support and helpfulness during the extraordinary three years.

Finally but foremost, I would like to thank my parents for their everlasting support. Although they do not exactly know what kind of things I have been busy doing, they do believe I am busy with things that I am really interested in.

Aalborg, September 2015 Zili Zhang

Summary in English

There are significant dynamic challenges associated with the tendencies towards large-scale wind and wave energy installations. As the size increases without a proportional increase of the stiffness, the wind turbines become more and more flexible and exhibit high susceptibility to wind or wave-induced vibrations. In order to reduce such vibrations it may become necessary to add passively or actively controlled damping elements to the system in order to remove mechanical energy from the primary structure. For wave energy converters (WEC) the objective is oppositely to control the motion of the system in such a way that a maximum mechanical energy is supplied to the absorber. In both cases, the modeling and control of dynamic systems turns out to be the most essential problem, which is the main focus of the present thesis.

In contrast to flap-wise blade vibrations and fore-aft tower vibrations, edgewise blade vibrations and lateral tower vibrations in wind turbines are related with insignificant aerodynamic damping, and may be prone to large dynamic responses or even aeroelastic instability. Active vibration control via pitch control or aerodynamic damping devices (such as trailing edge flaps) fail to effectively damp these vibrations. Therefore, in this thesis, various structural control techniques, which have achieved significant success in vibration suppression of civil engineering structures, will be extensively investigated for damping edgewise vibrations and lateral tower vibrations.

To mitigate edgewise vibrations in rotating blades, different passive control devices are proposed in the thesis, such as the roller damper, the tuned liquid column damper (TLCD), the circular liquid column damper (CLCD) and the tuned liquid damper (TLD). In traditional application the motion of the roller or liquid mass is governed by the gravitational acceleration. At implementation in the outer end of the rotating wind turbine blade the motion is controlled by the centrifugal acceleration, which for a blade of the length 63 m may attain a magnitude of 7-8 g. This makes it possible to use these dampers with rather small mass ratios for effectively suppressing edgewise vibrations. Based on an Euler-Lagrange formulation of the equations of motion, different 2-degrees-of-freedom (DOF) nonlinear models have been established for the coupling between edgewise blade motion and the motion of the mass of the roller damper, the TLCD, or the CLCD. The edgewise motion of the blade is modeled by 1-DOF defined in the blade-fixed rotating coordinate system. Parametric optimizations of these dampers have been performed using the 2-DOF models, and the optimized dampers are incorporated into a more sophisticated 13-DOF aeroelastic

model, where the coupling between the lateral tower vibration and the edgewise blade vibrations is taken into consideration. As for the TLD (sloshing damper) the analysis is based on a Galerkin variation of the field equations for the velocity field and for the free surface condition, leading to a system of coupled non-linear, ordinary differential equations. The mode shape of the linear standing waves governed by the centrifugal force is used as functional basis, which also determines the shape function s in the discretization of the free surface condition.

The second part of the thesis focuses on active and passive control of lateral tower vibrations. By means of modern power electronics, the generator torque can be prescribed to a certain value with a time delay below 10^{-2} s. In the analysis the details of the force transmission between the nacelle and the tower is described with special focus on the influence on the lateral tower motion from the reaction of the generator torque. Both the gear-driven and direct-driven offshore wind turbines are investigated, with combined excitations from aerodynamic and hydrodynamic loads. Next, as an alternative to the active generator controller, passive control of lateral tower vibrations using TLDs has also been investigated, since it is a more cost-effective and robust method. The nonlinear model established for the blade-TLD system has been modified so the rotation of the TLD-fixed coordinate system is now only due to the rotational deformation of the top of the tower. Furthermore, a state-of-the-art testing method, the real-time hybrid testing (RTHT), has been performed to verify the validity of the proposed equivalent linear damping mechanism for the fluid in the suggested theoretical model, and also to evaluate the actual behavior of TLD in damping lateral tower vibrations. In the RTHT, a full scale TLD (which prevents the scale effect) is manufactured and tested as the physical substructure, while the 13-DOF wind turbine model is employed as the numerical substructure formulated in Matlab/Simulink. Various values of damper parameters and different load cases have been considered.

The last part of the thesis focuses on the modeling and control of wave energy point absorbers, which are WECs that absorb energy from waves propagating in any direction, and with horizontal dimensions much smaller than the dominating wave length. At first, the optimal control law for a single nonlinear point absorber in irregular sea-state is derived, and proven to be a closed-loop controller with feedback from the present measured displacement and acceleration of the floater together with a non-causal integral control component dependent on future velocities. To circumvent this problem, a causal closed-loop controller is proposed by slightly modifying the optimal control law. The basic idea is to enforce the stationary velocity of the absorber into phase with the wave excitation force in order to ensure a positive power supply to the absorber at any time. It is shown that the devised causal controller absorbs almost the same power as the optimal controller in plane irregular sea states. Finally, a new principle for wave energy absorption, the so-called Gyroscopic power take-off point absorber, is proposed as a possible solution of delivering constant power to the grid without introducing expensive power electronics. Assuming monochromatic waves simplified equations are derived, valid at synchronization of the precession angular frequency of the spin axis of the gyro to the angular wave frequency. Stability conditions and the basins of attraction to the point attractors in the phase plane of the synchronized motion of the ring are also determined.

Resumé på dansk

Der er væsentlige dynamiske problemer forbundet med vind- og bølgeenergiinstallationer i stor skala. Da størrelsen forøges uden proportionelt at forøge stivheden, bliver vindmøller stadig mere fleksible og udviser som følge heraf øget vibrationsfølsomhed over for dynamiske vind- eller bølgelaster. For at reducere sådanne svingninger kan det blive nødvendigt at tilkoble passive eller aktive dæmpningselementer med henblik på at fjerne mekanisk energi fra primærkonstruktionen. For bølgeenergianlæg søger man omvendt aktivt at kontrollere anlægget, således at maksimal mekanisk energi tilføres absorberen. I begge tilfælde er kontrollen af de dynamiske systemer det mest fundamentale problem, hvilket er hovedfokus i denne afhandling.

I modsætning til flapvise bladsvingninger og tårnsvingninger i vindretningen er kantvise bladsvingninger og tårnsvingninger i lateralretningen forbundet med ubetydelig aerodynamisk dæmpning, der kan medføre store dynamiske responser, og i værste tilfælde aero-elastisk ustabilitet. Aktiv svingningsdæmpning via pitchregulering eller trailing edge flaps er ikke i stand til effektivt at dæmpe disse vibrationer. Derfor vil denne afhandling i stort omfang undersøge muligheden for at anvende forskellige strukturelle kontrolteknikker, der har haft succes i vibrationsundertrykkelse af bygningskonstruktioner, med henblik på dæmpning af kant- og laterale tårnvibrationer.

Til begrænsning af kantsvingninger undersøges i denne afhandling virkningen af forskellige passive dæmpere, såsom rulledæmpere, tunede væskesøjledæmpere (TLCD), cirkulære væskesøjledæmpere (CLCD) og tunede væskedæmpere (TLD). I sædvanlige anvendelser er rulle eller væskebevægelsen styret af tyngdeaccelerationen. Ved implementering i den ydre ende af roterende vindmøllevinger er bevægelsen i stedet styret af centrifugalaccelerationen, der for en vinge på 63 m kan antage en størrelse af 7-8 g. Dette muliggør et tilsvarende lavt masseforhold til opnåelse af en given dæmpning af kantsvingningerne. Baseret på en Euler-Lagrange fremgangsmåde er der opstillet ikke-lineære modeller til analyse af koblingen mellem bladets kantsvingninger og bevægelsen af massen af rulledæmperen, TLCD, CLCD og TLD. Vingens kantbevægelse er modelleret med en enkelt frihedsgrad, der defineres i et roterende koordinatsystem, og dæmpermasernes bevægelse ved en enkelt frihedsgrad. Baseret på 2-frihedsgraders model er udført en parametrisk optimering af de anførte dæmpere. Gyldigheden af denne fremgangsmåde er dernæst verificeret ved inkorporering af de optimerede dæmpere i en mere sofistikeret 13-frihedsgrads aero-elastisk model, hvor

der tages hensyn til koblingen mellem laterale tårn-og kantsvingninger. Hvad angår den tunede vaskedæmper er analysen baseret på Galerkin variation af feltligningerne for hastighedsfeltet og for den frie overfladebetingelse i det roterende koordinatsystem, der fører til et system af koblede ikke-lineære, ordinære differentialligninger. Som funktional basis er benyttet egensvingningsformerne i stående lineære bølger styret af centrifugalaccelerationen, der også bestemmer formfunktionerne i diskretiseringen af den frie overfladebetingelse.

Anden del af afhandlingen fokuserer på aktiv og passiv kontrol af laterale tårnvibrationer. Ved brug af moderne elektronik kan generatorens drejningsmoment foreskrives en bestemt værdi med en tidsforsinkelse på under 10^{-2} s. I undersøgelsen er detaljerne i kraftoverføringen mellem nacelle og tårn beskrevet med speciel fokus på indvirkningen af generatorens drejningsmoment på den laterale bevægelse af tårnet. Både offshore vindmøller med gear box og med direkte drev på generatoren er analyseret. Derefter, som et alternativ til den aktive generator kontrol af den laterale tårnbevægelse, er virkningen af en TLD. Den ikkelineære model udviklet til dæmpning af kantsvingninger er blevet modificeret, så rotationen af koordineringssystemet fikseret til dæmperhuset nu kun sker på grund af den rotationen af toppen af tårnet. Ydermere udføres en state-of-the-art realtime hybrid testing (RTHT), for at verificere gyldigheden af den benyttede ækvivalente lineære dæmpningsmekanisme for væsken i den foreslåede teoretiske model, og for at evaluere den faktiske adfærd af en tunet væskedæmper i fuld skala ved dæmpning af laterale tårnvibrationer. I RTHT anvendes en TLD i fuld skala som fysisk substruktur, hvilket eliminerer skala-effekter, mens 13-frihedsgrads vindmøllemodellen bruges som den numeriske sub-struktur, der formuleres i Matlab/Simulink. Undersøgelsen tager adskillige værdier for dæmpningsparametre og forskellige belastningstilfælde i betragtning.

Sidste del af afhandlingen fokuserer på modelleringen og den optimale kontrol af bølgenenergi punktbsorbere. I undersøgelsen er først udledt den optimale kontrollov for en enkelt ikkelineær punktabsorber i uregelmæssige plane bølger, der viser sig at være en lukket-løkke kontrol med feedback af den øjeblikkelige flytning og acceleration af flyderen, og af fremtidige hastigheder af denne. På grund af den sidstnævnte ikkekausale kontrolkomponent, er der foreslået en alternativ kausal lukket-løkke kontrollov, baseret på en mindre modificering af den optimale kontrollov. Ideen er at tvinge absorberens hastighed i fase med bølgekraften for herved at sikre en positiv effekttilførsel til absorberen til ethvert tidspunkt. Undersøgelsen viser, at den foreslåede kausale kontrollov kontrollov i uregelmæssige plane bølger absorberer tæt ved den samme effekt som den optimale. Endelig er foreslået et nyt princip for bølgeenergi absorption, en såkaldt Gyroscopic power take-off punktabsorber, som en mulig løsning på at levere konstant effekt til forsyningsnettet uden at introducere stærkstrømselektronik. Ved antagelse af monokromatiske bølger udledes der forenklede ligninger, gyldige ved synkronisering af præcessionen af gyroens spinaksel til vinkelfrekvensen af bølgebelastningen. Der fastlægges tillige stabilitetsbetingelser og tiltrækningsområder i faseplanen for den synkroniserede bevægelse af ringen.

Contents

CHAPTER 1
Introduction

This chapter gives the background, motivation and organization of this work. The vibration and stability problems of wind turbines, state-of-the-art of different control devices employed for wind turbines, as well as the control strategies widely used for wave energy point convertors are presented. Based on this literature survey, the objectives and structure of this thesis are outlined.

1.1 Background

As two important renewable energy sources, wind energy and wave energy have received significant attention in energy and policy agendas. An important goal in research and development of renewable energy technologies is to reduce the cost per unit of delivered electrical energy. This has led to the development of larger wind turbines with increased rotor diameters and tower heights, to capture more energy throughout its lifetime and reduce the cost of energy. Modern commercial 5 MW wind turbines have blades lengths over 60 m, and prototype turbines currently under development with ratings of 8-10 MW may have blade lengths of 80 m or more (Bak *et al.* 2013). While increasing the blade lengths and tower heights has the clear benefit of increased energy capture, this trend also leads to increased flexibility of wind turbine components, which are susceptible to experience large amplitude vibrations or even aeroelastic instability.

Wind turbines are aeroelastic systems, where strong couplings between aerodynamics and structural dynamics take place. The aerodynamic forces on wind turbine structures depend on the relative velocities of the air passing the structure. If the structure is deformed, the change in shape due to the elastic deformation and the time derivatives of the deformation will both affect the aerodynamic forces, e.g. due to a changed effective angle of attack. In turn the aerodynamic forces influence the deformation and the velocity of the structure. There is energy transfer between the vibrating structure and the air around it. If energy flows from the wind turbine structure to the air (which is normally the case), this acts like any other type of damping to reduce the amplitude of the structural motion, and it is called aerodynamic damping. However under certain circumstances it is possible for energy to flow the other way around and cause the vibration to increase. This is sometimes referred to as "negative

aerodynamic damping". If the negative aerodynamic damping exceeds the structural damping, the system renders into aeroelastic instability.

Aerodynamic damping plays an important role in the dynamic behaviors of wind turbines. Normally, the bending modes of the blades are classified as flap-wise and edgewise modes (Hansen 2003). Edgewise vibrations are vibrations close to the rotor plane, while flap-wise vibrations take place out of the rotor plane. The tower bending modes are classifed as fore-aft (longitudinal) tower mode and lateral tower mode, corresponding to along-wind and cross-wind vibrations, respectively. For different modes of the wind turbine system, the corresponding aerodynamic damping is different. Generally, for pitch regulated wind turbines, the aerodynamic damping of flap-wise rotor and longitudinal tower modes is high, whereas the damping of edgewise whirling, drivetrain torsion, and lateral tower modes is low (Hansen 2007). For example, Figure 1.1 shows the aeroelastic damping (structural damping plus aerodynamic damping) of the first nine modes of the 2.75 MW pitch-regulated, variable speed NM80 prototype turbine (Hansen *et al.* 2006). The aeroelastic damping (in terms of modal logarithmic decrement) of the first two edgewise whirling modes is around 5%, while the logarithmic decrement of the three flap-wise modes varies from 140% to 200% under normal operational conditions. The logarithmic decrement of the 1st lateral tower mode is around 5%, much less than that of the 1st fore-aft tower mode (around 30%).

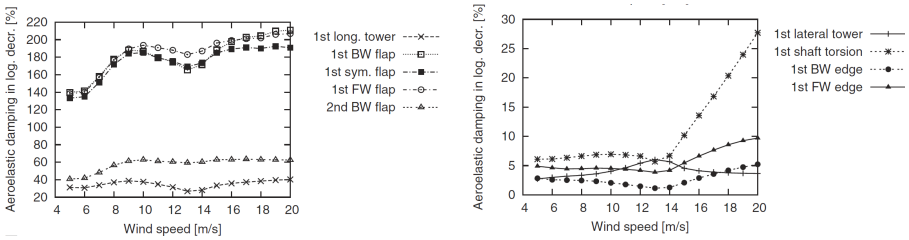

Figure 1.1 Predicted aeroelastic damping of the first nine modes of the NM80 turbine, obtained from eigenvalue analysis (Hansen *et al*. 2006).

Further, increased flexibility also causes a greater likehood of aeroelastic instability, where aeroelastic damping of certain modes become negative. The aeroelastic instability expected to occur in modern mega-watt wind turbines can be divided into two categories: stall induced vibrations during separated flow and classical flutter during attached flow (Hansen 2007). Pitch-regulated variable speed wind turbines normally do not operate in stall and the risk of stall-induced vibration is not as serious as for stall-regulated wind turbines. Exception may take place at parked conditions. It has been shown that under idle conditions, both the 1st lateral tower and 1st edgewise modes of the 5 MW NREL wind turbine exhibit negative modal damping when the nacelle yaw is either -30 or 20 degree (Bir and Jonkman 2007). Long slender blades of pitch-regulated turbines operating in attached flow may have the risk of classical flutter if the frequency ratio between flap-wise bending and torsional modes is sufficiently low, the rotor speed is sufficiently high, and the center of mass is sufficiently aft on the blade cross sections (Lobitz 2004; Hansen 2004). During flutter, the first torsional mode couples to a flap-wise bending mode through the aerodynamic forces,

and this flutter mode has highly negative damping. Although historically flutter has not been a driving issue in wind turbine design, it is believed that flutter may become a major design consideration with the growing trend of larger and more flexible blades (Hansen 2007; Pourazarm *et al.* 2015).

Large-amplitude edgewise and lateral tower vibrations not only contribute to structural fatigue damage with increased operation and maintenance costs, but also interfere with the power production, affecting the productivity and reducing efficiency (Ahlström 2006). On the other hand, aeroelastic instabilities, although not frequently occur, are potentially much more destructive and can lead to rapid failure of the wind turbine. Therefore, it becomes necessary to passively or actively add damping to the system by different control devices and control strategies, in order to remove mechanical energy from the primary structure.

1.2 Vibration control of wind turbine components

There has been continued interest among researcher in the past decade to control structural vibrations in wind turbines. Different types of vibration control systems have been proposed, either by changing aerodynamic loads experienced by the rotor (which is equivalent as increasing aerodynamic damping of the aeroelastic system), or by introducing extra damping to the primary structure through installed mechanical devices.

1.2.1 Pitch controller

Blade collective pitch controller is primarily used to limit the aerodynamic power in above-rated wind speeds in order to keep the turbine within its design limits (Burton *et al.* 2001). However, the collective pitch controller can be modified to add damping into fore-aft tower mode, since changes in pitch also have a major effect on the trust load and thus the fore-after tower vibration (Bossanyi 2000). Further, by pitching each blade individually, it is possible to reduce the low-frequency 1P (once-per-revolution) load peak (resulted from wind shear, tower shadow, yaw misalignment and rotational sampled turbulence) experienced by blade in-plane (dominantly flap-wise) vibrations (Bossanyi 2003). As illustrated in the individual pitch control (IPC) scheme in Figure 1.2, the measured out-of-plane bending moment signals at the root of each of the three blades are transformed into two orthogonal d- and q- axis by means of a transformation based on blade azimuthal angles. A feedback controller (such as PID, LQG) for each axis generates a pitch demand for that axis, and the two d- and q- axis pitch demands are converted by the reverse transformation to give pitch demand increments for each blade. These are summed with the collective pitch demand to give a total pitch demand for each blade. Furthermore, based on a nonlinear observer (extended Kalman filter) for estimating the turbine states together with the blade-effective wind speeds, IPC has been applied to reduce 1P blade loads under extreme gust with direction change (Kanev and van Engelen 2010).

This procedure is based on local blade response measurement. An alternative

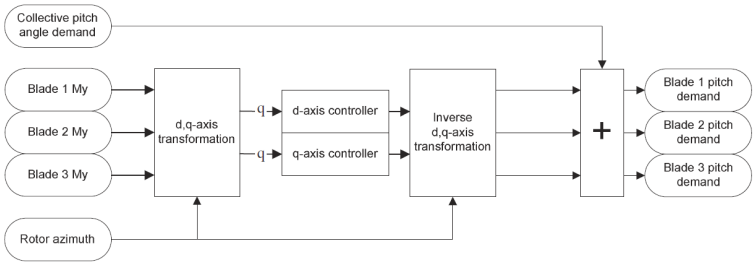

Figure 1.2 Individual pitch control (IPC) scheme (Bossanyi. 2005).

feed-forward control strategy is to measure the local inflow angle and relative flow velocity on each of the blades, and adjust the individual pitch angles accordingly (Larsen *et al.* 2005). The rapid variations in inflow conditions can be compensated faster by the inflow-based IPC than the normal IPC, leading to higher load reduction without loss of power production. Clearly, the pitch actuator will experience even greater activity in this case.

More recently, IPC was developed to improve power output and to reduce pitch motions of the platform of floating offshore wind turbines (Namik and Stol 2010). The individual blade pitching creates asymmetric aerodynamic loads in addition to the symmetric loads created by collective blade pitching to increase the platform restoring moments. Results show that the IPC reduces power fluctuations, platform rolling rate and platform pitching, comparing with a baseline collective pitch controller. Again, the blade pitch actuator usage increases significantly.

The pitch controller functions by changing the effective angle of attack along the blades and thus the aerodynamic loads experienced by the rotor. Therefore this vibration control method falls into the category which increases aerodynamic damping of the wind turbine system. The pitch controller primarily affects the fore-aft tower mode and out-of-plane (flap-wise) blade mode by reducing the low-frequency (mainly 1P) loads. However, it almost has no effect on the lightly damped lateral tower mode and edgewise blade mode. The increased usage of pitch actuator (especially the IPC) may also cause problems regarding maintenance as blade becomes longer.

1.2.2 Aerodynamic devices

In order to prevent excessive wear of the blade pitch system and to reduce the loads on the rotor in a more efficient way, several concepts of "smart rotor control" have been proposed. In this approach, aerodynamic load control devices are distributed along the span of the blade, and through a combination of sensing, control and actuation, these devices dynamically control the aerodynamic loads on the blades at any azimuthal positions.

Inspired by existing technology in aircraft and rotorcraft applications, the trailing edge flap (TEF) is a small movable control surface to directly control lift on a blade. By increasing or decreasing the camber of the airfoil, TEFs generate substantial

change in the lift coefficient of the airfoil (change in maximum lift, lift curve slope and zero-lift angle of attack), by altering the pressure distribution along the chord (Barlas and Van Kuik 2010). As illustrated in Figure 1.3, TEFs can be employed in two manners: either discrete rigid flaps or continuous deformable trailing edge. Discrete flaps are mounted on the blade (hinged) and require a moment over the hinge to achieve the required position, while continuous deformable trailing edge shows a more smooth change in shape which avoids sharp change in the camber and increases its effectiveness.

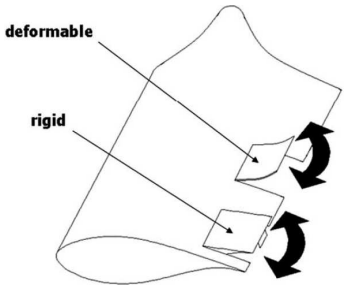

Figure 1.3 Trailing edge flaps concept (Barlas and van Kuik. 2010).

Load reduction capabilities of the rigid TEFs on blade out-of-plane vibrations have been investigated and compared with the IPC (Lackner and van Kuik 2010). It is shown that both TEFs and IPC are capable of achieving sizable load reductions, and the relative performance depends on the specific load case. While IPC more substantially reduces the 1P load peak, the individual flap controller appears to be more effective at reducing high-frequency loads, due to its low inertia and thus fast reaction. Hybrid control approaches which utilizes both IPC and TEFs offers possibilities of maximizing the load reductions or achieving large load reductions and reduced pitch usage compared to IPC. Further, both wind tunnel measurements on a small-scale wind turbine (Barlas *et al.* 2013) and full-scale tests of a Vestas V27 wind turbine (Castaignet *et al.* 2014) have been carried out for evaluating the performance of TEFs on load reduction. Promising results were observed which enhance the proof-of-concept of a "smart" wind turbine rotor.

Another aerodynamic devices for load control on wind turbine, the microtabs (Chow and Van Dam 2007; Barlas *et al.* 2013), are small (deployment height in the order of the boundary layer thickness) translational devices placed near the trailing edge of an airfoil (Figure 1.4). The deployment of such tabs changes the trailing edge flow development, so the effective camber of the airfoil, providing changes in lift. Lift enhancement is achieved by deploying the tab on the lower (pressure) side of the airfoil, while lift mitigation is achieved by deploying the tab on the upper side (suction). There are different actuation systems designed that could be used to control the tab motion. One possible design includes modular assemblies of micro-electro-mechanical translational tabs (actuated by small integrated electronic circuits) designed with a two-position control, either fully retracted (off) or fully deployed (on). Their effect on lift has been shown as powerful as flaps. The small size of these de-

vises lead to faster response and overall reduction of complexity and cost. Wind tunnel results demonstrate that careful design of tab height and location, combined with the selection of an appropriate baseline airfoil, can yield an effective active load control system (Johnson *et al.* 2010).

Figure 1.4 Microtab concept (Barlas and van Kuik. 2010).

Both TEFs and microtabs are functioning by changing lift coefficients of the airfoil, and thereby mainly affect the out-of-plane (flap-wise) blade loads. The lightly damped edgewise vibration is almost not affected by these devises.

Further, boundary layer control methods have also been used for load control on wind turbine blades. Most know methods are boundary layer suction method (Barlas *et al.* 2013) which consists in operating a powered system to suck boundary layer flow from closely spaced vertical slots, synthetic jets (Maldonado *et al.* 2010) which are zero-net mass flux jets created by employing an oscillatory surface within a cavity, and (active) vortex generators (Barrett and Farokhi 1993) which are aerodynamic surfaces consisting of small vanes to create a vortex. Traditionally these methods are used for flow separation control at moderate or large angle attack, thereby altering the airfoil pressure distribution and delaying the stall effect. Due to their simplicity, minute size and small actuating power needed, boundary layer control methods also appear high attractive to affect lift and reduce loads on the blade in normal operating conditions, although much more further investigations need to be carried out.

Alternatively, stall strips are used as a means for reducing edgewise vibrations (Riziotis *et al.* 2004; Thirstrup Petersen *et al.* 1998). Stall strips are small lists with triangular cross section at the leading edge of the blade, extending only few meters radially on a blade. Researchers have also found that blades installed with stall strips perform better with regard to edgewise vibrations; however, this beneficial effect is overshadowed by the negative impact on the power production since a substantial amount of power is lost at the same time.

1.2.3 Structural control devices

All the above-mentioned methods focus on changing aerodynamic loads experienced by the rotor, where controller conflicts may take place due to multiple objectives such as the power smoothing and load reduction. On the other hand, structural control technologies, which have achieved significant success in mitigating vibrations of civil engineering structures, turn out to be a promising alternative and in recent years are being increasingly investigated for application in wind turbines.

In the past few years, structural control of wind turbine towers has drawn more and more attention from both academia and industry. Several passive and active control devices have been developed and implemented for tower vibration control. Pendulum dampers immersing in oil have been proposed (Argyriadis and Hille 2004; Faber

and Dalhoff 2008) to be mounted inside the wind turbine tower, and highly reduced 2-DOF models have been established for this system. Tuned mass damper (TMD) is the most extensively investigated device, and its schematic diagram is illustrated in Figure 1.5(a). Taking the tower-blade interaction as well as the rotational effect into consideration, the performance of a passive TMD in mitigating along-wind tower vibrations was investigated using a simplified wind turbine model. To yield more realistic results, an advanced modeling tool has been developed and incorporated into the aeroelastic code, FAST (Fatigue, Aerodynamics, Structures and Turbulence), allowing the investigation of passive TMDs in vibration control of offshore wind turbine systems (Lackner and Rotea 2011a; Stewart and Lackner 2014). Rotea *et al.* (2010) designed and constructed active TMD for offshore wind turbine towers, and simulation results showed a clear improvement of response using active TMD compared to its passive counterpart. Passive and active TMD has also been investigated for a floating barge-type wind turbine (Lackner and Rotea 2011b). Simulation results from FAST-SC show superior performance of active TMD in reducing fore-aft tower vibrations, at the expense of active power and large strokes.

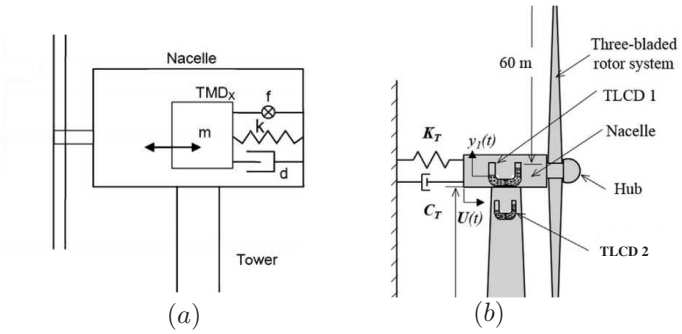

Figure 1.5 Schematic diagram of two extensively-investigated dampers for wind turbine tower. (a) TMD (Lackner and Rotea. 2011). (b) TLCD (Mensah and Duenas-Osorio. 2014).

Tuned liquid column damper (TLCD) was also introduced for wind turbine towers, and its schematic diagram is illustrated in Figure 1.5(b). Wilmink and Hengeveld (2006) simplified the wind turbine tower to be a SDOF model and concluded that TLCD was more effective than the pendulum damper. Colwell and Basu (2009) examined the effectiveness of TLCD in reducing dynamic responses of monopile offshore wind turbines under wind and wave loads, and simulation results show that response reduction of up to 55% might be achieved. Structural reliability improvement of wind turbine towers using TLCD were presented (Mensah and Dueñas-Osorio 2014), and it illustrates significant reductions in the vulnerability of towers to wind forces owing to the inclusion of the damper. Some other passive control devices, such as the ball vibration absorber (BVA) (Zhang *et al.* 2014), the spherical tuned liquid damper (TLD) (Chen and Georgakis 2013), the toggle-brace-damper (Brodersen and Høgsberg 2014) were also proposed for wind turbine towers. The effectiveness of these devices have been verified by either theoretical or experimental studies.

Most of the works described above focus on the fore-aft tower vibrations, which

are already highly damped due to the high aerodynamic damping in this mode. Therefore, more works need to be carried out on the structural control of lateral tower vibrations.

Structural control of wind turbine blades are mainly focused on active and semi-active control solutions. Arrigan *et al.* (2011) proposed a semi-active tuned mass damper (TMD) for the control of flap-wise vibrations in wind turbine blades, although the modal damping in this direction is already very high due to the aerodynamic damping. Active TMDs have also been studied for mitigating blade edgewise vibrations, and the active TMD achieves greater response reductions than the passive counterpart (Fitzgerald *et al.* 2013). Further, Krenk *et al.* (2012) proposed an active strut mounted near the root of each blade for suppressing blade vibrations, as illustrated in Figure 1.6. The active control concept developed in this research is based on resonant interaction between the rotor and the controller, which is inspired by the concept of TMDs. Staino *et al.* (2012) presented the use of active tendons mounted inside each blade for active control of edgewise vibrations (Figure 1.7). The controller allows a variable control force to be applied in the edgewise direction, and the control forces are manipulated according to a prescribed control law. Simulation results show that the use of the proposed control scheme significantly improves the response of the blade and promising performances can be achieved.

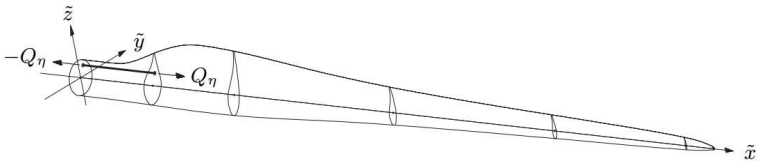

Figure 1.6 Rotor blade with an active strut attached at two cross-sections near the root (Krenk *et al.* 2012).

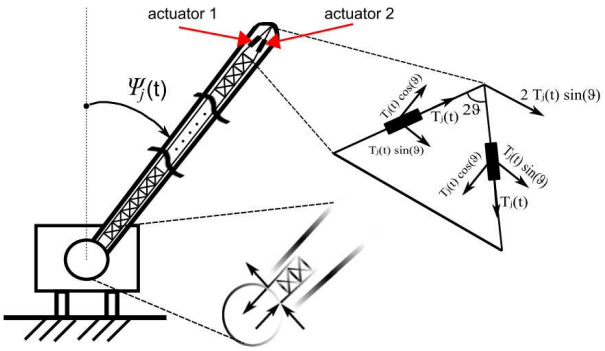

Figure 1.7 Actuator configuration for the proposed active tendon control system (Staino *et al.* 2012).

Both active and semi-active control solutions need relatively complicated controller configurations and some amount of power input. This indicates the importance and necessity of developing simple and robust vibration control devices for wind tur-

bine blades, although the existing solutions exhibit promising damping effect.

1.3 Control of wave energy point absorbers

In contrast to vibration control of wind turbine components that seeks to minimize mechanical energy from the primary structure, for wave energy point absorbers the objective is to control the motion of the system in such a way that a maximum mechanical energy is supplied to the absorber. The presence of a hydraulic power take-off mechanism (PTO) provides a reaction force (control force) that can influence the motion of the point absorber, making the optimal performance of the device possible. An schematic diagram of the point absorber with a PTO system is illustrated in Figure 1.8 (António 2008).

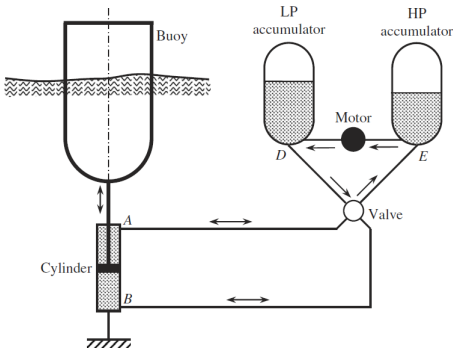

Figure 1.8 Schematic representation of the wave energy point absorber with a PTO system (António. 2008).

Basically, the point absorber is a mechanical oscillator, performing better as the wave frequency approaches its natural frequency. Theoretical studies on oscillating point absorber under regular waves revealed that the optimal performance is obtained when it's operating at resonance conditions, i.e. the frequency of oscillation should match the frequency of the incoming wave (António 2010). It is also shown that under resonance conditions, the wave excitation force and the velocity response are in phase with each other. This condition for maximizing energy production has already been reported by Budal and Falnes (1980) in the early 80's.

For real irregular waves featuring continuous frequency wave spectrum, several strategies (Falnes *et al.* 2002) have been proposed for approaching the theoretical optimal controller, which is non-causal, i.e. the present control demand depends on future wave loads or responses of the absorber. To handle this problem, non-predictive causal controllers have been proposed and tested by various authors, of which some of the recent are Valério *et al* (2007) and Lopes *et al* (2009). Such control strategies are basically suboptimal in irregular sea-states. In Valério *et al* (2007) it is demonstrated that the causal control at optimal tuning tends to enforce the velocity of the absorber into phase with the wave excitation force, which is in agreement with the

condition proposed by Budal and Falnes (1980). Other causal control methods are based on prediction of the incoming waves and the related future response of the absorber (Schoen *et al.* 2008a; Schoen *et al.* 2008b). Hence, such approaches combine elements of open- and closed-loop control. Optimal control with constraint on the displacements and the control force has also been considered (Hals *et al.* 2011). Still, the non-causality of the optimal control was handled by prediction of wave excitation force by means of an augmented Kalman filter.

The most extensively investigated causal control method is the so-called latching control (Falnes and Budal 1978; French 1979), which is inspired by the condition that the absorber velocity is kept in phase with the wave excitation. Latching control consists in locking the motion of the absorber at the very moment when its velocity vanishes at the end of one oscillation, and waiting for the most favorable situation to release the body, so as to achieve approximate optimal phase control. The principle is illustrated in Figure 1.9 for monochromatic wave excitation with the angular frequency $\omega < \omega_0 \Rightarrow T > T_0$, where ω_0 and $T_0 = \frac{2\pi}{\omega_0}$ denote the angular frequency and eigenperiod of the point absorber, and $T = \frac{2\pi}{\omega}$ is the period of the wave load. $u(t)$, $\dot{u}(t)$ and $f_e(t)$ denote the absorber displacement, absorber velocity and the wave excitation force, respectively.

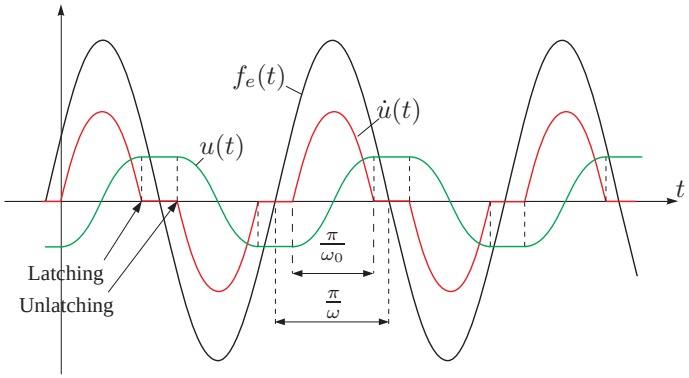

Figure 1.9 Optimal latching control under monochromatic wave excitation.

To optimally determine the latched time-intervals in real random waves is the problem to be solved, which requires the prediction of the incoming irregular waves some time into the future (Babarit *et al.* 2004). For the latching control strategy to be feasible in real sea conditions, it is required that the dynamic hydrodynamic force can be observed and predicted at least a semi-period ahead based on observation of the sea-surface elevation. In broad-banded irregular sea-states, the prediction of hydrodynamic force is related with uncertainty. Normally a significant loss of correlation of the sea-surface elevation process occurs at the time interval of half peak period $\frac{1}{2}T_p$. This lack of correlation is carried over into the dynamic hydrodynamic force, which makes the prediction of next semi-period of this quantity uncertain. Further, the non-continuous activation of the power outtake causes problems for the mechanical implementation of the control action.

1.4 Objective of the thesis

The objective of this study is to carry out fundamental research on passive and active vibration control of renewable structures, and to provide useful models for practical applications. Effective and robust vibration control methods will be explored for mitigating the lightly damped edgewise blade vibration and lateral tower vibration in wind turbines, with the main focus on structural control devices. Rigorous theoretical modeling of different dynamic systems is to be established, based on which detailed design and analysis of the proposed control devices can be carried out.

Besides, this study will explore technical solutions for wave energy point absorbers, in order to maximize the mean absorbed power and also to deliver more smooth power to the grid. A novel suboptimal causal control law will be established for controlling the motion of the point absorber, and a new type of point absorber will be proposed with detailed modeling and analysis.

1.5 Outline of the thesis

Chapter 1 presents the introduction and motivation of the whole thesis, where the background, objectives, and structure are addressed.

Chapter 2 describes the details of the 13-DOF aeroelastic wind turbine model. It clearly demonstrates how the equations of motion are derived and how the aerodynamic loads are calculated for the wind turbine system.

Chapter 3 addresses damping of edgewise vibrations in rotating wind turbine blades by means of different passive dampers. The working principal, the advantage, the disadvantage and potential improvement of each damper is explained.

Chapter 4 addresses mitigation of lateral tower vibrations in wind turbines. Active vibration control using the generator torque and passive control using TLD are both explored. Real-time hybrid testing of a full-scale TLD is also described in this chapter.

Chapter 5 presents dynamics and control of wave energy point absorbers. A suboptimal causal controller is proposed for the heave point absorber by slightly modifying the non-causal optimal control law. The Gyroscopic power take-off point absorber is modeled and stability analysis is carried out.

Chapter 6 provides the general conclusion drawn from this study and possible future extensions.

Appendix A provides the detailed descriptions of the system matrices of 13-DOF model.

Appendix B contains the enclosed journal paper: "Mitigation of edgewise vibrations

in wind turbine blades by means of roller dampers".

Appendix C contains the enclosed journal paper: "Tuned liquid column dampers for mitigation of edgewise vibrations in rotating wind turbine blades".

Appendix D contains the enclosed journal paper: "Damping of edgewise vibration in wind turbine blades by means of circular liquid dampers".

Appendix E contains the enclosed journal paper: "Nonlinear modeling of tuned liquid dampers (TLDs) in rotating wind turbine blades for damping edgewise vibrations".

Appendix F contains the enclosed journal paper: "Dynamics and control of lateral tower vibrations in offshore wind turbines by means of active generator torque".

Appendix G contains the enclosed journal paper: "Full-scale real-time hybrid testing of tuned liquid dampers (TLDs) for vibration control of wind turbine towers".

Appendix H contains the enclosed journal paper: "Optimal control of nonlinear wave energy point converters".

Appendix I contains the enclosed journal paper: "Stability analysis of the Gyroscopic Power Take-Off wave energy point absorber".

Appendix J provides detailed results from the real-time hybrid testing.

CHAPTER 2
The 13-degree-of-freedom aeroelastic wind turbine model

The details of the 13-degree-of-freedom (13-DOF) wind turbine model is presented in this chapter. The indicated reduced order model is based on linear structural dynamics together with nonlinear aerodynamics. The blades and the tower are modeled by Bernoulli-Euler beams, and the drivetrain is modeled by the St.Venant torsional theory. The blade element momentum (BEM) method is employed for calculating the lift and drag forces along each blade, taking the deformation velocities of the structure into consideration. Further, a collective PI pitch controller and a generator controller are also included in the model for power control of the machine. Despite its simplicity, this 13-DOF aeroelastic model takes into account many important characteristics of a wind turbine, including time-dependent system matrices, forward and backward whirling mods of the rotor, coupling of the tower-blade-drivetrain vibrations, aerodynamic damping in different modes of the system, as well as flexibility in the drivetrain. This model has been used as a basic tool for both the theoretical and experimental studies throughout the thesis.

2.1 General description of the structural model

A schematic representation of the wind turbine model is shown in Figure 2.1. The motions of the tower and the drivetrain are described in a fixed, global (X_1, X_2, X_3)-coordinate, while the motion of each blade is described in a moving, local (x_1, x_2, x_3)-coordinate system with its origin at the center of the hub. Neglecting the tilt and possible coning of the rotor, the X_1 and x_1 axis are unidirectional to the mean wind velocity. The (X_2, X_3)- and (x_2, x_3)- coordinate planes are placed at the rotor plane. The X_3-axis is vertical, and the x_3- axis is placed along the undeformed blade axis oriented from the hub towards the blade tip. The position of the local coordinated system attached to blade j is specified by the azimuthal angle $\Psi_j(t)$, which is considered positive when rotating clockwise seen from an upwind position.

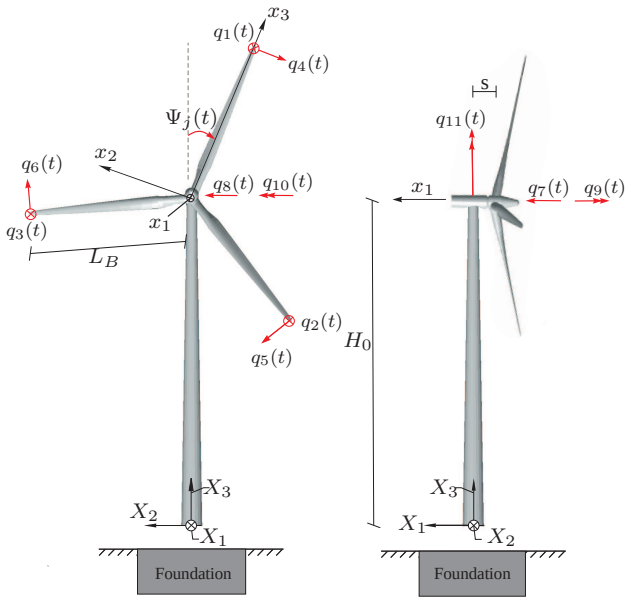

Figure 2.1 the 13-DOF aeroelastic wind turbine model. Definition of fixed and moving coordinate systems and the degrees of freedom $q_1(t), \ldots, q_{11}(t)$.

The blades are modeled as Bernoulli–Euler beams with the bending stiffness $EI_1(x_3)$ in the flap-wise direction and $EI_2(x_3)$ in the edgewise direction. The mass per unit length is $\mu(x_3)$. The flap-wise and edgewise motions of the three blades are modeled by the degrees of freedom (DOFs) $q_j(t)$ and $q_{j+3}(t)$, $j = 1, 2, 3$, indicating the tip displacement in the positive x_1-direction and in the negative x_2-direction, respectively. The related mode shapes are taken as the undamped fundamental eigenmodes $\Phi_f(x_3)$ and $\Phi_e(x_3)$ in the flap-wise and edgewise directions when the blade is clamped at the hub, i.e. the rotational speed of the rotor $\Omega = 0$ rad/s.

The tower motion is defined by five degrees of freedom $q_7(t), \ldots, q_{11}(t)$. $q_7(t)$ and $q_8(t)$ signify the displacements of the tower at the height of the hub in the global X_1-and X_2-directions. $q_9(t)$ specifies the elastic rotation of the top of the tower in the negative X_1-direction, while $q_{10}(t)$ and $q_{11}(t)$ indicate the corresponding rotations in the positive X_2-and X_3-directions. The height of the tower from the base to the nacelle is denoted H_0, and the horizontal distance from the center of the tower top to the origin of the moving coordinate systems is denoted s.

As shown in Figure 2.2, the drivetrain is modeled by the DOFs $q_{12}(t)$ and $q_{13}(t)$. The sign definition shown in Figure 2.2 applies to a gearbox with an odd number of stages. $q_{12}(t)$ and $q_{13}(t)$ indicate the deviations of the rotational angles at the hub and the generator from the nominal rotational angles Ωt and $N\Omega t$, respectively, where N is the gear ratio. Correspondingly, $\dot{q}_{12}(t)$ and $\dot{q}_{13}(t)$ are the deviations of the rotational speeds at the hub and the generator from the nominal values. In case of an even number of stages, the sign definitions for $q_{13}(t)$ and $f_{13}(t)$ are considered positive in the opposite direction. J_r and J_g denote the mass moment of inertia of the

rotor and the generator; and k_r and k_g denote the St. Venant torsional stiffness of the rotor shaft and the generator shaft.

Then, the azimuthal angle $\Psi_j(t)$ of blade j (Figure 2.1) is given by

$$\Psi_j(t) = \Omega t + \frac{2\pi}{3}(j-1) + q_{12}(t), \quad j = 1,2,3 \tag{2.1}$$

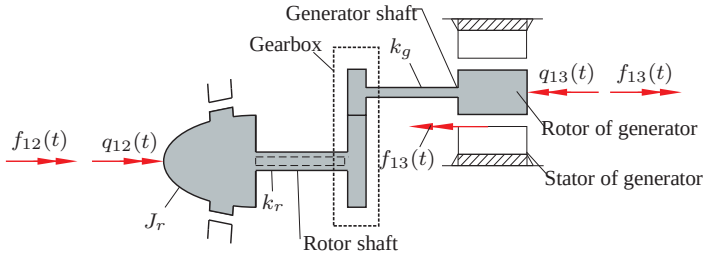

Figure 2.2 2-DOF model of the flexible drivetrain with odd number of gear stages. Definition of degrees of freedom $q_{12}(t)$ and $q_{13}(t)$.

The DOFs of the structure are assembled in the vector $\mathbf{q}(t)$. This vector can always be partitioned into a sub-vector $\mathbf{q}_l(t)$ storing the local DOFs (defined in the moving coordinate system), and a sub-vector $\mathbf{q}_g(t)$ storing the global DOFs

$$\mathbf{q}(t) = \begin{bmatrix} \mathbf{q}_l(t) \\ \mathbf{q}_g(t) \end{bmatrix} \tag{2.2}$$

In the present case we have

$$\mathbf{q}_l(t) = \begin{bmatrix} q_1(t) \\ \vdots \\ q_6(t) \end{bmatrix} \quad , \quad \mathbf{q}_g(t) = \begin{bmatrix} q_7(t) \\ \vdots \\ q_{13}(t) \end{bmatrix} \tag{2.3}$$

2.2 Establishing equations of motion

Let $\bar{u}_{1,j}(x_3,t)$ and $\bar{u}_{2,j}(x_3,t)$ denote the *local displacement fields* of the blade, i.e. the local x_1- and x_2- components of the elastic displacement vector seen by an observer fixed to the moving coordinate system. As described in the above section, the modal-based attached mode approach is applied for modeling the blade vibrations. Hence, the displacement fields $\bar{u}_{1,j}(x_3,t)$ and $\bar{u}_{2,j}(x_3,t)$ can be interpolated from the selected degrees of freedom $q_j(t)$ and $q_{j+3}(t)$ as follows

$$\left.\begin{aligned} \bar{u}_{1,j}(x_3,t) &\simeq \Phi_f(x_3) q_j(t), \qquad j = 1,2,3 \\ \bar{u}_{2,j}(x_3,t) &\simeq -\Phi_e(x_3) q_{j+3}(t) \end{aligned}\right\} \tag{2.4}$$

Due to definitions of $q_j(t)$ and $q_{j+3}(t)$ as the tip displacements, the eigenmodes must be normalized to one at the tip, i.e. $\Phi_f(L_B) = \Phi_e(L_B) = 1$. Then, the local

displacements in (2.4) lead to the following velocity components in the local x_1- and x_2- directions of a cross-section of blade j at the position x_3

$$\left.\begin{aligned}\dot{u}_{1,j}(x_3,t) &= \frac{d}{dt}\bar{u}_{1,j}(x_3,t) \simeq \Phi_f(x_3)\dot{q}_j(t)\\ \dot{u}_{2,j}(x_3,t) &= \frac{d}{dt}\bar{u}_{2,j}(x_3,t) \simeq -\Phi_e(x_3)\dot{q}_{j+3}(t)\end{aligned}\right\} \tag{2.5}$$

Further, due to the rotational angular velocity $\dot{\Psi}_j(t) = \dot{q}_{12}(t) + \Omega$ of the moving coordinate system, the local displacement vector $\bar{u}_{2,j}(x_3,t)$ induces a velocity in the local x_3- direction, which can be written as

$$\begin{aligned}\dot{u}_{3,j}(x_3,t) = \dot{\Psi}_j(t)\bar{u}_{2,j}(x_3,t) &\simeq -\Big(\dot{q}_{12}(t)+\Omega\Big)\Phi_e(x_3)q_{j+3}(t)\\ &\simeq -\Omega\Phi_e(x_3)q_{j+3}(t)\end{aligned} \tag{2.6}$$

where the 2^{nd} order term $\dot{q}_{12}(t)q_{j+3}(t)$ has been ignored in the last statement of (2.6).

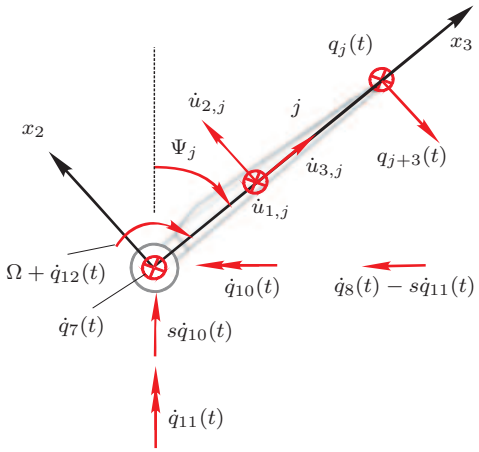

Figure 2.3 Velocities at a cross-section of blade j.

As shown in Figure 2.3, in addition to these velocity contributions, the globally defined DOFs $\mathbf{q}_g(t)$ also induce velocity contributions at the considered cross-section.

At the hub, the translational DOFs $q_7(t)$ and $q_8(t)$, and the rotational DOFs $q_{10}(t)$ and $q_{11}(t)$ induce the translational velocity components $\dot{q}_7(t)$, $\dot{q}_8(t) - s\dot{q}_{11}(t)$ and $s\dot{q}_{10}(t)$ in the global X_1-, X_2-, X_3- directions, respectively. The corresponding moving frame components for blade j are expressed as

$$\left.\begin{aligned}\dot{u}_{1,j}(x_3,t) &= \dot{q}_7(t)\\ \dot{u}_{2,j}(x_3,t) &= \sin\Psi_j\, s\dot{q}_{10}(t) + \cos\Psi_j\,\Big(\dot{q}_8(t) - s\dot{q}_{11}(t)\Big)\\ \dot{u}_{3,j}(x_3,t) &= \cos\Psi_j\, s\dot{q}_{10}(t) - \sin\Psi_j\,\Big(\dot{q}_8(t) - s\dot{q}_{11}(t)\Big)\end{aligned}\right\} \tag{2.7}$$

Further, the angular velocity of the hub induces a velocity component in the local x_2- direction at the considered cross-section

$$\dot{u}_{2,j}(x_3,t) = -x_3\Big(\Omega + \dot{q}_{12}(t)\Big) \tag{2.8}$$

Finally, at the hub the rotational DOFs $q_{10}(t)$ and $q_{11}(t)$ result in angular velocities $\dot{q}_{10}(t)$ and $\dot{q}_{11}(t)$ in the global X_2- and X_3- directions. In turn, these angular velocities induce the velocity component in the local x_1- direction

$$\dot{u}_{1,j}(x_3,t) = x_3\cos\Psi_j\,\dot{q}_{10}(t) + x_3\sin\Psi_j\,\dot{q}_{11}(t) \tag{2.9}$$

Summing up the contributions from (2.5), (2.6), (2.7), (2.8), (2.9) provides the following components of the velocity vector of a cross-section of blade j, in the moving coordinate system

$$\left.\begin{aligned}
\dot{u}_{1,j}(x_3,t) &= \Phi_f(x_3)\dot{q}_j(t) + \dot{q}_7(t) + x_3\cos\Psi_j\,\dot{q}_{10}(t) + x_3\sin\Psi_j\,\dot{q}_{11}(t)\\
\dot{u}_{2,j}(x_3,t) &= -\Phi_e(x_3)\dot{q}_{j+3}(t) + \sin\Psi_j\,s\dot{q}_{10}(t) +\\
&\qquad \cos\Psi_j\,\Big(\dot{q}_8(t) - s\dot{q}_{11}(t)\Big) - x_3\Big(\Omega + \dot{q}_{12}(t)\Big)\\
\dot{u}_{3,j}(x_3,t) &= -\Omega\Phi_e(x_3)q_{j+3}(t) + \cos\Psi_j\,s\dot{q}_{10}(t) -\\
&\qquad \sin\Psi_j\,s\Big(\dot{q}_8(t) - s\dot{q}_{11}(t)\Big)
\end{aligned}\right\} \tag{2.10}$$

Defined in the global coordinate system (Figure 2.4), the displacement components of the tower in X_1- and X_2- directions can be expressed as

$$\left.\begin{aligned}
u_{X_1}(X_3,t) &= N_1(X_3)q_7(t) - N_2(X_3)q_{10}(t)\\
u_{X_2}(X_3,t) &= N_1(X_3)q_8(t) + N_2(X_3)q_9(t)
\end{aligned}\right\} \tag{2.11}$$

where $N_1(X_3)$ and $N_2(X_3)$ are cubic Hermite interpolation functions in the following form

$$\left.\begin{aligned}
N_1(X_3) &= 3\Big(\frac{X_3}{H_0}\Big)^2 - 2\Big(\frac{X_3}{H_0}\Big)^3\\
N_2(X_3) &= H_0\Big(\frac{X_3}{H_0}\Big)^3 - H_0\Big(\frac{X_3}{H_0}\Big)^2
\end{aligned}\right\} \tag{2.12}$$

Hence, the total kinetic energy of the wind turbine including the blade, the tower and the generator becomes

$$\begin{aligned}
T\Big(\mathbf{q}(t),\dot{\mathbf{q}}(t)\Big) &= \frac{1}{2}\sum_{j=1}^{3}\int_0^{L_B}\mu(x_3)\Big(\dot{u}_{1,j}^2(x_3,t) + \dot{u}_{3,j}^2(x_3,t) + \dot{u}_{3,j}^2(x_3,t)\Big)dx_3\\
&+ \int_0^{H_0}\mu_0(X_3)\Big(\dot{u}_{X_1}^2(X_3,t) + \dot{u}_{X_2}^2(X_3,t)\Big)dX_3 + \frac{1}{2}M_0\Big(\dot{q}_7^2(t) + \dot{q}_8^2(t)\Big)\\
&+ \frac{1}{2}J_g\Big(N\Omega + \dot{q}_{13}(t)\Big)^2
\end{aligned}$$

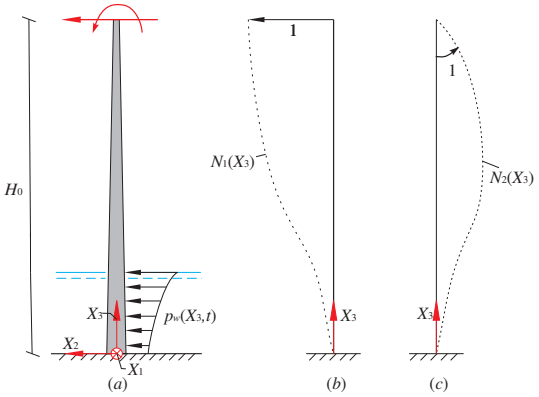

Figure 2.4 Modeling of the tower vibrations. (a) Two DOFs model for the fore-aft tower vibration or lateral tower vibration. (b) Shape function $N_1(X_3)$. (c) Shape function $N_2(X_3)$.

(2.13)

where $\mu_0(X_3)$ is the mass per unit length of the tower, M_0 is the mass of the nacelle. The first term on the right hand side of Eq. (2.13) indicates the kinetic energy stored in the rotor. The second and third terms represents the kinetic energy stored in the tower and the nacelle related to the globally defined degrees of freedom. Finally, the last term indicates the kinetic energy stored in the rotor of the generator.

Next, the total potential energy (strain energy) of the wind turbine is given by

$$U\Big(\mathbf{q}(t)\Big) = \frac{1}{2}\mathbf{q}^T(t)\mathbf{K}_s\mathbf{q}(t) \tag{2.14}$$

where $\mathbf{K}_s$ denotes the structural stiffness matrix including centrifugal stiffening in the rotating blades. $\mathbf{K}_s$ is symmetric and time-independent, as will be given later.

Based on Eqs. (2.13) and (2.14), the equations of motion can be obtained from the Euler-Lagrange stationary condition of the action integral in analytical mechanics (Pars 1965)

$$\frac{d}{dt}\left(\frac{\partial T}{\partial \dot{\mathbf{q}}}\right) - \frac{\partial T}{\partial \mathbf{q}} + \frac{\partial U}{\partial \mathbf{q}} = \mathbf{f}_a\big(\dot{\mathbf{q}}(t), \beta(t), t\big) - (\mathbf{C}_s + \mathbf{C}_{gen})\dot{\mathbf{q}}(t) \tag{2.15}$$

The right hand side of Eq. (2.15) is the load vector including all external and internal conservative and non-conservative load components. $\mathbf{f}_a\big(\dot{\mathbf{q}}(t), \beta(t), t\big)$ is the aerodynamic loads as a function of the structural response $\dot{\mathbf{q}}(t)$ and the pitch angle $\beta(t)$, as will be specified in the next subsection. $-\mathbf{C}_s\dot{\mathbf{q}}(t)$ is the linear viscous damping load term, and $\mathbf{C}_s$ indicates the structural damping matrix that is symmetric and positive definite. $-\mathbf{C}_g\dot{\mathbf{q}}(t)$ is the generator torque, which can be specified to actively damp tower vibrations as will be shown in Section 4.

The resulting equations of motion of the wind turbine system become

$$\mathbf{M}(t)\ddot{\mathbf{q}}(t) + \mathbf{C}(t)\dot{\mathbf{q}}(t) + \mathbf{K}(t)\mathbf{q}(t) = \mathbf{f}_a\big(\dot{\mathbf{q}}(t), \beta(t), t\big) \tag{2.16}$$

where $\mathbf{M}(t)$ is the mass matrix that is symmetric and positive definite, $\mathbf{C}(t)$ is the damping matrix and $\mathbf{K}(t)$ is the stiffness matrix. All three matrices are time dependent. In the general case these matrices depend on $\mathbf{q}(t)$, i.e. $\mathbf{M} = \mathbf{M}(\mathbf{q})$, $\mathbf{C} = \mathbf{C}(\mathbf{q})$ and $\mathbf{K} = \mathbf{K}(\mathbf{q})$. In the present case, the dependence is merely on $\Psi_j(t) = q_{12}(t) + \Omega t + \frac{2\pi}{3}(j-1)$. Ignoring $q_{12}(t)$ the system matrices all become periodic time-dependent matrix functions with the constant rotational period $T = \frac{2\pi}{\Omega}$.

$$\mathbf{M}(t) = \mathbf{M}(t+T), \quad \mathbf{C}(t) = \mathbf{C}(t+T), \quad \mathbf{K}(t) = \mathbf{K}(t+T) \tag{2.17}$$

The time-dependence in Eq. (2.17) can be eliminated by a coordinate transformation, e.g. the Coleman transformation or the multiblade transformation (Bir 2008). Only in this case it is meaningful to carry out eigenvalue analysis of the wind turbine system.

For detailed description of $\mathbf{M}(t)$, $\mathbf{C}(t)$ and $\mathbf{K}(t)$, see Appendix A.

Further, a full-span collective pitch control system is assumed. The time delay due to mechanical inertia in the pitch actuator system can be modeled by a linear first order filter

$$\dot{\beta}(t) = \frac{1}{\tau}\Big(\beta_0(q_{12}, \dot{q}_{12}, \ddot{q}_{12}) - \beta(t)\Big) \tag{2.18}$$

where τ is the response time. β_0 is the pitch demand, which is specified by the following PID controller here, partly due to its wide range of application in the wind turbine industry, and partly due to its relative simplicity (Ogata 2010)

$$\beta_0(q_{12}, \dot{q}_{12}, \ddot{q}_{12}) = G\Big(\dot{q}_{12}(t) + \frac{1}{\tau_i} q_{12}(t) + \tau_d \ddot{q}_{12}(t)\Big) \tag{2.19}$$

where G is the controller gain, τ_i is the integral control time constant and τ_d is the derivative control time constant. Inserting Eq. (2.19) into Eq. (2.18), the following linear control law is obtained

$$\dot{\beta}(t) = d_1 q_{12}(t) + d_2 \dot{q}_{12}(t) + d_3 \ddot{q}_{12}(t) - \frac{1}{\tau}\beta(t) \tag{2.20}$$

where $d_1 = \frac{G}{\tau\tau_i}$, $d_2 = \frac{G}{\tau}$, $d_1 = \frac{G\tau_d}{\tau}$.

In combination, Eqs.(2.16) and (2.20) form a closed system of differential equations for determination of the response vector **q**(t) and the pitch angle $\beta(t)$, driven by the turbulence in the inflow to the rotor.

2.3 Aerodynamic loads

In the present study, the blade element momentum (BEM) with Prandtl's tip loss factor and Glauert correction is adopted to calculate aerodynamic forces along the blade (Hansen 2000). Quasi-static aerodynamics is assumed without considering time delay of the obtained lift force on the airfoil, i.e. any changes of the instantaneous angle of attach $\alpha(x_3, t)$ is assumed to be felt immediately in the aerodynamic loads. If necessary the time delay can be modeled by a rational filtration of the aerodynamic loads at

the expense of introducing additional state variable in the dynamic system. It should be noted that if a dynamic stall model (Leishman and Beddoes 1989; Larsen *et al.* 2007) is applied in this 13-DOF model, such an extended state vector formulation become mandatory.

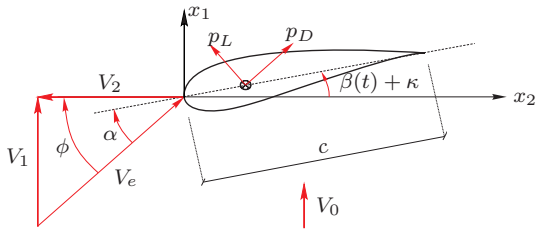

Figure 2.5 Local velocities and forces in the aerodynamic model.

Figure 2.5 shows the local velocities and forces on an airfoil (blade section) that has a distance x_3 away from the hub. $V_1(x_3,t)$ and $V_2(x_3,t)$ denote the wind velocities seen by an observer fixed to the moving (x_1,x_2,x_3)- coordinate system, which are given as

$$\left.\begin{aligned} V_1(x_3,t) &= (1-a)V_0 + v_1(x_3,t) - \dot{u}_1(x_3,t) \\ V_2(x_3,t) &= (1+a')\Omega x_3 + v_2(x_3,t) - \dot{u}_2(x_3,t) \end{aligned}\right\} \tag{2.21}$$

where V_0 is the mean wind velocity far up-stream of the rotor, $v_1(x_3,t)$ and $v_2(x_3,t)$ are the rotational sampled turbulence (Connell 1982) components in x_1- and x_2- directions, respectively. $\dot{u}_1(x_3,t)$ and $\dot{u}_2(x_3,t)$ are the velocity components of the blade in x_1- and x_2- directions, due to elastic deformations of the blade, the tower and the drivetrain. $a(x_3)$ and $a'(x_3)$ are axial and tangential induction factors determined by the modified BEM method (Hansen 2000). The instantaneous flow angle $\phi(x_3,t)$ and the effective wind velocity $V_e(x_3,t)$ defined in Figure 2.5 are given by

$$\phi(x_3,t) = \arctan\left(\frac{V_1(x_3,t)}{V_2(x_3,t)}\right), \quad V_e(x_3,t) = \sqrt{V_1^2(x_3,t)+V_2^2(x_3,t)} \tag{2.22}$$

The instantaneous angle of attack $\alpha(x_3,t)$ is written as

$$\alpha(x_3,t) = \phi(x_3,t) - \beta(t) - \kappa(x_3) \tag{2.23}$$

where $\kappa(x_3)$ is the pre-twist of the blade section. Based on the quasi-static assumption, the lift and drag forces per unit length are given by

$$\left.\begin{aligned} p_L(x_3,t) &= 0.5\rho V_e^2(x_3,t)c(x_3)c_L(\alpha) \\ p_D(x_3,t) &= 0.5\rho V_e^2(x_3,t)c(x_3)c_D(\alpha) \end{aligned}\right\} \tag{2.24}$$

where ρ denotes the mass density of air, $c(x_3)$ is the chord length of the airfoil, $c_L(\alpha)$ and $c_D(\alpha)$ are the static lift and drag coefficients of the airfoil. Correspondingly, the

normal and tangential loads per unit length become

$$\left.\begin{aligned} p_N(x_3,t) &= p_L(x_3,t)\cos\phi + p_D(x_3,t)\sin\phi \\ p_T(x_3,t) &= p_L(x_3,t)\sin\phi - p_D(x_3,t)\cos\phi \end{aligned}\right\} \tag{2.25}$$

Having $p_N(x_3,t)$ and $p_T(x_3,t)$, the external load vector $\mathbf{f}_a\big(\dot{\mathbf{q}}(t),\beta(t),t\big)$ on the right hand side of Eq. (2.16) can be obtained. This 13-dimensional load vector stores the external loads work-conjugated to the defined degrees of freedom. In the present case, the components of $\mathbf{f}_a\big(\dot{\mathbf{q}}(t),\beta(t),t\big)$ are given as

$$\left.\begin{aligned} f_j(t) &= \int_0^{L_B} \Phi_1(x_3) p_{N,j}(x_3,t)dx_3, \quad j=1,2,3 \\ f_{j+3}(t) &= \int_0^{L_B} \Phi_2(x_3) p_{T,j}(x_3,t)dx_3, \quad j=1,2,3 \\ f_7(t) &= \sum_{j=1}^{3}\int_0^{L_B} p_{N,j}(x_3,t)dx_3 \\ f_8(t) &= -\sum_{j=1}^{3}\int_0^{L_B} \cos\Psi_j\, p_{T,j}(x_3,t)dx_3 \\ f_{10}(t) &= \sum_{j=1}^{3}\int_0^{L_B} \big(x_3\cos\Psi_j\, p_{N,j}(x_3,t) - s\sin\Psi_j\, p_{T,j}(x_3,t)\big)dx_3 \\ f_{11}(t) &= \sum_{j=1}^{3}\int_0^{L_B} \big(x_3\sin\Psi_j\, p_{N,j}(x_3,t) + s\cos\Psi_j\, p_{T,j}(x_3,t)\big)dx_3 \\ f_{12}(t) &= (1-\mu)\sum_{j=1}^{3}\int_0^{L_B} x_3\, p_{T,j}(x_3,t)dx_3 \end{aligned}\right\} \tag{2.26}$$

$f_7(t)$ and $f_8(t)$ indicate the force resultants of the loads on the blades in the direction of the global translational degrees of freedom $q_7(t)$ and $q_8(t)$. Similarly, $f_{10}(t)$ and $f_{11}(t)$ signify the moment resultants in the direction of the global rotational degrees of freedom $q_{10}(t)$ and $q_{11}(t)$. $f_{12}(t)$ denotes the effective torque on the drivetrain available for power production. It is reduced by the factor $(1-\mu)$ relative to the aerodynamic torque on the rotor, due to friction in the bearings and the gearbox, as specified by the friction coefficient μ.

Further, $f_{13}(t)$ is the generator torque that can be specified in different forms for damping lateral tower and drivetrain vibrations, as will be shown in Eq. (4.3) in Chapter 4. $f_9(t)$ is related to $f_{12}(t)$ and $f_{13}(t)$ due to the load transfer from the drivetrain to the nacelle, as also will be shown in Chapter 4.

CHAPTER 3
Damping of edgewise vibrations in rotating wind turbine blades

In this chapter, different passive control devices have been proposed for mitigating edgewise vibrations in rotating blades. Normally, damping effects of these dampers are governed by the gravitational acceleration. For rotating wind turbine blades, the corresponding damping effect are governed by the centrifugal acceleration, which can reach to a magnitude of 7-8 g for the outboard portion of a 63-m-long blade. This makes it possible to use these dampers with rather small mass ratios for effectively suppressing edgewise vibrations. Formulations and analysis of the blade-damper systems have been established, where the blade edgewise motion is modeled by SDOF defined in the blade-fixed rotating coordinate system. The dynamics of different dampers are either described in the global fixed coordinate system, or in local moving coordinate systems. The formulated nonlinear models for the blade-damper systems have been used for the parametric optimizations of the dampers, and the optimized dampers are incorporated into the more sophisticated 13-DOF aeroelastic model (Chapter 2) to verify the application of these reduced-order models. Simulation results show promising performance of these passive dampers on mitigating edgewise vibrations.

3.1 Dynamics of blade edgewise vibrations

As mentioned in Chapter 1, in contrast with flap-wise blade vibrations, edgewise blade vibrations in wind turbines are related with insignificant aerodynamic damping. Therefore, it is of great importance to add damping into edgewise mode. In the following sections, different types of blade-mounted dampers have been proposed for damping edgewise vibrations in rotating wind turbine blades.

Edgewise vibrations of a wind turbine blade are coupled to the lateral tower vibrations (Hansen 2007). Therefore, besides the blade edgewise vibration, the motion of the lateral tower motion which will also influence the motion of the dampers mounted inside the blade. Since the focus in this study is on the interaction between the damper and the blade, as well as the damping effect of the damper on edgewise vibrations,

the basic assumption here is that the influence from the tower motions can be ignored. Therefore, the design of the dampers are totally based on the local dynamics of the rotating blade. The validity of this assumption has been evaluated by the more sophisticated 13-DOF wind turbine model (Zhang *et al.* 2014; Zhang *et al.* 2015; Basu *et al.* 2015), and this coupling has been proved to be of minor importance for the optimal design of the passive dampers inside a blade.

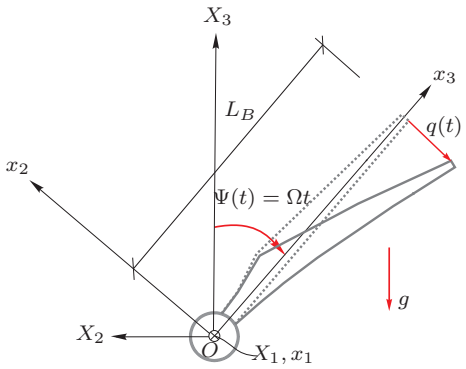

Figure 3.1 Dynamics of the blade edgewise vibration.

As shown in Figure 3.1, in this chapter the blade edgewise vibration is described by the single degree of freedom $q(t)$ in the local rotating coordinate system, without considering the coupling from the lateral tower vibration. The equation of motion of this SDOF model can be simply obtained from the Euler-Lagrange equation (Pars 1965)

$$m_0\,\ddot{q}(t) \,+\, c_0\,\dot{q}(t) \,+\, (k_0 - \Omega^2 m_0)\,q(t) \;=\; f_0(\dot{q},t) \,+\, f_g(t) \tag{3.1}$$

where m_0, c_0 and k_0 are the modal mass, modal damping and modal stiffness, respectively. k_0 includes both the elastic and geometric contributions (centrifugal stiffening due to rotation and centrifugal softening caused by the variation of axial force due to the weight of the blade). $f_0(\dot{q},t)$ denotes the wind induced edgewise modal load on the primary structure, taking the aerodynamic damping into consideration (see Chapter 2). $f_g(t)$ denotes the modal load from gravity, which will result in a harmonic motion in edgewise direction with an angular frequency of 1P (corresponding to the rotational speed of the rotor). The detailed expressions of these parameters are given by Appendix C.

In Eq. (3.1), the negative stiffness term $-\Omega^2 m_0$ is the result of the centripetal softening effect, where the blade deflection in the edgewise direction induces a component of the centrifugal force in the same direction (tending to further increase the blade edgewise deflection) in the rotor plane. The centrifugal softening effect almost cancels the centrifugal stiffening effect, and thus the rotation of the rotor has insignificant effect on the stiffness of the edgewise blade bending mode.

Based on this 1-DOF blade model, different reduced-order models for the blade-damper system have been established for the proposed dampers.

3.2 Roller damper

The idea of the roller damper (named ball vibration absorber) emerged for the first time in Czech proposed for controlling vibration of a suspended prestressed concrete footbridge, although it was not installed because the vibration ceased with the completion of the bridge deck (Pirner 1994). This kind of damper has been adopted successfully on two television towers (Pirner 2002), as shown in Figure 3.2(a). Recently, the roller damper (ball vibration absorber) was investigated for mitigating tower vibrations of offshore wind turbines (Zhang *et al.* 2014), as shown in Figure 3.2(b). Both experimental and numerical results show the efficacy of roller dampers in reducing dynamic responses of wind turbine towers. These successful applications give us motivations for investigating the performance of roller dampers on mitigating edgewise vibrations in rotating wind turbine blades.

(a) (b)

Figure 3.2 Previous investigations of the roller damper. (a) The ball vibration absorber used on two TV towers (Pirner 1994). (b) Shaking table tests on the performance of roller dampers for controlling wind turbine tower vibrations (Zhang *et al.* 2014).

The roller damper consists of a roller rolling along an arc track. The energy input to the primary structure from dynamic loads could thus be absorbed through the rolling motion of the roller. Figure 3.3 shows three possible layouts of the roller, i.e. a homogeneous ball, a homogeneous cylinder and a flywheel. The flywheel is less compact but more efficient than the ball and the cylinder since it has the largest mass moment of inertia.

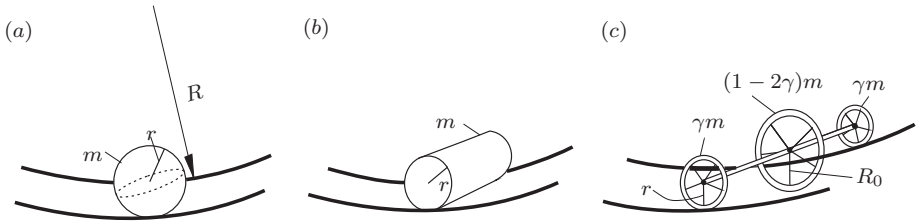

Figure 3.3 Possible layouts of the roller damper, with the same mass m. (a) homogeneous ball, $J = \frac{2}{5}mr^2$, (b) homogeneous cylinder, $J = \frac{1}{2}mr^2$, (c) a flywheel and two small rail wheels, $J = 2\gamma mr^2 + (1-2\gamma)mR_0^2$.

In the case of tower vibrations the damping effect of the roller damper is governed

by the gravitational acceleration g. For the rotating blade, the corresponding damping effect is governed by the centrifugal acceleration, which can reach up to a magnitude of 7-8g for a blade with a length of 63 m. This makes it possible to use the roller damper (or dampers with similar principles described in the following sections) with rather small mass ratios for effectively suppressing edgewise vibrations.

The roller damper is described by four parameters r, R, m and J, representing the radius of the roller, the outer radius of the track, the mass of the roller, and the mass moment of inertia around the gravitational center of the roller, respectively. In order to ease the notation as well as the derivation of the equation of motion, these four parameters can be combined into merely two parameters, namely the equivalent mass m_e and the equivalent length R_e, which may be interpreted as the mass and length of an equivalent mathematical pendulum, as shown in Figure 3.4. Based on the principle that the equivalent mathematical pendulum should represent the same kinetic and potential energy as the roller damper (Appendix B), the expressions of m_e and R_e become

$$m_e = m + \frac{J}{r^2}\frac{R^2}{(R-r)^2}, \quad R_e = R - r \tag{3.2}$$

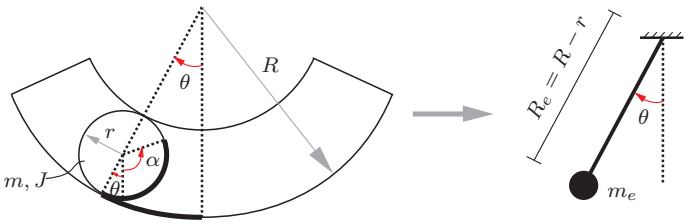

Figure 3.4 Equivalent mathematical pendulum for the roller damper.

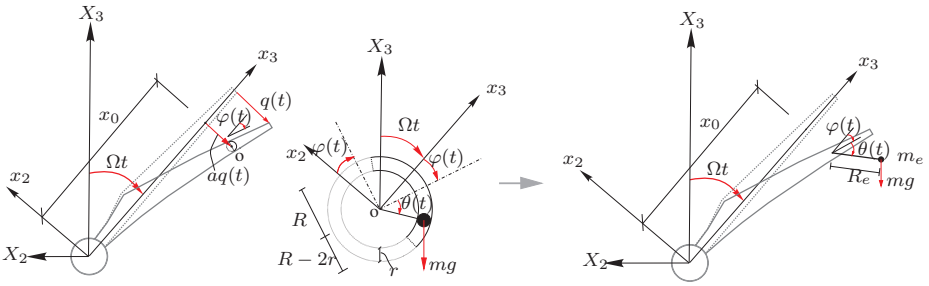

Figure 3.5 Schematic diagram of the reduced 2-DOF model, where the roller damper is presented by the equivalent mathematical pendulum.

Figure 3.5 shows the reduced 2-DOF model for the blade-damper system, where the roller damper has been replaced by the equivalent mathematical pendulum. The position of the damper mass is defined by the local degree of freedom $\theta(t)$, which is

the clockwise rotation from the deformed blade axis. Describing the position vector and velocity vector of the roller in the fixed global (X_2, X_3)- coordinate system (the blade edgewise vibration is described in the local (x_2, x_3)- coordinate system), the kinetic and potential energy of the blade-roller damper system can be formulated (see Appendix B). Employing the Euler-Lagrange equations (Pars 1965), the equations of motion of the 2-DOF system can be obtained, which turn out to be nonlinear ordinary differential equations with parametric-excited terms (Eqs. (21) and (22) in Appendix B).

Ignoring the influence of gravity, the angular eigenfrequency of the roller can be obtained as

$$\omega_d = \sqrt{\frac{m_e \Omega^2 x_0}{m_e R_e}} = \sqrt{\frac{x_0 \Omega^2}{R_e}} \tag{3.3}$$

It is shown from Eq. (J.1) that the motion of the roller is controlled by the centrifugal acceleration $x_0\Omega^2$, which is much larger than g if x_0 is large enough. The roller damper should be devised such that ω_d is approximately equal to the fundamental frequency of the blade. This can be achieved by adjusting R_e when the position of the damper x_0 and the rotational speed of the rotor Ω (the rated rotational speed) are fixed. However even during rated operation conditions the rotational speed of the rotor is varied around the rated value within 5%, which results in the slight change of the eigenfrequency of the damper and thus detuning to the blade frequency (as mentioned in section 3.1, stiffness of the rotating blade in edgewise mode is almost unchanged with different Ω due to both centrifugal stiffening and softening effects). This slight detuning effect can be counteracted by increasing bandwidth of the damper via a damping mechanism (Krenk 2005). The damping mechanism of the roller results from the rolling friction between the contacting surfaces of the roller and the track (see Appendix B). However the damping property is not easy to quantify accurately and difficult to adjust during operation, which is the main disadvantage of the roller damper.

Based on the 2-DOF blade-damper model, parametric optimizations of the tuning ratio and the coefficient of rolling friction have been carried out using 2-dimensional numerical optimization (Appendix B). It is shown that as the mass ratio (mass of the roller to the modal mass of the blade) increases, the optimal tuning ratio decreases and the optimal friction coefficient decreases very slightly. The detuning effect becomes less sensitive with larger mass ratios, and acceptable control effect of the damper can be obtained at a wider range of parameter variations. Further, as the mass ratio increases and as the damper is mounted closer to the blade tip (with larger centrifugal acceleration), the damping effect on edgewise vibrations becomes more pronounced. However, the mass of the damper and its mounting position should be constrained by the available space inside the blade, making the chosen of these two parameters a tradeoff problem.

Figure 3.6 presents the performance of a roller damper with optimized parameters for mitigating edgewise vibrations, when the mean wind speed is 15m/s and the turbulence intensity is 0.1. The mass ratio is 0.03 and the mounting position is x_0=45 m. As

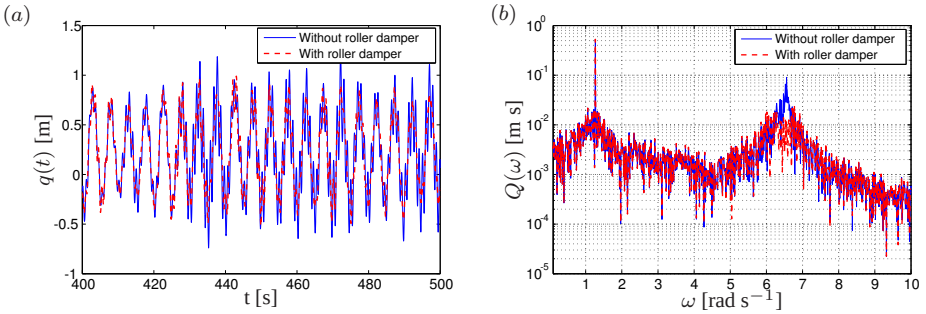

Figure 3.6 Performance of the roller damper for wind turbines under normal operational conditions, $V_0 = 15$ m s^{-1}, I=0.1, $m = 0.03m_0$, $x_0 = 45$ m, optimal tuning ratio and friction coefficient, $R_e = 1.785$m. (a) Time series of the edgewise vibration, (b) Fourier amplitude of the edgewise vibration.

shown in Figure 3.6(a), the modal loads from gravity result in a large harmonic motion in edgewise direction with an angular frequency of 1P. On top of this deterministic harmonic-varying motion, oscillations related to the edgewise eigenvibration are also presented in the time history. The roller damper has no effect on the gravity induced 1P motion (very low frequency) since it's a inertia based vibration absorber, but it effectively adds damping into the edgewise eigenvibration. The blade edgewise motion with the roller damper become almost pure harmonic (with the 1P frequency) since the high frequency oscillation has been significantly mitigated the the roller damper (with a mass of 39 kg). From the Fourier amplitude spectrum (in semi-logarithmic chart) of $q(t)$ in Figure 3.6(b), it is more clearly seen that the roller damper effectively suppress the peak around 6.85 rad/s corresponding to the fundamental edgewise angular frequency. This means that a properly designed roller damper is able to absorb almost all the energy in the fundamental edgewise mode of the blade. However, the 1P frequency peak is not influenced at all by the roller damper.

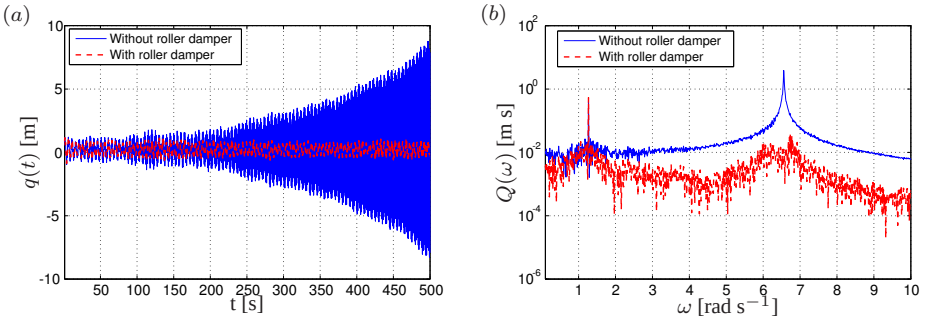

Figure 3.7 Performance of the roller damper for wind turbines under aeroelastic instability (here mimicked by manually set the damping ratio $\zeta_0 = -0.001$), $m = 0.03m_0$, $x_0 = 45$ m, optimal tuning ratio and friction coefficient, $R_e = 1.785$m. (a) Time series of the edgewise vibration, (b) Fourier amplitude of the edgewise vibration.

In contrast to the gravity induced motion, the edgewise vibration (in the fundamental edgewise mode) is stochastic in nature, and is influenced by both the turbu-

lent wind and the operational condition of the turbine. The aerodynamic damping may become negative under certain conditions (Hansen 2007). Figure 3.7 shows the performance of the roller damper (same parameters used as in Figure 3.6) when the aeroelastic instability takes place. In the present numerical example, the modal damping ratio ζ_0 of the blade is manually set to be -0.001 (in principle ζ_0 is always positive) in order to mimic the negative total damping (the structural damping plus the aerodynamic damping) under aeroelastic instability. It is seen that the edgewise response increases exponentially with time when there is no roller damper mounted. The instability is totally eliminated by the attached roller damper, implying that significant damping is introduced by the roller damper into the fundamental edgewise mode to overwhelm the negative aerodynamic damping.

The roller damper has the advantage that its mass moment of inertia can be adjusted (with the same mass) during design process by using different layouts of the roller. However as mentioned earlier, the damping property (friction between the roller and the track) is difficult to quantify and adjust. This makes the roller damper a device with relatively narrow bandwidth, i.e. the detuning effect becomes significant when the rotational speed of the rotor changes (during starting up or closing down of the rotor), since the damping property can not be adjusted accordingly. Therefore, liquid dampers, the damping property of which can be controlled easily, become interesting to be investigated.

3.3 Tuned liquid column damper (TLCD)

Among different liquid dampers, tuned liquid column damper (TLCD) is one of the favored options because it has several advantages, including low cost, easy installation and maintenance, easy adjustment of damper geometry to the target frequency and controllable damping property by the orifice opening. The controllable damping property is important for wind turbine blades since detuning of the damper occasionally takes place when the rotor speed deviates from the rated value, such as in the below-rated region (Burton *et al.* 2001).

TLCD imparts external damping to a structure through the inertial force of an oscillating liquid column in a U-shaped container (Sakai *et al.* 1989). Energy of the liquid column is dissipated when the liquid passes through an orifice opening in the middle of the horizontal tube. This kind of damper has been successfully implemented in Hotel Cosima, Hyatt Hotel and Ichida Building in Osaka (Shimizu and Teramura 1994) and also in One Wall Centre in Vancouver (Colwell and Basu 2008). A number of studies (Balendra *et al.* 1995; Balendra *et al.* 1999; Won *et al.* 1996) have shown that a properly tuned TLCD could significantly reduce structural responses under wind and earthquake excitations. TLCD was developed mainly for the purpose of suppressing horizontal motion of structures (Gao *et al.* 1997), as shown in Figure 3.8(a), but it was also propose for suppressing pitching motion of structures such as bridge deck (Xue *et al.* 2000), as shown in Figure 3.8(b). Investigation has also been carried out for comparing the performance of TLCDs with TMDs, and it was concluded that TLCDs were as effective as TMDs in damping structural vibrations (Xu *et al.* 1992).

Lee et al. (Lee *et al.* 2006) investigated the TLCD in reducing the wave induced vibrations of the floating platform system. Both the analytical and experimental results show promising performance of the TLCD when it is accurately tuned. More recently, Colwell and Basu (Colwell and Basu 2009) carried out a thorough theoretical study on the performance of a TLCD for vibration control of offshore wind turbine towers and observed that a single TLCD could reduce the tower displacement by up to 55%.

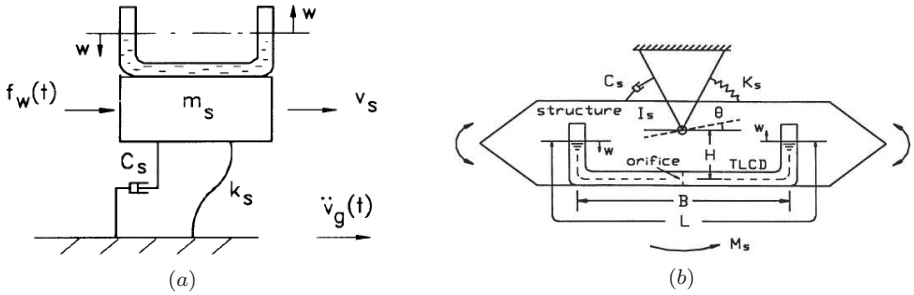

Figure 3.8 Previous investigations of TLCD. (a) TLCD for suppressing horizontal motion of the structure (Gao *et al* 1997). (b) TLCD for suppressing pitching motion of the structure (Xue *et al* 2000).

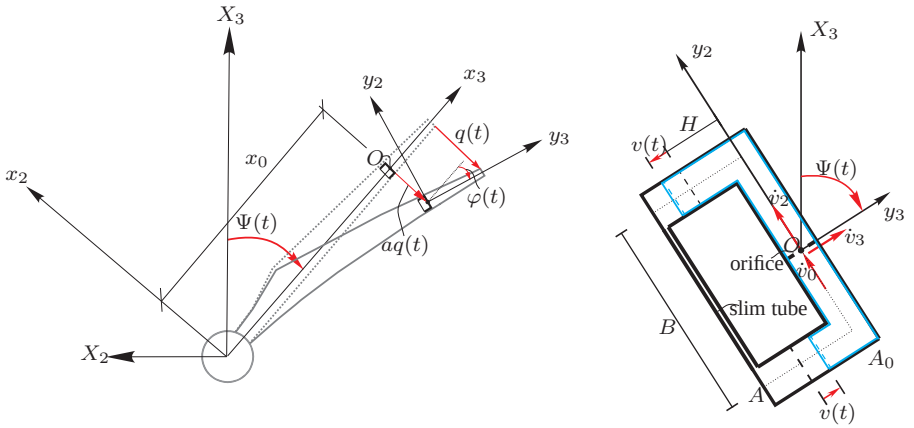

Figure 3.9 A rotating blade equipped with a TLCD, 2-DOF model proposed in the present study.

The successful applications of TLCD in civil engineering structures again motivate us to utilized it in wind turbine blades. Same as the roller damper, damping effect of the blade-mounted TLCD is governed by the large centrifugal acceleration $x_0\Omega^2$. As shown in Figure 3.9, the TLCD mounted inside the blade is composed of a U-shaped tube with an orifice installed at the center O of the horizontal tube. Since the U-shaped container is mounted inside a rotating blade with a changing azimuthal angle, it should be manufactured in a closed form to prevent the liquid from leaking out of the tube. In this case, an extra slim tube connecting two vertical tubes is fixed in order to balance the pressure above the liquid column during oscillation. The

cross-sectional area of the TLCD can be non-uniform, where the vertical and horizontal column cross-sectional areas are denoted as A and A_0, respectively. The density, the horizonal width, the vertical height and the overall length of the liquid inside the TLCD are represented by ρ, H, B and L, respectively, where $L = 2H + B$.

A moving (y_2, y_3)- coordinate system fixed to the damper has been introduced to describe the liquid motion $v(t)$ relative to the U-shaped tube. Describing the liquid motion in (y_2, y_3)- coordinate system and the blade edgewise vibration in (x_2, x_3)- coordinate system, the kinetic and potential energy of the blade-TLCD system can be formulated (see Appendix C). Employing the Euler-Lagrange equation, the equations of motion of the 2-DOF blade-TLCD system can be obtained, which turn out to be nonlinear ordinary differential equations (Eqs. (18) and (19) in Appendix C).

Ignoring the influence of gravity, the circular eigenfrequency of the TLCD can be obtained as

$$\omega_d = \sqrt{\frac{2(x_0 - H)}{2H + \alpha B}}\,\Omega = \sqrt{\frac{2x_0 - L(1-\gamma)}{L + (\alpha - 1)\gamma L}}\,\Omega \tag{3.4}$$

where $\alpha = A/A_0$ is the area ratio. The horizontal length ratio γ is defined as $\gamma = \frac{B}{L}$. It is clearly seen that the motion of the liquid is governed by the centrifugal acceleration $x_0\Omega^2$. For gravity-based TLCDs with uniform cross sections, the circular frequency is given by the well-known expression $\omega_d = \sqrt{2g/L}$. Gao *et al* (1997) further give the expression of circular frequency for the TLCD (gravity-based) with different cross-sectional areas in its vertical and horizontal sections, which is written as $\omega_d = \sqrt{2g/L_{ee}}$, where $L_{ee} = L + (\alpha - 1)B = L + (\alpha - 1)\gamma L$. Eq. (3.4) is analogous to this expression, with the gravitational acceleration replaced by the centrifugal acceleration.

Further, it should be noted that the damping force of liquid motion (due to the orifice) can be expressed as (Sakai *et al.* 1989)

$$F_d = -\frac{1}{2}\xi\,\rho\,A_0|\dot{v}_0|\,\dot{v}_0 \tag{3.5}$$

where v_0 is the displacement of the liquid in the horizontal tube. ξ is the head loss coefficient by the opening ratio of the orifice. The value of ξ can be easily adjusted by changing the orifice opening. Even semi-active control of the TLCD can be carried out by varying the orifice opening in real-time according to certain optimal control laws (Yalla *et al.* 2001). This makes the TLCD a device with relatively large bandwidth, and it is a major advantage of the TLCD comparing with the roller damper.

Based on the 2-DOF nonlinear model for the blade-TLCD system, parametric optimizations of the turning ratio and the head loss coefficient have been performed for various values of mass ratios, the area ratio α and the horizontal length ratio γ, using 2-dimensional numerical searching (Appendix C). Among other findings, it is shown that better control performance of the TLCD can be obtained by increasing γ. This is because the mass of the horizontal part of liquid is the only effective mass of TLCD acting on the structure, and a damper with a higher value of γ has a larger effective mass. However, γ should be limited by the space restriction inside the blade.

Moreover, an increase in α leads to a shortening of the total length of the liquid L as well as the horizontal length B, but to a slightly reduced control efficiency of the TLCD. This characteristic is meaningful for applying TLCD into the wind turbine blades where the available space in the vicinity of the tip is limited.

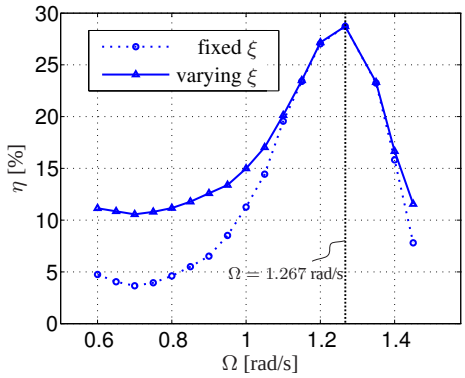

Figure 3.10 Behavior of the TLCD under various rotational speeds of the rotor, $V_0 = 15$ m/s, $I = 0.1$, $x_0 = 55$ m, mass ratio=0.03, $\alpha = 2$, $\gamma = 0.7$.

When the rotational speed of the rotor deviates from the rated value, the damping effect of the damper will be reduced due to detuning. However, by varying the head loss coefficient (orifice opening) in response to the change of the rotational speed, the performance of the TLCD can be enhanced. Figure 3.10 shows the control performance of the TLCD under various rotational speeds of the rotor. As expected, when Ω deviates from the rated value, the control efficiency of the TLCD is drastically reduced because of the frequency detuning. Nevertheless, it is observed that its performance is improved by semi-actively varying the head loss coefficient in response to the rotor speed. As for the passive TLCD with fixed head loss coefficient, the reduction ratio drops to below 10% for $\Omega < 1$ rad/s. On the other hand, the reduction ratio remains above 10% for all Ω between 0.6 and 1.267 rad/s when different optimal values of ξ are used for different Ω.

When the rotor speed is fixed to the rated value, the TLCD with optimal parameters is less effective than the optimized roller damper with a same physical mass m. This is because the effective mass of the roller damper is larger than m, as revealed by Eq. (3.2), while the effective mass of the TLCD (the liquid in the horizontal tube) is always less than m. However, in practice the rotor speed will always be varied within a certain range, and TLCD with controllable orifice opening may perform better than the roller damper in this respect. The controllable damping property of the TLCD makes it promising to be applied in an operating wind turbines.

3.4 Circular liquid column damper (CLCD)

The roller damper has the advantage of larger effective mass and the TLCD has the advantage of controllable damping property. Is it possible to devise a damper that

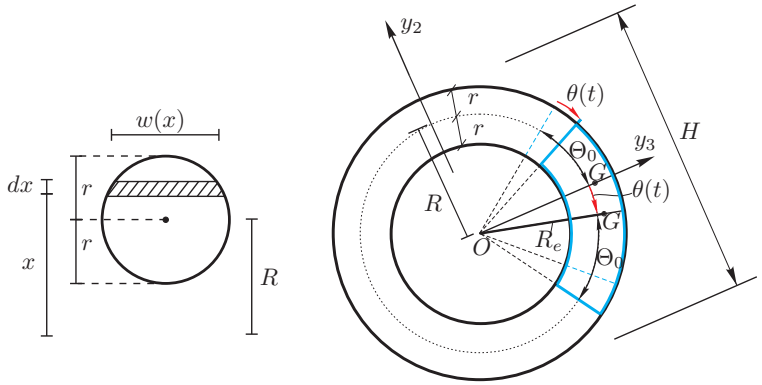

Figure 3.11 Geometries of the circular liquid damper.

includes both characteristics? The answer is yes.

Motivated by the idea of TLCD together with the roller damper, a new type of liquid column damper (LCD) has been proposed here for edgewise vibration control of wind turbine blades. The damper is circular in shape or geometry and hence is termed as the circular liquid column damper (CLCD). Figure 3.11 shows the schematic diagram of the CLCD. It is virtually a circular tube partly filled with certain amount of liquid that could oscillate back and forth inside the tube. The liquid and the circular tube behave as the roller and the track, respectively. On the other hand, orifices can be installed inside the circular tube for providing damping mechanism of the CLCD.

The radius of the circular tube (distance from the center point O to the central axis of the tube) is denoted R, and the radius of the cross-section of the tube is denoted by r. Therefore, the total dimension of the damper can be calculated as $H = 2(R+r)$. The liquid inside the tube is assumed to be connected, filling a segment with central angle $2\Theta_0$ of the complete circle and the center of gravity is denoted by G. A moving (y_2, y_3)-coordinate system fixed to the damper has been introduced. This coordinate system has its origin at the center point O of the circular damper, with y_3-axis placed on the symmetry line of the damper as shown in Figure 3.11. The motion of the liquid is described by the degree of freedom $\theta(t)$, which measures the clockwise rotation of the center of gravity of the liquid from the y_3- axis.

From the dynamics point of view, the working principle of the CLCD is exactly the same as the roller damper. Therefore, the liquid inside the circular tube is again represented by an equivalent mathematical pendulum with the equivalent mass m_e and the equivalent radius R_e. Based on the principle that the equivalent mathematical pendulum should represent the same kinetic and potential energy as the CLCD (Appendix D), the expressions of m_e and R_e become

$$R_e = R\left(1+\frac{1}{4}\alpha^2\right), \quad m_e = m\,\frac{\left(1+\frac{3}{4}\alpha^2\right)}{\left(1+\frac{1}{4}\alpha^2\right)^2} \tag{3.6}$$

where $\alpha = r/R$ is defined as the radius ratio between the cross-section and circular tube. It can be seen from Eq. (3.6) that the effective mass m_e is always larger than

the physical mass m for $0 < \alpha < 1$, making the CLCD a more effect damping device than the TLCD ($m_e < m$) when the rotor is operating in rated rotational speed. On the other hand, the effective mass of CLCD is generally smaller than that of the roller damper (Eq. (3.2)) when same physical mass is used for both dampers.

Having R_e and m_e, the resulting equations of motion of the blade-CLCD system can be obtained following the same procedure as for the roller damper, and are almost same as that for the blade-roller damper system, except for the damping force terms. Same as the TLCD, the damping force acting on the oscillating liquid is due to the energy dissipation when the liquid passes through the orifice inside the CLCD. Therefore, the CLCD possesses the same advantage of TLCD with controllable damping properties, and has larger bandwidth when the rotational speed of the rotor deviates from the rated value. Even semi-active control can be carried out by changing the orifice opening in real-time according to certain optimal control laws. For detailed equations of motion of the blade-CLCD, as well as the results and analysis of the performance of the CLCD, please see Appendix D.

Having both characteristics of the roller damper and the TLCD, CLCD turns out to be a quite promising device for damping edgewise vibrations in rotating wind turbine blades.

3.5 Tuned liquid damper (TLD)

Another kind of liquid damper, namely tuned liquid damper (TLD), has also been widely used in civil engineering structures, and becomes a natural candidate for damping edgewise vibrations in wind turbine blades. The large centrifugal acceleration of the rotating blades again makes it possible to use TLD with rather small mass ratios.

The TLD, which consists of a tank partially filled with fluid, mitigates structural vibrations by utilizing the sloshing fluid. Therefore, it also has the name of tuned sloshing damper (Fujii *et al.* 1990; Kareem 1990). Normally, the fundamental sloshing frequency of the liquid is tuned to the fundamental frequency of the primary structure. When the TLD is excited by the motion of the primary structure, the liquid in the tank begins to slosh, imparting inertial forces onto the structure, out of phase with its motion, thus absorbing and dissipating energy. The main advantages of the TLD are the ease of fabrication and installation, especially where space constraints exist, and minimal maintenance after installation, which make the device even more cost-effective than the TLCD and the CLCD.

The TLD has been shown to effectively suppress the wind-induced vibration of structures (Fujii *et al.* 1990; Tamura *et al.* 1995; Chang and Gu 1999). It is also proposed for seismic control of structures. Both experimental and theoretical studies (Banerji *et al.* 2000; Lee *et al.* 2007; Jin *et al.* 2007) have shown that a TLD does reduce the vibrations of flexible structures subjected to earthquake excitations.

For the roller damper, the TLCD and the CLCD, the local dynamics of the damper can be well accounted for by a single degree of freedom model. Hence, reduced order 2-DOF blade-damper models have been established for the analysis and design of these devices. However for the TLD, the highly nonlinear nature of the sloshing liquid

makes the modeling of TLD much more challenging.

Numerous methods have been proposed to predict the response of sloshing liquid. Equivalent mechanical models based on TMD analogy (Sun *et al.* 1995; Yu *et al.* 1999) simplify the TLD to an equivalent tuned mass damper, with the equivalent mass, stiffness and damping calibrated from the experimental results. This kind of model is able to predict the energy dissipation through liquid sloshing and is useful in the preliminary design of the TLD. However, the nonlinear fluid response cannot be captured by such simple models. Nonlinear shallow water wave theory (Sun and Fujino 1994; Reed *et al.* 1998) has been proposed for predicting the response of fluid sloshing in rectangular tanks. Although the nonlinear shallow-water wave equations can be solved numerically, it is computational inefficient and does not provide an effective design tool for engineering application. Modal expansion techniques (Faltinsen *et al.* 2000; Faltinsen and Timokha 2001; Love and Tait 2010) have been used to model the sloshing problem, where the fluid flow is assumed to be inviscid, irrotational, incompressible and without rigid-body rotations. The velocity potential and the free surface are expressed as a summation of sloshing modes, and a system of coupled ordinary differential equations are developed by applying calculus of variations (Faltinsen et al., 2000; Faltinsen and Timokha, 2001).

Similar as in the work of Faltinsen et al. (Faltinsen *et al.* 2000) and Faltinsen and Timokha (Faltinsen and Timokha 2001), modal expansion technique has been used in this paper for the sloshing problem. However, the main obstacle in modeling the TLD in rotating blades is that strong non-inertial forces appear in the Euler equations in terms of the angular acceleration, the Coriolis acceleration and the centripetal acceleration. These effects render the use of potential flow theory invalid even for inviscid and irrotational fluid flow. Therefore, modal expansion is carried out directly on the velocity field of the fluid rather than the velocity potential. The basic idea for the modeling of TLD is as follows.

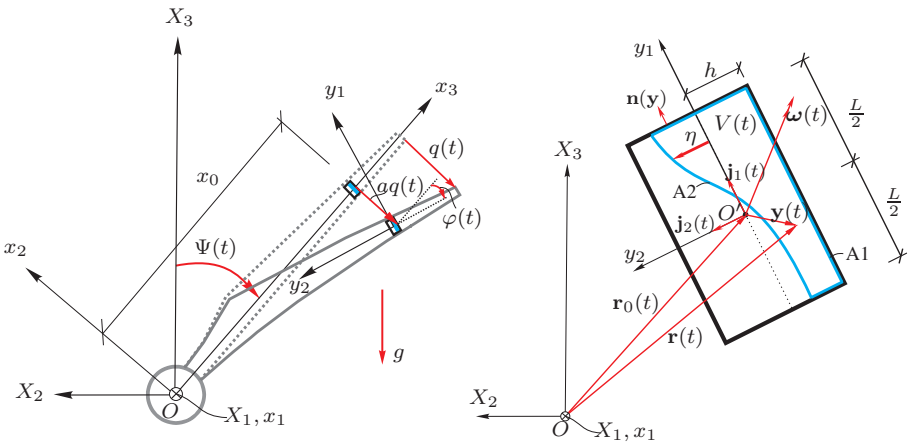

Figure 3.12 Schematic diagram of the blade-TLD model.

As shown in Figure 3.12, the motion of the fluid relative to the tank is described

in (y_1, y_2, y_3)-coordinate system fixed to the damper with its origin O' placed at the center of the mean water level (MWL). The free surface is defined by a single variable of the surface elevation $\eta(y_1, y_3, t)$ measured from the mean water level. By reformulating the Lagrangian description of the particle motion into Eulerian description (Malvern 1969), the boundary value problem (Euler equation with nonlinear boundary conditions) is established in (y_1, y_2, y_3)-coordinate system (see Appendix E). Since inviscid flow has been assumed , no dissipation terms exist in the Euler equation. The indicated dissipation mechanism will be modeled by introducing an equivalent linear damping term in the Euler equation. This linear damping term accommodate the overall energy dissipation arising from both the fluid viscosity and the flow restricting devices such as damping screens and baffles (Appendix E). The validity of the modeling of this equivalent damping has been verified by the real-time hybrid testing (RTHT) described in the next chapter.

A weak form of the boundary value problem can be obtained by the Galerkin variational method, where the modal expansions of the velocity field $\mathbf{v}(\mathbf{y}, t)$ and its virtual variation $\delta\mathbf{v}(\mathbf{y})$ are expressed as:

$$\left.\begin{aligned} \mathbf{v}(\mathbf{y}, t) &= \sum_{i=1}^{N} r_i(t)\, \mathbf{V}_i(\mathbf{y}) \quad , \quad \mathbf{y} \in V(t) \\ \delta\mathbf{v}(\mathbf{y}) &= \sum_{i=1}^{N} \delta r_i\, \mathbf{V}_i(\mathbf{y}) \quad , \quad \mathbf{y} \in V(t) \end{aligned}\right\} \tag{3.7}$$

where $\mathbf{v}(\mathbf{y}, t)$ is the velocity vectors of the fluids particle as seen by an observer fixed to the (y_1, y_2, y_3)-coordinate system. $V(t)$ is the time-varying fluid domain. $r_i(t)$ and δr_i denote the generalized coordinates of the velocity field and the variational field. The shape functions $\mathbf{V}_i(\mathbf{y})$ are not required to fulfill any mechanical boundary conditions on the free surface. However, they need to have zero divergence and to fulfill vanishing kinematical boundary conditions on the side walls.

Being placed close to the blade tip with small blade thickness, the width B of the TLD will be small compared to h and L. Due to this geometric constrain, the flow is predominantly 2-dimensional, taking place in the (y_1, y_2)- plane. Hence it is assumed that $v_3(\mathbf{y}, t) \equiv 0$ in the present study. The eigenmodes of standing waves in linear wave theory have been used as shape functions:

$$\mathbf{V}_i(\mathbf{y}) = \begin{bmatrix} -\sin\left(k_i(y_1 + \frac{L}{2})\right)\cosh\left(k_i(y_2 + h)\right) \\ \cos\left(k_i(y_1 + \frac{L}{2})\right)\sinh\left(k_i(y_2 + h)\right) \\ 0 \end{bmatrix}, (y_1, y_2) = \left[-\frac{L}{2}, \frac{L}{2}\right] \times \left[-h, \eta(y_1, t)\right] \tag{3.8}$$

where h is the mean water depth and $k_i = i\,\frac{\pi}{L}$ is the wave number. The angular eigenfrequencies ω_i of the standing waves are approximately determined from the dispersion relation

$$\omega_i^2 \simeq x_0 \Omega^2\, k_i\, \tanh(k_i h) \tag{3.9}$$

which is identical to the corresponding dispersion relation for gravity waves (Svendsen *et al.* 1976), except that the gravitational acceleration g has been replaced by the centrifugal acceleration $x_0\Omega^2$.

Next, the boundary condition on the free surface is discretized in a similar manner. Modal expansions of the surface elevation $\eta(y_1,t)$ and its virtual variation $\delta\eta(y_1)$ are formulated:

$$\left.\begin{aligned}\eta(y_1,t) &= \sum_{i=1}^{N} s_i(t)\,\cos\left(k_i\left(y_1+\frac{L}{2}\right)\right)\\ \delta\eta(y_1) &= \sum_{i=1}^{N} \delta s_i\,\cos\left(k_i\left(y_1+\frac{L}{2}\right)\right)\end{aligned}\right\} \tag{3.10}$$

where $s_i(t)$ and δs_i denote the generalized coordinates of $\eta(y_1,t)$ and $\delta\eta(y_1)$. The selected shape functions in Eq. (3.10) is motivated by the linear wave theory, where the free surface condition reduces to $v_2(y_1,0,t)=\frac{\partial}{\partial t}\eta(y_1,t)$. Hence, the distribution with y_1 for each shape function in Eq. (3.10) should be pairwise proportional to its counterpart in Eq. (3.8).

Finally, coupled nonlinear differential equations for $r_i(t)$ and $s_i(t)$ can be obtained by substituting Eqs. (3.7), (3.8) and (3.10) into the weak formulation of the boundary value problem (Appendix E). As mentioned earlier, a linear damping term $\mu\mathbf{v}(\mathbf{y},t)$ has been incorporated into the Euler equation, accounting for the overall energy dissipation from both the viscous effect and the damping screens. Upon inserting the modal expansions into the weak formulation, this linear damping term turns out to be $\sum_{j=1}^{\infty}\frac{\mu}{\rho}m_{ij}(t)r_j(t)$, where $m_{ij}(t)$ is the modal mass terms given in Eq. (19) in Appendix E. Upon reformulation, this term can be further written as $\sum_{j=1}^{\infty}\xi\omega_1 m_{ij}(t)r_j(t)$, where the non-dimensional damping parameter ξ is introduced as $\xi=\mu/(\rho\omega_1)$, and ω_1 is the first sloshing eigenfrequency. Equivalent with μ, ξ also accounts for the overall energy dissipation and will be used as the only damping parameter in our theoretical model. In next chapter, this assumed linear damping model will be verified through real-time hybrid testing, and the value of ξ will also be calibrated under different cases. Obviously, including damping screens results in larger dissipation in the flow and thus larger values of ξ.

As shown in Figure 3.13, $\mathbf{f}_c(t)$ with the non-vanishing moving frame components $f_{c,1}(t)$ and $f_{c,2}(t)$, denotes the external reaction force vector on the liquid due to the pressure $p(\mathbf{y},t)$ from inner side of the tank. This force vector, when transferred to the primary structure, represents the passive control force for edgewise vibrations. The analytical expression of $\mathbf{f}_c(t)$ can be obtained by integrating the pressure $p(\mathbf{y},t)$ over inner surfaces of the tank, in combination with the divergence theorem (Zhang *et al.* 2015), which turns out to be dependent on the state variables $s_i(t)$ through the time-varying fluid domain $V(t)$. This force vector is then incorporated into the equation of motion of blade edgewise vibrations, i.e. Eq. (3.1).

In contrary to the other three types of dampers that are described by 1-DOF models, the motion of the liquid in the TLD is described by a $2N$-DOF model, as shown in the modal expansions in Eqs. (3.7) and (3.10). Truncations at the order N=1 and

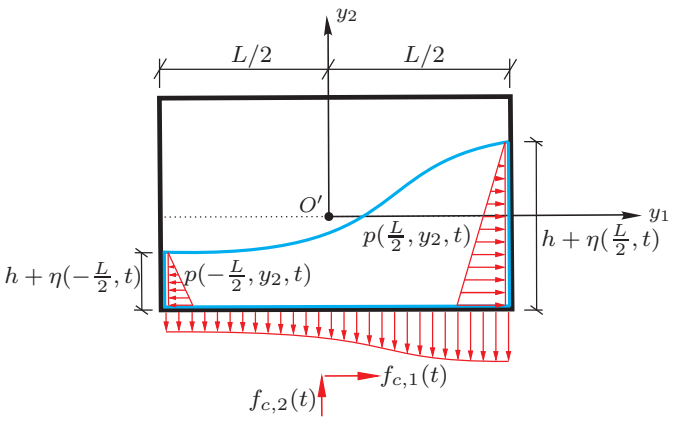

Figure 3.13 Pressure distribution on inner surfaces of the TLD tank.

N=3 have been considered in the present study, representing one and three sloshing modes, respectively. Figure 3.14(a) shows the simulation results of time histories of the sloshing force in y_1- direction. In general, the result from the one-mode model agrees well with that from the three-mode model. At certain instants of time such as t=319.7 s, relatively large discrepancies can be observed between the two models. This is due to the higher frequency contributions from the second and third sloshing modes in the three-mode model, which can not be captured by the single-mode model. Figure 3.14(b) shows the corresponding edgewise tip displacement of the blade when a TLD is mounted inside. The structural responses from the one-mode and three-mode models are in excellent agreement with each other. Essentially, the primary structure behaves like a filter, which filters out high frequency disturbances in the sloshing force, leading to almost identical results in Figure 3.14(b). Hence, the one-mode model is sufficient to accurately predict the TLD-damped structural response, and can be utilized for optimal design of the TLD.

Figure 3.15 illustrates the fluid surface elevation at various instants of time for the one-mode and three-mode models. The general behaviors of the sloshing liquid are similarly predicted by both models since the first sloshing mode contributes most to the liquid motion. On the other hand, it is also obviously seen that the second and third sloshing modes have larger effect on the fluid surface elevation than on the sloshing force and the structural response. The one-mode model only represents the first sloshing mode (cosine function), resulting in zero surface elevation at the middle of the tank at all time, which is surely unrealistic. Therefore, for accurately predicting the surface elevation, modal expansions to three or more sloshing modes need to be carried out. Furthermore, it can be seen by comparing Figure 3.14(a) and Figure 3.15 that there is a strong correlation between the sloshing force and the surface elevation, i.e., the sloshing force agrees well with each other when $\eta(t)$ is in good agreement (such as t=306 s, 315.4 s).

To sum up, the TLD is proposed as a competitive candidate for damping edgewise blade vibrations in this project. The main contribution here is to establish a

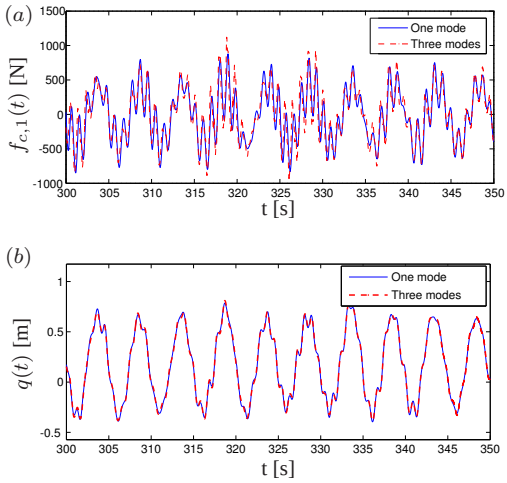

Figure 3.14 Comparison of the control performance from the one-mode and three-mode models, $V_0 = 15$ m s^{-1}, $I = 0.1$, $x_0 = 55$ m, mass ratio $= 0.03$, $L = 2.5$ m, $h = 0.3468$ m. (a) Control force (sloshing force) in y_1- direction, (b) Blade edgewise tip displacement with TLD.

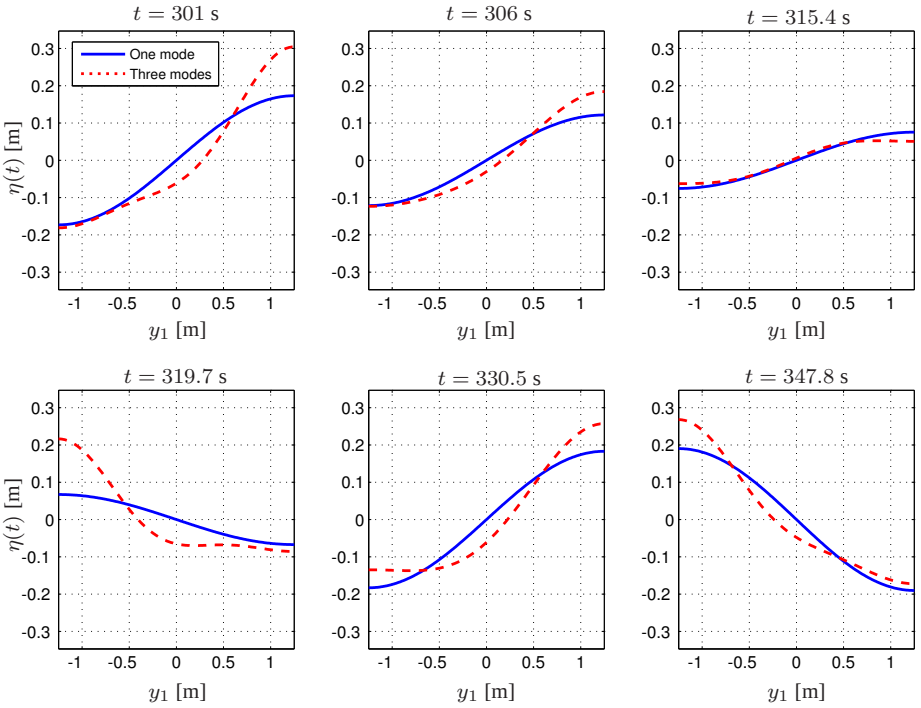

Figure 3.15 Surface elevation at various instants of time, $V_0 = 15$ m s^{-1}, $I = 0.1$, $x_0 = 55$ m, mass ratio $= 0.03$, $L = 2.5$ m, $h = 0.3468$ m.

useful engineering model for modeling the blade-TLD system using modal expansion technique, where the total energy dissipation during fluid sloshing has been accounted for by incorporating linear viscous damping terms. Different levels of accuracy can be achieved by using different numbers of sloshing modes in the modal expansion. In the simplest case, one-sloshing-mode model can be used for predicting the controlled structural response, while it fails to predict the sloshing response of the liquid and higher modes need to be included. In next chapter, the validity of this theoretical model will be further verified by RTHT using a full-scale TLD.

Besides its advantage of cost-effectiveness, TLD also has the potential of being a semi-active device with rotatable baffles installed inside the tank (Zahrai *et al.* 2012), as shown in Figure 3.16. The main idea behind installing such baffles is to compensate the effects of probable mistuning of the TLD, since the eigenfrequency of the TLD can be adjusted with different angles of the baffle. This characteristic of controllable eigenfrequency makes the TLD a even more promising device for rotating wind turbine blades than the TLCD and CLCD (with only controllable damping properties). Further experimental investigations (RTHT) are planned to be carried out in this respect in the future.

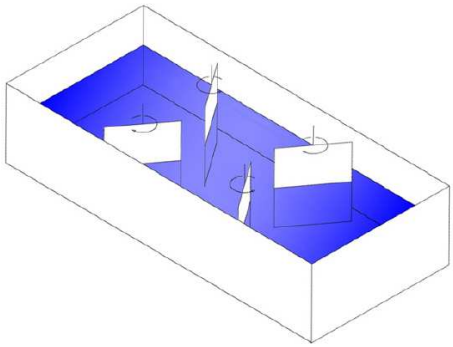

Figure 3.16 TLD with some standing rotatable baffles (Zahrai *et al* 2012).

CHAPTER 4
Mitigation of lateral tower vibrations in wind turbines

This chapter deals with both active and passive control of lateral tower vibrations. By means of modern power electronics, the generator torque can be prescribed to a certain value with a time delay below 10^{-2} s and affects the lateral tower vibration through the reaction on the generator stator. Using this property, feedback control of lateral tower vibrations can be performed. The load transfer mechanisms from the drivetrain and the generator to the nacelle are derived, and the interaction between the generator torque and the lateral tower vibration are presented in a generalized manner. Next, as an alternative to the active generator controller, passive control of lateral tower vibrations using TLDs have also been investigated, since it is a more cost-effective and robust method. The nonlinear model established for the blade-TLD system in the preceding chapter has been modified to deal with the tower-TLD system. Furthermore, to verify the proposed theoretical model as well as the assumed linear damping term in the model, and to evaluate the actual behavior of TLDs in damping lateral tower vibrations, a series of real-time hybrid tests (RTHT) have been performed on a full-scale TLD (physical substructure), with the 13-DOF model formulated in Matlab/Simulink (numerical substructure).

4.1 Active generator control of tower vibrations

Similar to the blade edgewise vibration, lateral tower vibrations are also very lightly damped due to low aerodynamic damping present in this mode. There is also a possibility of aeroelastic instability in lateral tower mode for some combinations of aerodynamic properties and operational conditions, especially for the parked turbine with nacelle yaw errors (Bir and Jonkman 2007). Moreover, for offshore wind turbines placed at shallow water, the wave load may act in a different direction of the mean wind direction due to refraction, and significant lateral tower vibrations may be initiated by the wave load in combination with the resultant aerodynamic loads from the three blades in the lateral tower direction.

The idea of providing active damping to lateral tower vibration using generator torque was first proposed by Van der Hooft *et al.* (Van der Hooft *et al.* 2003) and

was further investigated by de Corcuera *et al*. (De Corcuera *et al.* 2012) and Fleming *et al*. (Fleming *et al.* 2011). Essentially, the generator torque affects the lateral tower vibration through the reaction on the generator stator, which is rigidly fixed to the nacelle. By means of modern power electronics, the generator torque can be prescribed to a certain value with a delay below 10^{-2} s (Blaabjerg *et al.* 2004). By using this property, feedback control of the lateral tower vibrations can be performed. Van der Hooft *et al*. (Van der Hooft *et al.* 2003) simplified the tower by a single-degree-of-freedom (SDOF) representing the lateral translational motion, and the tower top rotation was neglected. Since the generator torque is affecting the lateral tower motion via the tower top rotation, this SDOF tower model does not adequately account for the transfer of the generator torque. De Corcuera *et al*. (De Corcuera *et al.* 2012) demonstrated a strategy to design a multi-variable controller based on the H_∞ norm reduction for reducing both the drivetrain torsional vibration and the tower side-to-side vibration, with simulations carried out in the GH Bladed software. This study focuses on the controller design procedure. However, the torque transfer mechanism from the generator to the tower vibration and the effect of the generator torque on other components of the wind turbine are not demonstrated. Fleming *et al*. (Van der Hooft *et al*. 2003) presented the field-testing results of the effect of active generator control on the drivetrain and lateral tower vibrations in a 600-kW wind turbine. A multi-SISO (single-input-single-output) controller is compared with the H_∞ controller, and a similar effect for damping the lateral tower vibration was obtained.

Actually, the edgewise vibrations of the blades are coupled to the lateral tower vibration, as well as to the torsional drivetrain vibration through the collective mode. Since very low, even negative, aerodynamic damping takes place in edgewise vibration, it is important to investigate the effect of the active generator torque on this mode of vibration. Moreover, as the basis of implementing active generator control, the load transfer mechanisms from the drivetrain and the generator to the nacelle, as well as the interaction between the generator torque with the lateral tower vibration are not clearly demonstrated in the above-mentioned studies. The mechanisms need to be revealed clearly. Further, all the previous studies focus on the gear-driven wind turbines. With offshore wind turbines becoming larger and being moved out further at sea, there is huge application potential of direct-driven systems, where the turbine rotor is coupled directly to the electrical generator without the gearbox. For the direct-driven wind turbines, the electric torque in the generator is much larger comparing with the gear-driven wind turbines, making it possible to damp the lateral tower vibration more effectively. Therefore, cases of both the gear-driven and direct-driven offshore wind turbines have been considered in the present study.

The 13-DOF model described in Chapter 2 is used for deriving the load transfer mechanisms from the generator to the nacelle. All notations given in Chapter 2 are kept the same here. As shown in Figure 4.1, using D'Alembert's principle, the load work-conjugated to $q_9(t)$ becomes (Appendix F)

$$f_9(t) = \begin{cases} f_{9,w}(t) - \mu f_{12}(t) + f_{13}(t) - k_0\left(1+\frac{1}{N}\right)\left(q_{12}(t) - \frac{1}{N}q_{13}(t)\right) & \text{(odd)} \\ f_{9,w}(t) - \mu f_{12}(t) - f_{13}(t) - k_0\left(1-\frac{1}{N}\right)\left(q_{12}(t) - \frac{1}{N}q_{13}(t)\right) & \text{(even)} \end{cases} \tag{4.1}$$

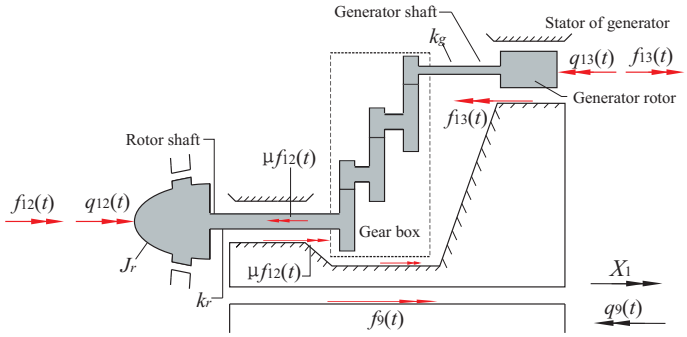

Figure 4.1 Schematic diagram of the torque transfer mechanism between the drivetrain and the tower.

where the first equation corresponds to the case with odd number of grea stages and the second equation for even number of gear stages. The acceleration terms $\ddot{q}_{12}(t)$ and $\ddot{q}_{13}(t)$ have been eliminated by means of the equations of motion of the drivetrain (Chapter 2). μ denotes the friction coefficient due to friction in the bearings and the gear box, N is the gear ratio. $f_{9,w}(t)$ is the load conjugated to $q_9(t)$ induced by waves propagating in the X_2 direction (Appendix F).

Especially for direct-driven wind turbines, where $N = 1$, we get from the second equation in Eq. (4.1) that

$$f_9(t) = f_{9,w}(t) - \mu f_{12}(t) - f_{13}(t) \tag{4.2}$$

Hence, based on the relationship (transfer mechanism) between $f_9(t)$ and $f_{13}(t)$ in Eqs. (4.1) and (4.2), the lateral tower vibrations can be controlled by specifying the format of the generator torque $f_{13}(t)$. Modern power electronics makes it possible to specify the generator torque within certain limits almost instantly. The generator torque can thus be used as an actuator in the active control of lateral tower vibrations. In the present study, the generator controller with feedback from lateral tower vibrations is proposed as:

$$f_{13}(t) = f_{13,0} + \Delta f_{13,0}(t) = f_{13,0} + c_0 \dot{q}_{13}(t) + c_a \dot{q}_8(t) \tag{4.3}$$

where $f_{13,0}$ is the constant nominal torque and $\Delta f_{13,0}(t)$ is the torque increment which can be used as actuator and specified in various ways. $c_0 \dot{q}_{13}(t)$ is the torsional damping term for the drivetrain with feedback from measured generator speed (Licari *et al.* 2013), which is very commonly included in the generator torque. For mitigating lateral tower vibrations, a damping term $c_a \dot{q}_8(t)$ (derivative controller) is included with feedback from $\dot{q}_8(t)$ to add damping into the lateral tower mode, and c_a is the gain factor. Generally speaking, the tower controller can be augmented with a torque component proportional to either the displacement $q_8(t)$ (proportional control) or the acceleration $\ddot{q}_8(t)$ (acceleration control), so that the eigenfrequency of the tower can be changed to a certain extent. This has not been further pursued in the present study, since the derivative controller alone is very effective in mitigating lateral tower vibrations as shown below.

In practical applications, the feedback signal $\dot{q}_8(t)$ is obtained by integrating the measured tower top acceleration from accelerometers placed in the nacelle. From a vibration point of view, it is favorable to have larger c_a and introducing higher damping into the lateral tower mode. However from a power electronic point of view, it is favorable that c_a is as small as possible in order to have a small power output. Consequently there is tradeoff between these two objects. The gain factor c_a is chosen such that the performance criterion considering both the structural vibration and the power smoothness is minimized (Appendix F).

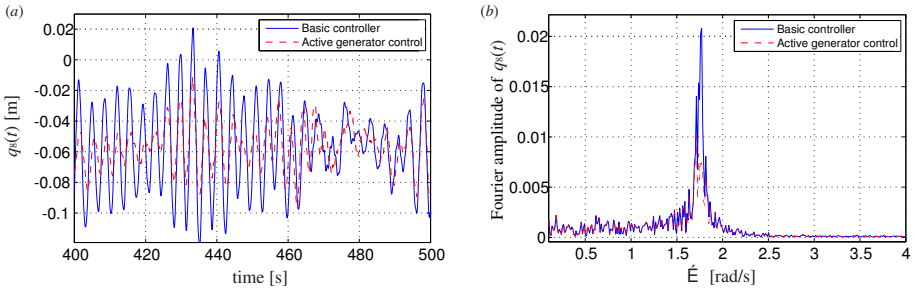

Figure 4.2 Lateral tower vibration with and without active generator control, gear-driven wind turbine. (**a**) Time history in 400–500 s. (**b**) Fourier amplitude of lateral tower vibration.

Figure 4.2 shows the lateral tower top displacements $q_8(t)$ in both the time and frequency domain. There is a reduction of 17.8% in the maximum responses and a reduction of 37.6% in the standard deviations. The FFT of the response $q_8(t)$ is presented in Figure 4.2(b). For a system without active generator control, a clear peak corresponding to the tower eigenfrequency (around 1.76 rad/s) is observed without other visible peaks, owing to the fact that very low aerodynamic damping takes place in this mode. This peak is reduced to approximately $\frac{1}{3}$ by the active generator torque due to the introduced damping to the lateral tower mode.

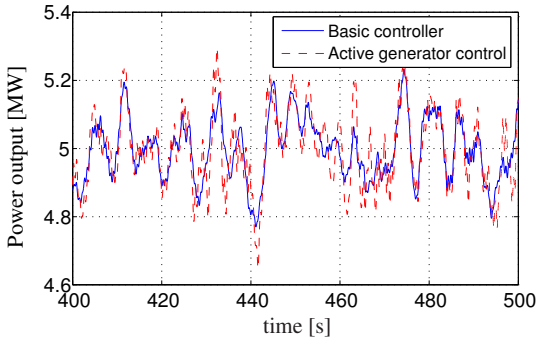

Figure 4.3 Influence of the active generator torque on the power output, gear-driven wind turbine.

With the extra torque component $c_a\dot{q}_8(t)$ for tower vibration control, fluctuating of the power output is introduced on top of the nominal torque. As shown in Figure

4.3, due to this torque increment, the generated power becomes more fluctuated with an increase of 1.3% in the maximum value and an increase of 33.0% in the standard deviation. Since the stiffness and mass of the tower for the offshore wind turbine is very large, it is inevitable that effective control of the tower vibration is at the expense of a little more fluctuated power output, which is unfavorable for the grid side. One possible solution to accommodate this problem is to increase the energy storage in the power converter by increasing the size of the capacitor.

Further, it is also favorable to observe from simulation (Appendix F) that the edgewise vibration is slightly suppressed by the active generator controller due to the coupling of edgewise vibration to the lateral tower vibration. The maximum response and the standard deviation are reduced by 5.5% and 5.0%, respectively (Appendix F).

For direct-driven wind turbines, the nominal generator torque is increased by N times comparing with the gear-driven wind turbine, while the nominal rotational speed of the generator is reduced by N times. Figure 4.4 shows the remarkable capability of the active generator controller in suppressing lateral tower vibrations for the direct-driven wind turbine. The maximum response of $q_8(t)$ is reduced by 26.6%, and the standard deviation is reduced by 54.0%. The Fourier spectrum of the lateral tower top displacement (Figure 4.4(b)) shows that the peak around 1.76 rad/s, corresponding to the tower eigenfrequency, is almost totally eliminated by the active generator controller, comparing with that of the uncontrolled case. The reason for the superior performance is that the nominal generator torque $f_{13,0}$ is much larger in the direct-driven wind turbine, and thus, the additive torque are also increased accordingly.

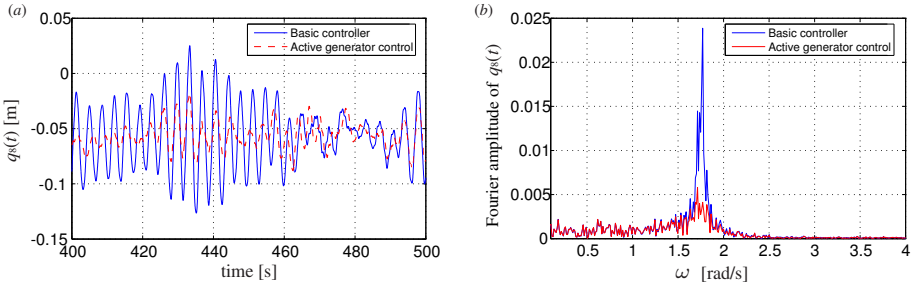

Figure 4.4 Lateral tower vibration with and without active generator control, direct-driven wind turbine. (**a**) Time history in 400–500 s. (**b**) Fourier amplitude of lateral tower vibration.

Figure 4.5 shows the time-history of the power output from the generator of the direct-driven wind turbine. A little negative effect on the smoothness of the power output is observed after the implementation of the active generator control. The maximum value of the power output is increased from 5.41 MW to 5.48 MW (increased by 1.3%), and the standard deviation is increased from 0.108 MW to 0.125 MW (increased by 15.7%), which means less impact on the grid side than that of the gear-driven case. For direct-driven wind turbines, the value of $f_{13,0}$ is significantly increased, and the relative magnitude between $c_a\dot{q}_8(t)$ and $f_{13,0}$ is smaller comparing with that of the gear-driven turbine; thus, the smoothness of the power output is less affected by the active control.

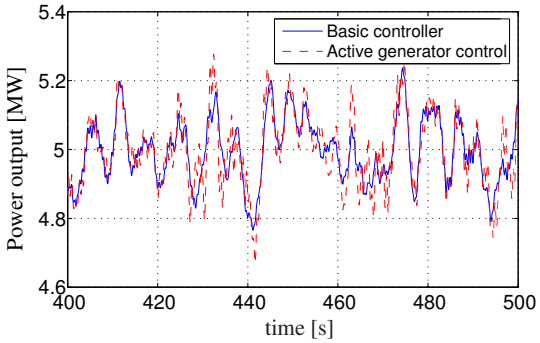

Figure 4.5 Influence of the active generator torque on the power output, direct-driven wind turbine.

To sum up, the effective control of lateral tower vibration is at the expense of somewhat more fluctuated power output, and a tradeoff between the vibration aspect and the power electronic aspect should be considered by properly choosing the controller gain. The active generator controller shows superior performance for the direct-driven wind turbine, since a better vibration control efficacy can be obtained with less impact on the smoothness of the power output. Further, it is also favorable to observe that the active controller has slightly positive influence (although negligible) on the lightly damped edgewise vibration.

Since this method introduces negative impact on the smoothness of the power output (even for the direct-driven wind turbine), it is suggested that the controller should only be switched on when significant lateral tower vibrations take place, e.g. due to wave excitation or sudden shift of wind directions. Further efforts should be paid on exploring alternative methods for mitigating lateral tower vibrations without influencing the power output. Once again, structural control technique turns out to be a promising solution.

4.2 Damping of lateral tower vibrations using TLD

Unlike for the case of rotating blade, the widely used structural control techniques can be easily applied to wind turbine towers, with the modeling and analysis methodologies almost unchanged.

As introduced in Chapter 1, pendulum damper, TMD, TLCD and BVA etc. have been proposed for structural control of wind turbine towers. All these dampers can be used to effectively mitigate lateral tower vibrations. However, the pendulum-oil damper and the TMD suffer from the problem of constrained strokes and the BVA has the disadvantage that the damping property is difficult to quantify and adjust. Being a very cost-effective device, the TLD again draws our attention since it is free of the stroke problem and its damping property can be easily adjusted by attaching damping screens with various mesh sizes. Consequently, the TLD becomes a natural candidate for mitigating lateral tower vibrations in wind turbines.

Different theoretical methods (with different accuracy and complexity) have been proposed for predicting the performance of TLD on the buildings or towers, as described in Chapter 3. In principal, all these methods can be applied directly to wind turbine towers. However to make the thesis consistent, the modal based approach proposed in Chapter 3 for the blade-TLD system will be employed for the tower as well. Slight modifications are needed since the rotation of the local coordinate system is now only due to the rotational deformation of the top of the tower.

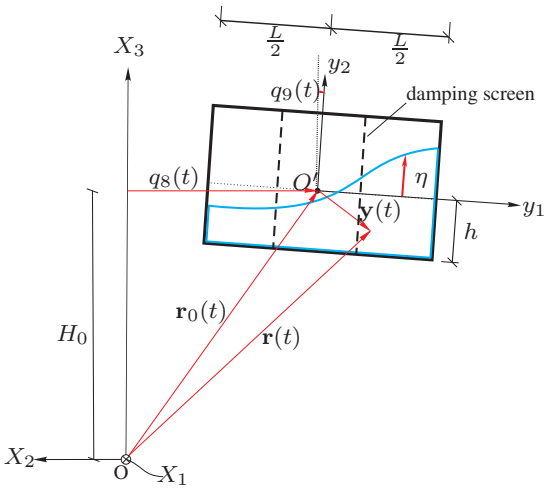

Figure 4.6 Modeling of the tower mounted TLD.

As shown in Figure 4.6, the TLD is assumed to be mounted at the top of the wind turbine tower (with the height of H_0), where the elastic displacement and elastic rotation at this position are $q_8(t)$ and $q_9(t)$, respectively. Since $\dot{q}_9(t)$ is very small, the motion of the liquid is governed by the gravitational acceleration g. The modeling procedure follows almost the same as for the blade-TLD system, except that the azimuthal angle Ωt of the local (y_1, y_2)- coordinate system is eliminated. The nonlinear differential equations Eqs. (25), (31) and (36) in Appendix E can be easily modified to obtain the differential equations for the tower-TLD system.

It is always important to verify a theoretical model through experimental study, especially when high nonlinearity is involved such as for the sloshing problem here. Furthermore, as mentioned in Chapter 3, a linear damping term with a single damping parameter is incorporated into the Euler equation, to account for the total energy dissipation arising from both the fluid viscosity and the damping screens. This assumed damping model also needs to be verified. All these motivate us to carry out experimental studies on the TLD, with the purposes of getting a more clear understanding of the real behavior of the sloshing liquid, verifying the proposed theoretical model as well as the assumed linear damping model, and providing guidelines for the practical applications of the TLD.

4.3 Real-time hybrid testing of a full-scale TLD

It is not feasible to carry out a full-scale experiment of the wind turbine-TLD system in the lab. A scaled down model of the system tested in lab conditions will essentially suffer from the scale effect, particularly with respect to the liquid behavior in the damper (e.g., due to viscous effects), and it may be a challenge to keep appropriate proportion with dynamic similarities for the wind turbine structure and the TLD.

To circumvent these problems, a state-of-the-art testing method, the real-time hybrid testing (RTHT) (Nakashima *et al.* 1992; Nakashima and Masaoka 1999; Horiuchi *et al.* 1999), has been conducted for this system where the liquid damper is tested physically and the wind turbine is simulated. The fundamental idea of the RTHT is to split the entire system into two parts: a numerical substructure and a physical substructure. The former will be simulated in the computer by a developed numerical model. The latter, which generally has a complicated dynamic behavior (nonlinear or load rate-dependent), is manufactured and tested using dynamic testing equipment (shaking table or dynamic actuators) (Lee *et al.* 2007; Mercan and Ricles 2009). This method has several advantages, such as the possibility of manufacturing full scale physical substructure, the reduced cost of the experiment and safe evaluation of structures at extreme states. The RTHT has been widely adopted for the performance evaluation of energy dissipating and vibration absorbing devices, such as elastomeric dampers (Mercan and Ricles 2009), MR dampers (Christenson *et al.* 2008), TLDs (Lee *et al.* 2007) and TMDs (Igarashi *et al.* 2000).

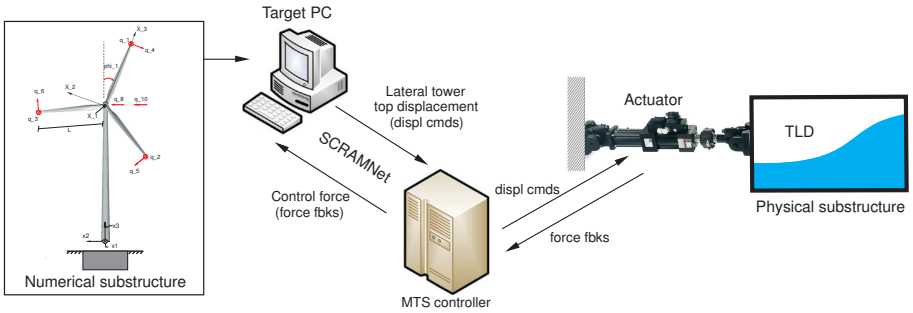

Figure 4.7 Conceptual view of the RTHT for the TLD-wind turbine system.

As shown in Figure 4.7, the present hybrid system includes the numerical substructure, the Target PC, the MTS controller, the actuator and the physical substructure. A full-scale TLD is manufactured and tested as the physical substructure, while the 13-DOF aeroelastic model (Chapter 2) is employed as the numerical substructure and established in Simulink/Matlab in a PC. The complied Simulink model is downloaded to another PC, the so-called Target PC, where real-time simulations can be run in Mathworks xPC Target environment. The MTS controller runs at a frequency of 1024 Hz, which is the update rate for the servo-valve commands. The communication through the target PC and the MTS controller is managed through the shared common random access memory network (SCRAMNet), which is a local high-speed network

ring. Such local high-speed connections drastically reduce delays and make it possible to perform real-time hybrid simulation. The MTS controller and the actuator are connected through SCRAMNet as well. At each time step, the tower displacement command calculated from the Target PC is sent to the MTS controller. The MTS controller generates an appropriate signal for the servo-valve which attempts to move the actuator to the commanded position. The actual displacement of the actuator and the reaction force (sloshing force) are measured at the same time. This reaction force is sent back to the Target PC through the MTS controller, and used for calculating the tower displacement at the next time step.

In the present case, the integration time step of the numerical substructure is set to be equal to the sampling time of the MTS controller (1/1024 s), since no iterations are needed for solving the numerical model and the actual task execution time is less than 1/1024 s. Therefore, synchronization is achieved without using the predictor-corrector technique (Mosqueda *et al.* 2005; Schellenberg 2008) that is normally used for nonlinear finite element models. Further, there is an inherent lag in the displacement response of servo-hydraulic actuator versus the command displacement. Consequently, the measured restoring forces are delayed relative to the command signal. To compensate for this delay, the compensation technique (Horiuchi *et al.* 1999) has been applied here, and satisfactory results have been achieved (Appendix G).

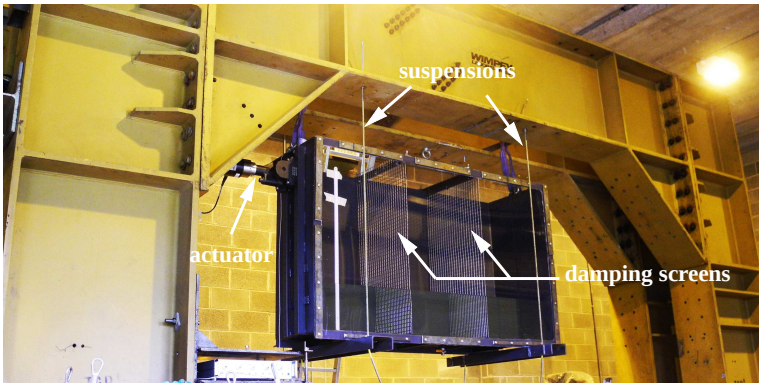

Figure 4.8 Test setup and the physical substructure (the TLD).

Figure 4.8 shows the test setup and the physical substructure (the TLD). The full-size TLD is made up of a closed rectangular tank, with a inner size of 1.93 m (length) $\times$ 0.59 m (width) $\times$ 1.2 m (height). Since the width of the tank is much smaller than the length, it is expected the sloshing of the water is predominately 2-dimensional. The TLD is suspended to top of the reaction frame by four steel cables in order to minimize the friction when the tank is enforced to move by the actuator. Further, a capacitance wave gauge (with a sampling rate of 10 Hz) is installed at the left end-wall of the tank to measure the liquid surface elevation. Unlike the previously reported reduced-scale tests on TLDs (Lee *et al.* 2007; Ashasi-Sorkhabi *et al.* 2013), the full-scale tests conducted here eliminate problems related to the scale effect and dynamic similarity, and reveal real behaviors of the sloshing liquid in a TLD that can be used

in prototype wind turbines.

Cases with and without damping screens have both been investigated. The inclusion of damping screens significantly increases the energy dissipation of the water sloshing, thus improving the performance of the TLD. For these scenarios, two damping screens are installed inside the tank at $1/3L$ and $2/3L$ positions, respectively, where L is the length of the tank. The size of each mesh for the present screen is 2.2 cm $\times$ 2.2 cm. It is expected that the damping parameter ξ in the theoretical model proposed in chapter 3 is much larger for the case with damping screens comparing with its counterpart, as will be shown below.

Detailed experimental results are presented in Appendix J and Appendix G. It is observed that the measured wave height at the left end wall contain a lot of high frequency components including both the higher sloshing modes and the nonlinear interaction effect. The measured sloshing force (reaction force), on the other hand, filters out most of the high frequency components since the force is the result of integrating liquid pressures over inner walls of the tank. By inserting damping screens, the remaining high frequency components are further mitigated, resulting in a sloshing force that is totally dominated by the first sloshing frequency. Consequently, it is shown from the results of structural responses that the inclusion of damping screens effectively improves the control performance of TLD on tower vibrations. Actually, it is only the first sloshing mode of the liquid motion that counteracts the fundamental lateral tower vibration. Although TLD effectively adds damping into lateral tower vibration even without damping screens, it is suggested that damping screens are included into the TLD for better damping performance.

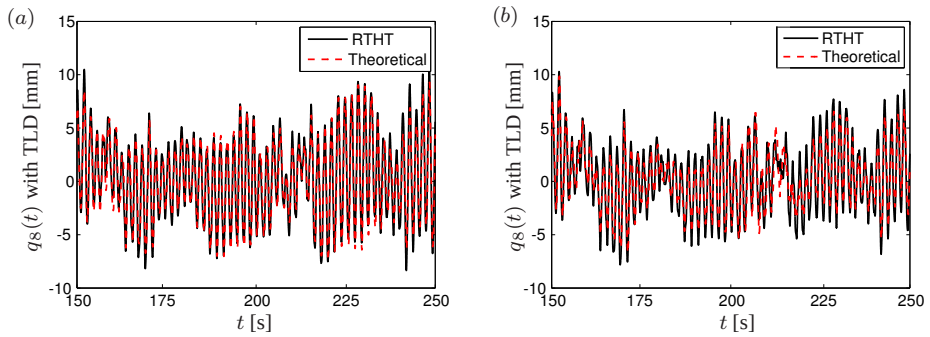

Figure 4.9 Comparison of the controlled tower displacements obtained by RTHT and theoretical model, 2 MW wind turbine, tuning ratio=1, $V_0 = 8$ m/s, I=0.1. (a) Without damping screens ($\xi = 0.004$ used in the theoretical model), (b) With damping screens ($\xi = 0.015$ used in the theoretical model).

Based on the experimental results, the theoretical model of the TLD-wind turbine system described in last section can be verified. Especially, it's rather important to verify the assumed equivalent linear damping term (with a single damping parameter ξ, as described in Chapter 3) in this model. Take one load case for example, Figure 4.9 shows the comparison of the controlled tower top displacements obtained by RTHT and the theoretical model for a 2 MW wind turbine. By setting the damping parameter ξ to be 0.004, the result from the theoretical model agrees very well with the test

result as shown in Figure 4.9(a). Acceptable agreement between the experimental and theoretical results is also obtained for the case with damping screens, by choosing the value of ξ to be 0.015. As expected, larger values of ξ should be used in the theoretical model when damping screens are installed in the TLD. For all other load cases, good agreements can also be achieved as long as correct values of ξ has been chosen in the model.

From the performed RTHT, a comprehensive evaluation of the full-size TLD for multi-megawatts wind turbines has been obtained, with a number of different load cases and various damper parameters considered (Appendix J). This provides some guidelines for the practical applications TLDs in wind turbines. One important finding is that best performance of the TLD is always obtained when the tuning ratio is 1.0 and damping screens are equipped.

Secondly (maybe more importantly), the good agreement between experimental and theoretical results shows the validity of the proposed model as well as the assumed equivalent linear damping modal, thus giving strong support to some of the previous sections in this thesis. However, it should be noted that trial-and-error procedures have been applied for finding a proper value of ξ, in order that theoretical result fits well with the experimental result. To make our model suitable for the design and analysis of a TLD, a reasonable expression between ξ and the parameters of the damping screens (the amount, the installing position and the mesh size) should be provided. In the future, more tests are planned to be carried out on this full-size TLD with various parameters of the damping screen considered. Sufficient data are to be collected, based on which an empirical expression of ξ is to be proposed with respect to the parameters of the damping screen.

CHAPTER 5
Dynamics and control of wave energy point absorbers

This chapter deals with dynamics and control of wave energy point absorbers. An optimal control law for a single nonlinear point absorber in irregular sea-state is first derived, in order to maximize the absorbed energy by the floater (the performance integral). It is proven to be a closed-loop controller with feedback from measured displacement, velocity and acceleration of the floater. However, a non-causal integral control component dependent on future velocities appears in the optimal control law. To circumvent this problem, a causal closed-loop controller is proposed by slightly modifying the optimal control law, with the basic idea that the stationary velocity of the absorber is enforced into phase with the wave excitation force at any time. Next, another type of point absorber, the Gyroscopic power take-off point absorber is proposed as a possible solution of delivering constant power to the grid without introducing power electronics. Assuming monochromatic waves simplified equations are derived, valid under synchronization of the ring to the angular frequency of the excitation. Stability conditions and the basins of attraction to the point attractors defining the synchronized motion are also determined.

5.1 Optimal control of wave energy point absorbers

A wave energy convertor (WEC) may be defined as a dynamic system with one or more degrees of freedom in order to convert the energy in the waves into mechanical energy stored in the oscillating system. A point absorber is a WEC that is capable of absorbing energy from waves propagating in any direction, and with horizontal dimensions that are small compared to the dominating wave length. In this thesis, only wave energy point absorbers are investigated. A type of the point absorber, the heave absorber, is modeled as SDOF and is shown in Figure 5.1.

As mentioned in Chapter 1, the optimal control law for a finite control horizon for achieving maximum absorbed power turns out to be non-causal. From this follows that any causal control law necessarily is suboptimal. Although all the causal controllers described in Chapter 1 work effectively, how to obtain the best causal controller is still a question. In the present study, the optimal control law for a point absorber in

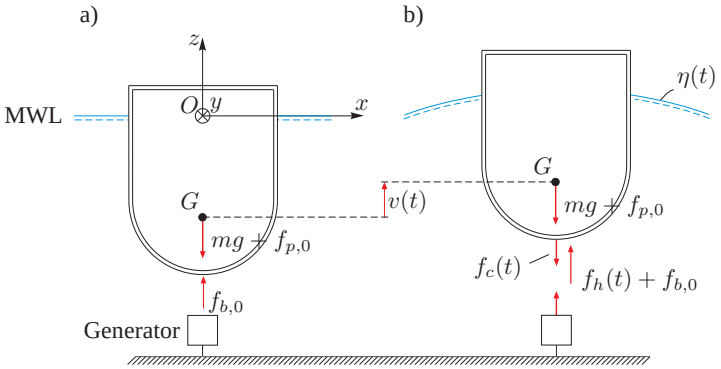

Figure 5.1 SDOF model of the heave absorber. a) Static equilibrium state. b) Dynamic state.

an irregular sea-state is at first devised based on optimal control theory (Meirovitch 1990; Naidu 2002). There are two approaches to the optimization problem, namely, the method of dynamic programming (Bellman 1956) and the Pontryagin's principle (Pontryagin 1987). Dynamic programming is completely equivalent to the Hamilton-Jacobi equation in analytical dynamics, and is now known as the Hamilton-Jacobi-Bellman (HJB) equation. The HJB equation provides the necessary and sufficient condition for optimality. In the present study, another method, the Pontryagin's principle has been used, which is a variational principle and essentially states that an optimal control must minimize or maximize a given function known as the Hamiltonian (Meirovitch 1990). In the analysis, first order wave theory is assumed, and no constraint on the absorber displacement and the control force is enforced. In reality, constraints are enforced on the control force to prevent large structural stresses in the floater at specific hot spots or due to the actuator saturation. Similarly the motion of the absorber is constrained, either due to limitations on the stroke of the actuator, or in order to prevent it from hitting the bottom of the sea or making unacceptable jumps out of water. Several forms of Pontryagin's principle have been proposed for optimal control problems with state variable inequality constraints, such as the direct adjoining approach where the Hamiltonian and Lagrangian are formulated directly from the constraints (state constraints, mixed constraints) (Jacobson *et al.* 1971), and the indirect adjoining approach where the derivative of the state constraints rather than the state constraints itself is adjoined to Hamiltonian in forming the Lagrangian (Pontryagin *et al.* 1962). A review of optimal control algorithms with constraints is given in Hartl *et al*. (1995). Optimal control of wave energy point absorbers with state and control force constraints is not dealt with in the present study.

The performance integral is taken as the absorbed mechanical energy during a given interval $[t_0, t_1]$ (Appendix H)

$$J[\mathbf{z}(t), f_c(t)] = \int_{t_0}^{t_1} f_c(\tau)\dot{v}(\tau)\, d\tau \tag{5.1}$$

where $\mathbf{z}(t)$ is the state vector, $\dot{v}(t)$ is the velocity of the absorber and $f_c(t)$ is the

control force. The control force is determined so the performance integral (the absorbed energy) is maximized under condition that the equations of motion with given initial conditions is fulfilled. The necessary condition for optimal control is that the 1st variation of the performance integral vanishes. Since it is only necessary but not sufficient, all the obtained stationary solutions from the Pontryagin's principle need to be examined to achieve the "true" optimal solution.

The resulting optimal control law is of the feedback type, with feedback from present displacement and acceleration, and future velocity of the absorber (Nielsen *et al.* 2013), given as

$$f_c(t) = -\big(m + m_h\big)\ddot{v}(t) - r\big(v(t)\big) + \int_t^\infty h_{r\dot{v}}(\tau - t)\dot{v}(\tau)\, d\tau \tag{5.2}$$

where m is the structural mass including ballast, m_h is the added water mass at infinite high frequencies, $r\big(v(t)\big)$ is the nonlinear buoyancy function and $h_{r\dot{v}}(t)$ is a causal impulse response function for the radiation force.

It is seen that the main effect of the optimal control force is to eliminate the inertial force and the buoyancy stiffness from the equations of motion, leading to the fact that at optimal control, all harmonic components of the velocity and the wave excitation force are in phase (Nielsen *et al.* 2013). This means that the Fourier transform of the control force and the floater velocity are related as

$$F_e(\omega) = C_h(\omega)\dot{V}(\omega) \tag{5.3}$$

where $C_h(\omega) = Re(H_{r\dot{v}}(\omega))$ is the frequency-dependent hydrodynamic radiation damping, and $H_{r\dot{v}}(\omega)$ is the frequency response function related to $h_{r\dot{v}}(t)$.

The non-causality (the control force depends on future velocities of the absorber) makes the optimal control law useless for practical applications, unless future velocities can be predicted. The prediction is difficult for broad-banded wave excitation, and is also related with errors, which inevitably results in a suboptimal control law. To circumvent this obstacle, a causal closed-loop controller is suggested by slightly modifying the optimal control law (Nielsen *et al.* 2013), written as

$$f_c(t) = -(m + m_h)\ddot{v}(t) + 2c_c\dot{v}(t) - r\big(v(t)\big) - \int_{-\infty}^t h_{r\dot{v}}(t - \tau)\dot{v}(\tau)\, d\tau \tag{5.4}$$

where the gain factor c_c is determined by maximizing the absorbed mean power. The rational of the proposed causal control law is that it also enforces the velocity of the absorber into phase with the wave excitation force at all frequencies. In this case, the Fourier transform of the control force and the floater velocity are related as

$$F_e(\omega) = 2c_c\dot{V}(\omega) \tag{5.5}$$

Eq. (5.5) is quite similar to Eq. (5.3) with the difference that the proportionality coefficient is frequency independent.

This causal controller is of course suboptimal, however, it is observed to absorb almost the same power as the optimal causal controller. Figure 5.2 shows the mean

power absorbed by the optimal controller and by the suboptimal causal controller calculated from analytical expressions (Nielsen *et al.* 2013), where all response processes are stationary Gaussian process since the wave excitation process is assumed to be so. Different values of the significant wave height H_s and the bandwidth parameter σ_f have been considered. As seen, the performance of the suboptimal causal controller is very close to that of the optimal controller at all parameter values.

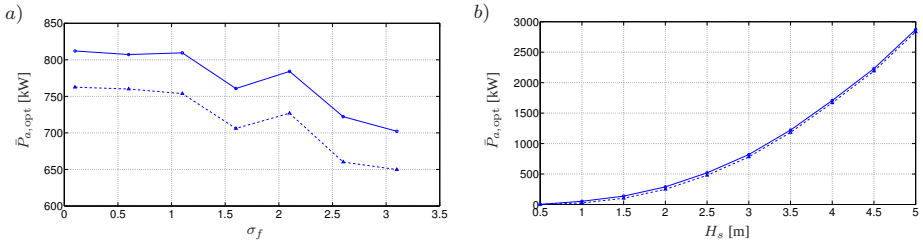

Figure 5.2 Absorbed mean power by optimal controller and sub-optimal causal controller. —: Optimal controller. - - -: Causal controller. a) Variation with σ_f, $H_s = 3\,\mathrm{m}$. b) Variation with H_s, $\sigma_f = 0.1$.

Again, it should be noted that no constraints on the floater displacement and the control force have been considered in the present study, and thus the unbounded optimal control force has been sought from stationarity of the Hamiltonian. Further works is to be done on optimal control of point absorbers with constraints on system state and control force.

5.2 Gyroscopic power take-off wave energy point absorber

For most point absorbers such as the heave absorber, the instantaneous absorbed energy varies significantly with time, making the expensive additional power electronics mandatory before the power can be supplied to the grid. This motivates a search for an alternative device which is able to deliver a more constant power to the grid without introducing power electronics.

The Gyroscopic power take-off (GyroPTO) wave energy point absorber is a possible solution to this problem. As shown in Figure 5.3, the GyroPTO wave energy point absorber consists of a float rigidly connected to a lever. In the other end the lever is supported by a hinge, which allows for rotations around a horizontal and vertical axis. Inside the float is a mechanical system made up of a spinning flywheel with a ring and a power take-off system connected to the ring along its rotational axis. The ring is free to rotate in a plane orthogonal to the lever. The spin axis of the flywheel is supported by a track on a ring with a width slightly larger than the diameter of the axis. The track forms a guidance for the precession of the spin axis, which is assumed to roll on the inner side of the track during rotations of the ring without any slip. The wave induced pitch and roll motions of the float produce a time varying rotation of the ring, which combined with the spinning velocity of the flywheel creates a gyroscopic torque parallel to the precession axis. This moment produces the necessary contact

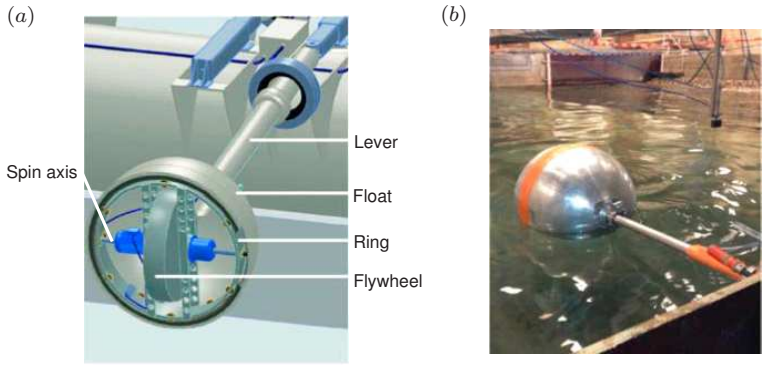

Figure 5.3 The GyroPTO point absorber. (a) Schematic details. (b) Scaled model tested in a wave tank.

force between the spin axis and the inner side of the track to provide the friction force making the rolling of the spin-axis possible. Hence, the gyroscopic moment enforces a non-holonomic kinematical constrain between the rotational velocities of the spin axis and the ring and makes the former to rotate at a larger angular velocity.

When synchronization of the angular frequency of the ring to the angular frequency of the wave loading takes place, the response of the ring becomes almost harmonic. This phenomenon is the basic reason for the functioning of the system. At synchronization, this means that the generated electric power becomes almost constant in time, making the need for expensive additional power electronics unnecessary before the power can be supplied to the grid.

Assuming monochromatic waves simplified equations are derived, valid under synchronization of the ring to the angular frequency of the excitation (Appendix I). It is demonstrated that the dynamics of the ring at synchronization can be described as an autonomous nonlinear SDOF system with parametric excitation. This equation is related with three different types of attractors depending on initial conditions of the ring. In one case, the ring vibrations are attracted to a state of rest indicating unstable synchronization. For the other two types of point attractors, the ring is synchronized to the wave angular frequency, either rotating in the positive or in the negative direction.

Figure 5.4 shows the responses of the ring for the initial values $(\psi_0, \dot{\psi}_0) = (\frac{\pi}{2}, \omega)$, where ω is the angular frequency of the wave load, and $\psi(t)$ and $\dot{\psi}(t)$ are the rotational angle and angular velocity of the ring, respectively. Synchronization with positive rotational speed of the ring ($\dot{\psi}(t) \simeq \omega$) takes place close to a given equilibrium point δ_1 of the said SDOF oscillator (see Appendix I). At synchronization, the quantity $\delta(t) = \psi(t) - \omega t - \mu_1$ converges towards δ_1, where μ_1 is a phase angle that can be determined from system parameters, and the fraction $\dot{\psi}(t)/\omega$ converge towards 1. In this stationary synchronized state, a forced harmonic oscillation (small amplitude) with the angular frequency 2ω can also be observed, which is cased by a parametric excitation term in the autonomous equation of the ring.

Figure 5.5 shows the corresponding results, when the initial conditions are changed to $\left(\psi_0, \dot{\psi}_0\right) = \left(-\frac{\pi}{2}, -\omega\right)$. In this case synchronization with negative rotational speed

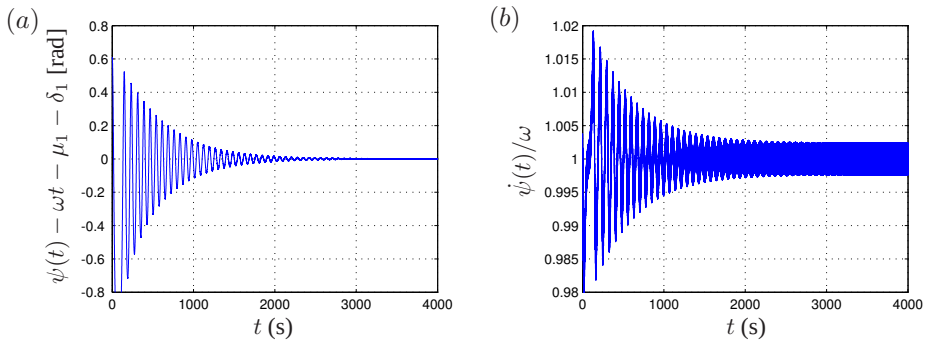

Figure 5.4 Synchronization with positive rotational speed of the ring. $\left(\psi_0, \dot{\psi}_0\right) = \left(\frac{\pi}{2}, \omega\right), T = 2$ s. (a) Time history of the rotational angle of the ring $\psi(t)$. (b) time history of the angular velocity of the ring $\dot{\psi}(t)$.

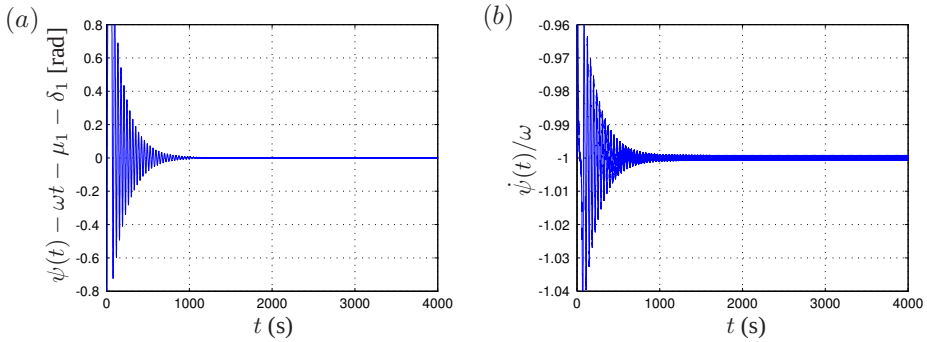

Figure 5.5 Synchronization with negative rotational speed of the ring. $\left(\psi_0, \dot{\psi}_0\right) = \left(\frac{-\pi}{2}, -\omega\right), T = 2$ s. (a) Time history of the rotational angle of the ring $\psi(t)$. (b) time history of the angular velocity of the ring $\dot{\psi}(t)$.

of the ring takes place to a different equilibrium point δ_1 (see Appendix I). At synchronization, the quantity $\delta(t) = \psi(t) + \omega t - \mu_2$ converges towards δ_1, where μ_2 is another phase angle that can be determined from system parameters, and the fraction $\dot{\psi}(t)/\omega$ converges towards -1. Again, the forced harmonic oscillations with the angular frequency 2ω around the equilibrium point in the stationary synchronized state is caused by the parametric excitation term in the autonomous equation of the ring.

It is clearly seen from the above results that the performance of the system depends strongly on the initial values $\left(\psi_0, \dot{\psi}_0\right)$. In order to analysis this problem further, the basins of attraction (or domain of attraction) (Nayfeh and Mook 2008) in the $\left(\delta(t), \dot{\delta}(t)\right)$ state space for synchronization to $\dot{\psi}(t) = \omega$ and $\dot{\psi}(t) = -\omega$ are determined. The basin of attraction of an equilibrium point indicates the subset of initial values $(\psi_0, \dot{\psi}_0)$ in the phase space for which the trajectories tend to approach the equilibrium point, although persistent oscillations may occur. The basins of attraction are separated by the separatrix manifolds originating from the saddle points.

In Figure 5.6(a) and 5.6(b), the grey colored areas show the basins of attraction in the the $(\delta, \dot{\delta})$-plane for the same systems as considered in Figures 5.4 and 5.5, re-

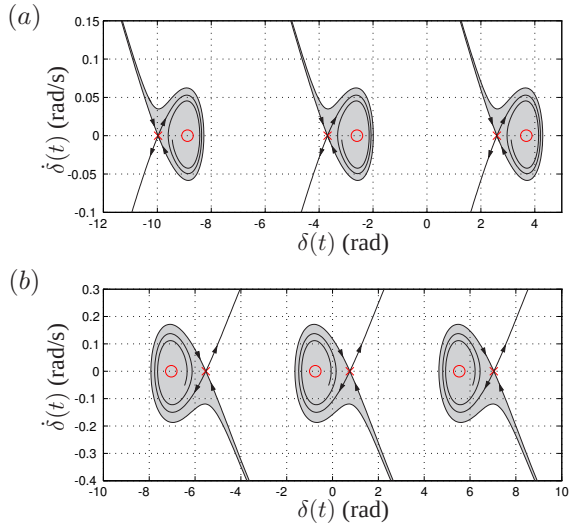

Figure 5.6 Basins of attraction, $T = 2$ s. (a) Synchronization to $\dot{\psi}(t) = \omega$. (b) Synchronization to $\dot{\psi}(t) = -\omega$. o: Stable equilibrium points, δ_1, x: Saddle points, δ_2.

spectively. In the disjoint white part of the state space, no synchronization is possible, and the system is attracted to a state of rest. As seen stable synchronization requires that $\delta(t)$ is confined to a finite interval centered around the equilibrium point δ_1.

The generator has a stator fixed to the ring and a rotor fixed to the spin axis of the flywheel, so the angular velocity of the generator is equal to the angular spin velocity $\dot{\theta}(t) = N\dot{\psi}(t)$, where N is the gear ratio between the angular spin velocity of the flywheel and the precession angular velocity of the ring. It is assumed to be an asynchronous generator with the characteristic (Simões and Farret 2014)

$$M_g(t) = M_{g,1}(V)N\dot{\psi}(t) \tag{5.6}$$

where $M_{g,1}(V)$ is a gain factor depending on the voltage V. Synchronization is possible only if the gain factor $M_{g,1}(V)$ fulfills (Appendix I)

$$M_{g,1} \leq \frac{\omega J_3^3}{2N}\sqrt{\Phi_1^2 + \Phi_3^2}\sqrt{1 \pm \sin(2\beta)\cos(\beta_1 - \beta_3)} \tag{5.7}$$

where the upper sign in $\pm$ refer to synchronization in the positive direction. J_3^3 is the polar moment of inertia of the flywheel. Let $\varphi_1^1(t)$ and $\varphi_3^1(t)$ denote the angular rotations of the float around the horizontal and vertical axis, respectively. At synchronization, $\varphi_1^1(t)$ and $\varphi_3^1(t)$ becomes almost harmonic with the angular wave frequency ω, the constant amplitudes Φ_1 and Φ_3, and the constant phases β_1 and β_3. $\beta = \arctan(\Phi_1/\Phi_3)$. The right hand side term in Eq. 5.7 is the maximum value of the gain parameter $M_{g,1}$ that can be used to achieve stable synchronization (the system state remains inside the grey colored areas in Figure 5.6).

In irregular sea-states, waves with different amplitudes and phases are exciting the structure, causing a broad-banded wave load. However, the response processes

of the float turn out to be narrow-banded with the central angular frequency equals the peak angular frequency of the wave spectrum ω_p. Then, the response processes indicated by the so-called Rice representation (Rice 1945; Gardner 1990)

$$\left.\begin{aligned}\varphi_1^1(t) &= \Phi_1(t)\cos\left(\omega_p t + \beta_1(t)\right)\\ \varphi_3^1(t) &= \Phi_3(t)\cos\left(\omega_p t + \beta_3(t)\right)\end{aligned}\right\} \tag{5.8}$$

where $\Phi_j(t)$ and $\beta_j(t), j = 1, 3$ are the slowly varying amplitude and phases. Eq. (5.7) still holds with ω replaced by ω_p, and the constant amplitude and phases replaced by the time-varying equivalents. Therefore, this opens up a need for a semi-active control for the stability of the synchronization, i.e. $M_{g,1}(V)$ should be reduced by changing the voltage V when the value of the right hand side term become smaller than the present value of $M_{g,1}(V)$. During operation, the time-varying amplitudes and phases need to be identified in real time from measured $\varphi_1^1(t)$, $\dot{\varphi}_1^1(t)$, $\varphi_3^1(t)$, $\dot{\varphi}_3^1(t)$, in order to check whether the system remains within the basin of attraction guaranteeing synchronization.

Further, from the generator torque in Eq. (5.6), the instantaneous generated electric power is given by

$$P_e(t) = M_g(t) N \dot{\psi}(t) = N^2 M_{g,1}\, \dot{\psi}^2(t) \tag{5.9}$$

On the other hand, the instantaneous absorbed power by the float is written as (Appendix I)

$$P_a(t) \;=\; M_{\varphi_1^1}(t)\, \dot{\varphi}_1^1(t) \;+\; M_{\varphi_1^3}(t)\, \dot{\varphi}_1^3(t) \tag{5.10}$$

where $M_{\varphi_1^1}(t)$ and $M_{\varphi_1^3}(t)$ are the external hydrodynamic moments work conjugated to $\varphi_1^1(t)$ and $\varphi_3^1(t)$, respectively.

Let $\overline{P}_a$ and $\overline{P}_e$ denote the time averages of $P_a(t)$ and $P_e(t)$, respectively. $P_a(t)$ varies strongly with time, whereas $P_e(t)$ is almost constant at synchronization since the angular velocity of the flywheel $\dot{\psi}(t)$ is almost constant. However, the time averages $\overline{P}_a$ and $\overline{P}_e$ must balance each other disregarding a small loss due to internal friction, leading to the following relation

$$\overline{P}_a \simeq \overline{P}_e \simeq P_e(t) \tag{5.11}$$

Eq. (5.11) implies that the generated electrical power can not exceed the mean absorbed power of the float. Generally, $\overline{P_a}$ is relatively small compared to the theoretical maximum where the motions of the float is actively controlled. This means the generated electric power $P_e(t)$ is also limited due to this power balance. For this reason the system may be improved if it is combined with an active control of the motion of the float somewhat similar to the heave point absorber described in the previous section, in order to increase $\overline{P}_a$ and thus the generated power $P_e(t)$. Both semi-active and active control of of this system under irregular waves will be pursued in a future study.

CHAPTER 6
Conclusions and future directions

The focus of the present study is to address two seemingly opposite but actually highly related issues: reducing structural vibrations of wind turbine components and increasing mechanical power supplied to wave energy point absorbers. Modeling of different dynamic systems have been carried out throughout the thesis. Various control solutions, both passively and actively, have been proposed and analyzed in detail. This final chapter gives the general conclusions drawn from this study and possible future extensions of this work.

6.1 General conclusions

(1) The lightly damped edgewise vibrations in wind turbine blades can be suppressed by various types of passive control devices, i.e. the roller damper, the TLCD, the CLCD and the TLD (sloshing damper). For rotating wind turbine blades, the large centrifugal acceleration governs the damping effect of these passive dampers, making it possible to use the dampers with rather small mass ratios for effectively reducing edgewise vibrations. Under certain circumstances when aeroelastic instability takes place in the edgewise mode, these passive dampers can also stabilize the structural response by introducing sufficient damping into the system.

(2) The roller damper has the advantage that its mass moment of inertia can be adjusted (with the same mass) during the design process by using different layouts of the roller. However, the damping property (friction between the roller and the track) is difficult to quantify and adjust once the damper has been manufactured. On the other hand, the damping property of the TLCD can be controlled easily by changing the orifice opening in real-time, making even the semi-active control applicable. The shortcoming of TLCD is that only the liquid in the horizontal tube acts as the effective mass, making the damper less effective than the roller damper with a same physical mass (when both dampers are optimized). The CLCD is as new type of liquid damper that combines the idea of TLCD with the roller damper. Therefore, it has both the advantages of large effective mass (larger than the TLCD, but not as large as the roller

damper) and the controllable damper property. Finally, another liquid damper, the TLD, turns out to be the most cost-effective device with the advantage of easy fabrication and minimal maintenance. Besides that, TLD also has the potential of being a semi-active device with rotatable baffles installed inside the tank, where the sloshing frequency can be adjusted by changing angles of the baffle.

(3) By means of modern power electronics, the generator torque can be prescribed to a certain value with a time delay below 10^-2 s and affects the lateral tower vibration through the reaction on the generator stator. It is shown that lateral tower vibrations can be effectively suppressed by active generator torque, for both the gear-driven and direct-driven wind turbines. However, the effective control of tower vibration is at the expense of somewhat more fluctuated power output, and a tradeoff between the vibration aspect and power electronic aspect should be considered. The negative impact on the smoothness of the power output can be avoided by using TLD in controlling lateral tower vibrations. A series of real-time hybrid tests have been carried out on a full-scale TLD, and proves the TLD to be very effective in reducing lateral tower vibrations in multi-megawatts wind turbines. It is shown that the best control effect of TLD is always achieved when the tuning ratio is 1.0 and damping screens are equipped. The good agreement between experimental and theoretical results also validates the theoretical model for TLD proposed in this thesis.

(4) From stationarity of the Hamiltonian, an optimal control law for a single wave energy point absorber in irregular sea-state is first derived. It is proven to be a closed-loop controller with feedback from measured displacement, velocity and acceleration of the floater, together with a non-causal integral component dependent on future velocities. A causal closed-loop controller is next proposed to circumvent this problem, by slightly modifying the optimal control law. The basic idea is to enforce the stationary velocity of the floater into phase with the wave excitation force at all frequencies in the excitation. It is shown that the devised causal controller absorbs almost the same power as the optimal controller in plane irregular sea states. For delivering more constant power to the grid without introducing power electronics, another type of point absorber, the Gyroscopic power take-off point absorber is proposed. It is shown that the dynamics of ring at synchronization (angular frequency of the ring equals to the angular frequency of the wave excitation) can be described as an autonomous nonlinear SDOF system, affected by three different types of point attractors. One where the ring vibrations are attracted to a state of rest indicating unstable synchronization, and the other two point attractors where the ring is synchronized to the wave angular frequency, either rotating in positive or negative directions. At stable synchronization, the generated electric power becomes almost constant.

6.2 Proposals for future directions

(1) Semi-active control of wind turbine components using liquid dampers

The dynamic properties (eigenfrequency, damping) of the wind turbine system

are dependent on various internal or external conditions, e.g. the rotor rotational speed, the mean wind speed and the turbulence intensity. Passive dampers with relatively narrow bandwidth may suffer from detuning effect when eigenfrequencies of the wind turbine components deviate from the designed values. Semi-active liquid dampers, such as the TLCD with controllable orifice opening, the TLD with rotatable baffles, are expected to have better performance for the time-varying wind turbine system. It will be important to carry out both theoretical and experimental studies on the semi-active liquid dampers for vibration control of wind turbine components. Especially, full-scale real-time hybrid testing of the semi-active damper using different control algorithms will be of great value for the application of liquid dampers in real multi-megawatts wind turbines.

(2) Flutter analysis of wind turbine systems and flutter suppression by means of control

With the increasing size, wind turbines also become more and more optimized with respect to structural dimensions and material usage. Future turbine designs will likely be stability-driven in contrast to the current loads-driven designs. Although classical flutter has not been observed on modern pitch-regulated wind turbines, it is believed to become a very important design consideration as wind turbine blades become more flexible.

Actually besides the 13-DOF wind turbine model, a detailed finite element (FE) model for the wind turbine system (not shown in the present thesis) has also been developed during the period of this Ph.D. study. The FE model takes into account the following effects: (i) offsets between the center of gravity, the shear center and the aerodynamic center of each cross-section along the blade, which have significant influence on the coupling between the flap-wise bending mode and the torsional mode. (ii) the distribution of pre-twist along the blade, which has significant influence on the coupling between the flap-wise mode and the edgewise mode. (iii) couplings between the blade vibrations with tower and drivetrain vibrations (as have already been considered in the 13-DOF model), which means there will be energy transfer between different components of the wind turbine. All these effects are important for accurately carrying out flutter analysis and predicting the critical flutter speed of a wind turbine system.

The indicated FE model can be used as a basic tool for flutter analysis of wind turbines. However, it might be necessary to develop a novel stability criteria rather than the widely-used eigenvalue analysis. More importantly, how to suppress flutter when it takes place under certain circumstances? One possible solution may be the so-called "small rotor", where rotatable flaps are mounted at outer part of the blades, and aerodynamic properties of the blade can be adjusted semi-actively when the angle of flap changes. Another idea is to devise certain novel dampers for torsional mode of the blade, and the damping of the torsional mode can be increased by installing this kind of damper inside the blade. The proper design and accurate modeling of the torsional damper become very important.

(3) Stochastic optimal control of wave energy point absorbers with state con-

straint

No constraints on the floater displacement and the control force have been considered in the present study, and thus the unbounded optimal control force has been obtained from the classical optimal control theory. In reality, constraints are enforced on the control force to prevent large structural stresses in the floater at specific hot spots or due to the actuator saturation. Similarly the motion of the absorber is constrained, either due to limitations on the stroke of the actuator, or in order to prevent it from hitting the bottom of the sea or making unacceptable jumps out of water.

Several forms of Pontryagin's principle have been proposed by other researchers for optimal control problems with state variable inequality constraints, such as the direct adjoining approach where the Hamiltonian and Lagrangian are formulated directly from the constraints, and the indirect adjoining approach where the derivatives of the state constraints rather than the state constraints are adjoined to Hamiltonian in forming the Lagrangian. These methods are applicable for the optimal control of wave energy point absorbers with state and control force constraints.

(4) Stochastic filtering theory and its application to the control of renewable energy structures

To control the system performance, we must accurately capture the state of the system at any instant of time. In reality, physical systems are subjected to random disturbance, so that the system state may itself be random. In order to determine the state of the indicated system, one may build a measuring device and takes measurements or observations on this system. These measurements are generally contaminated with noise caused by electronic and mechanical components of the measuring device.

The problem of determining the state of a system from noisy measurements is called filtering or estimation, and is of central importance for the control of system. The dynamic system can be modeled by a finite-dimensional Markov process, the output of a stochastic differential equation. The goal is to obtain the conditional probability density function of the state, given the measurements. This conditional density embodies all the information about the state of the system which is contained in the available measurements, and all estimates of the state can be constructed from this density.

Definitely, it is of both theoretical and practical values to apply filtering theory to the control of renewable energy structures.

Bibliography

Ahlström, Anders (2006). Influence of wind turbine flexibility on loads and power production. *Wind Energy* **9**(3), 237–249.

António, F de O (2008). Phase control through load control of oscillating-body wave energy converters with hydraulic pto system. *Ocean Engineering* **35**(3), 358–366.

António, F de O (2010). Wave energy utilization: A review of the technologies. *Renewable and sustainable energy reviews* **14**(3), 899–918.

Argyriadis, Kimon and Hille, Nikolai (2004). Determination of fatigue loading on a wind turbine with oil damping device. *Germanischer Lloydt, Hamburg*.

Arrigan, John, Pakrashi, Vikram, Basu, Biswajit, and Nagarajaiah, Satish (2011). Control of flapwise vibrations in wind turbine blades using semi-active tuned mass dampers. *Structural Control and Health Monitoring* **18**(8), 840–851.

Ashasi-Sorkhabi, Ali, Malekghasemi, Hadi, and Mercan, Oya (2013). Implementation and verification of real-time hybrid simulation (rths) using a shake table for research and education. *Journal of Vibration and Control*, 1077546313498616.

Babarit, Aurélien, Duclos, Gaelle, and Clément, AH (2004). Comparison of latching control strategies for a heaving wave energy device in random sea. *Applied Ocean Research* **26**(5), 227–238.

Bak, C, Zahle, F, Bitsche, R, Kim, T, Yde, A, Henriksen, LC, Natarajan, A, and Hansen, M (2013). Description of the dtu 10 mw reference wind turbine. *DTU Wind Energy Report-I-0092*.

Balendra, T, Wang, CM, and Cheong, HF (1995). Effectiveness of tuned liquid column dampers for vibration control of towers. *Engineering Structures* **17**(9), 668–675.

Balendra, T, Wang, CM, and Rakesh, G (1999). Vibration control of various types of buildings using tlcd. *Journal of Wind Engineering and Industrial Aerodynamics* **83**(1), 197–208.

Banerji, Pradipta, Murudi, Mohan, Shah, Arvind H, and Popplewell, Neil (2000). Tuned liquid dampers for controlling earthquake response of structures. *Earthquake engineering & structural dynamics* **29**(5), 587–602.

Barlas, Thanasis K and Van Kuik, GAM (2010). Review of state of the art in smart rotor control research for wind turbines. *Progress in Aerospace Sciences* **46**(1), 1–27.

Barlas, Thanasis K, Wingerden, W, Hulskamp, AW, Kuik, GA, and Bersee, HE (2013). Smart dynamic rotor control using active flaps on a small-scale wind turbine: aeroelastic modeling and comparison with wind tunnel measurements. *Wind Energy* **16**(8), 1287–1301.

Barrett, Ron and Farokhi, Saeed (1993). On the aerodynamics and performance of active vortex generators. *AIAA Paper* **3447**, 1993.

Basu, Biswajit, Zhang, Zili, and Nielsen, Søren RK (2015). Damping of edgewise vibration in wind turbine blades by means of circular liquid dampers. *Wind Energy*.

Bellman, Richard (1956). Dynamic programming and lagrange multipliers. *Proceedings of the National Academy of Sciences of the United States of America* **42**(10), 767.

Bir, Gunjit (2008). Multiblade coordinate transformation and its application to wind turbine analysis. In *ASME Wind Energy Symposium*.

Bir, Gunjit and Jonkman, Jason (2007). Aeroelastic instabilities of large offshore and onshore wind turbines. In *Journal of Physics: Conference Series*, Volume 75, pp. 012069. IOP Publishing.

Blaabjerg, Frede, Chen, Zhe, and Kjaer, Soeren Baekhoej (2004). Power electronics as efficient interface in dispersed power generation systems. *Power Electronics, IEEE Transactions on* **19**(5), 1184–1194.

Bossanyi, EA (2000). The design of closed loop controllers for wind turbines. *Wind energy* **3**(3), 149–163.

Bossanyi, EA (2003). Individual blade pitch control for load reduction. *Wind energy* **6**(2), 119–128.

Brodersen, Mark L and Høgsberg, Jan (2014). Damping of offshore wind turbine tower vibrations by a stroke amplifying brace. *Energy Procedia* **53**, 258–267.

Budal, K and Falnes, J (1980). Interacting point absorbers with controlled motion. *Power from sea waves*, 381–399.

Burton, T., Sharpe, D., Jenkins, N., and Bossanyi, E. (2001). *Wind Energy Handbook*. John Wiley & Sons.

Castaignet, Damien, Barlas, Thanasis, Buhl, Thomas, Poulsen, Niels K, Wedel-Heinen, Jens Jakob, Olesen, Niels A, Bak, Christian, and Kim, Taeseong (2014). Full-scale test of trailing edge flaps on a vestas v27 wind turbine: active load reduction and system identification. *Wind Energy* **17**(4), 549–564.

Chang, CC and Gu, M (1999). Suppression of vortex-excited vibration of tall buildings using tuned liquid dampers. *Journal of Wind Engineering and Industrial Aerodynamics* **83**(1), 225–237.

Chen, Jun-Ling and Georgakis, Christos T (2013). Spherical tuned liquid damper for vibration control in wind turbines. *Journal of Vibration and Control*, 1077546313495911.

Chow, Raymond and Van Dam, CP (2007). Computational investigations of deploying load control microtabs on a wind turbine airfoil. *45th AIAA Aerosp. Sci. Meet. Exhibit (ASME), Reno, NV*.

Christenson, Richard, Lin, Yi Zhong, Emmons, Andrew, and Bass, Brent (2008). Large-scale experimental verification of semiactive control through real-time hybrid simulation 1. *Journal of Structural Engineering* **134**(4), 522–534.

Colwell, Shane and Basu, Biswajit (2008). Experimental and theoretical investigations of equivalent viscous damping of structures with tlcd for different fluids. *Journal of structural engineering* **134**(1), 154–163.

Colwell, Shane and Basu, Biswajit (2009). Tuned liquid column dampers in offshore wind turbines for structural control. *Engineering Structures* **31**(2), 358–368.

Connell, James R (1982). The spectrum of wind speed fluctuations encountered by a rotating blade of a wind energy conversion system. *Solar Energy* **29**(5), 363–375.

De Corcuera, Asier Diaz, Pujana-Arrese, Aron, Ezquerra, Jose M, Segurola, Edurne, and Landaluze, Joseba (2012). H_∞ based control for load mitigation in wind turbines. *Energies* **5**(4), 938–967.

Faber, Torsten and Dalhoff, Peter (2008). Dynamic behaviour of oil dampers in wind turbine towers. *Germanischer Lloyd WindEnergie GmbH*.

Falnes, Johannes *et al.* (2002). Optimum control of oscillation of wave-energy converters. *International Journal of Offshore and Polar Engineering* **12**(02).

Falnes, Johannes and Budal, K (1978). Wave-power conversion by point absorbers. *Norwegian Maritime Research* **6**(4), 2–11.

Faltinsen, Odd M, Rognebakke, Olav F, Lukovsky, Ivan A, and Timokha, Alexander N (2000). Multidimensional modal analysis of nonlinear sloshing in a rectangular tank with finite water depth. *Journal of Fluid Mechanics* **407**, 201–234.

Faltinsen, Odd M and Timokha, Alexander N (2001). An adaptive multimodal approach to nonlinear sloshing in a rectangular tank. *Journal of Fluid Mechanics* **432**, 167–200.

Fitzgerald, Breiffni, Basu, Biswajit, and Nielsen, Søren RK (2013). Active tuned mass dampers for control of in-plane vibrations of wind turbine blades. *Structural Control and Health Monitoring* **20**(12), 1377–1396.

Fleming, Paul, Van Wingerden, Jan-Willem, and Wright, Alan D (2011). *Comparing State-space Multivariable Controls to Multi-SISO Controls for Load Reduction of Drivetrain-coupled Modes on Wind Turbines Through Field-testing: Preprint*. National Renewable Energy Laboratory,[National Wind Technology Center.

French, MJ (1979). A generalized view of resonant energy transfer. *Journal of Mechanical Engineering Science* **21**(4), 299–300.

Fujii, K, Tamura, Y, Sato, T, and Wakahara, T (1990). Wind-induced vibration of tower and practical applications of tuned sloshing damper. *Journal of Wind Engineering and Industrial Aerodynamics* **33**(1), 263–272.

Gao, H, Kwok, KCS, and Samali, B (1997). Optimization of tuned liquid column dampers. *Engineering structures* **19**(6), 476–486.

Gardner, William A (1990). *Introduction to random processes*. McGraw-Hill.

Hals, Jørgen, Falnes, Johannes, and Moan, Torgeir (2011). Constrained optimal control of a heaving buoy wave-energy converter. *Journal of Offshore Mechanics and Arctic Engineering* **133**(1), 011401.

Hansen, M.O.L. (2000). *Aerodynamics of Wind Turbines: Rotors, Loads and Structure*. Aktuelle Problems in der Angiologie. Earthscan.

Hansen, MH (2003). Improved modal dynamics of wind turbines to avoid stall-induced vibrations. *Wind Energy* **6**(2), 179–195.

Hansen, MH (2004). Stability analysis of three-bladed turbines using an eigenvalue approach. In *2004 ASME Wind Energy Symposium*, pp. 192–202.

Hansen, M. H. (2007). Aeroelastic instability problems for wind turbines. *Wind Energy* **10**(6), 551–577.

Hansen, Morten Hartvig, Thomsen, Kenneth, Fuglsang, Peter, and Knudsen, T (2006). Two methods for estimating aeroelastic damping of operational wind turbine modes from experiments. *Wind Energy* **9**(1-2), 179–191.

Hartl, Richard F, Sethi, Suresh P, and Vickson, Raymond G (1995). A survey of the maximum principles for optimal control problems with state constraints. *SIAM review* **37**(2), 181–218.

Horiuchi, T, Inoue, M, Konno, T, and Namita, Y (1999). Real-time hybrid experimental system with actuator delay compensation and its application to a piping system with energy absorber. *Earthquake Engineering & Structural Dynamics* **28**(10), 1121–1141.

Igarashi, Akira, Iemura, Hirokazu, and Suwa, Takanori (2000). Development of substructured shaking table test method. In *Proceedings of the 12th World Conference on Earthquake Engineering*.

Jacobson, David H, Lele, MM, and Speyer, Jason L (1971). New necessary conditions of optimality for control problems with state-variable inequality constraints. *Journal of mathematical analysis and applications* **35**(2), 255–284.

Jin, Qiao, Li, Xin, Sun, Ning, Zhou, Jing, and Guan, Jiong (2007). Experimental and numerical study on tuned liquid dampers for controlling earthquake response of jacket offshore platform. *Marine Structures* **20**(4), 238–254.

Johnson, Scott J, Baker, Jonathon P, Van Dam, CP, and Berg, Dale (2010). An overview of active load control techniques for wind turbines with an emphasis on microtabs. *Wind Energy* **13**(2-3), 239–253.

Kanev, Stoyan and van Engelen, Tim (2010). Wind turbine extreme gust control. *Wind Energy* **13**(1), 18–35.

Kareem, Ahsan (1990). Reduction of wind induced motion utilizing a tuned sloshing damper. *Journal of Wind Engineering and Industrial Aerodynamics* **36**, 725–737.

Krenk, Steen (2005). Frequency analysis of the tuned mass damper. *Journal of applied mechanics* **72**(6), 936–942.

Krenk, Steen, Svendsen, Martin Nymann, and Høgsberg, J (2012). Resonant vibration control of three-bladed wind turbine rotors. *AIAA journal* **50**(1), 148–161.

Lackner, Matthew A and Rotea, Mario A (2011a). Passive structural control of offshore wind turbines. *Wind energy* **14**(3), 373–388.

Lackner, Matthew A and Rotea, Mario A (2011b). Structural control of floating wind turbines. *Mechatronics* **21**(4), 704–719.

Lackner, Matthew A and van Kuik, Gijs (2010). A comparison of smart rotor control approaches using trailing edge flaps and individual pitch control. *Wind Energy* **13**(2-3), 117–134.

Larsen, Jesper Winther, Nielsen, Søren RK, and Krenk, Steen (2007). Dynamic stall model for wind turbine airfoils. *Journal of Fluids and Structures* **23**(7), 959–982.

Larsen, Torben Juul, Madsen, Helge A, and Thomsen, Kenneth (2005). Active load reduction using individual pitch, based on local blade flow measurements. *Wind Energy* **8**(1), 67–80.

Lee, HH, Wong, S-H, and Lee, R-S (2006). Response mitigation on the offshore floating platform system with tuned liquid column damper. *Ocean engineering* **33**(8), 1118–1142.

Lee, Sung-Kyung, Park, Eun Churn, Min, Kyung-Won, Lee, Sang-Hyun, Chung, Lan, and Park, Ji-Hun (2007). Real-time hybrid shaking table testing method for the performance evaluation of a tuned liquid damper controlling seismic response of building structures. *Journal of Sound and Vibration* **302**(3), 596–612.

Leishman, JG and Beddoes, TS (1989). A semi-empirical model for dynamic stall. *Journal of the American Helicopter society* **34**(3), 3–17.

Licari, John, Ugalde-Loo, Carlos E, Ekanayake, Janaka B, and Jenkins, Nick (2013). Damping of torsional vibrations in a variable-speed wind turbine. *Energy Conversion, IEEE Transactions on* **28**(1), 172–180.

Lobitz, Don W (2004). Aeroelastic stability predictions for a mw-sized blade. *Wind Energy* **7**(3), 211–224.

Lopes, MFP, Hals, J, Gomes, RPF, Moan, T, Gato, LMC, and Falcao, AF de O (2009). Experimental and numerical investigation of non-predictive phase-control strategies for a point-absorbing wave energy converter. *Ocean Engineering* **36**(5), 386–402.

Love, JS and Tait, MJ (2010). Nonlinear simulation of a tuned liquid damper with damping screens using a modal expansion technique. *Journal of Fluids and Structures* **26**(7), 1058–1077.

Maldonado, Victor, Farnsworth, John, Gressick, William, and Amitay, Michael (2010). Active control of flow separation and structural vibrations of wind turbine blades. *Wind Energy* **13**(2-3), 221–237.

Malvern, Lawrence E (1969). *Introduction to the Mechanics of a Continuous Medium*. Number Monograph.

Meirovitch, Leonard (1990). *Dynamics and control of structures*. John Wiley & Sons.

Mensah, Akwasi F and Dueñas-Osorio, Leonardo (2014). Improved reliability of wind turbine towers with tuned liquid column dampers (tlcds). *Structural Safety* **47**, 78–86.

Mercan, Oya and Ricles, James M (2009). Experimental studies on real-time testing of structures with elastomeric dampers. *Journal of structural engineering* **135**(9), 1124–1133.

Mosqueda, Gilberto, Stojadinović, Božidar, and Mahin, Stephen A (2005). *Implementation and accuracy of continuous hybrid simulation with geographically distributed substructures*. Earthquake Engineering Research Center, University of California.

Naidu, D Subbaram (2002). *Optimal control systems*. CRC press.

Nakashima, Masayoshi, Kato, Hiroto, and Takaoka, Eiji (1992). Development of real-time pseudo dynamic testing. *Earthquake Engineering & Structural Dynamics* **21**(1), 79–92.

Nakashima, Masayoshi and Masaoka, Nobuaki (1999). Real-time on-line test for mdof systems. *Earthquake engineering & structural dynamics* **28**(4), 393–420.

Namik, H and Stol, K (2010). Individual blade pitch control of floating offshore wind turbines. *Wind Energy* **13**(1), 74–85.

Nayfeh, Ali H and Mook, Dean T (2008). *Nonlinear oscillations*. John Wiley & Sons.

Nielsen, Søren RK, Zhou, Qiang, Kramer, Morten M, Basu, Biswajit, and Zhang, Zili (2013). Optimal control of nonlinear wave energy point converters. *Ocean Engineering* **72**, 176–187.

Ogata, K. (2010). *Modern Control Engineering*. Instrumentation and controls series. Prentice Hall.

Pars, Leopold Alexander (1965). *A treatise on analytical dynamics*. Wiley.

Pirner, M (1994). Dissipation of kinetic energy of large-span bridges. *Acta technica CSAV* **39**, 645–645.

Pirner, Miroš (2002). Actual behaviour of a ball vibration absorber. *Journal of Wind Engineering and Industrial Aerodynamics* **90**(8), 987–1005.

Pontryagin, LS, Boltyanskii, VG, Gamkrelidze, RV, and Mishchenko, E (1962). The mathematical theory of optimal processes (international series of monographs in pure and applied mathematics). *Interscience, New York*.

Pontryagin, Lev Semenovich (1987). *Mathematical theory of optimal processes*. CRC Press.

Pourazarm, Pariya, Modarres-Sadeghi, Yahya, and Lackner, Matthew (2015). A parametric study of coupled-mode flutter for mw-size wind turbine blades. *Wind Energy*.

Reed, Dorothy, Yu, Jinkyu, Yeh, Harry, and Gardarsson, Sigurdur (1998). Investigation of tuned liquid dampers under large amplitude excitation. *Journal of Engineering Mechanics* **124**(4), 405–413.

Rice, Stephen O (1945). Mathematical analysis of random noise. *Bell System Technical Journal, The* **24**(1), 46–156.

Riziotis, VA, Voutsinas, SG, Politis, ES, and Chaviaropoulos, PK (2004). Aeroelastic stability of wind turbines: the problem, the methods and the issues. *Wind Energy* **7**(4), 373–392.

Rotea, M, Lackner, M, and Saheba, Ruchir (2010). Active structural control of offshore wind turbines. In *48th AIAA aerospace sciences meeting and exhibit. Orlando, FL, pp CD–ROM*.

Sakai, F, Takaeda, S, and Tamaki, T (1989). Tuned liquid column damper-new type device for suppression of building vibrations. In *International Conference on Highrise Buildings, Nanjing, China, Mar*, pp. 25–27.

Schellenberg, Andreas Heinrich (2008). *Advanced implementation of hybrid simulation*. Ph. D. thesis, University of California, Berkeley.

Schoen, Marco P, Hals, Jorgen, and Moan, Torgeir (2008a). Robust control of heaving wave energy devices in irregular waves. In *Control and Automation, 2008 16th Mediterranean Conference on*, pp. 779–784. IEEE.

Schoen, Marco P, Hals, Jorgen, and Moan, Torgeir (2008b). Wave prediction and fuzzy logic control of wave energy converters in irregular waves. In *Control and Automation, 2008 16th Mediterranean Conference on*, pp. 767–772. IEEE.

Shimizu, K and Teramura, A (1994). Development of vibration control system using u-shaped tank. In *Proceedings of the 1st international workshop and seminar on behavior of steel structures in seismic areas, Timisoara, Romania*, Volume 7, pp. 25–34.

Simões, M Godoy and Farret, Felix A (2014). *Modeling and Analysis with Induction Generators*. Crc Press.

Staino, A, Basu, B, and Nielsen, Søren RK (2012). Actuator control of edgewise vibrations in wind turbine blades. *Journal of Sound and Vibration* **331**(6), 1233–1256.

Stewart, Gordon M and Lackner, Matthew A (2014). The impact of passive tuned mass dampers and wind–wave misalignment on offshore wind turbine loads. *Engineering Structures* **73**, 54–61.

Sun, LM and Fujino, Y (1994). A semi-analytical model for tuned liquid damper (tld) with wave breaking. *Journal of Fluids and Structures* **8**(5), 471–488.

Sun, LM, Fujino, Y, Chaiseri, P, and Pacheco, BM (1995). The properties of tuned liquid dampers using a tmd analogy. *Earthquake engineering & structural dynamics* **24**(7), 967–976.

Svendsen, Ib A, Svendsen, Ib A, and Jonsson, Ivar G (1976). *Hydrodynamics of coastal regions*. Den Private ingeniørfond, Technical University of Denmark.

Tamura, Yukio, Fujii, Kunio, Ohtsuki, Tamio, Wakahara, Toshihiro, and Kohsaka, Ryuichi (1995). Effectiveness of tuned liquid dampers under wind excitation. *Engineering structures* **17**(9), 609–621.

Thirstrup Petersen, J, Thomsen, Kenneth, and Aagaard Madsen, H (1998). Stall strips can control edgewise vibrations. Technical report.

Valério, D, Beirão, P, da Costa, J Sá, *et al.* (2007). Reactive control and phase and amplitude control applied to the archimedes wave swing. In *The Seventeenth International Offshore and Polar Engineering Conference*. International Society of Offshore and Polar Engineers.

Van der Hooft, EL, Schaak, P, Van Engelen, TG, *et al.* (2003). Wind turbine control algorithms. *DOWEC project-DOWEC-F1W1-EH-03-094/0, Task-3 report*.

Wilmink, AJ and Hengeveld, JF (2006). Application of tuned liquid column dampers in wind turbines. In *Proceedings of the European Wind Energy Conference*.

Won, AYJ, Pires, JA, and Haroun, MA (1996). Stochastic seismic performance evaluation of tuned liquid column dampers. *Earthquake engineering & structural dynamics* **25**(11), 1259–1274.

Xu, YL, Samali, B, and Kwok, KCS (1992). Control of along-wind response of structures by mass and liquid dampers. *Journal of Engineering Mechanics* **118**(1), 20–39.

Xue, SD, Ko, JM, and Xu, YL (2000). Tuned liquid column damper for suppressing pitching motion of structures. *Engineering Structures* **22**(11), 1538–1551.

Yalla, Swaroop K, Kareem, Ahsan, and Kantor, Jeffrey C (2001). Semi-active tuned liquid column dampers for vibration control of structures. *Engineering Structures* **23**(11), 1469–1479.

Yu, Jin-Kyu, Wakahara, Toshihiro, and Reed, Dorothy A (1999). A non-linear numerical model of the tuned liquid damper. *Earthquake Engineering and structural dynamics* **28**(6), 671–686.

Zahrai, Seyed Mehdi, Abbasi, Saeed, Samali, Bijan, and Vrcelj, Zora (2012). Experimental investigation of utilizing tld with baffles in a scaled down 5-story benchmark building. *Journal of Fluids and Structures* **28**, 194–210.

Zhang, Z., Basu, B., and Nielsen, S.R.K. (2015). Tuned liquid column dampers for mitigation of edgewise vibrations in rotating wind turbine blades. *Structural Control and Health Monitoring* **22**(3), 500–517.

Zhang, Zili, Li, Jie, Nielsen, Søren RK, and Basu, Biswajit (2014). Mitigation of edgewise vibrations in wind turbine blades by means of roller dampers. *Journal of Sound and Vibration* **333**(21), 5283–5298.

Zhang, Zili, Nielsen, Søren RK, Basu, Biswajit, and Li, Jie (2015). Nonlinear modeling of tuned liquid dampers (tlds) in rotating wind turbine blades for damping edgewise vibrations. *Journal of Fluids and Structures*, In review.

Zhang, Zi-Li, Chen, Jian-Bing, and Li, Jie (2014). Theoretical study and experimental verification of vibration control of offshore wind turbines by a ball vibration absorber. *Structure and Infrastructure Engineering* **10**(8), 1087–1100.

APPENDIX A
System Matrices of the 13-DOF model

A.1 Mass matrix

The mass matrix **M**(t) is symmetric and positive definite, and is made up of the following two contributions

$$\mathbf{M}(t) = \mathbf{M}_1(t) + \mathbf{M}_2 \tag{A.1}$$

where $\mathbf{M}_1(t)$ indicates the mass matrix that is attributed to the rotor, $\mathbf{M}_2$ indicates the contribution from the tower, the nacelle and the drivetrain.

(1) $\mathbf{M}_1(t)$ has the structure

$$\mathbf{M}_1(t) = \begin{bmatrix} \mathbf{M}_{1,ll} & \mathbf{M}_{1,lg}(t) \\ \mathbf{M}_{1,gl}(t) & \mathbf{M}_{1,gg} \end{bmatrix} \tag{A.2}$$

$\mathbf{M}_{1,ll}$ is given as

$$\mathbf{M}_{1,ll} = \begin{bmatrix} m_1 & 0 & 0 & 0 & 0 & 0 \\ 0 & m_1 & 0 & 0 & 0 & 0 \\ 0 & 0 & m_1 & 0 & 0 & 0 \\ 0 & 0 & 0 & m_2 & 0 & 0 \\ 0 & 0 & 0 & 0 & m_2 & 0 \\ 0 & 0 & 0 & 0 & 0 & m_2 \end{bmatrix} \tag{A.3}$$

where m_1 and m_2 are modal masses related to the fundamental flap-wise and edgewise eigenvibrations $\big(q_j(t)$ and $q_{j+3}(t)\big)$ defined as

$$\left.\begin{aligned} m_1 &= \int_0^{L_B} \mu(x_3)\Phi_1^2(x_3)dx_3 \\ m_2 &= \int_0^{L_B} \mu(x_3)\Phi_2^2(x_3)dx_3 \end{aligned}\right\} \tag{A.4}$$

$\mathbf{M}_{1,lg}(t) = \mathbf{M}_{1,gl}^{T}(t)$ is given as

$$\mathbf{M}_{1,lg}(t) = \begin{bmatrix} m_3 & 0 & 0 & m_5\cos\Psi_1 & m_5\sin\Psi_1 & 0 & 0 \\ m_3 & 0 & 0 & m_5\cos\Psi_2 & m_5\sin\Psi_2 & 0 & 0 \\ m_3 & 0 & 0 & m_5\cos\Psi_3 & m_5\sin\Psi_3 & 0 & 0 \\ 0 & -m_4\cos\Psi_1 & 0 & -m_4 s\sin\Psi_1 & -m_4 s\cos\Psi_1 & m_6 & 0 \\ 0 & -m_4\cos\Psi_2 & 0 & -m_4 s\sin\Psi_2 & -m_4 s\cos\Psi_2 & m_6 & 0 \\ 0 & -m_4\cos\Psi_3 & 0 & -m_4 s\sin\Psi_3 & -m_4 s\cos\Psi_3 & m_6 & 0 \end{bmatrix} \tag{A.5}$$

where

$$\left.\begin{aligned} m_3 &= \int_0^{L_B} \mu(x_3)\Phi_1(x_3)dx_3, \quad m_4 = \int_0^{L_B} \mu(x_3)\Phi_2(x_3)dx_3 \\ m_5 &= \int_0^{L_B} \mu(x_3)x_3\Phi_1(x_3)dx_3, \quad m_6 = \int_0^{L_B} \mu(x_3)x_3\Phi_2(x_3)dx_3 \end{aligned}\right\} \tag{A.6}$$

$\mathbf{M}_{1,gg}$ is given as

$$\mathbf{M}_{1,gg} = \begin{bmatrix} 3m_0 & 0 & 0 & 0 & 0 & 0 & 0 \\ 0 & 3m_0 & 0 & 0 & 0 & 0 & 0 \\ 0 & 0 & 0 & 0 & 0 & 0 & 0 \\ 0 & 0 & 0 & 3m_0 s^2 + \frac{1}{2}J_r & 0 & 0 & 0 \\ 0 & 0 & 0 & 0 & 3m_0 s^2 + \frac{1}{2}J_r & 0 & 0 \\ 0 & 0 & 0 & 0 & 0 & J_r & 0 \\ 0 & 0 & 0 & 0 & 0 & 0 & 0 \end{bmatrix} \tag{A.7}$$

where m_0 is the mass of a single blade and J_r is the mass moment of inertia of the rotor, given by

$$m_0 = \int_0^{L_B} \mu(x_3)dx_3, \quad J_r = 3\int_0^{L_B} \mu(x_3)x_3^2 dx_3 \tag{A.8}$$

(2) $\mathbf{M}_2$ has the structure

$$\mathbf{M}_2 = \begin{bmatrix} \mathbf{0} & \mathbf{0} \\ \mathbf{0} & \mathbf{M}_{2,gg} \end{bmatrix} \tag{A.9}$$

$$\mathbf{M}_{2,gg} = \begin{bmatrix} m_{7,7}+M_0 & 0 & 0 & m_{7,10} & 0 & 0 & 0 \\ 0 & m_{8,8}+M_0 & m_{8,9} & 0 & 0 & 0 & 0 \\ 0 & m_{9,8} & m_{9,9}+J_9 & 0 & 0 & 0 & 0 \\ m_{7,10} & 0 & 0 & m_{10,10}+J_{10} & 0 & 0 & 0 \\ 0 & 0 & 0 & 0 & m_{11,11}+J_{11} & 0 & 0 \\ 0 & 0 & 0 & 0 & 0 & 0 & 0 \\ 0 & 0 & 0 & 0 & 0 & 0 & J_g \end{bmatrix} \tag{A.10}$$

where M_0 is the mass of nacelle including drivetrain and equipment. J_9, J_{10} and J_{11} are the mass moment of inertia of the nacelle related to $q_9(t)$, $q_{10}(t)$ and $q_{11}(t)$, respectively. $m_{7,7} = m_{8,8}$, $m_{7,10} = m_{10,7} = m_{8,9} = m_{9,8}$, $m_{10,10} = m_{9,9}$, these are the consistent mass coefficients of tower related to $q_7(t)$ and $q_{10}(t)$ (the fore-aft tower vibration), and $q_8(t)$ and $q_9(t)$ (the lateral tower vibration), respectively. As mentioned in Chapter 2, cubic Hermite polynomial interpolation functions have been applied for tower displacements (Bernoulli-Euler beam theory). Further, $m_{11,11}$ is the consistent mass moment of inertia of the tower related to $q_{11}(t)$, with linear interpolation of tower rotations (St. Venant torsional theory). J_g is the mass moment of inertia of the rotor of the generator.

A.2 Stiffness matrix

The stiffness matrix $\mathbf{K}(t)$ is made up of the following two contributions

$$\mathbf{K}(t) = \mathbf{K}_s + \mathbf{K}_g(t) \tag{A.11}$$

where K_s is the structural stiffness matrix that is symmetric and positive definite. $\mathbf{K}_g(t)$ is the gyroscopic stiffness matrix.

(1) $\mathbf{K}_s$ has the structure

$$\mathbf{K}_s = \begin{bmatrix} \mathbf{K}_{s,ll} & \mathbf{0} \\ \mathbf{0} & \mathbf{K}_{s,gg} \end{bmatrix} \tag{A.12}$$

$\mathbf{K}_{s,ll}$ is given as

$$\mathbf{K}_{s,ll} = \begin{bmatrix} k_1 & 0 & 0 & 0 & 0 & 0 \\ 0 & k_1 & 0 & 0 & 0 & 0 \\ 0 & 0 & k_1 & 0 & 0 & 0 \\ 0 & 0 & 0 & k_2 & 0 & 0 \\ 0 & 0 & 0 & 0 & k_2 & 0 \\ 0 & 0 & 0 & 0 & 0 & k_2 \end{bmatrix} \tag{A.13}$$

where k_1 and k_2 are the modal stiffness for the fundamental flap-wise and edgewise modes under normal operation, i.e. including centrifugal stiffening. There are written as

$$\left.\begin{aligned} k_1 &= \int_0^{L_B} \left(EI_1(x_3) \left(\frac{d^2\Phi_1(x_3)}{dx_3^2} \right)^2 + F(x_3) \left(\frac{d\Phi_1(x_3)}{dx_3} \right)^2 \right) dx_3 \\ k_2 &= \int_0^{L_B} \left(EI_2(x_3) \left(\frac{d^2\Phi_2(x_3)}{dx_3^2} \right)^2 + F(x_3) \left(\frac{d\Phi_2(x_3)}{dx_3} \right)^2 \right) dx_3 \end{aligned}\right\} \tag{A.14}$$

where $F(x_3) = \Omega^2 \int_{x_3}^{L} \mu(\xi)\xi d\xi$ is the centrifugal axial force per unit length along the blade.

$\mathbf{K}_{s,gg}$ is given as

$$\mathbf{K}_{s,gg}=\begin{bmatrix} k_{7,7} & 0 & 0 & k_{7,10} & 0 & 0 & 0 \\ 0 & k_{8,8} & k_{8,9} & 0 & 0 & 0 & 0 \\ 0 & k_{9,8} & k_{9,9} & 0 & 0 & 0 & 0 \\ k_{7,10} & 0 & 0 & k_{10,10} & 0 & 0 & 0 \\ 0 & 0 & 0 & 0 & k_{11,11} & 0 & 0 \\ 0 & 0 & 0 & 0 & 0 & k_0 & -\frac{1}{N}k_0 \\ 0 & 0 & 0 & 0 & 0 & -\frac{1}{N}k_0 & \frac{1}{N^2}k_0 \end{bmatrix} \tag{A.15}$$

$k_{7,7} = k_{8,8}$, $k_{7,10} = k_{10,7} = k_{8,9} = k_{9,8}$, $k_{10,10} = k_{9,9}$, these are the consistent stiffness coefficients of tower related to $q_7(t)$ and $q_{10}(t)$ (the fore-aft tower vibration), and $q_8(t)$ and $q_9(t)$ (the lateral tower vibration), respectively. $k_{11,11}$ is the torsional stiffness coefficient related to $q_{11}(t)$, with linear interpolation of tower rotations (St. Venant torsional theory). k_0 is the equivalent St. Venant torsional stiffness of the drivetrain, given as

$$\frac{1}{k_0} = \frac{1}{k_r} + \frac{1}{N^2 k_g} \quad \Rightarrow \quad k_0 = \frac{N^2 k_r k_g}{k_r + N^2 k_g} \tag{A.16}$$

where k_r and k_g denote the St. Venant torsional stiffness of the rotor shaft and the generator shaft, and N is the gear ratio of the gearbox.

(2) $\mathbf{K}_g(t)$ has the structure

$$\mathbf{K}_s = \begin{bmatrix} \mathbf{K}_{g,ll} & \mathbf{0} \\ \mathbf{K}_{g,gl}(t) & \mathbf{0} \end{bmatrix} \tag{A.17}$$

$\mathbf{K}_{g,ll}$ is given as

$$\mathbf{K}_{g,ll} = \begin{bmatrix} 0 & 0 & 0 & 0 & 0 & 0 \\ 0 & 0 & 0 & 0 & 0 & 0 \\ 0 & 0 & 0 & 0 & 0 & 0 \\ 0 & 0 & 0 & -\Omega^2 m_2 & 0 & 0 \\ 0 & 0 & 0 & 0 & -\Omega^2 m_2 & 0 \\ 0 & 0 & 0 & 0 & 0 & -\Omega^2 m_2 \end{bmatrix} \tag{A.18}$$

$\mathbf{K}_{g,ll}$ introduces negative stiffness into equations of motion for edgewise degrees of freedom $q_4(t)$, $q_5(t)$ and $q_6(t)$, the so-called centrifugal softening effect.

$\mathbf{K}_{g,gl}(t)$ is given as

$$\mathbf{K}_{g,gl}(t)=\Omega^2\begin{bmatrix}0&0&0&0&0&0\\0&0&0&m_4\cos\Psi_1&m_4\sin\Psi_2&m_4\sin\Psi_3\\0&0&0&0&0&0\\0&0&0&m_4 s\sin\Psi_1&m_4 s\sin\Psi_2&m_4 s\sin\Psi_3\\0&0&0&-m_4 s\cos\Psi_1&-m_4 s\cos\Psi_2&-m_4 s\cos\Psi_3\\0&0&0&0&0&0\\0&0&0&0&0&0\end{bmatrix} \tag{A.19}$$

A.3 Damping matrix

The damping matrix $\mathbf{C}(t)$ is made up of the following two contributions

$$\mathbf{C}(t) = \mathbf{C}_s + \mathbf{C}_g(t) + \mathbf{C}_{gen} \tag{A.20}$$

where C_s is the structural damping matrix that is symmetric and positive definite. $\mathbf{C}_g(t)$ is the gyroscopic damping matrix, and $\mathbf{C}_{gen}$ is the generator damping matrix that can be specified by the active generator controller.

(1) $\mathbf{C}_s$ has the structure

$$\mathbf{C}_s = \begin{bmatrix}\mathbf{C}_{s,ll} & \mathbf{0}\\ \mathbf{0} & \mathbf{C}_{s,gg}\end{bmatrix} \tag{A.21}$$

$\mathbf{C}_{s,ll}$ is given as

$$\mathbf{C}_{s,ll} = \begin{bmatrix}c_1&0&0&0&0&0\\0&c_1&0&0&0&0\\0&0&c_1&0&0&0\\0&0&0&c_2&0&0\\0&0&0&0&c_2&0\\0&0&0&0&0&c_2\end{bmatrix} \tag{A.22}$$

where c_1 and c_2 denote the modal damping coefficients of the fundamental flap-wise and edgewise modes. $c_j = 2\zeta_j\sqrt{m_j k_j}, j = 1, 2$, and ζ_j is the corresponding modal damping ratios.

$\mathbf{C}_{s,gg}$ is given as

$$\mathbf{C}_{s,gg}=\begin{bmatrix}c_{7,7}&0&0&c_{7,10}&0&0&0\\0&c_{8,8}&c_{8,9}&0&0&0&0\\0&c_{9,8}&c_{9,9}&0&0&0&0\\c_{7,10}&0&0&c_{10,10}&0&0&0\\0&0&0&0&c_{11,11}&0&0\\0&0&0&0&0&0&0\\0&0&0&0&0&0&0\end{bmatrix} \tag{A.23}$$

$c_{7,7} = c_{8,8}$, $c_{7,10} = c_{10,7} = c_{8,9} = c_{9,8}$, $c_{10,10} = c_{9,9}$, these are the damping constants of tower (without nacelle) specified by means of Rayleigh damping model. $c_{11,11}$ is the modal damping constant of the fundamental torsional mode of the tower without nacelle.

(2) $\mathbf{C}_g(t)$ has the structure

$$\mathbf{C}_g(t) = \begin{bmatrix} \mathbf{0} & \mathbf{C}_{g,lg}(t) \\ \mathbf{C}_{g,gl}(t) & \mathbf{0} \end{bmatrix} \tag{A.24}$$

$\mathbf{C}_{g,lg}(t)$ is given as

$$\mathbf{C}_{g,lg}(t) = \Omega \begin{bmatrix} 0 & 0 & 0 & -m_5 \sin\Psi_1 & m_5 \cos\Psi_1 & 0 & 0 \\ 0 & 0 & 0 & -m_5 \sin\Psi_2 & m_5 \cos\Psi_2 & 0 & 0 \\ 0 & 0 & 0 & -m_5 \sin\Psi_3 & m_5 \cos\Psi_3 & 0 & 0 \\ 0 & 0 & 0 & 0 & 0 & 0 & 0 \\ 0 & 0 & 0 & 0 & 0 & 0 & 0 \\ 0 & 0 & 0 & 0 & 0 & 0 & 0 \end{bmatrix} \tag{A.25}$$

$\mathbf{C}_{g,gl}(t)$ is given as

$$\mathbf{C}_{g,gl}(t) = \Omega \begin{bmatrix} 0 & 0 & 0 & 0 & 0 & 0 \\ 0 & 0 & 0 & 2m_4 \sin\Psi_1 & 2m_4 \sin\Psi_2 & 2m_4 \sin\Psi_3 \\ 0 & 0 & 0 & 0 & 0 & 0 \\ -m_5 \sin\Psi_1 & -m_5 \sin\Psi_2 & -m_5 \sin\Psi_3 & -2m_4 s \cos\Psi_1 & -2m_4 s \cos\Psi_2 & -2m_4 s \cos\Psi_3 \\ m_5 \cos\Psi_1 & m_5 \cos\Psi_2 & m_5 \cos\Psi_3 & -2m_4 s \sin\Psi_1 & -2m_4 s \sin\Psi_2 & -2m_4 s \sin\Psi_3 \\ 0 & 0 & 0 & 0 & 0 & 0 \\ 0 & 0 & 0 & 0 & 0 & 0 \end{bmatrix} \tag{A.26}$$

APPENDIX B
Mitigation of Edgewise Vibrations in Wind Turbine Blades by Means of Roller Dampers

Paper 1
The paper presented in this appendix is published in *Journal of Sound and Vibration*, 2014, Volume 333, Pages 5283-5298. DOI: 10.1016/j.jsv.2014.06.006.

http://www.sciencedirect.com/science/article/pii/S0022460X1400491X

B.1 Author's Right

Journal author rights

In order for Elsevier to publish and disseminate research articles, we need publishing rights. This is determined by a publishing agreement between the author and Elsevier. This agreement deals with the transfer or license of the copyright to Elsevier and authors retain significant rights to use and share their own published articles. Elsevier supports the need for authors to share, disseminate and maximize the impact of their research and these rights, in Elsevier proprietary journals* are defined below:

For subscription articles	For open access articles
Authors transfer copyright to the publisher as part of a journal publishing agreement, but have the right to: • Share their article for Personal Use, Internal Institutional Use and Scholarly Sharing purposes, with a DOI link to the version of record on ScienceDirect (and with the Creative Commons CC-BY-NC- ND license for author manuscript versions) • Retain patent, trademark and other intellectual property rights (including raw research data). • Proper attribution and credit for the published work.	Authors sign an exclusive license agreement, where authors have copyright but license exclusive rights in their article to the publisher**. In this case authors have the right to: • Share their article in the same ways permitted to third parties under the relevant user license (together with Personal Use rights) so long as it contains a CrossMark logo, the end user license, and a DOI link to the version of record on ScienceDirect. • Retain patent, trademark and other intellectual property rights (including raw research data). • Proper attribution and credit for the published work.

http://www.elsevier.com/journal-authors/author-rights-and-responsibilities

Journal of Sound and Vibration 333 (2014) 5283–5298

Contents lists available at ScienceDirect

Journal of Sound and Vibration

journal homepage: www.elsevier.com/locate/jsvi

Mitigation of edgewise vibrations in wind turbine blades by means of roller dampers

Zili Zhang [a,*], Jie Li [b], Søren R.K. Nielsen [a], Biswajit Basu [c]

[a] Department of Civil Engineering, Aalborg University, 9000 Aalborg, Denmark
[b] School of Civil Engineering, Tongji University, Shanghai 200092, PR China
[c] Department of Civil, Structural and Environmental Engineering, Trinity College Dublin, Dublin 2, Ireland

ARTICLE INFO

Article history:
Received 18 November 2013
Received in revised form
6 June 2014
Accepted 6 June 2014
Handling Editor: W. Lacarbonara
Available online 30 June 2014

ABSTRACT

Edgewise vibrations in wind turbine blades are lightly damped, and large amplitude vibrations induced by the turbulence may significantly shorten the fatigue life of the blade. This paper investigates the performance of roller dampers for mitigation of edgewise vibrations in rotating wind turbine blades. Normally, the centrifugal acceleration of the rotating blade can reach to a magnitude of 7–8g, which makes it possible to use this kind of damper with a relatively small mass ratio for suppressing edgewise vibrations effectively. The parameters of the damper to be optimized are the mass ratio, the frequency ratio, the coefficient of rolling friction and the position of the damper in the blade. The optimization of these parameters has been carried out on a reduced 2-DOF nonlinear model of the rotating wind turbine blade equipped with a roller damper in terms of a ball or a cylinder, ignoring the coupling with other degrees of freedom of the wind turbine. The edgewise modal loading on the blade has been calculated from a more sophisticated 13-DOF aeroelastic wind turbine model with due consideration to the indicated couplings, the turbulence and the aerodynamic damping. Various turbulence intensities and mean wind speeds have been considered to evaluate the effectiveness of the roller damper in reducing edgewise vibrations when the working conditions of the wind turbine are changed. Further, the optimized roller damper is incorporated into the 13-DOF wind turbine model to verify the application of the decoupled optimization. The results indicate that the proposed damper can effectively improve the structural response of wind turbine blades.

1. Introduction

Modern multi-megawatt wind turbines are designed with increasingly larger rotors in order to capture more energy throughout their lifetime and reduce the cost of energy. As the rotor diameters increase in size, the stiffness of the blades is not proportionally increased, which renders the blades more flexible and thus more sensitive to dynamic excitations. Traditionally, the modes of vibration in the blades are clarified as flap-wise and edgewise modes. Flap-wise vibrations are vibrations out of the plane of the rotating rotor, whereas edgewise vibrations take place in the rotor plane. Normally, modal damping in the flap-wise direction is relatively high due to the strong aerodynamic damping when the turbulent flow is attached to the blade [1]. Hence, the vibrations merely turn out to be quasi-static responses to the turbulence present in the

* Corresponding author. Tel.: +45 9226 6226.
E-mail addresses: zlz@civil.aau.dk (Z. Zhang), lijie@tongji.edu.cn (J. Li), soren.nielsen@civil.aau.dk (S.R.K. Nielsen), basub@tcd.ie (B. Basu).

http://dx.doi.org/10.1016/j.jsv.2014.06.006
0022-460X/

incoming wind. In contrast, edgewise vibrations are associated with insignificant aerodynamic damping [1,2] and may be prone to large dynamic responses. There is also a possibility of instability for some combinations of blade properties and operational conditions. This corresponds to the case in which the aerodynamic loads pump energy into the vibrational mode in the edgewise direction, and the sum of the structural damping and the aerodynamic damping becomes negative [3]. For all these reasons, the reduction of edgewise vibrations has become an increasingly active area of research in the wind power industry.

Structural control technologies, which have achieved significant success in mitigating vibrations of civil engineering structures, are being increasingly investigated for application in wind turbines in recent years. Most of these studies focus on the vibration control of wind turbine towers using external dampers [4–7]. Limited studies have been carried out regarding the structural control of blade vibrations. A semi-active tuned mass damper (TMD) is investigated in [8] for the control of flap-wise vibrations in wind turbine blades, although the modal damping in this direction is already very high due to the aerodynamic damping. Active TMDs have also been studied for the mitigation of edgewise vibrations in wind turbine blades, and the active TMD achieved greater response reductions than the passive TMD for the edgewise vibration [9]. An active strut mounted near the root of each blade has been proposed in [10] for the control of blade vibrations. The active control concept developed in this research is based on resonant interaction between the rotor and the controller, which is inspired by the concept of TMD. The use of active tendons mounted inside each blade is described in [11] for the active control of edgewise vibrations. The controller allows a variable control force to be applied in the edgewise direction, and the control forces are manipulated according to a prescribed control law. However, both semi-active and active control solutions need relatively complicated controller configurations and some amount of power input. This indicates the importance and necessity of developing simple and robust dampers for wind turbine blades. An earlier investigation on passive dampers in rotating wind turbine blades has been carried out by Anderson et al. [12]. A pendulum-typed passive damper was tested on an operational rotor, and the damper effectively mitigated edgewise stall vibrations of a 600 kW commercial wind turbine. However, no detailed analytical model was present for optimizing and designing the passive damper.

In this paper, roller dampers are proposed for passive control of edgewise vibrations in rotating wind turbine blades. This kind of damper was first proposed in [13] to control wind induced vibrations in two television towers. Recently, the roller damper was investigated in [7] for mitigating tower vibrations of offshore wind turbines, and both experimental and numerical results show the efficacy of roller dampers in reducing dynamic response of wind turbine towers. In the case of tower vibrations the control effect of the roller damper is governed by the gravitational acceleration g. For the rotating blade the corresponding control effect is governed by the centrifugal acceleration, which can reach up to a magnitude of 7–8g for a blade with a length of 65 m. This makes it possible to use the roller damper with rather small mass ratios for effectively suppressing edgewise vibrations. A similar idea has also been proposed by Basu et al. [14] using a liquid damper which consists of a circular tube partly filled with certain amount of liquid that could oscillate back and forth inside the tube. The main difference between the roller damper and the liquid damper is the dissipation mechanism. The inherent damping of the roller is due to the rolling friction between the surfaces, while the inherent damping of the liquid is due to the liquid passage through an orifice opening in the middle of the tube. The latter has its advantage that the damping property of the liquid damper can be controlled by changing the orifice opening, making the semi-active control solution possible. On the other hand, the roller damper has its advantage that the control efficiency can be enhanced by increasing the mass moment of inertia of the roller with a fixed physical mass.

The focus of the present paper is to carry out a comprehensive theoretical study on the performance of roller dampers in suppressing blade edgewise vibrations. First, a reduced 2-degree-of-freedom (2-DOF) nonlinear model based on an analytical dynamic formulation is established for a rotating blade with a roller damper mounted inside. The blade is modeled as a rotating cantilever beam using data calibrated to the National Renewable Energy Laboratory (NREL) 5 MW baseline wind turbine [15], and the coupling with other components of the wind turbine is ignored. The parameters of the damper to be optimized are the mass ratio, the frequency ratio, the coefficient of rolling friction and the mounting position of the damper along the blade. The optimization of these parameters has been carried out on the reduced 2-DOF model, with the modal loads obtained from a more sophisticated 13-DOF aeroelastic wind turbine model subjected to a 3-dimensional turbulence field. Parametric studies are also performed to evaluate the effect of the mass ratio and the mounting position on the performance of the roller damper. Based on these results, tradeoffs can be made when designing a roller damper in practical application. Moreover, various mean wind speeds, turbulence intensities and rotational speeds of the rotor have been considered to evaluate the effectiveness of the damper in reducing edgewise vibrations when the working condition of the wind turbine is changed. Finally, the optimized damper is incorporated into the 13-DOF aeroelastic model to verify the application of the decoupled optimization as well as the control effect of the damper in the highly coupled wind turbine system.

2. Aeroelastic model of the wind turbine system

A 13-DOF aeroelastic wind turbine model is presented in this section. The indicated model takes several important characteristics of a wind turbine into account, including time dependent system matrices, coupling of the tower-blades-drivetrain vibrations as well as nonlinear aeroelasticity. Fig. 1 shows a schematic representation of the wind turbine model with definitions of the coordinate system and the degrees of freedom. Motions of the structural components are described either in a fixed, global (X_1, X_2, X_3)−coordinate system, or in moving (x_1, x_2, x_3)−coordinate systems attached to each blade

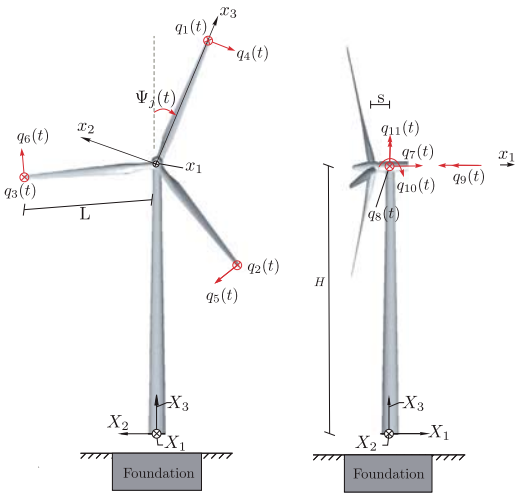

Fig. 1. 13-DOF aeroelastic model of three bladed wind turbine. Definition of fixed and moving frames of reference and the degrees of freedom $q_1(t), \ldots, q_{11}(t)$.

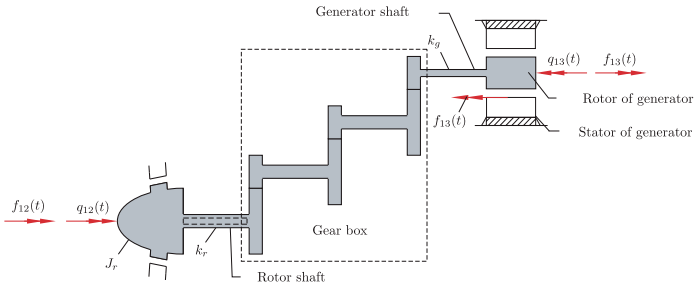

Fig. 2. 2-DOF model of flexible drivetrain with odd number of gear stages. Definition of degrees of freedom $q_{12}(t)$ and $q_{13}(t)$.

with origin at the center of the hub. The X_1- and x_1-axis are unidirectional to the mean wind velocity. The (X_2, X_3)- and (x_2, x_3)-coordinate planes are placed at the rotor plane. The X_3-axis is vertical, and the x_3-axis is placed along the undeformed blade axis oriented from the hub towards the blade tip. Moreover, the position of the local coordinated system attached to blade j is specified by the azimuthal angle $\Psi_j(t)$, which is considered positive when rotating clockwise seen from an upwind position.

Each blade is modeled as a Bernoulli–Euler beam with variable mass and stiffness per unit length, and is related with two degrees of freedom. $q_1(t), q_2(t), q_3(t)$ denote the flap-wise tip displacement of each blade in the positive x_1-direction. $q_4(t), q_5(t), q_6(t)$ denote the edgewise tip displacement of each blade in the negative x_2-direction. Further, the tower motion is defined by five degrees of freedom $q_7(t), \ldots, q_{11}(t)$. $q_7(t)$ and $q_8(t)$ signify the displacements of the tower at the height of the hub in the global X_1- and X_2-directions. $q_9(t)$ specifies the elastic rotation of the top of the tower in the negative X_1-direction, while $q_{10}(t)$ and $q_{11}(t)$ indicate the corresponding rotations in the positive X_2- and X_3-directions. The height of the tower from the base to the nacelle is denoted H, and the horizontal distance from the center of the tower top to the origin of the moving coordinate systems is denoted s.

The drivetrain is modeled by the degrees of freedom $q_{12}(t)$ and $q_{13}(t)$ (Fig. 2). The sign definition shown in Fig. 2 applies to a gearbox with odd number of stages. $q_{12}(t)$ and $q_{13}(t)$ indicate the deviations of the rotational angles at the hub and the generator from the nominal rotational angles Ωt and $N\Omega t$, respectively, where N is the gear ratio. Correspondingly, $\dot{q}_{12}(t)$ and $\dot{q}_{13}(t)$ are the deviations of the rotational speeds at the hub and the generator from the nominal values. In case of even number of stages the sign definitions for $q_{13}(t)$ and $f_{13}(t)$ are considered positive in the opposite direction. J_r and J_g denote

the mass moment of inertia of the rotor and the generator, and k_r and k_g denote the St. Venant torsional stiffness of the rotor shaft and the generator shaft.

Further, a full-span rotor-collective pitch controller is included with time delay modeled by a first-order filter. The pitch demand is modeled by a PI controller [16] with feedback from $\dot{q}_{12}(t)$ and $q_{12}(t)$. A gain-scheduled PI controller is used in this paper, i.e. the controller gains are dependent on the blade-pitch angle [15].

The Blade Element Momentum (BEM) with Prandtl's tip loss factor and Glauert correction is adopted to calculate aerodynamic forces along the blade [17]. Nonlinear aeroelasticity is considered by introducing the local deformation velocities of the blade into calculations of the flow angle and the angle of attack. As a result, this model possesses high aerodynamic damping in the blade flap-wise and the fore-aft tower vibrations, but relatively low aerodynamic damping in the blade edgewise and the lateral tower vibrations.

3. Theory of the reduced 2-DOF model for blade–damper system

The 13-DOF wind turbine model displays a highly coupled dynamical system. Lateral displacement and rotations of the tower around a horizontal line parallel to the mean wind direction will couple with the equations of motion of the edgewise blade vibration and the roller damper. Since we are interested in studying the interaction between the damper and the blade and the control effect of the damper on edgewise vibrations, we make the basic assumption for the following theory that the coupling between the tower and the blade can be ignored. Hence, only blade edgewise vibrations are considered, and the design of the damper is totally based on the local dynamics of the rotating blade.

3.1. Definition of the problem

Fig. 3 shows the schematic representation of a rotating blade equipped with a roller damper. The edgewise vibration of the blade is described in the moving (x_1, x_2, x_3)-coordinate system while the motion of the roller is described in the fixed global (X_1, X_2, X_3)-coordinate system. The mass per unit length and the bending stiffness in the edgewise direction of each blade are denoted $\mu(x_3)$ and $EI(x_3)$, respectively. The damper is merely devised to control the fundamental edgewise mode described by the degree of freedom $q_{3+j}(t)$, $j=1,2,3$, which is also a common practice when applying passive vibration control techniques.

The rotation of each blade is assumed to take place with a constant rotational speed Ω. Hence, the azimuthal angle $\Psi_j(t)$ for blade j is given as

$$\Psi_j(t) = \Omega t + \frac{2\pi}{3}(j-1), \quad j = 1, 2, 3 \tag{1}$$

In the following, only blade $j=1$ is considered since all three blades behave identical with the same geometrical and structural parameters. Consequently, all the subscripts j in Fig. 3 can be skipped, e.g. $q_{3+j}(t) = q(t)$ and $\Psi_j(t) = \Psi(t)$. Then, the local edgewise displacement $u_2(x_3, t)$ of the rotating blade in the x_2-direction can be described by the single modal coordinate $q(t)$ as

$$u_2(x_3, t) = -\Phi(x_3) q(t) \tag{2}$$

where $\Phi(x_3)$ indicates the fundamental fixed bay eigenmode of the edgewise vibration. This is normalized to 1 at the tip, i.e. $\Phi(L) = 1$, where L denotes the blade length.

The roller damper consists of a roller rolling inside an arc track. The mass and the mass moment of inertia around the gravitational center of the roller are denoted m and J, respectively. The radius of the roller and the outer radius of the track are denoted r and R, respectively. Depending on the available space inside the hollow blade, the track may be devised in the form of a complete circle or an arc. As shown in Fig. 3, the position of the damper mass inside the arc track is defined by the

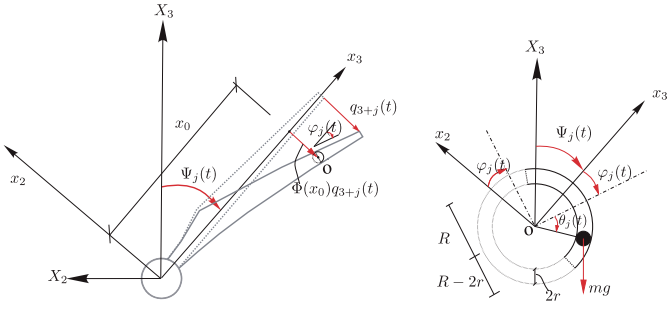

Fig. 3. Definition of coordinate systems, geometry and degrees of freedom.

clockwise rotation $\theta(t)$ from the deformed beam axis. Hence, $q(t)$ and $\theta(t)$ make up the degrees of freedom of this system. It is assumed that the damper is placed at the coordinate $x_3 = x_0$ in the blade. Then, the local displacement and rotation of the blade at this position with the sign definitions in Fig. 3 are given as

$$\left.\begin{aligned} u_{2,d}(t) &= -\Phi(x_0)q(t) \\ \varphi(t) &= \Phi'(x_0)q(t) \end{aligned}\right\} \tag{3}$$

where $\Phi'(x_0) = (\mathrm{d}/\mathrm{d}x_3)\Phi(x_3)|_{x_3 = x_0}$. For ease of notation the following auxiliary parameters are introduced:

$$\left.\begin{aligned} a &= \Phi(x_0) \\ b &= \Phi'(x_0) \end{aligned}\right\} \tag{4}$$

3.2. Local kinematics of the roller damper

Fig. 4 shows three possible layouts of the roller, i.e. a homogeneous ball, a homogeneous cylinder and a flywheel. The track for the ball or the cylinder as illustrated in Fig. 4(a) and (b) may be devised in the form of either a tube or a frame with four rails. A more efficient but less compact layout of the roller damper as shown in Fig. 4(c) consists of two small wheels with the radius r rolling on the rails and a flywheel with the radius R_0 attached in the middle of a massless bar. It is assumed that the wheels in contact to the rails may absorb negative contact forces if necessary. The mass αm of each rail wheel and the mass $(1-2\alpha)m$ of the flywheel are concentrated in the outer edge of the wheels. Hence in this case the mass moment of inertia of the roller around its mass center becomes $J = 2\alpha m r^2 + (1-2\alpha)mR_0^2$, which is larger than that of the ball or the cylinder with the same physical mass m.

For all these layouts, the roller damper is described by four parameters, i.e. r, R, m and J. In order to ease the notation as well as the following derivation of the equations of motion, these four parameters can be combined into merely two parameters as shown below, namely the equivalent mass m_e and the equivalent length R_e, which may be interpreted as the mass and length of an equivalent mathematical pendulum. The equivalent mathematical pendulum should represent the same kinetic and potential energy as the roller damper. As shown in Fig. 5, the kinetic energy of the roller mass during rotation can be written as

$$T = \tfrac{1}{2}m(R-r)^2\dot{\theta}^2 + \tfrac{1}{2}J(\dot{\alpha}+\dot{\theta})^2 \tag{5}$$

where α is the rotational angle of the roller relative to the line of gravity. By imposing a sufficient friction coefficient between the surfaces, sliding of the damper mass is prevented. Thus the relationship between α and θ is given by the

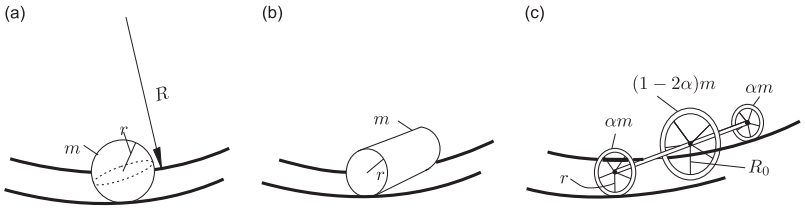

Fig. 4. Possible layouts of the roller damper. (a) Homogeneous ball, $J = \frac{2}{5}mr^2$, (b) homogeneous cylinder, $J = \frac{1}{2}mr^2$, (c) a flywheel and two small rail wheels, $J = 2\alpha mr^2 + (1-2\alpha)mR_0^2$.

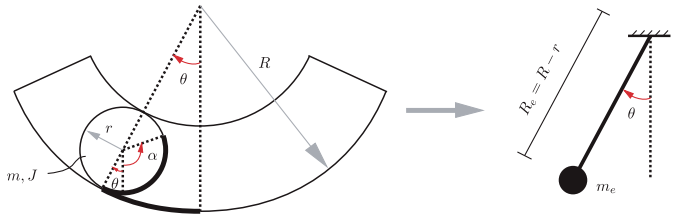

Fig. 5. Equivalent mathematical pendulum for the roller damper.

kinematical relation (see Fig. 5):

$$r(\alpha+\theta)=R\theta \quad \Rightarrow \quad r\alpha=(R-r)\theta \quad \Rightarrow \quad \dot{\alpha}=\frac{R-r}{r}\dot{\theta} \tag{6}$$

Substituting Eq. (6) into Eq. (5), the kinetic energy becomes

$$T=\frac{1}{2}\left(m+\frac{J}{r^2}\frac{R^2}{(R-r)^2}\right)(R-r)^2\dot{\theta}^2=\frac{1}{2}m_eR_e^2\dot{\theta}^2 \tag{7}$$

where

$$m_e=m+\frac{J}{r^2}\frac{R^2}{(R-r)^2}, \quad R_e=R-r \tag{8}$$

m_e can be regarded as a measure of the control efficiency of the damper. The larger the value of m_e is, the higher efficiency is achieved by the roller damper. For a given physical mass m of the roller, the value of m_e can be increased by increasing J. In this respect, the ball damper shown in Fig. 4(a) is less efficient than the cylinder in Fig. 4(b), which in turn is less efficient than the device shown in Fig. 4(c). It should be noted that m_e is only used for calculating the kinetic energy of the system. The potential energy for both systems in Fig. 5 is given by

$$V=mg(R-r)(1-\cos\ \theta)=mgR_e(1-\cos\ =\theta) \tag{9}$$

Here the physical mass m is used since the potential energy is always related to the gravity of an object. In the following derivations of the equations of motion of the 2-DOF system, m_e and R_e are used to calculate the kinetic energy, and m and R_e are used to calculate the potential energy of the system.

3.3. Modeling and analysis of the 2-DOF system

Fig. 6 shows the reduced 2-DOF model for a blade equipped with a roller damper, where the roller damper is represented by the mathematical pendulum. It should be noted that the equivalent length R_e ($R_e \ll x_0$) is locally amplified in the figure in order to clarify the geometry, which is helpful in deriving the kinetic and potential energy of the system. With sign definitions in Fig. 6, the velocity components of the blade in the moving (x_2,x_3)−coordinate system can be written as

$$\left.\begin{aligned} v_2(x_3,t)&=-\Omega x_3-\Phi(x_3)\dot{q}(t)\\ v_3(x_3,t)&=-\Omega\Phi(x_3)q(t)\end{aligned}\right\} \tag{10}$$

The components of the position vector and velocity vector of the damper mass in the fixed global (X_2,X_3)−coordinate system are given by

$$\left.\begin{aligned} X_{2,d}(t)&=-x_0\ \sin\ \Psi-aq\ \cos\ \Psi-R_e\ \sin\ (\Psi+\varphi+\theta)\\ X_{3,d}(t)&=x_0\ \cos\ \Psi-aq\ \sin\ \Psi+R_e\ \cos\ (\Psi+\varphi+\theta)\end{aligned}\right\} \tag{11}$$

$$\left.\begin{aligned} V_{2,d}(t)&=-(x_0\Omega+a\dot{q})\cos\ \Psi+aq\Omega\ \sin\ \Psi-R_e(\Omega+\dot{\varphi}+\dot{\theta})\cos(\Psi+\varphi+\theta)\\ V_{3,d}(t)&=-(x_0\Omega+a\dot{q})\sin\ \Psi-aq\Omega\ \cos\ \Psi-R_e(\Omega+\dot{\varphi}+\dot{\theta})\sin(\Psi+\varphi+\theta)\end{aligned}\right\} \tag{12}$$

The total kinetic energy of the system (i.e. one blade and one roller damper) becomes

$$T=\frac{1}{2}\int_0^L\mu(x_3)\left(v_2^2(x_3,t)+v_3^2(x_3,t)\right)\,\mathrm{d}x_3+\frac{1}{2}m_e\left(V_{2,d}^2(t)+V_{3,d}^2(t)\right)$$

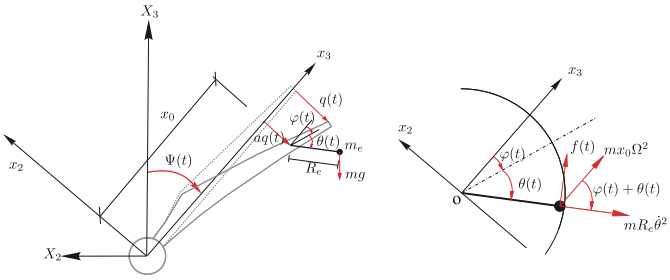

Fig. 6. Schematic diagram of the reduced 2-DOF model.

$$= \frac{1}{2}m_0(\dot{q}^2+\Omega^2q^2)+m_1\Omega\dot{q}+\frac{1}{2}\Omega^2m_2$$
$$+\frac{1}{2}m_e[(x_0\Omega+a\dot{q})^2+a^2q^2\Omega^2+R_e^2(\Omega+b\dot{q}+\dot{\theta})$$
$$+2R_e(\Omega+b\dot{q}+\theta)((x_0\Omega+a\dot{q})\cos(bq+\theta)+aq\Omega\ \sin(bq+\theta))] \tag{13}$$

where $m_0=\int_0^L \mu(x_3)\Phi^2(x_3)\,\mathrm{d}x_3$ denotes the modal mass of the blade. Further, $m_1=\int_0^L \mu(x_3)x_3\Phi(x_3)\,\mathrm{d}x_3$, $m_2=\int_0^L \mu(x_3)x_3^2\,\mathrm{d}x_3$. The total potential energy of the system is

$$U=mg(x_0\ \cos\ \Psi-aq\ \sin\ \Psi+R_e\ \cos(\Psi+bq+\theta))+\tfrac{1}{2}k_0q^2 \tag{14}$$

where g is the acceleration of gravity, and k_0 denotes the modal stiffness of the blade including the geometric stiffness effect from centrifugal accelerations. k_0 is expressed as

$$k_0=\int_0^L\left(EI(x_3)\left(\frac{\mathrm{d}^2\Phi(x_3)}{\mathrm{d}x_3^2}\right)^2+F(x_3)\left(\frac{\mathrm{d}\Phi(x_3)}{\mathrm{d}x_3}\right)^2\right)\mathrm{d}x_3 \tag{15}$$

where $F(x_3)=\Omega^2\int_{x_3}^L \mu(\xi)\xi\,\mathrm{d}\xi$ is the centrifugal axial force per unit length along the blade. Thus the fundamental angular eigenfrequency of the blade can be obtained as

$$\omega_0=\sqrt{\frac{k_0}{m_0}} \tag{16}$$

As the damper mass rolls along the track, a friction force $f(t)$ takes place due to the rolling friction between the contacting surfaces. The magnitude of this force is proportional to the normal force acting on the roller through the track. In a rotating blade, this normal force is governed by the centrifugal force since it is much larger than the gravity force. As shown in Fig. 6, the total normal force on the damper mass can be expressed as

$$N(t)=mR_e\dot{\theta}^2+mx_0\Omega^2\cos(bq+\theta) \tag{17}$$

Then, the friction force $f(t)$ can be given by

$$f(t)=\mu(mR_e\dot{\theta}^2+mx_0\Omega^2\ \cos(bq+\theta))\mathrm{sign}(\dot{\theta}) \tag{18}$$

where μ is the coefficient of rolling friction between the surfaces. A reaction force in the opposite direction is acting on the track which is fixed inside the blade. The projection of this force on the blade in the negative x_2-direction becomes co-directional to the degree of freedom $q(t)$. The modal load from this reaction force can be expressed as

$$f_r(t)=a\mu(mR_e\dot{\theta}^2+mx_0\Omega^2\ \cos(bq+\theta))\cos(bq+\theta)\mathrm{sign}(\dot{\theta}) \tag{19}$$

where a is defined in Eq. (4). Then the generalized loads for each DOF are given by

$$F_q(t)=f_0(\dot{q},t)-c_0\dot{q}+f_r(t)$$
$$F_\theta(t)=-f(t)R_e=-\mu R_e(mR_e\dot{\theta}^2+mx_0\Omega^2\ \cos(bq+\theta))\mathrm{sign}(\dot{\theta}) \tag{20}$$

where $f_0(\dot{q},t)$ denotes the turbulence induced modal load on the blade considering aerodynamic damping and couplings between the blade with other components of the wind turbine, and $c_0\dot{q}$ indicates the linear viscous damping load. $f_0(\dot{q},t)$ is calculated using the more sophisticated 13-DOF aeroelastic wind turbine model introduced in the previous section. $c_0=2\zeta_0m_0\omega_0$ indicates the modal damping coefficient of the primary structure, ζ_0 is the related modal damping ratio.

It can be proved that the magnitude of $f_r(t)$ is much smaller than that of $f_0(\dot{q},t)$ and $c_0\dot{q}$, thus this term is ignored in the following derivation.

Using Eqs. (12), (13) and the two generalized loads, the equations of motion of this 2-DOF system can be obtained from the stationarity conditions of the Euler–Lagrange equations [18]:

$$\frac{\mathrm{d}}{\mathrm{d}t}\left(\frac{\partial T}{\partial\dot{q}}\right)-\frac{\partial T}{\partial q}+\frac{\partial U}{\partial q}=f_0(\dot{q},t)-c_0\dot{q}$$
$$\Rightarrow(m_0+m_e(a^2+R_e^2b^2))\ddot{q}+m_eR_e^2b\ddot{\theta}+c_0\dot{q}+(k_0-\Omega^2(m_0+m_ea^2)ig)q$$
$$+m_eR_e(2ab\ddot{q}+a\ddot{\theta}-ab\Omega^2q)\cos(bq+\theta)-m_eR_e((a-bx_0)\Omega^2+2a\Omega\dot{\theta}+a(b\dot{q}+\dot{\theta})^2)\sin(bq+\theta)$$
$$-mg(a\ \sin\ (\Omega t)+bR_e\ \sin(\Omega t+bq+\theta))=f_0(\dot{q},t) \tag{21}$$

$$\frac{\mathrm{d}}{\mathrm{d}t}\left(\frac{\partial T}{\partial\dot{\theta}}\right)-\frac{\partial T}{\partial\theta}+\frac{\partial U}{\partial\theta}=F_\theta(t)$$
$$\Rightarrow m_eR_eb\ddot{q}+m_eR_e\ddot{\theta}+\mu(mR_e\dot{\theta}^2+mx_0\Omega^2\ \cos(bq+\theta))\mathrm{sign}(\dot{\theta})$$
$$+m_ea(\ddot{q}-\Omega^2q)\cos(bq+\theta)+m_e(2a\Omega\dot{q}+\Omega^2x_0)\sin(bq+\theta)$$
$$-mg\ \sin\ (\Omega t+bq+\theta)=0 \tag{22}$$

In the following numerical simulations, Eqs. (21) and (22) are solved directly instead of carrying out linearization. There are two reasons for avoiding linearization. Firstly, it may be impossible to perform linearization of the nonlinear equations of motion in some cases when the value of θ is large. Secondly, even if linearization has been performed, there still remain some parametric-excited terms and hence time-varying system parameters in the equations of motion. To obtain the system responses accurately, numerical integration is still needed as in the nonlinear case, making the linearization meaningless.

To calculate the angular eigenfrequency of the roller when it is rolling in the vicinity of the equilibrium position, we set $q(t)=0$ and assume small values of $\theta(t)$ in Eq. (22), resulting in the following equation:

$$m_e R_e \ddot{\theta}(t)+\mu(mR_e\dot{\theta}^2+mx_0\Omega^2)\mathrm{sign}(\dot{\theta})+m_e\Omega^2 x_0\theta(t)-mg\ \sin(\Omega t+\theta(t))=0 \tag{23}$$

Ignoring the influence of gravity, the angular eigenfrequency of the roller can be calculated from Eq. (23) as

$$\omega_d=\sqrt{\frac{m_e\Omega^2 x_0}{m_e R_e}}=\sqrt{\frac{x_0\Omega^2}{R_e}} \tag{24}$$

It is shown that the motion of the roller is controlled by the centrifugal acceleration $x_0\Omega^2$, which is much larger than g if x_0 is large enough. Normally, the roller damper should be devised such that $\omega_d \simeq \omega_0$. This can be achieved by adjusting R_e when the rotational speed of the rotor Ω and the position of the damper x_0 are fixed.

From Eqs. (21) and (22), it can be seen that the performance of the roller damper is affected by parameters m, ω_d, μ and x_0, which need to be optimized when designing this kind of damper for different wind turbines. The optimization procedure will be carried out directly on this 2-DOF nonlinear model, with the turbulence induced modal loads $f_0(\dot{q},t)$ as the external excitation. It should be noted that in the optimization the couplings of the blade edgewise vibration to other degrees of freedom are ignored. But the decoupled optimization will be verified by incorporating the damper into the highly coupled 13-DOF wind turbine model.

The reduction ratio η is defined as

$$\eta=\frac{\sigma_{q,0}-\sigma_q}{\sigma_{q,0}} \tag{25}$$

where $\sigma_{q,0}$ and σ_q are the standard deviations of the edgewise tip displacements of the blade without and with control, respectively. The optimal parameters of the roller damper can be found by maximizing the reduction ratio.

4. Numerical simulations

The NREL 5 MW baseline wind turbine [15] is utilized to calibrate both the 13-DOF and 2-DOF models. In both models, each blade has a length of 63 m and an overall mass of 17 740 kg. Eight different airfoil profiles are used for the blade from hub to tip, the lift and drag coefficients of which are obtained from wind tunnel test. The related data of modal shapes, the bending stiffness, the mass per unit length of the blade can also be found in [15].

In agreement with [19], the turbulence modeling is based on Taylor's hypothesis of frozen turbulence, corresponding to a frozen filed convected into the rotor plane in global X_1-direction with a mean velocity V_0 and a turbulence intensity I. The turbulence intensity is defined as $I=\sigma_v/V_0$, where σ_v is the standard deviation of the turbulence component in the mean wind direction. The frozen field is assumed to be homogeneous and isotropic, with a covariance structure given by [20]. Calibrated from this theoretical covariance structure, the first-order AR model as proposed by [10] performs a first-order filtering of the white noise input, resulting in continuous, non-differentiable sample curves of the turbulence field at the rotor plane. Next, the turbulence encountered in the moving frame of reference fixed to the rotating blade is obtained by linear interpolation between the turbulence at different grid points in the fixed frame of reference, resulting in the rotational sampled turbulence. Due to the longitudinal correlation of the incoming turbulence, a periodicity is present as spectral peaks at 1Ω, 2Ω, $3\Omega\cdots$ in the auto-spectrum density function of the rotational sampled turbulence.

By applying this turbulence field to the rotor of the 13-DOF wind turbine, we can obtain edgewise modal loads for each blade. The calculated modal load $f_0(\dot{q},t)$ is exerted to the 2-DOF model, based on which the optimization and parametric studies of the damper are to be carried out. In the simulation, the fourth-order Runge–Kutta method was applied to solve the nonlinear ordinary differential equations of the 2-DOF system.

4.1. Optimization and parametric study of the damper

Using data from the NREL baseline wind turbine, the constant parameters employed in the reduced 2-DOF model are calculated and illustrated in Table 1. The parameters of the damper to be determined are the mass m, the frequency ω_d, the coefficient of rolling friction μ and the mounting position x_0 along the blade. Since the control effect of the proposed damper is dominated by the centrifugal acceleration $x_0\Omega^2$, it is expected that we can obtain better control effect by mounting the damper closer to the blade tip. On the other hand, the available space inside the blade is decreasing towards tip, which makes the determination of x_0 a practical tradeoff problem. In the following optimization procedure x_0 is set to be 45 m, which means that the damper is mounted at a position approximately $\frac{2}{3}$ of the total blade length. The effect of various values of x_0 on the performance of the damper will also be investigated later. Furthermore, it is well known that the larger mass

Table 1
Parameters in the 2-DOF blade–damper model.

Parameter	Value	Unit
m_0	1.3×10^3	kg
k_0	5.8×10^4	N m^{-1}
ω_0	6.67	rad s^{-1}
ζ_0	0.005	–
L	63	m
Ω	1.27	rad s^{-1}
g	9.81	m s^{-2}

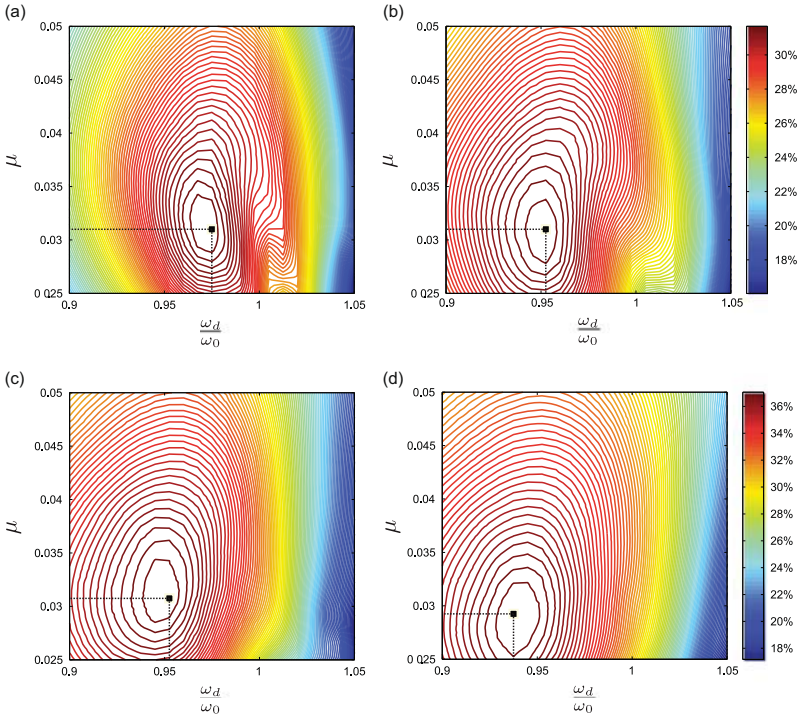

Fig. 7. Contour diagrams of the reduction ratios for optimization of ω_d and μ, $V_0=15$ m s^{-1}, I=0.1, $x_0=45$ m. (a) $m=0.01m_0$, optimization results: $\omega_d=0.975\omega_0$, $\mu=0.0312$, $\eta=26.79$ percent, R_e=1.703 m, (b) $m=0.02m_0$, optimization results: $\omega_d=0.952\omega_0$, $\mu=0.0310$, $\eta=31.84$ percent, R_e=1.785 m, (c) $m=0.03m_0$, optimization results: $\omega_d=0.952\omega_0$, $\mu=0.0308$, $\eta=34.79$ percent, R_e=1.785 m, (d) $m=0.04m_0$, optimization results: $\omega_d=0.938\omega_0$, $\mu=0.0295$, $\eta=37.26$ percent, R_e=1.842 m. (For interpretation of the references to color in this figure caption, the reader is referred to the web version of this paper.)

ratio m/m_0 would give a better control performance for a passive damper. However the damper mass should be limited according to the construction and maintenance considerations. Thus four sets of mass ratios are considered in the optimization procedure, i.e. $m=0.01m_0$, $m=0.02m_0$, $m=0.03m_0$, $m=0.04m_0$. In the simulation, only a ball is considered for the roller damper. Since the equivalent mass of a cylinder or a flywheel is larger than that of a ball, it is expected that a cylinder or a flywheel could obtain a better control effect comparing with a ball, and actually the results obtained in the simulation are conservative. With m_0=1300 kg, the roller mass will vary between 13 kg and 52 kg. For each assigned value of the mass ratio, we search for the optimal value of the turning ratio ω_d/ω_0 and the optimal value of the friction coefficient μ by maximizing the value of η.

Fig. 7 shows the 2-dimensional numerical optimization results of ω_d/ω_0 and μ for various mass ratios and a given x_0. The modal load is calculated from a turbulence field with a mean wind speed of 15 m s^{-1} and a turbulence intensity of 0.1. The color bar indicates the reduction ratio η by the damper. It can be seen from Fig. 7 that different mass ratios require different

optimal values for the frequency ratio and the friction coefficient. As the mass ratio increases from 1 percent to 4 percent, the optimal value of ω_d/ω_0 decreases from 0.975 to 0.938, and the optimal value of μ decreases very slightly from 0.0312 to 0.0295. As expected, the corresponding maximum reduction ratio increases from 26.79 percent for $m=0.01m_0$ to 37.26 percent for $m=0.04m_0$. It can also be seen in Fig. 7(a) that a local maxima exists at the right side of the optimal point, due to the nonlinearity of the system. As the mass ratio increases, no local maxima can be observed anymore. Moreover, the increase of the mass ratio broadens the read areas in the contour diagram. This means that the detuning of ω_d/ω_0 and μ becomes less sensitive with larger mass ratios, and acceptable control effect can be obtained at a wider range of parameter variations.

If the roller damper parameters shift away from their respective optimal values, the control effect is expected to degrade. Fig. 8(a) shows the effect of detuning of the frequency ratio, where the optimal values of μ obtained from Fig. 7 are used for different mass ratios. The value of η decreases faster when ω_d/ω_0 shifts towards larger values compared with that towards smaller values and it becomes very small when the frequency ratio is larger than 1. This means that the detuning effect of ω_d/ω_0 is more pronounced when it shifts from the optimal value towards larger values and the damper is more robust in the frequency range of $0.9<\omega_d/\omega_0<1$. Fig. 8(b) shows the effect of various values of friction coefficient on the damper performance with the optimal values of ω_d/ω_0. The detuning effect of μ is more pronounced when it shifts towards 0. As long as the friction coefficient is set to be larger than 0.02, reduction ratio of the edgewise vibration is not very sensible to the value of μ. Acceptable control effect can always be obtained when μ is set between 0.025 and 0.05. This is favorable when the friction coefficient between the roller and the circular tube increases slightly due to corrosion during the operational period.

Fig. 9 shows the influence of the mounting position and the mass ratio on the mitigation effect of the roller damper. Optimal values of ω_d/ω_0 and μ have been used for each value of m. Fig. 9(a) shows an expected result that a damper mounted closer to the tip can reduce the edgewise vibration more efficiently, owing to the larger centrifugal acceleration. As

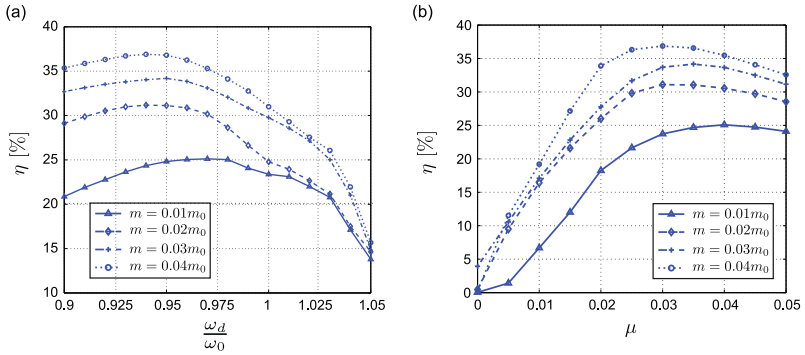

Fig. 8. Effect of detuning, $V_0=15$ m s^{-1}, $I=0.1$, $x_0=45$ m. (a) Reduction ratio versus ω_d/ω_0 for various mass ratios, μ optimal for each value of m. (b) Reduction ratio versus μ for various mass ratios, ω_d/ω_0 optimal for each value of m.

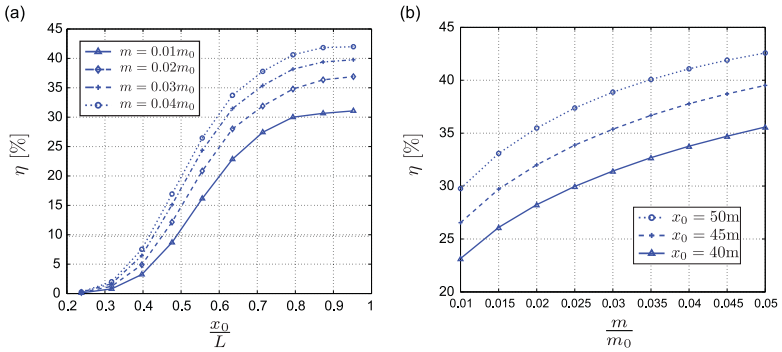

Fig. 9. Influence of the damper position and the mass ratio on the reduction ratio, $V_0=15$ m s^{-1}, $I=0.1$, ω_d and μ optimal for each value of m. (a) Reduction ratio versus x_0/L for various mass ratios, (b) reduction ratio versus m_0/m for various mounting positions.

x_0/L goes below 0.5, the control effect is not acceptable even though the mass ratio is large. The control effect increases rapidly as the value of x_0/L goes up to around 0.7, but it is not improved much as x_0/L increases further. This is a favorable observation since practically it is difficult to mount a damper in the vicinity of the blade tip due to lack of space. Fig. 9(b) indicates a well known result that as the mass ratio increases the control effect increases. However, one valuable observation is that the increase of the reduction ratio is not proportional to the increase of the mass ratio. For example, as the mass ratio goes from 0.02 to 0.05 (increased by 150 percent) for the case of $x_0 = 45$ m, the reduction ratio is only improved from 31.84 percent to 38.94 percent (increased by 22.30 percent). Considering the ease of maintenance and the improvement of control performance, it is not worthwhile to devise a damper with large mass ratios. When mounted at the position between 40 m and 50 m along the blade, a damper with a mass ratio of 0.02 (m=26 kg) can always achieve reasonably good control effect.

The motion of the roller is also investigated in various cases. Fig. 10(a) and (b) corresponds to the reduction ratios in Fig. 8(b) and (a), respectively. As shown in Fig. 10(a) the increase of the friction coefficient μ will reduce the maximum rotational angle $\theta(t)$ of the roller. The motion of the roller varies slightly as long as μ is set to be larger than 0.01. Fig. 10(b) shows that a closer mounting position of the damper to the tip will result in a more drastic motion of the roller for a given mass ratio. This explains the result in Fig. 9(a) that better control performance can be obtained when the damper is set closer to the tip, since a roller having more drastic motions absorbs more energy from the structural response. Again, the mass ratio effect is observed that a damper with a bigger mass ratio can achieve a better mitigation effect with a lower roller peak response. Further, it can be seen that the maximum rotational angle varies from 0.3 rad to 0.95 rad (17–54.4°) when optimal damper parameters are applied. This means that the rolling motion of the damper mass only takes place in a part of the circle, making it possible to devise a damper with an arc tube or a finite segment of the circular track. This becomes necessary in the present case, where R_e varies from 1.703 m to 1.842 m according to the results of Fig. 7, and the chord of the blade section at $x_0 = 45$ m is about 3 m [15].

4.2. Performance of the damper

Fig. 11 presents the control performance of the roller damper on the blade edgewise vibration, when $V_0 = 15$ m s^{-1} and I=0.1. The mass ratio is 0.02 and the mounting position of the damper is 45 m. Further, the optimal values of ω_d and μ are utilized. It is observed from Fig. 11(a) that a damper with a mass of 26 kg significantly improves the dynamic response of the blade. The maximum edgewise tip displacement is reduced from 0.770 m to 0.637 m (reduced by 17.27 percent), and the standard deviation is reduced from 0.1684 m to 0.1148 m (reduced by 31.84 percent). The Fourier amplitude spectrum of $q(t)$ as presented in Fig. 11(b) shows that the roller damper effectively suppresses the peak around 6.67 rad s^{-1} corresponding to the eigenvibration of the blade in edgewise direction. This means that a properly designed roller damper could almost totally absorb energy from the eigenvibration of the blade. However, a low peak around 1.27 rad s^{-1} is hardly affected by the roller. This is associated with the rotational speed of the blade, and the roller damper is not functioning at this frequency. It should be noted that much more energy is concentrated around the frequency of 6.67 rad s^{-1} for the uncontrolled response since aerodynamic damping is low in the edgewise direction. As a result, although not functioning around the frequency of Ω, a well tuned roller damper still exhibits promising performance in suppressing edgewise vibrations in a rotating wind turbine blade.

Fig. 11(c) illustrates the time history of the rotational angle of the roller damper with a mean value of $\theta(t) = 0$. The maximum rotational angle of the roller is 0.6287 rad, which means that the motion of the roller is restricted within a small segment of a circle. Fig. 11(d) shows the Fourier amplitude spectrum of $\theta(t)$. A clear peak corresponding to the rotational

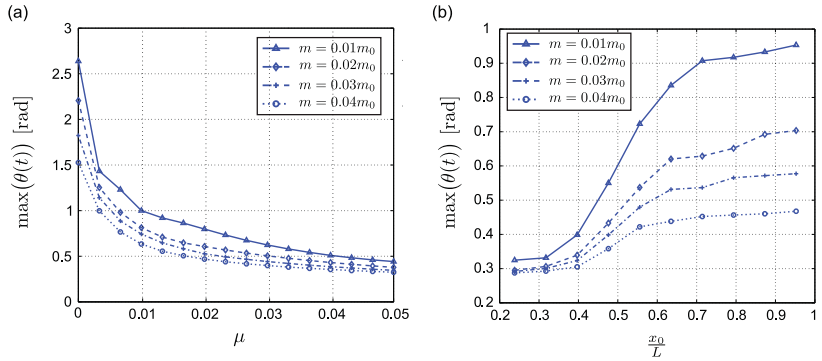

Fig. 10. Maximum rotational angle of the roller in various cases, $V_0 = 15$ m s^{-1}, I=0.1. (a) Maximum angle versus μ, ω_d optimal for each value of m, (b) maximum angle versus x_0/L, ω_d and μ optimal for each value of m.

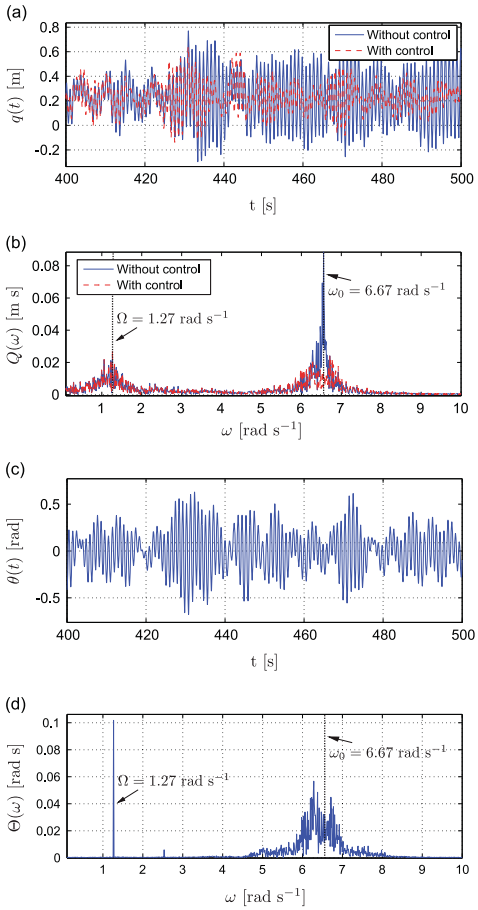

Fig. 11. Control performance of the roller damper, $V_0 = 15$ m s^{-1}, I=0.1, $m = 0.02m_0$, $x_0 = 45$ m, optimal ω_d and μ, R_e=1.785 m. (a) Time series of the edgewise vibration, (b) Fourier amplitude of the edgewise vibration, (c) time series of the roller motion, (d) Fourier amplitude of the roller motion.

speed of the rotor is observed, which can be explained by the last term in Eq. (22). Moreover, two low peaks can be observed at two sides of the fundamental edgewise frequency, which displays the angular eigenfrequencies of the 2-DOF system.

It is of importance to study the performance of roller dampers when the working condition of the wind turbine is changed. In the following, different combinations of V_0 and I are investigated to evaluate the control effect of the roller damper with optimal parameters determined from the case of $V_0 = 15$ m s^{-1} and I=0.1.

The cut-in, cut-out and rated wind speed of the NREL 5-MM wind turbine are 3 m s^{-1}, 25 m s^{-1} and 11.4 m s^{-1}, respectively. With the functioning of the pitch controller, the mean rotational speed of the rotor keeps constant for mean wind speeds ranging from 11.4 m s^{-1} to 25 m s^{-1}. Fig. 12 shows the edgewise tip displacement of the blade when $V_0 = 25$ m s^{-1} and I=0.1. The roller damper again works well in this case. There is a reduction of 30.72 percent in the maximum value and a reduction of 26.38 percent in the standard deviation of $q(t)$ by installing a roller damper in the blade. Similarly, the frequency component corresponding to eigenvibration of the blade is almost totally eliminated by the damper. Further, Fig. 13 shows the result in the case of the rated wind speed V_0=11.4 m s^{-1} with the same turbulence intensity. The optimized damper achieves similar performance as in the previous cases, with a reduction of 21.98 percent in the maximum value and a reduction of 26.52 percent in the standard deviation. It is observed that in all cases, the mean value of $q(t)$ with or without control remains identical, which equals to 0.240 m, 0.225 m, 0.118 m for V_0=11.4 m s^{-1}, 15 m s^{-1}, 25 m s^{-1}, respectively. The reason for the decreased mean edgewise displacement with the increased mean wind speed is that the pitch angle tends to be increased as V_0 increases from the rated speed to the cut-out speed, so that a constant rated power

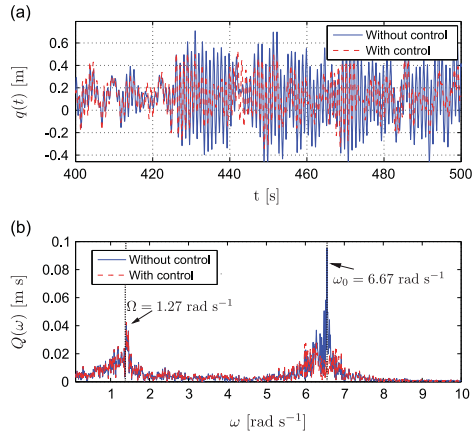

Fig. 12. Blade edgewise vibrations with and without the roller damper, $V_0 = 25$ m s^{-1}, $I = 0.1$, $m = 0.02m_0$, $x_0 = 45$ m, $R_e = 1.785$ m, $\mu = 0.031$. (a) Time series, (b) Fourier amplitude.

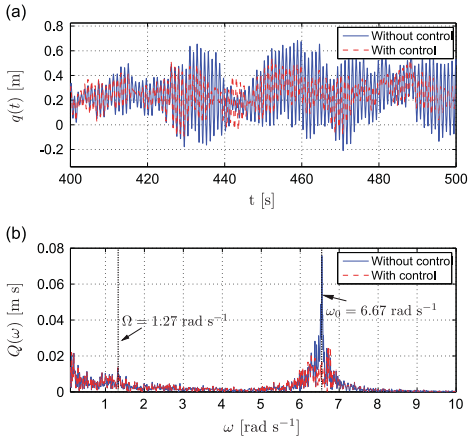

Fig. 13. Blade edgewise vibrations with and without the roller damper, $V_0 = 11.4$ m s^{-1}, $I = 0.1$, $m = 0.02m_0$, $x_0 = 45$ m, $R_e = 1.785$ m, $\mu = 0.031$. (a) Time series, (b) Fourier amplitude.

(5 MW in this case) is produced. With increased pitch angle, the mean values of the angles of attack along the blade and hence the mean modal loads are reduced. This is typical for the variable speed, pitch regulated wind turbines.

The turning of the roller damper is based on the rated rotational speed of the rotor (1.27 rad/s). As the blade rotational speed varies, e.g. when V_0 is below rated, or during the starting up or closing down procedures of the wind turbine, the control efficiency of the roller damper is expected to be reduced due to the frequency detuning. Table 2 shows the influence of the blade rotational speed on the values of ω_0, ω_d and the control efficiency of the roller damper. It is seen that ω_0 is slightly reduced as Ω decreases since the centrifugal axial force and hence k_0 are reduced, as indicated by Eq. (14). With fixed x_0 and R_e, ω_d decreases significantly with decreased Ω, resulting in more pronounced frequency detuning of the roller damper. Consequently, the reduction ratio of the damper is significantly reduced from 31.84 percent to 6.21 percent when Ω decreases from 1.27 rad s^{-1} to 0.8 rad s^{-1}.

Larger values of the turbulence intensity imply larger amplitude vibrations of the blade. As I increases from 0.1 to 0.3, the standard deviation of the uncontrolled edgewise vibration increases from 0.1684 m to 0.3915 m. Nevertheless, the roller damper works similarly well as in Fig. 11. However, by increasing I further to the value of 0.35, one can observe an interesting phenomenon of the damper performance. As shown in Fig. 14(a), the blade instantaneously vibrates at high amplitudes and the damper has ceased working in the interval between 200 s and 300 s, where the response of the

Table 2
Influence of the blade rotational speed on ω_0, ω_d and the damper performance.

Ω (rad/s)	ω_0 (rad/s)	ω_d (rad/s)	η (%)
1.27	6.679	6.362	31.84
1.20	6.639	6.025	27.53
1.15	6.627	5.774	23.09
1.10	6.610	5.523	19.37
1.05	6.598	5.272	15.82
1.00	6.587	5.021	13.20
0.95	6.575	4.770	11.01
0.90	6.563	4.519	9.45
0.85	6.552	4.268	7.79
0.80	6.540	4.017	6.21

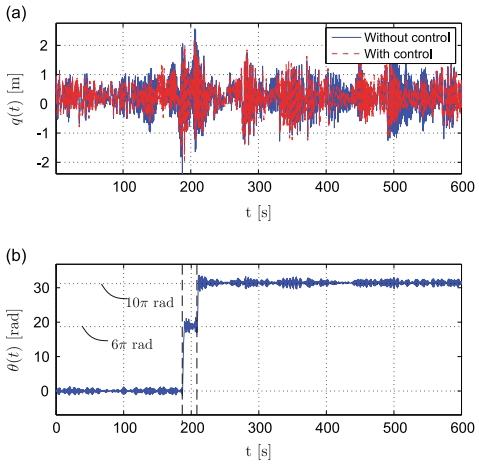

Fig. 14. Performance of the roller damper, $V_0 = 15\ \mathrm{m\,s^{-1}}$, I=0.35, $m = 0.02m_0$, $x_0 = 45$ m, R_e=1.785 m, μ=0.031. (a) Time series of the edgewise tip displacement, (b) time series of the rotational angle of the roller.

controlled system is even increased. This can be explained by the time series of the rotational angle of the roller illustrated in Fig. 14(b). The strong turbulence enforces the roller to perform 3 clockwise full rotations of a magnitude 2π at t=190 and 2 clockwise full rotations at t=210. As seen, the reestablishment of the damping effect on the blade requires almost one minute after the roller starts to move forth and back again around the equilibrium position. It should be noted that due to the symmetry of the roller damper about its center, both clockwise and counterclockwise full rotations can take place, depending on the vibration of the blade and hence the turbulence field applied to the rotor. Since the turbulence is stochastic, the direction of the full rotational is also random. The results in Fig. 14 correspond to the turbulence field used in that specific simulation. Using different realizations of the turbulence field, the roller may have counterclockwise full rotations. Obviously, such full rotations of the roller are unfavorable for control of edgewise vibrations. In reality, a turbulence intensity of 0.35 might be encountered when a wind turbine is placed in the wake of other wind turbines. In such situations, the control efficiency of the roller damper is expected to be reduced compared with the cases when I is less than 0.35.

Further, for some combinations of blade properties and operational conditions, the sum of the structural damping and the aerodynamic damping becomes negative, and aeroelastic instability may take place in the edgewise direction. In this case, the blade vibrates at the first edgewise eigenfrequency with exponentially increasing amplitude. Since the vibrational energy is completely concentrated in the first edgewise mode, the roller damper which is tuned to this frequency will effectively add damping into this mode, resulting in a more stable system.

4.3. Evaluation by the 13-DOF aeroelastic wind turbine model

To verify the applicability of the decoupled optimization and the control effect of the damper in highly coupled wind turbine systems, the optimized damper is incorporated into the 13-DOF aeroelastic wind turbine model. For each blade, a roller damper is mounted at the position of $x_0 = 45$ m. Therefore, a 16-DOF system is obtained for the wind turbine with totally

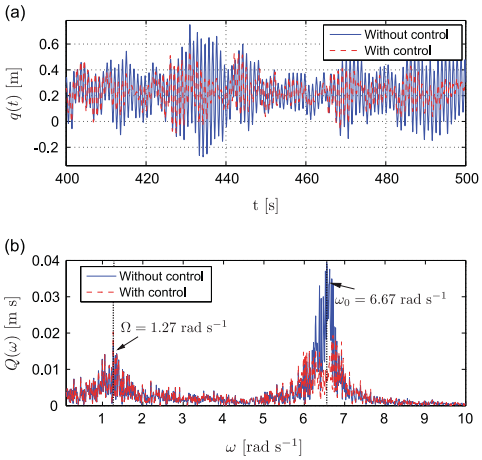

Fig. 15. Blade edgewise vibrations with and without the roller damper, obtained from the 16-DOF model. $V_0 = 15$ m s^{-1}, I=0.1, $m = 0.02m_0$, $x_0 = 45$ m, R_e=1.785 m, μ=0.031. (a) Time series, (b) Fourier amplitude.

Table 3
Effects of the roller damper on other degrees of freedom (std: standard deviation).

Cases	q_1 (m)	q_7 (m)	q_8 (m)	$\dot{q}_{12}$ (rad/s)	Pitch angle (rad)
std without damper	0.9732	0.0759	0.0145	0.0149	0.04519
std with damper	0.9738	0.0760	0.0143	0.0147	0.04522

three roller dampers installed. Rewriting the equations of motion in the state vector form and including the first-order differential equation of the pitch controller, the dynamics of the system is described by a 33-dimensional state vector. Again, this can be solved by the fourth-order Runge–Kutta method. Fig. 15 shows the edgewise vibration in blade 1 obtained from the 16-DOF model, with the same damper parameters and the same turbulence field as used in Fig. 11. It is shown from Fig. 15(a) that the optimized roller damper effectively mitigates the blade edgewise vibration. The maximum edgewise tip displacement is reduced from 0.751 m to 0.628 m (reduced by 16.38 percent), and the standard deviation is reduced from 0.138 m to 0.099 m (reduced by 28.26 percent). Similar to Fig. 11(b), Fig. 15(b) shows that the frequency component corresponding to eigenvibration of the blade is significantly reduced by the damper, whereas the frequency component related to Ω is unaffected. Comparing with the results obtained from the 2-DOF model as illustrated in Fig. 11, the control effect of the roller damper is slightly reduced when it is incorporated into the highly coupled 13-DOF model. This is because the couplings of blade edgewise vibration to other degrees of freedom cause a transfer of mechanical energy from edgewise vibration to other vibrational modes, resulting in a slightly reduced damping efficiency of the damper. Nevertheless, the roller damper with parameters optimized from the reduced 2-DOF model could achieve equally promising performance on the highly coupled 13-DOF model. Similar results have also been obtained for edgewise vibrations in the other two blades.

Table 3 shows the effects of the roller damper on other degrees of freedom of the wind turbine system. It can be seen that the standard deviations of the lateral tower vibration (q_8) and the deviation of the rotor rotational speed ($\dot{q}_{12}$) are slightly reduced when roller dampers are mounted. This is due to the direct coupling from the edgewise vibration to the lateral tower vibration and the drivetrain torsional vibration, which in turn results in some energy flow from these modes to the motion of the roller. It is favorable to obtain slightly reduced lateral tower vibrations since aerodynamic damping in this mode is very low. Further, the blade flap-wise vibration (q_1), the fore-aft tower vibration (q_7) and the collective pitch angle are almost unchanged, with negligibly increased standard deviations. Since $\dot{q}_{12}(t)$ is slightly affected by the roller damper, the pitch controller produces slightly different pitch angles as feedback from $\dot{q}_{12}(t)$. Due to the dependence of the aerodynamic loads on the pitch angle, $q_1(t)$ and $q_7(t)$ are also insignificantly affected although there is no direct coupling between these two modes with the edgewise vibration.

5. Concluding remarks

This paper investigated the performance of roller dampers for mitigation of edgewise vibrations in rotating wind turbine blades. A reduced 2-DOF nonlinear model based on an analytical dynamic formulation has been established for a rotating

blade equipped with a roller damper. The blade is modeled as a rotating cantilever beam using data from the NREL 5-MW baseline wind turbine, and the coupling with other degrees of freedom in the wind turbine system is ignored. To ease the derivation of the equations of motion, the roller damper is represented by an equivalent mathematical pendulum, which possesses the same kinetic and potential energy as the roller damper. The optimization of the damper parameters has been carried out on this 2-DOF model, with the modal loads obtained from a more sophisticated 13-DOF aeroelastic wind turbine model subjected to a 3-dimensional turbulence field.

Optimal parameters have been determined for the roller damper with different mass ratios by minimizing the standard deviation of the controlled response. Extensive parametric studies are presented to evaluate the influence of various system parameters, such as mass ratio, frequency ratio, friction coefficient and mounting position of the damper. The results reveal that better performance of the roller damper can be obtained by increasing the mass ratio and mounting the damper closer to tip. Variations of the frequency ratio and the friction coefficient have significant effect on the control effect. However, the performance of the damper becomes less sensitive to the friction coefficient when the value of μ is set to be larger than 0.02. It is shown that a roller damper with a mass of 26 kg can significantly attenuate edgewise blade vibrations, when it is properly tuned and is placed at outer part along the blade. This kind of damper performs well in operational wind turbines with a cut-in wind speed of 3 m s^{-1} (the pitch controller is turned off) and a cut-of speed of 25 m s^{-1}. Robust control effect of the damper is observed in suppressing edgewise vibrations as long as the turbulence intensity is less than 0.35. However, stronger turbulence as encountered in the wake of other wind turbines may enforce the roller to perform full rotations in a short time, resulting in a poor control effect during a certain succeeding transient time intervals.

Further, the roller damper with optimal parameters has been incorporated into the 13-DOF aeroelastic wind turbine model to verify the decoupled optimization. Simulation results show that the optimized damper performs almost equally well in the highly coupled wind turbine model as in the reduced 2-DOF model. The slight reduction in the control effect is attributed to the energy flow between the blade edgewise vibration with other degrees of freedom of the highly coupled system. In conclusion, the proposed roller damper and the 2-DOF reduced model for parametric optimization are promising for practical use in wind energy industries.

Acknowledgments

The first author gratefully acknowledge the financial support from the Chinese Scholarship Council under the State Scholarship Fund (File no. 201206260081).

References

[1] M.H. Hansen, Aeroelastic instability problems for wind turbines, *Wind Energy* 10 (6) (2007) 551–577.
[2] K. Thomsen, J.T. Petersen, E. Nim, S. Øye, B. Petersen, A method for determination of damping for edgewise blade vibrations, *Wind Energy* 3 (4) (2000) 233–246.
[3] V.A. Riziotis, S.G. Voutsinas, E.S. Politis, P.K. Chaviaropoulos, Aeroelastic stability of wind turbines: *the problem, the methods and the issues*, *Wind Energy* 7 (4) (2004) 373–392.
[4] P.J. Murtagh, A. Ghosh, B. Basu, B.M. Broderick, Passive control of wind turbine vibrations including blade/tower interaction and rotationally sampled turbulence, *Wind Energy* 11 (4) (2008) 305–317.
[5] R. Colwell, B. Basu, Tuned liquid column dampers in offshore wind turbines for structural control, *Engineering Structures* 31 (2) (2009) 358–368.
[6] M.A. Lackner, M.A. Rotea, Passive structural control of offshore wind turbines, *Wind Energy* 14 (3) (2011) 373–388.
[7] Z.L. Zhang, J.B. Chen, J. Li, Theoretical study and experimental verification of vibration control of offshore wind turbines by a ball vibration absorber, *Structure and Infrastructure Engineering* 10 (8) (2014) 1087–1100.
[8] J. Arrigan, V. Pakrashi, B. Basu, S. Nagarajaiah, Control of flapwise vibrations in wind turbine blades using semi-active tuned mass dampers, *Structural Control and Health Monitoring* 18 (8) (2011) 840–851.
[9] B. Fitzgerald, B. Basu, S.R.K. Nielsen, Active tuned mass dampers for control of in-plane vibrations of wind turbine blades, *Structural Control and Health Monitoring* 20 (12) (2013) 1377–1396.
[10] S. Krenk, M.N. Svendsen, J. Høgsberg, Resonant vibration control of three-bladed wind turbine rotors, *AIAA Journal* 50 (1) (2012) 148–161.
[11] A. Staino, B. Basu, S.R.K. Nielsen, Actuator control of edgewise vibrations in wind turbine blades, *Journal of Sound and Vibration* 331 (6) (2012) 1233–1256.
[12] C. Anderson, H. Heerkes, R. Yemm, The use of blade-mounted dampers to eliminate edgewise stall vibration, *1999 European Wind Energy Conference*, 1999, pp. 207–211.
[13] M. Pirner, Actual behaviour of a ball vibration absorber, *Wind Engineering and Industrial Aerodynamics* 90 (8) (2002) 987–1005.
[14] B. Basu, Z.L. Zhang, S.R.K. Nielsen, Damping of edgewise vibrations in wind turbine blades by means of liquid dampers, *Wind Energy* (2014), submitted for publication.
[15] J. Jonkman, S. Butterfield, W. Musial, G. Scott, Definition of 5-MW reference wind turbine for offshore system development, Technical Report NREL/TP-500-38060, National Renewable Energy Laboratory (NREL), 2009.
[16] K. Ogata, *Morden Control Engineering*, 5th ed. Prentice Hall, New Jersey, 2009.
[17] M.O.L. Hansen, *Aerodynamics of Wind Turbines*, Earthscan, London, 2008.
[18] L.A. Pars, *A Treatise on Analytical Dynamics*, Ox Bow Press, Woodbridge, 1979.
[19] IEC. 61400-1, Wind turbine part 1; design requirements, International Electrotechnical Committee, 2005.
[20] G.K. Batchelor, *The Theory of Homogeneous Turbulence*, Cambridge University Press, Cambridge, 1953.

APPENDIX C
Tuned Liquid Column Dampers for Mitigation of Edgewise Vibrations in Rotating Wind Turbine Blades

Paper 2
The paper presented in this appendix is published in *Structural Control and Health Monitoring*, 2015, Volume 22, Pages 500-517, DOI: 10.1002/stc.1689.

http://onlinelibrary.wiley.com/doi/10.1002/stc.1689/abstract

C.1 Author's Right

AUTHORS - If you wish to reuse your own article (or an amended version of it) in a new publication of which you are the author, editor or co-editor, prior permission is not required (with the usual acknowledgements). However, a formal grant of license can be downloaded free of charge from RightsLink by selecting "Author of this Wiley article" as your requestor type.

http://onlinelibrary.wiley.com/journal/10.1002/(ISSN)1545-2263/homepage/Permissions.html

STRUCTURAL CONTROL AND HEALTH MONITORING
Struct. Control Health Monit. (2014)
Published online in Wiley Online Library (wileyonlinelibrary.com). DOI: 10.1002/stc.1689

Tuned liquid column dampers for mitigation of edgewise vibrations in rotating wind turbine blades

Zili Zhang[1,*,†], Biswajit Basu[2] and Søren R. K. Nielsen[1]

[1]*Department of Civil Engineering, Aalborg University, 9000 Aalborg, Denmark*
[2]*Department of Civil, Structural & Environmental Engineering, School of Engineering, Trinity College Dublin, Dublin 2, Ireland*

SUMMARY

Edgewise vibrations in wind turbine blades are lightly damped, and large amplitude vibrations induced by the turbulence may significantly shorten the fatigue life of the blade. This paper investigates the performance of tuned liquid column dampers (TLCDs) for mitigating edgewise vibrations in rotating wind turbine blades. Normally, the centrifugal acceleration at the outboard portion of a rotating blade can reach to a magnitude of 7–8 g, which makes it possible to use a TLCD with a very small mass for suppressing edgewise vibrations effectively. The parameters of the TLCD to be optimized are the mounting position, the mass ratio, the geometries, and the head loss coefficient of the damper. Based on a reduced 2-DOF nonlinear model developed by the authors, the optimization of these parameters are carried out by minimizing the standard deviation of the edgewise tip displacement, with the consideration of both the space limitation inside the blade and the constraint of the liquid motion. The edgewise modal load for the 2-DOF model has been calculated from a more sophisticated 13-DOF aeroelastic wind turbine model, which includes the coupling of the blade-tower-drivetrain vibration and the aerodynamic damping presented in different modes. Various turbulence intensities and rotational speeds of the rotor have been considered to evaluate the performance of the TLCD. Further, the optimized damper is incorporated into the 13-DOF model to verify the application of the decoupled optimization. The investigation shows promising results for the use of the TLCD in mitigating edgewise vibrations in wind turbine blades. Copyright © 2014 John Wiley & Sons, Ltd.

Received 10 April 2014; Revised 14 June 2014; Accepted 29 July 2014

KEY WORDS: tuned liquid column damper; wind turbine; blade edgewise vibration; vibration control; parametric study

1. INTRODUCTION

Recent developments in the wind energy industry aim at obtaining more economic and productive configurations in order to compete in the energy sector. As a result, modern multi-megawatt wind turbines are designed with increasingly larger rotors to capture more energy throughout their lifetime and to reduce the cost of energy. As the size of the rotor increases, the stiffness of the blades is not proportionally increased. These slender and flexible blades exhibit high susceptibility to wind-induced vibrations, which may significantly shorten the fatigue life of the blade and reduce the efficiency of wind energy conversion to electrical power.

Normally, the modes of vibration in the blades are classified as flap-wise and edgewise modes. Flap-wise vibrations are vibrations out of the plane of the rotating rotor, whereas edgewise vibrations take place in the rotor plane. In operational conditions, flap-wise vibrations are highly damped because of the strong aerodynamic damping as long as the boundary layer on the back side of the profile is attached [1]. Hence, the out-of-plane motions merely turn out to be quasi-static responses to the turbulent wind. In contrast, edgewise vibrations are associated with much smaller aerodynamic damping [1,2],

*Correspondence to: Zili Zhang, Department of Civil Engineering, Aalborg University, 9000 Aalborg, Denmark.
†E-mail: zlz@civil.aau.dk; zzl_1116@126.com

which gives rise to the increased dynamic responses and fatigue damage. Further, the edgewise vibrations will increase the fluctuations of the generator torque, and hence the quality of the generated power. There is also a possibility of aeroelastic instability in the edgewise direction for some combinations of blade properties and operational conditions, especially for high performance wind turbines operating close to stall [1,3]. This corresponds to the case in which the aerodynamic loadings pump energy into the vibrational mode in the edgewise direction, and the sum of the structural damping and the aerodynamic damping becomes negative [4]. For these reasons, the suppression of excessive edgewise vibrations has become a vital design consideration to protect wind turbine blades from the fatigue damage during the design period and to improve their overall performance.

The use of passive, semi-active, and active control devices has been extensively investigated for controlling structural vibrations and protecting structures from the damage effect of the environment [5]. In recent years, structural control technologies are being increasingly investigated for application in wind turbines. For wind turbine towers, several kinds of passive dampers have been studied to suppress the vibrations induced by the wind and wave loads [6–8]. Investigations regarding the mitigation of blade vibrations are mainly focused on the semi-active and active control solutions. Arrigan *et al.* [9] proposed a semi-active tuned mass damper (TMD) for the control of flap-wise vibrations in wind turbine blades, although the modal damping in this direction is already very high because of the aerodynamic damping. Active TMDs have also been studied for mitigating edgewise vibrations, and the active TMD achieves greater response reductions than the passive counterpart [10]. Krenk *et al.* [11] proposed an active strut mounted near the root of each blade for suppressing blade vibrations. The active control concept developed in this research is based on resonant interaction between the rotor and the controller, which is inspired by the concept of TMDs. Staino *et al.* [12] presented the use of active tendons mounted inside each blade for active control of edgewise vibrations. The controller allows a variable control force to be applied in the edgewise direction, and the control forces are manipulated according to a prescribed control law. Recently, Zhang *et al.* [13] investigated the performance of a passive roller damper equipped inside a rotating blade. Because of the large centrifugal acceleration of the rotating blade, it was shown that a roller damper with a very small mass ratio could effectively mitigate edgewise vibrations in different working conditions of the wind turbine.

Tuned liquid column damper (TLCD) imparts external damping to a structure through the inertial force of an oscillating liquid column in a U-shaped container [14]. Energy of the liquid column is dissipated when the liquid passes through an orifice opening in the middle of the horizontal tube. The TLCD has several advantages over other damping devices including its low cost, easy installation and maintenance, easy adjustment of damper geometry to the target frequency, and controllable damping property by the orifice opening. A number of studies [15–17] have shown that a properly tuned TLCD could significantly reduce structural responses under wind and earthquake excitations. Investigation has also been carried out for comparing the performance of TLCDs with TMDs, and it was concluded that TLCDs were as effective as TMDs in damping structural vibrations [18]. Lee *et al.* [19] investigated the TLCD in reducing the wave-induced vibrations of the floating platform system. Both the analytical and experimental results show promising performance of the TLCD when it is accurately tuned. More recently, Colwell and Basu [7] carried out a thorough theoretical study on the performance of a TLCD for vibration control of offshore wind turbine towers and observed that a single TLCD could reduce the tower displacement by up to 55%.

In this paper, TLCDs are proposed for mitigation of edgewise vibrations in rotating wind turbine blades. In the case of the building or tower vibrations, the oscillation of the liquid column and thus the control effect of the TLCD are governed by the gravitational acceleration g. For the rotating blade, the corresponding control effect is governed by the centrifugal acceleration, which can reach to a magnitude of 7–8 g for the outboard portion of a 65-m-long blade. This makes it possible to use the TLCD with a rather small mass for effectively suppressing edgewise vibrations. The focus of this paper is to present a comprehensive theoretical study on the performance of TLCDs in mitigating blade edgewise vibrations. A reduced 2-DOF nonlinear model is established for a rotating blade equipped with a TLCD, ignoring couplings between the edgewise vibration with lateral tower and drivetrain vibrations. The parameters of the TLCD to be optimized are the mass ratio, the tuning ratio, the head loss coefficient, the cross-sectional area ratio (vertical/horizontal), and the horizontal length ratio. Parametric studies have been carried out on the 2-DOF model, with the turbulence induced modal

DOI: 10.1002/stc

loads obtained from a more sophisticated 13-DOF aeroelastic wind turbine model subjected to a three-dimensional turbulence field. Different turbulence intensities and rotational speeds of the rotor have been considered to evaluate the performance of both the passive TLCD with fixed orifice area and the TLCD with varying head loss coefficient. Finally, the optimized damper is incorporated into the 13-DOF model to validate the application of the decoupled optimization as well as the control effect of the TLCD in the highly coupled wind turbine system.

2. AEROELASTIC MODEL OF THE WIND TURBINE SYSTEM

In this section, a 13-DOF aeroelastic wind turbine model is presented. The indicated model displays several important characteristics of a wind turbine, including time-dependent system matrices, coupled tower-blades-drivetrain vibrations, and nonlinear aeroelasticity. Figure 1 shows a schematic representation of the wind turbine model with definitions of the coordinate systems and the degrees of freedom. The motion of the tower is described in a fixed, global (X_1, X_2, X_3)-coordinate, while the motion of each blade is described in a moving, local (x_1, x_2, x_3)-coordinate system with origin at the center of the hub. The X_1- and x_1-axis are unidirectional to the mean wind velocity. The X_3-axis is vertical, and the x_3-axis is placed along the undeformed blade axis orientated from the hub toward the blade tip. Assuming a constant rotational speed Ω for the rotation of each blade, the position of the local coordinated system attached to blade j is specified by the azimuthal angle $\Psi_j(t)$, given by the following equation:

$$\Psi_j(t) = \Omega t + \frac{2\pi}{3}(j-1), j = 1, 2, 3 \tag{1}$$

which is positive when rotating clockwise as observed from an upwind position.

Each blade is modeled as a Bernoulli–Euler beam with variable mass per unit length and variable bending stiffness in the flap-wise and edgewise directions. The flap-wise and edgewise motions of the three blades are modeled by the degrees of freedom $q_j(t)$ and $q_{j+3}(t), j = 1, 2, 3$, indicating the tip

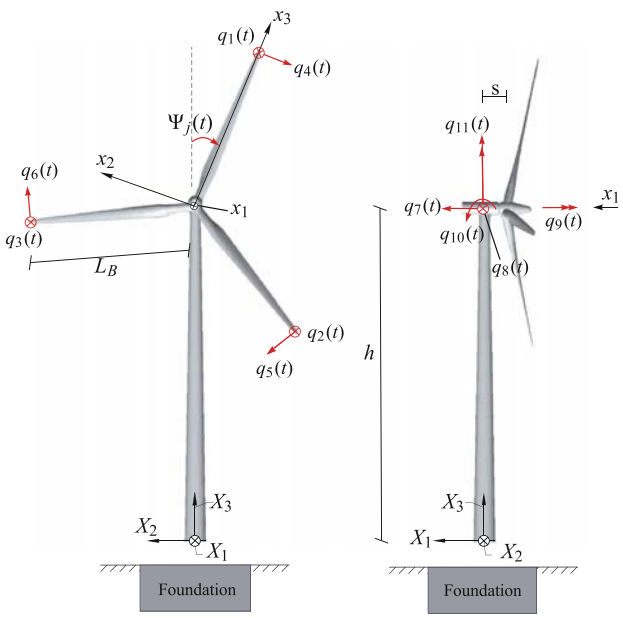

Figure 1. 13-DOF aeroelastic model of three bladed wind turbine. Definition of fixed and moving frames of reference and the degrees of freedom $q_1(t), \ldots, q_{11}(t)$.

DOI: 10.1002/stc

displacement in the positive x_1-direction and the negative x_2-direction, respectively. The related attached modes are taken as the undamped fundamental eigenmodes $\Phi_f(x_3)$ and $\Phi_e(x_3)$ in the flap-wise and edgewise directions, when the blade is fixed at the hub. Because of the definition of $q_j(t)$ and $q_{j+3}(t)$, these modes must be normalized to 1 at the tip, $\Phi_f(L_B) = \Phi_e(L_B) = 1$, where L_B denotes the length of the blade.

The tower motion is defined by the translational degrees of freedom $q_7(t)$ and $q_8(t)$ in the global X_1- and X_2-directions, and the rotational degrees of freedom $q_9(t)$, $q_{10}(t)$, $q_{11}(t)$ in the global X_1-, X_2-, and X_3-directions. The height of the tower from the base to the nacelle is denoted h, and the horizontal distance from the center of the tower top to the origin of the moving coordinate systems is denoted s.

The drivetrain is modeled by the degrees of freedom $q_{12}(t)$ and $q_{13}(t)$ as shown in Figure 2. The sign definition applies to a gearbox with odd number of stages. $q_{12}(t)$ and $q_{13}(t)$ indicate the deviations of the rotational angles at the hub and the generator from the nominal rotational angles Ωt and $N\Omega t$, respectively, where N is the gear ratio. Correspondingly, $\dot{q}_{12}(t)$ and $\dot{q}_{13}(t)$ are the deviations of the rotational speeds at the hub and the generator from the nominal values. In case of even number of stages, the sign definitions for $q_{13}(t)$ and $f_{13}(t)$ are considered positive in the opposite direction. J_r and J_g denote the mass moment of inertia of the rotor and the generator, and k_r and k_g denote the St. Venant torsional stiffness of the rotor shaft and the generator shaft.

Further, a full-span collective pitch controller is included with time delay modeled by a first-order filter. The pitch demand is modeled by a PI controller [20] with feedback from $q_{12}(t)$ and $\dot{q}_{12}(t)$. A gain-scheduled PI controller is used for this model, that is, the controller gains are dependent on the blade pitch angle [21]. The blade element momentum method with Prandtl's tip loss factor and Glauert's correction for large axial induction coefficients is adopted to calculate aerodynamic forces along the blade [22]. Nonlinear quasi-static aeroelasticity is considered by introducing the local deformation velocities of the blade into the calculation of the flow angle and the angle of attack. As a result, this model possesses high aerodynamic damping in the blade flap-wise and the fore-aft tower vibrations, but relatively low aerodynamic damping in the blade edgewise and the lateral tower vibrations.

3. THEORETICAL MODEL FOR THE BLADE-TLCD SYSTEM

The 13-DOF wind turbine model displays a highly coupled dynamical system. The couplings of the blade edgewise vibration to the lateral tower vibration and the drivetrain torsional vibration will influence the motion of the liquid inside the U-shaped container. Because the focus of this study is on the interaction between the TLCD and the blade as well as the control efficiency of the TLCD on edgewise vibrations, the basic assumption in the following theory is that the influence from the tower and drivetrain motions can be ignored. Therefore, the analysis and tuning of the damper is totally based on the local dynamics of the rotating blade. The feasibility of this assumption will be later evaluated by the 13-DOF model.

3.1. Definition of the problem

In the following, only blade $j = 1$ is considered because all three blades behave identical with the same geometrical and structural parameters. Consequently, all the subscripts j representing different blades

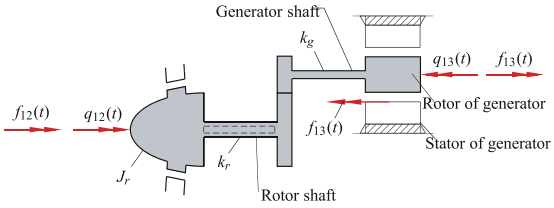

Figure 2. 2-DOF model of the flexible drivetrain with odd number of gear stages. Definition of degrees of freedom $q_{12}(t)$ and $q_{13}(t)$.

DOI: 10.1002/stc

can be skipped, that is, $q_{3+j}(t) = q(t)$, $\Psi_j(t) = \Psi(t)$. Figure 3 shows the schematic representation of a rotating blade equipped with a TLCD. The edgewise vibration of the blade is described by the local degree of freedom $q(t)$ representing the tip displacement in the negative x_2-direction. Hence, the local edgewise displacement field $u(x_3, t)$ of the rotating blade in the positive x_2-direction can be described by $q(t)$ as

$$u_2(x_3, t) = -\Phi(x_3) q(t) \tag{2}$$

where $\Phi(x_3) = \Phi_e(x_3)$ is the fundamental edgewise eigenmode of the blade, which is normalized to 1 at the tip.

Assuming the TLCD to be mounted at the coordinate $x_3 = x_0$, the local displacement and rotation of the blade at this position with the sign definition in Figure 3 are given by

$$\left.\begin{aligned} u_2(x_0, t) &= -aq(t) \\ \varphi(t) &= bq(t) \end{aligned}\right\} \tag{3}$$

where the auxiliary parameters a and b have been introduced: $a = \Phi(x_0)$, $b = \Phi'(x_0)$. Further, the mass per unit length and the edgewise bending stiffness of each blade are denoted $\mu(x_3)$ and $EI(x_3)$, respectively.

3.2. Modeling of the TLCD

As shown in Figure 4, the TLCD considered in this paper is composed of a U-shaped tube with an orifice installed at the center O of the horizontal tube. Because the U-shaped container is mounted inside a rotating blade with a changing azimuthal angle, it should be manufactured in a closed form to prevent the liquid from leaking out of the tube. In this case, an extra slim tube connecting two vertical tubes is fixed in order to balance the pressure above the liquid column during oscillation. The cross-sectional area of the TLCD can be non-uniform, where the vertical and horizontal column cross-sectional areas are denoted as A and A_0, respectively. The density, the horizontal width, the vertical height, and the overall length of the liquid inside the TLCD are represented by ρ, H, B, and L, respectively, where $L = 2H + B$. Thus, the overall mass of the liquid inside the TLCD can be calculated as

$$m = \rho(2HA + BA_0) \tag{4}$$

The displacements of the liquid in the vertical and horizontal tube are defined as $v(t)$ and $v_0(t)$, respectively. Assuming the liquid to be incompressible, the continuity of liquid motion indicates that the liquid velocities at different locations have the following relationship:

$$\dot{v}_0(t) A_0 = \dot{v}(t) A \quad \Rightarrow \quad \dot{v}_0(t) = \alpha \dot{v}(t) \tag{5}$$

where $\alpha = A/A_0$ is the area ratio.

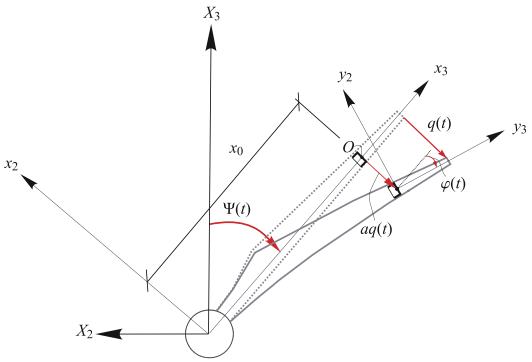

Figure 3. A rotating blade equipped with a tuned liquid column damper.

DOI: 10.1002/stc

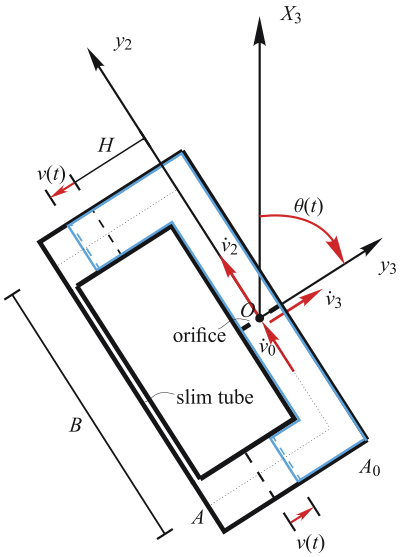

Figure 4. Geometry of the U-shaped tuned liquid column damper.

In order to describe the liquid motion $v(t)$ relative to the U-shaped tube inside the rotating blade, a moving (y_2, y_3)-coordinate system fixed to the damper has been introduced. The origin of this coordinate system is fixed at O, and the y_3-axis is placed on the symmetry line of the damper, resulting in a time-varying angle $\theta(t)$ between the y_3- and the global X_3-axis (Figure 4) as given by

$$\theta(t) = \Psi(t) + \varphi(t) = \Omega t + bq(t) \tag{6}$$

Further, describing the velocity vector of the point O in the moving (y_2, y_3)-coordinate system, the resulting velocities $\dot{v}_2(t)$ and $\dot{v}_3(t)$ of O in the y_2- and y_3-direction can be expressed as

$$\left.\begin{aligned} \dot{v}_2(t) &= -\left(x_0\dot{\Psi}(t) + a\dot{q}(t)\right)\cos\varphi(t) = -(\Omega x_0 + a\dot{q}(t))\cos(bq(t)) \\ \dot{v}_3(t) &= \left(x_0\dot{\Psi}(t) + a\dot{q}(t)\right)\sin\varphi(t) = (\Omega x_0 + a\dot{q}(t))\sin(bq(t)) \end{aligned}\right\} \tag{7}$$

Therefore, the kinetic and potential energy of the liquid inside the container can be obtained as

$$\begin{aligned} T_d = {} & \frac{1}{2}\rho A \int_{-(H-v)}^{0} \left(\left(\dot{v}_2 - y_3\dot{\theta}\right)^2 + \left(\dot{v}_3 + \dot{v} - \frac{1}{2}B\dot{\theta}\right)^2\right) dy_3 + \frac{1}{2}\rho A \int_{-(H+v)}^{0} \left(\left(\dot{v}_2 - y_3\dot{\theta}\right)^2 + \left(\dot{v}_3 - \dot{v} + \frac{1}{2}B\dot{\theta}\right)^2\right) dy_3 \\ & + \frac{1}{2}\rho A_0 \int_{-B/2}^{B/2} \left(\left(\dot{v}_2 + \dot{v}_0\right)^2 + \left(\dot{v}_3 + y_2\dot{\theta}\right)^2\right) dy_2 \\ = {} & \rho A\left[\left(H^3 + 3Hv^2\right)\frac{\dot{\theta}^2}{3} + \left(H^2 + v^2\right)\dot{\theta}\dot{v}_2 + \frac{1}{4}H\left(4\dot{v}_2^2 + 4\dot{v}_3^2 + \left(2\dot{v} - B\dot{\theta}\right)^2\right) - v\left(2\dot{v} - B\dot{\theta}\right)\dot{v}_3\right] \\ & + \frac{1}{24}\rho A_0 B\left(12(\dot{v}_0 + \dot{v}_2)^2 + 12\dot{v}_3^2 + B^2\dot{\theta}^2\right) \end{aligned} \tag{8}$$

DOI: 10.1002/stc

$$\begin{aligned} U_d &= mg(x_0\cos\Psi - aq\sin\Psi) - \rho Avg\left(-\frac{1}{2}(2H-v)\cos\theta - \frac{1}{2}B\sin\theta\right) \\ &\quad + \rho Avg\left(-\frac{1}{2}(2H+v)\cos\theta + \frac{1}{2}B\sin\theta\right) \\ &= mg(x_0\cos\Psi - aq\sin\Psi) + \rho Avg(-v\cos\theta + B\sin\theta) \end{aligned} \tag{9}$$

where g denotes the gravitational acceleration.

3.3. Equations of motion

The velocity components of the blade in the moving (x_2, x_3)-coordinate system are given by

$$\left.\begin{aligned} \dot{u}_2(x_3,t) &= -\Omega x_3 - \Phi(x_3)\dot{q}(t) \\ \dot{u}_3(x_3,t) &= -\Omega\Phi(x_3)q(t) \end{aligned}\right\} \tag{10}$$

Thus, the kinetic energy of the primary structure becomes

$$\begin{aligned} T_p &= \frac{1}{2}\int_0^L \mu(x_3)\left(\dot{u}_2^2(x_3,t) + \dot{u}_3^2(x_3,t)\right)dx_3 \\ &= \frac{1}{2}m_0\left(\dot{q}^2 + \Omega^2 q^2\right) + m_1\Omega\dot{q} + \frac{1}{2}\Omega^2 m_2 \end{aligned} \tag{11}$$

where $m_0 = \int_0^L \mu(x_3)\Phi^2(x_3)dx_3$ is the modal mass of the blade. Further, $m_1 = \int_0^L \mu(x_3)\Phi(x_3)x_3dx_3$, $m_2 = \int_0^L \mu(x_3)x_3^2dx_3$.

The potential energy (strain energy) of the primary structure can be written as

$$U_p = \frac{1}{2}k_0(t)q^2 \tag{12}$$

where $k_0(t)$ denotes the modal stiffness of the primary structure including the elastic and geometric contributions:

$$k_0(t) = k_e + k_1\Omega^2 - k_2 g\cos(\Omega t) \tag{13}$$

k_e is the elastic stiffness of the blade without geometrical contributions. The second term indicates the geometrical stiffening due to the centrifugal acceleration. The last term indicates the geometrical softening caused by the variation of the axial force during rotating due to the weight of the blade. The parameters k_e, k_1, and k_2 are given by

$$\left.\begin{aligned} k_e &= \int_0^L EI(x_3)\left(\frac{d^2\Phi(x_3)}{dx_3^2}\right)^2 dx_3 \\ k_1 &= \int_0^L N_1(x_3)\left(\frac{d\Phi(x_3)}{dx_3}\right)^2 dx_3 \quad , \quad N_1(x_3) = \int_{x_3}^L \mu(y_3)y_3dy_3 \\ k_2 &= \int_0^L N_2(x_3)\left(\frac{d\Phi(x_3)}{dx_3}\right)^2 dx_3 \quad , \quad N_2(x_3) = \int_{x_3}^L \mu(y_3)dy_3 \end{aligned}\right\} \tag{14}$$

The fundamental edgewise circular eigenfrequency of a static blade can be calculated using the following equation:

$$\omega_0 = \sqrt{k_e/m_0} \tag{15}$$

From Equations (8) and (11), the total kinetic energy of the 2-DOF blade-TLCD system is given by

DOI: 10.1002/stc

$$
\begin{aligned}
T = T_p + T_d = {} & \frac{1}{2}m_0\left(\dot{q}^2 + \Omega^2 q^2\right) + m_1\Omega\dot{q} + \frac{1}{2}\Omega^2 m_2 \\
& + \rho A\left[\left(H^3 + 3Hv^2\right)\frac{\dot{\theta}^2}{3} + \left(H^2 + v^2\right)\dot{\theta}\dot{v}_2 + \frac{1}{4}H\left(4\dot{v}_2^2 + 4\dot{v}_3^2 + \left(2\dot{v} - B\dot{\theta}\right)^2\right) - v\left(2\dot{v} - B\dot{\theta}\right)\dot{v}_3\right] \\
& + \frac{1}{24}\rho A_0 B\left(12(\dot{v}_0 + \dot{v}_2)^2 + 12\dot{v}_3^2 + B^2\dot{\theta}^2\right)
\end{aligned} \tag{16}
$$

The total potential energy of the system follows from Equations (9) and (12) is given by

$$
\begin{aligned}
U &= U_p + U_d \\
&= \frac{1}{2}\,k_0 q^2 + mg(x_0\cos\Psi - aq\sin\Psi) + \rho A v g(-v\cos\theta + B\sin\theta)
\end{aligned} \tag{17}
$$

Based on the kinetic and potential energy presented in Equations (16) and (17), the equations of motion of this 2-DOF system can be obtained from the Euler–Lagrange equations [23]:

$$
\begin{aligned}
& \frac{d}{dt}\left(\frac{\partial T}{\partial \dot{q}}\right) - \frac{\partial T}{\partial q} + \frac{\partial U}{\partial q} = f_0(\dot{q}, t) + f_g(t) - c_0\dot{q} \qquad \Rightarrow \\
& \quad m_4\ddot{q} + m_5\ddot{v} + c_0\dot{q} + 2m_6 v\dot{v} + m_7(2v\dot{v}\dot{q} + v^2\ddot{q}) + \left(k_0 - m_0\Omega^2\right)q \\
& \qquad + k_1 v\cos(\Omega t + bq) + k_2 v^2\sin(\Omega t + bq) - mga\sin(\Omega t) + \\
& \quad \sin bq[-(bm_8 + m_{23}) - (bm_9 + m_{24})\dot{q} - (bm_{10} - m_{13} + m_{25})\dot{v} - (bm_{11} + m_{27})v^2 \\
& \qquad - m_{26}\dot{q}^2 + m_{15}\dot{v}^2 + \frac{1}{2}m_{14}\dot{v}\dot{q} + m_{14}v\ddot{q} + m_{15}v\ddot{v} - (bm_{12} + m_{28})v^2\dot{q} - m_{29}v^2\dot{q}^2] + \\
& \quad \cos bq[m_9\ddot{q} + m_{10}\ddot{v} + (bm_{13} - m_{19})v + (bm_{14} - m_{20})v\dot{q} \\
& \qquad + (2m_{11} + bm_{15} - m_{21})v\dot{v} + m_{12}v\dot{v}\dot{q} - m_{22}v\dot{q}^2 + m_{12}v^2\ddot{q}] = f_0(\dot{q}, t) + f_g(t)
\end{aligned} \tag{18}
$$

$$
\begin{aligned}
& \frac{d}{dt}\left(\frac{\partial T}{\partial \dot{v}}\right) - \frac{\partial T}{\partial v} + \frac{\partial U}{\partial v} = -c_d|\dot{v}_0|\dot{v}_0 \qquad \Rightarrow \\
& \quad m_5\ddot{q} + m_{16}\ddot{v} + c_d\alpha^2|\dot{v}|\dot{v} + (-m_{30})v - 2m_6 v\dot{q} - m_7 v\dot{q}^2 + k_3\sin(\Omega t + bq) + k_4 v\cos(\Omega t + bq) \\
& \qquad + \sin bq\left[-(bm_{17} + m_{32}) - (bm_{10} + m_{13})\dot{q} + (m_{18} - m_{19})\dot{v} - \frac{1}{2}m_{14}\dot{q}^2 + m_{15}v\ddot{q}\right] \\
& \qquad + \cos bq\left[m_{10}\ddot{q} + (bm_{18} - m_{31})v + (bm_{15} - 2m_{11})v\dot{q} - m_{12}v\dot{q}^2\right] = 0
\end{aligned} \tag{19}
$$

where the constant parameters $m_4 - m_{32}$ and $k_3 - k_6$ have been defined in Appendix A. $f_0(\dot{q}, t)$ denotes the wind-induced modal load on the primary structure, taking the aerodynamic damping into consideration. $f_g(t)$ denotes the modal load from gravity expressed as

$$
f_g(t) = sin\ \Psi(t)\int_0^L \mu(x_3)g\Phi(x_3)dx_3 = m_3 g\sin(\Omega t) \tag{20}
$$

where $m_3 = \int_0^L \mu(x_3)\Phi(x_3)dx_3$.

$c_0 = 2\zeta_0 m_0\omega_0$ indicates the modal damping coefficient of the primary structure, where ζ_0 is the corresponding modal damping ratio. c_d is the damping coefficient of the TLCD, indicating the energy dissipation due to the passage of liquid through an orifice, as specified in the following form:

$$
c_d = \frac{1}{2}\xi\,\rho\,A_0 \tag{21}
$$

where ξ is the head loss coefficient governed by the opening ratio of the orifice placed at O.

By setting $q(t) = 0$ and assuming small values of $\theta(t)$, the circular frequency ω_d of the TLCD can be obtained from Equation (19) as

DOI: 10.1002/stc

$$\omega_d = \sqrt{\frac{-m_{30} - m_{31}}{m_{16}}} = \sqrt{\frac{2(x_0 - H)}{2H + \alpha B}}\,\Omega = \sqrt{\frac{2x_0 - L(1-\gamma)}{L + (\alpha - 1)\gamma L}}\,\Omega \tag{22}$$

where the horizontal length ratio γ is defined as

$$\gamma = \frac{B}{L} \tag{23}$$

Further, the mass ratio μ and the tuning ratio χ are introduced as design parameters, defined as

$$\mu = \frac{m}{m_0}, \quad \chi = \frac{\omega_d}{\omega_0} \tag{24}$$

It is shown from Equation (22) that the liquid motion is dominated by the centrifugal acceleration $x_0\Omega^2$, which is much larger than g if x_0 is large enough. Normally, the TLCD should be devised such that $\chi \simeq 1$. Because the rated rotational speed Ω is known for the wind turbine, the tuning of the TLCD can be achieved by adjusting L when x_0, γ, and α are specified. Next, for given values of L, μ, γ and α, B, H, A_0, A can also be determined, thus fixing the geometries of the TLCD. Parametric studies of x_0, μ, γ, and α on the control efficiency of TLCD will be carried out in the following section, which provides a guideline for choosing the values of x_0, μ, γ, and α reasonably.

As a measure of the efficiency of the damper, the reduction ratio η is defined as

$$\eta = \frac{\sigma_{q,0} - \sigma_q}{\sigma_{q,0}} \tag{25}$$

where σ_q and $\sigma_{q,0}$ are the standard deviations of the edgewise tip displacements of the blade with and without the TLCD, respectively. The optimal parameters of the TLCD can be found by maximizing the reduction ratio.

4. RESULTS AND DISCUSSIONS

In the numerical simulations carried out for the present study, data from the NREL 5-MW reference wind turbine have been used to calibrate the 13-DOF and the 2-DOF models. In both models, each blade has a length of 63 m and an overall mass of 17740 kg, with the fundamental edgewise modal shape, the bending stiffness, and the mass per unit length provided in [21]. Eight different airfoil profiles are employed for the blade from the hub to the tip, the lift and drag coefficients of which are obtained from wind tunnel test [21].

Based on Taylor's hypothesis of frozen turbulence [24] together with the first-order AR model [11], a three-dimensional rotational sampled turbulence field has been generated with specified mean wind speed V_0 and turbulence intensity I. Applying this turbulence field to the rotor of the 13-DOF model, the edgewise modal load can be obtained for each blade. The calculated modal load $f_0(\dot{q}, t)$ is applied to the 2-DOF, based on which the optimization and parametric studies of the TLCD are performed.

4.1. Optimization procedure

The basic parameters employed in the 2-DOF blade-TLCD model are presented in Table I. Although procedures for design of efficient TLCD are known for linear system [25], they may not be exactly

Table I. Parameters used in the 2-DOF model.

Parameter	Value	Unit	Parameter	Value	Unit
L_B	63	m	k_1	$2.09\cdot 10^3$	kg
m_0	$1.41\cdot 10^3$	kg	k_2	47.25	kg/m
k_e	$6.62\cdot 10^4$	N/m	Ω	1.267	s^{-1}
ω_0	6.85	s^{-1}	g	9.81	m/s^2
ζ_0	0.005	—	ρ	$1.0\cdot 10^3$	kg/m^3

DOI: 10.1002/stc

applicable in the present problem considered. Because of the nonlinearity of Equations (18) and (19), it is difficult to obtain an analytical solution for the optimal damper parameters. However, they may be obtained by numerical search, where various combinations of damper parameters are investigated in a systematic manner until the best combination that maximizes the reduction ratio η is reached. In each numerical simulation, the fourth-order Runge–Kutta method has been used to solve the nonlinear differential equations of the 2-DOF system with a time step of 0.02 s.

The parameters of the TLCD to be determined during the design procedure are the mounting position x_0, the mass ratio μ, the horizontal length ratio γ, the area ratio α, the tuning ratio χ, and the head loss coefficient ξ. Because the damping effect of the oscillating liquid on the structure is governed by the centrifugal acceleration $x_0\Omega^2$, better control performance can be achieved by equipping the TLCD closer to the blade tip. However, the available space inside the hollow blade is diminishing toward the tip, making the determination of x_0 a tradeoff problem. In the following optimization procedure, x_0 is set to be 55 m, corresponding to approximately 7/8 of the total blade length. The effect of various values of x_0 on the control efficiency of the TLCD will be investigated later as well. With a fixed value of x_0, we first search for the optimal values of χ and ξ, while μ, γ, α are assigned certain values. By specifying different values to μ, γ, and α, one can determine the effect of each parameter on the optimal tuning ratio, the optimal head loss coefficient, and the system response. Four sets of mass ratios are considered in the optimization, that is, $\mu = 0.02, 0.03, 0.04, 0.05$. With the modal mass $m_0 = 1412$ kg, the liquid mass will vary between 28.24 and 70.6 kg, corresponding to 0.16–0.40% of the overall mass of each blade. The choices of γ and α have a significant influence on the geometries of the TLCD and should be decided according to the available space inside the blade. In the present study, three different values of γ and three different values of α have been taken into consideration, that is, $\gamma = 0.5, 0.6, 0.7$ and $\alpha = 1, 1.5, 2$.

It should be noted that the optimization has been conducted with the constraint that the maximum displacement of the liquid v_m in the vertical tube should not exceed the vertical height of the liquid column H, that is, $v_m \leqslant H$, so that the fluid remains in the vertical portions of the U-shaped tube at all times.

4.2. Parametric study of the TLCD

Table II gives the values of optimal tuning ratio χ_{opt}, optimal head loss coefficient ξ_{opt}, reduction ratio of the optimized TLCD, and the ratio of maximum liquid response to the vertical length of the liquid

Table II. Optimal parameters of the tuned liquid column damper and their effects on system responses, $V_0 = 15$ m/s, $I = 0.1$, $x_0 = 55$ m.

α	γ	χ_{opt}	ξ_{opt}	η (%)	v_m/H	B (m)	χ_{opt}	ξ_{opt}	η (%)	v_m/H	B (m)
			$\mu = 2\%$						$\mu = 3\%$		
1	0.5	1.000	1.4	24.97	0.974	1.833	0.998	2.2	26.80	0.761	1.860
	0.6	0.998	2.7	26.55	0.998	2.239	0.990	2.9	28.88	0.909	2.273
	0.7	0.998	7.0	25.09	0.996	2.622	0.982	5.7	29.98	0.999	2.701
1.5	0.5	1.000	1.2	24.65	0.991	1.471	0.998	1.7	26.49	0.785	1.493
	0.6	0.998	2.4	26.02	0.990	1.728	0.990	2.4	28.59	0.922	1.754
	0.7	0.998	6.3	24.55	0.994	1.947	0.982	5.2	29.51	0.997	2.006
2	0.5	1.000	1.1	24.01	0.988	1.229	0.998	1.4	25.98	0.821	1.247
	0.6	0.998	2.2	25.25	0.997	1.407	0.990	2.0	28.12	0.958	1.428
	0.7	0.998	5.9	23.67	0.999	1.549	0.982	5.0	28.72	0.998	1.596
			$\mu = 4\%$						$\mu = 5\%$		
1	0.5	0.990	3.0	27.91	0.653	1.888	0.982	3.7	28.69	0.592	1.916
	0.6	0.982	3.9	30.07	0.786	2.310	0.975	4.9	31.00	0.695	2.342
	0.7	0.975	5.0	31.99	0.989	2.743	0.960	5.9	33.14	0.918	2.828
1.5	0.5	0.990	2.3	27.59	0.671	1.515	0.982	2.9	28.35	0.606	1.538
	0.6	0.982	3.2	29.76	0.804	1.781	0.975	4.0	30.66	0.712	1.808
	0.7	0.975	4.4	31.69	0.998	2.037	0.960	5.1	32.80	0.929	2.101
2	0.5	0.990	1.9	27.05	0.691	1.266	0.982	2.3	27.79	0.640	1.285
	0.6	0.982	2.7	29.26	0.837	1.450	0.975	3.4	30.11	0.740	1.472
	0.7	0.975	4.3	31.15	0.999	1.620	0.960	4.5	32.27	0.956	1.645

DOI: 10.1002/stc

column. The horizontal length B for each case is also presented in Table II to check the possibility of equipping the TLCD inside the blade.

From Table II, there are five observations to be made:

(i) As the mass ratio μ increases with the values of α and γ unchanged, the reduction ratio η increases but the value of v_m/H decreases, indicating that a TLCD with a larger mass can achieve higher efficiency with a lower liquid peak response. The horizontal length B increases slightly as μ increases because of the increased volume of the liquid.

(ii) The optimal tuning ratio and the optimal head loss coefficient highly depend on other parameters of the TLCD. χ_{opt} decreases as μ and γ increases, whereas the variation of α has no effect on χ_{opt}. ξ_{opt} increases as γ increases and diminishes as α increases. The variation of μ has no clear effect on ξ_{opt}. As will be shown later, the turbulence intensity also has a significant influence on ξ_{opt}.

(iii) For $\mu = 3\,\%$, $4\,\%$, $5\,\%$, better control performance of the TLCD can be obtained by increasing γ. This is because the mass of the horizontal part of liquid is the only effective mass of TLCD acting on the structure, and a damper with a higher value of γ has a more effective liquid mass. However, both v_m/H and B increase monotonously with γ. Therefore, γ should be limited by the constraint $v_m \leqslant H$ and the space restriction inside the blade.

(iv) For $\mu = 2\,\%$, η decreases as γ increases from 0.6 to 0.7 even though the mass of the horizontal liquid column (effective mass) becomes bigger. The reason is that v_m/H tends to be relatively large for TLCD with a small liquid mass, especially when $\gamma = 0.7$. In this case, ξ_{opt} should be large enough in order that the constrain $v_m \leqslant H$ is fulfilled, which results in the fact that η is even smaller compared to the case of $\gamma = 0.6$. Therefore, when μ is small and γ is large, the constraint $v_m \leqslant H$ becomes a decisive factor for ξ_{opt} as well as the control efficiency of TLCD.

(v) An increase in α leads to a shortening of the total length of the liquid L as well as the horizontal length B, but to a slightly reduced control efficiency of the TLCD as revealed by η. This characteristic is meaningful for applying TLCD into the wind turbine blades where the available horizontal space in the vicinity of the tip is rather limited. The installation of TLCD can be realized by choosing a reasonably large α, at the expense of slightly reduced mitigation effect.

Figure 5 shows the influence of the mounting position of the TLCD on its control performance. Optimal values of tuning ratio and head loss coefficient have been used for each combination of x_0, μ, α, and γ. The results in Figure 5(a) correspond to the case when the space restriction inside the blade is not considered, that is, the horizontal length B and thus the selection of α and γ are not limited by the available horizontal space inside the hollow blade. As expected, it is shown that a TLCD mounted closer to the tip suppresses the edgewise vibration more efficiently because of the increased centrifugal acceleration. Again, one can observe that the increase of the TLCD mass provides a better control performance, but the increase of the reduction ratio is not proportional to the increase of the mass ratio.

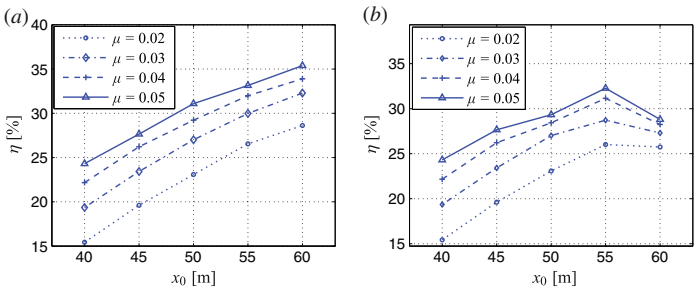

Figure 5. Influence of the damper position on the reduction ratio, $V_0 = 15\,\mathrm{m\,s^{-1}}$, $I = 0.1$, χ_{opt}, and ξ_{opt} used in each case. (a) α and γ chosen without consideration of the space restriction inside the blade, (b) α and γ chosen considering the space restriction inside the blade.

DOI: 10.1002/stc

Figure 5(b) shows the corresponding results obtained with consideration of the space restriction inside the blade, using the geometry of NREL 5-MW wind turbine blade [21]. In the present study, we set the available horizontal length at different positions along the blade to be 0.8 times the chord length c of the corresponding cross section [21], resulting in the constraint of $B \leqslant 0.8c$ when determining the value of α and γ. It can be observed from Figure 5(b) that the control efficiency of TLCD increases monotonously until x_0 reaches 55 m, but decreases as x_0 increases from 55 to 60 m. This is due to the limitation of horizontal space at the cross section of $x_0 = 60$ m (0.8c equals to 1.4 m for the NREL blade), which inevitably requires a large value of α and a small value of γ. Hence, the control performance of TLCD is reduced when equipping it at $x_0 = 60$ m even though the centrifugal acceleration is increased. In reality, results in Figure 5(b) should be utilized in the design procedure, indicating that $x_0 = 55$ m is the best mounting position of TLCD for the NREL 5-MW wind turbine.

In order to evaluate the effect of turbulence intensity I on the optimal tuning ratio and head loss coefficient, various turbulence intensities have been used to generate the wind field for the 13-DOF model with a constant mean wind speed ($V_0 = 15$ m/s). The modal load $f_0(\dot{q}, t)$ for the 2-DOF is then obtained from the 13-DOF model subjected to the generated wind field. From simulation results, it is observed that I has no influence on the optimal tuning ratio and the value of χ_{opt} is unchanged when I is varied. On the other hand, I has a noticeable influence on the optimal head loss coefficient. As shown in Figure 6, different values of I dictate different values of ξ_{opt}. ξ_{opt} is insensitive to I in the cases of $\gamma = 0.5$ and 0.6. However, ξ_{opt} increases significantly as I increases from 0.1 to 0.25 when $\gamma = 0.7$. In this case, ξ_{opt} is dominated by the constraint of $v_m \leqslant H$, because the liquid motion tends to be increased under strong turbulence field and H tends to be small when γ is large. Only with large ξ_{opt}, the liquid motion can be kept within a certain range to maintain a U-shaped liquid column.

Figure 7 shows the control performance of a TLCD under various turbulence intensities. The results in Figure 7(a) correspond to the case when a passive TLCD with a fixed head loss coefficient (fixed orifice) is mounted inside the blade. The constant head loss coefficient is chosen according to $I = 0.25$. Hence, the damping property of the TLCD is non-optimal for all turbulence intensities except for $I = 0.25$. However, it is seen that the reduction ratio decreases monotonously as I increases from 0.05 to 0.25, and that the mitigation effect of TLCD turns out to be the worst when $I = 0.25$. This is because the value of ξ_{opt} for $I = 0.25$ is totally governed by the constraint $v_m \leqslant H$, which is at the cost of a significantly reduced control efficiency. As I decreases, the influence from this constraint on the control efficiency becomes less significant. Therefore, even though non-optimal head loss coefficient is used for low turbulence intensities, the TLCD still exhibits better control performance than that under higher turbulence intensities. Figure 7(b) illustrates the corresponding results when the TLCD is used with varying optimal head loss coefficients in response to different turbulence intensities as given in Figure 6. The control efficiency remains almost unchanged in the range of $I = 0.05$ to $I = 0.1$, but again decreases monotonously as I increases from 0.1 to 0.25. Comparing the reduction ratios in Figure 7(a and b), it is observed that the TLCD with varying head loss coefficient exhibits

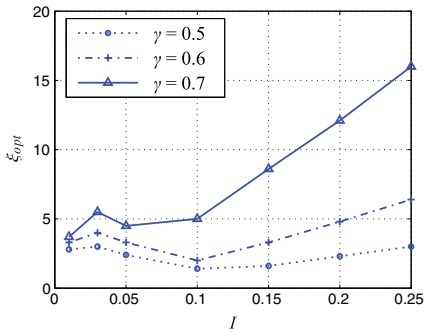

Figure 6. Influence of the turbulence intensity on the optimal head loss coefficient, $V_0 = 15\ \text{m s}^{-1}$, $x_0 = 55$ m, $\mu = 0.03$, $\alpha = 2$.

DOI: 10.1002/stc

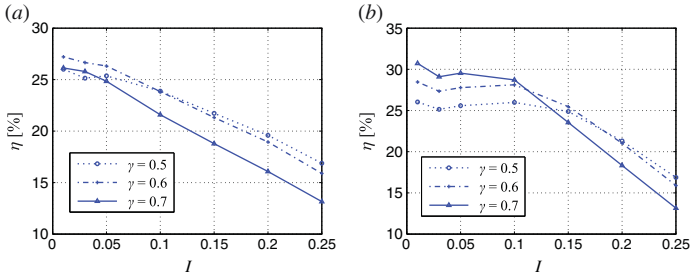

Figure 7. Behavior of a tuned liquid column damper under various turbulence intensities, $V_0 = 15\,\mathrm{m\,s^{-1}}$, $x_0 = 55$ m, $\mu = 0.03$, $\alpha = 2$. (a) Fixed head loss coefficient chosen according to $I = 0.25$, (b) varying optimal head loss coefficient for different turbulence intensities.

better mitigation performance than that of the passive TLCD for all turbulence intensities below $I = 0.25$. The additional reduction provided by the former ranges from 0.30% to 7.13%.

From the previous observations, it is concluded that the efficiency of the TLCD can be improved if the head loss coefficient can be semi-actively varied in response to the actual turbulence intensity. This can be realized by changing the orifice area of the valve through a command voltage [26]. It should also be noted that the optimal tuning ratio χ_{opt} is unaffected by the turbulence intensity, which means that the same TLCD with fixed geometry will perform well under all excitation intensities as long as the area ratio of the orifice/valve is varied adaptively.

4.3. Wind turbine with variable rotational speeds

Figure 8 presents the comparison of the edgewise vibration with and without TLCD when $V_0 = 15$ m/s and $I = 0.1$, where the same turbulence field has been used for both controlled and uncontrolled cases. The tuning of the TLCD is based on the rated rotational speed of the wind turbine, that is, $\Omega = 1.267$ rad/s in the present study. Given $x_0 = 55$ m, $\mu = 0.03$, $\alpha = 2$, and $\gamma = 0.7$, the optimal tuning ratio and head loss coefficient used in the simulation are determined as $\chi_{opt} = 0.982$ and $\xi_{opt} = 5.0$, respectively. The resulting horizontal length B is 1.596 m, which meets the horizontal space limitation at the cross section of $x_0 = 55$ m ($0.8c$ equals to 1.906 m for the NREL blade).

As shown in Figure 8(a), a TLCD with a mass of 42.36 kg significantly mitigates the edgewise vibration of the blade. The maximum edgewise tip displacement is reduced from 0.550 to 0.440 m (reduced by 20.00%), and the standard deviation is reduced from 0.1147 to 0.0817 m (reduced by 28.72%). The Fourier amplitude spectrum of $q(t)$ in Figure 8(b) shows that the TLCD effectively reduces the peak around 6.85 rad/s corresponding to the edgewise eigenvibration of the blade. This indicates that a properly designed TLCD is able to absorb almost all energy in the fundamental edgewise mode of the blade. Further, it is noted that all frequencies below 6.85 rad/s are hardly affected by the damper, including a low peak corresponding to the rated rotational speed (1.267 rad/s). It should be noted that much more energy is concentrated around the frequency of 6.85 rad/s for the uncontrolled

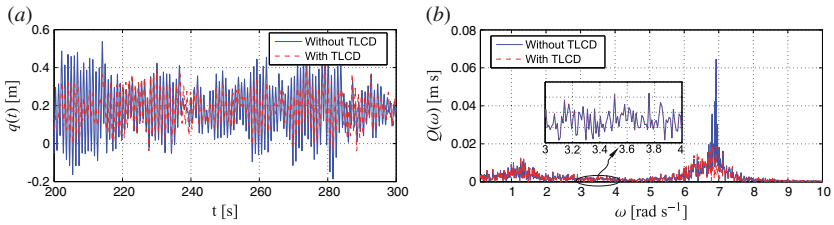

Figure 8. Blade edgewise vibrations with and without tuned liquid column damper (TLCD), $V_0 = 15\,\mathrm{m\,s^{-1}}$, $I = 0.1$, $x_0 = 55$ m, $\mu = 0.03$, $\alpha = 2$, $\gamma = 0.7$. (a) Time series, (b) Fourier amplitude.

DOI: 10.1002/stc

response because aerodynamic damping is low in the edgewise direction. Therefore, although not functioning below the edgewise eigenfrequency, a well-designed TLCD still exhibits promising performance in suppressing edgewise vibrations in a rotating wind turbine blade.

Because the TLCD is optimized according to the rated rotational speed of the rotor, it is of interest to evaluate its performance when the rotational speed of the rotor is varied, for example, during starting up or closing down procedures of the wind turbine. With fixed geometries of the TLCD, all the parameters are invariable except for the head loss coefficient if the orifice area can be changed semi-actively. Table III gives the values of ξ_{opt} for various rotational speeds. It is observed that ξ_{opt} increases significantly as Ω decreases from the nominal value (1.267 rad/s) to 0.6 rad/s. As Ω decreases further, the centrifugal acceleration will be overwhelmed by the gravitational acceleration, that is, $x_0\Omega^2 < g$, resulting in malfunctioning of the TLCD and inapplicability of the equations derived in this paper. The critical value of Ω can be obtained by balancing the centrifugal acceleration with the gravitational acceleration, that is, $x_0\Omega_{cr}^2 = g \Rightarrow \Omega_{cr} = \sqrt{g/x_0}$. In the present case, we have $\Omega_{\mathrm{cr}} = 0.422$ rad/s. Moreover, even for Ω slightly above Ω_{cr}, the influence of the gravity becomes so large that the U-shaped liquid column cannot be maintained (the liquid motion turns out to be very drastic). Hence, we set the lower limit of Ω to be 0.6 rad/s for the operational range of the TLCD.

Figure 9 shows the control performance of the TLCD under various rotational speeds of the rotor. As expected, when Ω deviates from the rated value, the control efficiency of the TLCD is drastically reduced because of the frequency detuning of the damper. Nevertheless, it is observed that the performance of the damper can be enhanced by semi-actively varying the head loss coefficient in response to the change of the rotational speed. As for the passive TLCD with fixed head loss coefficient, the reduction ratio drops to below 10% for $\Omega < 1.00$ rad/s. On the other hand, the reduction ratio remains above 10% for all Ω between 0.6 and 1.267 rad/s when ξ_{opt} given in Table III are used for different Ω. Further, it is noted that the control efficiency decreases even faster as Ω increases from the nominal value, indicating a more significant frequency detuning when $\Omega > 1.267$ rad/s. For modern multi-megawatt wind turbines, however, the rotational speed of the rotor is limited to the rated value by the pitch controller. This makes it promising to apply the TLCD in an operating wind turbine, especially the TLCD with varying head loss coefficients.

4.4. Evaluation by the 13-DOF aeroelastic model

To verify the applicability of the decoupled optimization and the control effect of the TLCD in highly coupled wind turbine system, the optimized damper is incorporated into the 13-DOF model. For each blade, a TLCD is mounted at the position of $x_0 = 55$ m. Hence, a 16-DOF system is obtained for the wind turbine with a total of three TLCDs installed. Figure 10 shows the edgewise vibration in blade 1, with the same damper parameters and the same wind field as used in Figure 8. It is shown from Figure 10(a) that the damper with parameters optimized from the reduced 2-DOF model effectively mitigates the blade edgewise vibration of the highly coupled wind turbine system. The maximum edgewise tip displacement is reduced from 0.481 to 0.400 m (reduced by 16.84 %), and the standard deviation is reduced from 0.0895 to 0.0698 m (reduced by 21.94 %). Similar to Figure 8(b), Figure 10(b) demonstrates that frequency component corresponding to fundamental edgewise mode of the blade is significantly reduced by the damper, whereas the frequencies below ω_0 are unaffected. Comparing with

Table III. Optimal head loss coefficients for different rotational speeds of the rotor, $x_0 = 55$ m, $\mu = 0.03$, $\alpha = 2$, $\gamma = 0.7$.

Ω (rad/s)	ξ_{opt}	Ω (rad/s)	ξ_{opt}
1.40	7.9	0.95	23.5
1.35	4.3	0.90	28.5
1.267	5.0	0.85	32.5
1.20	4.0	0.80	37.0
1.15	6.1	0.75	39.5
1.10	9.0	0.70	43.0
1.05	14.4	0.65	44.0
1.00	18.2	0.60	45.0

DOI: 10.1002/stc

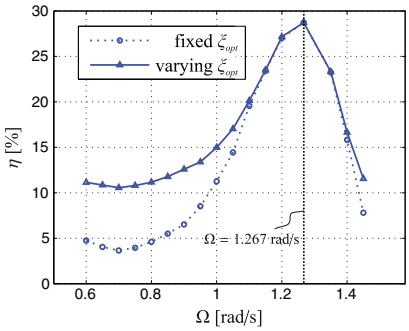

Figure 9. Behavior of the tuned liquid column damper under various rotational speeds of the rotor, $V_0 = 15$ m/s, $I = 0.1$, $x_0 = 55$ m, $\mu = 0.03$, $\alpha = 2$, $\gamma = 0.7$.

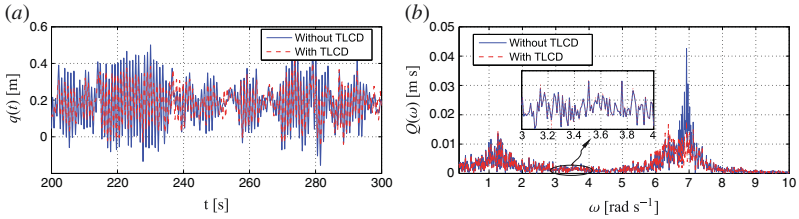

Figure 10. Blade edgewise vibrations with and without tuned liquid column damper (TLCD), obtained from the 16-DOF model. $V_0 = 15\,\mathrm{m\,s^{-1}}$, $I = 0.1$, $x_0 = 55$ m, $\mu = 0.03$, $\alpha = 2$, $\gamma = 0.7$. (a) Time series, (b) Fourier amplitude.

the results obtained from the 2-DOF model as illustrated in Figure 8, the control efficiency of the TLCD is to some extent reduced when it is incorporated into the highly coupled system. This is because the couplings of blade edgewise vibration to other degrees of freedom cause a transfer of mechanical energy from edgewise vibration to other vibrational modes, resulting in a slightly worse damping performance of the damper. Nevertheless, the TLCD with parameters optimized from the reduced 2-DOF model is still able to achieve promising control performance on the highly coupled 13-DOF model.

5. CONCLUSIONS

In the present paper, a comprehensive theoretical study has been carried out on the performance of TLCDs for mitigating edgewise vibrations in wind turbine blades. Parametric studies have been carried out using a reduced 2-DOF nonlinear model developed by the authors for a rotating blade equipped with a TLCD. The results reveal that a TLCD with a very small mass can effectively suppress edgewise vibrations in a rotating wind turbine blade. Better control performance can be obtained by increasing the liquid mass and equipping the damper closer to the blade tip. However, the damper mass and the mounting position should be limited according to the installation capacity and the available space inside the blade. It is also found that increasing the area ratio of the vertical tube to the horizontal tube can greatly reduce the horizontal width of the TLCD at the cost of slightly reduced control efficiency, making it possible to mount the damper in the vicinity of the tip. Further, it is shown that the optimal head loss coefficient is changed with the variation of turbulence intensity, while the turbulence intensity has no influence on the optimal tuning ratio. Therefore, the performance of a TLCD with fixed geometries can be improved by

DOI: 10.1002/stc

continuously changing the orifice ratio in response to the actual turbulence intensity. Although the control effect of the damper is drastically reduced when the rotational speed of the rotor deviates from the nominal value (e.g., during the starting up or closing down procedure of the wind turbine), it can be enhanced by semi-actively varying the head loss coefficient according to the change of the rotational speed. Finally, the optimized damper has been incorporated into the 13-DOF aeroelastic wind turbine model to verify the decoupled optimization. Simulation results show that the optimized damper achieves promising performance in the highly coupled model. The slight reduction in the control effect is attributed to the energy flow between the blade edgewise vibration and other degrees of freedom specifying the tower and drivetrain motions.

Validation of the performance of the TLCD through testing is to be performed in future research. It is not feasible to carry out a full-scale experiment of such a system with rotating elements in the lab. A scaled down model of the system tested in lab conditions will essentially suffer from scale effects, particularly with respect to the liquid behavior in the damper (e.g., due to viscous effects), and it may be a challenge to keep appropriate proportion with dynamic similarities for the wind turbine structure and the damper. One option is to conduct real-time hybrid testing of the system where the liquid damper is tested physically in full scale and the rest of the wind turbine is simulated. However, such facilities are not available generally in many labs, with full-scale capability. The authors have plans for implementation of the system and to conduct experimentation in a real-time hybrid simulation framework in a lab where such a facility is available.

APPENDIX A

The constant parameters in Equations (18) and (19) are given by

$$
\left.\begin{array}{ll}
m_4 = m_0 + \dfrac{2}{3}\rho A b^2 H^3 + \dfrac{1}{2}\rho AH\left(4a^2 + b^2B^2\right) + \dfrac{1}{12}\rho A_0 B\left(12a^2 + b^2B^2\right) & \\
m_5 = -\rho ABHb & m_6 = 2\rho AHb\Omega \\
m_7 = 2\rho AHb^2 & m_8 = -\rho A(a + bx_0)H^2\Omega \\
m_9 = -2\rho AabH^2 & m_{10} = -\rho AaB \\
m_{11} = -\rho A(a + bx_0)\Omega & m_{12} = -2\rho Aab \\
m_{13} = \rho A(a + bx_0)B\Omega & m_{14} = 2\rho AabB \\
m_{15} = -2\rho Aa & m_{16} = \rho A(2H + \alpha B) \\
m_{17} = -\rho AB\,\Omega x_0 & m_{18} = -2\rho A\Omega x_0 \\
m_{19} = \rho ABbx_0\Omega^2 & m_{20} = \rho ABb(a + bx_0)\Omega \\
m_{21} = -2\rho Abx_0\Omega & m_{22} = \rho ABab^2 \\
m_{23} = \rho AH^2bx_0\Omega^2 & m_{24} = \rho AbH^2(a + bx_0)\Omega \\
m_{25} = \rho ABbx_0\Omega & m_{26} = \rho AH^2ab^2 \\
m_{27} = \rho Abx_0\Omega^2 & m_{28} = \rho Ab(a + bx_0)\Omega \\
m_{29} = \rho Aab^2 & m_{30} = 2\rho AH\Omega^2 \\
m_{31} = -2\rho Ax_0\Omega^2 & m_{32} = \rho ABx_0\Omega^2 \\
k_3 = \rho AgBb & k_4 = \rho Agb \\
k_5 = \rho AgB & k_6 = -2\rho Ag
\end{array}\right\} \qquad \text{(A1)}
$$

DOI: 10.1002/stc

APPENDIX B: NOMENCLATURE

A	Cross-sectional area of the vertical column of the TLCD
$a = \Phi(x_0)$	Auxiliary parameter related to the local displacement of the blade
A_0	Cross-sectional area of the horizontal column of the TLCD
B	Horizontal length of the liquid inside the TLCD
$b = \Phi'(x_0)$	Auxiliary parameter related to the local rotation of the blade
c_0	Modal damping coefficient of the blade
$EI(x_3)$	Edgewise bending stiffness of the blade
$f_0(\dot{q}, t)$	Wind-induced modal load considering aerodynamic damping
g	Gravitational acceleration
H	Vertical length of the liquid inside the TLCD
I	Turbulence intensity
$k_0(t)$	Modal stiffness of the blade
k_1, k_2	Stiffness related parameters given by Equation (19)
k_e	Elastic stiffness of the blade
L	Overall length of the liquid inside the TLCD
L_B	Length of the blade
m	Overall mass of the liquid
m_0	Modal mass of the blade
$q(t)$	Edgewise tip displacement of the blade
T, U	Total kinetic and total potential energy of the blade-TLCD system
t	Time
T_d, U_d	Kinetic and potential energy of the liquid
T_p, U_p	Kinetic and potential energy of the blade
$v(t)$	Displacement of the liquid in the vertical tube
V_0	Mean wind speed
$v_0(t)$	Displacement of the liquid in the horizontal tube
$\dot{v}_2(t)$	Local velocity of the center point O of the horizontal tube in y_2-direction
$\dot{v}_3(t)$	Local velocity of the center point O of the horizontal tube in y_3-direction
v_m	Maximum displacement of the liquid in the vertical tube
$(X_1, X_2, X_3) -$	Global coordinate system
x_0	Mounting position of the TLCD
$(x_1, x_2, x_3) -$	Local coordinate system fixed to the rotating blade
$(y_1, y_2, y_3) -$	Local coordinate system fixed to the U-shaped tube
$\alpha = A/A_0$	Cross-sectional area ratio of the vertical column versus horizontal column
$\gamma = B/L$	Ratio of the horizontal length to overall length of the liquid column
ζ_0	Modal damping ratio of the blade
ζ_d	Damping coefficient of the TLCD
η	Reduction ratio of the edgewise vibration
$\theta(t)$	Angle between the local y_3- and global X_3-axis
$\mu = m/m_0$	Ratio of the liquid mass to the modal mass of the blade
$\mu(x_3)$	Mass per unit length of the blade
ξ	Head loss coefficient due to the orifice
ξ_{opt}	Optimal head loss coefficient
ρ	Liquid density
$\Phi(x_3)$	Fundamental edgewise eigenmode of the blade
$\varphi(t)$	Local elastic rotation of the blade where the TLCD is mounted
$\chi = \omega_d/\omega_0$	Frequency tuning ratio of the TLCD to the blade
χ_{opt}	Optimal frequency tuning ratio
$\Psi(t)$	Azimuthal angle of blade 1
Ω	Rotational speed of the rotor
ω_0	Fundamental edgewise circular eigenfrequency of the blade
ω_d	Circular frequency of the TLCD

ACKNOWLEDGEMENTS

The first author gratefully acknowledges the financial support from the Chinese Scholarship Council under the State Scholarship Fund.

DOI: 10.1002/stc

REFERENCES

1. Hansen MH. Aeroelastic instability problems for wind turbines. *Wind Energy* 2007; **10**(6):551–577. doi:10.1002/we.242.
2. Thomsen K, Petersen JT, Nim E, Øye S, Petersen B. A method for determination of damping for edgewise blade vibrations. *Wind Energy* 2000; **3**(4):233–246. doi:10.1002/we.42.
3. Bir G, Jonkman J. Aeroelastic instabilities of large offshore and onshore wind turbines. EAWE 2007 Torque from Wind Conference, Lyngby, Denmark, 2007. DOI:10.1088/1742-6596/75/1/012069.
4. Riziotis VA, Voutsinas SG, Politis ES, Chaviaropoulos PK. Aeroelastic stability of wind turbines: the problem, the methods and the issues. *Wind Energy* 2004; **7**(4):373–392. doi:10.1002/we.133.
5. Spencer BF, Nagarajaiah S. State of the art of structural control. *Journal of Structural Engineering* 2003; **129**(7):845–856. doi:10.1061/(ASCE)0733-9445(2003)129:7(845.
6. Murtagh PJ, Ghosh A, Basu B, Broderick BM. Passive control of wind turbine vibrations including blade/tower interaction and rotationally sampled turbulence. *Wind Energy* 2008; **11**(4):305–317. doi:10.1002/we.249.
7. Colwell S, Basu B. Tuned liquid column dampers in offshore wind turbines for structural control. *Engineering Structures* 2009; **31**(2):358–368. doi:10.1016/j.engstruct.2008.09.001.
8. Zhang ZL, Chen JB, Li J. Theoretical study and experimental verification of vibration control of offshore wind turbines by a ball vibration absorber. *Structure and Infrastructure Engineering* 2014; **10**(8):1087–1100. doi:10.1080/15732479.2013.792098.
9. Arrigan J, Pakrashi V, Basu B, Nagarajaiah S. Control of flapwise vibrations in wind turbine blades using semi-active tuned mass dampers. *Structural Control and Health Monitoring* 2011; **18**(8):840–851. doi:10.1002/stc.404.
10. Fitzgerald B, Basu B, Nielsen SRK. Active tuned mass dampers for control of in-plane vibrations of wind turbine blades. *Structural Control and Health Monitoring* 2013; **20**(12):1377–1396. doi:10.1002/stc.1524.
11. Krenk S, Svendsen MN, Høgsberg J. Resonant vibration control of three-bladed wind turbine rotors. *AIAA Journal* 2012; **50**(1):148–161. doi:10.2514/1.J051164.
12. Staino A, Basu B, Nielsen SRK. Actuator control of edgewise vibrations in wind turbine blades. *Journal of Sound and Vibration* 2012; **331**(6):1233–1256. doi:10.1016/j.jsv.2011.11.003.
13. Zhang Z, Li J, Nielsen SRK, Basu B. Mitigation of edgewise vibrations in wind turbine blades by means of roller dampers. *Journal of Sound and Vibration* 2014; **333**(21):5283–5298. doi:10.1016/j.jsv.2014.06.006.
14. Sakai F, Takaeda S. Tuned liquid column damper – new type device for suppression of building vibrations. In Proceedings International Conference on High-rise Building, Nanjing, China, 1989.
15. Balendra T, Wang CM, Cheong HF. Effectiveness of tuned liquid column dampers for vibration control of towers. *Engineering Structures* 1995; **17**(9):668–675. doi:10.1016/0141-0296(95)00036-7.
16. Balendra T, Wang CM, Rakesh G. Effectiveness of TLCD on various structural systems. *Engineering Structures* 1999; **21**(4):291–305.
17. Won AYJ, Pires JA, Haroun MA. Stochastic seismic performance evaluation of tuned liquid column dampers. *Earthquake Engineering and Structural Dynamics* 1996; **25**(11):1259–1274. doi:10.1016/S0141-0296(97)00156-9.
18. Xu YL, Samali B, Kwok KCS. Control of along-wind response of structures by mass and liquid dampers. *Journal of Engineering Mechanics* 1992; **118**(1):20–39. doi:10.1061/(ASCE)0733-9399(1992)118:1(20.
19. Lee HH, Wong SH, Lee RS. Response mitigation on the offshore floating platform system with tuned liquid column damper. *Ocean Engineering* 2006; **33**(8-9):1118–1142. doi:10.1016/j.oceaneng.2005.06.008.
20. Ogata K. Modern Control Engineering (5 edn). Prentice Hall: New Jersey, 2009.
21. Jonkman J, Butterfield S, Musial W, Scott G. Definition of 5-MW reference wind turbine for offshore system development. National Renewable Energy Laboratory, Technical Report, NREL/TP-500-38060, Golden, Colorado; 2009. DOI: 10.2172/947422.
22. Hansen MOL. Aerodynamics of Wind Turbines. Earthscan: London, 2008.
23. Pars LA. A Treatise on Analytical Dynamics. Ox Bow Press: Woodbridge, 1979.
24. IEC. 61400-1; *Wind turbine part 1; design requirements*, International Electrotechnical Committee, 2005.
25. Wu JC, Shih MH, Lin YY, Shen YC. Design guidelines for tuned liquid column damper for structures responding to wind. *Engineering Structures* 2005; **27**(13):1893–1905. doi:10.1016/j.engstruct.2005.05.009.
26. Yalla SK, Kareem A, Kantor JC. Semi-active tuned liquid column dampers for vibration control of structures. *Engineering Structures* 2001; **23**(11):1469–1479. doi:10.1016/S0141-0296(01)00047-5.

APPENDIX D
Damping of Edgewise Vibration in Wind Turbine Blades by Means of Circular Liquid Dampers

Paper 3
The paper presented in this appendix is published in *Wind Energy*, 2015, Early view, DOI: 10.1002/we.1827.

http://onlinelibrary.wiley.com/doi/10.1002/we.1827/abstract

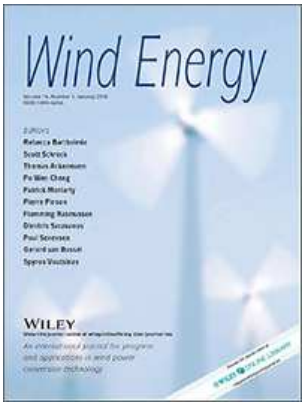

D.1 Author's Right

AUTHORS - If you wish to reuse your own article (or an amended version of it) in a new publication of which you are the author, editor or co-editor, prior permission is not required (with the usual acknowledgements). However, a formal grant of license can be downloaded free of charge from RightsLink by selecting "Author of this Wiley article" as your requestor type.

http://onlinelibrary.wiley.com/journal/10.1002/(ISSN)1099-1824/homepage/Permissions.html

Wind Energy

WIND ENERGY
Wind Energ. (2015)
Published online in Wiley Online Library (wileyonlinelibrary.com). DOI: 10.1002/we.1827

RESEARCH ARTICLE

Damping of edgewise vibration in wind turbine blades by means of circular liquid dampers

Biswajit Basu[1], Zili Zhang[2] and Søren R. K. Nielsen[2]

[1] Department of Civil, Structural & Environmental Engineering, School of Engineering, Trinity College Dublin, Dublin 2, Ireland
[2] Department of Civil Engineering, Aalborg University, DK-9000 Aalborg, Denmark

ABSTRACT

This paper proposes a new type of passive vibration control damper for controlling edgewise vibrations of wind turbine blades. The damper is a variant of the liquid column damper and is termed as a circular liquid column damper (CLCD). Rotating wind turbine blades generally experience a large centrifugal acceleration. This centrifugal acceleration makes the use of this kind of oscillatory liquid damper feasible with a small mass ratio to effectively suppress edgewise vibrations. A reduced 2-DOF non-linear model is used for tuning the CLCD attached to a rotating wind turbine blade, ignoring the coupling between the blade and the tower. The performance of the damper is evaluated under various rotational speeds of the rotor. A special case in which the rotational speed is so small that the gravity dominates the motion of the liquid is also investigated. Further, the legitimacy of the decoupled optimization is verified by incorporating the optimized damper into a more sophisticated 13-DOF aeroelastic wind turbine model with due consideration to the coupled blade-tower-drivetrain vibrations of the wind turbine as well as a pitch controller. The numerical results from the illustrations on a 5 and a 10 MW wind turbine machine indicate that the CLCD at an optimal tuning can effectively suppress the dynamic response of wind turbine blades. Copyright © 2015 John Wiley & Sons, Ltd.

KEYWORDS
wind turbines; edgewise vibrations; circular liquid damper; parametric optimization

Correspondence
Biswajit Basu, Department of Civil, Structural & Environmental Engineering, School of Engineering, Trinity College Dublin, Dublin 2, Ireland.
E-mail: basub@tcd.ie

Received 21 June 2014; Revised 11 November 2014; Accepted 27 November 2014

1. INTRODUCTION

The control of edgewise vibrations in wind turbine blades is an area of topical interest because of the presence of light to almost no aerodynamic damping in this mode. This problem is expected to persist in the future because of the growth of the wind energy leading to larger rotors, particularly for offshore deployments. Edgewise vibrations not only contribute to structural fatigue damage with increased operation and maintenance costs but also interfere with the power production.[1]

There has been continued interest among researchers in the past few years to control structural vibrations in wind turbines. Passive structural control techniques[2–4] have been used by researchers for controlling vibrations in both onshore and offshore wind turbines. To cater to variation in environmental/operational changes, semi-active strategies using tuned mass dampers (TMDs) have been proposed by Arrigan *et al.*[5,6] Researchers[7,8] have found that blades installed with stall strips perform better with regard to edgewise vibrations; however, this beneficial effect is overshadowed by the negative impact on the power production. Some other researchers have used synthetic jet actuators,[9] microtabs and trailing edge flaps.[10,11] More recently, some active control strategies for wind turbine blades have been proposed. All of these concepts take advantage of the hollow nature of the blades and utilize the space inside to install the dampers. Svendsen *et al.*[12] proposed the use of active strut elements based on resonant controllers inspired by the concept of TMDs; Staino *et al.*[13] developed a controller based on active tendon/actuator, and Fitzgerald *et al.*[14] used active TMD (ATMD) for edgewise vibration control. Fitzgerald and Basu[15] proposed a variant of ATMD called the cable-connected ATMD in order to reduce the force demand on the actuator of the ATMD. Although a number of the proposed solutions work well, there is still a

need to find simple, maintenance-free and easy to install solutions for vibration control of edgewise vibrations in wind turbine blades.

Among the passive structural control solutions available, liquid column dampers (LCDs) are one of the favored options because of the consistent behavior over a range of excitation levels, the self-containing passive damping capability with little auxiliary equipment, personnel or power required to maintain it and the fact that they are easy to install. An investigation on the effects of liquid storage tanks containing glycol on the dynamic response of offshore structures indicated that a proper selection of the tank geometry could dampen the offshore platform vibration.[16] Colwell and Basu[4] have used tuned liquid column dampers (TLCDs) for supressing vibration in offshore wind turbine towers/nacelle.

Motivated by the TLCDs, a new type of LCD has been proposed in this paper for edgewise vibration control of wind turbine blades. The damper is circular in shape or geometry and hence is termed as a circular liquid column damper (CLCD). The circular shape allows for consistent definition of local dynamic behavior of the liquid irrespective of the position at the damper. This is due to the axisymmetric nature of the liquid column damper geometry. The presence of a large centrifugal acceleration in wind turbine blades makes it possible to use this kind of oscillatory liquid damper with a rather small mass for effectively suppressing edgewise vibrations. To optimize the design of the proposed CLCD, the interaction between the tower and the blades are ignored. The optimization for tuning of the CLCD to the rotating blades is based on a reduced 2-DOF non-linear model. In order to evaluate the vibration suppression performance of the proposed new damper, a more sophisticated 13-DOF aeroelastic wind turbine model with due consideration to the coupled blade-tower-drivetrain vibrations of the wind turbine as well as a pitch controller are used and numerical simulations are carried out with the optimally tuned CLCD. Two wind turbines, a 5 and a 10 MW machine, are considered to illustrate the effectiveness of the proposed damper in suppressing vibrations.

2. THEORY FOR THE BLADE-DAMPER SYSTEM

The edgewise vibrations of a wind turbine blade is coupled to the lateral tower and drivetrain vibrations, which also influence the motion of the liquid damper. Because the focus of this study is on the interaction between the damper and blade, as well as the control effect of the damper on edgewise vibrations, the basic assumption in the following theory is that this coupling from the tower and drivetrain motion can be ignored. Therefore, the design of the damper is totally based on the local dynamics of the rotating blade. The validity of this assumption will be evaluated later by a more sophisticated 13-DOF wind turbine model, which takes into consideration the coupling of blade-tower-drivetrain vibration, the non-linear aeroelasticity and a collective pitch controller.

2.1. Definition of the problem

Figure 1 illustrates the schematic representation of a rotating blade equipped with a circular liquid damper. The edgewise vibration of the blade is described in the moving (x_2, x_3)-coordinate system, while the motion of the liquid inside the damper is described by another local coordinate system (y_2, y_3) fixed to the damper. The mass per unit length and the bending stiffness in the edgewise direction of each blade are denoted $\mu(x_3)$ and $EI(x_3)$, respectively. The liquid damper is devised to control the fundamental edgewise mode, as described by the degree of freedom $q(t)$. Further, the rotation of

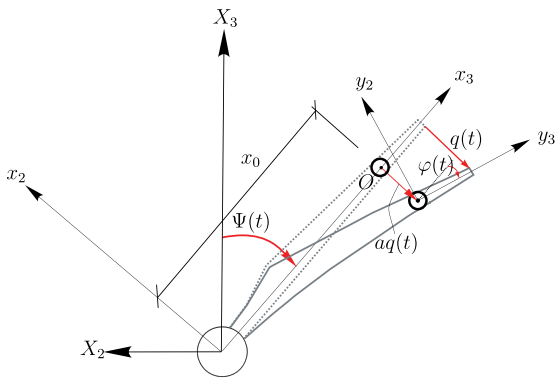

Figure 1. Definition of the coordinate systems, the geometry and the degrees of freedom.

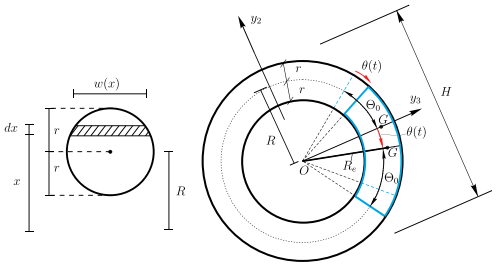

Figure 2. Geometries of the circular liquid damper.

each blade is assumed to take place with a constant rotational speed Ω. Hence, the azimuthal angle $\Psi(t)$ of the blade is given as

$$\Psi(t) = \Omega t \tag{1}$$

The local edgewise displacement $u_2(x_3, t)$ of the rotating blade in the x_2 direction can by described by $q(t)$ as

$$u_2(x_3, t) = -\Phi(x_3)\, q(t) \tag{2}$$

where $\Phi(x_3)$ indicates the fundamental edgewise mode of the blade. This is normalized to 1 at the tip, i.e., $\Phi(L) = 1$, where L denotes the blade length. The negative sign in Equation (2) refers to the definition of $q(t)$ in the negative direction of the x_2-axis. Hence, $q(t)$ represents the edgewise tip displacement in the negative x_2 direction.

The circular liquid damper is virtually a circular tube partly filled with certain amount of liquid that could oscillate back and forth inside the tube. As shown in Figure 2, the radius of the circular tube (distance from the center point O to the central axis of the tube) is denoted by R, and the radius of the cross-section of the tube is denoted by r. Therefore, the total dimension of the damper can be calculated as $H = 2(R + r)$. The liquid inside the tube is assumed to be connected, filling a segment with a central angle $2\Theta_0$ of the complete circle, and the center of gravity is denoted by G.

It is assumed that the liquid damper is placed at the coordinate $x_3 = x_0$ of the blade. Hence, the local displacement and rotation of the blade at this position with the sign definition in Figure 1 are given as

$$\left.\begin{aligned} u_2(x_0, t) &= -aq(t) \\ \varphi(t) &= bq(t) \end{aligned}\right\} \tag{3}$$

where the auxiliary parameters introduced are $a = \Phi(x_0)$ and $b = \Phi'(x_0)$.

2.2. Modeling of the circular liquid damper

A moving (y_2, y_3)-coordinate system fixed to the damper has been introduced for describing the motion of the liquid. This coordinate system has its origin at the center point O of the circular damper, with y_3-axis placed on the symmetry line of the damper as shown in Figure 2. Hence, the azimuthal angle of the y_3-axis is described by the clockwise rotation $\Psi(t) + \varphi(t)$ from the fixed global X_3-axis. The motion of the liquid is described by the degree of freedom $\theta(t)$, which measures the clockwise rotation of the center of gravity of the liquid from the y_3-axis. Thus, $q(t)$ and $\theta(t)$ make up the degrees of freedom of the blade-damper system.

From the geometries illustrated in Figure 2, the mass of the liquid can be calculated as

$$m = \rho \int_{-\Theta_0}^{\Theta_0} \int_{R-r}^{R+r} w(x) x \, d\theta \, dx \tag{4}$$

where ρ denotes the mass density of the fluid. The term $w(x)$ is the width of the cross-section at a distance x from the center point O and is given as

$$w(x) = 2\sqrt{r^2 - (x - R)^2} \tag{5}$$

Substituting Equation (5) into Equation (4), the mass of the liquid becomes

$$m = 4\rho\Theta_0 \int_{R-r}^{R+r} \sqrt{r^2 - (x - R)^2}\, x \, d\theta \, dx = \rho \pi r^2 2\Theta_0 R \tag{6}$$

Defining R_G as the distance from G to O, R_G can be given by

$$m R_G = \rho \int_{-\Theta_0}^{\Theta_0} \int_{R-r}^{R+r} w(x) x^2 \, d\theta \, dx = 4\rho\Theta_0 \int_{R-r}^{R+r} \sqrt{r^2 - (x-R)^2}\, x^2 \, d\theta \, dx = \rho \pi r^2 \, 2\Theta_0 R^2 \left(1 + \frac{1}{4}\frac{r^2}{R^2}\right) \tag{7}$$

From Equations (6) and (7), it follows that

$$R_G = R\left(1 + \frac{1}{4}\frac{r^2}{R^2}\right) = R\left(1 + \frac{1}{4}\alpha^2\right) \tag{8}$$

where $\alpha = \frac{r}{R}$ is defined as the radius ratio of the circular cross-section and the damper.

From the dynamics point of view, the liquid inside the circular damper virtually acts as a physical pendulum during its oscillation. The idea in the following is to represent the liquid damper as an equivalent mathematical pendulum with the equivalent mass m_e and the equivalent length R_e. The equivalent mass m_e is approximately equal to the liquid mass m, if the radius r of the cross-section is small compared with R. The equivalent mathematical pendulum should represent the same kinetic and potential energy as the circular liquid damper. Because the kinetic energy stored in the local rotation of the liquid mass can be ignored compared with the translational kinetic energy, the total kinetic energy of the liquid mass with the angular velocity $\dot{\theta}$ can be written as

$$\begin{aligned} T &= \frac{1}{2}\rho \int_{-\Theta_0}^{\Theta_0} \int_{R-r}^{R+r} w(x) x \left(x\dot{\theta}\right)^2 d\theta dx = 2\rho\Theta_0 \, \dot{\theta}^2 \int_{R-r}^{R+r} \sqrt{r^2 - (x-R)^2}\, x^3 \, d\theta \, dx \\ &= \frac{1}{2}\rho \pi r^2 \, 2\Theta_0 R^3 \left(1 + \frac{3}{4}\alpha^2\right)\dot{\theta}^2 = \frac{1}{2} m R^2 \left(1 + \frac{3}{4}\alpha^2\right)\dot{\theta}^2 \end{aligned} \tag{9}$$

The kinetic energy of the equivalent mathematical pendulum is

$$T = \frac{1}{2} m_e R_e^2 \, \dot{\theta}^2 \tag{10}$$

Equating the kinetic energy of the equivalent mathematical pendulum to that of the oscillating liquid, the relationship between m_e and R_e follows from

$$m_e R_e^2 = m R^2 \left(1 + \frac{3}{4}\alpha^2\right) \tag{11}$$

In order to facilitate the calculation of the potential energy of the liquid mass, we shall choose R_e as

$$R_e = R_G = R\left(1 + \frac{1}{4}\alpha^2\right) \tag{12}$$

Then, from Equations (11) and (12), the equivalent mass of the mathematical pendulum is given by

$$m_e = m \frac{\left(1 + \frac{3}{4}\alpha^2\right)}{\left(1 + \frac{1}{4}\alpha^2\right)^2} \tag{13}$$

2.3. Equations of motion of the 2-DOF model

The velocity components of the primary structure in the moving (x_2, x_3)-coordinate system can be written as

$$\left.\begin{aligned} \dot{u}_2(x_3, t) &= -\Omega \, x_3 - \Phi(x_3) \, \dot{q}(t) \\ \dot{u}_3(x_3, t) &= -\Omega \, \Phi(x_3) q(t) \end{aligned}\right\} \tag{14}$$

The fixed frame components of the displacement vector and velocity vector of the center of gravity G of the liquid becomes

$$\left.\begin{aligned} U_{2,G}(t) &= -x_0 \sin\Psi - aq\cos\Psi - R_e \sin(\Psi + \varphi + \theta) \\ U_{3,G}(t) &= x_0 \cos\Psi - aq \sin\Psi + R_e \cos(\Psi + \varphi + \theta) \end{aligned}\right\} \tag{15}$$

$$\left.\begin{aligned} \dot{U}_{2,G}(t) &= -(x_0\Omega + a\dot{q})\cos\Psi + aq\Omega \sin\Psi - R_e\left(\Omega + \dot{\varphi} + \dot{\theta}\right)\cos(\Psi + \varphi + \theta) \\ \dot{U}_{3,G}(t) &= -(x_0\Omega + a\dot{q})\sin\Psi - aq\Omega \cos\Psi - R_e\left(\Omega + \dot{\varphi} + \dot{\theta}\right)\sin(\Psi + \varphi + \theta) \end{aligned}\right\} \tag{16}$$

Thus, the total kinetic energy of the 2-DOF system becomes

$$\begin{aligned} T &= \frac{1}{2}\int_0^L \mu(x_3)\left(\dot{u}_2^2(x_3,t)+\dot{u}_3^2(x_3,t)\right)dx_3 + \frac{1}{2}m_e\left(\dot{U}_{2,O}^2(t)+\dot{U}_{3,O}^2(t)\right) \\ &= \frac{1}{2}m_0\left(\dot{q}^2+\Omega^2 q^2\right)+m_1\Omega\dot{q}+\frac{1}{2}\Omega^2 m_2 \\ &\quad + \frac{1}{2}m_e\left(((x_0\Omega+a\dot{q})^2+a^2q^2\Omega^2+R_e^2\left(\Omega+b\dot{q}+\dot{\theta}\right)\right. \\ &\qquad \left. + 2R_e\left(\Omega+b\dot{q}+\theta\right)\left((x_0\Omega+a\dot{q})\cos(bq+\theta)+aq\Omega\sin(bq+\theta)\right)\right) \end{aligned} \tag{17}$$

where $m_0=\int_0^L \mu(x_3)\Phi^2(x_3)dx_3$ is the modal mass of the blade, and $m_1=\int_0^L \mu(x_3)\Phi(x_3)x_3dx_3, m_2=\int_0^L \mu(x_3)x_3^2dx_3$.

The total potential energy of the system is

$$U = mg\left(x_0\cos\Psi - aq\sin\Psi + R_e\cos(\Psi+bq+\theta)\right)+\frac{1}{2}k_0(t)q^2 \tag{18}$$

where g is the acceleration of gravity. The term $k_0(t)$ denotes the modal stiffness of the blade and is given by

$$k_0(t) = k_e + k_g(t) \tag{19}$$

where k_e and $k_g(t)$ specify the elastic and geometric contributions to the modal stiffness. The term $k_g(t)$ is expressed as

$$k_g(t) = k_1\,\Omega^2 - k_2\,g\cos(\Omega t) \tag{20}$$

The first term indicates the geometrical stiffening due to the centrifugal acceleration, whereas the second term is caused by the variation of the axial force during rotation due to the weight of the blade. The parameters k_e, k_1 and k_2 are given by

$$\left.\begin{aligned} k_e &= \int_0^L EI(x_3)\left(\frac{d^2\Phi(x_3)}{dx_3^2}\right)^2 dx_3 \\ k_1 &= \int_0^L N_1(x_3)\left(\frac{d\Phi(x_3)}{dx_3}\right)^2 dx_3 \quad , \quad N_1(x_3)=\int_{x_3}^L \mu(y_3)\,y_3\,dy_3 \\ k_2 &= \int_0^L N_2(x_3)\left(\frac{d\Phi(x_3)}{dx_3}\right)^2 dx_3 \quad , \quad N_2(x_3)=\int_{x_3}^L \mu(y_3)\,dy_3 \end{aligned}\right\} \tag{21}$$

The fundamental edgewise angular eigenfrequency of the blade when it is in stand-still position is obtained as

$$\omega_0 = \sqrt{k_e/m_0} \tag{22}$$

The equations of motion of the 2-DOF system are obtained from the stationarity conditions using Euler–Lagrange equations

$$\begin{aligned} \frac{d}{dt}\left(\frac{\partial T}{\partial\dot{q}}\right)-\frac{\partial T}{\partial q}+\frac{\partial U}{\partial q} &= F_0(t)+F_g(t)-c_0\dot{q} \\ &\Rightarrow \left(m_0+m_e\left(a^2+R_e^2b^2\right)\right)\ddot{q}+m_eR_e^2b\,\ddot{\theta}+(c_0+c_a)\,\dot{q}+\left(k_0-\Omega^2(m_0+m_ea^2)\right)q \\ &\quad + m_eR_e\left(2ab\,\ddot{q}+a\ddot{\theta}-ab\Omega^2 q\right)\cos(bq+\theta) \\ &\quad - m_eR_e\left((a-bx_0)\,\Omega^2+2a\Omega\,\dot{\theta}+a\left(b\dot{q}+\dot{\theta}\right)^2\right)\sin(bq+\theta) \\ &\quad - mg\left(a\sin(\Omega t)+R_eb\sin(\Omega t+bq+\theta)\right) \\ &= F_0(t)+F_g(t) \end{aligned} \tag{23}$$

$$\begin{aligned} \frac{d}{dt}\left(\frac{\partial T}{\partial\dot{\theta}}\right)-\frac{\partial T}{\partial\theta}+\frac{\partial U}{\partial\theta} &= -c_d\,|\dot{\theta}|\,\dot{\theta} \\ &\Rightarrow m_eR_e^2b\,\ddot{q}+m_eR_e^2\,\ddot{\theta}+c_d\,|\dot{\theta}|\,\dot{\theta}+m_eR_ea\left(\ddot{q}-\Omega^2 q\right)\cos(bq+\theta) \\ &\quad + m_eR_e\left(2a\Omega\,\dot{q}+\Omega^2x_0\right)\sin(bq+\theta)-mgR_e\,\sin(\Omega t+bq+\theta) \\ &= 0 \end{aligned} \tag{24}$$

where c_0 indicates the structural damping coefficient of the primary structure, as specified by the related modal damping ratio ζ_0 as $c_0 = 2\zeta_0 m_0 \omega_0$. The term $F_0(t)$ specifies the modal load on the primary structure from turbulence and pitch control loads, taking into account aerodynamic damping. The term $F_g(t)$ denotes the modal load on the blade from gravity and is given by

$$F_g(t) = m_3 g \sin(\Omega t) \tag{25}$$

where $m_3 = \int_0^L \mu(x_3)\Phi(x_3)dx_3$. The term c_d indicates the damping coefficient of the liquid damper specifying the energy dissipation due to the passage of liquid through an orifice, as given by the form

$$c_d = \frac{1}{2}\xi\rho r^2 R^3 \tag{26}$$

where ξ denotes the non-dimensional head loss coefficient, which is governed by the opening ratio of the orifice.

Assuming small values of $q(t)$ and $\theta(t)$ and ignoring the influence of gravity, the angular eigenfrequency of the oscillating liquid can be obtained from Equation (24) as

$$\omega_d = \sqrt{\frac{x_0}{R_e}}\,\Omega \tag{27}$$

Defining μ as the mass ratio between the damper and the modal mass of the structure, and χ as the natural frequency ratio between the liquid and the structure, the following relationships follow:

$$\mu = \frac{m}{m_0}, \quad \chi = \frac{\omega_d}{\omega_0} \tag{28}$$

Further, the reduction ratio η of the structural response with and without the damper is defined as

$$\eta = \frac{\sigma_{q,0} - \sigma_q}{\sigma_{q,0}} \tag{29}$$

where $\sigma_{q,0}$ and σ_q are the standard deviations of the edgewise tip displacements of the blade without and with control, respectively. The optimal parameters of the circular liquid damper can be found by maximizing the value of η.

2.4. 13-DOF wind turbine model for validation

A 13-DOF aeroelastic model is presented for validating the effectiveness of the circular liquid damper in a highly coupled wind turbine system. The model displays several important characteristics of a wind turbine, including time-dependent system matrices, coupled tower-blade-drivetrain vibrations as well as non-linear aeroelasticity. Figure 3 shows a schematic representation of the wind turbine model with definition of the coordinate systems and the degrees of freedom.

The motions of the blade are described in a moving, local (x_1, x_2, x_3)-coordinate system with origin at the center of the hub. Each blade is modeled as a Bernoulli–Euler beam with variable mass per unit length and variable bending stiffness in the flap-wise and edgewise directions. The flap-wise and edgewise motions of the three blades are modeled by the degrees of freedom $q_j(t)$ and $q_{j+3}(t)$, $j = 1, 2, 3$, with the tip displacement in the positive x_1 direction and the negative x_2 direction, respectively. The related attached modes are taken as the undamped fundamental eigenmodes $\Phi_f(x_3)$ and $\Phi(x_3)$ in the flap-wise and edgewise directions, when the blade is fixed at the hub. Similar to $\Phi(x_3)$, $\Phi_f(x_3)$ should also be normalized to one at the tip, i.e., $\Phi_f(L) = 1$.

The motions of the tower are described in a fixed, global (X_1, X_2, X_3)-coordinate system. The coordinates $q_7(t)$ and $q_8(t)$ define the translational motions of the tower in the X_1 and X_2 directions, respectively. The coordinates $q_9(t), q_{10}(t), q_{11}(t)$ define the rotational motions of the tower in the X_1, X_2 and X_3 directions. The height of the tower from the base to the nacelle is denoted by h, and the horizontal distance from the center of the tower top to the origin of the moving coordinate systems is denoted by s.

The drivetrain is modeled by the degrees of freedom $q_{12}(t)$ and $q_{13}(t)$ as shown in Figure 4. The sign definition applies to a gearbox with odd number of stages. The degrees of freedom $q_{12}(t)$ and $q_{13}(t)$ indicate the deviations of the rotational angles at the hub and the generator from the nominal rotational angles Ωt and $N\Omega t$, respectively, where N is the gear ratio. Correspondingly, $\dot{q}_{12}(t)$ and $\dot{q}_{13}(t)$ are the deviations of the rotational speeds at the hub and the generator from the nominal values. In case of even number of stages, the sign definitions for $q_{13}(t)$ and $f_{13}(t)$ are considered positive in the opposite direction. The terms J_r and J_g denote the mass moment of inertia of the rotor and the generator, and k_r and k_g denote the St.Venant torsional stiffness of the rotor shaft and the generator shaft.

Further, a full-span collective pitch controller is included with time delay modeled by a first-order filter. The pitch demand is modeled by a proportional integral (PI) controller[17] with feedback from $q_{12}(t)$ and $\dot{q}_{12}(t)$. A gain-scheduled

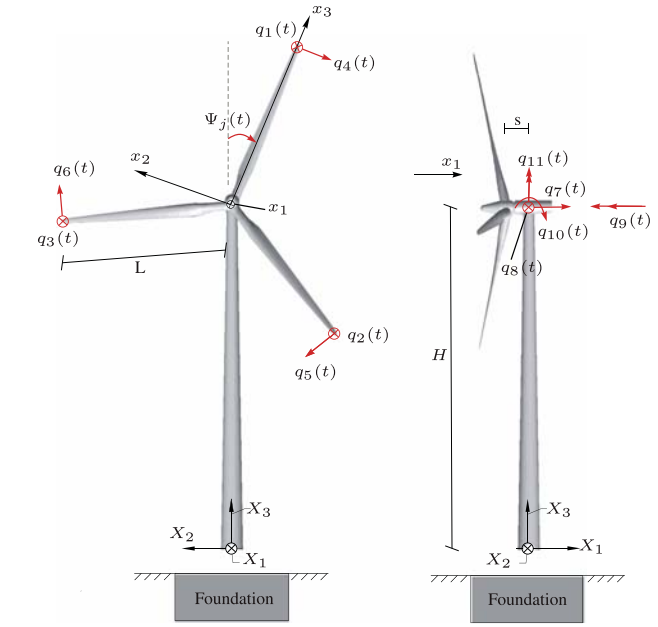

Figure 3. 13-DOF aeroelastic model of a three-bladed wind turbine. Definition of fixed and moving frames of reference and the degrees of freedom $q_1(t), \ldots, q_{11}(t)$.

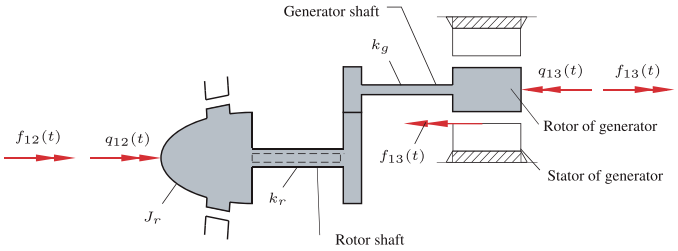

Figure 4. 2-DOF model of the flexible drivetrain with odd number of gear stages. Definition of degrees of freedom $q_{12}(t)$ and $q_{13}(t)$.

PI controller is used for this model, i.e., the controller gains are dependent on the blade pitch angle.[18] The blade element momentum method with Prandtl's tip loss factor and Glauert's correction for large axial induction coefficients is adopted to calculate aerodynamic forces along the blade.[19] Non-linear quasi-static aeroelasticity is considered by introducing the local deformation velocities of the blade into the calculation of the flow angle and the angle of attack. As a result, this model possesses high aerodynamic damping in the blade flap-wise and the fore–aft tower vibrations but relatively low aerodynamic damping in the blade edgewise and the lateral tower vibrations.

3. RESULTS AND DISCUSSION

In the first phase of numerical simulations, data from the National Renewable Energy Laboratory (NREL) 5 MW reference wind turbine[18] have been used to calibrate both the 2-DOF and the 13-DOF models. Each blade has a length of 63 m and

Table I. Parameters in 2-DOF blade-damper model.

Parameter	Value	Unit
L	63	m
x_0	45	m
Ω_0	1.267	rad s^{-1}
m_0	$1.412{\cdot}10^3$	kg
m_1	$3.049{\cdot}10^3$	kg
k_e	$6.623{\cdot}10^4$	N m^{-1}
k_1	$2.086{\cdot}10^3$	kg
k_2	47.25	kg m^{-1}
ξ_0	0.005	—
a	0.5267	—
b	0.0238	m^{-1}
ρ	$1.0{\cdot}10^3$	kg m^{-3}
g	9.81	m s^{-2}
ω_0	6.848	rad s^{-1}

an overall mass of 17,740 kg, with the fundamental modal shape, the bending stiffness and the mass per unit length given by Jonkman *et al.*[18] The constant parameters employed in the 2-DOF model are calculated and provided in Table I.

On the basis of Taylor's hypothesis of frozen turbulence[20] together with the first-order auto-regressive (AR) model,[21] a three-dimensional (3D) rotational sampled wind field has been generated with a given mean wind speed and turbulence intensity. By applying this turbulence field to the rotor of the 13-DOF wind turbine, the edgewise modal loads for each blade can be obtained. The calculated modal load $F_0(t)$ is exerted on the 2-DOF model, on the basis of which the optimization and parametric studies of the damper are to be carried out. In the simulation, the fourth-order Runge–Kutta method was applied to solve the non-linear ordinary differential equations of the 2-DOF system.

3.1. Optimization and parametric studies

The parameters of the liquid damper to be determined are the mass ratio μ, the frequency ratio χ, the radius ratio α, the head loss coefficient ξ and the mounting position of the damper x_0. Because the damping effect of the oscillating liquid on the structure is governed by the centrifugal acceleration $x_0\Omega^2$, better performance of vibration reduction can be obtained by mounting the liquid damper closer to the tip of the blade. However, the available space inside the hollow blade decreases toward the tip, making the determination of x_0 a trade-off problem. In the following optimization procedure, x_0 is set to be 45 m, corresponding to approximately two thirds of the total blade length. Further, four sets of mass ratios are considered in the optimization, i.e., $\mu = 0.01, 0.02, 0.03, 0.04$. With the modal mass $m_0 = 1412$ kg, the liquid mass varies between 14.12 and 56.48 kg, corresponding to 0.08–0.32% of the total mass of each blade. Moreover, four different values of the radius ratio have been compared, i.e., $\alpha = 0.03, 0.05, 0.07, 0.09$. It should be noted that the tuning of the damper is based on the nominal rotational speed of the NREL 5 MW wind turbine, i.e., $\Omega_0 = 1.267$ rad s^{-1}.

In the optimization procedure, the optimal frequency ratio χ_{opt} and head loss coefficient ξ_{opt} are sought such that the reduction coefficient η is maximized, for prescribed values of the mass ratio μ and the radius ratio α. Table II gives the

Table II. Optimal parameters of the liquid damper and their effects on system responses, $x_0 = 45$ m.

	μ=1%					μ=2%				
$\alpha = \frac{r}{R}$	χ_{opt}	ξ_{opt}	η (%)	$2\Theta_0$ (rad)	H (m)	χ_{opt}	ξ_{opt}	η (%)	$2\Theta_0$ (rad)	H (m)
0.03	1.00	1.57	25.19	1.36	3.17	0.99	6.40	29.40	2.58	3.24
0.05	1.00	0.55	25.19	0.50	3.23	0.99	2.35	29.40	0.92	3.30
0.07	1.00	0.29	25.19	0.26	3.29	0.99	1.22	29.41	0.48	3.36
0.09	1.00	0.18	25.20	0.086	3.35	0.99	0.75	29.41	0.28	3.42
	μ=3%					μ=4%				
$\alpha = \frac{r}{R}$	χ_{opt}	ξ_{opt}	η (%)	$2\Theta_0$ (rad)	H (m)	χ_{opt}	ξ_{opt}	η (%)	$2\Theta_0$ (rad)	H (m)
0.03	0.98	15.40	31.62	3.62	3.30	0.97	27.70	33.24	4.56	3.37
0.05	0.98	5.68	31.62	1.30	3.36	0.97	9.90	33.24	1.64	3.43
0.07	0.98	2.89	31.63	0.68	3.43	0.97	5.14	33.24	0.84	3.50
0.09	0.98	1.72	31.63	0.40	3.49	0.97	3.07	33.25	0.50	3.56

values of χ_{opt}, ξ_{opt}, as well as the corresponding η, the central angle of the liquid mass $2\Theta_0$ and the total width of the damper $H = 2(R+r)$. Values of $2\Theta_0$ and H are calculated in each case to check the possibility of practical implementation of the liquid damper with such geometries.

From Table II, four observations are to be made: (i) The reduction ratio η increases non-proportionally as the mass ratio μ increases. (ii) As μ increases with a given α, χ_{opt} decreases while ξ_{opt} increases. Both $2\Theta_0$ and H increase as μ increases. (iii) As α varies between 0.03 and 0.09 for a prescribed value of μ, the value of χ_{opt} is unchanged, and η is almost unaffected as well. On the other hand, ξ_{opt} decreases significantly as α increases. (iv) As α increases, $2\Theta_0$ decreases significantly and H increases slightly. For very small values of α, the value of $2\Theta_0$ may become so large that the annular tube is almost completely filled with liquid, resulting in ineffectiveness of the damper. On the other hand, a large value of α may lead to a large value of H, making it impossible to mount the liquid damper inside the blade. Therefore, the determination of α becomes a trade-off problem depending only on the geometries of the damper and the liquid inside the tube, as α has almost no effect on the maximum reduction ratio when optimal values of χ and ξ are used.

3.2. Performance of the liquid damper

Figure 5 presents the comparison of the edgewise vibration with and without the liquid damper, when the mean wind speed is 15 m s^{-1} and the turbulence intensity is 0.1. The same turbulence field has been used for cases with and without control to make the comparison meaningful. Given the mounting position $x_0 = 45$ m, the mass ratio $\mu = 0.03$ and the radius ratio $\alpha = 0.05$, the optimal frequency ratio and head loss coefficient of the damper used in the simulation are determined as $\chi_{opt} = 0.98$ and $\xi_{opt} = 5.68$, respectively.

As shown in Figure 5(a), a liquid damper with a mass of 42.36 kg significantly mitigates the edgewise vibration of the blade. The maximum edgewise tip displacement is reduced from 0.550 to 0.417 m (reduced by 24.18%), and the standard deviation is reduced from 0.1147 to 0.0784 m (reduced by 31.62%). The Fourier amplitude spectrum of $q(t)$ as illustrated in Figure 5(b) shows that the liquid damper effectively suppresses the peak around 6.85 rad s^{-1} corresponding to the eigen-vibration of the blade in edgewise direction. This means that a properly designed liquid damper is able to absorb almost all the energy in the fundamental edgewise mode of the blade. Further, it is noted that all frequencies below 6.85 rad s^{-1} are hardly affected by the dampers, including a low peak corresponding to a rotational speed of 1.267 rad s^{-1}. It should be noted that much more energy is concentrated around the frequency of 6.85 rad s^{-1} for the uncontrolled response as aerodynamic damping is low in the edgewise direction. Therefore, although not functioning below the edgewise eigenfrequency, a well-tuned liquid damper still exhibits promising performance in suppressing edgewise vibrations in a rotating wind turbine blade.

In order to evaluate the performance of the liquid damper during starting up or closing down procedures of the wind turbine system, results have been calculated at various rotational speeds $\Omega < \Omega_0$. Figure 6 demonstrates the behavior of the liquid under two scenarios, i.e., $x_0\Omega^2 > g$ and $x_0\Omega^2 < g$, respectively. When the centrifugal acceleration overwhelms the gravitational acceleration [Figure 6(a)], the liquid is centrifuged toward the tip of the blade, and it oscillates around a mean value of $\theta = 0$ rad according to the definition of $\theta(t)$ in the (y_2, y_3)-coordinate system. On the other hand when $x_0\Omega^2 < g$, the motion of the liquid is dominated by gravity, and the liquid will gravitate downwards and remain close to the bottom of the circular tube no matter where the blade is placed, as shown in Figure 6(b).

Table III shows the reduction ratios of the damper on edgewise vibrations as well as the corresponding standard deviations of the liquid motion. It is noted that as Ω decreases from the nominal value Ω_0, the control efficiency of the liquid damper is drastically reduced as revealed by the value of η, as a result of detuning of the damper. Acceptable control performance can be achieved only when Ω is no less than 1.1 rad s^{-1}, which means the band width of the damper is rather limited. Moreover, the standard deviation σ_θ of $\theta(t)$ increases from 0.16 to 0.50 rad as Ω decreases from 1.267to 0.6 rad s^{-1}. One interesting observation is that when Ω changes from 0.5 to 0.4 rad s^{-1}, the value of σ_θ increases significantly from 0.74

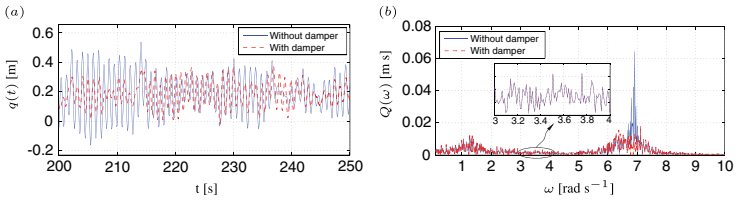

Figure 5. Blade edgewise vibrations with and without liquid damper, $\Omega = 1.267$ rad s^{-1}, $V_0 = 15$ m s^{-1}, $I = 0.1$, $\mu = 0.03$, $\alpha = 0.05$, $x_0 = 45$ m, $\Omega = 1.267$ rad s^{-1}. (a) Time series, (b) Fourier amplitude.

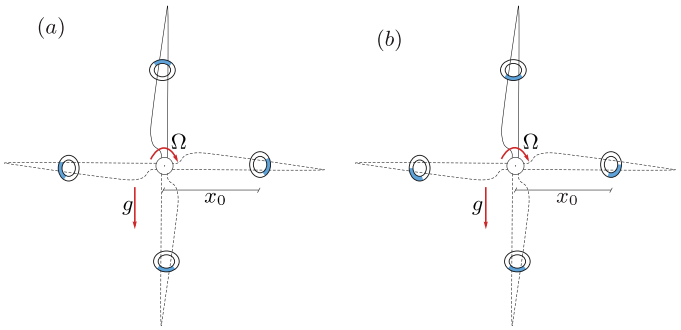

Figure 6. Position of the liquid mass. (a) $x_0\Omega^2 > g$, (b) $x_0\Omega^2 < g$.

Table III. Performance of the circular liquid damper for various rotational speeds of the rotor.

Ω (rad s^{-1})	$x_0\Omega^2\,g^{-1}$	η (%)	σ_θ (rad)	Ω (rad s^{-1})	$x_0\Omega^2\,g^{-1}$	η (%)	σ_θ (rad)
1.267	7.41	31.62	0.16	0.6	1.65	8.10	0.50
1.2	6.61	29.60	0.16	0.5	1.15	7.40	0.74
1.1	5.56	23.67	0.17	0.4	0.73	6.30	2.23
1.0	4.59	16.03	0.18	0.3	0.41	4.65	2.09
0.9	3.72	11.55	0.21	0.2	0.18	3.98	2.00
0.8	2.94	9.28	0.26	0.1	0.05	4.00	1.86
0.7	2.25	7.80	0.35	0.0	0	3.33	0.17

to 2.23 rad. The critical value of Ω is obtained when the centrifugal acceleration balances the acceleration of gravity, i.e., $x_0\Omega^2 = g \Rightarrow \Omega_{cr} = \sqrt{g/x_0}$. In the present case, we have $\Omega_{cr} = 0.467\,\text{rad s}^{-1}$. For $\Omega < \Omega_{cr}$, the liquid tends to gravitate downwards no matter where the blade is positioned, as shown in Figure 6(b).

Figure 7 presents the motion of the liquid mass in both time and frequency domain, under three different rotational speeds. As shown in Figure 7(a), when $\Omega = \Omega_0$ the liquid moves in an oscillatory manner with the mean value of $\theta(t)$ equal to 0 rad, verifying the phenomenon illustrated in Figure 6(a). The dominant angular frequency of $\theta(t)$ is around $6.85\,\text{rad s}^{-1}$, and the liquid damper absorbs energy from fundamental edgewise eigenvibrations. Peaks corresponding to 1Ω and 2Ω are also visible in the frequency domain. As Ω decreases to $0.5\,\text{rad s}^{-1}$ [Figure 7(b)], the liquid motion becomes quasi-periodic with the dominant frequency equal to $0.5\,\text{rad s}^{-1}$. The reason is that the liquid motion $\theta(t)$ is defined in the moving (y_2, y_3)-coordinate system; because of more significant influence from gravity, $\theta(t)$ turns out to be quasi-periodic with its dominant frequency equal to the rotational speed of the rotor. One can also observe peaks corresponding to integral multiples of Ω, as well as a very low peak around the edgewise eigenfrequency, indicating a very weak coupling to the fundamental edgewise mode of the blade. As Ω decreases further to $0.4\,\text{rad s}^{-1}$ [Figure 7(c)], the acceleration due to gravity overwhelms the centrifugal acceleration. The dominant angular frequency of the quasi-periodic liquid motion is still the rotational speed of the rotor, and contributions from integral multiples of Ω can also be observed in the frequency domain. It is seen from Figure 7(c) that when $x_0\Omega^2 < g$, the amplitude of $\theta(t)$ varies between 0 and -2π rad in one periodical motion, verifying the physical fact that the liquid tends to gravitate downwards regardless of the azimuthal angle of the blade.

To verify the applicability of the decoupled optimization and the control effect of the circular liquid damper in a highly coupled wind turbine system, the optimized damper is incorporated into the 13-DOF model. For each blade, a circular liquid damper is mounted at the position of $x_0 = 45$ m. Hence, a 16-DOF system is obtained for the wind turbine with a total of three liquid dampers installed. Figure 8 shows the edgewise vibration in blade 1, with the same damper parameters and the same wind field as used in Figure 5. It is shown from Figure 8(a) that the damper with parameters optimized from the reduced 2-DOF model effectively mitigates the blade edgewise vibration of the highly coupled wind turbine system. The maximum edgewise tip displacement is reduced from 0.515 to 0.436 m (reduced by 15.33%), and the standard deviation is reduced from 0.1015 to 0.0776 m (reduced by 23.55%). Similar to Figure 5(b), Figure 8(b) demonstrates that the frequency component corresponding to fundamental edgewise mode of the blade is significantly reduced by the damper, whereas the frequencies below ω_0 are unaffected. Compared with the results obtained from the 2-DOF model as illustrated in Figure 5, the control efficiency of the liquid damper is slightly reduced when it is incorporated into the highly coupled system. This is because the couplings of blade edgewise vibration to other degrees of freedom cause a transfer of mechanical energy

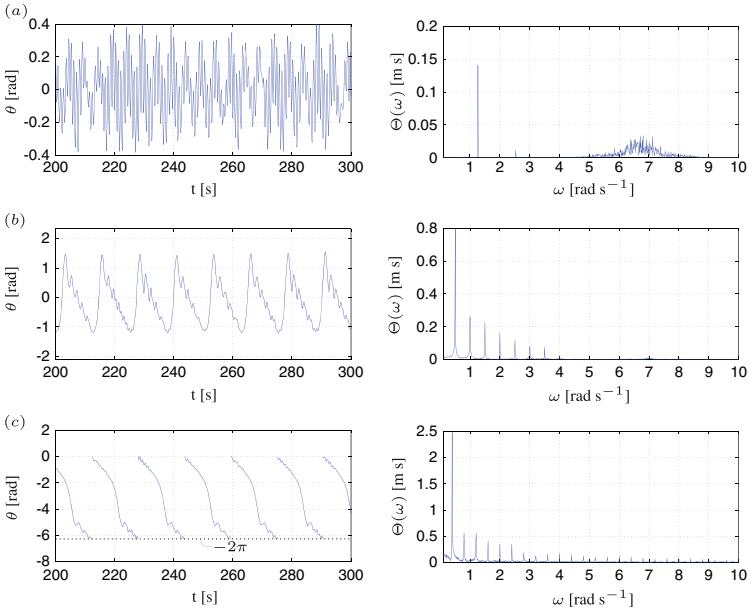

Figure 7. Time series and related Fourier spectrum of the liquid motion for various values of Ω, $V_0 = 15\,\mathrm{m\,s^{-1}}$, $l = 0.1$, $\mu = 0.03$, $\alpha = 0.05$, $x_0 = 45\,\mathrm{m}$. (a) $\Omega = 1.267\,\mathrm{rad\,s^{-1}}$. (b) $\Omega = 0.5\,\mathrm{rad\,s^{-1}}$. (c) $\Omega = 0.4\,\mathrm{rad\,s^{-1}}$.

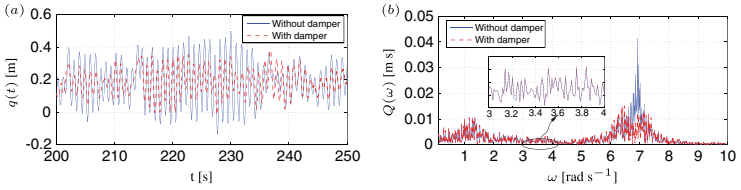

Figure 8. Blade edgewise vibrations with and without the liquid damper, obtained from the 16-DOF model. $\Omega = 1.267\,\mathrm{rad\,s^{-1}}$, $V_0 = 15$, $l = 0.1$, $\mu = 0.03$, $\alpha = 0.05$, $x_0 = 45\,\mathrm{m}$, optimal ω_d and ξ. (a) Time series, (b) Fourier amplitude.

from edgewise vibration to other vibrational modes, resulting in a slightly worse damping performance of the damper. Nevertheless, the circular liquid damper with parameters optimized from the reduced 2-DOF model is able to achieve equally promising results on the highly coupled 13-DOF model.

3.3. Further case study on a 10 MW wind turbine

In the deployment of offshore wind power, a clear trend toward larger wind turbines can be observed. It is believed that larger wind turbines can help to reduce the cost of energy for offshore wind farms, and designs for 10 MW turbines are being developed, such as the Danish Technical University (DTU) 10 MW reference wind turbine.[22,23] To evaluate the performance of CLCD in even larger blades, a case study on a 10 MW wind turbine is carried out. In this case, data from the DTU 10 MW reference wind turbine[22,23] are used to calibrate both the 2-DOF and 13-DOF models. Each blade has a length of 89.2 m and an overall mass of 41,788 kg, which is much larger compared with the blade of the 5 MW wind turbine. As a result of the increased maximum tip speed ($90\,\mathrm{m\,s^{-1}}$ for the 10 MW turbine and $80\,\mathrm{m\,s^{-1}}$ for the 5 MW turbine), the rotational speed of the 10 MW wind turbine is slightly reduced to $1.00\,\mathrm{rad\,s^{-1}}$, even though the blade length is significantly increased. Table IV presents the parameters employed in the 2-DOF model for the larger turbine, where the

Table IV. Parameters in 2-DOF blade-damper model for the 10 MW wind turbine.

Parameter	Value	Unit
L	89.2	m
x_0	60	m
Ω_0	1.00	rad s^{-1}
m_0	$2.207{\cdot}10^3$	kg
m_1	$5.652{\cdot}10^3$	kg
k_e	$7.530{\cdot}10^4$	N m^{-1}
k_1	$3.287{\cdot}10^3$	kg
k_2	53.446	kg m^{-1}
ζ_0	0.005	—
a	0.4102	—
b	0.0160	m^{-1}
ρ	$1.0{\cdot}10^3$	kg m^{-3}
g	9.81	m s^{-2}
ω_0	5.840	rad s^{-1}

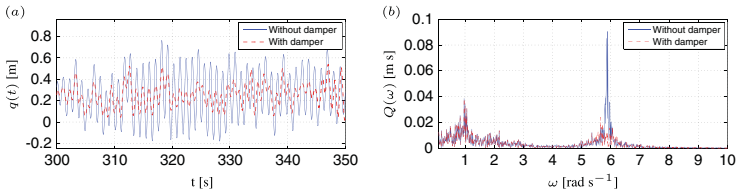

Figure 9. Blade edgewise vibrations with and without the liquid damper, for the 10 MW wind turbine. $L = 89.2$ m, $\Omega = 1.00$ rad s^{-1}, $V_0 = 15$, $I = 0.1$, $\mu = 0.03$, $\alpha = 0.03$, $x_0 = 60$ m, optimal ω_d and ξ. (a) Time series, (b) Fourier amplitude.

modal parameters are calculated in the same way as in Table I. It should be noted that we obtain the mode shapes of the blade by establishing a 3D finite element model of the blade with 51 beam elements. Further, sixth-order polynomials are used to fit the fundamental flap-wise and edgewise mode shapes:

$$\left.\begin{aligned}\Phi_f(x_3) &= -1.13\bar{x}^6 + 2.533\bar{x}^5 - 2.255\bar{x}^4 + 1.423\bar{x}^3 + 0.4294\bar{x}^2\\ \Phi(x_3) &= -0.5087\bar{x}^6 - 0.011\bar{x}^5 + 1.068\bar{x}^4 + 0.3317\bar{x}^3 + 0.12\bar{x}^2\end{aligned}\right\} \tag{30}$$

with $\bar{x} = \frac{x_3}{L}$.

In the same manner, the edgewise modal load for the 2-DOF model is obtained by applying a 3D rotational sampled wind field to the rotor of the 13-DOF model with $V_0 = 15\,\mathrm{m\,s^{-1}}$, $I = 0.1$. Extensive parametric studies of the damper are not carried out here. With the assigned values of the following parameters, $\mu = 0.03, \alpha = 0.03$, $x_0 = 60$ m (two thirds of the total blade length), the optimal frequency ratio and head loss coefficient can be determined. Figure 9 shows the comparison of edgewise vibration with and without the optimized liquid damper for the 10 MW turbine. A CLCD with a mass ratio of 0.03 ($m = 66.2$ kg) significantly mitigates the edgewise vibration of the blade, with the standard deviation reduced by 30.05%. The Fourier amplitude spectrum in Figure 9(b) clearly shows two peaks corresponding to the fundamental edgewise frequency (5.840 rad s^{-1}) and the rotational speed of the rotor (1.00 rad s^{-1}), both of which have lower frequencies compared with the 5 MW turbine. The CLCD almost totally eliminates the peak corresponding to the fundamental edgewise mode, which proves the effectiveness of the CLCD in a very large wind turbine blade. Because the calculated edgewise modal loads for the 5 and 10 MW turbines are different, quantitative comparison of the performance of the CLCD is meaningless. Nevertheless, one can observe from Figures 5 and 9 that CLCD with optimal parameters performs equally well in reducing edgewise vibrations for the NREL 5 MW turbine and the DTU 10 MW turbine.

4. CONCLUDING REMARKS

A new type of liquid column damper termed as a circular liquid column damper (CLCD) has been proposed in the paper in order to suppress edgewise vibrations in wind turbine blades. An investigation is then carried out to evaluate the

effectiveness of the proposed CLCD in mitigating edgewise vibrations in wind turbine blades. Parametric optimization for tuning of the damper has been carried out using a reduced order (2-DOF) non-linear model developed for a rotating blade equipped with a CLCD. The optimally tuned damper is then used on a 13-DOF aeroelastic wind turbine model that incorporates coupled blade-tower-drivetrain vibrations as well as a pitch controller.

Simulation results show that an optimized CLCD with a very small mass ratio can effectively eliminate fundamental edgewise eigenvibrations of the blade in rated rotational speed. Better control performance can be obtained by increasing the liquid mass and equipping the damper closer to the blade tip. However, the damper mass and mounting position should be restricted according to the installation capacity and the available space inside the blade. The size of the damper can be regulated by changing the value of the radius ratio ($\alpha = r/R$). Further, it is observed that the performance of the CLCD falls drastically as the rotational speed of the rotor decreases as a result of detuning of the damper. When Ω is less than a critical value, the acceleration of gravity overwhelms the centrifugal acceleration, resulting in a situation such that the liquid tends to gravitate downwards regardless of the azimuthal angle of the blade.

Most of the simulations are based on the NREL 5 MW wind turbine. An additional case study on the DTU 10 MW turbine has also been carried out to evaluate the effect of the CLCD in a very large blade. It is shown that an optimally tuned CLCD performs equally well in the 10 MW wind turbine blade, even though the rated rotor rotational speed and the fundamental edgewise frequency are slightly reduced. All these results show that the proposed CLCDs are promising passive damper devices and can be utilized in wind turbine blades for edgewise vibration control.

ACKNOWLEDGEMENT

The second author gratefully acknowledges the financial support from the Chinese Scholarship Council under the State Scholarship Fund.

REFERENCES

1. Ahlström A. Influence of wind turbine flexibility on loads and power production. *Wind Energy* 2006; **9**(3): 237–249.
2. Murtagh PJ, Ghosh A, Basu B, Broderick BM. Passive control of wind turbine vibrations including blade/tower interaction and rotationally sampled turbulence. *Wind Energy* 2008; **11**(4): 305–317.
3. Lackner MA, Rotea MA. Passive structural control of offshore wind turbines. *Wind Energy* 2011; **14**(3): 373–388.
4. Colwell S, Basu B. Tuned liquid column dampers in offshore wind turbines for structural control. *Engineering Structures* 2009; **31**(2): 358–368.
5. Arrigan J, Pakrashi V, Basu B, Nagarajaiah S. Control of flapwise vibrations in wind turbine blades using semi-active tuned mass dampers. *Structural Control and Health Monitoring* 2011; **18**(8): 840–851.
6. Arrigan J, Huang C, Staino A, Basu B, Nagarajaiah S. A frequency tracking semi-active algorithm for control of edgewise vibrations in wind turbine blades. *Smart Structures and Systems, Special Issue on Passive and Smart Tuned Mass Dampers* 2013; **13**(82): 177–201.
7. Riziotis VA, Voutsinas SG, Politis ES, Chaviaropoulos PK. Aeroelastic stability of wind turbines: the problem, the methods and the issues. *Wind Energy* 2004; **7**(4): 373–392.
8. Petersen JT, Thomsen K, Madsen H A, *Stall strips can control edgewise vibrations*, Technical Report AED-RB-6(EN), Risø National Laboratory, Denmark, 1998.
9. Maldonado V, Farnsworth J, Gressick W, Amitay M. Active control of flow separation and structural vibrations of wind turbine blades. *Wind Energy* 2010; **13**(2-3): 221–237.
10. Johnson SJ, Baker JP, van Dam CP, Berg D. An overview of active load control techniques for wind turbines with an emphasis on microtabs. *Wind Energy* 2010; **13**(2-3): 239–253.
11. Lackner MA, van Kuik G. A comparison of smart rotor control approaches using trailing edge flaps and individual pitch control. *Wind Energy* 2010; **13**(2-3): 117–134.
12. Svendsen MN, Krenk S, Høgsberg J. Resonant vibration control of rotating beams. *Journal of Sound and Vibration* 2011; **330**(9): 1877–1890.
13. Staino A, Basu B, Nielsen SRK. Actuator control of edgewise vibrations in wind turbine blades. *Journal of Sound and Vibration* 2012; **331**(6): 1233–1256.
14. Fitzgerald B, Basu B, Nielsen SRK. Active tuned mass dampers for control of in-plane vibrations of wind turbine blades. *Structural Control and Health Monitoring* 2013; **20**(12): 1377–1396.
15. Fitzgerald B, Basu B. Cable connected active tuned mass dampers for control of in-plane vibrations of wind turbine blades. *Journal of Sound and Vibration* 2014; **333**(23): 5980–6004.

16. Vandiver JK, Mitone SK. Effect of liquid storage tanks on the dynamic response of offshore platforms. *Applied Ocean Research* 1979; **1**(2): 67–74.
17. Ogata K. *Morden Control Engineering* 5ed. Prentice Hall: New Jersey, 2009.
18. Jonkman J, Butterfield S, Musial W, Scott G, *Definition of 5-MW reference wind turbine for offshore system development*, Technical Report NREL/TP-500-38060, National Renewable Energy Laboratory (NREL), 2009.
19. Hansen MOL. *Aerodynamics of Wind Turbines*. Earthscan: London, 2008.
20. IEC. 61400-1. Wind turbine part 1; design requirements, International Electrotechnical Committee, 2005.
21. Krenk S, Svendsen MN, Hogsberg J. Resonant vibration control of three-bladed wind turbine rotors. *AIAA Journal* 2012; **50**(1): 148–161.
22. Bak C, Bitsche R, Yde A, Kim T, Hansen MH, Zahle F, Gaunaa M, Blasques J, Døssing M, Heinen J-JW, Behrens T, *Description of the DTU 10 MW Reference Wind Turbine*, DTU Wind Energy Report-I-0092, 2013.
23. Bak C, Bitsche R, Yde A, Kim T, Hansen MH, Zahle F, Gaunaa M, Blasques J, Døssing M, Heinen J-JW, Behrens T. Design and performance of a 10 MW wind turbine. *Wind Energy* 2014. to be accepted.

APPENDIX E

Nonlinear modeling of tuned liquid dampers (TLDs) in rotating wind turbine blades for damping edgewise vibrations

Paper 4

The paper presented in this appendix has been submitted to *Journal of Fluids and Structures*, 2015, In review.

E.1 Author's Right

Journal author rights

In order for Elsevier to publish and disseminate research articles, we need publishing rights. This is determined by a publishing agreement between the author and Elsevier. This agreement deals with the transfer or license of the copyright to Elsevier and authors retain significant rights to use and share their own published articles. Elsevier supports the need for authors to share, disseminate and maximize the impact of their research and these rights, in Elsevier proprietary journals* are defined below:

For subscription articles	For open access articles
Authors transfer copyright to the publisher as part of a journal publishing agreement, but have the right to: • Share their article for Personal Use, Internal Institutional Use and Scholarly Sharing purposes, with a DOI link to the version of record on ScienceDirect (and with the Creative Commons CC-BY-NC- ND license for author manuscript versions) • Retain patent, trademark and other intellectual property rights (including raw research data). • Proper attribution and credit for the published work.	Authors sign an exclusive license agreement, where authors have copyright but license exclusive rights in their article to the publisher**. In this case authors have the right to: • Share their article in the same ways permitted to third parties under the relevant user license (together with Personal Use rights) so long as it contains a CrossMark logo, the end user license, and a DOI link to the version of record on ScienceDirect. • Retain patent, trademark and other intellectual property rights (including raw research data). • Proper attribution and credit for the published work.

http://www.elsevier.com/journal-authors/author-rights-and-responsibilities

Nonlinear modeling of tuned liquid dampers (TLDs) in rotating wind turbine blades for damping edgewise vibrations

Zili Zhang[a,*], Søren R.K. Nielsen[a], Biswajit Basu[b], Jie Li[c]

[a]*Department of Civil Engineering, Aalborg University, 9000 Aalborg, Denmark*
[b]*Department of Civil, Structural & Environmental Engineering, School of Engineering, Trinity College Dublin, Dublin 2, Ireland*
[c]*School of Civil Engineering, Tongji University, Shanghai 200092, PR China*

Abstract

Tuned liquid dampers (TLDs) utilize the sloshing motion of the fluid to suppress structural vibrations and become a natural candidate for damping vibrations in rotating wind turbine blades. The centrifugal acceleration at the tip of a wind turbine blade can reach a magnitude of 7-8 g. This facilitates the use of a TLD with a relatively small fluid mass and with feasible geometric dimensions to mitigate the lightly-damped edgewise vibrations effectively. In the present paper, modal expansions are carried out directly on the velocity field and the free surface of the sloshing liquid in the rotating coordinate system. A formulation has been proposed leading to coupled nonlinear ordinary differential equations, which have been obtained through the Galerkin variational approach together with the modal expansion technique. Two models, with one sloshing mode and three sloshing modes have been studied in the numerical simulation. It is shown that the one-mode model is able to predict the sloshing force and the damped structural response accurately, since the primary damping effect on the structure is achieved by the first sloshing mode of the fluid. Although it is unable to predict the fluid free-surface elevation equally well, the one-mode model can still be utilized for the design of TLD. Parametric optimization of the TLD is carried out based on the one-mode model, and the optimized damper effectively improve the dynamic response of wind turbine blades.

Keywords: tuned liquid dampers, wind turbine blade, edgewise vibration, modal expansion

1. Introduction

Recent development in the wind energy industry aims at obtaining more economic and productive configurations in order to compete in the energy sector. This has led to larger multi-megawatt wind turbines with increased rotor diameters of over 160m, allowing more wind resource to be captured throughout their lifetime and lowering the cost of energy. On the other hand, as the size of the rotor increases, the blades are becoming more flexible and hence are more vulnerable to wind-induced vibrations. The large amplitude vibrations may significantly

*Corresponding author, Tel: +45 50256836
Email addresses: zlz@civil.aau.dk (Zili Zhang), srkn@civil.aau.dk (Søren R.K. Nielsen), basub@tcd.ie (Biswajit Basu), lijie@tongji.edu.cn (Jie Li)

shorten the fatigue life of the blade and reduce the operational efficiency in converting the wind energy to electrical power.

Conventionally, the modes of vibration for the blades are classified as flap-wise and edgewise modes. Flap-wise vibrations are vibrations out of the plane of the rotating rotor, whereas edgewise vibrations take place in the rotor plane. During normal operations, flap-wise vibrations are highly damped due to the strong aerodynamic damping as long as the boundary layer on the suction side of the profile is attached (Hansen, 2007). Therefore, motion in this direction merely turns out to be quasi-static responses to the incoming turbulent wind, containing only low frequency components from the wind shear and the stagnation during tower passage. In contrast, the modal damping in the edgewise direction is much lower due to low aerodynamic damping (Hansen, 2007; Thomsen et al., 2000), leading to more violent vibrations and increased fatigue damage of the blade. Moreover, due to the coupling between the blade edgewise motion and the drivetrain torsional motion, the unfavorable edgewise vibrations will increase the fluctuations of the generator torque, and hence the quality of the generated power. Further, there is also a possibility of aeroelastic instability in the edgewise direction for some combinations of blade properties and operational conditions, especially around rated wind speeds for turbines with high performance rotors operating close to stall (Hansen, 2007; Bir and Jonkman, 2007). When aeroelastic instability takes place, the sum of the structural damping and the aerodynamic damping becomes negative in the edgewise direction (Riziotis et al., 2004), and the motion grows exponentially, which may potentially lead to the failure of the overall system. Therefore, the mitigation of violent edgewise vibrations becomes a vital design consideration to improve the overall performance of wind turbine blades and to protect them from the fatigue damage during the design period.

The use of passive, semi-active and active damping devices, which introduce additional damping to suppress the damaging effect of wind, wave and earthquake loads on engineering structures, have been extensively investigated in the last few decades (Spencer and Nagarajaiah, 2003). In recent years, an increasing number of investigations are being carried out on vibration mitigation of wind turbine components using external devices. For wind turbine towers, several types of passive dampers have been proposed for reducing the vibrations induced by the wind and wave loads (Murtagh et al., 2008; Colwell and Basu, 2009; Lackner and Rotea, 2011; Stewart and Lackner, 2014; Zhang et al., 2014a). On the other hand, investigations regarding the mitigation of blade vibrations are mainly focused on the semi-active and active control solutions (Arrigan et al., 2011; Staino and Basu, 2013; Fitzgerald and Basu, 2014; Staino and Basu, 2015). Fitzgerald et al. (2013) investigated active TMDs for mitigating edgewise vibrations, and the active TMD achieved greater response reductions than its passive counterpart. Active struts mounted near the root of each blade was proposed by Krenk et al. (2012) for suppressing blade vibrations. Inspired by the concept of TMDs, the active control concept developed in this study is based on resonant interaction between the rotor and the controller. Staino et al. (2012) presented the use of active tendons mounted inside each blade for the control of edgewise vibrations. Manipulated according to a prescribed control law, a variable control force can be applied in the edgewise direction, improving the dynamic response of the blade significantly. However, both semi-active and active control solutions need relatively complicated controller configurations and some amount of power input. Recently, investigations have been carried out on the performance of both a roller damper (Zhang et al., 2014b) and a tuned liquid column damper (TLCD) (Zhang et al., 2015a) equipped inside a rotating blade. Because of the large centrifugal acceleration of the rotating blade, it was shown that both the roller damper and the TLCD with small mass ratios could effectively mitigate edgewise vibrations.

Added fluid mass can be used to effectively counteract undesired oscillations of structures (Langthjem and Nakamura, 2014). The tuned liquid damper (TLD), which consists of a tank partially filled with fluid, is a passive damping device for mitigation of structural vibrations by utilizing the sloshing fluid. Normally, the fundamental sloshing frequency of the liquid is tuned to the fundamental frequency of the primary structure. When the TLD is excited by the motion of the primary structure, the liquid in the tank begins to slosh, imparting inertial forces onto the structure, out of phase with its motion, thus absorbing and dissipating energy. The main advantages of the TLD are the ease of fabrication and installation, especially where space constraints exist, and minimal maintenance after installation, which make the device very cost-effective. The TLD has been shown to effectively suppress the wind-induced vibration of structures (Fujii et al., 1990; Tamura et al., 1995; Chang and Gu, 1999). It is also proposed for seismic control of structures. Both experimental and theoretical studies (Banerji et al., 2000; Lee et al., 2007; Jin et al., 2007) have shown that a TLD does reduce the vibrations of flexible structures subjected to earthquake excitations. The primary difficulties associated with TLDs arise from the nonlinear nature of the sloshing liquid, which makes modeling and designing these devices challenging. Numerous methods have been employed to predict the response of sloshing liquid. Equivalent mechanical models based on TMD analogy (Sun et al., 1995; Yu et al., 1999) simplify the TLD to an equivalent tuned mass damper, with the equivalent mass, stiffness and damping calibrated from the experimental results. This kind of model is able to predict the energy dissipation through liquid sloshing and is useful in the preliminary design of the TLD. However, the nonlinear fluid response cannot be captured by such simple models. Nonlinear shallow water wave theory (Sun et al., 1994; Reed et al., 1998) has been proposed for predicting the response of fluid sloshing in rectangular tanks. Although the nonlinear shallow-water wave equations can be solved numerically, it is computational inefficient and does not provide an effective design tool for engineering application. Modal expansion techniques (Faltinsen et al., 2000; Faltinsen and Timokha, 2001; Love and Tait, 2010) have been used to model the sloshing problem, where the fluid flow is assumed to be inviscid, irrotational, incompressible and without rigid-body rotations. The velocity potential and the free surface are expressed as a summation of sloshing modes, and a system of coupled ordinary differential equations are developed by applying calculus of variations (Faltinsen et al., 2000; Faltinsen and Timokha, 2001).

In this paper, the TLD is proposed for mitigating edgewise vibrations in rotating wind turbine blades. In the case of the building or tower vibrations, the sloshing of the liquid and thus the damping effect of the TLD is governed by the gravitational acceleration, g. For a rotating wind turbine blade, the corresponding damping effect is governed by the centrifugal acceleration, which can reach up to a magnitude of 7-8 g at the tip of a 65m-long blade. This makes it possible to use the TLD with a rather small mass for effectively suppressing edgewise vibrations.

Similar as in the work of Faltinsen et al. (2000) and Faltinsen and Timokha (2001), modal expansion technique has been used in this paper for the sloshing problem. However, the main obstacle in modeling the TLD in rotating blades is that strong non-inertial forces appear in the Euler equations in terms of the angular acceleration, the Coriolis acceleration and the centripetal acceleration. These effects render the use of potential flow theory invalid even for inviscid and irrotational fluid flow. Therefore, modal expansion is carried out directly on the velocity field of the fluid rather than the velocity potential. The basic idea for the modeling of the TLD in this paper is as follows. First of all, boundary value problem (Euler equations with the nonlinear boundary conditions) for the liquid inside the TLD is derived in the local, rotating coordinate system. Next, the Galerkin variational approach has been used to develop two equations, one for the velocity field, and the other one for the kinematical boundary condition at the free surface.

These two equations are used with the modal expansions to develop a system of coupled ordinary differential equations. Here the shape functions in the modal expansion of the velocity field are taken as the eigenmodes of standing waves in linear wave theory, based on which the shape functions for the surface elevation can also be obtained. Finally, the differential equations of the fluid are combined with the equation of motion of the edgewise blade vibration, which completes the modeling of the problem.

In the numerical simulation, both the one-sloshing-mode model and three-sloshing-mode model have been considered for study. The sloshing force, the damped structural response and the fluid surface elevation are compared between the two models. Parametric studies have also been performed for the TLD with different mass ratios and tank lengths.

2. Theoretical model for the TLD installed in a rotating blade

The edgewise vibrations of a wind turbine blade are coupled to the lateral tower and drivetrain vibrations, which may also influence the motion of the fluid inside the TLD. However, previous studies (Zhang et al., 2014b; Zhang et al., 2015a; Basu et al., 2015) have proved that this coupling is of minor importance for the optimal design of passive dampers inside a blade. It has been shown that the optimally tuned passive dampers perform almost equally well in a highly-coupled 13-DOF wind turbine model, even though the optimal tuning is based on a reduced 2-DOF blade-damper model ignoring the coupling with the tower and drivetrain vibrations. Therefore, in the present paper only the mode corresponding to blade edgewise vibrations is considered, and the analysis of the TLD is totally based on the local dynamics of the rotating blade without considering the influence from other components of the wind turbine.

2.1. Definition of the problem

Figure 1 appears about here.

Fig. 1 shows the schematic representation of a rotating blade equipped with a TLD. (X_1, X_2, X_3)- is the global fixed coordinated system with its origin O fixed at the center of the hub. The edgewise vibration of the blade is described in the moving (x_1, x_2, x_3)- coordinate system, while the motion of the liquid inside the TLD is described by another local coordinate system (y_1, y_2, y_3) fixed to the damper. For each blade, the mass per unit length and bending stiffness in the edgewise direction are denoted by $\mu(x_3)$ and $EI(x_3)$, respectively. Similar to other inertial based dampers for passive vibration control such as a tuned mass damper (TMD), the TLD has a rather limited bandwidth (although might be wider than a TMD due to nonlinear sloshing effects), and is likely only to mitigate vibrations in a single mode at optimal tuning. In the present case the aim is to damp the fundamental edgewise mode, which is described by the degree of freedom $q(t)$. Further, the azimuthal angle $\Psi(t)$ of the blade is given as:

$$\Psi(t) = \Omega t \tag{1}$$

where Ω is the angular rotational speed of the blade, which is assumed constant in time.

Further, the local edgewise displacement $u_2(x_3, t)$ of the rotating blade in the x_2-direction can be described by the single modal coordinate $q(t)$ as:

$$u_2(x_3, t) = -\Phi(x_3)\, q(t) \tag{2}$$

where $\Phi(x_3)$ is the fundamental eigenmode of the blade edgewise vibration. This is normalized to 1 at the tip, i.e. $\Phi(L_B) = 1$, where L_B denotes the blade length. The negative sign refers to the definition of $q(t)$ in the negative direction of the x_2-axis, as shown in Fig. 1.

Assuming the TLD to be mounted at the coordinate $x_3 = x_0$, the elastic displacement and rotation of the blade at this position are given by

$$\left.\begin{aligned} u_2(x_0, t) &= -b\, q(t) \\ \varphi(t) &= c\, q(t) \end{aligned}\right\} \tag{3}$$

where the following auxiliary parameters have been introduced:

$$\left.\begin{aligned} b &= \Phi(x_0) \\ c &= \Phi'(x_0) \end{aligned}\right\} \tag{4}$$

The TLD is made up of a closed rectangular tank with the length L and the width B. The height of the tank is assumed to be sufficiently larger than the mean water depth h, so that there is enough free board and the surface elevation η will not reach the ceiling of the damper. The mass of the oscillating liquid becomes:

$$m_l = \rho h L B \tag{5}$$

where ρ denotes the mass density of the liquid.

2.2. Boundary value problem in the rotating coordinate system

As shown in Fig. 2, the motion of the fluid relative to the tank is described in (y_1, y_2, y_3)-coordinate system fixed to the damper with its origin O' placed at the center of the mean water level (MWL). It is assumed that the free surface can be defined by a single variable of the surface elevation $\eta(y_1, y_3, t)$ measured from the mean water level. Hence, overturning waves, slamming or breaking waves are not covered by the following theory. Further, the fluid is considered incompressible, inviscid and irrotational.

Figure 2 appears about here.

A given fluid particle is described by the position vector $\mathbf{r}(t)$, which is decomposed as follows:

$$\mathbf{r}(t) = \mathbf{r}_0(t) + \mathbf{y}(t) \tag{6}$$

where $\mathbf{r}_0(t)$ and $\mathbf{y}(t)$ denote the position vector from the fixed origin O to the point O' and the position vector from the point O' to the fluid particle. Further, $\boldsymbol{\omega}(t)$ denotes the angular velocity vector of the moving (y_1, y_2, y_3)-coordinate system relative to the (X_1, X_2, X_3)-coordinate system (Fig. 2). Then the following result can be derived for the velocity vector and acceleration vector of the fluid particle in the (y_1, y_2, y_3)-coordinate system:

$$\left.\begin{aligned}
\dot{\mathbf{r}}(t) &= \dot{\mathbf{r}}_0(t) + \mathbf{v}(\mathbf{y}(t),t) + \boldsymbol{\omega}(t)\times\Big(\mathbf{r}_0(t)+\mathbf{y}(t)\Big)\\
\ddot{\mathbf{r}}(t) &= \ddot{\mathbf{r}}_0(t) + \dot{\mathbf{v}}(\mathbf{y}(t),t) + \dot{\boldsymbol{\omega}}(t)\times\Big(\mathbf{r}_0(t)+\mathbf{y}(t)\Big) + 2\,\boldsymbol{\omega}(t)\times\Big(\dot{\mathbf{r}}_0(t)+\mathbf{v}(\mathbf{y}(t),t)\Big) +\\
&\quad \boldsymbol{\omega}(t)\times\Big(\boldsymbol{\omega}(t)\times(\mathbf{r}_0(t)+\mathbf{y}(t))\Big)
\end{aligned}\right\} \tag{7}$$

where $\dot{\boldsymbol{r}}_{\mathbf{0}}$ is the vector with components $\dot{r}_{0,j}$ in the local (y_1,y_2,y_3)-coordinate system. $\ddot{\boldsymbol{r}}_{\mathbf{0}}$ is the vector with components $\ddot{r}_{0,j}$ in (y_1,y_2,y_3)-coordinate system. $\dot{\boldsymbol{\omega}}(t)\times\Big(\mathbf{r}_0(t)+\mathbf{y}(t)\Big)$, $2\,\boldsymbol{\omega}(t)\times\Big(\dot{\mathbf{r}}_0(t)+\mathbf{v}(\mathbf{y}(t),t)\Big)$ and $\boldsymbol{\omega}(t)\times\Big(\boldsymbol{\omega}(t)\times(\mathbf{r}_0(t)+\mathbf{y}(t))\Big)$ indicate the contributions to the acceleration vector from the angular acceleration, the Coriolis acceleration and the centripetal acceleration, respectively. It should be noted that $\mathbf{v}(\mathbf{y}(t),t)$ and $\dot{\mathbf{v}}(\mathbf{y}(t),t)$ indicate the velocity and acceleration vectors of the fluid particle as seen by an observer fixed to the (y_1,y_2,y_3)-coordinate system.

Up to now a Lagrangian description of the motion of a certain fluid particle has been followed. Next, the description is reformulated in Eulerian coordinates. This means that the acceleration $\dot{\mathbf{v}}(\mathbf{y},t)$ of the particle occupying the position $\mathbf{y}$ at the time t is calculated as $\dot{\mathbf{v}}(\mathbf{y},t) = \frac{\partial}{\partial t}\mathbf{v}(\mathbf{y},t) + (\mathbf{v}(\mathbf{y},t)\cdot\nabla)\,\mathbf{v}(\mathbf{y},t)$ (Malvern, 1969), resulting in the following boundary value problem:

$$\left.\begin{aligned}
&\rho\Big(\frac{\partial}{\partial t}\mathbf{v}(\mathbf{y},t) + \Big(\mathbf{v}(\mathbf{y},t)\cdot\nabla\Big)\mathbf{v}(\mathbf{y},t)\Big) + \rho\,\ddot{\mathbf{r}}_0(t) + \rho\,\dot{\boldsymbol{\omega}}(t)\times\Big(\mathbf{r}_0(t)+\mathbf{y}\Big) +\\
&2\,\rho\,\boldsymbol{\omega}(t)\times\Big(\dot{\mathbf{r}}_0(t)+\mathbf{v}(\mathbf{y},t)\Big) + \rho\,\boldsymbol{\omega}(t)\times\Big(\boldsymbol{\omega}(t)\times(\mathbf{r}_0(t)+\mathbf{y})\Big) = -\nabla p(\mathbf{y},t) + \rho\,\mathbf{g}\,, \quad \mathbf{y}\in V(t)\\
&\nabla\cdot\mathbf{v}(\mathbf{y},t) = 0 \quad , \quad \mathbf{y}\in V(t)\\
&\mathbf{v}(\mathbf{y},t)\cdot\mathbf{n}(\mathbf{y}) = 0 \quad , \quad \mathbf{y}\in A_1(t)\\
&p(\mathbf{y},t) = 0 \quad , \quad \mathbf{y}\in A_2(t)\\
&v_2(\mathbf{y},t) = \frac{\partial\eta(y_1,y_3,t)}{\partial t} + v_1(\mathbf{y},t)\frac{\partial\eta(y_1,y_3,t)}{\partial y_1} + v_3(\mathbf{y},t)\frac{\partial\eta(y_1,y_3,t)}{\partial y_3} \quad , \quad \mathbf{y}\in A_2(t)
\end{aligned}\right\} \tag{8}$$

where $\mathbf{g}$ denotes the acceleration due to gravity vector. All the components of the vectors entering Eq. (8) will be indicated in the (y_1,y_2,y_3)-coordinate system, in which the components of $\mathbf{g}$ become time-dependent. Due to the assumed incompressibility, the volume of the fluid is constant in time. However, the shape as specified by the surface elevation $\eta(y_1,y_3,t)$ is changing with time. Therefore, the domain $V(t)$ occupied by the fluid, the wet part of the boundary $A_1(t)$, and the free surface $A_2(t)$ will be time varying as well.

The boundary condition $\mathbf{v}(\mathbf{y},t)\cdot\mathbf{n}(\mathbf{y}) = 0$ at $A_1(t)$ specifies that the velocity component of the fluid in the outward direction must be zero, where $\mathbf{n}(\mathbf{y})$ is the unit normal vector at $A_1(t)$. At the free surface $A_2(t)$, the pressure above atmospheric pressure $p(\mathbf{y},t)$ must vanish. Further, a fluid particle at the free surface must remain there at all time, which is specified by the other boundary condition at $A_2(t)$.

Being placed close to the blade tip with small blade thickness, the width B of the TLD will be small compared to h and L. Due to this geometric constrain, the flow is predominantly 2-dimensional, taking place in the (y_1,y_2)- plane. Hence it is assumed that $v_3(\mathbf{y},t)\equiv 0$ in the present study. Due to the incompressibility of the fluid the surface elevation needs to fulfill the

integral condition:

$$\int_{-L/2}^{L/2} \eta(y_1,t)\,dy_1 \;=\; 0 \tag{9}$$

The components of $\mathbf{r}_0(t)$, $\mathbf{g}$ and $\boldsymbol{\omega}(t)$ in the (y_1,y_2,y_3)-coordinate system are given by (see Fig. 1):

$$\mathbf{r}_0(t) \;=\; \begin{bmatrix} x_0\sin\varphi(t) - bq(t)\cos\varphi(t) \\ -x_0\cos\varphi(t) - bq(t)\sin\varphi(t) \\ 0 \end{bmatrix},\; \mathbf{g}(t) \;=\; g\begin{bmatrix} -\sin\big(\Psi(t)+\varphi(t)\big) \\ \cos\big(\Psi(t)+\varphi(t)\big) \\ 0 \end{bmatrix},\; \boldsymbol{\omega}(t) \;=\; \begin{bmatrix} 0 \\ 0 \\ -\dot{\Psi}(t)-\dot{\varphi}(t) \end{bmatrix} \tag{10}$$

where the components have been presented in matrix formulation for ease. The term g is the scalar magnitude of acceleration due to gravity (i.e. 9.8 m/s^2).

2.3. The Galerkin variational method and the modal expansion

Faltinsen et al. (2000) proposed the use of potential theory for the sloshing problem, where the rotation of the TLD is around the origin O'. The rotation of the TLD is around the origin O (the hub center) in the present case, which causes a centrifugal acceleration of the fluid particles of the magnitude $\Omega^2\,x_0$, much larger than the centrifugal acceleration of the magnitude $\Omega^2\,|\mathbf{y}|$ caused by a rotation around O'. In the present study, the solution to the problem will be based on a discretization of the velocity field equation and non-linear boundary conditions in Eq. (8), rather than based on potential theory.

In order to derive a weak representation of the boundary value problem in Eq. (8), a virtual variation $\delta\mathbf{v}(\mathbf{y})$ of the fluid velocity field is considered with the following properties:

$$\left.\begin{aligned} \nabla\cdot\delta\mathbf{v}(\mathbf{y}) \;&=\; 0 \quad,\quad \mathbf{y}\in V(t) \\ \delta\mathbf{v}(\mathbf{y})\cdot\mathbf{n}(\mathbf{y}) \;&=\; 0 \quad,\quad \mathbf{y}\in A_1(t) \end{aligned}\right\} \tag{11}$$

Scalar multiplication of the momentum equation with $\delta\mathbf{v}(\mathbf{y})$, followed by an integration over $V(t)$ provides:

$$\int_{V(t)} \delta\mathbf{v}(\mathbf{y})\cdot\left(\rho\left(\frac{\partial}{\partial t}\mathbf{v}(\mathbf{y},t) + \big(\mathbf{v}(\mathbf{y},t)\cdot\nabla\big)\mathbf{v}(\mathbf{y},t)\right) + 2\,\rho\,\boldsymbol{\omega}(t)\times\mathbf{v}(\mathbf{y},t) - \rho\,\mathbf{a}_e(\mathbf{y},t) + \nabla p(\mathbf{y},t)\right)dV \;=\; 0 \tag{12}$$

where $\mathbf{a}_e(\mathbf{y},t)$ is an effective acceleration vector on the fluid particle defined as:

$$\mathbf{a}_e(\mathbf{y},t) \;=\; \mathbf{g} \;-\; \ddot{\mathbf{r}}_0(t) \;-\; \dot{\boldsymbol{\omega}}(t)\times\big(\mathbf{r}_0(t)+\mathbf{y}\big) \;-\; 2\,\boldsymbol{\omega}(t)\times\dot{\mathbf{r}}_0(t) \;-\; \boldsymbol{\omega}(t)\times\Big(\boldsymbol{\omega}(t)\times\big(\mathbf{r}_0(t)+\mathbf{y}\big)\Big) \tag{13}$$

From the divergence theorem

$$\int_{V(t)} \delta\mathbf{v}(\mathbf{y})\cdot\nabla p(\mathbf{y},t)\,dV \;=\; p(\mathbf{y},t)\,\delta\mathbf{v}(\mathbf{y})\cdot\mathbf{n}(\mathbf{y})\Big|_{\mathbf{y}\in A_1(t)+A_2(t)} \;-\; \int_{V(t)} p(\mathbf{y},t)\nabla\cdot\delta\mathbf{v}\,dV \;=\; 0 \tag{14}$$

The vanishing of the volume integral follows from: 1) the mechanical boundary conditions for $p(\mathbf{y},t)$ on $A_2(t)$ and the kinematic boundary condition for $\delta v(\mathbf{y})$ on $A_1(t)$ as indicated in Eqs.

(8) and (11). 2) the assumed incompressibility of the variational field in $V(t)$. Then, Eq. (12) is simplified as:

$$\int_V \delta\mathbf{v}(\mathbf{y}) \cdot \left(\rho \left(\frac{\partial}{\partial t}\mathbf{v}(\mathbf{y},t) + \Big(\mathbf{v}(\mathbf{y},t)\cdot\nabla\Big)\mathbf{v}(\mathbf{y},t)\right) + 2\,\rho\,\boldsymbol{\omega}(t)\times\mathbf{v}(\mathbf{y},t) - \rho\,\mathbf{a}_e(\mathbf{y},t)\right) dV = 0 \quad (15)$$

This variational equation (Eq. (15)) has some resemblance to the variational principle (Luke, 1967) for potential flows in the sense that the pressure $p(\mathbf{y},t)$ disappears from the stationarity condition.

Next, the following modal expansion of the velocity field $\mathbf{v}(\mathbf{y},t)$ and its virtual variation $\delta\mathbf{v}(\mathbf{y})$ are formulated:

$$\left.\begin{aligned} \mathbf{v}(\mathbf{y},t) &= \sum_{i=1}^{\infty} r_i(t)\,\mathbf{V}_i(\mathbf{y}) \quad , \quad \mathbf{y}\in V(t) \\ \delta\mathbf{v}(\mathbf{y}) &= \sum_{i=1}^{\infty} \delta r_i\,\mathbf{V}_i(\mathbf{y}) \quad , \quad \mathbf{y}\in V(t) \end{aligned}\right\} \quad (16)$$

where $r_i(t)$ and δr_i denote the generalized coordinates of the velocity field and the variational field. As seen the same functional bases have been assumed for the two expansions, corresponding to a Galerkin variational method. The shape functions $\mathbf{V}_i(\mathbf{y})$ are not required to fulfill any mechanical boundary conditions on the free surface $A_2(t)$. However, they need to have zero divergence in $V(t)$ and to fulfill vanishing kinematical boundary conditions on $A_1(t)$:

$$\left.\begin{aligned} \nabla\cdot\mathbf{V}_i(\mathbf{y}) &= 0 \quad , \quad \mathbf{y}\in V(t) \\ \mathbf{V}_i(\mathbf{y})\cdot\mathbf{n}(\mathbf{y}) &= 0 \quad , \quad \mathbf{y}\in A_1(t) \end{aligned}\right\} \quad (17)$$

Substituting Eq. (16) into Eq. (15), and using that δr_i can be varied independently, the following infinite system of ordinary nonlinear differential equation are obtained for the generalized coordinates $r_i(t)$:

$$\sum_{j=1}^{\infty} m_{ij}(t)\,\dot{r}_j(t) + \sum_{j=1}^{\infty} n_{ij}(t)\,r_j(t) + \sum_{j=1}^{\infty}\sum_{k=1}^{\infty} o_{ijk}(t)\,r_j(t)\,r_k(t) = f_i(t) \quad , \quad i = 1,2,\ldots \quad (18)$$

$$\left.\begin{aligned} m_{ij}(t) &= \int_{V(t)} \rho\,\mathbf{V}_i(\mathbf{y})\cdot\mathbf{V}_j(\mathbf{y})\,dV \\ n_{ij}(t) &= \int_{V(t)} 2\rho\,\mathbf{V}_i(\mathbf{y})\cdot\Big(\boldsymbol{\omega}(t)\times\mathbf{V}_j(\mathbf{y})\Big)\,dV = 2\rho\,\boldsymbol{\omega}(t)\cdot\int_{V(t)}\mathbf{V}_j(\mathbf{y})\times\mathbf{V}_i(\mathbf{y})\,dV \\ o_{ijk}(t) &= \int_{V(t)} \rho\,\mathbf{V}_i(\mathbf{y})\cdot\Big((\mathbf{V}_j(\mathbf{y})\cdot\nabla)\,\mathbf{V}_k(\mathbf{y})\Big)\,dV \\ f_i(t) &= \int_{V(t)} \rho\,\mathbf{V}_i(\mathbf{y})\cdot\mathbf{a}_e(\mathbf{y},t)\,dV \end{aligned}\right\} \quad (19)$$

The tensor components in equation Eq. (16) are time-dependent due to the time-varying fluid domain $V(t)$. In Appendix A, semi-analytical expressions for these components have been given, based on which they can be calculated using one-dimensional numerical integration.

In the present paper, the shape functions in Eq. (19) are taken as the eigenmodes of standing waves in linear wave theory (Svendsen and Jonsson, 1976) given by:

$$\mathbf{V}_i(\mathbf{y}) = \begin{bmatrix} -\sin(k_i\,(y_1+\frac{L}{2}))\,\cosh(k_i\,(y_2+h)) \\ \cos(k_i\,(y_1+\frac{L}{2}))\,\sinh(k_i\,(y_2+h)) \\ 0 \end{bmatrix} \quad , \quad (y_1,y_2) = [-\frac{L}{2},\frac{L}{2}]\times[-h,\eta(y_1,t)] \tag{20}$$

The chosen shape functions are equivalent to the ones by Faltinsen et al. (2000), Love and Tait (2010), where the eigenfunctions in linear potential theory were used as functional basis in the expansion of the velocity potential $\Phi(\mathbf{y},t)$. The gradient of $\Phi(\mathbf{y},t)$ leads to exactly the same results as in Eq. (20). It can also be verified that $\mathbf{V}_i(\mathbf{y})$ has zero divergence for any value of the wave number k_i in the liquid domain. Further, the chosen shape functions fulfill certain orthogonality conditions, which will make the resulting system equations simpler. In order to fulfill the kinematic boundary condition on $A_1(t)$ the wave numbers must be chosen as:

$$k_i = i\frac{\pi}{L} \quad , \quad i = 1,2,\ldots \tag{21}$$

Mounted inside the rotating blade, the motion of the sloshing fluid in the TLD is primarily governed by the centrifugal acceleration $x_0\Omega^2$, which turns out to be the dominating component in Eq. (13). Hence, the angular eigenfrequencies ω_i of the standing waves are approximately determined from the dispersion relation:

$$\omega_i^2 \simeq x_0\Omega^2\,k_i\,\tanh(k_i h) \tag{22}$$

which is identical to the corresponding dispersion relation for gravity waves (Svendsen and Jonsson, 1976), except that the gravitational acceleration g has been replaced by the centrifugal acceleration $x_0\Omega^2$.

Further, the boundary condition on the free surface is discretized in a similar manner. Let $\delta\eta(y_1)$ denote a virtual displacement of the surface elevation $\eta(y_1,t)$. The multiplication of the boundary condition with $\delta\eta(y_1)$ followed by an integration over the interval $[-L/2,L/2]$ provides the stationarity condition:

$$\int_{-L/2}^{L/2}\delta\eta(y_1)\left(\frac{\partial\eta(y_1,t)}{\partial t}+v_1(\mathbf{y},t)\frac{\partial\eta(y_1,t)}{\partial y_1}-v_2(\mathbf{y},t)\right)dy_1 = 0 \tag{23}$$

The following modal expansion of the surface elevation $\eta(y_1,t)$ and its virtual variation $\delta\eta(y_1)$ are formulated:

$$\left.\begin{aligned} \eta(y_1,t) &= \sum_{i=1}^{\infty} s_i(t)\,\cos\left(k_i\left(y_1+\frac{L}{2}\right)\right) \\ \delta\eta(y_1) &= \sum_{i=1}^{\infty}\delta s_i\,\cos\left(k_i\left(y_1+\frac{L}{2}\right)\right) \end{aligned}\right\} \tag{24}$$

where $s_i(t)$ and δs_i denote the generalized coordinates of $\eta(y_1,t)$ and $\delta\eta(y_1)$. The selected shape functions in Eq. (24) is motivated by the linear wave theory, where the free surface condition reduces to $v_2(y_1,0,t) = \frac{\partial}{\partial t}\eta(y_1,t)$. Hence, the distribution with y_1 for each shape function in Eq. (24) should be pairwise proportional to its counterpart in Eq. (20). Further, the indicated shape

functions imply that the incompressibility condition in Eq. (9) is automatically fulfilled.

Substituting Eq. (24) into Eq. (23), and using that δs_j can be varied independently, the following infinite system of ordinary nonlinear differential equations are obtained for the generalized coordinates $s_i(t)$:

$$\dot{s}_i(t) = \frac{2}{L}\int_{-L/2}^{L/2} \cos\left(k_i\left(y_1+\frac{L}{2}\right)\right)\left[p_2\big(y_1,\eta(y_1,t)\big) + p_1\big(y_1,\eta(y_1,t)\big)\sum_{j=1}^{\infty} s_j(t)\,k_j\,\sin\left(k_j\left(y_1+\frac{L}{2}\right)\right)\right] dy_1 \tag{25}$$

where:

$$\left.\begin{aligned} p_1\big(y_1,\eta(y_1,t)\big) &= -\sum_{j=1}^{\infty} r_j(t)\,\sin\left(k_j\left(y_1+\frac{L}{2}\right)\right)\cosh\big(k_j\,(\eta(y_1,t)+h)\big) \\ p_2\big(y_1,\eta(y_1,t)\big) &= \sum_{j=1}^{\infty} r_j(t)\,\cos\left(k_j\left(y_1+\frac{L}{2}\right)\right)\sinh\big(k_j\,(\eta(y_1,t)+h)\big) \end{aligned}\right\} \tag{26}$$

2.4. Equations of motion for the coupled blade-TLD system

Obviously, the differential equations in Eqs. (18) and (25) are coupled, and both depend on $q(t)$, $\dot{q}(t)$, $\ddot{q}(t)$ via the vectors $\mathbf{r}_0(t)$, $\mathbf{g}$, $\boldsymbol{\omega}(t)$ and their time derivatives. The dependence on $\ddot{q}(t)$ can be eliminated via the equation of motion for $q(t)$ to be specified below. Hence, the dynamics of the fluid simply depends on the state variables $q(t)$, $\dot{q}(t)$ and the generalized coordinates $r_1(t)$, $r_2(t)$, ... and $s_1(t)$, $s_2(t)$, ... In practical applications the expansions in Eqs. (16) and (24) need to be truncated at the same finite order N. Hence, the fluid motion is described by the following state vector $\mathbf{z}(t)$ of dimension $2N+2$:

$$\mathbf{z}(t) = \begin{bmatrix} q(t) \\ \dot{q}(t) \\ \mathbf{r}(t) \\ \mathbf{s}(t) \end{bmatrix} \tag{27}$$

where:

$$\mathbf{r}(t) = \begin{bmatrix} r_1(t) \\ r_2(t) \\ \vdots \\ r_N(t) \end{bmatrix} \quad , \quad \mathbf{s}(t) = \begin{bmatrix} s_1(t) \\ s_2(t) \\ \vdots \\ s_N(t) \end{bmatrix} \tag{28}$$

Figure 3 appears about here.

As shown in Fig. 3, $\mathbf{f}_c(t) = \mathbf{f}_c(\mathbf{z}(t), t)$ with the non-vanishing moving frame components $f_{c,1}(t)$ and $f_{c,2}(t)$, denotes the external reaction force vector on the liquid due to the pressure $p(\mathbf{y}, t)$ from inner side of the tank. This force vector, when transferred to the primary structure, represents the sloshing force for mitigating edgewise vibrations in the rotating blade. The vector $\mathbf{f}_c(t)$ can be

obtained from the divergence theorem in combination with Eqs. (8) and (13):

$$\begin{aligned}
\mathbf{f}_c(t) \;&=\; -\int_{A_1(t)} p(\mathbf{y},t)\,\mathbf{n}(\mathbf{y})\,dA \;= \\
&\int_{V(t)} \rho\Big(\frac{\partial}{\partial t}\mathbf{v}(\mathbf{y},t) \;+\; \big(\mathbf{v}(\mathbf{y},t)\cdot\nabla\big)\mathbf{v}(\mathbf{y},t) \;+\; 2\,\boldsymbol{\omega}(t)\times\mathbf{v}(\mathbf{y},t) \;-\; \mathbf{a}_e(\mathbf{y},t)\Big)dV \;= \\
&\sum_{k=1}^{N}\mathbf{b}_i(t)\,\dot{r}_i(t) \;+\; \sum_{k=1}^{N}\mathbf{c}_i(t)\,r_i(t) \;+\; \sum_{i=1}^{N}\sum_{j=1}^{N}\mathbf{d}_{ij}(t)\,r_i(t)\,r_j(t) \;+\; \mathbf{e}(t)
\end{aligned} \tag{29}$$

where the vectors $\mathbf{b}_i(t)$, $\mathbf{c}_i(t)$, $\mathbf{d}_{ij}(t)$, $\mathbf{e}(t)$ are given by:

$$\left.\begin{aligned}
\mathbf{b}_i(t) \;&=\; \int_{V(t)} \rho\,\mathbf{V}_i(\mathbf{y})\,dV \\
\mathbf{c}_i(t) \;&=\; \int_{V(t)} 2\rho\,\boldsymbol{\omega}(t)\times\mathbf{V}_i(\mathbf{y})\,dV \;=\; 2\,\boldsymbol{\omega}(t)\times\mathbf{b}_i(t) \\
\mathbf{d}_{ij}(t) \;&=\; \int_{V(t)} \rho\,\big(\mathbf{V}_i(\mathbf{y})\cdot\nabla\big)\mathbf{V}_j(\mathbf{y})\,dV \\
\mathbf{e}(t) \;&=\; -\int_{V(t)} \rho\,\mathbf{a}_e(\mathbf{y},t)\,dV
\end{aligned}\right\} \tag{30}$$

Semi-analytical expressions for the moving frame component of the vectors $\mathbf{b}_i(t)$, $\mathbf{c}_i(t)$, $\mathbf{d}_{ij}(t)$, $\mathbf{e}(t)$ have been given in Appendix A. They depend on the state variables $\mathbf{s}(t)$ through the time-varying fluid domain $V(t)$.

From the linear wave theory, under the influence of the centrifugal acceleration $x_0\Omega^2$ alone, only the odd-number modes in the expansions in Eqs. (16) and (24) contribute to $f_{c,1}(t)$, and that the contribution from any mode to $f_{c,2}(t)$ vanishes totally. In the nonlinear case, with the time and space varying acceleration $\mathbf{a}_e(\mathbf{y},t)$ and the non-symmetric influence of the Coriolis acceleration, there will be non-vanishing contributions to both force components from all modes in the expansions. However, it is assumed that the odd terms have dominating contributions in the control force, and the number of retained terms N should be chosen as an odd number.

By using the Euler-Lagrange equation, the equation of motion for the edgewise vibration $q(t)$ can be formulated (Zhang et al., 2014b; Zhang et al., 2015a; Basu et al., 2015). Coupled with the sloshing force from the TLD, the following equation is obtained:

$$m_0\,\ddot{q}(t) + c_0\,\dot{q}(t) + (k_0 - \Omega^2 m_0)\,q(t) \;=\; f_0(\dot{q},t) + f_g(t) + B\Big(f_{c,1}(t)\cos\varphi(t) + f_{c,2}(t)\sin\varphi(t)\Big) \tag{31}$$

where $f_0(t)$ denotes the wind-induced modal load on the primary structure obtained from a more sophisticated 13-DOF aeroelastic model, taking the aerodynamic damping into consideration (Zhang et al., 2014c). $f_g(t) = \sin(\Omega t)\int_0^{L_B}\mu(x_3)g\Phi(x_3)dx_3$ denotes the modal load from gravity. The term $m_0 = \int_0^{L_B}\mu(x_3)\,\Phi^2(x_3)\,dx_3$ is the modal mass of the blade, and k_0 denotes the modal stiffness including the elastic and geometric contributions:

$$k_0(t) = k_e + k_1\Omega^2 - k_2 g\cos(\Omega t) \tag{32}$$

In Eq. (32), k_e is the elastic stiffness of the blade without geometrical contributions. $k_1\Omega^2$ indicates the geometrical stiffening due to the centrifugal acceleration. $-k_2 g\cos(\Omega t)$ indicates

the geometrical softening caused by the variation of the axial force during rotating due to the weight of the blade. The parameters k_e, k_1 and k_2 are given by:

$$\left.\begin{aligned} k_e &= \int_0^{L_B} EI(x_3)\left(\frac{d^2\Phi(x_3)}{dx_3^2}\right)^2 dx_3 \\ k_1 &= \int_0^{L_B} N_1(x_3)\left(\frac{d\Phi(x_3)}{dx_3}\right)^2 dx_3 \quad , \quad N_1(x_3) = \int_{x_3}^{L_B} \mu(y_3)\, y_3\, dy_3 \\ k_2 &= \int_0^{L_B} N_2(x_3)\left(\frac{d\Phi(x_3)}{dx_3}\right)^2 dx_3 \quad , \quad N_2(x_3) = \int_{x_3}^{L_B} \mu(y_3)\, dy_3 \end{aligned}\right\} \tag{33}$$

Further, the negative stiffness term $-\Omega^2 m_0$ in Eq. (31) is the result of the centripetal softening effect, where the blade deflection in the edgewise direction induces a component of the centrifugal force in the same direction (tending to further increase the blade edgewise deflection) in the rotor plane.

The fundamental edgewise circular eigenfrequency of a static blade can be calculated using the following equation:

$$\omega_0 = \sqrt{k_e/m_0} \tag{34}$$

Based on ω_0 and m_0, the damping coefficient of the primary structure is calculated as:

$$c_0 = 2\,\zeta_0\,\omega_0\,m_0 \tag{35}$$

where ζ_0 is the structural damping ratio.

The ordinary differential equations for the generalized coordinates $r_i(t)$ (Eq. (18)) do not contain terms to account for the energy losses of the sloshing liquid ($n_{ij}(t)$ is the gyroscopic damping term which does not dissipate energy). In principal, energy dissipations in the TLD arise from both the fluid viscosity present primarily in the boundary layer and the inclusion of flow restricting devices such as screens and baffles. Investigating how these two mechanisms contribute to the energy dissipation are beyond the scope of this paper. Instead, in Eq. (18) a linear viscous damping term is incorporated to accommodate the overall energy dissipation arising from the viscous effect and flow restricting devices:

$$\sum_{j=1}^{N} m_{ij}(t)\,\dot{r}_j(t) + \sum_{j=1}^{N} c_{ij}(t)\,r_j(t) + \sum_{j=1}^{N} n_{ij}(t)\,r_j(t) + \sum_{j=1}^{N}\sum_{k=1}^{N} o_{ijk}(t)\,r_j(t)\,r_k(t) = f_i(t) \tag{36}$$

In the present case, $c_{ij}(t)$ is modeled as

$$c_{ij}(t) = \xi\omega_1 m_{ij}(t) \tag{37}$$

where ξ is a non-dimensional damping parameter, representing both the dissipations from the fluid viscosity in the boundary layer and the flow restriction device. For practical applications this parameter should be calibrated from full scale eigenvibration tests.

Eqs. (31), (25) and (36) are combined into the following state vector differential equation, which describes the edgewise vibrations of the blade coupled to the fluid motion of the TLD:

$$\dot{\mathbf{z}}(t) = \mathbf{h}\Big(\mathbf{z}(t), t\Big) \tag{38}$$

Further, the mass ratio μ (ratio between the fluid mass and the modal mass of the structure) and the tuning ratio χ (ratio between the first sloshing frequency and the fundamental edgewise frequency) are introduced as design parameters, defined as:

$$\mu = \frac{m_l}{m_0}, \quad \chi = \frac{\omega_1}{\omega_0} \tag{39}$$

As a measure of the efficiency of the damper, the reduction ratio δ is defined as:

$$\delta = \frac{\int_{\omega_a}^{\omega_b} |Q_0(\omega)|^2 d\omega - \int_{\omega_a}^{\omega_b} |Q(\omega)|^2 d\omega}{\int_{\omega_a}^{\omega_b} |Q_0(\omega)|^2 d\omega} \tag{40}$$

where $Q(\omega)$ and $Q_0(\omega)$ are the Fourier amplitude of the edgewise tip displacements of the blade with and without the TLD, respectively. ω_a and ω_b are the lower and upper limits of the considered angular frequency range. The optimal parameters of the TLD can be found by maximizing the value of δ.

3. Numerical simulations

Data from the NREL 5-MW reference wind turbine (Jonkman et al., 2009) have been used to calibrate the structural model of the blade. Each blade has a length of 63 m and an overall mass of 17740 kg, with the fundamental edgewise modal shape, the bending stiffness and the mass per unit length provided by Jonkman et al. (2009). The constant parameters employed in the structure-TLD model are calculated and presented in Table 1.

Table 1 appears about here.

The edgewise modal loads $f_0(t)$ in Eq. (31) are obtained by applying a 3-dimensional rotational sampled wind field to the rotor of the 13-DOF aeroelastic model (Zhang et al., 2014c), with specified mean wind speed V_0 and turbulence intensity I. Having $f_0(t)$ as the external exitation, the nonlinear state vector differential equation (Eq. (38)) is numerically solved by the fourth-order Runge-Kutta method using a time interval of 0.02 s. At each time step, iterations need to be performed to obtain $\ddot{q}(t)$ since Eqs. (29) and (31) are nonlinearly coupled.

In the present study, modal expansions to one sloshing mode (N=1) and three sloshing modes (N=3) are evaluated, corresponding to the state vector $\mathbf{z}(t)$ of dimension 4 and 8, respectively. The one-sloshing-mode model is used for parametric optimization of the TLD, which has been justified by comparing the results from the one-mode and three-mode models.

3.1. Parametric optimization of the TLD using one-mode model

The parameters of the TLD to be determined are the mass ratio μ, the tuning ratio χ, the non-dimensional damping parameter ξ and the mounting position of the damper x_0. Because the damping effect of the sloshing liquid on the structure is governed by the centrifugal acceleration $x_0\Omega^2$, better performance of vibration reduction can be obtained by mounting the liquid damper closer to the tip of the blade. However, the available space inside the hollow blade decreases toward the tip, making the determination of x_0 a trade-off problem. In the following, x_0 is set

to be 55 m, corresponding to approximately $7/8$ of the total blade length. Further, four sets of mass ratios are considered in the optimization, i.e., μ=0.02, 0.03, 0.04, 0.05. With the modal mass m_0= 1412 kg, the liquid mass varies between 28.24 and 70.60 kg, corresponding to 0.16%-0.40% of the total mass of each blade. The choice of the tank length L has significant influence on the tank width and mean fluid depth of the TLD, and it should be decided according to the available space inside the blade. In the present study, three different values of L have been taken into consideration, i.e., L=1.5, 2, 2.5 m.

In the optimization procedure, the optimal tuning ratio χ_{opt} and the optimal non-dimensional damping parameter ξ_{opt} are sought such that the reduction ratio δ is maximized, for prescribed values of the mass ratio and the tank length. Considering the edgewise angular frequency to be 6.85 rad/s, $\omega_a = 3$ rad/s and $\omega_b = 10$ rad/s have been used in Eq. (40).

Table 2 gives the values of χ_{opt}, ξ_{opt}, as well as the corresponding δ, the mean fluid depth h and the tank width B. From Table 2, there are four observations to be made:

(i) the reduction ratio δ increases as the mass ratio μ increases, indicating that a TLD with a larger fluid mass can achieve higher damping effect;

(ii) as μ increases with a given L, both χ_{opt} and h decrease slightly, but B increases significantly. Actually when L is fixed, the adjustment of fluid mass is mainly achieved by the change of B, since h is determined by the tuning condition and the tuning ratio is always around 1. The variation of μ has almost no effect on ξ_{opt}.

(iii) as L increases from 1.5 m to 2.5 m for a prescribed value of μ, χ_{opt} decreases slightly while ξ_{opt} is almost not influenced. The variation of L has almost no effect on the reduction ratio δ. Therefore, it is mainly the mass ratio that determines the damping efficacy of the TLD.

(iv) as L increases, h increases significantly and B decreases significantly. The value of L should be constrained by the blade chord at the corresponding span-wise position. L should be limited also because large value of L will result in a very small value of B that is unrealistic for practical implementation. On the other hand, a very small value of L may lead to a large value of B that exceeds the available space inside the blade. Further, h becomes very small for a small value of L. The significant wave breaking for the shallow water cannot be captured by the present theoretical model. Therefore, the determination of L becomes a tradeoff problem, depending on the available space inside the blade, the resulting width and the mean fluid depth of the damper.

Table 2 appears about here.

Fig. 4 presents the performance of a TLD with optimized parameters for mitigating edgewise vibrations, when the mean wind speed is 15 m/s and the turbulence intensity is 0.1. Given $x_0 = 55$ m, $\mu = 0.03$ and L=2.5 m, the optimal tuning ratio $\chi_{opt} = 0.985$ (resulting in $h = 0.3468$ m) and damping parameter $\xi_{opt} = 0.165$ as given in Table 2 are used in the simulation.

Figure 4 appears about here.

As shown by the time history in Fig. 4(a), the modal loads from gravity result in a large harmonic motion in edgewise direction, with an angular frequency of 1P (1 per rev, corresponding to

the rotational speed of the rotor 1.267 rad/s). On top of this deterministically harmonic-varying motion, oscillations related to the edgewise eigenvibration are also presented in the time history. The TLD has no effect on the gravity induced 1P motion, but effectively adds damping into the edgewise eigenvibration. The blade edgewise motion with the TLD becomes almost pure harmonic (with the 1P frequency) since the high frequency oscillation has been significantly mitigated by the TLD. The maximum edgewise tip displacement is reduced from 0.974 m to 0.864 m. From the Fourier amplitude spectrum (in semi-logarithmic chart) of $q(t)$ in Fig. 4(b), it is more clearly seen that a TLD with a fluid mass of 42.36 kg effectively suppresses the peak around 6.85 rad/s corresponding to fundamental edgewise angular frequency. This means that a properly designed TLD is able to absorb almost all the energy in the fundamental edgewise mode of the blade. However, the 1P frequency peak is not influenced at all by the TLD.

Figure 5 appears about here.

On the contrast to the gravity induced motion, the edgewise vibration (in the fundamental edgewise mode) is stochastic in nature, and is influenced by both the turbulent wind field and the operational condition of the turbine. Under some conditions (Hansen, 2007), the aerodynamic damping in the edgewise mode becomes negative, and large amplitude oscillation or even aeroelastic instability may take place. Fig. 5 shows the performance of the TLD (same parameters used as in Fig. 4) under two conditions with different aerodynamic damping. In the present numerical example, the value of ζ_0 is manually changed (in principle ζ_0 is always positive) in order to mimic the change of the aerodynamic damping, and the same modal loads $f_0(t)$ as in Fig. 4 has been employed. In Fig. 5(a) ζ_0 is set to be 0, representing the case where the total damping (the structural damping plus the aerodynamic damping) is zero. Large amplitude oscillations take place in the fundamental edgewise mode, and the TLD effectively damped the edgewise eigenvibration, leaving only the 1P harmonic-varying motion in the edgewise direction. In Fig. 5(b) ζ_0 is set to be -0.001, representing a case with negative total damping (aeroelastic instability). It is seen that the edgewise response increases exponentially with time when there is no TLD mounted. The instability is totally eliminated by the attached TLD, implying that significant damping is introduced by the TLD into the fundamental edgewise mode to overwhelm the negative aerodynamic damping.

It should be mentioned that during the transient time period (not shown here), both the blade and the fluid are influenced by the initial conditions, and the liquid response contains some high frequency components. During this interval, the damping effect of the TLD is ignorable. It takes some time (several seconds) for the liquid to start sloshing in its dominating first sloshing mode, and hence to spark off the damping effect on the blade edgewise response. This phenomenon is also observed in other passive vibration absorbers, such as the TMD, the TLCD and the particle damper.

Moreover, previous studies on the roller damper (Zhang et al., 2014b) and the TLCD (Zhang et al., 2015a) have shown that when the rotational speed of the rotor decreases from its rated value (during starting up or closing down procedures of the turbine), the damping effect of the damper on edgewise vibrations will be drastically reduced due to frequency detuning. Nevertheless, the reduction ratio of the damper is always positive for rotational speed ranging from zero to the rated value. These observations also apply to the TLD.

3.2. Comparison between the one-mode and three-mode models

Simulation results from the one-mode model and three-mode model are compared, with the same TLD parameters utilized in both models, i.e. $x_0 = 55$ m, $\mu = 0.03$, $L = 2.5$ m, $\xi = 0.165$, $h = 0.3468$ m.

Fig. 6(a) shows the time histories of the sloshing force in y_1- direction, obtained from Eq. (29). In general, the result from the one-mode model agrees well with that from the three-mode model, indicating that the most significant damping effect is created by the fundamental sloshing mode. At certain instants of time such as t=319.7 s, relatively large discrepancies can be observed between the two models. This is due to the higher frequency contributions from the second and third sloshing modes in the three-mode model, which can not be captured by the single-mode model. Fig. 6(b) shows the corresponding edgewise tip displacement of the blade when a TLD is mounted inside. The structural responses from the one-mode and three-mode models are in excellent agreement with each other. Essentially, the primary structure behaves like a filter, which filters out high frequency disturbances in the sloshing force, leading to almost identical results in Fig. 6(b). Hence, the one-mode model is sufficient to accurately predict the TLD-damped structural response, and can be utilized for optimal design of the TLD as shown in the previous subsection.

Figure 6 appears about here.

Fig. 7 illustrates the fluid surface elevation at various instants of time for the one-mode and three-mode models. The general behaviors of the sloshing liquid are similarly predicted by both models since the first sloshing mode contributes most to the liquid motion. On the other hand, it is also obviously seen that the second and third sloshing modes have larger effect on the fluid surface elevation than on the sloshing force and the structural response. The one-mode model only represents the first sloshing mode (cosine function), resulting in zero surface elevation at the middle of the tank at all time, which is surely unrealistic. Therefore, for accurately predicting the surface elevation, modal expansions to three or more sloshing modes need to be carried out. Furthermore, it can be seen by comparing Fig. 6(a) and Fig. 7 that there is a strong correlation between the sloshing force and the surface elevation, i.e., the sloshing force agrees well with each other when $\eta(t)$ is in good agreement (such as t=306 s, 315.4 s).

Figure 7 appears about here.

In order to substantiate the results shown in Fig. 7, time histories of the surface elevation $\eta(t)$ at the end walls are illustrated in Fig. 8(a) and 8(b). Again, the solid and dashed curves indicate the results when the modal expansion in Eq. (24) is truncated after one mode and three modes, respectively. The results from the one-mode model (the solid curves) in Fig. 8(a) and 8(b) are absolutely symmetric about the zero axis, which is not the case for the three-mode model. Further, it is seen that the one-mode model underestimates the peak heights and overestimates the trough depths. This limitation of the one-mode model was also experienced for a TLD subjected to pure horizontal excitations (Love and Tait, 2010).

Figure 8 appears about here.

To further unfold the contributions from different sloshing modes on the surface elevation, Fig. 9 shows the time series and the corresponding Fourier amplitude spectra of the generalized coordinates $s_i(t)$ in the modal expansion of Eq. (24). Results from the one-mode model are shown in Fig. 9(a). As displayed by the Fourier amplitude spectrum to the right, $s_1(t)$ appears as a broad-banded random oscillation with the central frequency equal to the fundamental sloshing frequency ω_1 of the fluid. A clear peak corresponding to the rotational speed of the rotor (Ω=1.267 rad/s) is also observed. Fig. 9(b) shows the results from the three-mode model, where the responses of $s_1(t)$, $s_2(t)$ and $s_3(t)$ are compared. As expected, $s_1(t)$ is much more significant than $s_2(t)$ and $s_3(t)$. In the Fourier amplitude spectrum, $s_1(t)$ also displays small spectral peaks in the vicinity of the second and third sloshing frequencies ω_2 and ω_3. Similarly, spectral peaks around ω_1 and ω_2 are clearly observed in $s_3(t)$ besides the third sloshing frequency. This can be explained by the nonlinear couplings in Eq. (25). Hence, although very similar with each other, the time series of $s_1(t)$ in Figs. 9(a) and 9(b) are slightly different due to this coupling.

Figure 9 appears about here.

Finally, a widely-used simplified method (Reed et al., 1998) is employed to calculate the control force (sloshing force) of TLD in the local y_1-direction, and comparisons with the result calculated from Eq. (29) are illustrated in Fig. 10. The sloshing force in the simplified method is expressed as:

$$f_{st} = \frac{1}{2}\rho x_0 \Omega^2 B\Big[(h+\eta(-L/2))^2 - (h+\eta(L/2))^2\Big] \tag{41}$$

which is totally based on the linear hydrostatic pressure distributions (Fig. 3), neglecting all inertial effects. Again, the gravitational acceleration g in the original equation (Reed et al., 1998) has been replaced by the centrifugal acceleration $x_0\Omega^2$ in the present case.

Fig. 10(a) compares the results from the one-mode model. The sloshing forces calculated from hydrodynamic pressure (Eq. (29)) and hydrostatic pressure are in good agreement with each other, implying that the hydrostatic pressure force is a dominant part of the sloshing force. Fig. 10(b) shows the corresponding results for the three-mode model, where the discrepancy is somewhat larger and the simplified method overestimates the amplitude of the sloshing force. The reason is that the inertia/dynamic effects become more pronounced in the higher order sloshing modes. Therefore, Eq. (29) is recommended for calculating the sloshing force especially when modal expansions are truncated to higher modes.

Figure 10 appears about here.

Recently, a series of real-time hybrid testing on a full-scale TLD for mitigating lateral tower vibrations of wind turbines have been carried out by the authors (Zhang el al., 2015b). The theoretical model proposed in the present paper was slightly modified to handle the case where

the liquid motion is governed by gravitational acceleration rather than centrifugal acceleration. The test results agree very well with the results predicted by the modified theoretical model, which to some extent validates the present theoretical model.

4. Concluding Remarks

This paper presents the modeling of a rectangular TLD for the mitigation of edgewise vibrations in rotating wind turbine blades. For effectiveness, the TLD is required to be placed close to the blade tip where the thickness is small, and the width of the damper needs to be small accordingly. As a consequence the fluid motion of the damper becomes essentially 2-dimensional.

First of all, the boundary value problem (Euler equation with the nonlinear boundary conditions) is formulated in a coordinate system fixed to the rotating container. Next, the Euler equation and the nonlinear kinematic boundary condition of the free surface are discretized using the modal expansion technique, where the velocity field and the free surface are expressed as a summation of sloshing modes (eigenmodes of the standing wave under centrifugal acceleration are taken as the shape functions for the velocity field). A system of coupled ordinary differential equations are obtained, the time-dependent coefficients of which can be numerically calculated using the semi-analytical expressions (1-dimensional quadratures).

Based on a reduced order single-degree-of-freedom model for the rotating blade, it is demonstrated that the edgewise vibrations in the fundamental mode can be effectively damped by an optimally designed TLD. It is also shown that the one-sloshing-mode model is able to predict the sloshing force and the damped structural response accurately. This implies that the primary damping effect on the blade is achieved by the first sloshing mode of the fluid, and higher modes have minor effect on the performance of the damper. On the other hand, the one-mode model is unable to predict the fluid surface elevation equally well, and a model with three sloshing modes or even more modes should be employed to well capture the response of the fluid. Nevertheless, the one-mode model can be utilized for preliminary design/tuning of the TLD, with much less computational effort and equally good prediction of the damping effect on the primary structure.

5. Acknowledgements

The first author gratefully acknowledge the financial support from the Chinese Scholarship Council under the State Scholarship Fund.

Appendix A. Semi-analytical expressions for Eqs. (22) and (33)

$m_{ij}(t)$ is calculated as:

$$m_{ij}(t) = m_{ij}^{(1)}(t) + m_{ij}^{(2)}(t) \tag{42}$$

where:

$$\left.\begin{aligned} m_{ij}^{(1)}(t) &= \frac{m}{2}\cdot\int_0^1 \cos\Big((i-j)\,\pi\,\xi_1\Big)\,\frac{\sinh\Big((i+j)\,\pi\,\alpha\,\beta(\xi_1,t)\Big)}{(i+j)\,\pi\,\alpha}\,d\xi_1 \\ m_{ij}^{(2)}(t) &= -\frac{m}{2}\cdot\begin{cases} \dfrac{1}{2h}\,s_{2i}(t) & ,\quad i=j \\ \displaystyle\int_0^1 \cos\Big((i+j)\,\pi\,\xi_1\Big)\,\frac{\sinh\Big((i-j)\,\pi\,\alpha\,\beta(\xi_1,t)\Big)}{(i-j)\,\pi\,\alpha}\,d\xi_1 & ,\quad i\neq j \end{cases} \end{aligned}\right\} \tag{43}$$

$m = \rho h L$ is the fluid mass per unit width, and the following non-dimensional quantities have been introduced:

$$\left.\begin{aligned} \xi_1 &= \frac{1}{L}\Big(y_1 + L/2\Big) \\ \alpha &= \frac{h}{L} \\ \beta(\xi_1,t) &= \frac{h+\eta(\xi_1,t)}{h} \end{aligned}\right\} \tag{44}$$

$n_{ij}(t)$ is calculated as:

$$n_{ij}(t) = \begin{cases} 0 & ,\quad i=j \\ n_{ij}^{(1)}(t) + n_{ij}^{(2)}(t) & ,\quad i\neq j \end{cases} \tag{45}$$

where:

$$\left.\begin{aligned} n_{ij}^{(1)}(t) &= -m\Big(\dot{\Psi}(t)+\dot{\varphi}(t)\Big)\int_0^1 \sin\Big((i-j)\,\pi\,\xi_1\Big)\,\frac{\cosh\Big((i+j)\,\pi\,\alpha\,\beta(\xi_1,t)\Big)-1}{(i+j)\,\pi\,\alpha}\,d\xi_1 \\ n_{ij}^{(2)}(t) &= m\Big(\dot{\Psi}(t)+\dot{\varphi}(t)\Big)\int_0^1 \sin\Big((i+j)\,\pi\,\xi_1\Big)\,\frac{\cosh\Big((i-j)\,\pi\,\alpha\,\beta(\xi_1,t)\Big)-1}{(i-j)\,\pi\,\alpha}\,d\xi_1 \end{aligned}\right\} \tag{46}$$

$o_{ijk}(t)$ is calculated as:

$$o_{ijk}(t) = o_{ijk}^{(1)}(t) + o_{ijk}^{(2)}(t) + o_{ijk}^{(3)}(t) + o_{ijk}^{(4)}(t) \tag{47}$$

where:

$$
\begin{aligned}
o^{(1)}_{ijk}(t) &= \frac{m\,k}{4h}\int_0^1 \cos\Big((k-i-j)\,\pi\,\xi_1\Big)\,\frac{\sinh\Big((k+i+j)\,\pi\,\alpha\,\beta(\xi_1,t)\Big)}{k+i+j}\,d\xi_1 \\
o^{(2)}_{ijk}(t) &= \frac{m\,k}{4h}\cdot\begin{cases} \dfrac{\pi}{2L}\,s_{2i+2j}(t) & , \quad k=i+j \\ \displaystyle\int_0^1 \cos\Big((k+i+j)\,\pi\,\xi_1\Big)\,\frac{\sinh\Big((k-i-j)\,\pi\,\alpha\,\beta(\xi_1,t)\Big)}{k-i-j}\,d\xi_1 & , \quad k\neq i+j \end{cases} \\
o^{(3)}_{ijk}(t) &= -\frac{m\,k}{4h}\cdot\begin{cases} \dfrac{\pi}{2L}\,s_{2i-2j}(t) & , \quad k=i-j \\ \displaystyle\int_0^1 \cos\Big((k+i-j)\,\pi\,\xi_1\Big)\,\frac{\sinh\Big((k-i+j)\,\pi\,\alpha\,\beta(\xi_1,t)\Big)}{k-i+j}\,d\xi_1 & , \quad k\neq i-j \end{cases} \\
o^{(4)}_{ijk}(t) &= -\frac{m\,k}{4h}\cdot\begin{cases} \dfrac{\pi}{2L}\,s_{2j-2i}(t) & , \quad k=j-i \\ \displaystyle\int_0^1 \cos\Big((k-i+j)\,\pi\,\xi_1\Big)\,\frac{\sinh\Big((k+i-j)\,\pi\,\alpha\,\beta(\xi_1,t)\Big)}{k+i-j}\,d\xi_1 & , \quad k\neq j-i \end{cases}
\end{aligned}
\tag{48}
$$

$f_i(t)$ is calculated as:

$$
f_i(t) = f_i^{(1)}(t) + f_i^{(2)}(t) + f_i^{(3)}(t) + f_i^{(4)}(t) \tag{49}
$$

where

$$
\begin{aligned}
f_i^{(1)}(t) = m\Big(\ddot{\Psi}(t)+\ddot{\varphi}(t)\Big)\int_0^1 \Big\{&\frac{h}{i\pi\alpha}\big[(\beta-1)\sinh(i\pi\alpha\xi_1) - \frac{\cosh(i\pi\alpha\xi_1)-1}{i\pi\alpha}\big]\sin(i\pi\xi_1) \\
&+ (L\xi_1 - L/2)\frac{\cosh(i\pi\alpha\beta)-1}{i\pi\alpha}\cos(i\pi\xi_1)\Big\}d\xi_1
\end{aligned}
$$

$$
\begin{aligned}
f_i^{(2)}(t) = m\Big(\dot{\Psi}(t)+\dot{\varphi}(t)\Big)^2\int_0^1 \Big\{&\frac{h}{i\pi\alpha}\big[(\beta-1)\cosh(i\pi\alpha\xi_1) - \frac{\sinh(i\pi\alpha\xi_1)}{i\pi\alpha}+1\big]\cos(i\pi\xi_1) \\
&+ (L/2 - L\xi_1)\frac{\sinh(i\pi\alpha\beta)}{i\pi\alpha}\sin(i\pi\xi_1)\Big\}d\xi_1
\end{aligned}
$$

$$
\begin{aligned}
f_i^{(3)}(t) =& m\Big[\int_0^1 -\sin(i\pi\xi_1)\frac{\sinh(i\pi\alpha\beta)}{i\pi\alpha}d\xi_1\Big]\Big[-g\sin(\Psi+\varphi) - \Big(x_0\ddot{\varphi}\cos\varphi - x_0\dot{\varphi}^2\sin\varphi \\
&- b\ddot{q}\cos\varphi + b\dot{q}\dot{\varphi}\sin\varphi + b(\dot{q}\dot{\varphi}+q\ddot{\varphi})\sin\varphi + bq\dot{\varphi}^2\cos\varphi\Big) + (\ddot{\Psi}+\ddot{\varphi})(x_0\cos\varphi + bq\sin\varphi) \\
&- 2(\dot{\Psi}+\dot{\varphi})(x_0\dot{\varphi}\sin\varphi - b\dot{q}\sin\varphi - bq\dot{\varphi}\cos\varphi) + (\dot{\Psi}+\dot{\varphi})^2(x_0\sin\varphi - bq\cos\varphi)\Big]
\end{aligned}
$$

$$
\begin{aligned}
f_i^{(4)}(t) =& m\Big[\int_0^1 \cos(i\pi\xi_1)\frac{\cosh(i\pi\alpha\beta)-1}{i\pi\alpha}d\xi_1\Big]\Big[g\cos(\Psi+\varphi) - \Big(x_0\ddot{\varphi}\sin\varphi + x_0\dot{\varphi}^2\cos\varphi \\
&- b\ddot{q}\sin\varphi - b\dot{q}\dot{\varphi}\cos\varphi - b(\dot{q}\dot{\varphi}+q\ddot{\varphi})\cos\varphi + bq\dot{\varphi}^2\sin\varphi\Big) + (\ddot{\Psi}+\ddot{\varphi})(x_0\sin\varphi - bq\cos\varphi) \\
&+ 2(\dot{\Psi}+\dot{\varphi})(x_0\dot{\varphi}\cos\varphi - b\dot{q}\cos\varphi + bq\dot{\varphi}\sin\varphi) - (\dot{\Psi}+\dot{\varphi})^2(x_0\cos\varphi + bq\sin\varphi)\Big]
\end{aligned}
\tag{50}
$$

The moving frame components of $\mathbf{b}_i(t)$, $\mathbf{c}_i(t)$, $\mathbf{d}_{ij}(t)$, $\mathbf{e}(t)$ in Eq. (33) are calculated as:

$$\mathbf{b}_i(t) = \frac{m}{i\pi\alpha}\int_0^1 \begin{bmatrix} -\sin(i\pi\xi_1) & \sinh(i\pi\alpha\beta(\xi_1,t)) \\ \cos(i\pi\xi_1)\Big(\cosh(i\pi\alpha\beta(\xi_1,t)) - 1\Big) \end{bmatrix} d\xi_1 \tag{51}$$

$$\mathbf{c}_i(t) = \frac{2m}{i\pi\alpha}\Big(\dot{\Psi}(t)+\dot{\varphi}(t)\Big)\int_0^1 \begin{bmatrix} \cos(i\pi\xi_1)\Big(\cosh(i\pi\alpha\beta(\xi_1,t)) - 1\Big) \\ \sin(i\pi\xi_1) & \sinh(i\pi\alpha\beta(\xi_1,t)) \end{bmatrix} d\xi_1 \tag{52}$$

$$\mathbf{d}_{ij}(t) = \mathbf{d}_{ij}^{(1)}(t) + \mathbf{d}_{ij}^{(2)}(t) \tag{53}$$

where:

$$\mathbf{d}_{ij}^{(1)}(t) = \frac{j}{2(i+j)}\frac{m}{h}\int_0^1 \begin{bmatrix} \sin((i-1)\pi\xi_1) & \sinh((i+j)\pi\alpha\beta(\xi_1,t)) \\ \cos((i-1)\pi\xi_1)\Big(\cosh((i+j)\pi\alpha\beta(\xi_1,t)) - 1\Big) \end{bmatrix} d\xi_1$$

$$\mathbf{d}_{ij}^{(2)}(t) = \frac{jm}{h}\begin{cases} \dfrac{1}{2(i-j)}\displaystyle\int_0^1 \begin{bmatrix} \sin((i+1)\pi\xi_1) & \sinh((i-j)\pi\alpha\beta(\xi_1,t)) \\ \cos((i+1)\pi\xi_1)\Big(\cosh((i-j)\pi\alpha\beta(\xi_1,t)) - 1\Big) \end{bmatrix} d\xi_1 \ , \ i \neq j \\ -\dfrac{2i}{l}\begin{bmatrix} \displaystyle\sum_{n=1}^{\frac{1}{2}(N+1)} s_{2n-1}(t)\frac{1}{4i^2-(2n-1)^2} \\ 0 \end{bmatrix} \ , \ i = j \end{cases} \tag{54}$$

$$\mathbf{e}(t) = \mathbf{e}^{(1)}(t) + \mathbf{e}^{(2)}(t) \tag{55}$$

where

$$\mathbf{e}^{(1)}(t) = -m\Big(\int_0^1 \beta d\xi_1\Big)\Big(\mathbf{g} - \ddot{\mathbf{r}}_0 - \dot{\boldsymbol{\omega}}\times\mathbf{r}_0 - 2\boldsymbol{\omega}\times\dot{\mathbf{r}}_0 - \boldsymbol{\omega}\times(\boldsymbol{\omega}\times\mathbf{r}_0)\Big)$$

$$\mathbf{e}^{(2)}(t) = m\begin{bmatrix} \displaystyle\int_0^1 \Big[h(\ddot{\Psi}+\ddot{\varphi})(\frac{1}{2}\beta^2-\beta) - L(\dot{\Psi}+\dot{\varphi})^2(\xi_1-\frac{1}{2})\beta\Big]d\xi_1 \\ -\displaystyle\int_0^1 \Big[L(\ddot{\Psi}+\ddot{\varphi})(\xi_1-\frac{1}{2})\beta + h(\dot{\Psi}+\dot{\varphi})^2(\frac{1}{2}\beta^2-\beta)\Big]d\xi_1 \end{bmatrix} \tag{56}$$

REFERENCES

Arrigan, J., Pakrashi, V., Basu, B., Nagarajaiah, S., 2011. Control of flapwise vibrations in wind turbine blades using semi-active tuned mass dampers. *Structural Control and Health Monitoring* 18(8): 840-851.

Banerji, P., Murudi, M., Shah, A.H., Popplewell, N., 2000. Tuned liquid dampers for controlling earthquake response of structures. *Earthquake Engineering and Structural Dynamics* 29(5): 587-602.

Basu, B., Zhang, Z., Nielsen, S.R.K., 2015. Damping of edgewise vibration in wind turbine blades by means of circular liquid dampers. *Wind energy*. DOI: 10.1002/we.1827.

Bir, G., Jonkman, J., 2007. Aeroelastic instabilities of large offshore and onshore wind turbines. *EAWE 2007 Torque from Wind Conference*, August 28-31, Lyngby, Denmark.

Chang, C.C., Gu, M., 1999. Suppression of vortex-excited vibration of tall buildings using tuned liquid dampers. *Journal of Wind Engineering and Industrial Aerodynamics* 83(1-3): 225-237.

Colwell, S., Basu, B., 2009. Tuned liquid column dampers in offshore wind turbines for structural control. *Engineering Structures* 31(2): 358-368.

Faltinsen, O.M., Regnebakke, O.F., Lukovsky, I.A., Timokha, A.N., 2000. Multidimensional model analysis of nonlinear sloshing in a rectangular tank with finite water depth. *Journal of Fluid Mechanics* 407: 201-234.

Faltinsen, O.M., Timokha, A.N., 2001. An adaptive multimodal approach to nonlinear sloshing in a rectangular tank. *Journal of Fluid Mechanics* 432: 167-200.

Fitzgerald, B., Basu, B., Nielsen, S.R.K., 2013. Active tuned mass dampers for control of in-plane vibrations of wind turbine blades. *Structural Control and Health Monitoring* 20(12): 1377-1396.

Fitzgerald, B., Basu, B., 2014. Cable connected active tuned mass dampers for control of in-plane vibrations of wind turbine blades. *Journal of Sound and Vibration* 333(23): 59806004.

Fujii, K., Tamura, Y., Sato, T., Wakahara, T., 1990. Wind-induced vibration of tower and practical applications of tuned sloshing damper. *Journal of Wind Engineering and Industrial Aerodynamics* 33(1-2): 263-272.

Hansen, M.H., 2007. Aeroelastic instability problems for wind turbines. *Wind Energy* 10(6): 551-577. DOI: 10.1002/we.242.

Jin, Q., Li, X., Sun, N., Zhou, J., Guan, J., 2007. Experimental and numerical study on tuned liquid dampers for controlling earthquake response of jacket offshore platform. *Marine Structures* 20(4): 238-254.

Jonkman, J., Butterfield, S., Musial, W., Scott, G., 2009. Definition of 5-MW reference wind turbine for offshore system development. National Renewable Energy Laboratory, Technical Report, NREL/TP-500-38060, Golden, Colorado.

Krenk, S., Svendsen, M.N., Høgsberg, J., 2012. Resonant vibration control of three-bladed wind turbine rotors. *AIAA Journal* 50(1): 148-161.

Lackner, M.A., Rotea, M.A., 2011. Passive structural control of offshore wind turbines. *Wind Energy* 14(3): 373-388.

Langthjema, M.A., Nakamura, T., 2014. On the dynamics of the fluid balancer. *Journal of Fluids and Structures* 15: 1-19.

Lee, S.K., Park, E.C., Min, K.W., Lee, S.H., Chung, L., Park, J.H., 2007. Real-time hybrid shaking table testing method for the performance evaluation of a tuned liquid damper controlling seismic response of building structures. *Journal of Sound and Vibration* 302(3): 471-488.

Love, J.S., Tait, M.J., 2010. Nonlinear simulation of a tuned liquid damper with damping screens using a modal expansion technique. *Journal of Fluid and Structures* 26(7-8): 1058-1077.

Luke, J.C., 1967. A variational principle for a fluid with a free surface. *Journal of Fluid Mechanics* 27(2): 395-397.

Malvern, L.E., 1969. *Introduction to the Mechanics of a Continuous Medium.* Prentice Hall, New Jersey.

Murtagh, P.J., Ghosh, A., Basu, B., Broderick, B.M., 2008. Passive control of wind turbine vibrations including blade/tower interaction and rotationally sampled turbulence, *Wind Energy* 11(4): 305-317.

Reed, D., Yu, J., Yeh, H., Gardarsson, S., 1998. Investigation of tuned liquid dampers under large amplitude excitation. *Journal of Engineering Mechanics* 124(4): 405-413.

Riziotis, V.A., Voutsinas, S.G., Politis, E.S., Chaviaropoulos, P.K., 2004 Aeroelastic stability of wind turbines: the problem, the methods and the issues. *Wind Energy* 7(4): 373-392.

Staino, A., Basu, B., Nielsen, S.R.K., 2012. Actuator control of edgewise vibrations in wind turbine blades. *Journal of Sound and Vibration* 331(6): 1233-1256.

Staino, A., Basu, B., 2013. Dynamics and control of vibrations in wind turbines with variable rotor speed. *Engineering Structures* 56: 5867.

Staino, A., Basu, B., 2015. Emerging trends in vibration control of wind turbines: a focus on a dual control strategy. *Philosophical Transactions of the Royal Society A: Mathematical, Physical and Engineering Sciences* 373(2035): 20140069.

Stewart, G.M., Lackner, M.A., 2014. The impact of passive tuned mass dampers and wind-Cwave misalignment on offshore wind turbine loads. *Engineering Structures* 73: 54-61.

Sun, L.M., Fujino, Y., 1994. A semi-analytical model for tuned liquid damper (TLD) with wave breaking. *Journal of Fluids and Structures* 8(5): 471-488.

Sun, L.M., Fujino, Y., Chaiseri, P., Pacheco, B.M., 1995. The properties of tuned liquid dampers using a TMD analogy. *Earthquake Engineering and Structural Dynamics* 24(7): 967-976.

Spencer, B.F., Nagarajaiah, S., 2003. State of the art of structural control. *Journal of Structural Engineering* 129(7): 845-856.

Svendsen, I.A., Jonsson, I.G., 1976. *Hydrodynamics of Coastal Regions*. Den Private Ingeniørfond, Technical University of Denmark.

Tamura, Y., Fujii, K., Ohtsuki, T., Wakahara, T., Kohsaka, R., 1995. Effectiveness of tuned liquid dampers under wind excitation. *Engineering Structures* 17(9): 609-621.

Thomsen, K., Petersen, J.T., Nim, E., Øye, S., Petersen, B., 2000. A method for determination of damping for edgewise blade vibrations. *Wind Energy* 3(4): 233-246.

Yu, J.K., Wakahara, T., Reed, D., 1999. A nonliner numerical model for the tuned liquid damper. *Earthquake Engineering and Structural Dynamics* 28(6): 671-686.

Zhang, Z.L., Chen, J.B., Li, J., 2014a. Theoretical study and experimental verification of vibration control of offshore wind turbines by a ball vibration absorber. *Structure and Infrastructure Engineering* 10(8): 1087-1100.

Zhang, Z., Li, J., Nielsen, S.R.K., Basu, B., 2014b. Mitigation of edgewise vibrations in wind turbine blades by means of roller dampers. *Journal of Sound and Vibration* 333(21), 5283-5298.

Zhang, Z., Nielsen, S.R.K., Blaabjerg, F., Zhou, D., 2014c. Dynamics and control of lateral tower vibrations in offshore wind turbines by means of active generator torque. *Energies* 7(11): 7746-7772.

Zhang, Z., Basu, B., Nielsen, S.R.K., 2015a. Tuned liquid column dampers for mitigation of edgewise vibrations in rotating wind turbine blades. *Structural Control and Health Monitoring* 22(3), 500-517.

Zhang, Z., Staino, A., Basu, B., Nielsen, S.R.K., 2015b. Full-scale real-time hybrid testing of tuned liquid dampers (TLDs) for vibration control of wind turbine towers. *Engineering Structures*. submitted.

Table 1: Parameters used in the structure-TLD model.

Parameter	Value	Unit	Parameter	Value	Unit
L_B	63	m	k_1	$2.09{\cdot}10^3$	kg
m_0	$1.41{\cdot}10^3$	kg	k_2	47.25	kg/m
k_e	$6.62{\cdot}10^4$	N/m	Ω	1.267	s^{-1}
ω_0	6.85	s^{-1}	g	9.81	m/s^2
ζ_0	0.005	–	ρ	$1.0{\cdot}10^3$	kg/m^3

Table 2: Optimal parameters of the TLD, V_0 = 15 m/s, I = 0.1, x_0 = 55 m

	μ=2%					μ=3%				
L [m]	χ_{opt}	ξ_{opt}	δ [%]	h [m]	B [m]	χ_{opt}	ξ_{opt}	δ [%]	h [m]	B [m]
1.5	1.040	0.165	41.77	0.1344	0.1400	1.010	0.165	46.18	0.1264	0.2234
2.0	1.030	0.165	42.61	0.2390	0.0591	1.005	0.165	46.91	0.2266	0.0935
2.5	1.030	0.136	43.35	0.3842	0.0294	0.985	0.165	46.48	0.3468	0.0489
	μ=4%					μ=5%				
L [m]	χ_{opt}	ξ_{opt}	δ [%]	h [m]	B [m]	χ_{opt}	ξ_{opt}	δ [%]	h [m]	B [m]
1.5	0.985	0.194	49.08	0.1200	0.3139	0.975	0.194	51.66	0.1174	0.4008
2.0	0.975	0.194	49.39	0.2122	0.1331	0.965	0.194	51.91	0.2075	0.1701
2.5	0.965	0.194	49.19	0.3311	0.0682	0.960	0.194	51.85	0.3273	0.0863

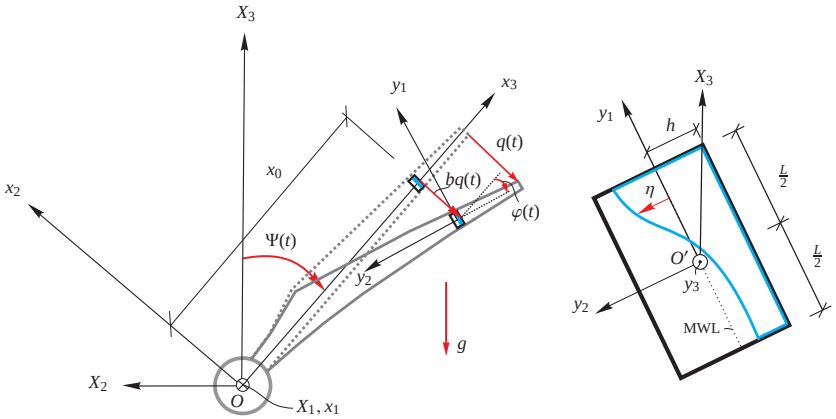

Figure 1: Definition of the coordinate systems, the geometry and the degrees of freedom.

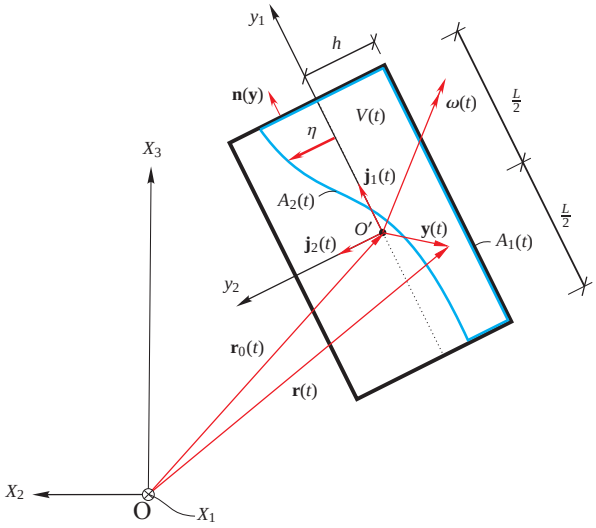

Figure 2: Modeling of the TLD.

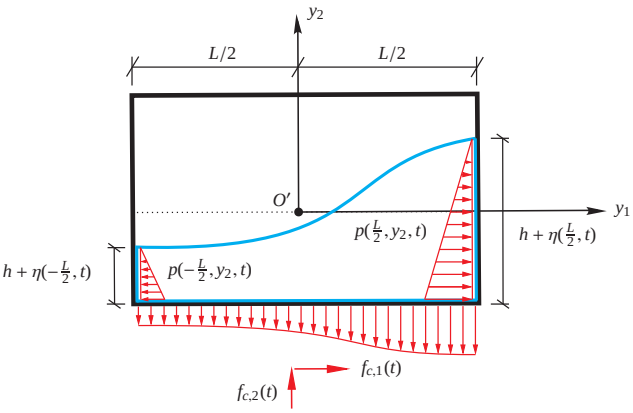

Figure 3: Pressure distribution on inner surfaces of the TLD tank.

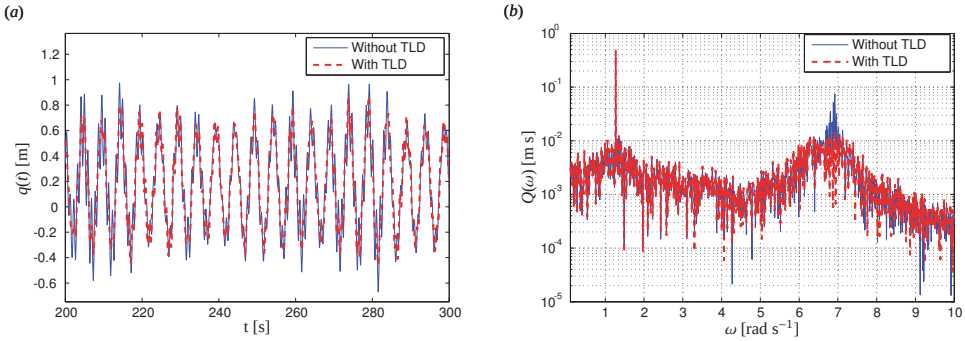

Figure 4: Blade edgewise vibrations with and without TLD, normal operational condition, $V_0 = 15$ m s^{-1}, $I = 0.1$, $x_0 = 55$ m, $\mu = 0.03$, $L = 2.5$ m, $h = 0.3468$ m. (a) Time series, (b) Fourier amplitude in semi-logarithmic chart.

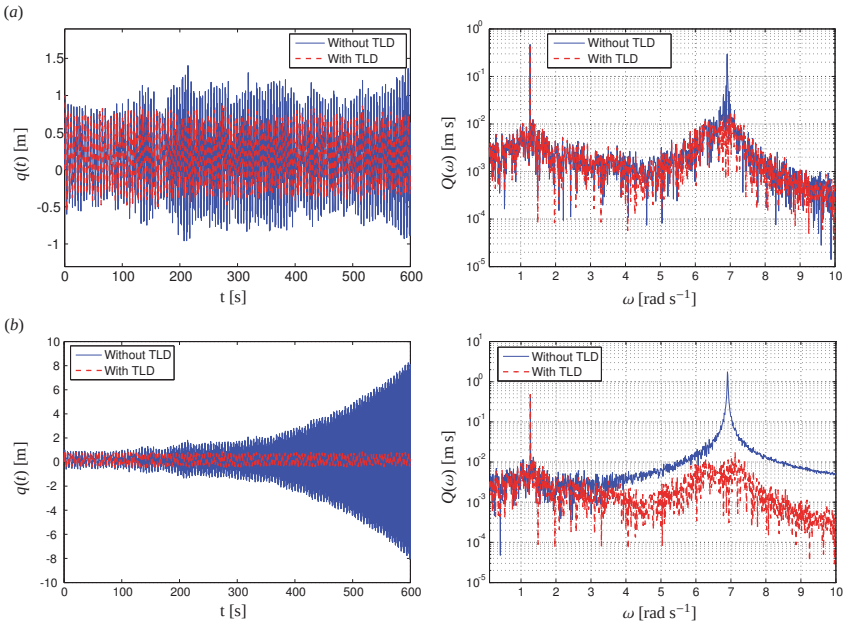

Figure 5: Performance of the TLD when aerodynamic damping changes (here mimicked by manually changing ζ_0 as illustration). $x_0 = 55$ m, $\mu = 0.03$, $L = 2.5$ m, $h = 0.3468$ m. (a) $\zeta_0 = 0$, (b) $\zeta_0 = -0.001$, aeroelastic instability.

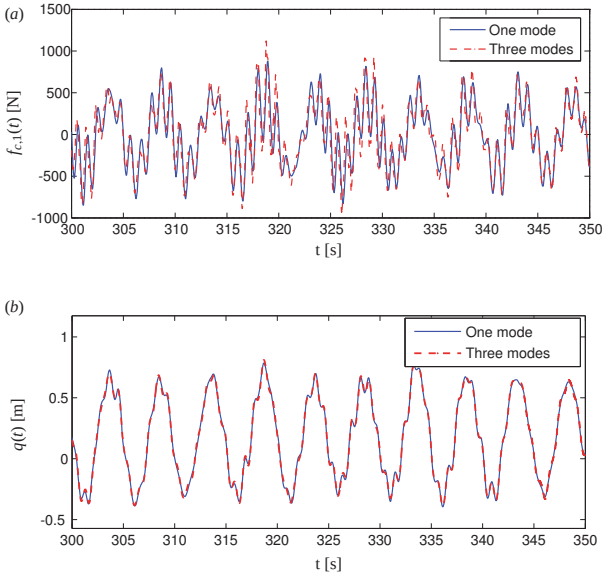

Figure 6: Comparison of the control performance from the one-mode and three-mode models, $V_0 = 15$ m s^{-1}, $I = 0.1$, $x_0 = 55$ m, $\mu = 0.03$, $L = 2.5$ m, $h = 0.3468$ m. (a) Control force (sloshing force) in y_1- direction, (b) Blade edgewise tip displacement with TLD.

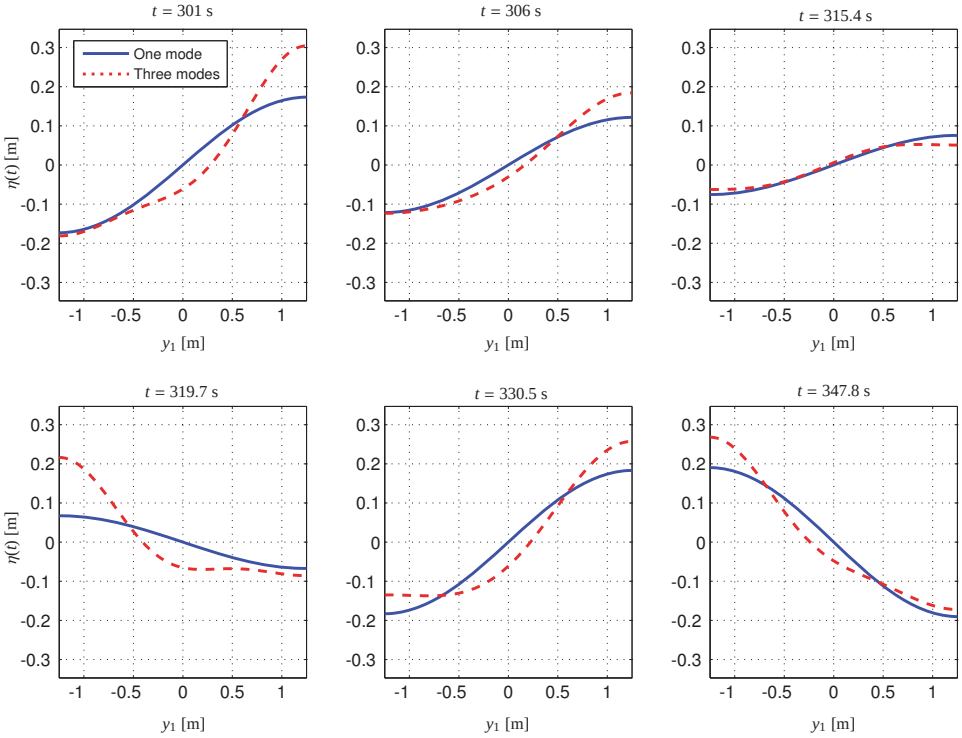

Figure 7: Surface elevation at various instants of time, $V_0 = 15$ m s^{-1}, $I = 0.1$, $x_0 = 55$ m, $\mu = 0.03$, $L = 2.5$ m, $h = 0.3468$ m.

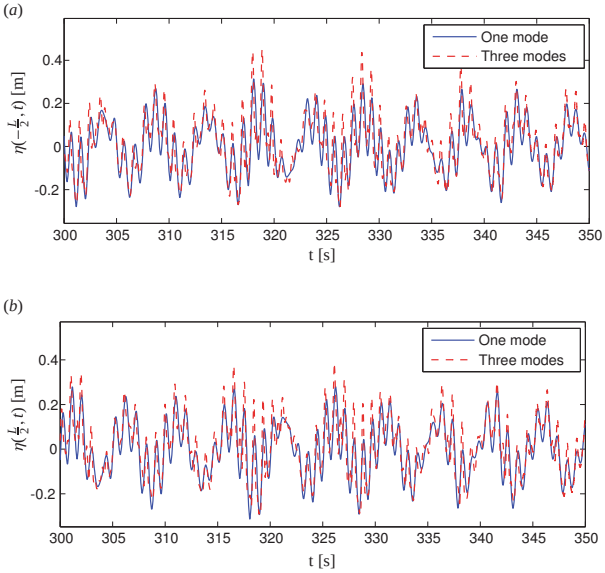

Figure 8: Time histories of the wave heights at the end walls, $V_0 = 15$ m s^{-1}, $I = 0.1$, $x_0 = 55$ m, $\mu = 0.03$, $L = 2.5$ m, $h = 0.3468$ m. (a) On the left side, i.e., $y_1 = -\frac{L}{2}$. (b) On the right side, i.e., $y_1 = \frac{L}{2}$.

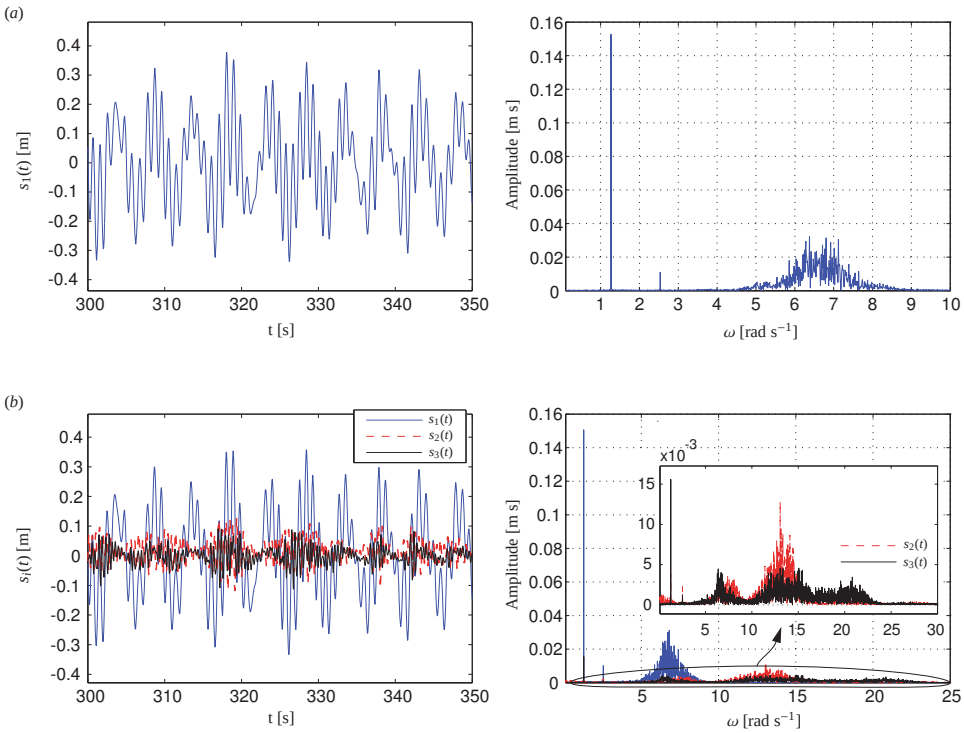

Figure 9: Responses of the generalized coordinates $s_i(t)$ in both time and frequency domains, $V_0 = 15$ m s^{-1}, $I = 0.1$, $x_0 = 55$ m, $\mu = 0.03$, $L = 2.5$ m, $h = 0.3468$ m. (a) One-mode model. (b) Three-mode model.

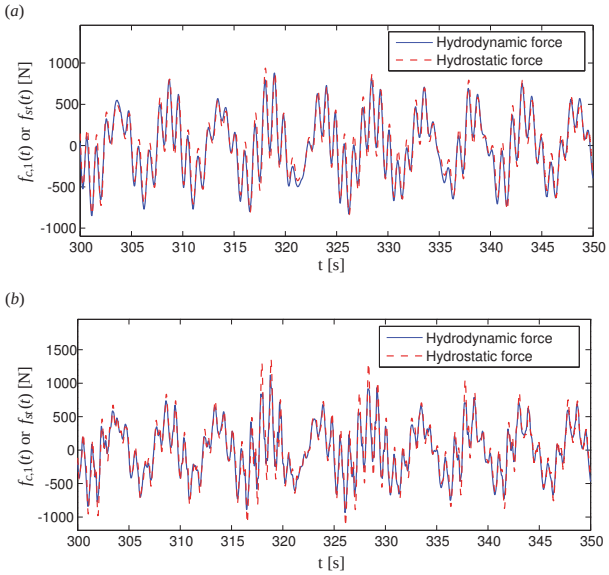

Figure 10: Comparison of the sloshing forces calculated from hydrodynamic pressure (Eq. (32)) and hydrostatic pressure (Eq. (44)), $V_0 = 15\,\mathrm{m\,s^{-1}}$, $I = 0.1$, $x_0 = 55\,\mathrm{m}$, $\mu = 0.03$, $L = 2.5\,\mathrm{m}$, $h = 0.3468\,\mathrm{m}$. (a) One-mode model. (b) Three-mode model.

APPENDIX F

Dynamics and Control of Lateral Tower Vibrations in Offshore Wind Turbines by Means of Active Generator Torque

Paper 5
The paper presented in this appendix is published in *Energies*, 2014, Volume 7, Pages 7746-7772, DOI: 10.3390/en7117746.

http://www.mdpi.com/1996-1073/7/11/7746

F.1 Author's Right

For Authors and Readers Open Access Means:

- **free availability** of the literature on the Internet without any subscription or price barriers
- **immediate open access** once an article is released (no embargo period)
- **authors retain all copyrights** - authors will not be forced to sign any copyright transfer agreements
- **permission of re-use** the published material if proper accreditation is given (Creative Commons Attribution License)

This is a human-readable summary of (and not a substitute for) the **license**.

Disclaimer

You are free to:

Share — copy and redistribute the material in any medium or format

Adapt — remix, transform, and build upon the material

for any purpose, even commercially.

The licensor cannot revoke these freedoms as long as you follow the license terms.

http://www.mdpi.com/authors

Energies **2014**, *7*, 7746-7772; doi:10.3390/en7117746

OPEN ACCESS

energies

ISSN 1996-1073

www.mdpi.com/journal/energies

Article

Dynamics and Control of Lateral Tower Vibrations in Offshore Wind Turbines by Means of Active Generator Torque

Zili Zhang [1,*], Søren R. K. Nielsen [1], Frede Blaabjerg [2] and Dao Zhou [2]

[1] Department of Civil Engineering, Aalborg University, Sofiendalsvej 11, 9200 Aalborg SV, Denmark; E-Mail: srkn@civil.aau.dk

[2] Department of Energy Technology, Aalborg University, Pontoppidanstraede 101, 9220 Aalborg East, Denmark; E-Mails: fbl@et.aau.dk (F.B.); zda@et.aau.dk (D.Z.)

* Author to whom correspondence should be addressed; E-Mail: zlz@civil.aau.dk; Tel.: +45-92-266-226.

External Editor: Simon J. Watson

Received: 6 July 2014; in revised form: 6 November 2014 / Accepted: 13 November 2014 / Published: 21 November 2014

Abstract: Lateral tower vibrations of offshore wind turbines are normally lightly damped, and large amplitude vibrations induced by wind and wave loads in this direction may significantly shorten the fatigue life of the tower. This paper proposes the modeling and control of lateral tower vibrations in offshore wind turbines using active generator torque. To implement the active control algorithm, both the mechanical and power electronic aspects have been taken into consideration. A 13-degrees-of-freedom aeroelastic wind turbine model with generator and pitch controllers is derived using the Euler–Lagrangian approach. The model displays important features of wind turbines, such as mixed moving frame and fixed frame-defined degrees-of-freedom, couplings of the tower-blade-drivetrain vibrations, as well as aerodynamic damping present in different modes of motions. The load transfer mechanisms from the drivetrain and the generator to the nacelle are derived, and the interaction between the generator torque and the lateral tower vibration are presented in a generalized manner. A three-dimensional rotational sampled turbulence field is generated and applied to the rotor, and the tower is excited by a first order wave load in the lateral direction. Next, a simple active control algorithm is proposed based on active generator torques with feedback from the measured lateral tower vibrations. A full-scale power converter configuration with a cascaded loop control structure is also introduced to produce the feedback control torque in real time. Numerical simulations have been carried out using

data calibrated to the referential 5-MW NREL (National Renewable Energy Laboratory) offshore wind turbine. Cases of drivetrains with a gearbox and direct drive to the generator are considered using the same time series for the wave and turbulence loadings. Results show that by using active generator torque control, lateral tower vibrations can be significantly mitigated for both gear-driven and direct-driven wind turbines, with modest influence on the smoothness of the power output from the generator.

Keywords: offshore wind turbine; active generator control; lateral tower vibration; feedback control; aeroelastic model

1. Introduction

Modern multi-megawatt wind turbines are designed with increasingly larger rotors and higher towers, in order to capture more energy throughout their lifetime and, thereby, reduce the cost of energy. As wind turbines grow in size, the stiffness of the blades and the tower are not increased proportionally, rendering the structure more sensitive to dynamic excitations. Normally, vibrations in the flap-wise direction and tower vibration in the mean wind direction are highly damped due to the strong aerodynamic damping [1]. In contrast, edgewise vibrations and lateral tower vibrations are related with insignificant aerodynamic damping [1,2]. Hence, these modes of vibrations may be prone to large dynamic responses. Most offshore wind turbines are placed at shallow water. Due to refraction, the approaching waves tend to propagate in a direction normal to the level curves of the sea bottom. In turn, this means that the wave load may act in a different direction of the mean wind direction, and significant lateral tower vibrations may be initiated by the wave load in combination with the resultant aerodynamic load from the three blades in the lateral direction.

Some studies have been carried out for the structural control of tower vibrations, most of which focus on passive structural control techniques. Theoretical investigations have been performed on the effectiveness of a tuned mass damper (TMD) [3] and tuned liquid column damper (TLCD) [4] for mitigating along-wind vibrations of wind turbine towers, ignoring the aerodynamic properties of the blades. To yield more realistic results, an advanced modeling tool has been developed and incorporated into the aeroelastic code, FAST (Fatigue, Aerodynamics, Structures and Turbulence), allowing the investigation of passive TMDs in vibration control of offshore wind turbine systems [5]. Recently, a series of shaking table tests have been carried out to evaluate the effect of the ball vibration absorber (BVA) on the vibration mitigation of a reduced scale wind turbine model, which proves the effectiveness of the passive damping device [6]. However, the focus of this study is still on along-wind vibrations without considering the aerodynamic damping. Active structural control of floating wind turbines is investigated by Lackner and Rotea [7]. Simulation results in FAST show that active control is a more effective way of reducing structural loads than the passive control method, at the expense of active power and larger TMD strokes.

For modern variable speed wind turbines, advanced pitch control and generator torque control techniques for the mitigation of structural loads are being increasingly investigated. In a basic variable

speed wind turbine control system, torque control is used in below-rated wind speeds to obtain maximum energy output. Above the rated speed, a pitch controller is utilized to regulate the rotor speed to the desired value, and the generator torque is held constant (nominal torque) [8]. Additional pitch control loops as feedback from measured nacelle fore-aft acceleration are usually used to damp fore-aft tower vibrations [9], although vibration in this direction is already highly damped due to the aerodynamic damping. Generator torque control is widely used to provide damping into the drivetrain torsional vibrations [9–11]. Instead of demanding a constant generator torque above the rated one, an additive torque as feedback from the measured generator speed is added to the torque demand, which is effective at damping vibrations of the resonant mode of the drivetrain.

The idea of providing active damping to lateral tower vibration using generator torque was first proposed by Van der Hooft *et al*. [12] and was further investigated by de Corcuera *et al*. [13] and Fleming *et al*. [14]. Essentially, the generator torque affects the lateral tower vibration through the reaction on the generator stator, which is rigidly fixed to the nacelle. By means of modern power electronics, the generator torque can be prescribed to a certain value with a delay below 10^{-2} s [15]. By using this property, feedback control of the lateral tower vibrations can be performed. Van der Hooft *et al*. [12] simplified the tower by a single-degree-of-freedom (SDOF) representing the lateral translational motion, and the tower top rotation was neglected. Since the generator torque is affecting the lateral tower motion via the tower top rotation, this SDOF tower model does not adequately account for the transfer of the generator torque. De Corcuera *et al*. [13] demonstrated a strategy to design a multi-variable controller based on the H_∞ norm reduction for reducing both the drivetrain torsional vibration and the tower side-to-side vibration, with simulations carried out in the GH Bladed software. This study focuses on the controller design procedure. However, the torque transfer mechanism from the generator to the tower vibration and the effect of the generator torque on other components of the wind turbine are not demonstrated. Fleming *et al*. [14] presented the field-testing results of the effect of active generator control on the drivetrain and lateral tower vibrations in a 600-kW wind turbine. A multi-SISO (single-input-single-output) controller is compared with the H_∞ controller, and a similar effect for damping the lateral tower vibration was obtained. Again, the effect of the generator torque on other components of the wind turbine, such as the blades, was ignored. Actually, the edgewise vibrations of the blades are coupled to the lateral tower vibration, as well as to the torsional drivetrain vibration through the collective mode. Since very low, even negative, aerodynamic damping takes place in edgewise vibration, it is important to investigate the effect of the active generator torque on this mode of vibration. Moreover, as the basis of implementing active generator control, the load transfer mechanisms from the drivetrain and the generator to the nacelle, as well as the interaction between the generator torque with the lateral tower vibration are not clearly demonstrated in the above-mentioned studies. Further, all of the previous studies focus on the gear-driven wind turbines. With offshore wind turbines becoming larger and being moved out further at sea, there is huge application potential of direct-driven systems, where the turbine rotor is coupled directly to the electrical generator without the gearbox. The generators operate at the same rotational speed as the turbine's rotor and must therefore be much bigger in size. However, by using permanent magnets in the generators' rotor and eliminating the gearbox, the weight of the nacelle can be significantly decreased compared to that of the gear-driven system, which, in turn, reduces the shipping and installation costs for offshore wind farms. Further, since the gearbox causes

the greatest downtime resulting in lost revenue, the use of a direct-driven system definitely avoids the cost of overhauling, removing and reinstalling the gearbox, thus reducing operating costs over the long term and making electricity from wind farms more competitive. This is especially important for offshore wind farms, because doing maintenance at sea is a lot more complex and expensive than on the ground. For the direct-driven wind turbines, the electric torque in the generator is much larger comparing with the gear-driven wind turbines, making it possible to damp the lateral tower vibration more effectively.

This paper presents a comprehensive investigation into the modeling and control of lateral tower vibrations in offshore wind turbines using active generator torque, taking into consideration the consequences of the control on the edgewise blade vibrations and the quality of the produced power. The load transfer mechanisms from the generator to the tower are derived in a generalized form for gear-driven wind turbines with an odd or even number of gear stages, as well as for the direct-driven wind turbines. The active generator control algorithm is investigated based on a 13-degrees-of-freedom (13-DOF) wind turbine model developed by the authors, which has been calibrated to the referential 5-MW NREL (National Renewable Energy Laboratory) offshore wind turbine [16]. A three-dimensional (3D) turbulence field is modeled by a low order auto-regressive (AR) model [17]. The dynamic loading from the rotational sampled turbulence and the non-linear aeroelasticity is assumed to be quasi-static, *i.e.*, the changes of aerodynamic forces due to changes of the angle of attack are felt without time delay. The wave load is modeled by the Morison formula [18] in combination with the first order wave theory and applied to the tower in the lateral direction. A generator model is proposed with a complete solution to provide the feedback control torque. Cases of gear-driven and direct-driven wind turbines are both investigated. Simulation results show that lateral tower vibration can be significantly suppressed, and the edgewise vibrations are also slightly mitigated by the active generator control, while only modest influence on the smoothness of the power output are brought about by the additive generator torque.

2. Wind Turbine Model

In this section, a 13-DOF aeroelastic wind turbine model is presented with coupled edgewise, lateral tower and torsional drivetrain vibrations. The torque transfer mechanism between the drivetrain and the tower are derived in a generalized manner, which forms the basis for active control of tower vibrations using the generator torque.

2.1. General Description

Despite its simplicity, the 13-DOF aeroelastic model takes into account several important characteristics of a wind turbine, including time-dependent system matrices, coupling of the tower-blades-drivetrain vibration, as well as non-linear aeroelasticity. A schematic representation of the wind turbine model is shown in Figure 1. The motion of structural components is described either in a fixed, global frame of reference (X_1, X_2, X_3) or in moving frames of reference (x_1, x_2, x_3), attached to each blade with the origin at the center of the hub. Neglecting the tilt of the rotor, the X_1 and x_1 axis are unidirectional to the mean wind velocity. The (X_2, X_3) and (x_2, x_3) coordinate planes are placed in the rotor plane. The X_3 axis is vertical, and the x_3 axis is placed along the blade axis oriented from the hub

towards the blade tip. The position of the moving frame attached to blade j is specified by the azimuthal angle $\Psi_j(t)$, which is considered positive when rotating clockwise seen from an upwind position.

Figure 1. Thirteen DOFs model of a three-bladed wind turbine. Definition of fixed and moving frames of reference and the degrees of freedom $q_1(t), \ldots, q_{11}(t)$.

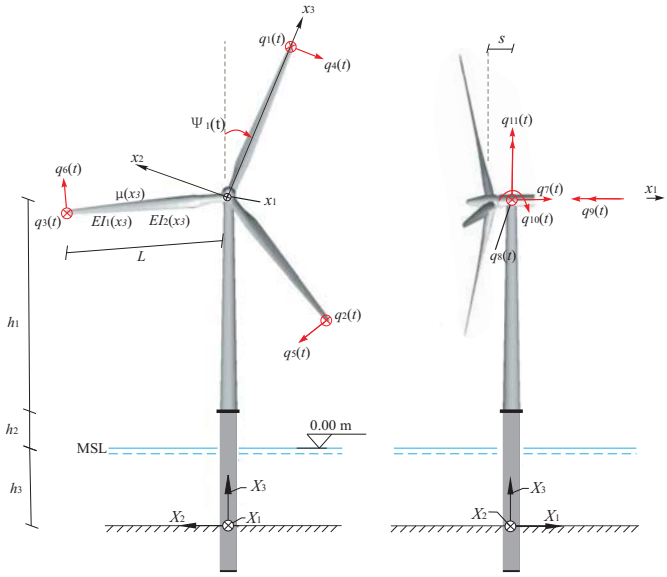

The blades are modeled as Bernoulli–Euler beams with the bending stiffness $EI_1(x_3)$ in the flap-wise direction and $EI_2(x_3)$ in the edgewise direction. The mass per unit length is $\mu(x_3)$. Each blade is related with two degrees of freedom (DOFs). $q_1(t)$, $q_2(t)$, $q_3(t)$ denote the flapwise tip displacement in the positive x_1 direction. $q_4(t)$, $q_5(t)$, $q_6(t)$ denote the edgewise tip displacement in the negative x_2 direction. The length of each blade is denoted L. The tower motion is defined by five DOFs $q_7(t), \ldots, q_{11}(t)$. $q_7(t)$ and $q_8(t)$ signify the displacements of the tower at the height of the hub in the global X_1 and X_2 directions. $q_9(t)$ specifies the elastic rotation of the top of the tower in the negative X_1 direction, and $q_{10}(t)$ and $q_{11}(t)$ indicate the corresponding rotations in the positive X_2 and X_3 directions. The height of the tower from the base to the nacelle is denoted h_1, and the tower base begins at an elevation of h_2 above mean sea level (MSL), with a monopile extending from the tower base to the mud line. The water depth from the mud line to the MSL is denoted h_3, and the horizontal distance from the center of the tower top to the origin of the moving coordinate systems is denoted s (Figure 1).

The drivetrain is modeled by the DOFs $q_{12}(t)$ and $q_{13}(t)$ (Figure 2). The sign definition shown in Figure 2 applies to a gearbox with an odd number of stages. $q_{12}(t)$ and $q_{13}(t)$ indicate the deviations of the rotational angles at the hub and the generator from the nominal rotational angles Ωt and $N\Omega t$, respectively, where N is the gear ratio. Correspondingly, $\dot{q}_{12}(t)$ and $\dot{q}_{13}(t)$ are the deviations of the rotational speeds at the hub and the generator from the nominal values. In case of an even number of stages, the sign definitions for $q_{13}(t)$ and $f_{13}(t)$ are considered positive in the opposite direction. J_r and

J_g denote the mass moment of inertia of the rotor and the generator; and k_r and k_g denote the St. Venant torsional stiffness of the rotor shaft and the generator shaft. The azimuthal angle of the blade j (Figure 1) becomes $\Psi_j(t) = \Omega\, t + q_{12}(t) + \frac{2\pi}{3}\,(j-1),\ j = 1, 2, 3.$

Figure 2. Two DOFs model of flexible drivetrain with an odd number of gear stages. Definition of degrees of freedom $q_{12}(t)$ and $q_{13}(t)$.

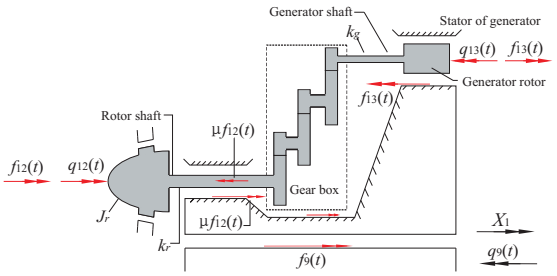

Further, a full-span rotor-collective pitch controller is included in the model with time delay modeled by a first order filter. The pitch demand is modeled by a PI controller [19] with feedback from $\dot{q}_{12}(t)$ and $q_{12}(t)$. A gain-scheduled PI controller is used in this paper, *i.e.*, the controller gains are dependent on the blade-pitch angle [16].

2.2. Coupled Edgewise, Lateral Tower and Torsional Drivetrain Vibrations

The equations of motion of the 13-DOF wind turbine model can be derived from the Euler–Lagrange equation [20]:

$$\frac{d}{dt}\left(\frac{\partial T}{\partial \dot{\mathbf{q}}}\right) - \frac{\partial T}{\partial \mathbf{q}} + \frac{\partial U}{\partial \mathbf{q}} = \mathbf{f}(t) \tag{1}$$

where $\mathbf{q}^{\mathrm{T}}(t) = \left[q_1(t), \ldots, q_{13}(t)\right]$ is a 13-dimensional column vector storing all DOFs. $T = T(\mathbf{q}, \dot{\mathbf{q}})$ signifies the kinetic energy, and $U = U(\mathbf{q})$ is the potential energy of the system. The key step in setting up the coupled equation is to formulate the kinetic energy of each blade with velocity contributions from both the locally and globally defined DOFs. For example, $\dot{q}_1(t), \dot{q}_7(t), \dot{q}_{10}(t)$ and $\dot{q}_{11}(t)$ induce the velocity component of a cross-section of Blade 1 in the x_1 direction, while $\dot{q}_4(t), \dot{q}_8(t), \dot{q}_{10}(t), \dot{q}_{11}(t)$ and $\dot{q}_{12}(t)$ induce the velocity component of Blade 1 in the x_2 direction. $\mathbf{f}(t)$ is the force vector work conjugated to $\mathbf{q}(t)$, including structural damping forces, aerodynamic and hydrodynamic forces, as well as generator control forces.

Assuming linear structural dynamics and substituting the expressions for kinetic and potential energies into Equation (1), the equations of motion of the 13-DOF wind turbine model are obtained of the form:

$$\mathbf{M}(t)\,\ddot{\mathbf{q}}(t) + \mathbf{C}(t)\,\dot{\mathbf{q}}(t) + \mathbf{K}(t)\,\mathbf{q}(t) = \mathbf{f}_{\mathrm{e}}(t) \tag{2}$$

where $\mathbf{M}(t)$ is the mass matrix, $\mathbf{C}(t)$ is the damping matrix, including the structural damping and the gyroscopic damping, and $\mathbf{K}(t)$ is the stiffness matrix taking into account the geometric stiffness

and the gyroscopic stiffness. Both the gyroscopic damping matrix and gyroscopic stiffness matrix are obtained by substituting the kinetic energy of the system into the Euler–Lagrange equation. Through this procedure, the coriolis forces and the centrifugal softening effect are taken into account. $\mathbf{f}_e(t)$ is the external dynamic load vector work conjugated to $\mathbf{q}(t)$, which is composed of the non-linear aerodynamic loads, the generator torque and the wave loads. All of the indicated system matrices are time dependent, due to the fact that the DOFs of the blades are formulated in the moving frames of reference, and others are formulated in a fixed frame of reference.

Next, the DOFs vector $\mathbf{q}(t)$ may be partitioned in the following way:

$$\mathbf{q}(t) = \begin{bmatrix} \mathbf{q}_1(t) \\ \mathbf{q}_2(t) \end{bmatrix} \tag{3}$$

$$\begin{aligned} \mathbf{q}_1^{\mathrm{T}}(t) &= \begin{bmatrix} q_4(t) & q_5(t) & q_6(t) & q_8(t) & q_9(t) & q_{12}(t) & q_{13}(t) \end{bmatrix} \\ \mathbf{q}_2^{\mathrm{T}}(t) &= \begin{bmatrix} q_1(t) & q_2(t) & q_3(t) & q_7(t) & q_{10}(t) & q_{11}(t) \end{bmatrix} \end{aligned} \tag{4}$$

The main focus of the present study is on the dynamic coupling of edgewise, lateral tower and torsional drivetrain motions and the effect of active generator torque on these vibrations. To clearly unfold this coupling, only the sub-system related to DOFs $\mathbf{q}_1(t)$ is picked out from Equation (2) and is demonstrated in detail. It should be noted that the numerical simulations in the subsequent section will always be based on Equation (2), where all of the 13 DOFs are activated. As a part of Equation (2), the equations of motion related to the above-mentioned sub-system, which show the coupling of edgewise, lateral tower and torsional drivetrain vibrations, are demonstrated by the following matrix differential equations:

$$\mathbf{M}_1(t)\,\ddot{\mathbf{q}}_1(t) + \mathbf{C}_1(t)\,\dot{\mathbf{q}}_1(t) + \mathbf{K}_1(t)\,\mathbf{q}_1(t) = \mathbf{f}_{e,1}(t) \tag{5}$$

$$\mathbf{M}_1(t) = \begin{bmatrix} m_2 & 0 & 0 & -m_1\cos\Psi_1 & 0 & m_3 & 0 \\ 0 & m_2 & 0 & -m_1\cos\Psi_2 & 0 & m_3 & 0 \\ 0 & 0 & m_2 & -m_1\cos\Psi_3 & 0 & m_3 & 0 \\ -m_1\cos\Psi_1 & -m_1\cos\Psi_2 & -m_1\cos\Psi_3 & m_{88}+M_0+3m_0 & m_{89} & 0 & 0 \\ 0 & 0 & 0 & m_{98} & m_{99} & 0 & 0 \\ m_3 & m_3 & m_3 & 0 & 0 & J_r & 0 \\ 0 & 0 & 0 & 0 & 0 & 0 & J_g \end{bmatrix}$$

$$\mathbf{C}_1(t) = \begin{bmatrix} c_2 & 0 & 0 & 0 & 0 & 0 & 0 \\ 0 & c_2 & 0 & 0 & 0 & 0 & 0 \\ 0 & 0 & c_2 & 0 & 0 & 0 & 0 \\ 2\Omega m_1\sin\Psi_1 & 2\Omega m_1\sin\Psi_2 & 2\Omega m_1\sin\Psi_3 & c_{88} & c_{89} & 0 & 0 \\ 0 & 0 & 0 & c_{98} & c_{99} & 0 & 0 \\ 0 & 0 & 0 & 0 & 0 & 0 & 0 \\ 0 & 0 & 0 & 0 & 0 & 0 & 0 \end{bmatrix}$$

$$\mathbf{K}_1(t) = \begin{bmatrix} k_2 - k_g & 0 & 0 & 0 & 0 & 0 & 0 \\ 0 & k_2 - k_g & 0 & 0 & 0 & 0 & 0 \\ 0 & 0 & k_2 - k_g & 0 & 0 & 0 & 0 \\ \Omega^2 m_1 \cos\Psi_1 & \Omega^2 m_1 \cos\Psi_2 & \Omega^2 m_1 \cos\Psi_3 & k_{88} & k_{89} & 0 & 0 \\ 0 & 0 & 0 & k_{98} & k_{99} & 0 & 0 \\ 0 & 0 & 0 & 0 & 0 & k_0 & -\frac{k_0}{N} \\ 0 & 0 & 0 & 0 & 0 & -\frac{k_0}{N} & \frac{k_0}{N^2} \end{bmatrix} \tag{6}$$

where:

$$\begin{gathered} m_0 = \int_0^L \mu(x_3)dx_3, m_1 = \int_0^L \Phi(x_3)\mu(x_3)dx_3, m_2 = \int_0^L \Phi^2(x_3)\mu(x_3)dx_3, m_3 = \int_0^L \Phi(x_3)\mu(x_3)x_3 dx_3 \\ k_2 = \int_0^L \left(EI_2(x_3)\left(\frac{d^2\Phi(x_3)}{dx_3^2}\right)^2 + F(x_3)\left(\frac{d\Phi(x_3)}{dx_3}\right)^2 \right) dx_3, \quad k_g = \Omega^2 m_2, \quad J_r = 3\int_0^L \mu(x_3)x_3^2 dx_3 \end{gathered} \tag{7}$$

$\Phi(x_3)$ is the undamped eigenmode in the edgewise direction, when the blade is fixed at the hub. Due to the definition of $q_{j+3}(t)$, $j = 1, 2, 3$, this mode must be normalized to one at the tip, *i.e.*, $\Phi(L) = 1$. $F(x_3) = \Omega^2 \int_{x_3}^L \mu(\xi)\xi d\xi$ is the centrifugal axial force on the blade. m_0 is the mass of each blade, and M_0 is the mass of the nacelle. $c_2 = 2\zeta_2\sqrt{m_2 k_2}$ is the modal damping coefficient of the edgewise vibration, calculated from the given damping ratio ζ_2.

As shown in Figure 3, the lateral tower vibration is modeled by two DOFs, $q_8(t)$ and $q_9(t)$, with cubic shape functions $N_8(X_3)$ and $N_9(X_3)$, respectively. The consistent mass and stiffness terms for $q_8(t)$ and $q_9(t)$ are calculated from the tower itself without considering the nacelle and the rotor, as given by the following equation:

$$\begin{gathered} m_{88} = \int_0^H \mu_0(X_3)N_8^2(X_3)dX_3, \quad m_{89} = \int_0^H \mu_0(X_3)N_8(X_3)N_9(X_3)dX_3, \quad m_{99} = \int_0^H \mu_0(X_3)N_9^2(X_3)dX_3 \\ k_{88} = \int_0^H EI_0(X_3)(\frac{\partial N_8}{\partial X_3})^2 dX_3, \quad k_{89} = \int_0^H EI_0(X_3)(\frac{\partial N_8}{\partial X_3})(\frac{\partial N_9}{\partial X_3})dX_3, \quad k_{99} = \int_0^H EI_0(X_3)(\frac{\partial N_9}{\partial X_3})^2 dX_3 \end{gathered} \tag{8}$$

where $\mu_0(X_3)$ and $EI_0(X_3)$ are the mass per unit length and bending stiffness in the lateral direction of the tower, respectively. $N_8(X_3) = 3\left(\frac{X_3}{H}\right)^2 - 2\left(\frac{X_3}{H}\right)^3$, $N_9(X_3) = H\left(\left(\frac{X_3}{H}\right)^3 - \left(\frac{X_3}{H}\right)^2\right)$, $H = h_1 + h_2 + h_3$ is the total height of the tower structure. The related damping terms c_{88}, c_{89}, c_{98}, c_{99} are specified by the Rayleigh damping model [21] from the consistent mass and stiffness terms, with given damping ratios ζ_8 and ζ_9. k_0 indicates an equivalent torsional stiffness of the shaft of the drivetrain, given as:

$$\frac{1}{k_0} = \frac{1}{k_r} + \frac{1}{N^2 k_g} \quad \Rightarrow \quad k_0 = \frac{N^2 k_r k_g}{k_r + N^2 k_g} \tag{9}$$

Figure 3. Modeling of the lateral tower vibration. (**a**) Two DOFs model for lateral tower vibration with wave loads. (**b**) Shape function for the degree of freedom $q_8(t)$. (**c**) Shape function for the degree of freedom $q_9(t)$.

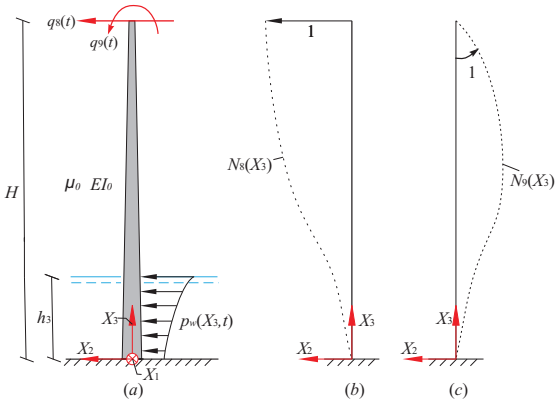

From Equation (6), it is noted that the edgewise vibrations are coupled to the lateral tower vibration through the mass matrix, damping matrix and stiffness matrix and coupled to the drivetrain torsional vibration through the mass matrix alone. Actually, only the collective mode of the edgewise vibration is coupled with the torsional vibration of the drivetrain.

2.3. Torque Transfer Mechanism between the Drivetrain and the Tower

In Equation (5), the external dynamic load vector work conjugated to $\mathbf{q}_1(t)$ is expressed as:

$$\mathbf{f}_{e,1}^{\mathrm{T}}(t) = \begin{bmatrix} f_4(t) & f_5(t) & f_6(t) & f_8(t) & f_9(t) & (1-\mu)f_{12}(t) & -f_{13}(t) \end{bmatrix} \tag{10}$$

where $f_4(t)$, $f_5(t)$, $f_6(t)$ and $f_{12}(t)$ are dynamic loads work-conjugated to the defined DOFs, resulting from aerodynamic loads. $f_8(t)$ is the load work-conjugated to the degree of freedom $q_8(t)$, due to both aerodynamic loads and wave forces. $(1-\mu)f_{12}(t)$ denotes the effective torque on the drivetrain available for power production due to friction in the bearings and the gear box, as specified by the friction coefficient μ. $f_{13}(t)$ indicates the generator torque.

Using D'Alembert's principle, the net torque on the drivetrain in the global X_1 direction becomes $(1-\mu)f_{12}(t) - J_r\ddot{q}_{12}(t) \pm (f_{13}(t) + J_g\ddot{q}_{13}(t))$, where the plus sign applies for a gearbox with an odd number of gear stages (as shown in Figure 2) and the minus sign for an even number of stages. The torque is transferred to the nacelle in the positive X_1 direction via the bearings of the shaft and the gearbox. On the nacelle, the transferred torque is added to the reaction of the friction torque $\mu f_{12}(t)$ (always in the positive X_1 direction) and the generator torque on the stator $f_{13}(t)$, which is acting in the negative X_1 direction for an odd number of stages or acting in the positive X_1 direction for an even number of stages. Hence, the resultant torque on the bottom of the nacelle becomes $f_{12}(t) - J_r\ddot{q}_{12}(t) \pm J_g\ddot{q}_{13}(t)$ (plus sign for an odd number of gear stages). With $q_9(t)$ defined as positive when acting in the negative X_1 direction, the torque work-conjugated to $q_9(t)$ resulting from the nacelle becomes $-f_{12}(t) + J_r\ddot{q}_{12}(t) \mp J_g\ddot{q}_{13}(t)$

(minus sign for an odd number of gear stages). Then, together with the contribution from the wave load, the total load work-conjugated to $q_9(t)$ becomes:

$$f_9(t) = \begin{cases} f_{9,w}(t) - f_{12}(t) + J_r\ddot{q}_{12}(t) - J_g\ddot{q}_{13}(t) & \text{(odd number of gear stages)} \\ f_{9,w}(t) - f_{12}(t) + J_r\ddot{q}_{12}(t) + J_g\ddot{q}_{13}(t) & \text{(even number of gear stages)} \end{cases} \tag{11}$$

where $f_{9,w}(t)$ is the load conjugated to $q_9(t)$ induced by waves propagating in the X_2 direction. As shown in Figure 3, $p_w(X_3, t)$ denotes the distributed wave force acting on the tower, which can be calculated by the Morison formula. Then, the loads conjugated to $q_8(t)$ and $q_9(t)$ induced by the distributed wave force can be written as:

$$\begin{bmatrix} f_{8,w}(t) \\ f_{9,w}(t) \end{bmatrix} = \int_0^{h_3} \begin{bmatrix} N_8(X_3) \\ N_9(X_3) \end{bmatrix} p_w(X_3, t) dX_3 \tag{12}$$

The control of the lateral tower vibration is actually applied via the torque $f_9(t)$ conjugated to $q_9(t)$. For this reason, the relation between $f_9(t)$ and $f_{13}(t)$ is analyzed. The equation of motion of the drivetrain reads from Equations (5) and (10):

$$\begin{bmatrix} J_r & 0 \\ 0 & J_g \end{bmatrix} \begin{bmatrix} \ddot{q}_{12}(t) \\ \ddot{q}_{13}(t) \end{bmatrix} + k_0 \begin{bmatrix} 1 & -\frac{1}{N} \\ -\frac{1}{N} & \frac{1}{N^2} \end{bmatrix} \begin{bmatrix} q_{12}(t) \\ q_{13}(t) \end{bmatrix} = \begin{bmatrix} (1-\mu) f_{12}(t) \\ -f_{13}(t) \end{bmatrix} \tag{13}$$

The acceleration terms in Equation (11) can be eliminated by means of the equation of motion of the drivetrain, resulting in the equivalent expression for $f_9(t)$:

$$f_9(t) = \begin{cases} f_{9,w}(t) - \mu f_{12}(t) + f_{13}(t) - k_0 \left(1 + \frac{1}{N}\right) \left(q_{12}(t) - \frac{1}{N} q_{13}(t)\right) & \text{(odd number of gear stages)} \\ f_{9,w}(t) - \mu f_{12}(t) - f_{13}(t) - k_0 \left(1 - \frac{1}{N}\right) \left(q_{12}(t) - \frac{1}{N} q_{13}(t)\right) & \text{(even number of gear stages)} \end{cases} \tag{14}$$

Especially for direct-driven wind turbines, where $N = 1$, we get from the second equation in Equation (14) that:

$$f_9(t) = f_{9,w}(t) - \mu f_{12}(t) - f_{13}(t) \tag{15}$$

It is seen from the last part of the two sub-equations in Equation (14) that for gear-driven wind turbines, there are extra coupling terms between the degree of freedom $q_9(t)$ and the two DOFs of the drivetrain, which can be transferred and added to the stiffness matrix in Equation (6). Based on the relationship between $f_9(t)$ and $f_{13}(t)$ in Equations (14) and (15), the lateral tower vibrations can be controlled by specifying the format of the generator torque $f_{13}(t)$, as will be shown in the subsequent section.

2.4. Aerodynamic and Wave Loads

In agreement with [22], the turbulence modeling is based on Taylor's hypothesis of frozen turbulence, corresponding to a frozen turbulence field that is convected into the rotor in the global X_1 direction with a mean velocity V_0, which provides the relation between spatial coordinates and time. The frozen field is assumed to be a zero mean homogeneous and isotropic stochastic field, with a spatial covariance structure given by [23]. Calibrated from the theoretical covariance structure, the first order AR model as proposed by [17] performs a first-order filtering of the white noise input, resulting in continuous, non-differentiable

sample curves of the turbulence field at the rotor plane in the fixed frame of reference. As shown in Figure 4, the fixed frame components of the convected turbulence are generated at $n_n = n_a \cdot n_r + 1$ nodal points at the discrete instants of time $t = 0, \Delta t, 2\Delta t, \cdots$, where n_a is the number of radial lines in the mesh from the center Node 1 and n_r is the number of equidistantly placed nodes along a given radial line. Next, the fixed frame components of the rotational sampled turbulence vector on each blade with the azimuthal angle Ψ_j are obtained by linear interpolation of the turbulence of the adjacent radial lines according to the position of the blade at each time step. Finally, the moving frame components of the rotational sampled turbulence are obtained by the following coordinate transformation:

$$\begin{bmatrix} v_{1,j}(x_3,t) \\ v_{2,j}(x_3,t) \\ v_{3,j}(x_3,t) \end{bmatrix} = \begin{bmatrix} 1 & 0 & 0 \\ 0 & \cos\Psi_j & \sin\Psi_j \\ 0 & -\sin\Psi_j & \cos\Psi_j \end{bmatrix} \begin{bmatrix} \bar{v}_{1,j}(\mathbf{X},t) \\ \bar{v}_{2,j}(\mathbf{X},t) \\ \bar{v}_{3,j}(\mathbf{X},t) \end{bmatrix} \tag{16}$$

where $v_{1,j}(x_3,t)$, $v_{2,j}(x_3,t)$ and $v_{3,j}(x_3,t)$ are rotational sampled turbulence components for blade j at the position x_3, in the moving frames of reference. $\bar{v}_{1,j}(\mathbf{X},t)$, $\bar{v}_{2,j}(\mathbf{X},t)$, $\bar{v}_{3,j}(\mathbf{X},t)$ are rotational sampled turbulence components at the same position for blade j in the fixed frame of reference with $\mathbf{X} = [0, -x_3 \sin\Psi_j, x_3 \cos\Psi_j]^{\mathrm{T}}$. Due to the longitudinal correlation of the incoming turbulence, a certain periodicity is present as spectral peaks at $1\Omega, 2\Omega, 3\Omega$... in the frequency domain representation of the rotational sampled turbulence. The simple AR model used here does not represent the low-frequency, large-scale turbulent structures very well, due to the homogeneity and isotropy assumption. On the other hand, the dynamics of the tower are more related to the frequency component of turbulence in the vicinity of the tower frequency. In this respect, the rotational sampled effect seems to be more important and is well accounted for by the present model.

The blade element momentum (BEM) method with Prandtl's tip loss factor and Glauert correction is adopted to calculate aerodynamic forces along the blade [24]. Non-linear aeroelasticity is considered by including the local deformation velocities of the blade into the calculation of the flow angle and the angle of attack. As a result, high aerodynamic damping is introduced in the blade flap-wise and the fore-aft tower vibrations, but relatively low aerodynamic damping in the blade edgewise and the lateral tower vibrations.

Figure 4. Nodal points in the rotor plane of the discretized turbulence field. n_a = 8, n_r = 5.

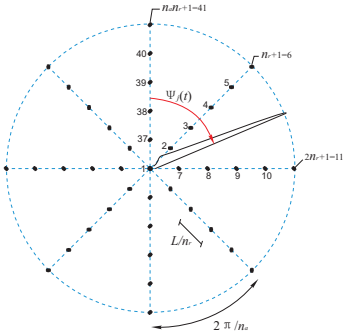

Sea surface elevation is modeled as a zero mean, stationary Gaussian process defined by the single-sided version of the JONSWAP (Joint North Sea Wave Project) spectrum [25], which is determined by the significant wave height H_s and the peak period T_p. Assuming first order wave theory, the realization of the stationary wave surface elevation process can be obtained by the following random phase model:

$$\eta(X_2,t)=\sum_{j=1}^{J}\sqrt{2}\eta_j\cos(\omega_j t-k_jX_2+\phi_j) \tag{17}$$

where J is the number of harmonic components in the spectral decomposition, ω_j and k_j are the angular frequency and wave number of the j-th harmonic component related through the dispersion relationship $\omega_j^2=gk_j\tanh(k_jh)$. ϕ_j denotes samples of the random phase Φ_j, which are mutually independent and uniformly distributed in $[0,2\pi]$. $\eta_j=\sqrt{S_\eta(\omega_j)\Delta\omega_j}$ denotes the standard deviation of the j-th harmonic component, and $S_\eta(\omega_j)$ is the single-sided JONSWAP spectrum.

Following the linear wave theory, the horizontal velocity $v(X_3,t)$ and acceleration $\dot{v}(X_3,t)$ of the water particle at the position $X_2=0$ can be written as:

$$\begin{aligned}v(X_3,t)&=\sum_{j=1}^{J}\sqrt{2}\eta_j\omega_j\frac{\cosh(k_jX_3)}{\sinh(k_jh)}\cos(\omega_jt+\phi_j)\\ \dot{v}(X_3,t)&=-\sum_{j=1}^{J}\sqrt{2}\eta_j\omega_j^2\frac{\cosh(k_jX_3)}{\sinh(k_jh)}\sin(\omega_jt+\phi_j)\end{aligned} \tag{18}$$

The distributed wave force acting at the position X_3 of the tower can be calculated by the Morison Equation [18]:

$$p_w(X_3,t)=\frac{1}{2}\rho_wC_dDv(X_3,t)\left|v(X_3,t)\right|+\frac{\pi}{4}\rho_wC_mD^2\dot{v}(X_3,t) \tag{19}$$

where ρ_w is the fluid density, C_d is the drag coefficient, C_m is the inertia coefficient and D is the diameter of the turbine monopile. The total wave forces can then be calculated by Equation (12), which are acting on the wind turbine tower perpendicularly to the mean wind direction.

3. Active Generator Control

A simple active control algorithm is proposed based on active generator torque with feedback from the measured lateral tower vibrations. Closed-loop equations are obtained from the active control. A full-scale power converter configuration with a cascaded loop control structure is also introduced to produce the feedback torque in real time.

3.1. Closed-Loop Equations from Active Control

Only the above rated region (Region 3 according to [16]) is considered where the mean wind speed is higher than the rated value, and the wind turbine produces nominal power with the functioning of the collective pitch controller. In the basic control system for Region 3, the collective pitch controller is activated to regulate the rotor speed to the nominal value, while the generator torque is held constant [9]. Modern power electronics makes it possible to specify the generator torque within certain limits almost instantly (time delay below 10^{-2} s). Then, the generator torque $f_{13}(t)$ can be used as an actuator in the

active vibration control of the structure. Sometimes, a torsional damping term as feedback control is included in the generator torque to damp the resonant mode of the drivetrain [10]. Since the focus is to investigate the effectiveness of active generator control of lateral tower vibrations and the influence of the controller on the power output, as well as on the responses of other components, the torsional damping term is not taken into account in the present study. The generator controller with feedback from lateral tower vibrations is proposed as:

$$f_{13}(t) = f_{13,0} + \Delta f_{13,0}(t) = f_{13,0} + c_a \dot{q}_8(t) \tag{20}$$

where $f_{13,0} = \frac{P_0}{N\Omega}$ is the constant nominal torque and P_0 is the nominal power produced by the wind turbine. With the functioning of the collective pitch controller, $f_{13,0}$ is balanced by the mean value of the aerodynamic torque on the rotor. $c_a \dot{q}_8(t)$ is the feedback torque components from lateral tower velocity, and c_a is the gain factor. In practical applications, the feedback signal $\dot{q}_8(t)$ is obtained by integrating the measured tower top acceleration from accelerometers placed in the nacelle.

Then, the generated power becomes:

$$P(t) = \Big(f_{13,0} + \Delta f_{13,0}(t)\Big)\Big(N\Omega + \dot{q}_{13}(t)\Big) = P_0(t) + \Delta P(t) \tag{21}$$

where $P_0 = N\Omega f_{13,0}$ is the nominal power of the wind turbine, and $\Delta P(t) = \Delta f_{13,0}(t)\left(N\Omega + \dot{q}_{13}(t)\right) + f_{13,0}\dot{q}_{13}(t)$ indicates a time-varying deviation from the nominal power. In the absence of the active generator control, *i.e.*, $c_a = 0$, the deviation of power output only contains the term $f_{13,0}\dot{q}_{13}(t)$. With active generator control, fluctuation of the power output is introduced by the term $\Delta f_{13,0}(t)\left(N\Omega + \dot{q}_{13}(t)\right)$ due to the torque increment $\Delta f_{13,0}(t)$. From a power electronic point of view, it is favorable that $\Delta P(t)$ is as small as possible in comparison with P_0 in order to have a smooth power output. From a vibration point of view, it is favorable to have larger c_a and, hence, $\Delta P(t)$, introducing higher damping to the lateral tower mode. Consequently, there is a tradeoff between these two objectives. In this respect, the gain factors c_a is chosen such that the following performance criterion is minimized:

$$J(c_a) = W\frac{\sigma_{q_8}}{\sigma_{q_8,0}} + (1-W)\frac{\sigma_P}{\sigma_{P,0}}, \quad 0 < W < 1 \tag{22}$$

where $\sigma_{q_8,0}$ and $\sigma_{P,0}$ signify the standard deviation of the lateral tower top displacement $q_8(t)$ and the power output without active generator control, *i.e.*, the generator torque is kept constant as $f_{13,0}$. σ_{q_8} and σ_P denote the standard deviation of $q_8(t)$ and the power output, when active generator control is implemented using Equation (20), and W is the weighting factor for the lateral tower vibration. It is clear that by increasing the value of W, more importance is placed on maintaining small values for the lateral tower vibration.

The torque $f_9(t)$ work-conjugated to $q_9(t)$ for wind turbines with an active generator controller follows from Equations (14) and (20):

$$f_9(t) = \begin{cases} f_{9,w}(t) - \mu f_{12}(t) + f_{13,0} + c_a\dot{q}_8(t) - k_0\left(1+\frac{1}{N}\right)\left(q_{12}(t) - \frac{1}{N}q_{13}(t)\right) & \text{(odd stages)} \\ f_{9,w}(t) - \mu f_{12}(t) - f_{13,0} - c_a\dot{q}_8(t) - k_0\left(1-\frac{1}{N}\right)\left(q_{12}(t) - \frac{1}{N}q_{13}(t)\right) & \text{(even stages)} \end{cases} \tag{23}$$

Substituting Equations (20) and (23) into the load vector (Equation (10)) at the right-hand side of Equation (5), the equation of motion of the system with active generator controller is given by:

$$\mathbf{M}_1(t)\,\ddot{\mathbf{q}}_1(t) + \Big(\mathbf{C}_1(t) + \mathbf{C}_a(t)\Big)\,\dot{\mathbf{q}}_1(t) + \mathbf{K}_1(t)\,\mathbf{q}_1(t) = \mathbf{f}_{e,1}(t) \tag{24}$$

where:

$$\mathbf{C}_a(t) = \begin{bmatrix} 0 & 0 & 0 & 0 & 0 & 0 & 0 \\ 0 & 0 & 0 & 0 & 0 & 0 & 0 \\ 0 & 0 & 0 & 0 & 0 & 0 & 0 \\ 0 & 0 & 0 & 0 & 0 & 0 & 0 \\ 0 & 0 & 0 & \mp c_a & 0 & 0 & 0 \\ 0 & 0 & 0 & 0 & 0 & 0 & 0 \\ 0 & 0 & 0 & c_a & 0 & 0 & 0 \end{bmatrix} \tag{25}$$

The system matrices $\mathbf{M}_1(t)$, $\mathbf{C}_1(t)$, $\mathbf{K}_1(t)$ and the load vector $\mathbf{f}_{e,1}(t)$ are unchanged, except that an extra damping matrix $\mathbf{C}_a(t)$ is introduced by the active generator controller. Therefore by making use of the extra damping matrix, it is possible to mitigate lateral tower vibrations, as will be shown in the following simulation results. The upper sign in Equation (25) refers to the gearbox with an odd number of stages, while the lower sign corresponds to the case with an even number of gear stages, which also applies to the direct-driven wind turbines (the number of stages is zero).

3.2. Power Electronic Solution for Torque Control

In order to realize the objective of active control of lateral tower vibration using the generator torque, a generator model is introduced. As seen in Figure 5, a full-scale power converter configuration equipped with a permanent magnet synchronous generator (PMSG) or an induction generator (IG) is considered [15]. Normally, a PMSG-based wind turbine may become a direct-driven system, which avoids the fatigue-prone gearbox. The principle of the full-scale power converter is the same for both IG and PMSG. The generator stator winding is connected to the grid through a full-scale back-to-back power converter, which performs the reactive power compensation and a smooth grid connection. Due to different positions, the back-to-back power converter is named as the generator-side converter and the grid-side converter, respectively. The grid-side converter is used to keep the DC-link voltage V_{DC} fixed and to meet the reactive power demand according to the grid codes [26].

The active generator control scheme for lateral tower vibration is carried out via the generator-side converter. With the aid of the stator field oriented control (as shown in Figure 5), a cascaded loop control structure is realized by two controllers: outer speed loop and inner current loop. According to the maximum power tracking point, the rotor speed demand is calculated by the measured power fed into grid. Above the rated region, the speed control loop provides a torque demand of $f_{13,0}$. Along with additive generator torque demand $c_a\dot{q}_8(t)$, the total torque demand is given in the same form as Equation (20). The electromagnetic torque T_e of the generator can be expressed as [27]:

$$T_e = \frac{3}{2} p \Psi_m i_{sq} \tag{26}$$

where p denotes the number of pole pairs, Ψ_m denotes the flux induced by the magnet and i_{sq} denotes the stator current in the q axis. It is noted that the electromagnetic torque is only in line with the q axis stator current. As a consequence, the electromagnetic torque can be simply controlled by the inner current loop together with the demand of the d axis current setting at zero for minimum power loss.

Figure 5. Control diagram in a wind turbine with a permanent magnet synchronous generator or an induction generator.

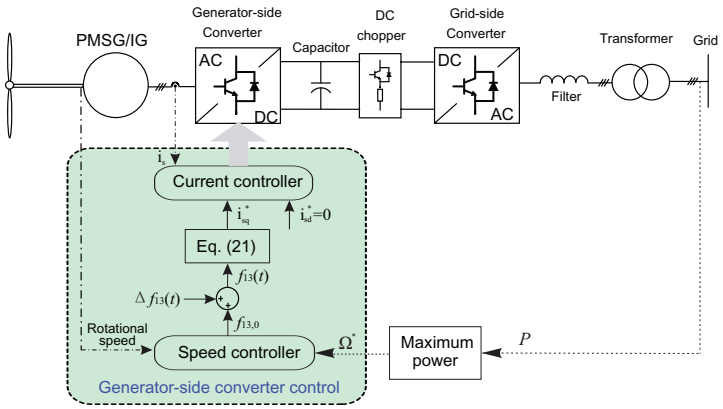

From the power electronic point of view, direct driven and gear-driven wind turbines are basically dependent on which kind of generator the manufacturer prefers to use. If the synchronous generator is selected, due to the relatively low speed of the generator rotor, the wind turbine system could have less stages of the gearbox or even becomes direct-driven if the poles of the generator are high enough (e.g., permanent-magnet synchronous generator). On the other hand, if the induction generator is chosen, the gearbox must be employed because of its high rotor speed range, which cannot match the speed of the wind turbine rotor directly.

4. Results and Discussion

Numerical simulations are carried out on the calibrated 13-DOF model subjected to the wave and wind loads. In all simulations, the same turbulent wind field and wave loads have been used, with the mean wind velocity $V_0 = 15$ m/s, the turbulence intensity $I = 10\%$, the significant wave height $H_s = 2$ m and the time interval Δt = 0.02 s. The worst case study scenario is considered, *i.e.*, the wave loads are acting on the tower in the lateral direction perpendicular to the mean wind velocity. Both gear-driven and direct-driven wind turbines are investigated to evaluate the effectiveness of active generator torque on mitigating lateral tower vibrations.

4.1. Model Calibration

The NREL 5-MW referential wind turbine [16] together with the monopile-type support structure documented by [28] are used to calibrate the proposed 13-DOF aeroelastic model. The rotor-nacelle

assembly of the NREL 5-MW wind turbine, including the aerodynamic, structural and pitch control system properties, remains the same as in [16]. This wind turbine is mounted atop a monopile foundation at a 20-m water depth, and the tower base begins at an elevation of 10 m above mean sea level (MSL). As for the rotor, each blade has eight different airfoil profiles from hub to tip, the lift and drag coefficients of which are obtained by wind tunnel tests. The related data of the modal shapes, the bending stiffness and the mass per unit length of the blade are also given by [16]. As for the support-structure, the distributed properties of the tower and monopile are given by [28]. Based on these data, we can calculate the parameters of the rotor and the support structure (the geometries, the mass parameters and the stiffness parameters) in the 13-DOF model, as presented in Table 1. Next, to evaluate the validity and feasibility of the proposed 13-DOF model, comparisons of some results obtained from the present model and from the NREL FAST program [16] are carried out. Table 2 shows the results for the natural frequencies of the blade and the tower, as well as the steady-state responses of the blade, the tower and the pitch controller at different mean wind speeds. The steady-state responses of the present model are obtained by running simulations on the 13-DOF system at three given, steady and uniform wind speeds, when the turbulence field is inactivated. The simulation lengths are long enough to ensure that all transient behavior has died out. The FAST results for the blade and the pitch controller are given by [16], and the results for the tower are given by [28]. The agreement between FAST and the 13-DOF model is quite good, which validates the present model.

Table 1. Parameters in the 13-DOF wind turbine model.

Parameter	Value	Unit	Parameter	Vale	Unit
L	61.50	m	k_2	5.80×10^4	N/m
h_1	77.60	m	k_{88}	5.14×10^6	N/m
h_2	10.00	m	k_{89}	-1.77×10^8	N
h_3	20.00	m	k_{99}	8.50×10^9	N m
s	2.50	m	k_0	8.70×10^8	N m/rad
Ω	1.27	rad/s	ζ_2	0.005	–
m_0	1.70×10^4	kg	ζ_8	0.01	–
m_1	2.80×10^3	kg	ζ_9	0.01	–
m_2	1.30×10^3	kg	μ	0.01	–
m_3	1.17×10^5	kg m	H_s	2.00	m
m_{88}	1.05×10^5	kg	T_p	6.00	s
m_{89}	-1.76×10^6	kg m	ρ	1.25	kg/m^3
m_{99}	3.65×10^7	kg m^2	ρ_w	1000	kg/m^3
J_r	3.68×10^7	kg m^2	C_d	1.20	–
J_g	5.30×10^2	kg m^2	C_m	2.00	–
M_0	2.98×10^5	kg	D	6.00	m

Table 2. Results obtained from the 13-DOF model and FAST.

Item	13-DOF			FAST		
1st flap-wise frequency (HZ)	0.669			0.668		
1st edgewise frequency (HZ)	1.062			1.079		
1st tower fore-aft frequency (Hz)	0.280			0.280		
1st tower lateral frequency (Hz)	0.280			0.280		
Mean Wind Speed (m/s)	**11.4**	**15**	**20**	**11.4**	**15**	**20**
Collective pitch angle (degrees)	0.40	10.17	17.24	0.00	10.20	17.50
flap-wise tip displacement (m)	5.70	2.77	1.22	5.65	2.75	1.20
tower fore-aft displacement (m)	0.35	0.21	0.16	0.40	0.20	0.15
tower lateral displacement (m)	−0.06	−0.06	−0.06	−0.06	−0.06	−0.06

Based on the the model described in Section 2.4, the rotational sampled turbulence field has been generated. Figure 6 shows the Fourier amplitude spectrum obtained by FFT (fast Fourier transformation) of the sample curves of the rotational sampled turbulence, at the middle point of Blade 1. A very clear $1P$ (1.267 rad/s) frequency component of the turbulence in the x_2 direction can be observed in Figure 6b. Less obviously from Figure 6a, the $1P$ peak can still be observed in the turbulence acting on the blade in the x_1 direction. Figure 7 shows the influence of aeroelasticity on tower vibrations in the case of a gear-driven wind turbine with gear ratio N equal to 97. It is seen that the aerodynamic damping almost completely removes the dynamic response of the fore-aft tower vibration $q_7(t)$, while the lateral tower vibration $q_8(t)$ is almost unaffected by aerodynamic damping, justifying the necessity of implementing active vibration control algorithms in this direction.

Figure 6. Fourier amplitude spectrum of the sample curves of the rotational sampled turbulence, at the middle point of Blade 1. $V_0 = 15$ m/s, $I = 10\%$. (**a**) The moving frame component of the rotational sampled turbulence in the x_1 direction. (**b**) The moving frame component of the rotational sampled turbulence in the x_2 direction.

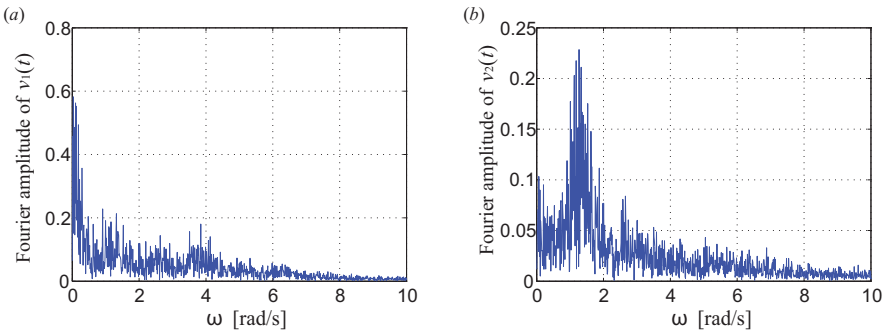

Figure 7. Tower responses with and without aerodynamic damping, gear-driven wind turbine. (**a**) Fore-aft tower top displacement. (**b**) Lateral tower top displacement. Blue curve: aerodynamic damping not considered. Red curve: aerodynamic damping considered.

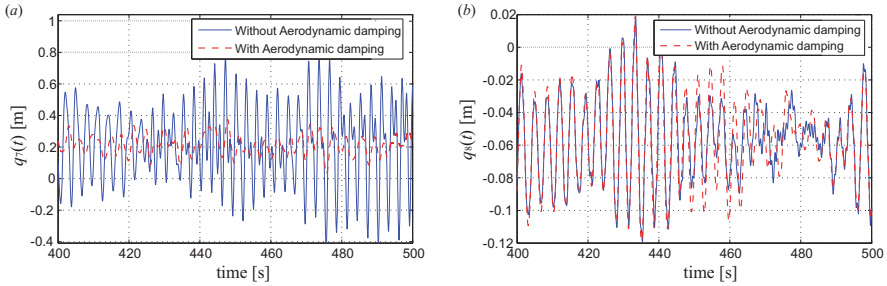

Normally, in an irregular sea-state, the mean wind direction and the mean direction of wave propagation are correlated. Hence, the wave loads and the turbulent wind loads on the structure tend to be somewhat unidirectional in most cases. However, we are focusing on the lightly damped lateral tower vibration rather than the along-wind response of the tower with relatively strong aerodynamic damping. Thus, the most conservative load combination is considered in this study, *i.e.*, the wave loads are acting on the tower in the lateral direction perpendicular to the mean wind velocity, in order to fully excite the lateral tower vibration. There is also a clear physical explanation for this load combination. Due to the relatively shallow water, the waves are occasionally refracted tending to propagate orthogonal to the level curves of the sea bottom, meaning that sometimes the direction of wave propagation may take place orthogonal to the mean wind velocity. This load scenario is not expected to take place as often as the unidirectional case. However, considering an offshore wind farm with many wind turbines, there is a high chance that at all times there is a certain amount of wind turbines under such a scenario. The related parameter values used in the aerodynamic and wave loads simulation are also listed in Table 1. In [29], wave measurements were carried out at the German North Sea coast, where the water depth is 29 m. During a severe storm surge on 2 October 2009, the measured significant height was 5.23 m. This data to some extent justify the significant wave height we use ($H_s = 2$ m) for the 20-m water depth in the simulations. Extensive load cases with different combinations of V_0 and H_s (correlated with each other) are not considered in the present study.

4.2. Gear-Driven Wind Turbine

Firstly, simulations are performed considering a gear-driven wind turbine with gear ratio $N = 97$, which is in accordance with the NREL 5-MW wind turbine. In this case, the rotational speed of the generator is almost N times that of the rotor, and the magnitude of the generator torque is reduced by N times comparing with the aerodynamic torque acting at the rotor. The performance of the wind turbine system is almost the same whether the number of gear stages is odd or even, as long as the gear ratio N is unchanged. Therefore, only the results of the wind turbine with odd-numbered gear stages are illustrated.

By setting the weighting factor $W = 0.5$, meaning the same importance is placed on mitigating the tower vibration, and keeping the smoothness of the power output, the gain factor c_a is determined as

$c_a = 2.0 \times 10^4$ Ns in order to minimize the performance criterion $J(c_a)$ in Equation (22). The following figures compare the performance of the wind turbine system with the basic controller and with the active generator controller. Figure 8 shows the lateral tower top displacements $q_8(t)$ in both the time and frequency domain, where the blue line denotes the responses without active generator control and the red line with active generator control. There is a reduction of 17.8% in the maximum responses and a reduction of 37.6% in the standard deviations. For both cases, the same static displacement equal to -0.057 m is observed. This is caused by the mean value of the tower torque, which is equal to the negative mean value of the aerodynamic torque at the rotor, *i.e.*, $E[f_9(t)] = -E[f_{12}(t)]$, as explained by Equation (11). The FFT of the response $q_8(t)$ is presented in Figure 8b. For a system without active generator control, a clear peak corresponding to the tower eigenfrequency (around 1.76 rad/s) is observed without other visible peaks, owing to the fact that very low aerodynamic damping takes place in this mode. This peak is reduced to approximately $\frac{1}{3}$ by the active generator torque due to the introduced damping matrix in Equation (25). Further, it is observed that base moment of the tower in lateral direction is effectively suppressed, as well, with the standard deviation reduced from 5.12×10^6 to 3.32×10^6 Nm and the maximum value reduced from 19.63×10^6 to 15.40×10^6 Nm. The stress at the tower base in the lateral direction is calculated accordingly. There is a reduction of 35.2% (6.80 to 4.41 Mpa) in the standard deviation and a reduction of 21.6% (26.07 to 20.44 Mpa) in the maximum response, which means the fatigue lives of the tower and the foundation are effectively increased by active control.

Figure 8. Lateral tower vibration with and without active generator control, gear-driven, $W = 0.5$. (**a**) Time history in 400–500 s. (**b**) Fourier amplitude of lateral tower vibration.

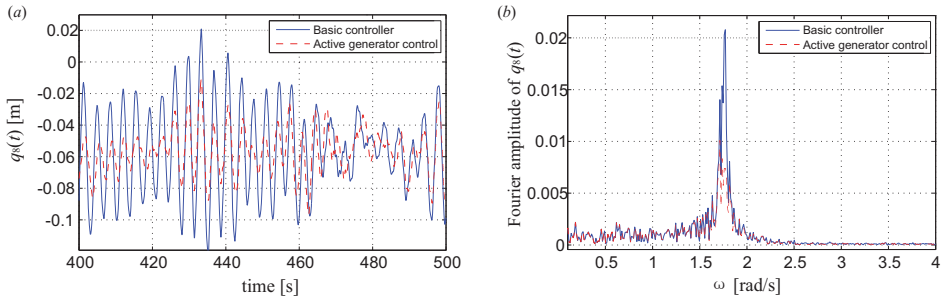

Figure 9 shows the impact of the active control on the performance of the drivetrain shafts, the gearbox and the collective pitch controller. The deviations of the rotational speed at the rotor $\dot{q}_{12}(t)$ and at the generator $\dot{q}_{13}(t)$ are very slightly affected with the standard deviations increased by 1.0% and 0.92%, respectively, reflecting a very weak coupling between the torsional vibration of the drivetrain with the lateral tower vibration. Based on Equation (13), the dynamic torque acting at the gearbox can also be obtained from $q_{12}(t)$ and $q_{13}(t)$, as shown in Figure 9c. It is seen that the active generator controller introduces a frequency component corresponding to the tower frequency in the gearbox torque, and a little more fluctuated torque is observed with an increase of 12.6% in the standard deviation, which is unfavorable for the fatigue life of the gearbox. By reducing the controller gain c_a, the negative effect can be diminished. Further, the performance of the pitch controller is almost unaffected by the

active generator control (Figure 9d) with the standard deviation increased by 0.93%. It is observed from Figure 10a,b that the flap-wise tip displacement $q_1(t)$ and tower fore-aft top displacement $q_7(t)$ are also insignificantly affected with the standard deviations increased by 0.85% and 2.2% after the implementation of active generator control. This is expected, since there is no direct coupling between these two modes of vibration with the generator torque and the lateral tower vibration. The coupling is indirectly via the pitch controller performance, which changes the effective angle of attack and the corresponding aerodynamic loads on the blade sections. Figure 10c shows an interesting result that the edgewise vibration $q_4(t)$ is slightly suppressed by the active generator control due to the coupling of edgewise vibration to the lateral tower vibration, as shown in Equation (6). The maximum response and the standard deviation are reduced by 5.5% and 5.0%, respectively. Although the focus is to control the lateral tower vibration through active generator torque, it is favorable to see that the edgewise vibration with very low aerodynamic damping is also suppressed a little, rather than being negatively affected.

Figure 9. Influence of the active generator control on the drivetrain, the gearbox and the pitch controller, gear-driven, $W = 0.5$. (**a**) Deviation of rotational speed of the rotor. (**b**) Deviation of rotational speed of the generator. (**c**) Torque on the gearbox. (**d**) Collective pitch angle.

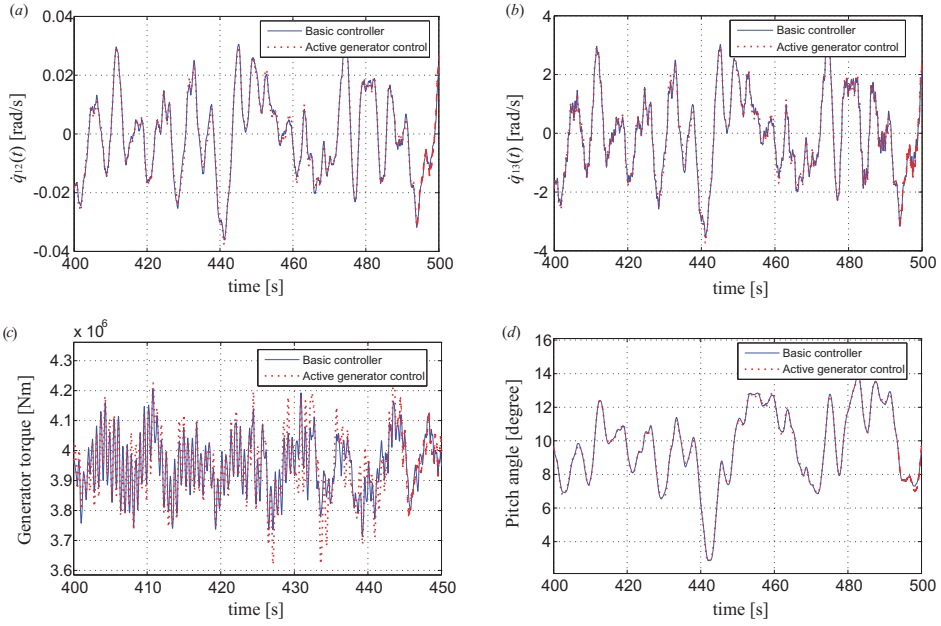

The time history of power output from the generator is presented in Figure 11. Since the generated power is related to the lift forces along the blade and, hence, the longitudinal turbulence, the resulting power output also presents periodicity around $1P$ frequency, similarly with that in Figure 6a. Due to the torque increment $c_a\dot{q}_8(t)$, the generated power becomes more fluctuated with an increase of 1.3% in the maximum value and an increase of 33.0% in the standard deviation, relative to the values without active generator control. Since the stiffness and mass of the tower for the offshore wind turbine is very large,

it is inevitable that effective control of the tower vibration is at the expense of a little more fluctuated power output, which is unfavorable for the grid side. One possible solution to accommodate this problem is to increase the energy storage in the power converter by increasing the size of the capacitor in Figure 5. To give more clear insight into the tradeoff between the structural vibration and the power output, five different values of weighting factor W are used, *i.e.*, W is chosen to be 0.1, 0.3, 0.5, 0.7 and 0.9. For each W, an optimal value of c_a can be obtained through the optimization procedure given by Equation (22). Table 3 presents the optimized c_a and the corresponding standard deviations of $q_8(t)$ and the power output in different cases. It is shown that as the value of W increases, allowing larger values in the control effort, better structural performance, but worse power quality are achieved. For the extreme case of $W = 0.9$, the standard deviation of the lateral tower vibration can be reduced by 60%, but the fluctuation of the power output is increased by 121.7%. In this case, one solution may be to turn on the active generator controller merely when large lateral tower vibrations take place.

Figure 10. Influence of the active generator control on the flap-wise, fore-aft tower and edgewise vibrations, gear-driven, $W = 0.5$. (**a**) Flap-wise tip displacement. (**b**) Fore-aft tower top displacement. (**c**) Edgewise tip displacement.

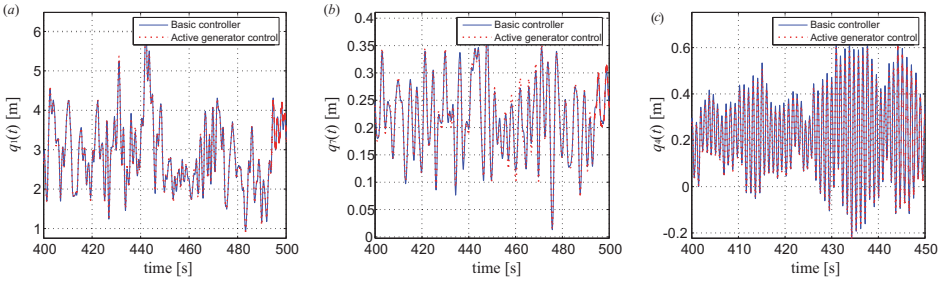

Figure 11. Time series of power output, gear-driven, $W = 0.5$.

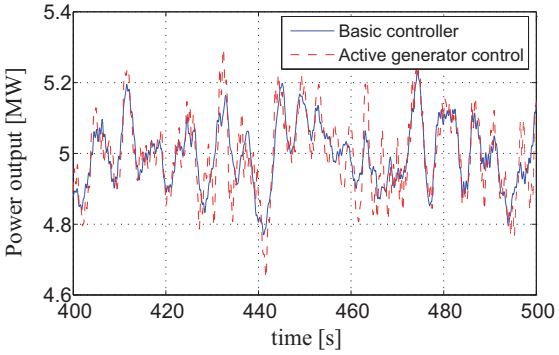

Table 3. Performance of the tower controller for the gear-driven case.

Case	c_a (Ns)	σ_{q_8} (m)	σ_P (MW)
Basic system	0	0.0330	0.106
$W = 0.1$	0	0.0330	0.106
$W = 0.3$	1.0×10^4	0.0246	0.121
$W = 0.5$	2.0×10^4	0.0206	0.141
$W = 0.7$	4.0×10^4	0.0167	0.177
$W = 0.9$	8.0×10^4	0.0132	0.235

4.3. Direct-Driven Wind Turbine

Next, simulations of the direct driven wind turbine are carried out. Comparing with the gear-driven wind turbine, the nominal generator torque is increased by N times, while the nominal rotational speed of the generator is reduced by N times. Since the magnitude of the generator is increased significantly, we take the mass moment of inertia of the generator J_g to be N times the original value in the simulation. This is justified by the data of a 3-MW wind turbine [30], where the mass moment of inertia of the generator for the direct driven wind turbine is about 150-times that of the gear-driven one (the total mass is six-times larger and the radius of the stator is five-times larger). The same turbulence field and wave loads as in the previous case are applied to the wind turbine system in order to make meaningful comparisons.

Similarly, by setting $W = 0.5$, the value of the gain factor c_a is determined as 2.0×10^6 in order to minimize the performance criterion $J(c_a)$. Figures 12–14 show the results corresponding to similar parameters studied in the previous case. Results in Figure 12 show the remarkable capability of the active generator controller in suppressing lateral tower vibrations. The maximum response of $q_8(t)$ is reduced from 0.143 to 0.105 m (reduced by 26.6%), and the standard deviation is reduced by 54.0%. Again, a static displacement equal to -0.057 m is always present with or without active control. This value is also unchanged comparing with the gear-driven case, because the mean value of the aerodynamic torque acting at the rotor is unchanged whether it is a gear-driven or direct-driven wind turbine. Further, the stress at the tower base is calculated, with the standard deviation reduced from 6.72 to 3.39 Mpa (49.6%) and the maximum response reduced from 26.12 to 18.90 Mpa (27.6%). The Fourier spectrum of the lateral tower top displacement (Figure 12b) shows that the peak around 1.76 rad/s, corresponding to the tower eigenfrequency, is almost totally eliminated by the active generator controller, comparing with that of the uncontrolled case. The reason for the superior performance is that the nominal generator torque $f_{13,0}$ is much larger in the direct-driven wind turbine, and thus, the optimized controller gain c_a, as well as the additive torque are also increased accordingly.

Figure 13 shows the impact of the active generator controller on the responses of other components of the wind turbine. Similarly, the negative influences on the drivetrain oscillation, the flap-wise vibration, the fore-aft tower vibration and the performance of the pitch controller are negligible. The lightly-damped edgewise vibration in Blade 1 ($q_4(t)$) is again slightly suppressed by the active generator control, due to its coupling to the lateral tower vibration. Similar results have been confirmed for the

other two blades. It should be noted that the gearbox is eliminated in the direct-driven system, and the negative impact from the active generator torque on the gearbox as stated in the gear-driven case is no longer a problem for the direct-driven case.

Figure 12. Lateral tower vibration with and without active generator control, direct-driven, $W = 0.5$. (**a**) Time history in 400–500 s. (**b**) Fourier amplitude of lateral tower vibration.

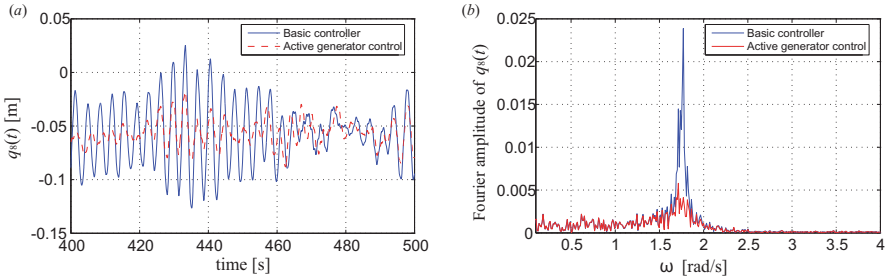

Figure 13. Influence of the active generator control on system responses, direct-driven, $W = 0.5$. (**a**) Deviation of rotational speed of the rotor. (**b**) Deviation of rotational speed of the generator. (**c**) Collective pitch angle. (**d**) Flap-wise tip displacement. (**e**) Fore-aft tower top displacement. (**f**) Edgewise tip displacement.

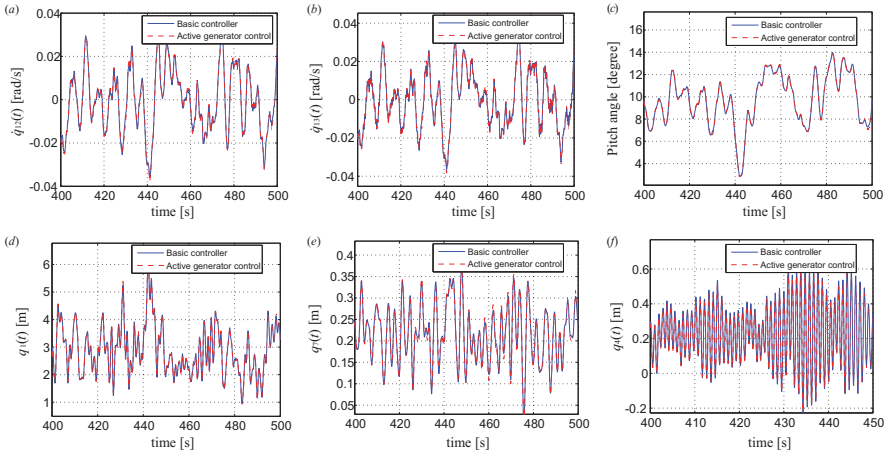

Figure 14 shows the time-history of the power output from the generator. A little negative effect on the smoothness of the power output is observed after the implementation of the active generator control. The maximum value of the power output is increased from 5.41 MW to 5.48 MW (increased by 1.3%), and the standard deviation is increased from 0.108 MW to 0.125 MW (increased by 15.7%), which means less impact on the grid side than that of the gear-driven case. For direct-driven wind turbines, the value of $f_{13,0}$ is significantly increased, and the relative magnitude between $c_a\dot{q}_8(t)$ and $f_{13,0}$ is smaller comparing with that of the gear-driven turbine; thus, the smoothness of the power output is less affected by the active

control. Similarly, the tradeoff between the tower vibration and the power output is illustrated in Table 4, showing that as the value of the weighting factor W increases, better structural performance, but worse power quality are obtained. However, acceptable results for the power quality can always be obtained when the tower vibration is significantly reduced.

Figure 14. Time series of power output, direct-driven, $W = 0.5$.

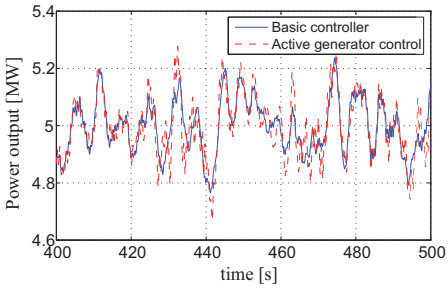

Table 4. Performance of the tower controller for the direct drive case.

Case	c_a (Ns)	σ_{q_s} (m)	σ_P (MW)
Basic system	0	0.0328	0.108
$W = 0.1$	0	0.0328	0.108
$W = 0.3$	1.0×10^6	0.0189	0.116
$W = 0.5$	2.0×10^6	0.0151	0.125
$W = 0.7$	3.0×10^6	0.0132	0.134
$W = 0.9$	8.0×10^6	0.0099	0.175

5. Conclusions

This paper presents a comprehensive investigation into the modeling and control of lateral tower vibrations of offshore wind turbines using active generator torque. A 13-DOF wind turbine model has been developed using a Euler–Lagrangian approach, taking into consideration the quasi-static nonlinear aeroelasticity. The equation of motion was derived, and the coupling of the blade-tower-drivetrain motion, as well as the load transfer mechanisms from the generator to the tower are demonstrated. A simple feedback controller was proposed for lateral tower vibrations through the active generator torque, and a generator model was introduced as the power electronic solution for providing the additive generator torque in real time.

Numerical simulations have been carried out using data calibrated to the referential 5-MW NREL offshore wind turbine. Cases of the gear-driven and the direct-driven wind turbines were both considered to evaluate the effectiveness of the active generator torque for mitigating lateral tower vibrations. The non-linear time-history results demonstrate that for both gear-driven and direct-driven wind turbines, the active generator controller is successfully able to reduce the lateral tower vibration induced by the combined aerodynamic and hydrodynamic loads. The effective control of lateral tower vibration is at the expense of a little more fluctuated power output, and a tradeoff between the vibration aspect and

the power electronic aspect should be considered by properly choosing the controller gain. The active generator controller has negligible affects on the drivetrain oscillation, the flap-wise vibration, the fore-aft tower vibration and the performance of the controller. It is also favorable to observe that the lightly-damped edgewise vibration is slightly suppressed by the active generator controller due to its coupling to the lateral tower vibration. The active generator controller shows superior performance for the direct-driven wind turbine, since a better vibration control efficacy can be obtained with less impact on the smoothness of the power output.

In further works, a more sophisticated and realistic consideration of the wind-wave correlation needs to be investigated. The controller will also be developed in more detail, such as to include filters and to design the controller when there is a slight rotor imbalance.

Acknowledgments

The first author gratefully acknowledges the financial support from the Chinese Scholarship Council under the State Scholarship Fund.

Author Contributions

This paper is a result of the collaboration of all co-authors. Zili Zhang and Søren R.K. Nielsen established the wind turbine model and designed the controller. Frede Blaabjerg and Dao Zhou proposed the power electronic solution for the active generator control. Zili Zhang was mainly responsible for numerical simulation, results interpretation and initial writing. All co-authors performed editing and reviewing of the paper.

Conflicts of Interest

The authors declare no conflict of interest.

References

1. Hansen, M.H. Aeroelastic instability problems for wind turbines. *Wind Energy* **2007**, *10*, 551–577.
2. Thomsen, K.; Petersen, J.T.; Nim, E.; Oye, S.; Petersen, B. A method for determination of damping for edgewise blade vibrations. *Wind Energy* **2000**, *3*, 233–246.
3. Murtagh, P.J.; Ghosh, A.; Basu, B.; Broderick, B.M. Passive control of wind turbine vibrations including blade/tower interaction and rotationally sampled turbulence. *Wind Energy* **2008**, *11*, 305–317.
4. Colwell, R.; Basu, B. Tuned liquid column dampers in offshore wind turbines for structural control. *Eng. Struct.* **2009**, *31*, 358–368.
5. Lackner, M.A.; Rotea, M.A. Passive structural control of offshore wind turbines. *Wind Energy* **2011**, *14*, 373–388.
6. Zhang, Z.L.; Chen, J.B.; Li, J. Theoretical study and experimental verification of vibration control of offshore wind turbines by a ball vibration absorber. *Struct. Infrastruct. Eng.* **2014**, *10*, 1087–1100.

7. Lackner, M.A.; Rotea, M.A. Structural control of floating wind turbines. *Mechatronics* **2011**, *21*, 704–719.
8. Burton, T.; Sharpe, D.; Jenkins, N.; Bossanyi, E.A. *Wind Energy Handbook*; John Wiley Sons, Ltd.: West Sussex, UK, 2001.
9. Bossanyi, E.A. Wind turbine control for load reduction. *Wind Energy* **2003**, *6*, 229–244.
10. Licari, J.; Ugalde-Loo, C.E.; Ekanayake, J.B.; Jenkins, N. Damping of torsional vibrations in a variable-speed wind turbine. *IEEE Trans. Energy Convers.* **2013**, *28*, 172–180.
11. Dixit, A.; Suryanarayanan, S. Towards pitch-scheduled drive train damping in variable-speed, horizontal-axis large wind turbines. In Proceedings of the 44th IEEE Conference on Decision and Control, and the European Control Conference 2005, Seville, Spain, 12–15 December 2005.
12. Van der Hooft, E.; Schaak, P.; van Engelen, T. *Wind Turbine Control Algorithms*; Technical Report ECN-C-03-111; Energy Research Center of the Netherlands (ECN): Petten, The Netherlands, 2003.
13. De Corcuera, A.D.; Pujana-Arrese, A.; Ezquerra, J.M.; Segurola, E.; Landaluze, J. H_∞ based control for load mitigation in wind turbines. *Energies* **2012**, *5*, 938–967.
14. Fleming, P.A.; van Wingerden, J.W.; Wright, A.D. Comparison state-space multivariable controls to multi-SISO controls for load reduction of drivetain-coupled modes on wind turbines through field-testing. In Proceedings of 50th AIAA Aerospace Sciences Meeting, Nashville, TN, USA, 9–12 January 2012.
15. Blaabjerg, F.; Chen, Z.; Kjaer, S.B. Power electronics as efficient interface in dispersed power generation systems. *IEEE Trans. Power Electron.* **2004**, *19*, 1184–1194.
16. Jonkman, J.; Butterfield, S.; Musial, W.; Scott, G. *Definition of 5-MW Reference Wind Turbine for Offshore System Development*; Technical Report NREL/TP-500-38060; National Renewable Energy Laboratory (NREL): Golden, CO, USA, 2009.
17. Krenk, S.; Svendsen, M.N.; Høgsberg, J. Resonant vibration control of three-bladed wind turbine rotors. *AIAA J.* **2012**, *50*, 148–161.
18. Sarpkaya, T.; Isaacson, M. *Mechanics of Wave Forces on Offshore Structures*; Van Nostrand Reinhold: New York, NY, USA, 1981.
19. Ogata, K. *Morden Control Engineering*; Prentice Hall: Upper Saddle River, NJ, USA, 2009.
20. Pars, L.A. *A Treatise on Analytical Dynamics*; Ox Bow Press: Woodbridge, ON, Canada, 1979.
21. Clough, R.W.; Penzien, J. *Dynamics of Structures*; McGraw-Hill: New York, NY, USA, 1993.
22. *Wind Turbine Part 1; Design Requirements*; IEC 61400-1; International Electrotechnical Committee: Geneva, Switzerland, 2005.
23. Batchelor, G.K. *The Theory of Homogeneous Turbulence*; Cambridge University Press: Cambridge, UK, 1953.
24. Hansen, M.O.L. *Aerodynamics of Wind Turbines*; Earthscan: London, UK, 2008.
25. Hasselmann, K.; Barnett, T.P.; Bouws, E.; Carlson, H.; Cartwright, D.E.; Enke, K.; Ewing, J.A.; Gienapp, H.; Hasselmann, D.E.; Kruseman, P.; *et al*. *Measurement of Wind-Wave Growth and Swell Decay during the Joint North Sea Wave Project (JONSWAP)*; Deutches Hydrographisches Institut: Hamburg, Germany, 1973.

26. Chinchilla, M.; Arnaltes, S.; Burgos, J.C. Control of permanent-magnet generators applied to variable-speed wind-energy systems connnected to the grid. *IEEE Trans. Energy Convers.* **2006**, *12*, 130–135.
27. Novotny, D.W.; Lipo, T.A. *Vector Control and Dynamics of ac Drives*; Clarendon Press: Oxford, UK, 1996.
28. Jonkman, J.; Musial, W. *Offshore Code Comparison Collaboration (OC3) for IEA Task 23 Offshore Wind Technology and Deployment*; Technical Report NREL/TP-5000-48191; National Renewable Energy Laboratory (NREL): Golden, CO, USA, 2010.
29. Mai, S.; Wilhelmi, J.; Barjenbruch, U. Wave height distributions in shallow waters. *Coast. Eng. Proc.* **2010**, *32*, doi:10.9753/icce.v32.waves.63.
30. Polinder, H.; van der Pijl, F.F.A.; de Vilder, G.-J.; Tavner, P.J. Comparison of direct-drive and geared generator concepts for wind turbines. *IEEE Trans. Energy Convers.* **2006**, *21*, 725–733.

APPENDIX G
Full-Scale Real-Time Hybrid Testing of Tuned Liquid Dampers (TLDs) for Vibration Control of Wind Turbine Towers

Paper 6
The paper presented in this appendix has been submitted to *Engineering Structures*, 2015, In review.

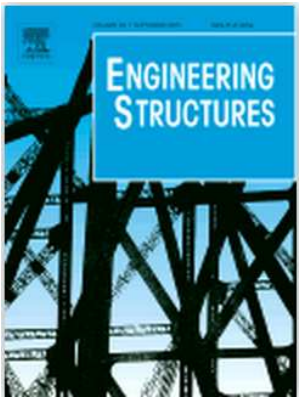

G.1 Author's Right

Journal author rights

In order for Elsevier to publish and disseminate research articles, we need publishing rights. This is determined by a publishing agreement between the author and Elsevier. This agreement deals with the transfer or license of the copyright to Elsevier and authors retain significant rights to use and share their own published articles. Elsevier supports the need for authors to share, disseminate and maximize the impact of their research and these rights, in Elsevier proprietary journals* are defined below:

For subscription articles	For open access articles
Authors transfer copyright to the publisher as part of a journal publishing agreement, but have the right to: • Share their article for Personal Use, Internal Institutional Use and Scholarly Sharing purposes, with a DOI link to the version of record on ScienceDirect (and with the Creative Commons CC-BY-NC- ND license for author manuscript versions) • Retain patent, trademark and other intellectual property rights (including raw research data). • Proper attribution and credit for the published work.	Authors sign an exclusive license agreement, where authors have copyright but license exclusive rights in their article to the publisher**. In this case authors have the right to: • Share their article in the same ways permitted to third parties under the relevant user license (together with Personal Use rights) so long as it contains a CrossMark logo, the end user license, and a DOI link to the version of record on ScienceDirect. • Retain patent, trademark and other intellectual property rights (including raw research data). • Proper attribution and credit for the published work.

http://www.elsevier.com/journal-authors/author-rights-and-responsibilities

Full-scale real-time hybrid testing of tuned liquid dampers (TLDs) for vibration control of wind turbine towers

Zili Zhang[a], Andrea Staino[b], Biswajit Basu[b,*], Søren R.K. Nielsen[a]

[a]*Department of Civil Engineering, Aalborg University, 9000 Aalborg, Denmark*
[b]*Department of Civil, Structural & Environmental Engineering, School of Engineering, Trinity College Dublin, Dublin 2, Ireland*

Abstract

Tuned liquid dampers (TLDs) utilize the sloshing motion of the fluid to suppress structural vibrations and become a natural candidate for vibration control of wind turbines. Lateral tower vibrations of wind turbines are normally lightly damped, and large amplitude vibrations induced by wind and wave loads in this direction may significantly shorten the fatigue life of the tower. In this paper, a real-time hybrid testing (RTHT) method is implemented for evaluating the performance of a TLD in mitigating lateral tower vibrations of megawatt wind turbines. During the RTHT, a full-size TLD is tested as the physical substructure while the structural responses of the wind turbine system are calculated numerically in real time using a 13-degree-of-freedom (13-DOF) aeroelastic model in the Matlab/Simulink environment. Both the 3 MW and 2 MW wind turbines have been considered in establishing the Simulink model. Cases of the TLD with and without damping screens have both been tested, in order to evaluate the performance of the TLD with different damping ratios. Further, the effect of tuning ratios on the damper performance has been studied by changing the mean water level of the tank. Finally, the RTHT results are compared to the results obtained from an analytical model of the TLD-wind turbine system. The comparative results indicate that the test method provides an accurate and cost-effective procedure for performing full-scale tests of passive or semi-active dampers.

Keywords: real-time hybrid testing, tuned liquid dampers, wind turbines, lateral tower vibration, full scale test

1. Introduction

Recent development in the wind energy industry aims at obtaining more economic and productive configurations in order to compete in the energy sector. Multi-megawatt wind turbines are designed with increasingly larger rotors and higher towers, in order to capture more energy throughout their lifetime and, thereby, reduce the cost of energy. As wind turbines grow in size, the stiffness of the blades and the tower are not increased proportionally, rendering the structure more sensitive to dynamic excitations. The large amplitude vibrations may significantly shorten

*Corresponding author, Tel: +45 50256836
Email addresses: zlz@civil.aau.dk (Zili Zhang), stainoa@tcd.ie (Andrea Staino), basub@tcd.ie (Biswajit Basu), srkn@civil.aau.dk (Søren R.K. Nielsen)

the fatigue life of the structural components and reduce the operational efficiency in converting the wind energy to electrical power.

Normally, flap-wise blade vibration and fore-aft tower vibration (along-wind direction) are highly damped due to the strong aerodynamic damping as long as the flow is attached at the blade [1]. In contrast, edgewise blade vibration and lateral tower vibration (side-side direction) are related with insignificant aerodynamic damping [1,2]. Hence, these modes of vibrations may be prone to large amplitude vibrations. There is also a possibility of aeroelastic instability in the lateral tower mode for some combinations of aerodynamic properties and operational conditions, especially for the parked turbine with nacelle yaw errors [3]. Moreover, for offshore wind turbines placed at shallow water, the wave load may act in a different direction of the mean wind direction due to refraction, and significant lateral tower vibrations may be initiated by the wave load in combination with the resultant aerodynamic loads from the three blades in the lateral direction. Finally, due to the coupling between the lateral tower vibration with the drivetrain torsional motion, the unfavorable tower vibrations will increase the fluctuations of the generator torque, and hence the quality of the generated power.

Some studies have been carried out for the structural control of wind turbine towers. Theoretical investigations have been performed on the effectiveness of a tuned mass damper (TMD) [4] and tuned liquid column damper (TLCD) [5] for mitigating along-wind tower vibrations, ignoring the aerodynamic properties of the blades. To yield more realistic results, an advanced modeling tool has been developed and incorporated into the aeroelastic code, FAST (Fatigue, Aerodynamics, Structures and Turbulence), allowing the investigation of passive TMDs in vibration control of offshore wind turbine systems [6]. A series of shaking table tests have been carried out to evaluate the performance of the ball vibration absorber (BVA) on vibration control of a reduced scale wind turbine model, through which the effectiveness of the passive damping device was proven [7]. However, the focus of this study is still on the fore-aft tower vibration without considering the aerodynamic damping. Therefore, it is of great importance and necessity to carry out a comprehensive investigation on structural control of the lightly-damped lateral tower vibrations.

Tuned liquid damper (TLD), which consists of a tank partially filled with liquid, is a passive control device for suppressing structural vibrations. The fundamental sloshing frequency of the liquid is normally tuned to the fundamental frequency of the primary structure. When the TLD is excited by the motion of the primary structure, the liquid inside the tank begins to slosh, imparting inertial forces onto the structure, out of phase with its motion, thus absorbing and dissipating energy. The main advantages of the TLD are the ease of fabrication and installation, especially where space constraints exist, and minimal maintenance after installation, which make the device cost-effective. The TLD has been proved to effectively control the wind-induced vibration of structures [8-10]. It is also proposed for seismic control of structures. Both experimental and theoretical studies [11-13] have shown that TLDs successfully suppress vibrations of the flexible structures subjected to earthquake excitations.

The main difficulties associated with TLDs arise from the nonlinear nature of the sloshing liquid, which makes modeling and designing of these devices challenging. Different methods have been employed to predict the response of sloshing liquid. Equivalent mechanical models based on TMD analogy [14, 15] simplify the TLD into an equivalent tuned mass damper, with the equivalent mass, stiffness and damping calibrated from the experimental results. This model is able to predict the energy dissipation through liquid sloshing and is useful in the preliminary design of the TLD. However, the nonlinear fluid response cannot be captured. Nonlinear shallow water wave theory [16, 17] has been proposed for predicting the response of fluid sloshing

in rectangular tanks. Although the nonlinear shallow-water wave equations can be numerically solved, it is computational inefficient and does not provide an effective design tool for engineering application. Modal expansion techniques [18-20] have been used for modeling the sloshing problem, where the fluid flow is assumed to be inviscid, irrotational, incompressible and without rigid-body rotations. The velocity potential and the free surface are expressed as a summation of sloshing modes, and a system of coupled ordinary differential equations are developed by applying calculus of variations [18,19].

In principle, all the above-mentioned models have errors in capturing the real dynamic characteristics of the sloshing liquid and the control force generated by the TLD. Therefore, it is necessary to obtain the response of the TLD-structure system through experiments. In the present paper, a state-of-the-art testing method, real-time hybrid testing (RTHT) [21-23] has been employed for evaluating the performance of the TLD in vibration control of wind turbine towers. The fundamental idea of the RTHT is to split the entire system into two parts: a numerical substructure and a physical substructure. The former will be simulated in the computer by a developed numerical model. The latter, which generally has a complicated dynamic behavior (nonlinear or load rate-dependent), is manufactured and tested using dynamic testing equipment (shaking table or dynamic actuators) [12, 24]. This method has several advantages, such as the reduced cost of the experiment, the possibility of manufacturing full scale physical substructure and safe evaluation of structures at extreme states. The RTHT has been widely adopted for the performance evaluation of energy dissipating and vibration absorbing devices, such as elastomeric dampers [24], MR dampers [25], TLDs [12] and TMDs [26].

In the study reported here, the performance of the TLD in suppressing lateral tower vibrations of wind turbines is evaluated through RTHT. A full scale TLD is manufactured and tested as the physical substructure, while a 13-degree-of-freedom (13-DOF) aeroelastic wind turbine model is employed as the numerical substructure. The dynamic responses of the wind turbine system are numerically calculated in real time using the 13-DOF model formulated in Matlab/Simulink, with the measured control force and the pre-calculated wind-induced modal loads (with due consideration of the aerodynamic damping) acting as excitations. Both the 3 MW and 2 MW wind turbines have been considered in establishing the Simulink model. Cases of the TLD with and without damping screens have been tested for evaluating the control effect of the damper with different energy dissipations of the sloshing. Further, various values of the tuning ratio, the mean wind speed and the turbulence intensity are considered in the RTHT, so that a systematic evaluation of the damper performance can be revealed. Finally, simulation results from a pure theoretical model are compared with the recorded results from the RTHT, and the acceptable agreement verifies the accuracy of both the RTHT and the theoretical model.

2. Real-time hybrid testing

2.1. General description

The RTHT presented in this paper has been carried out using the MTS real-time hybrid testing system at Trinity College Dublin, Ireland [27]. The system allows to simultaneously combine physical testing of the TLD with the computer model of the wind turbine system. The RTHT system is mainly composed of the following:

1) a host PC running Matlab/Simulink, which is used to program Simulink models of the wind turbine system using the Real-Time Windows Target toolbox;

2) a target PC with the shared common random access memory network (SCRAMNet), on which compiled Simulink models are downloaded and the real-time simulation is run in Mathworks xPC Target environment;

3) a hybrid controller host PC, which runs the graphical user interface to the MTS servo-controller. The software Structural Test System (STS) can be used to calibrate and tune instrumentation, servo-valves and actuators prior to a test;

4) a MTS servo-controller hardware with SCRAMNet, which includes a digital PID actuator controller, signal conditioners, data acquisition system and interlock mechanisms. The controller is preset to run at a frequency of 1024 Hz, which is the update rate for the servo-valve commands;

5) a hydraulic actuator equipped with displacement and force sensors, which physically operate the desired commend to the physical substructure and allows to measure the quantities of interest.

The communication through the target PC and the MTS controller is managed through the SCRAMNet, which is a local high-speed network ring. Such local high-speed connections drastically reduce delays and make it possible to perform continuous and/or real-time hybrid simulation. Using SCRAMNet, memory-writes to the replicated shared memory at one computer are instantly sent to all other replicated shared memories at 150 MB/s via high-speed fiber optic cables.

A schematic diagram representing the RTHT system is illustrated in Figure 1. The MTS controller accepts a displacement or force command and generates the proper command signal for the servo-valve that moves the actuator to the commanded position. In order to access the MTS controller from the target PC, Simulink blocks are available to perform input/output operations through the SCRAMNet memory associated with the controller. The blocks contains the I/O signals that allow interaction with the experimental specimen. Hence, force and displacements commands can be sent from the target PC to the actuator, while measurement from the transducers can be fed back to the real-time simulation environment.

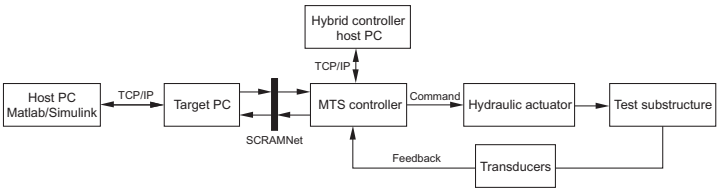

Figure 1: Layout of the RTHT system.

2.2. Implementation of the hybrid model

Figure 2 depicts the conceptual illustrations of the RTHT for the TLD-wind turbine system carried out in this paper. At each time step, the discrete equations of motion of the 13-DOF wind turbine model are solved on the target PC. The numerically obtained lateral tower vibration is sent as a displacement command over the SCRAMNet. The MTS controller generates an appropriate signal for the servo-valve which attempts to move the actuator to the commanded position. The actual displacement of the actuator and the interacting force (control force/ sloshing force) measured from the load cell are fed back to the SCRAMNet and accessed by the target

PC. With this TLD-generated control force, the equations of motion of the wind turbine system, where a TLD is installed, are solved numerically, and the displacement command is sent to the controller again. This process is carried out in real-time.

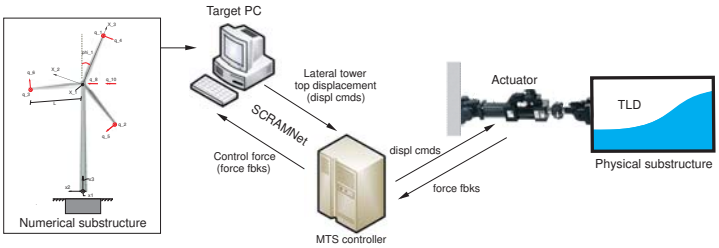

Figure 2: Conceptual view of the RTHT for the TLD-wind turbine system.

Applying the load history at fast rates, rather than a ramp-hold load history to the actuator, improves the performance and accuracy of the experiment by eliminating the hold phase and associated force relaxation [28]. Better control of the actuator is also achieved through a fast-rated command signal. Further, high performance actuators coupled with fast hybrid test methods can capture the rate-dependent behavior of the physical substructure, such as the TLD. In most of the recent hybrid tests [27-29], the MTS controller runs at a sampling rate of 1024 Hz (1/1024 s sampling time) to control the motion of the servo-hydraulic actuator using the SCRAMNet. When the integration time step of the numerical substructure is larger than 1/1024 s (for nonlinear finite element models), the predictor-corrector technique [22, 29] has been widely employed to generate the displacement command at the required rate (1024 Hz) and to synchronize the hybrid simulation.

In the present hybrid system, the integration time step of the numerical substructure (the 13-DOF wind turbine model) is set to be equal to the sampling time of the MTS controller (1/1024 s), since no iterations are needed for solving the numerical model and the actual task execution time is less than 1/1024 s. Therefore, synchronization is achieved without using the predictor-corrector technique.

There is an inherent lag in the displacement response of servo-hydraulic actuator versus the command displacement. Consequently, the measured restoring forces are delayed relative to the command signal. To compensate for this delay, the compensation technique proposed in [23] has been applied here. The time lag of the actuator response is measured first and polynomial extrapolation procedure is then used to predict the command of the actuator by advancing the current time in the algorithm by the delay time. Detailed results of the delay compensation will be given later.

2.3. Numerical substructure: the 13-DOF wind turbine model

The numerical substructure of the wind turbine system shown in Figure 3 is a 13-DOF aeroelastic model. The motions of the tower and the drivetrain are described in a fixed, global (X_1, X_2, X_3)-coordinate, while the motion of each blade is described in a moving, local (x_1, x_2, x_3)-coordinate system with its origin at the center of the hub. Assuming a constant rotational speed Ω of the rotor, the position of the local coordinate system attached to blade j is specified by the

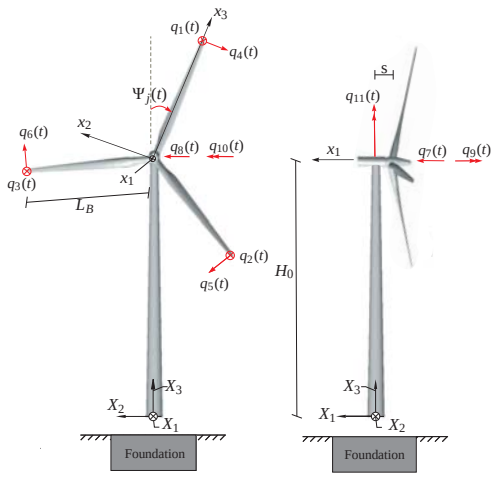

Figure 3: the 13-DOF aeroelastic wind turbine model. Definition of fixed and moving coordinate systems and the degrees of freedom $q_1(t), \ldots, q_{11}(t)$.

azimuthal angle $\Psi_j(t)$:

$$\Psi_j(t) = \Omega t + \frac{2\pi}{3}(j-1)\,,\ j = 1,2,3 \tag{1}$$

which is positive when rotating clockwise as observed from an upwind position.

Each blade is modeled as a Bernoulli-Euler beam with variable mass per unit length and variable bending stiffness. The flap-wise and edgewise motions of the three blades are modeled by the DOFs $q_j(t)$ and $q_{j+3}(t)$, $j = 1,2,3$, indicating the tip displacement in the positive x_1-direction and the negative x_2-direction, respectively. The related mode shapes are taken as the undamped fundamental eigenmodes $\Phi_f(x_3)$ and $\Phi_e(x_3)$ in the flap-wise and edgewise directions with $\Omega = 0$.

The tower motion is defined by the translational DOFs $q_7(t)$ and $q_8(t)$ in the global X_1- and X_2-directions, and the rotational DOFs $q_9(t)$, $q_{10}(t)$, $q_{11}(t)$ in the global X_1-, X_2- and X_3-directions. Hence, the lateral tower vibration is modeled by the top elastic displacement $q_8(t)$ and top elastic rotation $q_9(t)$, using cubic shape functions [30]. At each time step, the calculated $q_8(t)$ is sent to the MTS controller as the displacement command.

The drivetrain shown in Figure 4 is modeled by the DOFs $q_{12}(t)$ and $q_{13}(t)$, indicating the deviations of the rotational angles at the hub and the generator from the nominal rotational angles Ωt and $N\Omega t$, respectively, where N is the gear ratio. Correspondingly, $\dot{q}_{12}(t)$ and $\dot{q}_{13}(t)$ are the deviations of the rotational speeds at the hub and the generator from the nominal values. J_r and J_g denote the mass moment of inertia of the rotor and the generator, and k_r and k_g denote the St.Venant torsional stiffness of the rotor shaft and the generator shaft.

Assuming linear structural dynamics and substituting the kinetic and potential energies into the Euler-Lagrange equation [31], the equations of motion of the 13-DOF model are obtained of

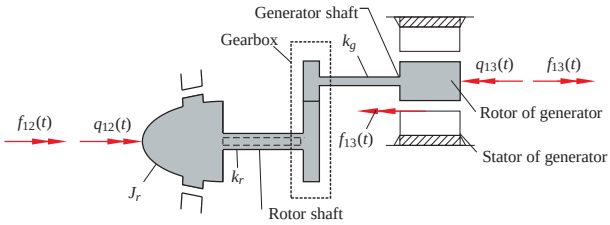

Figure 4: 2-DOF model of the flexible drivetrain with odd number of gear stages. Definition of degrees of freedom $q_{12}(t)$ and $q_{13}(t)$.

the form:

$$\mathbf{M}(t)\,\ddot{\mathbf{q}}(t) + \mathbf{C}(t)\,\dot{\mathbf{q}}(t) + \mathbf{K}(t)\,\mathbf{q}(t) = \mathbf{f}_e(t) \tag{2}$$

where $\mathbf{q}(t)$ is the DOFs vector. $\mathbf{M}(t)$ is the mass matrix, $\mathbf{C}(t)$ is the damping matrix including the structural and gyroscopic damping, and $\mathbf{K}(t)$ is the stiffness matrix taking into account the geometric and gyroscopic stiffness. $\mathbf{f}_e(t)$ is the external load vector work conjugated to $\mathbf{q}(t)$, including the non-linear aerodynamic loads and the generator torque. All the indicated system matrices contain the azimuthal angle $\Psi_j(t)$ and are thus time-varying. This is because the DOFs of the blades are modeled in the moving coordinate system, while others are formulated in a fixed coordinate system. Detailed expressions of the system matrices can be found in [30].

The 13-DOF model is formulated in Matlab/Simulink, where all the terms are discretized and the backward Euler method has been used for solving the discrete equations of motion. The time-varying system matrices are handled by user-defined Matlab functions. Two blocks, one receives inputs from SCRAMNet to the 13-DOF model and one sends commands from the 13-DOF model to SCRAMNet, are included in the Simulink model as well.

2.4. Experimental substructure test setup

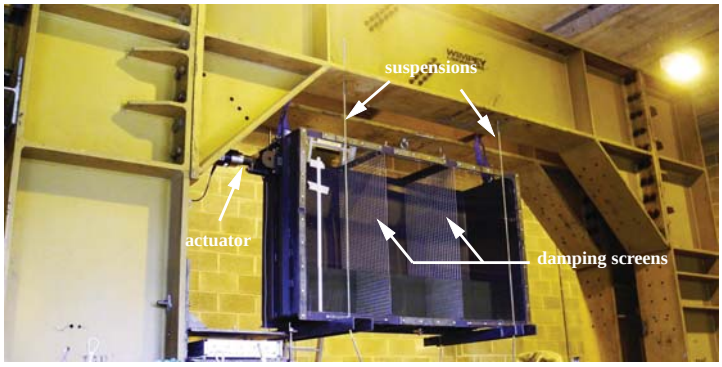

Figure 5: Test setup and the physical substructure (the TLD).

Figure 5 shows a photograph of the test setup and the physical substructure (the TLD). The setup has a hydraulic actuator in the horizontal direction, a reaction frame and the data acquisition system. The MTS 244 actuator, with a load capacity of 150 kN and a maximum stroke of ±125 mm, is bolted to the left side of the TLD. One load cell and one linear variable displacement transducer (LVDT) are attached at the actuator to measure the interaction force and the actuator displacement. The full-size TLD is made up of a closed rectangular tank, with a inner size of 1.93 m (length) × 0.59 m (width) × 1.2 m (height). Since the width of the tank is much smaller than the length, it is expected the sloshing of the water is predominately 2-dimensional. The TLD is suspended to top of the reaction frame by four steel cables in order to minimize the friction when the tank is enforced to move by the actuator. Further, a capacitance wave gauge (with a sampling rate of 10 Hz) is installed at the left end-wall of the tank to measure the liquid surface elevation.

The tank with installed damping screens have also been investigated during the tests. Actually, the inherent viscous damping of the water is usually much less than the optimal damping that results in optimal performance of the TLD. The inclusion of the damping screens significantly increases the damping ratio and energy dissipation of the water sloshing, thus improving the performance of the TLD. For these scenarios, two damping screens are installed inside the tank at $1/3L$ and $2/3L$ positions, respectively, where L is the length of the tank. The size of each mesh in the screen is 2.2 cm × 2.2 cm.

3. Analytical model to capture TLD-structure interaction

A nonlinear model for a TLD in a rotating coordinate system (wind turbine blade) has been established in [32], where the modal expansion technique was used for modeling the sloshing of the liquid under gravity, the angular acceleration, the Coriolis acceleration and the centripetal acceleration. Modal expansion was carried out directly on the velocity field of the liquid rather than the velocity potential [18-20] because the Coriolis acceleration renders the potential flow theory unvalid even for inviscous fluid flow. For wind turbine towers, either the methods proposed in [18-20] or in [32] can be employed to model the TLD-structure interaction (actually they are equivalent). In the present paper, the method proposed in [32] has been applied with slight modifications where the rotation of the coordinate system is now only due to the rotational deformation of the top of the tower. This modified theoretical model is briefly described in the following, and detailed formulation of the coupled nonlinear equations of motion can be found in [32].

3.1. Modal expansion technique for the sloshing problem

As shown in Figure 6, the TLD is assumed to be mounted at the top of the wind turbine tower (with the height of H_0), and the elastic displacement and elastic rotation at this position are given by

$$\left.\begin{aligned} q(t) &= -q_8(t) \\ \varphi(t) &= -q_9(t) \end{aligned}\right\} \tag{3}$$

where $q_8(t)$ and $q_9(t)$ are the 8th and 9th degree of freedom of the 13-DOF model as defined in Figure 3.

The motion of the fluid relative to the tank is described in (y_1, y_2, y_3)-coordinate system fixed to the damper with its origin O' placed at the center of the mean water level (MWL). The free surface is defined by a single variable of the surface elevation $\eta(y_1, t)$ measured from the mean

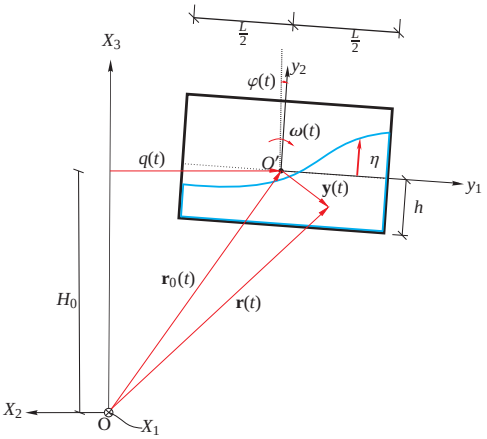

Figure 6: Modeling of the TLD.

water level. Hence, overturning waves, slamming or breaking waves are not covered by this theory. For a given fluid particle, the velocity vector and acceleration vector are given by

$$\left.\begin{aligned} \dot{\mathbf{r}}(t) &= \dot{\mathbf{r}}_0(t) + \mathbf{v}(\mathbf{y}(t),t) + \boldsymbol{\omega}(t)\times\mathbf{y}(t) \\ \ddot{\mathbf{r}}(t) &= \ddot{\mathbf{r}}_0(t) + \dot{\mathbf{v}}(\mathbf{y}(t),t) + \dot{\boldsymbol{\omega}}(t)\times\mathbf{y}(t) + 2\,\boldsymbol{\omega}(t)\times\mathbf{v}(\mathbf{y}(t),t) + \boldsymbol{\omega}(t)\times\Big(\boldsymbol{\omega}(t)\times\mathbf{y}(t)\Big) \end{aligned}\right\} \tag{4}$$

where $\mathbf{r}(t)$, $\mathbf{r}_0(t)$ and $\mathbf{y}(t)$ are defined in Figure 6. $\mathbf{v}(\mathbf{y}(t),t)$ and $\dot{\mathbf{v}}(\mathbf{y}(t),t)$ indicate the velocity and acceleration vectors of the fluid particle as seen by an observer fixed to (y_1,y_2,y_3)-coordinate system. $\boldsymbol{\omega}(t)$ is the angular velocity vector of (y_1,y_2,y_3)-coordinate system relative to (X_1,X_2,X_3)-coordinate system.

By reformulating the Lagrangian description in Eq. (4) into Eulerian description of the particle motion, the boundary value problem (Navier-Stokes equation with nonlinear boundary conditions) is established in (y_1,y_2,y_3)-coordinate system. Nest, a weak form of the boundary value problem can be obtained by the Galerkin variational method, where the modal expansions of the velocity field $\mathbf{v}(\mathbf{y},t)$ and its virtual variation $\delta\mathbf{v}(\mathbf{y})$ are expressed as:

$$\left.\begin{aligned} \mathbf{v}(\mathbf{y},t) &= \sum_{i=1}^{N} r_i(t)\,\mathbf{V}_i(\mathbf{y}) \quad , \quad \mathbf{y}\in V(t) \\ \delta\mathbf{v}(\mathbf{y}) &= \sum_{i=1}^{N} \delta r_i\,\mathbf{V}_i(\mathbf{y}) \quad , \quad \mathbf{y}\in V(t) \end{aligned}\right\} \tag{5}$$

where $V(t)$ is the time-varying fluid domain. $r_i(t)$ and δr_i denote the generalized coordinates of the velocity field and the variational field. The shape functions $\mathbf{V}_i(\mathbf{y})$ are not required to fulfill any mechanical boundary conditions on the free surface. However, they need to have zero divergence and to fulfill vanishing kinematical boundary conditions on the side walls.

Hence, the eigenmodes of standing waves in linear wave theory have been used as shape functions:

$$\mathbf{V}_i(\mathbf{y}) = \begin{bmatrix} -\sin(k_i\,(y_1+\frac{L}{2}))\,\cosh(k_i\,(y_2+h)) \\ \cos(k_i\,(y_1+\frac{L}{2}))\,\sinh(k_i\,(y_2+h)) \\ 0 \end{bmatrix} \quad , \quad (y_1,y_2) = [-\frac{L}{2},\frac{L}{2}]\times[-h,\eta(y_1,t)] \quad (6)$$

where h is the mean water depth and $k_i = i\,\frac{\pi}{L}$ is the wave number. The angular frequency of the ith sloshing mode is given by:

$$\omega_i^2 = g\,k_i\,\tanh(k_i h) \quad (7)$$

Next, the boundary condition on the free surface is discretized in a similar manner. Modal expansions of the surface elevation $\eta(y_1,t)$ and its virtual variation $\delta\eta(y_1)$ are formulated:

$$\left.\begin{aligned} \eta(y_1,t) &= \sum_{i=1}^{N} s_i(t)\,\cos\left(k_i\left(y_1+\frac{L}{2}\right)\right) \\ \delta\eta(y_1) &= \sum_{i=1}^{N} \delta s_i\,\cos\left(k_i\left(y_1+\frac{L}{2}\right)\right) \end{aligned}\right\} \quad (8)$$

where $s_i(t)$ and δs_i denote the generalized coordinates of $\eta(y_1,t)$ and $\delta\eta(y_1)$. The selected shape functions in Eq. (8) is motivated by the linear wave theory, where the free surface condition reduces to $v_2(y_1,0,t) = \frac{\partial}{\partial t}\eta(y_1,t)$. Hence, the distribution with y_1 for each shape function in Eq. (8) should be pairwise proportional to its counterpart in Eq. (6).

Finally, coupled nonlinear differential equations for $r_i(t)$ and $s_i(t)$ can be obtained by substituting Eqs. (5), (6) and (8) into the weak formulation of the boundary value problem [32]. Linear viscous damping terms are also incorporated to the equations related to $r_i(t)$ to accommodate the overall energy dissipation arising from both the viscous effect and the flow restricting devices such as the damping screen. The same damping ratio ξ has been used for all sloshing modes considered in the modal expansion [32].

3.2. The sloshing force

As shown in Fig. 7, $\mathbf{f}_c(t)$ with the non-vanishing moving frame components $f_{c,1}(t)$ and $f_{c,2}(t)$, denotes the external reaction force vector on the liquid due to the pressure $p(\mathbf{y},t)$ from inner side of the tank. This force vector, when transferred to the primary structure, represents the control force for lateral tower vibrations. The analytical expression of $\mathbf{f}_c(t)$ can be obtained by integrating the pressure $p(\mathbf{y},t)$ over inner surfaces of the tank, in combination with the divergence theorem [32]. This force vector is dependent on the state variables $s_i(t)$ through the time-varying fluid domain $V(t)$.

4. Test results and Analysis

Considering the size of the manufactured TLD, the suitable ratings of wind turbine could be 2 MW and 3 MW, and both of them have been considered in establishing the Matlab/Simulink model. To obtain data of these two configurations, a classical upscaling/downscaling method [33] has been used on the widely used NREL 5 MW reference turbine [34]. The resulting system parameters of the two turbines are provided in Table 1.

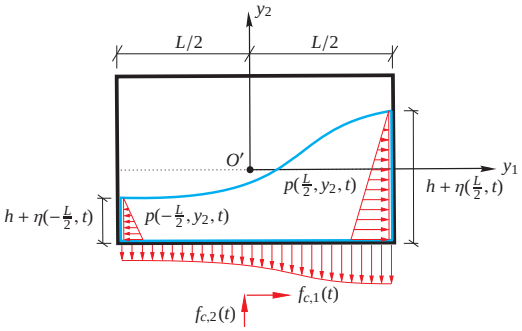

Figure 7: Pressure distribution on inner surfaces of the TLD tank.

Table 1: Parameters of the two wind turbines used in the Simulink model.

Parameter	2 MW	3 MW
Rotor rotational speed [rad/s]	2.000	1.633
Blade radius [m]	40	49
Blade mass [kg]	4488.0	8244.8
Blade structural damping ratio [-]	0.005	0.005
Rotor moment of inertia [kg m^2]	$3.768{\cdot}10^6$	$1.039{\cdot}10^7$
Nacelle+hub mass [kg]	$7.508{\cdot}10^4$	$1.379{\cdot}10^5$
Hub height [m]	55.4	67.9
Tower mass [kg]	$8.790{\cdot}10^4$	$1.615{\cdot}10^5$
Tower structural damping ratio [-]	0.01	0.01
First lateral tower frequency [rad/s]	3.369	2.751

Eq. (7) is used for tuning the TLD (by changing the mean water lever h), so that the first sloshing frequency is close to the first lateral tower frequency shown in Table 1. For each wind turbine model, tests were undertaken for three different tuning ratios (ratio between the first sloshing frequency to the first lateral tower frequency) of the TLD and using three different turbulent wind loads. Moreover, cases of the TLD with and without damping screens were both evaluated. Therefore, in total 36 ($= 2 \times 3 \times 3 \times 2$) real-time hybrid tests were conducted, and the duration for each test was set to be 5 minutes.

4.1. Delay compensation

The developed compensation method in [23] predicts the displacement of the actuator after the actuator delay δt from the present time by extrapolating an nth-order polynomial function based on the target (present) displacement and n previous calculated displacements ($\delta t \times i$ units of time ago, $i = 1, 2, ..., n$). Therefore, the predicted displacement is δt time ahead of the target counterpart.

By sending a sinusoidal signal to the actuator, the delay time δt was identified as 15 ms for the system in this study (it depends both on the actuator and the physical substructure). This delay

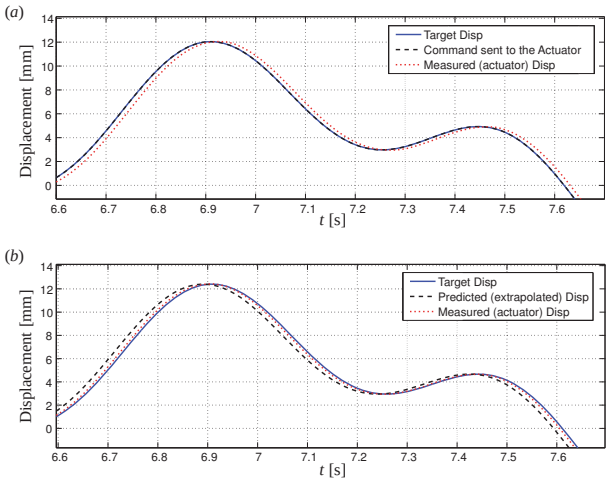

Figure 8: Accuracy of the applied delay compensation technique. (a) without compensation; (b) with compensation

time was used in the compensation technique for predicting (extrapolating) the actuator displacement during all tests. Figure 8(a) shows the results of one test case without delay compensation, where the solid line is the displacement calculated by the computer (target displacement) and dashed line is the displacement command sent to the actuator by the controller. They are identical when no compensation is applied. The dotted line is the measured displacement (feedback displacement from the actuator), which is observed to be about 15 ms delayed comparing with the target displacement. Figure 8(b) shows the corresponding results for the same load case with the delay compensation technique applied. The black dashed line is the predicted (extrapolated using the polynomial function) displacement, which is now about 15 ms ahead of the target displacement. By applying this predicted value as a command signal to the actuator, the resulting displacement becomes almost identical to the target one, since the command signal is delayed by the actuator.

4.2. Control effect of the TLD on tower vibrations

On the basis of Taylor's hypothesis of frozen turbulence together with the first-order autoregressive (AR) model, three-dimensional rotational sampled wind field can be generated with a given mean wind speed V_0 and turbulence intensity I [30]. For each wind turbine model, three different wind fields (with different combinations of V_0 and I) have been applied.

Table 2 shows the response reduction of lateral tower vibrations of the 2 MW wind turbine by the TLD. The water level of TLD varies from 46.74 cm to 64.80 cm corresponding to three values of tuning ratio η (0.95, 1.0, 1.05). With fixed size of the tank, the resulting water mass is only dependent on the water level, and it varies from 532.23 kg to 737.88 kg. Reductions of both the standard deviation (STD) and the maximum value of the tower top displacement are presented. From Table 2, there are three observations to be emphasized:

(i) For all load cases and all configurations, the TLD is effective in reducing the standard deviations and peak values of the tower top displacement. Hence, the dynamic response and fatigue life of the 2 MW wind turbine tower can be successfully improved by the TLD designed in this study.

(ii) The inclusion of damping screens in the TLD significantly improves the control performance of the damper, for all wind loads scenarios and all tuning ratios. By equipping two damping screens, more energies are dissipated during sloshing and larger response reductions are achieved by the TLD.

(iii) For the TLD without damping screens, the optimal tuning ratio depends on the mean wind speed and the turbulence intensity. On the other hand, the optimal tuning ratio is always 1 for cases with damping screens. Acceptable control performance of the TLD can be obtained for all three tuning ratios considered here, but the best performance is always achieved for all wind load cases when $\eta = 1$ with damping screens equipped.

Table 2: Response reduction of lateral tower vibrations of the 2 MW wind turbine by TLDs with different configurations.

Wind loads	Tuning ratio	Screen	Water level	Water mass	STD reduction	Peak reduction
$V_0 = 12$ m/s, $I = 0.08$	$\eta = 1.0$	no	54.61 cm	621.84 kg	39.80 %	33.63 %
		yes	54.61 cm	621.84 kg	51.98 %	47.35 %
	$\eta = 0.95$	no	46.74 cm	532.23 kg	28.01 %	35.46 %
		yes	46.74 cm	532.23 kg	31.28 %	38.52 %
	$\eta = 1.05$	no	64.80 cm	737.88 kg	41.55 %	15.03 %
		yes	64.80 cm	737.88 kg	49.95 %	25.44 %
$V_0 = 12$ m/s, $I = 0.1$	$\eta = 1.0$	no	54.61 cm	621.84 kg	43.55 %	32.75 %
		yes	54.61 cm	621.84 kg	52.90 %	48.83 %
	$\eta = 0.95$	no	46.74 cm	532.23 kg	29.50 %	37.06 %
		yes	46.74 cm	532.23 kg	33.03 %	40.85 %
	$\eta = 1.05$	no	64.80 cm	737.88 kg	37.39 %	9.79 %
		yes	64.80 cm	737.88 kg	50.28 %	26.91 %
$V_0 = 8$ m/s, $I = 0.1$	$\eta = 1.0$	no	54.61 cm	621.84 kg	20.38 %	8.80 %
		yes	54.61 cm	621.84 kg	32.26 %	13.34 %
	$\eta = 0.95$	no	46.74 cm	532.23 kg	22.13 %	14.56 %
		yes	46.74 cm	532.23 kg	25.77 %	15.61 %
	$\eta = 1.05$	no	64.80 cm	737.88 kg	9.46 %	2.17 %
		yes	64.80 cm	737.88 kg	25.40 %	20.98 %

Figure 9 shows the control effect of the TLD on tower vibrations of the 2 MW wind turbine in both time and frequency domains, for the case of V_0=12 m/s, $I = 0.08$, η=1.0. Figure 9(a) and (b) correspond to the TLD without and with damping screens, respectively. For both scenarios, the tower top displacement $q_8(t)$ is significantly reduced by the TLD, while the inclusion of damping screens further improves the reduction effect as shown in Figure 9(b). From the Fourier amplitude of $q_8(t)$ a clear peak corresponding to the first lateral tower frequency (3.369 rad/s) is observed due to very low aerodynamic damping in this mode. This peak is effectively suppressed by the damper, and is almost totally eliminated when damping screens are included in the TLD. Moreover, in the frequency domain two very small peaks (around 9 rad/s and 13 rad/s) can also been observed , resulting from the coupling between the lateral tower vibration to the edgewise blade vibrations. The TLD has no effect on these two peaks.

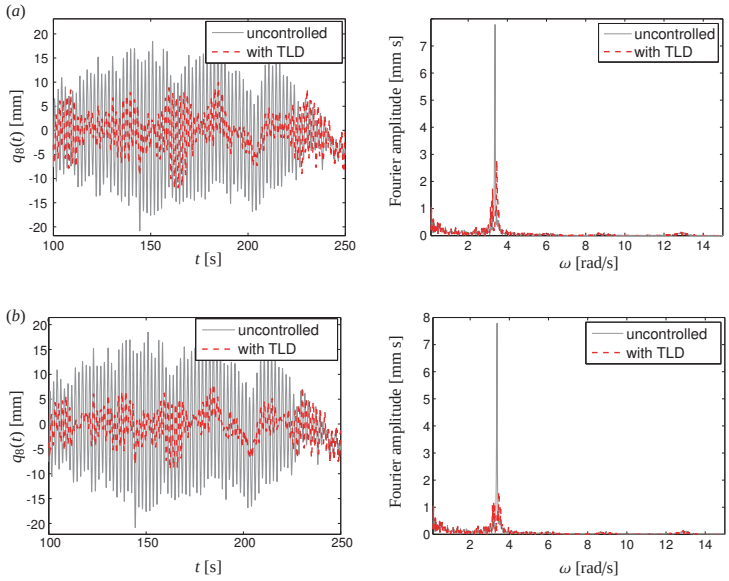

Figure 9: Control effect of the TLD on tower vibrations of the 2 MW wind turbine, tuning ratio=1, V_0 = 12 m/s, I=0.08. (a) without damping screens, (b) with damping screens.

Table 3 shows the performance of the TLD on the 3 MW wind turbine. Comparing with Table 2, slightly different results have been obtained, with the following observations to be highlighted:

(i) The overall control effect of the TLD is slightly worse comparing with the results in Table 2. Since the tower frequency of the 3 MW wind turbine is lowered to 2.751 rad/s, the mean water level (for tuning the sloshing frequency) and thus the water mass of the TLD are reduced, resulting in smaller mass ratio of the damper.

(ii) For very few cases (such as V_0 = 12 m/s, I=0.1, η = 0.95), the inclusion of damping screens even deteriorates the performance of the TLD. This might be attributed to the increased nonlinear effect when the water height is shallow in the tank.

(iii) Same as the results in Table 2, for all wind load cases the best performance of the TLD is always obtained when the tuning ratio is 1 and damping screens are equipped. This turns out to be the optimal design of the TLD for both 2 MW and 3 MW wind turbines.

Figure 10 shows the performance of the TLD on the 3 MW wind turbine in both time and frequency domains, for the case of V_0=12 m/s, I = 0.1, η=1.0. Again, Figure 10(a) and (b) correspond to the TLD without and with damping screens, respectively. It is observed that the equipped damping screens effectively improve the control effect of the TLD, and STD reduction calculated from the 5-minutes time histories is increased from 28.32% to 40.25%. The spectrum peak corresponding to the first lateral tower frequency (2.741 rad/s) is reduced by half in Figure 10(a) and by 1/3 in Figure 10(b) using the TLD with damping screens.

Table 3: Response reduction of lateral tower vibrations of the 3 MW wind turbine by TLDs with different configurations.

Wind loads	Tuning ratio	Screen	Water level	Water mass	STD reduction	Peak reduction
V_0 = 12 m/s, I = 0.08	η = 1.0	no	31.64 cm	360.28 kg	28.32 %	18.43 %
		yes	31.64 cm	360.28 kg	40.25 %	29.86 %
	η = 0.95	no	28.08 cm	319.75 kg	27.80 %	26.77 %
		yes	28.08 cm	319.75 kg	18.57 %	4.52 %
	η = 1.05	no	35.62 cm	405.60 kg	17.66 %	−3.10 %
		yes	35.62 cm	405.60 kg	27.78 %	13.09 %
V_0 = 12 m/s, I = 0.1	η = 1.0	no	31.64 cm	360.28 kg	29.43 %	25.59 %
		yes	31.64 cm	360.28 kg	44.19 %	29.86 %
	η = 0.95	no	28.08 cm	319.75 kg	32.62 %	24.68 %
		yes	28.08 cm	319.75 kg	21.81 %	9.67 %
	η = 1.05	no	35.62 cm	405.60 kg	13.77 %	−4.90 %
		yes	35.62 cm	405.60 kg	26.10 %	10.42 %
V_0 = 8 m/s, I = 0.1	η = 1.0	no	31.64 cm	360.28 kg	8.29 %	4.63 %
		yes	31.64 cm	360.28 kg	29.74 %	34.04 %
	η = 0.95	no	28.08 cm	319.75 kg	9.66 %	4.86 %
		yes	28.08 cm	319.75 kg	12.96 %	4.78 %
	η = 1.05	no	35.62 cm	405.60 kg	7.42 %	−5.02 %
		yes	35.62 cm	405.60 kg	18.84 %	11.78 %

4.3. Measured wave heights and control forces

Figure 11 compares the measured wave heights at the left end wall of the TLD with and without damping screens for the 2 MW wind turbine, where V_0 = 12 m/s, I = 0.08, η = 1.0. From the time histories in Figure 11(a), it is observed that the water sloshes in a similar trend for both cases, but much larger amplitude of the wave height is observed when there are no damping screens. Obviously the inclusion of damping screens leads to increased energy dissipation during sloshing and thus mitigated motion of the water. Moreover, for TLD with damping screens, the time history of the wave height near the tank wall turns out to be more symmetric about zero axis, implying a dominating 1^{st} sloshing mode.

The corresponding Fourier amplitude of the wave heights is illustrated in Figure 11(b). For the case without damping screens, several spectral peaks can be clearly observed, of which the most significant one corresponds to the 1^{st} sloshing mode. From Eq. (7), theoretical values (linear wave theory) of the 2^{nd}, 3^{rd} and 5^{th} sloshing frequencies are calculated as 5.492 rad/s, 6.888 rad/s and 8.934 rad/s, respectively. These three sloshing modes are also presented in Figure 11(b), implying significant contributions from higher modes in the sloshing of the liquid. Further, it is interesting to observe two other peaks at about 6.7 rad/s and 10.1 rad/s, corresponding to 2 times and 3 times the first sloshing frequency ω_1, respectively. This is due to the inherent nonlinear characteristics of the sloshing system, and higher-harmonics (multiples of the first frequency) are presented in the liquid response. On the other hand, for the case with damping screens, all the above mentioned peaks are effectively suppressed, resulting in a dominated peak of the first sloshing frequency (although this peak is suppressed as well). This again explains the more symmetric time history of the wave height about the zero axis in Figure 11(a). Finally, in both cases a peak at about 13 rad/s is presented with the same magnitude. As earlier remarked, this peak results from the coupling of the tower with blade edgewise vibrations, and the inclusion

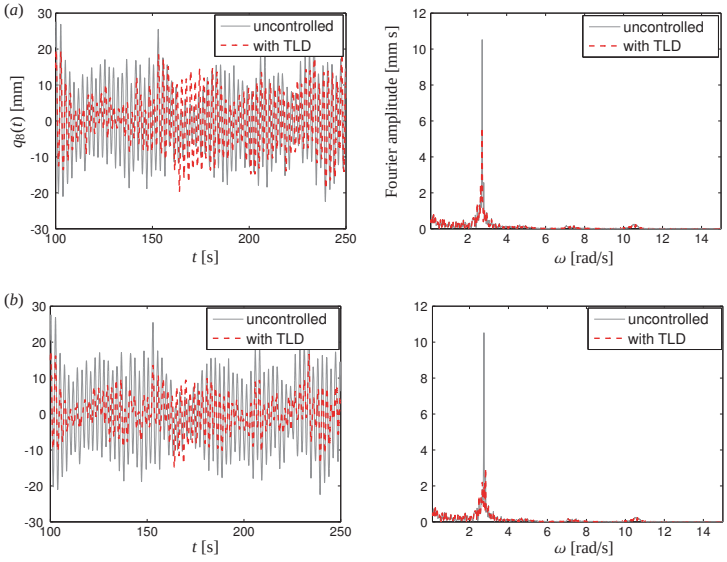

Figure 10: Control effect of the TLD on tower vibrations of the 3 MW wind turbine, tuning ratio=1, V_0 = 12 m/s, I=0.1. (a) without damping screens, (b) with damping screens.

of damping screens has no influence on it.

In connection to Figure 11, Figure 12 compares the measured (by the actuator) control force (sloshing force) for cases with and without damping screens. From Figure 12(a) it is seen that the insertion of damping screens reduces the magnitude of the control force, even though the control effect of the TLD is improved as shown in Figure 9. The corresponding Fourier amplitude in Figure 12(b) shows a dominating peak of the first sloshing mode as expected. Two small peaks at the 3^{rd} and 5^{th} sloshing angular frequencies are also observed for the case without damping screens. The 2^{nd} sloshing mode is totally gone because it has no contribution to the resulting control force. Moreover, peaks of $2 \times \omega_1$ and $3 \times \omega_1$ in Figure 11(b) are also filtered out since the force is the result of integrating liquid pressures over inner walls of the tank. By including damping screens, peaks of the 3^{rd} and 5^{th} sloshing modes are further eliminated, leaving only the fundamental peak and the peak due to the coupling effect with the blade vibrations.

For the 3 MW wind turbine with a lower tower frequency, the water depth (for tuning the damper) in the tank is more shallow and nonlinear effect of the sloshing system becomes more pronounced.

Figure 13 illustrates the measured wave height at the left end wall for the 3 MW wind turbine, with V_0=12 m/s, I = 0.08, η=1.0. Very drastic motion of the liquid is shown in Figure 13(a) for the case without damping screens. Actually, wave breaking was also observed during the test. Again the inclusion of damping screens mitigate the liquid motion effectively. From Figure 13(b), peaks corresponding to the 2^{nd} sloshing, the 3^{rd} sloshing, the 6^{th} sloshing, the 8^{th} sloshing

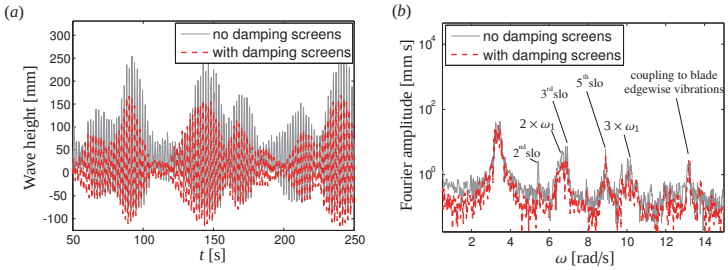

Figure 11: Measured wave heights at the left end wall of the tank, 2 MW wind turbine, tuning ratio=1, V_0 = 12 m/s, I=0.08. (a) Time histories, (b) Fourier amplitude in semi-logarithmic chart.

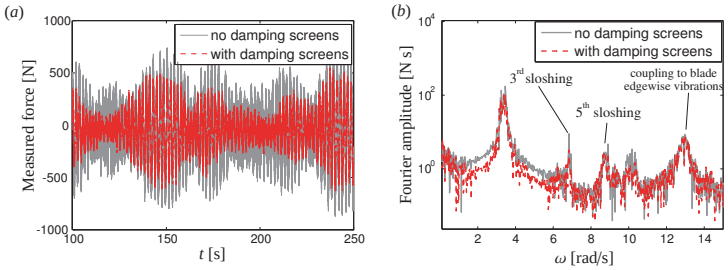

Figure 12: Measured control force from the TLD, 2 MW wind turbine, tuning ratio=1, V_0 = 12 m/s, I=0.08. (a) Time histories, (b) Fourier amplitude in semi-logarithmic chart.

are observed together with $2 \times \omega_1$ and $3 \times \omega_1$ peaks. By inserting damping screens, all peaks corresponding to the higher sloshing modes are almost totally eliminated , but the $2 \times \omega_1$ and $3 \times \omega_1$ peaks are still visible (although suppressed).

Correspondingly, Figure 14 shows the measured control force in both time and frequency domains. Observations similar to those in Figure 12 can be made, except that the frequency components of the control force (without damping screens) turn out to be the dominating 1^{st} sloshing, the 3^{rd} sloshing, together with $3 \times \omega_1$ and $5 \times \omega_1$ due to nonlinear interactions. This again shows the more pronounced nonlinear effect of the relatively shallow water for the 3 MW wind turbine, since peaks corresponding to nonlinear interactions are totally eliminated in Figure 12(b) for the 2 MW wind turbine.

For Figures 11-14, some further remarks are made as follows. Although the liquid motion contains a lot of frequency components including both the higher sloshing modes and the nonlinear interaction effects, the resulting control force filters out most of the high frequency components. Applied to the main structure, the remaind small amounts of high frequency components are further filtered out by the structure. Further, better control effect is achieved when the resulting control force is dominated by the first sloshing frequency without high frequency components.

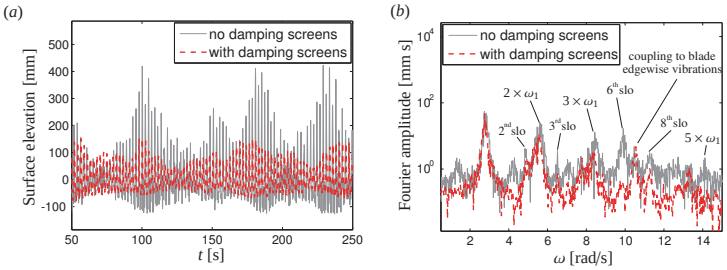

Figure 13: Measured wave heights at the left end wall of the tank, 3 MW wind turbine, tuning ratio=1, V_0 = 12 m/s, I=0.08. (a) Time histories, (b) Fourier amplitude in semi-logarithmic chart.

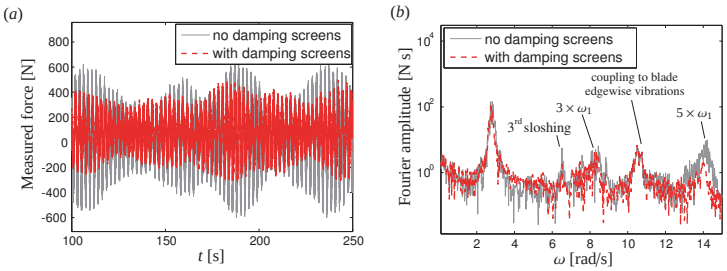

Figure 14: Measured control force from the TLD, 3 MW wind turbine, tuning ratio=1, V_0 = 12 m/s, I=0.1. (a) Time histories, (b) Fourier amplitude in semi-logarithmic chart.

4.4. Comparison of results from RTHT and analytical model

Modal expansions to three sloshing modes (N=3) in Eqs. (5) and (8) have been carried out in the numerical simulations using the analytical model. Two different values of the damping ratio ξ are used in the analytical model for cases with and without damping screens.

Figure 15 shows the comparison of the controlled tower top displacements obtained by RTHT and the analytical model for the 2 MW wind turbine, where V_0 = 12 m/s, I = 0.08, η = 1.0. By setting the damping ratio ξ to be 0.004, the result from the analytical model agrees very well with the test result as shown in Figure 15(a). Acceptable agreement between the experimental and analytical results is also obtained for the case with damping screens by choosing the value of ξ to be 0.02.

Figure 16 shows a similar comparison for the 2 MW wind turbine under the load scenario of V_0 = 8 m/s, I = 0.1, η = 1.0. Again, there is a good agreement between the test and analytical results for the case without damping screens. The analytical result fits slightly worse with the test result for the case with damping screens. This is reasonable because in fact the inclusion of damping screens not only increases energy dissipation but also introduces nonlinear interactions between the liquid and the screens, which is not accounted for by the analytical model.

As for the 3 MW wind turbine, comparison of the results obtained by RTHT and the analytical model are shown in Figure 17, where V_0 = 12 m/s, I = 0.1, η = 1.0. ξ is set to be 0.005 and

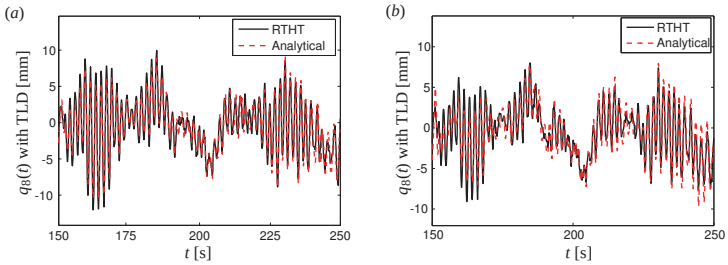

Figure 15: Comparison of the controlled tower displacements obtained by RTHT and analytical model, 2 MW wind turbine, tuning ratio=1, V_0 = 12 m/s, I=0.08. (a) Without damping screens (ξ = 0.004 used in the analytical model), (b) With damping screens (ξ = 0.02 used in the analytical model).

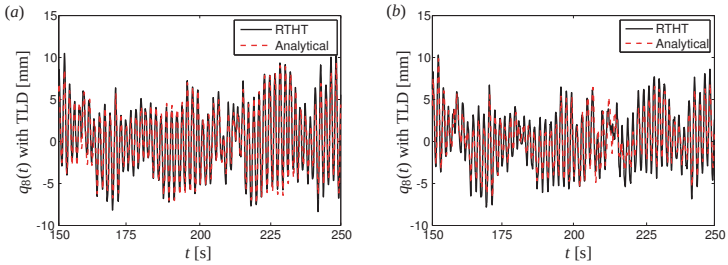

Figure 16: Comparison of the controlled tower displacements obtained by RTHT and analytical model, 2 MW wind turbine, tuning ratio=1, V_0 = 8 m/s, I=0.1. (a) Without damping screens (ξ = 0.004 used in the analytical model), (b) With damping screens (ξ = 0.015 used in the analytical model).

0.03 in the analytical model for cases without and with damping screens, respectively. Good agreement between the experimental and analytical results is obtained. Figure 18 shows the comparison under the load scenario of V_0 = 8 m/s, I = 0.1, η = 1.0. Similar observations are obtained, where the agreement is worse for the case with damping screens. Further, for TLDs used in the 3 MW turbine, larger values of ξ have been used in the analytical model comparing with its 2 MW counterpart, implying larger energy dissipations of the shallow water TLD due to nonlinear interactions and wave breaking.

5. Conclusions

In this paper, a real-time hybrid testing (RTHT) method is implemented for evaluating the performance of a TLD in mitigating lateral tower vibrations of megawatt wind turbines. During the RTHT, a full-size TLD is tested as the physical substructure while the structural responses of the wind turbine system are numerically calculated using a 13-DOF aeroelastic model in the Matlab/Simulink environment. A compensation technique based on polynomial extrapolation has been applied to compensate for the inherent actuator delay.

Both 3 MW and 2 MW wind turbine models have been established in Matlab/Simulink, and

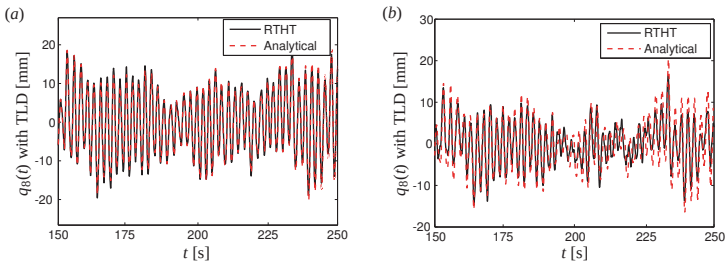

Figure 17: Comparison of the controlled tower displacements obtained by RTHT and analytical model, 3 MW wind turbine, tuning ratio=1, V_0 = 12 m/s, I=0.1. (a) Without damping screens (ξ = 0.005 used in the analytical model), (b) With damping screens (ξ = 0.03 used in the analytical model).

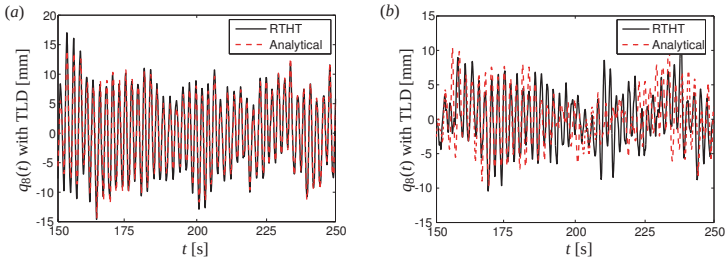

Figure 18: Comparison of the controlled tower displacements obtained by RTHT and analytical model, 3 MW wind turbine, tuning ratio=1, V_0 = 8 m/s, I=0.1. (a) Without damping screens (ξ = 0.005 used in the analytical model), (b) With damping screens (ξ = 0.04 used in the analytical model).

different water levels of the TLD are determined from frequency tuning conditions for the two turbines. The overall control effect of the TLD is slightly worse for the 3 MW wind turbine (with lower tower frequency) due to the reduced mean water level and thus the mass ratio of the damper. Moreover, it is shown from test results that the inclusion of damping screens effectively increases energy dissipation during liquid sloshing and in most cases improves the control performance of the TLD on tower vibrations. For both turbines under all load cases, the best performance of the TLD is always obtained when the tuning ratio is 1.0 and damping screens are equipped. Furthermore, the measured wave height at the left end wall is observed to contain a lot of frequency components including both the higher sloshing modes and the nonlinear interaction effect. The measured control force, on the other hand, filters out most of the high frequency components since the force is the result of integrating liquid pressures over inner walls of the tank. By inserting damping screens, the remaining high frequency components are further mitigated, resulting in a control force that is totally dominated by the first sloshing frequency.

Finally, the RTHT results are compared to the results obtained from an analytical model of the TLD-wind turbine system (based on modal expansion technique). Good agreement between tested and analytical results demonstrates that the proposed analytical method can yield acceptable estimates of the response of wind turbine-TLD system under turbulent wind loads. The

comparative results also indicate that the real-time hybrid test method provides an accurate and cost-effective procedure for performing full-scale tests of passive or semi-active dampers.

6. Acknowledgements

The first author gratefully acknowledge the financial support from the Chinese Scholarship Council under the State Scholarship Fund. The authors would like to acknowledge the contributions of the technical staffs (especially Dr. Kevin Ryan and Mr. David McAulay) in the Structures Laboratory at Trinity College Dublin.

REFERENCES

[1] Hansen MH. Aeroelastic instability problems for wind turbines. *Wind Energy* 2007; 10(6): 551-577.

[2] Thomsen K, Petersen JT, Nim E, Øye S, Petersen B. A method for determination of damping for edgewise blade vibrations. *Wind Energy* 2000; 3(4): 233-246.

[3] Bir G, Jonkman J. Aeroelastic instabilities of large offshore and onshore wind turbines. *EAWE 2007 Torque from Wind Conference*, Lyngby, Denmark, 2007.

[4] Murtagh PJ, Ghosh A, Basu B, Broderick BM. Passive control of wind turbine vibrations including blade/tower interaction and rotationally sampled turbulence. *Wind Energy* 2008; 11(4): 305-317.

[5] Colwell S, Basu B. Tuned liquid column dampers in offshore wind turbines for structural control. *Engineering Structures* 2009; 31(2): 358-368.

[6] Lackner MA, Rotea MA. Passive structural control of offshore wind turbines, *Wind Energy* 2011; 14(3): 373-388.

[7] Zhang ZL, Chen JB, Li J. Theoretical study and experimental verification of vibration control of offshore wind turbines by a ball vibration absorber. *Structure and Infrastructure Engineering* 2014; 10(8): 1087-1100.

[8] Fujii K, Tamura Y, Sato T, Wakahara T. Wind-induced vibration of tower and practical applications of tuned sloshing damper. *Journal of Wind Engineering and Industrial Aerodynamics* 1990; 33(1-2): 263-272.

[9] Tamura Y, Fujii K, Ohtsuki T, Wakahara T, Kohsaka R. Effectiveness of tuned liquid dampers under wind excitation. *Engineering Structures* 1995; 17(9): 609-621.

[10] Chang CC, Gu M. Suppression of vortex-excited vibration of tall buildings using tuned liquid dampers. *Journal of Wind Engineering and Industrial Aerodynamics* 1999; 83(1-3): 225-237.

[11] Banerji P, Murudi M, Shah AH, Popplewell N. Tuned liquid dampers for controlling earthquake response of structures. *Earthquake Engineering and Structural Dynamics* 2000; 29(5): 587-602.

[12] Lee SK, Park EC, Min KW, Lee SH, Chung L, Park JH. Real-time hybrid shaking table testing method for the performance evaluation of a tuned liquid damper controlling seismic response of building structures. *Journal of Sound and Vibration* 2007; 302(3): 471-488.

[13] Jin Q, Li X, Sun N, Zhou J, Guan J. Experimental and numerical study on tuned liquid dampers for controlling earthquake response of jacket offshore platform. *Marine Structures* 2007; 20(4): 238-254.

[14] Sun LM, Fujino Y, Chaiseri P, Pacheco BM. The properties of tuned liquid dampers using a TMD analogy. *Earthquake Engineering and Structural Dynamics* 1995; 24(7): 967-976.

[15] Yu JK, Wakahara T, Reed D. A nonliner numerical model for the tuned liquid damper. *Earthquake Engineering and Structural Dynamics* 1999; 28(6): 671-686.

[16] Sun LM, Fujino Y. A semi-analytical model for tuned liquid damper (TLD) with wave breaking. *Journal of Fluids and Structures* 1994; 8(5): 471-488.

[17] Reed D, Yu J, Yeh H, Gardarsson S. Investigation of tuned liquid dampers under large amplitude excitation. *Journal of Engineering Mechanics* 1998; 124(4): 405-413.

[18] Faltinsen OM, Regnebakke OF, Lukovsky IA, Timokha AN. Multidimensional model analysis of nonlinear sloshing in a rectangular tank with finite water depth. *Journal of Fluid Mechanics* 2000; 407: 201-234.

[19] Faltinsen OM, Timokha AN. An adaptive multimodal approach to nonlinear sloshing in a rectangular tank. *Journal of Fluid Mechanics* 2001; 432: 167-200.

[20] Love JS, Tait MJ. Nonlinear simulation of a tuned liquid damper with damping screens using a modal expansion technique. *Journal of Fluid and Structures* 2010; 26(7-8): 1058-1077.

[21] Nakashima M, Kato H. Development of real-time pseudo dynamic testing. *Earthquake Engineering and Structural Dynamics* 1992; 21(1): 79-92.

[22] Nakashima M, Masaoka N. Real-time on-line test for MDOF systems. *Earthquake Engineering and Structural Dynamics* 1999; 28(4): 393-420.

[23] Horiuchi T, Inoue M, Konno T, Namita Y. Real-time hybrid experimental system with actuator delay compensation and its application to a piping system with energy absorber. *Earthquake Engineering and Structural Dynamics* 1999; 28(10): 1121-1141.

[24] Mercan O, Ricles JM. Experimental studies on real-time testing of structures with elastomeric dampers. *Journal of Structural Engineering, ASCE* 2009; 135(9): 1124-1133.

[25] Christenson R, Lin Y, Emmons A, Bass B. Large-scale experimental verification of semiactie control through real-time hybrid simulation. *Journal of Structural Engineering, ASCE* 2008; 134(4): 522-534.

[26] Igarashi A, Iemura H, Suwa T. Development of substructured shaking table test method. *Proceedings of the 12th World Conference on Earthquake Engineering*. 2000.

[27] McCrum DP, Broderick BM. Evaluation of a substructured soft-real time hybrid test for performing seismic analysis of complex structural systems. *Computers and Structures* 2013; 129: 111-119.

[28] Mosqueda G, Stojadinovic B, Mahin S. Implementation and accuracy of continuous hybrid simulation with geographically distributed substructures. Technical Report. Earthquake Engineering Research Center, University of California, Berkeley, CA, USA. 2005.

[29] Schellenberg A, Mahin S, Fenves GL. Advanced implementation of hybrid simulation. Technical Report. Pacific Earthquake Engineering Research Center, University of California, Berkeley, CA, USA. 2009.

[30] Zhang Z, Nielsen SRK, Blaabjerg F, Zhou D. Dynamics and control of lateral tower vibrations in offshore wind turbines by means of active generator torque. *Energies* 2014; 7(11): 7746-7772.

[31] Pars LA. *A Treatise on Analytical Dynamics*. Ox Bow Press: Woodbridge, 1979.

[32] Zhang Z, Nielsen SRK, Basu B, Li J. Nonlinear modeling of tuned liquid dampers (TLDs) in rotating wind turbine blades for edgewise vibration control. *Journal of Fluids and Structures* 2015; submitted.

[33] Sieros G, Chaviaropoulos P, Sørensen JD, Bulder BH, Jamieson P. Upscaling wind turbines: theoretical and practical aspects and their impact on the cost of energy. *Wind Energy* 2012;

15(1): 3-17.

[34] Jonkman J, Butterfield S, Musial W, Scott G. Definition of 5-MW reference wind turbine for offshore system development. National Renewable Energy Laboratory, Technical Report, NREL/TP-500-38060, Golden, Colorado. 2009.

APPENDIX H
Optimal Control of Nonlinear Wave Energy Point Converters

Paper 7
The paper presented in this appendix is published in *Ocean Engineering*, 2013, Volume 72, Pages 176-187, DOI: 10.1016/j.oceaneng.2013.06.029.

http://www.sciencedirect.com/science/article/pii/S0029801813002758

H.1 Author's Right

Journal author rights

In order for Elsevier to publish and disseminate research articles, we need publishing rights. This is determined by a publishing agreement between the author and Elsevier. This agreement deals with the transfer or license of the copyright to Elsevier and authors retain significant rights to use and share their own published articles. Elsevier supports the need for authors to share, disseminate and maximize the impact of their research and these rights, in Elsevier proprietary journals* are defined below:

For subscription articles	For open access articles
Authors transfer copyright to the publisher as part of a journal publishing agreement, but have the right to: • Share their article for Personal Use, Internal Institutional Use and Scholarly Sharing purposes, with a DOI link to the version of record on ScienceDirect (and with the Creative Commons CC-BY-NC- ND license for author manuscript versions) • Retain patent, trademark and other intellectual property rights (including raw research data). • Proper attribution and credit for the published work.	Authors sign an exclusive license agreement, where authors have copyright but license exclusive rights in their article to the publisher**. In this case authors have the right to: • Share their article in the same ways permitted to third parties under the relevant user license (together with Personal Use rights) so long as it contains a CrossMark logo, the end user license, and a DOI link to the version of record on ScienceDirect. • Retain patent, trademark and other intellectual property rights (including raw research data). • Proper attribution and credit for the published work.

http://www.elsevier.com/journal-authors/author-rights-and-responsibilities

Ocean Engineering 72 (2013) 176–187

Contents lists available at SciVerse ScienceDirect

Ocean Engineering

journal homepage: www.elsevier.com/locate/oceaneng

Optimal control of nonlinear wave energy point converters

Søren R.K. Nielsen [a,*], Qiang Zhou [b], Morten M. Kramer [a], Biswajit Basu [c], Zili Zhang [a]

[a] Aalborg University, Department of Civil Engineering, Sohngaardsholsvej 57, 9000 Aalborg, Denmark
[b] Wuhan University of Technology, Hubei Key Laboratory of Roadway, Bridge and Structure Engineering, 430070 Wuhan, PR China
[c] School of Engineering, Trinity College Dublin, Dublin 2, Ireland

ARTICLE INFO

Article history:
Received 21 June 2012
Accepted 24 June 2013
Available online 24 July 2013

Keywords:
Wave energy converters
Nonlinear point absorbers
Optimal control
Feedback control
Irregular sea state

ABSTRACT

In this paper the optimal control law for a single nonlinear point absorber in irregular sea-states is derived, and proven to be a closed-loop controller with feedback from measured displacement, velocity and acceleration of the floater. However, a non-causal integral control component dependent on future velocities appears in the optimal control law, rendering the optimal control law less useful for real time implementation. To circumvent this problem a causal closed-loop controller with the same feedback information is proposed, based on a slight modification of the optimal control law. The basic idea behind the control strategy is to enforce the stationary velocity response of the absorber into phase with the wave excitation force at any time. The controller is optimal under monochromatic wave excitation. It is demonstrated that the devised causal controller, in plane irregular sea states, absorbs almost the same power as the optimal controller.

1. Introduction

A wave energy converter (WEC) may be defined as a dynamic system with one or more degrees of freedom in order to convert the energy in the waves into mechanical energy stored in the oscillating system. A point absorber is a WEC that is capable of absorbing energy from waves propagating in any direction, and with horizontal dimensions that are small compared to the dominating wave length. The WEC is typically equipped with an electric power generator via a hydraulic force system. The reaction forces from the latter influence the motion of the WEC. In a so-called reactive control these forces are used to control the motion of the WEC in such a way that a maximum mechanical energy is supplied to the absorber. With a certain loss due to friction in the hydraulic force actuators, the control forces are then transferred to the generator, where they are converted into electric energy. Within certain ranges these reaction forces can be specified at prescribed values.

The idea of extracting energy from the waves is very old and several types of WEC devices have been proposed (Falnes, 2002a). This has initiated commercial WEC projects using devices such as different buoy concepts, Oscillating-Water-Column (OWC) plants, the Pelamis WEC (Pelamis Wave, 2012), overtopping WEC types like the Wave Dragon (Wavedragon, 2005), point absorber approaches used for the Wavestar device (Wave Star, 2005), or the SEAREV device (Ruellan et al., 2010).

The total hydrodynamic force on the absorber consists of the quasi-static buoyancy force, the radiation force, and the wave excitation force. Under the action of these forces, the active control of a WEC may be classified as either open-loop (feed forward) or closed-loop (feedback) control. Open-loop control implies that the control effort is feed forward based on observation (measurement) of the dynamic hydrodynamic force. Open-loop does not affect the dynamics of the system, i.e. angular eigenfrequencies and structural damping ratios are unchanged by the control. Closed-loop control is entirely based on the observed motion of the absorbers. Typically, this involves the displacement, velocity or acceleration components, which easily can be measured by accelerometer or laser vibrometer measurements onboard the floating device. A closed-loop control always changes the dynamic properties of the system (inertia, damping or stiffness parameters) as specified by the poles and zeros of the frequency response function that relate the external wave force to the displacement response of the absorber system.

Many control strategies for WECs have been devised and reviewed in Falnes (2002b, 2007). Latching control, independently proposed in Falnes and Budal (1978) and French (1979), is probably the simplest and definitely the most investigated control strategy. The control is based on the observation of the dynamic hydrodynamic force. For this reason latching control should be classified as an open-loop control strategy. Further, latching control requires that the hydrodynamic force can be predicted for, at least, a semi-wave period ahead of the present time. In broad-banded irregular sea-states this

* Corresponding author. Tel.: +45 9940 8451.
E-mail addresses: srkn@civil.aau.dk (S.R.K. Nielsen), drzhouqiang@hotmail.com (Q. Zhou), mmk@civil.aau.dk (M.M. Kramer), BASUB@tcd.ie (B. Basu), zlz@civil.aau.dk (Z.L. Zhang).

0029-8018/$ - see front matter © 2013 Elsevier Ltd. All rights reserved.
http://dx.doi.org/10.1016/j.oceaneng.2013.06.029

prediction is related with uncertainty, which may affect the stability of the control. Normally, merely the sea surface elevation in the vicinity of the converter is observed. This makes the observation of the wave excitation force component difficult due to the non-causal dependence of this quantity on the sea-surface elevation (Falnes, 1995). Further, the power outtake from the control changes between finite time intervals with zero and non-zero power production and may cause problems for the mechanical implementation of the method.

The simplest closed-loop control law is achieved by a so-called derivative controller, where the reactive control force is specified to be proportional to and oppositely directed to the velocity of the WEC. The controller has insignificant influence on the eigenfrequency of the absorber. For this reason the controller only becomes optimal for frequencies in the auto-spectrum of the wave excitation force in the vicinity of the undamped eigenfrequency of the absorber. By augmenting the controller with a force component proportional to either the displacement (proportional control) or the acceleration (acceleration control), a broader spectrum of frequencies can be absorbed. Proportional control will change the stiffness of the absorber, and acceleration control will change the mass. In both cases the eigenfrequency can be changed to a certain extent. Finally, a so-called integral control force component can be introduced. Here the control force appears as a convolution integral of the absorber velocity weighted with respect to a given impulse response function. It turns out that integral control needs to be introduced, if a perfect phase locking between the wave excitation force and the velocity of the absorber is attempted at all frequencies.

The optimal control proves to be non-causal, i.e. the present control demand depends on future wave loads or displacements of the floater. To handle this problem various control laws have been suggested based on prediction of the incoming waves and the related future response of the absorber (Schoen, 2008a,b). Hence, such approaches combine elements of open and closed-loop control. Optimal control with constraint on the displacements and the control force has also been considered (Hals et al., 2011; Li et al., 2012). Still, the non-causality of the optimal control was handled by prediction of the wave excitation force by means of an augmented Kalman filter. Non-predictive phase control has been considered by many authors (Valerio et al., 2007; Lopez et al., 2009). Such control strategies are basically sub-optimal in irregular sea-states. In Valerio et al. (2007) it is demonstrated that the control at optimal tuning tends to enforce the velocity of the absorber into phase with the wave excitation force. The enforcement of this condition by the control force formed the guideline for the causal control law devised in the present paper.

Since the displacement response at optimal control is significant, the non-linear buoyancy component of the control forces needs to be considered, rather than a linearized version of this around the static equilibrium state. In this respect the optimal control law for a point absorber in an irregular sea-state is, at first, derived based on optimal control theory, assuming non-linear buoyancy response and linear wave theory. It turns out that the optimal control force eliminates the inertial and the non-linear stiffness (buoyancy) loads on the absorber completely. The derivation of the control law relies upon an initial rational approximation to the integral component of the radiation force, described by a number of additional state variables (Yu and Falnes, 1995). The rational approximation is merely used at the formal derivation of the optimal control law, and is eliminated again in the final expression for this quantity. The optimal controller proves to be of a closed-loop type, incorporating all of the proportional, derivative, acceleration and integral control force components. For this reason the control law is optimal in any 2D or 3D irregular sea-state, as well for transient vibrations induced by the initial conditions. The study demonstrates that the absorber velocity and the wave excitation are in phase at all frequencies, with the implication that mechanical energy is supplied to the absorbed at all instants of time. The integral control component of the optimal control is completely non-causal, depending merely on future velocities of the absorber. Because the velocity response at optimal control is significantly broad-banded, predictions of this quantity are difficult and, thereby, makes the control law useless for real time implementation.

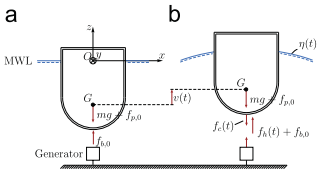

Fig. 1. Loads on heave absorber. (a) Static equilibrium state. (b) Dynamic state.

To circumvent this problem, a causal closed-loop controller is suggested with feedback from measurements of the present displacement and acceleration, and all velocities up to and including present time, based on a slight modification of the optimal control law. The rationale for the controller is that it enforces the velocity response of the point absorber into phase with the wave excitation force at all frequencies, as is the case for the optimal controller. The control law contains a single unspecified gain factor, which is determined so the absorbed power by the control force is maximum in a given 2D or 3D sea state. An analytical solution for the optimal gain factor is derived, when the absorber is exposed to a plane irregular wave excitation. The devised controller is shown to be optimal under monochromatic wave excitation, and a numeric example demonstrates that the devised causal controller absorbs almost the same power as the optimal controller in plane irregular sea states.

2. Equation of motion of a WEC

The $(x, y, z)-$coordinate system is introduced as shown in Fig. 1. Although, only the heave absorber shown in Fig. 1 will be analyzed, all results, including the equation of motion and control laws, may easily be carried over to other single-degree-of-freedom systems by slight modifications. Only two-dimensional (plane) regular or irregular waves are considered, which are assumed to propagate in the positive x direction. The motion $v(t)$ of the body in the vertical z direction is defined relative to the static equilibrium state, where the static buoyancy force $f_{b,0}$ balances the gravity force mg and a possible static pre-stressing force from the generator $f_{p,0}$. The structural mass including ballast is denoted by m, and g is the acceleration of gravity. Hence

$$f_{b,0} = mg + f_{p,0} \tag{1}$$

$f_{b,0}$ is given by Archimedes' law

$$f_{b,0} = \rho\, D(0) g \tag{2}$$

where ρ is the mass density of water, and $D(v(t))$ denotes the displaced water volume at the displacement $v(t)$.

In the dynamic state the WEC is excited by an additional dynamic hydrodynamic force, $f_h(t)$, on the top of the static buoyancy force, and by an additional dynamic reactive generator force, $f_c(t)$, on the top of the generator pre-stressing force. The force $f_c(t)$ can be prescribed to a certain extent, for which reason it may be used to control the motion of the WEC. Henceforth, $f_c(t)$ will be

referred to as the control force. Then, the equation of motion becomes

$$m\ddot{v}(t) = f_h(t) - f_c(t) \tag{3}$$

Assuming linear wave theory $f_h(t)$ may be written as a superposition of the following contributions:

$$f_h(t) = f_b(t) + f_r(t) + f_e(t) \tag{4}$$

where $f_b(t)$ is the quasi-static increment of the buoyancy force, $f_r(t)$ is the radiation force generated by the motion of the absorber in still water, and $f_e(t)$ is the wave excitation force caused by the wave action, when the absorber is fixed in the static equilibrium state. The term $f_r(t)$ removes mechanical energy by generating a wave train propagating away from the absorber, whereas $f_e(t)$ supplies energy to the absorber.

$f_b(t)$ is given as

$$f_b(t) = -\rho(D(v(t)) - D(0))g = -r(v(t)) \tag{5}$$

The non-linear buoyancy function $r(v(t))$ is limited between the value r_1 corresponding to a fully submerged absorber, and the value $r_0 = -f_{b,0}$, when the absorber is jumping out of the water. Assuming small vertical vibrations, Eq. (5) may be linearized around the static equilibrium state as (Newman, 1977)

$$f_b(t) = -kv(t), \quad k = r'(0) = \rho D'(0)g \tag{6}$$

The radiation force $f_r(t)$ may be written in terms of the following differential-integro relation (Cummins, 1962; Faltinsen, 1990):

$$f_r(t) = -m_h\ddot{v}(t) - f_{r,0}(t) \tag{7}$$

$$f_{r,0}(t) = \int_{-\infty}^{t} h_{r\dot{v}}(t-\tau)\dot{v}(\tau)\,d\tau \tag{8}$$

The term m_h is the added water mass at infinite high frequencies and $h_{r\dot{v}}(t)$ is a causal impulse response function for the radiation force brought forward by the absorber velocity $\dot{v}(\tau)$.

Due to the causality of the impulse response function, the related frequency response function becomes

$$H_{r\dot{v}}(\omega) = \int_0^{\infty} e^{-i\omega t} h_{r\dot{v}}(t)\,dt \tag{9}$$

Insertion of Eqs. (5), (7) and (8) in Eq. (2) provides the following integro-differential equation for $v(t)$ driven by the $f_e(t)$ and $f_c(t)$:

$$\left.\begin{array}{ll} (m+m_h)\ddot{v}(t) + r(v(t)) + \int_{t_0}^{t} h_{r\dot{v}}(t-\tau)\dot{v}(\tau)\,d\tau = f_e(t) - f_c(t), & t > t_0 \\ v(t_0) = v_0, & \dot{v}(t_0) = \dot{v}_0 \end{array}\right\} \tag{10}$$

where v_0 and $\dot{v}_0$ are given initial conditions at the time t_0.

$M_h(\omega)$ and $C_h(\omega)$ denote the hydrodynamic added mass and the hydrodynamic radiation damping coefficient respectively during monochromatic wave excitation. These are related to the imaginary and real parts of $H_{r\dot{v}}(\omega)$ by the following sine and cosine transforms:

$$\left.\begin{array}{l} M_h(\omega) = m_h + \dfrac{1}{\omega}\mathrm{Im}(H_{r\dot{v}}(\omega)) = m_h - \dfrac{1}{\omega}\int_0^{\infty} \sin(\omega t) h_{r\dot{v}}(t)\,dt \\ C_h(\omega) = \mathrm{Re}(H_{r\dot{v}}(\omega)) = \int_0^{\infty} \cos(\omega t) h_{r\dot{v}}(t)\,dt \end{array}\right\} \tag{11}$$

The indicated sine and cosine transforms of the impulse response function are consequences of $h_{r\dot{v}}(t)$ which is causal.

Then, under monochromatic wave excitation, the radiation force may be given by the following mixed time and frequency representation:

$$f_r(t) = -M_h(\omega)\ddot{v}(t) - C_h(\omega)\dot{v}(t) \tag{12}$$

The wave excitation force $f_e(t)$ may be given in terms of the following convolution integral of the sea-surface elevation $\eta(t)$ (Falnes, 2002a):

$$f_e(t) = \int_{-\infty}^{\infty} h_{e\eta}(t-\tau)\eta(\tau)\,d\tau \tag{13}$$

where $\eta(t)$ refers to the sea-surface elevation observed at a sufficient distant position, so no disturbances from radiation waves are present, and $h_{e\eta}(t)$ is a non-causal impulse response function.

The related frequency response function becomes

$$H_{e\eta}(\omega) = \int_{-\infty}^{\infty} e^{-i\omega t} h_{e\eta}(t)\,dt \tag{14}$$

The hydrodynamic parameters and functions k, m_h, $M_h(\omega)$, $C_h(\omega)$ and $H_{e\eta}(\omega)$ have been calculated by the program WAMIT, which is based on the boundary element method (WAMIT, 2011). Based on the indicated parameters, the frequency response function $H_{r\dot{v}}(\omega)$ is calculated from Eq. (11). Finally, the impulse response functions, $h_{r\dot{v}}(t)$ and $h_{e\eta}(t)$, are obtained numerically by inverse Fourier transform of Eqs. (9) and (14) respectively.

At first, the case of optimal control at stationary response under monochromatic wave excitation with the angular frequency ω is considered. Further, the linear buoyancy model (6) is applied, and the following parameterized feedback control law is presumed for the control force

$$f_c(t) = m_c\ddot{v}(t) + c_c\dot{v}(t) + k_c v(t) \tag{15}$$

where m_c, c_c and k_c represent the gain factors for the acceleration component, the velocity component and the displacement component, respectively.

Then, by insertion of Eqs. (6), (12), (15) in Eq. (3), the following linear equation of motion for the point absorber is obtained:

$$M\ddot{v}(t) + C\dot{v}(t) + Kv(t) = f_e(t) = |F_e|\,\cos(\omega t) \tag{16}$$

$$\left.\begin{array}{l} M = m + M_h + m_c \\ C = C_h + c_c \\ K = k + k_c \end{array}\right\} \tag{17}$$

$|F_e|$ denotes the amplitude of the wave excitation force. The stationary solution to (16) reads as

$$v(t) = \mathrm{Re}(Ve^{i\omega t}) = |V|\,\cos(\omega t - \Psi) \tag{18}$$

The displacement amplitude $|V|$ and the phase lag Ψ are given by the well-known results

$$|V| = \frac{|F_e|}{\sqrt{(K-\omega^2 M)^2 + \omega^2 C^2}}, \quad \tan\Psi = \frac{\omega C}{K - \omega^2 M} \tag{19}$$

The velocity and the control force become

$$\dot{v}(t) = \mathrm{Re}(i\omega V e^{i\omega t}) = \mathrm{Re}(i\omega V)\,\cos(\omega t) - \mathrm{Im}(i\omega V)\,\sin(\omega t) \tag{20}$$

$$\begin{aligned} f_c(t) &= \mathrm{Re}((k_c - \omega^2 m_c + i\omega c_c)Ve^{i\omega t}) \\ &= \mathrm{Re}((k_c - \omega^2 m_c + i\omega c_c)V)\,\cos(\omega t) - \mathrm{Im}((k_c - \omega^2 m_c + i\omega c_c)V)\,\sin(\omega t) \end{aligned} \tag{21}$$

The instantaneous power absorbed by the control force becomes

$$P_a(t) = f_c(t)\dot{v}(t) \tag{22}$$

Rather than the instantaneous absorbed power the time average $\overline{P}_a$ during a wave period $T = 2\pi/\omega$ is of interest. By the use of Eqs. (20) and (21), the time average becomes (Falnes, 2002a)

$$\overline{P}_a = \frac{1}{T}\int_0^T f_c(\tau)\dot{v}(\tau)\,d\tau = \frac{1}{2}|F_e|^2 \frac{\omega^2 c_c}{(K-\omega^2 M)^2 + \omega^2(C_h + c_c)^2} \tag{23}$$

Next, Eq. (23) is optimized with respect to k_c, c_c and m_c. The optimality conditions read as

$$K - \omega^2 M = k + k_c - \omega^2(m + M_h + m_c) = 0 \Rightarrow$$

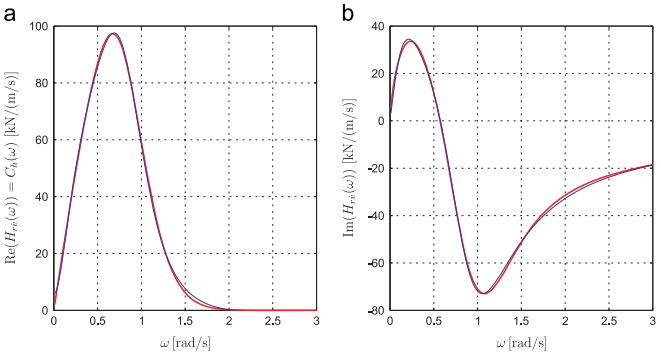

Fig. 2. Rational approximation of order $(m,n)=(2,3)$ to $H_{rv}(\omega)$. (a) $\mathrm{Re}(H_{rv}(\omega))$. (b) $\mathrm{Im}(H_{rv}(\omega))$. ——: Numerical determined target frequency response function. ——: Rational approximation.

$$k_c - \omega^2 m_c = -k + \omega^2(m + M_h) \tag{24}$$

$$c_c = C_h \tag{25}$$

Insertion of Eqs. (24) and (25) into Eq. (23) provides the following result for the optimal time-averaged power outtake (Falnes, 2002a):

$$\overline{P}_{a,\mathrm{opt}}(\omega) = \frac{1}{8}\frac{|F_e(\omega)|^2}{C_h(\omega)} \tag{26}$$

The tuning condition in Eq. (24) implies that the absorber is at resonance at optimal control. Under stationary harmonic excitation with the angular frequency ω, the condition is equivalent to $M\ddot{v}(t) + Kv(t) = 0$. Insertion of this relation in Eq. (16) provides the following relation between the wave excitation force and the absorber velocity at optimal control:

$$f_e(t) = (c_c + C_h)\dot{v}(t) = 2C_h\dot{v}(t) \tag{27}$$

Eq. (27) shows that the wave excitation force and the velocity response are in phase at optimal control, which is a well-known result for a linear single-degree-of-freedom oscillator at resonance under harmonic excitation.

With the tuning parameters determined by Eq. (24) and (25), the optimal control law for the stationary harmonic response due to monochromatic wave excitation may be written as

$$f_c(t) = m_c\ddot{v}(t) + k_c v(t) + c_c\dot{v}(t) = -(m + M_h)\ddot{v}(t) - kv(t) + C_h\dot{v}(t) \tag{28}$$

3. Rational approximation to the radiation force

The convolution integral defining the integral part $f_{r,0}(t)$ of the radiation force is replaced by an equivalent system of coupled first-order differential equations, which is solved along with the equations of motion of the absorber. The method is based on a replacement of the actual frequency response function $H_{r\dot{v}}(\omega)$ by an approximating rational function $\tilde{H}_{r\dot{v}}(\omega)$ given in the form

$$\tilde{H}_{r\dot{v}}(s) = \frac{P(s)}{Q(s)} \tag{29}$$

$$\left.\begin{aligned} P(s) &= p_0 s^m + p_1 s^{m-1} + \cdots + p_{m-1}s + p_m \\ Q(s) &= s^n + q_1 s^{n-1} + \cdots + q_{n-1,1}s + q_n \end{aligned}\right\}, \quad s = i\omega \tag{30}$$

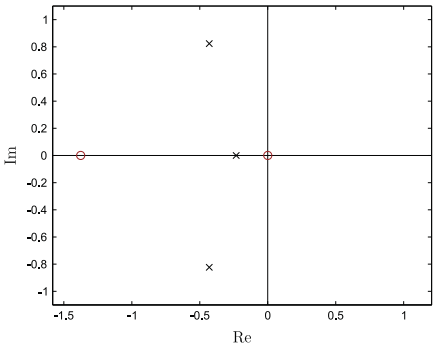

Fig. 3. Poles (x) and zeros (o) for the rational approximation of order $(m,n)=(2,3)$ to $H_{r\dot{v}}(\omega)$.

The parameters $p_0, p_1, \ldots, p_{m-1}, p_m$ and $q_1, \ldots, q_{n-1}, q_n$ are all real. Such a replacement is always possible, because the impulse response function $h_{r\dot{v}}(t)$ is causal. The order of the filter as given by the pair (m,n) may be chosen freely with the only restrictions that $m \le n$. Further, all poles must have negative real parts in order to ensure that the rational filter is asymptotic stable and strictly causal. The rational approximation may be obtained by the MATLAB control toolbox (Mathworks, 2011), as illustrated in Fig. 2. Fig. 3 shows the related zeros and poles of the approximation. Then, $f_{r,0}(t)$ may be obtained as output of the following system of differential equations:

$$f_{r,0}(t) = p_0\frac{d^m y}{dt^m} + p_1\frac{d^{m-1}y}{dt^{m-1}} + \cdots + p_{m-1}\frac{dy}{dt} + p_m y \tag{31}$$

$$\frac{d^n y}{dt^n} + q_1\frac{d^{n-1}y}{dt^{n-1}} + \cdots + q_{n-1}\frac{dy}{dt} + q_n y = \dot{v}(t) \tag{32}$$

where $y(t)$ is an auxiliary function, which cannot be related with any physical interpretation. Eq. (32) may be written in the following state vector form:

$$\frac{d}{dt}\mathbf{z}_r(t) = \mathbf{A}_r\mathbf{z}_r(t) + \mathbf{b}_r\dot{v}(t) \tag{33}$$

where

$$\mathbf{z}_r(t)=\begin{bmatrix} y(t)\\ \frac{d}{dt}y(t)\\ \frac{d^2}{dt^2}y(t)\\ \vdots\\ \frac{d^{n-2}}{dt^{n-2}}y(t)\\ \frac{d^{n-1}}{dt^{n-1}}y(t)\end{bmatrix},\quad \mathbf{b}_r=\begin{bmatrix}0\\0\\0\\\vdots\\0\\1\end{bmatrix} \tag{34}$$

$$\mathbf{A}_r=\begin{bmatrix} 0 & 1 & 0 & \cdots & 0 & 0\\ 0 & 0 & 1 & \cdots & 0 & 0\\ \vdots & \vdots & \vdots & \ddots & \vdots & \vdots\\ 0 & 0 & 0 & \cdots & 0 & 1\\ -q_n & -q_{n-1} & -q_{n-2} & \cdots & -q_2 & -q_1\end{bmatrix} \tag{35}$$

Similarly, Eq. (31) may be written in the vector form

$$f_{r,0}(t)=\mathbf{p}_r\mathbf{z}_r(t) \tag{36}$$

$$\mathbf{p}_r=[p_m\ \ p_{m-1}\ \ \cdots\ \ p_1\ \ p_0\ \ 0\ \ \cdots\ \ 0] \tag{37}$$

4. Optimal stochastic control

The determination of the optimal control in irregular sea-states involves a stochastic analysis of the dynamic system. In this respect the convention for indicating stochastic processes and random variable by upper case letters and their realizations by lower case letter will be adopted (Nielsen, 2007). The system is considered in the control interval $[t_0,t_1]$. Hence, the wave excitation process, the control force process and the displacement process are denoted as $\{F_e(t),t\in[t_0,t_1]\}$, $\{F_c(t),t\in[t_0,t_1]\}$ and $\{V(t),t\in[t_0,t_1]\}$, respectively, and arbitrary realizations of the said processes are denoted as $f_c(t)$, $f_e(t)$ and $v(t)$, respectively.

All state variables are assumed to be known at the initial time t_0, and are treated as deterministic quantities. We seek the control force process $\{F_c(t),t\in[t_0,t_1]\}$, which maximizes the absorbed mechanical energy $E_a=E_a[f_c(t),\dot v(t)]$ during the indicated control interval for almost all realizations of the involved process (also known as optimal control with probability one) subject to the initial value problem defined by Eq. (10), leading to the following optimization problem:

$$\begin{aligned}&\max\quad E_a[f_c(t),\dot v(t)]=\textstyle\int_{t_0}^{t_1} f_c(\tau)\dot v(\tau)\,d\tau\\ &\text{s.t.}\\ &\left\{\begin{array}{l}(m+m_h)\ddot v(t)+r(v(t))+\int_{t_0}^{t} h_{rv}(t-\tau)\dot v(\tau)\,d\tau=f_e(t)-f_c(\tau)\\ v(t_0)=v_0,\dot v(t_0)=\dot v_0\end{array}\right\}\end{aligned} \tag{38}$$

The optimal control is unchanged, if the performance functional is modified to $(1/t_1-t_0)E_a[f_c(t),\dot v(t)]$. We will assume that all involved stochastic processes are ergodic. Then, it follows for infinite control horizon, corresponding to $t_0\to-\infty$ and $t_1\to\infty$ (Nielsen, 2007)

$$\lim_{\substack{t_1\to\infty\\ t_0\to-\infty}}\frac{1}{t_1-t_0}\int_{t_0}^{t_1} f_c(\tau)\dot v(\tau)\,d\tau=E[F_c(t)\dot V(t)] \tag{39}$$

where $E[\,\cdot\,]$ indicates the expectation operator. Hence, at infinite control horizon and on condition of ergodic response processes the optimal control will be the one, which optimizes the expected (mean) value of the absorbed power $P_a(t)=F_c(t)\dot V(t)$. This represents the stochastic equivalence to the time averaging in Eq. (23) for harmonic monochromatic wave excitation.

The starting point is taken in Eqs. (10), (33) and (36), which may be combined in the following state vector equation of dimension $N=2+n$:

$$\left.\begin{array}{l}\dot{\mathbf{z}}(t)=\mathbf{g}(\mathbf{z}(t),f_c(t),t),\quad t\in]t_0,t_1]\\ \mathbf{z}(t_0)=\mathbf{z}_0\end{array}\right\} \tag{40}$$

where

$$\mathbf{z}(t)=\begin{bmatrix}v(t)\\ \dot v(t)\\ \mathbf{z}_r(t)\end{bmatrix} \tag{41}$$

$$\mathbf{g}(\mathbf{z}(t),f_c(t),t)=\begin{bmatrix}\dot v(t)\\ -\frac{1}{M}r(v(t))-\frac{1}{M}\mathbf{p}_r\mathbf{z}_r(t)+\frac{1}{M}(f_e(t)-f_c(t))\\ \mathbf{b}_r\dot v(t)+\mathbf{A}_r\mathbf{z}_r(t)\end{bmatrix} \tag{42}$$

where $M=m+m_h$.

Basically, there are two approaches to solve the indicated constrained optimization problem: the method of dynamic programming (Bellman, 1957), and the variational approach with Hamiltonian formalism (Pontryagin et al., 1964; Naidu, 2003). Here, the variational approach will be used. The Hamiltonian of the control problem is defined as

$$\begin{aligned}&H(\mathbf{z}(t),f_c(t),\boldsymbol\lambda(t),t)=f_c(t)\dot v(t)+\boldsymbol\lambda^T(t)\mathbf{g}(\mathbf{z}(t),f_c(t),t),\boldsymbol\lambda(t)=\begin{bmatrix}\lambda_v(t)\\ \lambda_{\dot v}(t)\\ \boldsymbol\lambda_r(t)\end{bmatrix}\\ &\Rightarrow H(\mathbf{z}(t),f_c(t),\boldsymbol\lambda(t),t)=-r(v(t))\frac{\lambda_{\dot v}(t)}{M}+\dot v(t)(f_c(t)+\lambda_v(t)+\mathbf{b}_r^T\boldsymbol\lambda_r(t))\\ &+\mathbf{z}_r^T(t)\left(-\mathbf{p}_r^T\frac{\lambda_{\dot v}(t)}{M}+\mathbf{A}_r^T\boldsymbol\lambda_r(t)\right)+\frac{\lambda_{\dot v}(t)}{M}\left(f_e(t)-f_c(t)\right)\end{aligned} \tag{43}$$

In the above equation, (43), $\boldsymbol\lambda(t)$ is the co-state vector, which forms the generalized momentum vector of the problem. The Euler–Lagrange stationarity conditions for optimal control become (Meirovitch, 1990; Soong, 1990)

State vector equation:

$$\dot{\mathbf{z}}(t)=\frac{\partial H}{\partial\boldsymbol\lambda}=\mathbf{g}(\mathbf{z}(t),f_c(t),t) \tag{44}$$

Co-state vector equation:

$$\dot{\boldsymbol\lambda}(t)=-\frac{\partial H}{\partial\mathbf{z}}=\begin{bmatrix}\frac{d}{dv}r(v(t))\frac{\lambda_{\dot v}(t)}{M}\\ -f_c(t)-\lambda_v(t)-\mathbf{b}_r\boldsymbol\lambda_r(t)\\ \mathbf{p}_r\frac{\lambda_{\dot v}(t)}{M}-\mathbf{A}_r^T\boldsymbol\lambda_r(t)\end{bmatrix} \tag{45}$$

Stationarity condition on the control force:

$$\begin{aligned}&\frac{\partial H(\mathbf{z}(t),f_c(t),\boldsymbol\lambda(t),t)}{\partial f_c}=\dot v(t)-\lambda_{\dot v}(t)\frac{1}{M}=\mathbf{0}\\ &\Rightarrow\lambda_{\dot v}(t)=M\dot v(t)\end{aligned} \tag{46}$$

Terminal condition on the co-state vector:

$$\boldsymbol\lambda(t_1)=\mathbf{0}\quad(\lambda_v(t_1)=\lambda_{\dot v}(t_1)=0,\boldsymbol\lambda_r(t_1)=\mathbf{0}) \tag{47}$$

Using Eq. (46) the first component equation in Eq. (45) provides the following solution for the co-state component $\lambda_v(t)$:

$$\begin{aligned}&\dot\lambda_v(t)=\frac{d}{dv}r(v(t))\dot v(t)=\frac{d}{dt}r(v(t))\\ &\Rightarrow\lambda_v(t)=r(v(t))-r(v(t_1))\end{aligned} \tag{48}$$

where the terminal condition (47) has been used in the last statement.

Using Eqs. (46) and (48) the second component equation in (45) provides the following solution for the optimal control force:

$$\dot{\lambda}_{\dot{v}}(t) = M\ddot{v}(t) = -f_c(t) - (r(v(t)) - r(v(t_1))) - \mathbf{b}_r^T \lambda_r(t)$$

$$\Rightarrow f_c(t) = -M\ddot{v}(t) - (r(v(t)) - r(v(t_1))) - \mathbf{b}_r^T \lambda_r(t) \tag{49}$$

Using Eq. (46) the third equation of (45) provides the following solution for the co-state sub-vector $\lambda_r(t)$:

$$\dot{\lambda}_r(t) = \mathbf{p}_r \dot{v}(t) - \mathbf{A}_r^T \lambda_r(t)$$

$$\Rightarrow \lambda_r(t) = -\int_t^{t_1} \mathrm{e}^{\mathbf{A}_r^T(\tau - t)} \mathbf{p}_r^T \dot{v}(\tau)\, d\tau \tag{50}$$

where the terminal condition (47) has been used, and $\mathrm{e}^{-\mathbf{A}_r^T t}$ represents the matrix exponential. Insertion of Eq. (50) in Eq. (49) provides the following representation for the optimal control force:

$$f_c(t) = -M\ddot{v}(t) - (r(v(t)) - r(v(t_1))) + \int_t^{t_1} \mathbf{p}_r\, \mathrm{e}^{\mathbf{A}_r(\tau - t)} \mathbf{b}_r \dot{v}(\tau)\, d\tau \tag{51}$$

The term $r(v(t_1))$ represents a static control force component useful for counteracting an external static force (time-averaged mean force) resulting in a non-zero mean displacement $v(t_1)$. However, the static reaction force has already been accounted for in the static equilibrium Eq. (1). Correspondingly, $f_c(t)$ has been defined as the dynamic component of the control force on the top of a possible static prestressing force. Hence, $f_c(t)$ must be zero in mean, so we will choose $v(t_1) = 0$. Then, the final form of the optimal control law in a finite control interval is given as

$$f_c(t) = -(m + m_h)\ddot{v}(t) - r(v(t)) + \int_t^{t_1} \mathbf{p}_r\, \mathrm{e}^{\mathbf{A}_r(\tau - t)} \mathbf{b}_r \dot{v}(\tau)\, d\tau \tag{52}$$

As seen the optimal control law is of the feedback type. This means that the control is optimal for both monochromatic and 2D and 3D irregular wave excitation, and during the transient phase, where the response is influenced by the initial conditions. The principal limitation of the control law (52) is that the integral component is non-causal, i.e. the control force component depends on future velocities ahead of the present time t. The velocity response process $\{\dot{V}(t), t \in [t_0, t_1]\}$ at optimal control is broad-banded reflecting a somewhat quasi-static dependence on the wave excitation process $\{F_e(t), t \in [t_0, t_1]\}$. So, prediction of the velocity response during a sufficiently long time interval ahead of the present time is related with significant uncertainty.

Next, consider the case of an infinite control horizon, i.e. $t_0 = -\infty$ and $t_1 = \infty$. Then, the solution to Eq. (33) becomes

$$\mathbf{z}_r(t) = \int_{-\infty}^{t} \mathrm{e}^{\mathbf{A}_r(t - \tau)} \mathbf{b}_r \dot{v}(\tau)\, d\tau \tag{53}$$

$f_{r,0}(t)$ follows from Eqs. (8) and (36)

$$f_{r,0}(t) = \int_{-\infty}^{t} h_{r\dot{v}}(t - \tau) \dot{v}(\tau)\, d\tau = \int_{-\infty}^{t} \mathbf{p}_r\, \mathrm{e}^{\mathbf{A}_r(t - \tau)}\, \mathbf{b}_r \dot{v}(\tau)\, d\tau \tag{54}$$

Hence, the following representation of the impulse response function in terms of the applied rational approximation applies

$$h_{r\dot{v}}(t) = \mathbf{p}_r\, \mathrm{e}^{\mathbf{A}_r t}\, \mathbf{b}_r \tag{55}$$

Then, Eq. (52) may be written as

$$f_c(t) = -(m + m_h)\ddot{v}(t) - r(v(t)) + \int_t^{\infty} h_{r\dot{v}}(\tau - t) \dot{v}(\tau)\, d\tau \tag{56}$$

The velocity response of the absorber at optimal control with infinite control horizon follows by insertion of Eq. (56) into Eq. (10), which is reduced to

$$\int_{-\infty}^{t} h_{r\dot{v}}(t - \tau) \dot{v}(\tau)\, d\tau + \int_t^{\infty} h_{r\dot{v}}(\tau - t) \dot{v}(\tau)\, d\tau = f_e(t)$$

$$\Rightarrow \int_{-\infty}^{\infty} h_{r\dot{v}}(|t - \tau|) \dot{v}(\tau)\, d\tau = f_e(t) \tag{57}$$

As seen from Eq. (57) the main effect of the optimal control force is to eliminate the inertial force and the buoyancy stiffness from the equation of motion. Since large motions take place during optimal control, it is important that the exact non-linear buoyancy function $r(v(t))$, and not merely the linear version $kv(t)$, is applied in the control law. Eq. (57) is a Fredholm integral equation of the first kind with infinite kernel support. Since the integral equation is linear, it follows that the velocity process $\{\dot{V}(t), t \in R\}$ and hence the displacement process $\{V(t), t \in R\}$ at optimal control become zero mean stationary Gaussian processes, if the wave excitation process $\{F_e(t), t \in R\}$ is modeled as a zero mean stationary Gaussian process, despite the physical system being intrinsic non-linear.

Fourier transformation of Eq. (57) provides the following relation between the Fourier transforms $\dot{V}(\omega)$ and $F_e(\omega)$ of the velocity at optimal control $\dot{v}(t)$ and the wave excitation force $f_e(t)$:

$$F_e(\omega) = 2C_h(\omega)\dot{V}(\omega) \tag{58}$$

where the following result has been used, cf. Eq. (11):

$$\int_{-\infty}^{\infty} \mathrm{e}^{-i\omega t} h_{r\dot{v}}(|t|)\, dt = 2\int_0^{\infty} \cos(\omega t) h_{r\dot{v}}(t)\, dt = 2C_h(\omega) \tag{59}$$

Since $C_h(\omega)$ is real, Eq. (58) shows that, at optimal control, all harmonic components of the velocity and the wave excitation force are in phase. Hence, Eq. (58) merely generalizes the condition (27) for optimal control at monochromatic wave excitation.

5. Optimal causal feedback control

The non-causality of the optimal control law given by Eq. (56) implies that it cannot be implemented for practical applications, unless future velocities can be predicted. To circumvent this obstacle a closely related causal control law is suggested in this section.

The starting point is taken from the optimal control law (56), where the non-causal integral part is replaced by the term $2c_c\dot{v}(t) - f_{r,0}(t)$, resulting in the following causal control law:

$$f_c(t) = -(m + m_h)\ddot{v}(t) - r(v(t)) + 2c_c\dot{v}(t) - f_{r,0}(t)$$

$$-(m + m_h)\ddot{v}(t) + 2c_c\dot{v}(t) - r(v(t)) - \int_{-\infty}^{t} h_{r\dot{v}}(t - \tau) \dot{v}(\tau)\, d\tau \tag{60}$$

The unspecified gain factor c_c is determined by an optimality criterion for the absorbed mean power of the control force under the given sea-state. The rationale for Eq. (60) is seen by insertion into Eq. (10), which is reduced to

$$f_e(t) = 2c_c\dot{v}(t) \tag{61}$$

Fourier transformation of Eq. (61) provides the following relation between the related Fourier transforms:

$$F_e(\omega) = 2c_c\dot{V}(\omega) \tag{62}$$

So the causal control law (60) also enforces the velocity of the absorber into phase with the wave excitation force at all frequencies. Eq. (62) is quite similar to Eq. (58) with the difference that the proportionality coefficient is frequency independent. Similarly, due to the linear relation in Eq. (61), the response vector process $\{(V(t), \dot{V}(t)), t \in R\}$ becomes a zero mean stationary Gaussian process, if this is the case for the wave excitation process $\{F_e(t), t \in R\}$.

Since an infinite control horizon is considered and ergodicity has been assumed for all involved processes, the optimal causal control must optimize the mean (expected) power outtake of the

control force. This criterion is used to find the optimal gain factor c_c in case of plane irregular wave excitation.

The expected power absorbed by the causal control force becomes

$$\overline{P}_a = E[F_c(t)\dot{V}(t)] = -(m+m_h)E[\dot{V}(t)\ddot{V}(t)] + 2c_c E[\dot{V}^2(t)] - E[\dot{V}(t)r(V(t))] - \int_{-\infty}^{t} h_{r\dot{v}}(t-\tau)E[\dot{V}(t)\dot{V}(\tau)]\,d\tau \quad (63)$$

In the stationary state, where the response from the initial values has been dissipated, the normal distributed random variables $V(t)$ and $\dot{V}(t)$ are stochastically independent with zero mean values $E[V(t)] = E[\dot{V}(t)] = 0$ (Nielsen, 2007). In turn, this implies that $\dot{V}(t)$ and $r(V(t))$ are also stochastically independent, which means

$$E[\dot{V}(t)r(V(t))] = E[\dot{V}(t)]E[r(V(t))] = 0 \cdot E[r(V(t))] = 0 \quad (64)$$

Further, the following expectations apply (Nielsen, 2007):

$$\left.\begin{aligned} &E[\dot{V}(t)\ddot{V}(t)] = 0 \\ &E[\dot{V}(t)\dot{V}(t)] = \frac{1}{4c_c^2}\sigma_{F_e}^2 \\ &E[\dot{V}(t)\dot{V}(\tau)] = \kappa_{\dot{V}\dot{V}}(\tau-t) = \kappa_{\dot{V}\dot{V}}(t-\tau) = \frac{1}{4c_c^2}\kappa_{F_eF_e}(t-\tau) \end{aligned}\right\} \quad (65)$$

where Eq. (61) has been used. The term $\kappa_{\dot{V}\dot{V}}(\tau)$ denotes the auto-covariance functions of the velocity process, and $\sigma_{F_e}^2$ and $\kappa_{F_eF_e}(\tau)$ indicate the variance and auto-covariance function of the wave excitation process, respectively.

Insertion of the relations (64) and (65) into Eq. (63) provides the following result for the absorbed mean power:

$$\overline{P}_a = \frac{1}{2c_c}\sigma_{F_e}^2 - \frac{1}{4c_c^2}\int_{-\infty}^{t} h_{r\dot{v}}(t-\tau)\kappa_{F_eF_e}(t-\tau)\,d\tau = \sigma_{F_e}^2\left(\frac{1}{2c_c} - \frac{1}{4c_c^2}\int_0^{\infty}\rho_{F_eF_e}(u)h_{r\dot{v}}(u)\,du\right) \quad (66)$$

$$\rho_{F_eF_e}(\tau) = \frac{\kappa_{F_eF_e}(\tau)}{\sigma_{F_e}^2} \quad (67)$$

$\rho_{F_eF_e}(\tau)$ denotes the auto-correlation coefficient function of the wave excitation process. The qualitative variation of $\rho_{F_eF_e}(\tau)$ has been shown in Fig. 4 for monochromatic, narrow- and broad-banded stochastic wave excitation forces defined by the band-width parameter σ_f of the JONSWAP spectrum. In order to make the comparison meaningful, the separation time τ has been normalized with respect to the peak period T_p of the irregular sea state.

Next, $\overline{P}_a$ given by Eq. (66) is optimized with respect to the gain parameter c_c. The optimal gain factor becomes

$$c_c = \int_0^{\infty}\rho_{F_eF_e}(u)h_{r\dot{v}}(u)\,du \quad (68)$$

Insertion into Eq. (66) provides the following result for the optimal absorbed mean power:

$$\overline{P}_{a,\mathrm{opt}} = \frac{1}{4}\frac{\sigma_{F_e}^2}{c_c} \quad (69)$$

Eq. (69) indicates the maximum mean power that can be absorbed under the considered control law on condition that the control force demand can be applied without significant time delay and without saturation problems.

For monochromatic wave excitation with the amplitude $|F_e|$ and the angular frequency ω, we have $\sigma_{F_e}^2 = \frac{1}{2}|F_e|^2$ and $\rho_{F_eF_e}(\tau) = \cos(\omega t)$. In this case Eqs. (68) and (69) become

$$c_c = \int_0^{\infty}\cos(\omega t)h_{r\dot{v}}(t)\,dt \quad (70)$$

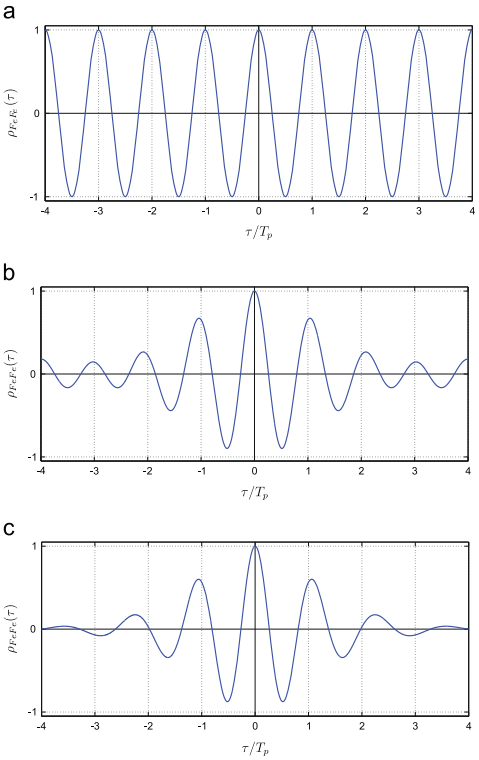

Fig. 4. Autocorrelation coefficient function of the wave excitation force. (a) Monochromatic wave excitation force. (b) Narrow-banded stochastic excitation force (swells, $\sigma_f = 0.01$). (c) Broad-banded stochastic wave excitation force (wind waves, $\sigma_f = 1.0$).

$$\overline{P}_{a,\mathrm{opt}} = \frac{1}{8}\frac{|F_e|^2}{c_c} \quad (71)$$

Upon comparison with Eq. (11) it follows that the optimal control gain in this case becomes $c_c = C_h(\omega)$. Then, the mean power absorbed by the suboptimal causal controller becomes identical to the optimal absorbed mean power under monochromatic wave excitation as given by Eq. (26). Hence, the suboptimal causal controller is optimal under monochromatic wave excitation with the tuning of the gain parameter given in Eq. (70).

The auto-covariance function of the wave excitation force is related to the double-sided auto-spectral density function $S_{F_eF_e}(\omega)$ by the Wiener–Khintchine relation (Nielsen, 2007):

$$\kappa_{F_eF_e}(\tau) = \int_{-\infty}^{\infty} e^{i\omega\tau}S_{F_eF_e}(\omega)\,d\omega \quad (72)$$

$S_{F_eF_e}(\omega)$ follows from (12) (Nielsen, 2007):

$$S_{F_eF_e}(\omega) = |H_{e\eta}(\omega)|^2 S_{\eta\eta}(\omega) \quad (73)$$

where $S_{\eta\eta}(\omega)$ is the double-sided auto-spectral density function of the sea-surface elevation process $\{\eta(t), t\in R\}$. This is modeled as a zero mean, stationary Gaussian process defined by the following slightly modified double-sided version of the JONSWAP spectrum

(Hasselmann et al., 1973):

$$S_{\eta\eta}(\omega)=\beta\frac{H_s^2}{\omega_p}\gamma^{\alpha}\left(\frac{|\omega|}{\omega_p}\right)^{-5}\exp\left(-\frac{5}{4}\left(\frac{\omega}{\omega_p}\right)^{-4}\right) \tag{74}$$

where

$$\left.\begin{aligned}&\alpha=\exp\left(-\frac{1}{2}\left(\frac{|\omega|-\omega_p}{\sigma_f\omega_p}\right)^2\right)\\&T_p=\frac{2\pi}{\omega_p}=\sqrt{\frac{180H_s}{g}}\\&\gamma=3.3\end{aligned}\right\} \tag{75}$$

T_p is the peak period, $\omega_p=2\pi/T_p$ is the related angular peak frequency, H_s is the significant wave height, and σ_f is a bandwidth parameter. β is a normalization parameter to be determined, so the relation $H_s=4.0\sigma_\eta$ is fulfilled, corresponding to Rayleigh-distributed wave heights. In the present version the bandwidth parameter σ_f is assumed to be frequency independent, in contrast to the original formulation of the spectrum (Hasselmann et al., 1973). As seen, the irregular sea-state is merely defined by the two parameters σ_f and H_s. The auto-spectral density function has been shown in Fig. 5 with various values of σ_f.

Finally, the expected absorbed power by the optimal control force given by Eq. (56) becomes

$$\begin{aligned}\overline{P}_{a,\mathrm{opt}}&=E[F_c(t)\dot{V}(t)]\\&=-(m+m_h)E[\dot{V}(t)\ddot{V}(t)]-E[\dot{V}(t)r(V(t))]+\int_t^\infty h_{r\dot{V}}(\tau-t)E[\dot{V}(t)\dot{V}(\tau)]\,d\tau\\&=\int_0^\infty\kappa_{\dot{V}\dot{V}}(u)h_{r\dot{V}}(u)\,du\end{aligned} \tag{76}$$

The auto-covariance function, $\kappa_{\dot{V}\dot{V}}(u)$, of the velocity process at optimal control follows from the Wiener–Khintchine relation, cf. Eq. (72):

$$\kappa_{\dot{V}\dot{V}}(\tau)=\int_{-\infty}^{\infty}e^{i\omega\tau}S_{\dot{V}\dot{V}}(\omega)\,d\omega=2\int_0^\infty\cos(\omega\tau)S_{\dot{V}\dot{V}}(\omega)\,d\omega \tag{77}$$

where the double-sided auto-spectral density function is given as, cf. Eqs. (58) and (73):

$$S_{\dot{V}\dot{V}}(\omega)=\frac{S_{F_eF_e}(\omega)}{4C_h^2(\omega)}=\frac{|H_{e\eta}(\omega)|^2}{4C_h^2(\omega)}S_{\eta\eta}(\omega) \tag{78}$$

$|H_{e\eta}(\omega)|$, $C_h(\omega)$ and $S_{\eta\eta}(\omega)$ all approach zero as $\omega\to\infty$. Especially $C_h(\omega)$ and $|H_{e\eta}(\omega)|$ are approaching zero quite fast as seen in Figs. 8a and 11. However, since these functions are determined numerically, the limit passing of the right-hand side of Eq. (78) is uncertain. Actually, spurious spectral peaks may evolve due to numerical discretization errors. Since very little energy is present in the auto-spectrum $S_{\eta\eta}(\omega)$ for $\omega>2\omega_p$, the indicated numerical problem may be circumvented simply by the assigning $C_h(\omega)=C_h(2\omega_p)$ for $\omega\geq2\omega_p$.

6. Numerical example

The theory is illustrated with the heave absorber in Fig. 6, consisting of a cylindrical volume with a diameter D. The bottom consists of a hemisphere with the same diameter as the cylinder. The bottom is filled with ballast to stabilize the floater from capsizing. The relevant data has been indicated in Table 1. The impulse response function for the radiation force and the wave excitation force are shown in Figs. 7 and 10. The real and imaginary parts of the related frequency response functions are shown in Figs. 8 and 11, respectively. Since the real parts are even functions of ω, and the imaginary parts are odd functions of ω, results have only been indicated for positive angular frequencies. Finally, Fig. 9 indicates the added hydrodynamic mass. Again, due to the symmetry of the function, results have only been shown for positive angular frequencies.

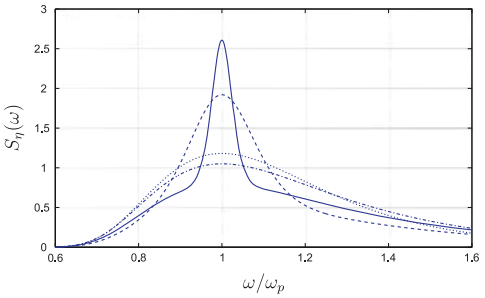

Fig. 5. One-sided modified JONSWAP auto-spectral density function as a function of the bandwidth parameter σ_f, $H_s=3$ m. ——: $\sigma_f=0.03$. – – –: $\sigma_f=0.1$. · · · : $\sigma_f=0.5$. — · — · —: $\sigma_f=1.0$.

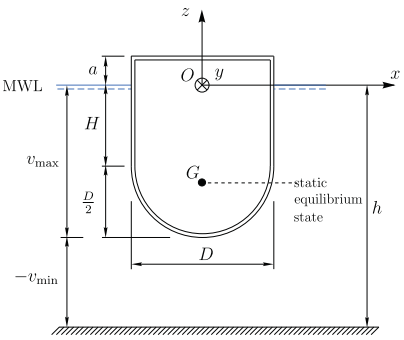

Fig. 6. Geometry of heave absorber.

Table 1
Heave absorber parameters.

a	8.00 m	m	1.84×10^6 kg
H	7.00 m	m_h	0.44×10^6 kg
D	14.00 m	ρ	1000 kg/m^3
h	30.00 m	g	9.81 m/s^2

Fig. 12 shows the mean power absorbed by the optimal control as given by Eq. (76) and by the optimal tuned causal controller as given by Eq. (69) as a function of H_s and σ_f. As seen, the performance of the suboptimal causal controller is very close to that of the optimal controller at all parameter values.

Fig. 13 shows the variation of the normalized mean power absorbed by the optimal tuned causal control force as a function of H_s for various values of the bandwidth parameter σ_f. The results have been normalized with respect to the $2\sigma_\eta^2=\frac{1}{8}H_s^2$. Notice, in case of monochromatic wave excitation with the wave amplitude η_0 the following relation is holds $2\sigma_\eta^2=\eta_0^2$. There is a significant variation of the normalized absorbed mean power with the significant wave height. This may be explained with reference to the second equation in (75), showing that the angular peak frequency ω_p has an inverse square root dependence on H_s. Hence, the peak value of the one-sided auto-spectral density function $S_\eta(\omega)$ will shift towards lower angular frequencies as H_s is

increased. Further, the modulus of the frequency response function $|H_{e\eta}(\omega)|$ is a decreasing function of ω, cf. Fig. 11. This means that the variance of the wave excitation force $\sigma_{F_e}^2$, with the main contribution given by the integral of $|H_{e\eta}(\omega)|^2 S_\eta(\omega)$ in the vicinity of $\omega = \omega_p$, will increase significantly with increasing H_s. On the other hand the optimal gain factor, c_c, as given by Eq. (68), only has a moderate dependence on H_s. As a result the optimal absorbed mean power increases with H_s, even after normalization with $2\sigma_\eta^2$.

Fig. 14 shows the corresponding variation of the normalized mean power absorbed by the optimal tuned causal control force as a function of σ_f for various values of H_s. The normalized absorbed mean power becomes almost independent of the bandwidth parameter for $\sigma_f > 0.5$. A possible explanation is that the one-sided auto-spectral density function $S_\eta(\omega)$ becomes increasingly independent of σ_f as the bandwidth parameter increased, as seen in Fig. 5.

Considering first-order wave theory the realizations of the stationary wave excitation force process may be obtained by the following random phase model (Nielsen, 2007):

$$f_e(t) = \sum_{j=1}^{J} \sqrt{2} f_j \cos(\omega_j t - \varphi_j), \quad \omega_j = (j-1)\Delta\omega \tag{79}$$

where, cf. (73):

$$f_j = \sqrt{2 S_{F_e F_e}(\omega_j)\Delta\omega} = \sqrt{2|H_{e\eta}(\omega_j)|^2 S_{\eta\eta}(\omega_j)\Delta\omega} \tag{80}$$

J is the number of harmonic components in the spectral decomposition, f_j denotes the standard deviation of harmonic components with angular frequencies in the interval $]\omega_j, \omega_j + \Delta\omega]$.

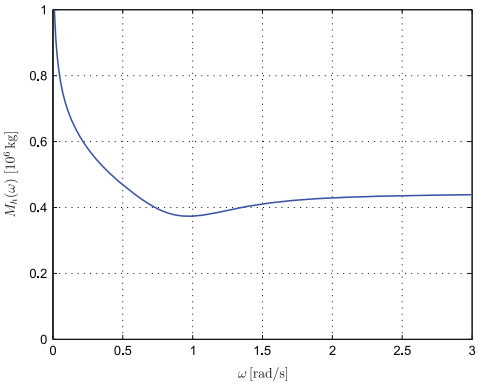

Fig. 9. Hydrodynamic added mass, $M_h(\omega)$.

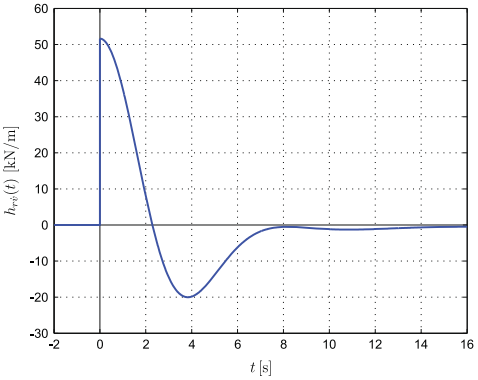

Fig. 7. Impulse response function for the radiation force, $h_{re}(t)$.

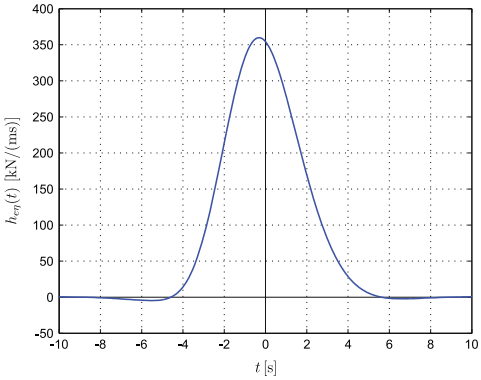

Fig. 10. Impulse response function for the wave excitation force, $h_{e\eta}(t)$.

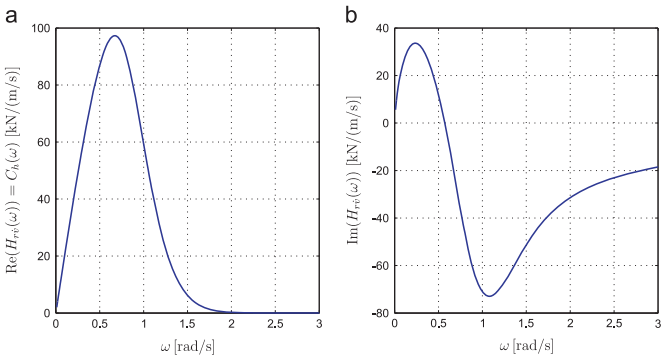

Fig. 8. Frequency response function for the radiation force. (a) $\mathrm{Re}(H_{re}(\omega))$. (b) $\mathrm{Im}(H_{re}(\omega))$.

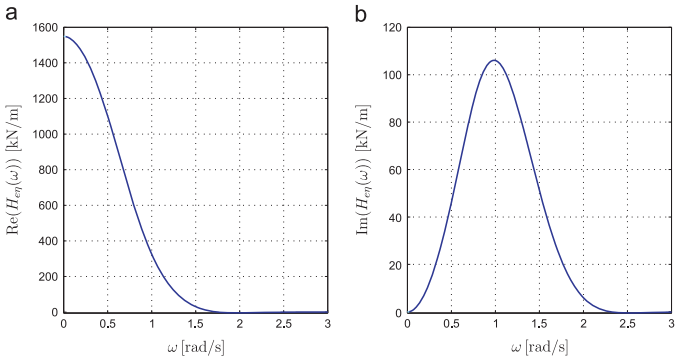

Fig. 11. Frequency response function for the wave excitation force. (a) $\mathrm{Re}(H_{e\eta}(\omega))$. (b) $\mathrm{Im}(H_{e\eta}(\omega))$.

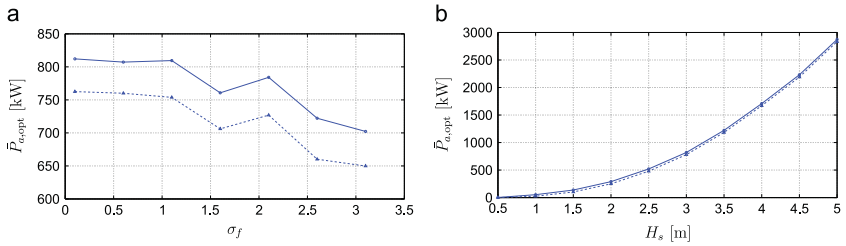

Fig. 12. Absorbed mean power by optimal control and optimal tuned causal control. — Optimal control. - - - Optimal tuned causal control. (a) Variation with σ_f, $H_s = 3$ m. (b) Variation with H_s, $\sigma_f = 0.1$.

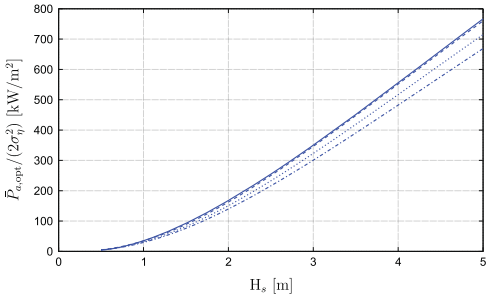

Fig. 13. Variation of normalized optimal absorbed mean power $\overline{P}_{a,\mathrm{opt}}/(2\sigma_\eta^2)$ by the causal controller as a function of H_s. — $\sigma_f = 0.1$. - - - $\sigma_f = 0.5$. ⋯ $\sigma_f = 1.0$. - · - · $\sigma_f = 5.0$.

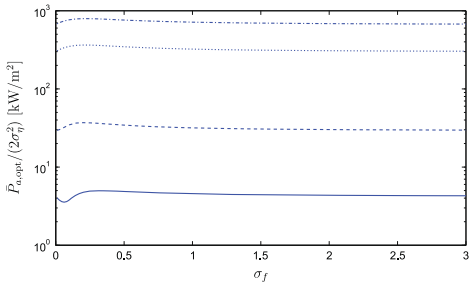

Fig. 14. Variation of normalized optimal absorbed mean power $\overline{P}_{a,\mathrm{opt}}/(2\sigma_\eta^2)$ by the causal controller as a function of σ_f. — $H_s = 0.5$ m. - - - $H_s = 1.0$ m. ⋯ $H_s = 3.0$ m. - · - · $H_s = 5.0$ m.

φ_j denote samples of the random variables Φ_j, which are mutually independent and uniformly distributed in $[0, 2\pi]$.

Then, by the use of Eqs. (61) and (79) the following time series of the displacement $v(t)$, the velocity $\dot{v}(t)$ and the acceleration $\ddot{v}(t)$ under optimal tuned causal control are obtained as follows:

$$\left.\begin{aligned} v(t) &= \sum_{j=1}^{J} \frac{f_j}{\sqrt{2}\omega_j c_c} \sin(\omega_j t - \varphi_j) \\ \dot{v}(t) &= \sum_{j=1}^{J} \frac{f_j}{\sqrt{2}c_c} \cos(\omega_j t - \varphi_j) \\ \ddot{v}(t) &= -\sum_{j=1}^{J} \frac{f_j \omega_j}{\sqrt{2}c_c} \sin(\omega_j t - \varphi_j) \end{aligned}\right\} \tag{81}$$

where c_c is given by Eq. (68). The corresponding time series at optimal control follow by the use of Eqs. (58) and (79):

$$\left.\begin{aligned} v(t) &= \sum_{j=1}^{J} \frac{f_j}{\sqrt{2}\omega_j C_h(\omega_j)} \sin(\omega_j - \varphi_j) \\ \dot{v}(t) &= \sum_{j=1}^{J} \frac{f_j}{\sqrt{2}C_h(\omega_j)} \cos(\omega_j t - \varphi_j) \\ \ddot{v}(t) &= -\sum_{j=1}^{J} \frac{f_j \omega_j}{\sqrt{2}C_h(\omega_j)} \sin(\omega_j t - \varphi_j) \end{aligned}\right\} \tag{82}$$

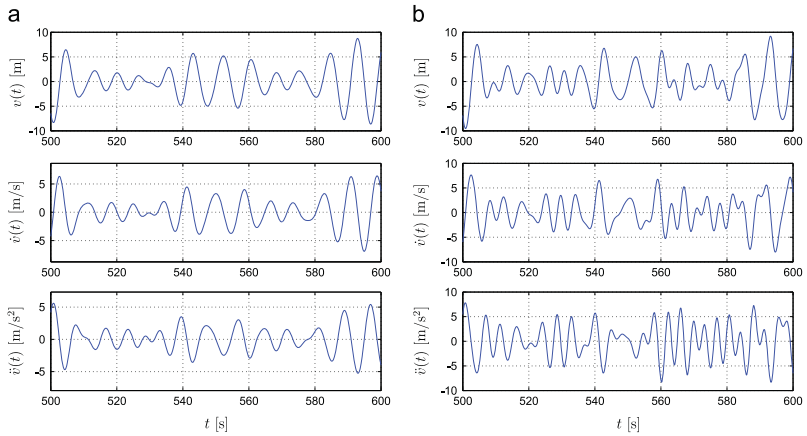

Fig. 15. Time series of the displacement $v(t)$, velocity $\dot{v}(t)$ and acceleration $\ddot{v}(t)$ of the absorber under feedback control, $\sigma_f = 0.1$, $H_s = 3$ m. (a) Optimal tuned causal control. (b) Optimal control.

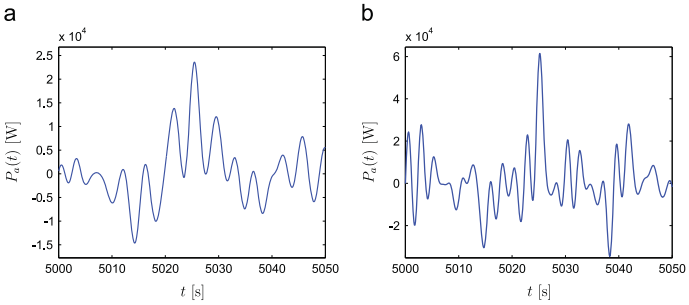

Fig. 16. Time series of instantaneous power outtake by optimal control and optimal tuned causal control, $\sigma_f = 0.1$, $H_s = 3$ m. — Optimal control. - - - Optimal tuned causal control.

In order to avoid spurious harmonics in the time series caused by discretization errors related to the numerical determination of $C_h(\omega)$, the assignment $C_h(\omega) = C_h(2\omega_p)$ for $\omega \geq 2\omega_p$ has been applied, cf. the remarks following Eq. (78).

The obtained time series are shown in Fig. 15a and b for the optimal tuned causal and optimal controllers, respectively. As seen, the response of the absorber is dominated by the peak angular frequency ω_p (T_p=7.42 s) in both cases.

Fig. 16a and b shows the time series of the instantaneous absorbed power for the optimal tuned causal controller and the optimal controllers, respectively. As seen, both time series are dominated by the angular frequency $2\omega_p$.

7. Concluding remarks

Based on optimal control theory, the optimal control law for a single point absorber in irregular sea-states has been derived, assuming nonlinear buoyancy stiffness and linear wave theory. The optimal controller is proved to be a closed-loop type, with feedback from the present displacement and acceleration and all future velocities of the absorber, making the control law non-causal. The study shows that the essential property of the optimal controller is to enforce all harmonic components of the wave excitation force into phase with the corresponding harmonic components of the absorber velocity with a frequency depending proportionality factor.

To circumvent the indicated non-causality problem, a causal closed-loop controller has been suggested with feedback from measurements of the present displacement and acceleration and all past velocities of the absorber, based on a slight modification of the optimal control law. The basic idea behind the control strategy is again to enforce the velocity response of the absorber into phase with the wave excitation force at any time. In this case the proportionality factor between the harmonic components is frequency independent. The said proportionality factor, which appears as an unspecified derivative gain parameter in the control law, has been optimized for a given irregular sea-state defined by the auto-spectral density function of the sea-surface elevation process. The optimal tuned causal controller is optimal under monochromatic wave excitation. In other sea states the controller is merely suboptimal. However, in case of plane irregular wave excitation, the study shows that the causal controller absorbs almost as much power as the optimal controller for all parameter values defining the auto-spectral density function.

Acknowledgements

The second author gratefully acknowledges the support from the Fundamental Research Funds for the Central Universities under Grant no. 2012-IV-016. The fifth author gratefully acknowledges the support from the Chinese Scholarship Council under the State Scholarship Fund.

References

Bellman, R.E., 1957. Dynamic Programming. Princeton University Press.
Cummins, W., 1962. The impulse response functions and ship motions. Schiffstechnik 9, 101–109.
Falnes, J., 1995. On non-causal impulse response functions related to propagating water waves. Applied Ocean Research 17 (6), 379–389.
Falnes, J., 2002a. Ocean Waves and Oscillating Systems: Linear Interactions Including Wave-Energy Extraction. Cambridge University Press.
Falnes, J., 2002b. Optimum control of oscillation of wave-energy converters. Journal of Offshore and Polar Engineering 12 (2).
Falnes, J., 2007. A review of wave-energy extraction. Marine Structures 20, 185–201.
Falnes, J., Budal, K., 1978. Wave Power Conversion by Point Absorbers. Norwegian Maritime Research.
Faltinsen, O., 1990. Sea Loads on Ships and Offshore Structures. Cambridge University Press.
French, M.J., 1979. A generalized view of resonant energy transfer. Journal Mechanical Engineering Science 21 (4), 299–300.
Hals, J., Falnes, J., Moan, T., 2011. Constrained optimal control of a heaving buoy wave-energy converter. Applied Offshore Mechanics and Arctic Engineering 133, 1–15.
Hasselmann, K., et al., 1973. Measurements of Wind Wave Growth and Swell Decay During the Joint North Sea Project (JONSWAP). Erganzungsheft zur Deutschen Hydrograph. Z., Reihe A, No. 12, Hamburg.
Li, G., Weiss, G., Mueller, M., Townley, S., Belmont, M.R., 2012. Wave energy converter control by wave prediction and dynamic programming. Renewal Energy 48, 392–403.
Lopez, M.F.P., Hals, J., Gomes, R.P.F., Moan, T., Gato, L.M.C., Falcao, A.F.O., 2009. Experimental and numerical investigation of non-predictive phase control strategies for a point-absorbing wave energy converter. Journal of Ocean Engineering 36, 386–402.
Mathworks, 2011. Control System Toolbox 9.1. Mathworks, Inc.
Meirovitch, L., 1990. Dynamics and Control of Structures. John Wiley & Sons, Inc.
Naidu, D.S., 2003. Optimal Control Systems. CRC Press, Boca Raton, FL.
Newman, J., 1977. Marine Hydrodynamics. The MIT Press.
Nielsen, S.R.K., 2007. Structural dynamics. In: Linear Stochastic Dynamics, 5th edition, vol. 3. Aalborg University (ISSN 1901-7286).
Pelamis Wave, 2012. Pelamis Wave Power ⟨http://www.pelamiswave.com/⟩.
Pontryagin, L.S., Boltyanskii, V.G., Gamkrelitze, R.V., Mishenko, E.F., 1964. The Mathematical Theory of Optimal Processes. MacMillan, New York.
Ruellan, M., BenAhmed, H., Multon, B., Josset, C., Babarit, A., Clement, A., 2010. Design methodology for a SEAREV wave energy converter. IEEE Transactions on Energy Conversion 25 (3), 760–767.
Schoen, M.P., Hals, J., Moan, T., 2008a. Robust control of heaving wave energy devices in irregular waves. In: Proceedings of the 16th Mediterranean Conference on Control and Automation, Ajaccio, France, June 25–27, 2008.
Schoen, M.P., Hals, J., Moan, T., 2008b. Wave prediction and fuzzy logic control of wave energy converters in irregular waves. In: Proceedings of the 16th Mediterranean Conference on Control and Automation, Ajaccio, France, June 25–27, 2008.
Soong, T.T., 1990. Active Structural Control: Theory and Practice. John Wiley & Sons, Inc.
Valerio, D., Beirao, P., Costa, J.S., 2007. Reactive control and phase and amplitude control applied to the archimedes wave swing. In: Proceedings of the Seventeenth International Offshore and Polar Engineering Conference, Lisbon, Portugal, July 1–6, 2007.
WAMIT, 2011. WAMIT User Manual, Version 7.0. WAMIT, Inc. Technical Report Manual ⟨http://www.wamit.com/⟩.
Wave Star, 2005. Wave Star A/S ⟨http://www.wavestarenergy.com/⟩.
Wavedragon, 2005. Wave Dragon ⟨http://www.wavedragon.net/⟩.
Yu, Z., Falnes, J., 1995. State-space modeling of a vertical cylinder in heave. Applied Ocean Research 17, 265–275.

APPENDIX I
Stability Analysis of the Gyroscopic Power Take-Off Wave Energy Point Absorber

Paper 8
The paper presented in this appendix is published in *Journal of Sound and Vibration*, 2015, Volume 355, Pages 418-433, DOI: 10.1016/j.jsv.2015.06.029.

http://www.sciencedirect.com/science/article/pii/S0022460X15005118

I.1 Author's Right

Journal author rights

In order for Elsevier to publish and disseminate research articles, we need publishing rights. This is determined by a publishing agreement between the author and Elsevier. This agreement deals with the transfer or license of the copyright to Elsevier and authors retain significant rights to use and share their own published articles. Elsevier supports the need for authors to share, disseminate and maximize the impact of their research and these rights, in Elsevier proprietary journals* are defined below:

For subscription articles	For open access articles
Authors transfer copyright to the publisher as part of a journal publishing agreement, but have the right to: • Share their article for Personal Use, Internal Institutional Use and Scholarly Sharing purposes, with a DOI link to the version of record on ScienceDirect (and with the Creative Commons CC-BY-NC- ND license for author manuscript versions) • Retain patent, trademark and other intellectual property rights (including raw research data). • Proper attribution and credit for the published work.	Authors sign an exclusive license agreement, where authors have copyright but license exclusive rights in their article to the publisher**. In this case authors have the right to: • Share their article in the same ways permitted to third parties under the relevant user license (together with Personal Use rights) so long as it contains a CrossMark logo, the end user license, and a DOI link to the version of record on ScienceDirect. • Retain patent, trademark and other intellectual property rights (including raw research data). • Proper attribution and credit for the published work.

http://www.elsevier.com/journal-authors/author-rights-and-responsibilities

Journal of Sound and Vibration 355 (2015) 418–433

Contents lists available at ScienceDirect

Journal of Sound and Vibration

journal homepage: www.elsevier.com/locate/jsvi

Stability analysis of the Gyroscopic Power Take-Off wave energy point absorber

Søren R.K. Nielsen [a,*], Zili Zhang [a], Morten M. Kramer [a], Jan Olsen [b]

[a] Department of Civil Engineering, Aalborg University, 9000 Aalborg, Denmark
[b] JOLTECH, Langbrogade 3, 6400 Sønderborg, Denmark

ARTICLE INFO

Article history:
Received 23 February 2015
Received in revised form
29 May 2015
Accepted 15 June 2015
Handling Editor: Ivan Kovacic
Available online 3 July 2015

ABSTRACT

The Gyroscopic Power Take-Off (GyroPTO) wave energy point absorber consists of a float rigidly connected to a lever. The operational principle is somewhat similar to that of the so-called gyroscopic hand wrist exercisers, where the rotation of the float is brought forward by the rotational particle motion of the waves. At first, the equations of motion of the system are derived based on analytical rigid body dynamics. Next, assuming monochromatic waves simplified equations are derived, valid under synchronisation of the ring of the gyro to the angular frequency of the excitation. Especially, it is demonstrated that the dynamics of the ring can be described as an autonomous nonlinear single-degree-of-freedom system, affected by three different types of point attractors. One where the ring vibrations are attracted to a static equilibrium point indicating unstable synchronisation and two types of attractors where the ring is synchronised to the wave angular frequency, either rotating in one or the opposite direction. Finally, the stability conditions and the basins of attraction to the point attractors defining the synchronised motion are determined.

1. Introduction

The idea of using the gyroscopic moment on a spinning flywheel to absorb wave energy from a floating structure is not new, see e.g. the OCEANTEC Wave Energy Converter [1], and the devices of Kanki et al. [2,3], and Bracco et al. [4,5]. Common to these previous developments is a mechanical system made up of a spinning flywheel with a gimbal and a power-take off system connected to the gimbal along its rotational axis. The wave induced pitch and roll motion of the float produces a time variation of the orientation of the spin axis, which combined with the spinning velocity of a flywheel creates a gyroscopic torque parallel to the precession axes. In turn, the gyroscopic torque induces a precession of the gimbal making the capture of wave energy possible. The underlying dynamics of the indicated developments was investigated by Townsend and Shenoi [6], who demonstrated that strong nonlinearities including period doubling were present in the dynamic responses of the float.

The operation principle of the GyroPTO wave energy point absorber is somewhat similar to that of the so-called gyroscopic hand wrist exerciser sold under the names Dynabee, Powerball or Dynaflex, the dynamics of which was described by Gulick and O'Reilly [7]. The spin-axis of the flywheel is supported by a track on a ring with a width slightly

* Corresponding author. Tel.: +45 9940 8451, fax: +45 9814 8552.
E-mail addresses: srkn@civil.aau.dk (S.R.K. Nielsen), zlz@civil.aau.dk (Z. Zhang), mmk@civil.aau.dk (M.M. Kramer), JAO@joltech.dk (J. Olsen).

http://dx.doi.org/10.1016/j.jsv.2015.06.029
0022-460X/

larger than the diameter of the axis. The track forms a guidance for the precession of the spin-axis, which is assumed to roll on the inner side of the track during rotations of the ring without any slip. If the ring is set in rotation with a certain angular frequency, a gyroscopic moment is generated in the plane of the ring and at right angle to the spin-axis. In turn this moment produces the necessary contact force between the spin axis and the inner side of the track to provide the friction force making the rolling of spin-axis possible. Hence, the gyroscopic moment enforces a kinematical constrain between the rotational velocities of the spin-axis and the ring and makes the former to rotate at a large angular velocity. Further, in case the ring is subjected to external harmonic vibrations with a given angular frequency and orientation, it turns out that the angular frequency of the ring may synchronise with the angular frequency of the excitation. The stator and the rotor of the electric power generator are fixed to the ring and the spin axis of the flywheel, respectively.

The principle has previously been under consideration for energy harvesting assuming that the system was subjected to a prescribed harmonic varying external rotation of the plane of the ring [8,9]. These studies demonstrated that stable synchronised precession of the ring only appears for some amplitude and frequency of the external excitation and that discontinuous state solutions exist for different initial conditions [9].

The GyroPTO wave energy absorber consists of a float rigidly connected to a lever. In the other end the lever is supported by a hinge, which allows for rotations around a horizontal and vertical axis. The construction may be classified as a socalled wave energy point absorber, which is defined as a device with geometrical dimensions that are small compared to a characteristic wavelength of the seastate and is capable of absorbing energy from waves propagating in all directions [10]. The equations of motion are nonlinear for which reason subharmonic or even chaotic response may occur under harmonic wave excitation. However, when synchronisation of the angular frequency of the ring to the angular frequency of the wave loading takes place, the response of the float becomes almost harmonic. This phenomenon is the basic reason for the functioning of the system. At synchronisation, this means that the generated electric power becomes almost constant in time, making the need for expensive additional power electronics unnecessary before the power can be supplied to the grid. This is in contrast to other wave energy point absorbers, where the instantaneous absorbed power varies significantly with time, making such power electronics mandatory.

In the paper, the equations of motion of the device are at first derived based on analytical rigid body dynamics. The wave loading on the float is described based on the first-order wave theory, where the related hydrodynamic coefficients are assumed to be calculated numerically. Next, the dynamics of the ring at synchronisation can be described by an autonomous nonlinear single-degree-of-freedom system with parametric excitation. The said equation is related with three types of point attractors. One where the ring vibrations are attracted to a state of rest indicating unstable synchronisation, and the other two types of point attractors where the ring is synchronised to the wave angular frequency, either rotating in one or the opposite direction. Finally, the stability and the basins of attraction of the synchronised point attractors are determined.

2. Mechanics of GyroPTO point absorber

2.1. Rigid body dynamics of GyroPTO point absorber

The point absorber consists of a float with a ring and a flywheel inside, see Fig. 1. The float of the GyroPTO device is made up of two semi-spheres with the diameter d connected with a cylindrical part with the height c, see Fig. 2. The spin-axis of the flywheel has the radius r_1, and the inner radius of the track of the ring is r_2. If the ring is set in motion with the angular

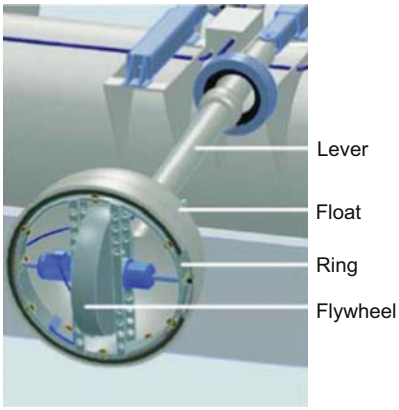

Fig. 1. Schematic details of the GyroPTO point absorber.

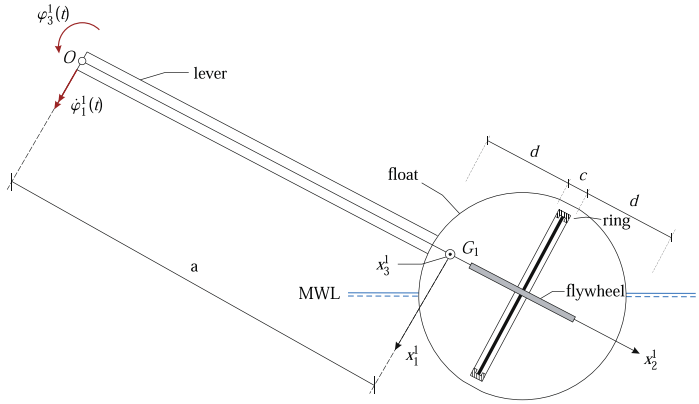

Fig. 2. Schematic geometry of GPTO point absorber. Definition of the (x_1^1, x_2^1, x_3^1)-coordinate system fixed to the float and lever.

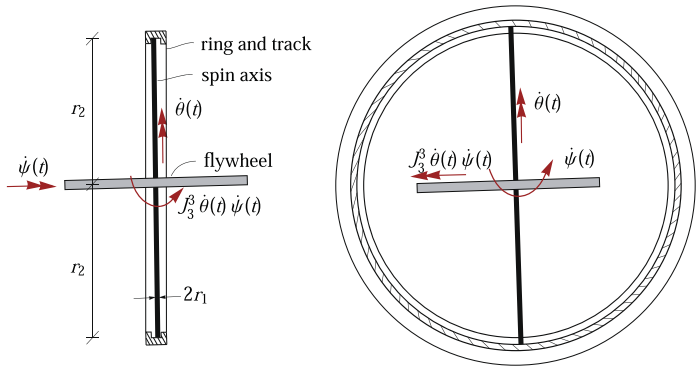

Fig. 3. Rolling contact between the precessing ring and the spinning flywheel.

frequency $\dot{\psi}(t)$, a gyroscopic moment $J_3^3\dot{\theta}(t)\dot{\psi}(t)$ on the flywheel is generated according to the law of moment of momentum, where J_3^3 is the polar mass moment of inertia, and $\dot{\theta}(t)$ is the angular spin frequency of the flywheel. With the sign definitions given in Fig. 3, the no-slip rolling of the axis of the flywheel on the track implies the following kinematical constrain between the indicated angular frequencies:

$$\dot{\theta}(t) = N\dot{\psi}(t) \tag{1}$$

where the gear ratio N is given as

$$N = \frac{r_2}{r_1} \tag{2}$$

Due to the constraint in Eq. (1) the internal dynamics of the device has merely a single degree of freedom, which we shall choose as $\psi(t)$.

In the following different principal axes coordinate systems attached to three rigid bodies moving relative to each other will be introduced. The components of a vector and quantities defined in relation to the kth principal axis coordinate system $(x_1^k, x_2^k, x_3^k), k = 1, 2, 3$ are indicated with an upper k. Hence, the jth component of a vector $\mathbf{v}$ in the kth principal axis coordinate system is denoted as v_j^k, and the principal mass moment of inertia of a rigid body at rotation around the coordinate axis x_j^k is denoted as J_j^k.

In Fig. 2 the mass center of gravity G_1 on of the lever and float is indicated, and an (x_1^1, x_2^1, x_3^1) principal axis coordinate system with origin at G_1 fixed to the float is introduced. Due to the rotational symmetry of the device, the centerline of the lever forms a principal axis, so G_1 is placed on this centerline a distance a from O. The x_2^1-axis is placed along the centerline

and orientated in the direction away from O. The x_3^1-axis is placed along the spin axis of the flywheel in a referential position. The ring is precessing around the x_2^1-axis, and the spin axis of the flywheel is supported to the ring via hinges. Hence, the plane of the flywheel is always orthogonal to the plane of the ring.

The mass of the lever and float is denoted m_1, and the principal axis mass moment of inertia at rotations around the x_j^1-axis is denoted J_j^1. Obviously, $J_1^1 = J_3^1$.

It is assumed that the device is undergoing rotations with the angular velocity vector $\dot{\boldsymbol{\varphi}}(t)$. The components of $\dot{\boldsymbol{\varphi}}(t)$ in the (x_1^1, x_2^1, x_3^1)-coordinate system are denoted $\dot{\varphi}_1^1(t),\ \dot{\varphi}_2^1(t),\ \dot{\varphi}_3^1(t)$. No rotations take place around the x_2^1-axis, so $\dot{\varphi}_2^1(t) \equiv 0$. Hence, $\dot{\varphi}_1^1(t)$ and $\dot{\varphi}_3^1(t)$ represent the degrees of freedom of the external structure.

The translational velocity vector $\dot{\mathbf{u}}(t)$ of G_1 has the following components in the (x_1^1, x_2^1, x_3^1)-coordinate system:

$$\begin{bmatrix} \dot{u}_1^1(t) \\ \dot{u}_2^1(t) \\ \dot{u}_3^1(t) \end{bmatrix} = \begin{bmatrix} -a\dot{\varphi}_3^1(t) \\ 0 \\ a\dot{\varphi}_1^1(t) \end{bmatrix} \tag{3}$$

So, the kinetic energy of the lever and float becomes

$$\left.\begin{aligned} T_1\left(\dot{\varphi}_1^1(t), \dot{\varphi}_3^1(t)\right) &= \frac{1}{2} m_1 \left(\left(\dot{u}_1^1(t)\right)^2 + \left(\dot{u}_3^1(t)\right)^2 \right) + \frac{1}{2} J_1^1 \left(\dot{\varphi}_1^1(t)\right)^2 + \frac{1}{2} J_3^1 \left(\dot{\varphi}_3^1(t)\right)^2 \\ &= \frac{1}{2} \left(J_1^1 + m_1 a^2\right) \left(\left(\dot{\varphi}_1^1(t)\right)^2 + \left(\dot{\varphi}_3^1(t)\right)^2 \right) \end{aligned}\right\} \tag{4}$$

Fig. 4 shows the position of the mass center of gravity G_2 of both the ring and the flywheel, placed along the x_2^1-axis at a distance b from G_1. The ring is precessing around the x_2^1-axis, and the spin-axis of the flywheel is fixed to the ring via a bearing, which allows merely for the spin. An (x_1^2, x_2^2, x_3^2) principal axis coordinate system with origin at G_2 is introduced fixed to the precessing ring. The x_2^2-axis is co-directional to the x_2^1-axis, and the x_3^2-axis is placed along the spin-axis of the flywheel. The angular precession velocity $\dot{\psi}(t)$ of the ring is considered positive in the x_2^2-direction.

The mass of the ring is denoted m_2, and the principal axis mass moment of inertia at rotations around the x_j^2-axis is denoted J_j^2. Obviously, $J_1^2 = J_3^2 = \frac{1}{2} J_2^2$. J_2^2 signifies the polar moment of inertia of the ring.

The translational velocity vector $\dot{\mathbf{v}}(t)$ of G_2 has the following components in the (x_1^1, x_2^1, x_3^1)-coordinate system:

$$\begin{bmatrix} \dot{v}_1^1(t) \\ \dot{v}_2^1(t) \\ \dot{v}_3^1(t) \end{bmatrix} = \begin{bmatrix} -(a+b)\dot{\varphi}_3^1(t) \\ 0 \\ (a+b)\dot{\varphi}_1^1(t) \end{bmatrix} \tag{5}$$

The components of $\dot{\boldsymbol{\varphi}}(t)$ in the (x_1^1, x_2^1, x_3^1)- and (x_1^2, x_2^2, x_3^2)-coordinate systems are related as

$$\begin{bmatrix} \dot{\varphi}_1^2(t) \\ \dot{\varphi}_2^2(t) \\ \dot{\varphi}_3^2(t) \end{bmatrix} = \begin{bmatrix} \cos\psi & 0 & -\sin\psi \\ 0 & 1 & 0 \\ \sin\psi & 0 & \cos\psi \end{bmatrix} \begin{bmatrix} \dot{\varphi}_1^1(t) \\ \dot{\varphi}_2^1(t) \\ \dot{\varphi}_3^1(t) \end{bmatrix} = \begin{bmatrix} \cos\psi\dot{\varphi}_1^1(t) - \sin\psi\dot{\varphi}_3^1(t) \\ 0 \\ \sin\psi\dot{\varphi}_1^1(t) + \cos\psi\dot{\varphi}_3^1(t) \end{bmatrix} \tag{6}$$

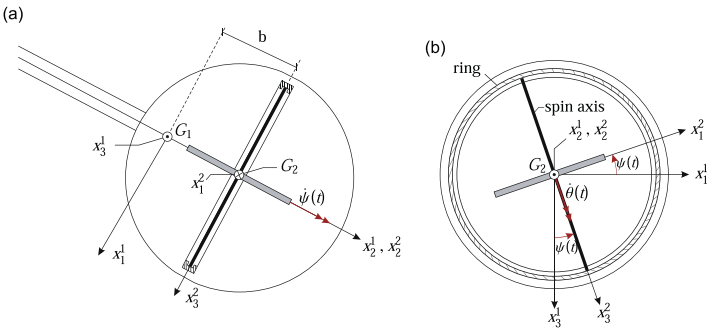

Fig. 4. Definition of the (x_1^2, x_2^2, x_3^2)-coordinate system fixed to the ring.

So, the components $(\dot{\psi}_1^2, \dot{\psi}_2^2, \dot{\psi}_3^2)$ of the angular velocity vector $\dot{\boldsymbol{\psi}}(t)$ of the ring in the (x_1^2, x_2^2, x_3^2)-coordinate system become

$$\begin{bmatrix} \dot{\psi}_1^2(t) \\ \dot{\psi}_2^2(t) \\ \dot{\psi}_3^2(t) \end{bmatrix} = \begin{bmatrix} \cos\psi\dot{\varphi}_1^1(t) - \sin\psi\dot{\varphi}_3^1(t) \\ \dot{\psi}(t) \\ \sin\psi\dot{\varphi}_1^1(t) + \cos\psi\dot{\varphi}_3^1(t) \end{bmatrix} \tag{7}$$

The kinetic energy of the ring becomes

$$\left.\begin{aligned} T_2\left(\dot{\varphi}_1^1(t), \dot{\varphi}_3^1(t), \dot{\psi}(t)\right) &= \frac{1}{2}m_2\left(\left(\dot{v}_1^1(t)\right)^2 + \left(\dot{v}_3^1(t)\right)^2\right) + \frac{1}{2}J_1^2\left(\dot{\psi}_1^2(t)\right)^2 + \frac{1}{2}J_2^2\left(\dot{\psi}_2^2(t)\right)^2 + \frac{1}{2}J_3^2\left(\dot{\psi}_3^2(t)\right)^2 \\ &= \frac{1}{2}\left(\frac{1}{2}J_2^2 + m_2(a+b)^2\right)\left(\left(\dot{\varphi}_1^1(t)\right)^2 + \left(\dot{\varphi}_3^1(t)\right)^2\right) + \frac{1}{2}J_2^2\left(\dot{\psi}(t)\right)^2 \end{aligned}\right\} \tag{8}$$

In Fig. 5 an (x_1^3, x_2^3, x_3^3) principal axis coordinate system with origin at G_2 fixed to the spinning flywheel has been defined. The x_3^3-axis is placed along the spin axis, co-directional to the x_3^2-axis. The angular spin velocity $\theta(t)$ is considered positive in the x_3^3-direction. The x_1^2- and x_2^2-axes are rotated into the x_1^3- and x_2^3-axes by the rotational angle θ around the x_3^2-axis.

The mass of the flywheel is denoted m_3, and the principal axis mass moment of inertia at rotations around the x_j^3-axis is denoted J_j^3. Obviously, $J_1^3 = J_2^3 = \frac{1}{2}J_3^3$. J_3^3 signifies the polar moment of inertia of the flywheel.

The translational velocity vector of the flywheel is identical to that of the ring and given by Eq. (5). The components of $\dot{\boldsymbol{\psi}}(t)$ in the (x_1^2, x_2^2, x_3^2)- and (x_1^3, x_2^3, x_3^3)-coordinate systems are related as

$$\begin{bmatrix} \dot{\psi}_1^3(t) \\ \dot{\psi}_2^3(t) \\ \dot{\psi}_3^3(t) \end{bmatrix} = \begin{bmatrix} \cos\theta & \sin\theta & 0 \\ -\sin\theta & \cos\theta & 0 \\ 0 & 0 & 1 \end{bmatrix} \begin{bmatrix} \dot{\psi}_1^2(t) \\ \dot{\psi}_2^2(t) \\ \dot{\psi}_3^2(t) \end{bmatrix} = \begin{bmatrix} \cos\theta\,\dot{\psi}_1^2(t) + \sin\theta\,\dot{\psi}_2^2(t) \\ -\sin\theta\,\dot{\psi}_1^2(t) + \cos\theta\,\dot{\psi}_2^2(t) \\ \dot{\psi}_3^2(t) \end{bmatrix} \tag{9}$$

So, the components $(\dot{\theta}_1^3, \dot{\theta}_2^3, \dot{\theta}_3^3)$ of the angular velocity vector $\dot{\boldsymbol{\theta}}(t)$ of the flywheel in the (x_1^3, x_2^3, x_3^3)-coordinate system become

$$\begin{bmatrix} \dot{\theta}_1^3(t) \\ \dot{\theta}_2^3(t) \\ \dot{\theta}_3^3(t) \end{bmatrix} = \begin{bmatrix} \cos\theta\,\dot{\psi}_1^2(t) + \sin\theta\,\dot{\psi}_2^2(t) \\ -\sin\theta\,\dot{\psi}_1^2(t) + \cos\theta\,\dot{\psi}_2^2(t) \\ \dot{\psi}_3^2(t) + \dot{\theta}(t) \end{bmatrix} \tag{10}$$

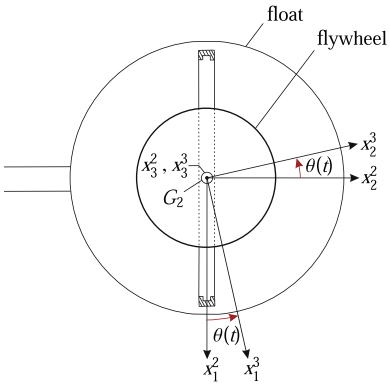

Fig. 5. Definition of the (x_1^3, x_2^3, x_3^3)-coordinate system fixed to the flywheel.

The kinetic energy of the flywheel becomes

$$\left.\begin{aligned} T_3\left(\dot{\varphi}_1^1(t),\dot{\varphi}_3^1(t),\psi(t),\dot{\psi}(t),\dot{\theta}(t)\right) &= \frac{1}{2}m_3\left(\left(\dot{v}_1^1(t)\right)^2+\left(\dot{v}_3^1(t)\right)^2\right)+\frac{1}{2}J_1^3\left(\dot{\theta}_1^3(t)\right)^2+\frac{1}{2}J_2^3\left(\dot{\theta}_2^3(t)\right)^2+\frac{1}{2}J_3^3\left(\dot{\theta}_3^3(t)\right)^2 \\ &= \frac{1}{2}m_3(a+b)^2\left(\left(\dot{\varphi}_1^1(t)\right)^2+\left(\dot{\varphi}_3^1(t)\right)^2\right)+\frac{1}{4}J_3^3\left(\left(\dot{\psi}_1^2(t)\right)^2+\left(\dot{\psi}_2^2(t)\right)^2\right)+\frac{1}{2}J_3^3\left(\dot{\psi}_3^2(t)+\dot{\theta}(t)\right)^2 \\ &= \frac{1}{2}\left(\frac{1}{2}J_3^3+m_3(a+b)^2\right)\left(\left(\dot{\varphi}_1^1(t)\right)^2+\left(\dot{\varphi}_3^1(t)\right)^2\right) \\ &\quad +\frac{1}{4}J_3^3\left(\left(\dot{\psi}(t)\right)^2+\left(\sin\psi\,\dot{\varphi}_1^1(t)+\cos\psi\,\dot{\varphi}_3^1(t)\right)^2+4\left(\sin\psi\,\dot{\varphi}_1^1(t)+\cos\psi\,\dot{\varphi}_3^1(t)\right)\dot{\theta}(t)+2\left(\dot{\theta}(t)\right)^2\right) \end{aligned}\right\} \tag{11}$$

The kinetic energy of the structure is obtained by adding the contributions defined in Eqs. (4), (8) and (11):

$$\left.\begin{aligned} T &= T\left(\dot{\varphi}_1^1(t),\dot{\varphi}_3^1(t),\psi(t),\dot{\psi}(t)\right) \\ &= T_1\left(\dot{\varphi}_1^1(t),\dot{\varphi}_3^1(t)\right)+T_2\left(\dot{\varphi}_1^1(t),\dot{\varphi}_3^1(t),\dot{\psi}(t)\right)+T_3\left(\dot{\varphi}_1^1(t),\dot{\varphi}_3^1(t),\psi(t),\dot{\psi}(t),\dot{\theta}(t)\right) \\ &= \frac{1}{2}J_1\left(\left(\dot{\varphi}_1^1(t)\right)^2+\left(\dot{\varphi}_3^1(t)\right)^2\right)+\frac{1}{2}J_2(\dot{\psi}(t))^2 \\ &\quad +\frac{1}{2}J_3\left(\left(\sin\psi\,\dot{\varphi}_1^1(t)+\cos\psi\,\dot{\varphi}_3^1(t)\right)^2+4N\left(\sin\psi\,\dot{\varphi}_1^1(t)+\cos\psi\,\dot{\varphi}_3^1(t)\right)\dot{\psi}(t)\right) \end{aligned}\right\} \tag{12}$$

where the frequency constrain in Eq. (1) has been used. Further, the following quantities have been introduced:

$$\left.\begin{aligned} J_1 &= J_1^1+\frac{1}{2}J_2^2+\frac{1}{2}J_3^3+m_1a^2+(m_2+m_3)(a+b)^2 \\ J_2 &= J_2^2+\left(N^2+\frac{1}{2}\right)J_3^3 \\ J_3 &= \frac{1}{2}J_3^3 \end{aligned}\right\} \tag{13}$$

$\varphi_1^1(t)$, $\varphi_3^1(t)$ and $\psi(t)$ make up the degrees of freedom of the system.

The equations of motions follow from the Euler–Lagrange stationarity conditions of the action integral [11]:

$$\left.\begin{aligned} \frac{\mathrm{d}}{\mathrm{d}t}\left(\frac{\partial T}{\partial\dot{\varphi}_1^1}\right) &= Q_{\varphi_1^1}(t) \\ \frac{\mathrm{d}}{\mathrm{d}t}\left(\frac{\partial T}{\partial\dot{\varphi}_1^3}\right) &= Q_{\varphi_1^3}(t) \\ \frac{\mathrm{d}}{\mathrm{d}t}\left(\frac{\partial T}{\partial\dot{\psi}}\right)-\frac{\partial T}{\partial\psi} &= Q_{\psi}(t) \end{aligned}\right\} \tag{14}$$

where $Q_{\varphi_1^1}(t)$, $Q_{\varphi_1^3}(t)$, $Q_{\psi}(t)$ denote the external conservative and non-conservative moments work-conjugated to the degrees of freedom $\varphi_1^1(t)$, $\varphi_3^1(t)$, $\psi(t)$, respectively.

The generator has a stator fixed to the ring and a rotor fixed to the spin axis of the flywheel. Hence, the power extract depends on the angular spin velocity $\dot{\theta}$ of the flywheel relative to the ring. Further, the generator torque $M_g(t)$ must be acting in the opposite direction of the spin, i.e. in the negative x_3^1-direction. The extracted electric power is $P_e(t)=M_g(t)\dot{\theta}(t)=NM_g(t)\dot{\psi}(t)$, which may be modelled by applying an external torque $Q_{\psi}(t)=-NM_g(t)$ on the right-hand side of the precession equation in Eq. (14).

Correspondingly, the reaction of the generator torque on the stator, and hence on the float, is positive, when acting in the positive x_3^2-direction. The components in the (x_1^1,x_2^1,x_3^1)-coordinate system follow from the inverse coordinate transformation given in Eq. (6):

$$\begin{bmatrix} Q_{\dot{\varphi}_1 1}(t) \\ Q_{\dot{\varphi}_2 1}(t) \\ Q_{\dot{\varphi}_3 1}(t) \end{bmatrix} = \begin{bmatrix} \cos\psi & 0 & \sin\psi \\ 0 & 1 & 0 \\ -\sin\psi & 0 & \cos\psi \end{bmatrix}\begin{bmatrix} 0 \\ 0 \\ M_g(t) \end{bmatrix} = \begin{bmatrix} \sin\psi\,M_g(t) \\ 0 \\ \cos\psi\,M_g(t) \end{bmatrix} \tag{15}$$

The kinetic energy given by Eq. (12) is inserted on the left-hand side and the indicated generalised loads on the right-hand sides, resulting in

$$\begin{aligned} &\left(J_1+J_3\sin^2\psi\right)\ddot{\varphi}_1^1+J_3\sin\psi\cos\psi\,\ddot{\varphi}_3^1+J_3\,2N\sin\psi\,\ddot{\psi} \\ &\quad +J_3\left(\sin(2\psi)\dot{\varphi}_1^1+\cos(2\psi)\dot{\varphi}_3^1\right)\dot{\psi}+J_3\,2N\cos\psi(\dot{\psi})^2 \quad = \sin\psi\,M_g(t)+M_{\varphi_1^1}(t) \end{aligned} \tag{16a}$$

$$\begin{aligned} &J_3\ \sin\psi\ \cos\psi\ \ddot{\varphi}_1^1+(J_1+J_3\ \cos^2\psi)\ddot{\varphi}_3^1+J_3\ 2N\ \cos\psi\ \ddot{\psi}\\ &+J_3\Big(\cos(2\psi)\dot{\varphi}_1^1-\sin(2\psi)\dot{\varphi}_3^1\Big)\dot{\psi}-J_3\ 2N\ \sin\psi(\dot{\psi})^2 \quad = \cos\psi\ M_g(t)+M_{\varphi_3^1}(t) \end{aligned} \tag{16b}$$

$$\begin{aligned} &J_3\ 2N\ \sin\psi\ \ddot{\varphi}_1^1+J_3\ 2N\ \cos\psi\ \ddot{\varphi}_3^1+J_2\ddot{\psi}\\ &-\frac{1}{2}J_3\Big(\sin(2\psi)\Big(\big(\dot{\varphi}_1^1\big)^2-\big(\dot{\varphi}_3^1\big)^2\Big)+2\ \cos(2\psi)\dot{\varphi}_1^1\dot{\varphi}_3^1\Big) \quad = -NM_g(t) \end{aligned} \tag{16c}$$

$M_{\varphi_1^1}(t)$ and $M_{\varphi_3^1}(t)$ denote the external hydrodynamic moments work conjugated to $\varphi_1^1(t)$ and $\varphi_3^1(t)$ with contributions from quasi-static buoyancy, radiation damping and external wave load, respectively. These moments will be indicated in a following section.

The generator is assumed to be asynchronous with the characteristic [12]

$$M_g(t)=M_{g,0}(t)+M_{g,1}\dot{\theta}(t)=M_{g,0}(t)+M_{g,1}N\dot{\psi}(t) \tag{17}$$

$M_{g,0}(t)$ is assumed to be applied without any significant time delay and make up the control demand of the problem.

The instantaneous absorbed power by the point absorber is given as

$$P_a(t)=M_{\varphi_1^1}(t)\dot{\varphi}_1^1(t)+M_{\varphi_1^3}(t)\dot{\varphi}_1^3(t) \tag{18}$$

The instantaneous generated electric power is given as

$$P_e(t)=NM_g(t)\dot{\psi}(t)=NM_{g,0}(t)\dot{\psi}(t)+N^2M_{g,1}\dot{\psi}^2(t) \tag{19}$$

$P_a(t)$ varies strongly with time, whereas $P_e(t)$ is almost constant. However, the time average $\overline{P_a(t)}$ is equal to $P_e(t)$, apart from a small amount of power loss due to mechanical friction.

2.2. Hydrodynamic loads on GyroPTO point absorber

We shall merely consider 2D monochromatic wave excitation with the wave period T and amplitude η_0 propagating in the positive x_3^1-direction. The water depth is h. Assuming linear wave theory, the hydrodynamics moments $M_{\varphi_1^1}(t)$ and $M_{\varphi_3^1}(t)$ may be written as

$$M_{\varphi_1^1}(t)=-k_1\varphi_1^1(t)-C_{h,1}(\omega)\dot{\varphi}_1^1(t)-J_{h,1}(\omega)\ddot{\varphi}_1^1(t)-M_1(\omega)\sin(\omega t) \tag{20a}$$

$$M_{\varphi_3^1}(t)=-k_3\varphi_3^1(t)-C_{h,3}(\omega)\dot{\varphi}_3^1(t)-J_{h,3}(\omega)\ddot{\varphi}_3^1(t)-M_3(\omega)\cos(\omega t+\alpha) \tag{20b}$$

Due to the symmetry of the structure, no self-induced couplings take place between the hydrodynamics moments $M_{\varphi_1^1}(t)$ and $M_{\varphi_3^1}(t)$, i.e. $M_{\varphi_1^1}(t)$ merely depends on the angular wave frequency $\varphi_1^1(t)$ and its derivatives, and $M_{\varphi_3^1}(t)$ on $\varphi_3^1(t)$ and its derivatives.

k_3 indicates the buoyancy stiffness coefficient at small rotations $\varphi_3^1(t)$ around the static equilibrium state. k_1 is a mechanical spring stiffness introduced in order to prevent drift in the unsupported degree of freedom $\varphi_1^1(t)$. This stiffness should be relatively small. In the numerical example it has been specified as $k_1\simeq 0.05k_3$.

$C_{h,1}(\omega)$, $C_{h,2}(\omega)$ and $J_{h,1}(\omega)$, $J_{h,3}(\omega)$ indicate the radiation damping coefficients and the added mass moments of inertia, respectively [10]. These quantities depend on the wave period via the angular wave frequency $\omega=2\pi/T$.

$M_1(\omega)$ and $M_3(\omega)$ denote the amplitudes of the moments on the float from the external wave loading. These are given as

$$\left.\begin{aligned} M_1(\omega)&=H_1(\omega)\eta_0\\ M_3(\omega)&=H_3(\omega)\eta_0 \end{aligned}\right\} \tag{21}$$

$H_1(\omega)$ and $H_3(\omega)$ indicate the moduli of the frequency response functions for the wave excitation moments with the surface elevation observed at the position of the float. $\alpha=\alpha(\omega)$ specifies the phase lag between the two load components, and is specified so M_3 in Eq. (20b) becomes positive.

The hydrodynamic parameters k_3, $C_{h,1}(\omega)$, $C_{h,2}(\omega)$, $J_{h,1}(\omega)$, $J_{h,3}(\omega)$, $M_1(\omega)$, $M_3(\omega)$ and $\alpha(\omega)$ have been calculated with the boundary element program WAMIT [13].

2.3. Simplified equations of motion

At synchronisation of the angular rotational frequency of the ring, we have $\dot{\psi}(t)\simeq\pm\omega\Rightarrow\ddot{\psi}(t)\simeq 0$ and $\psi(t)\simeq\pm(\omega t+\delta_0)$, where δ_0 is an unknown phase angle to be determined. Here and below the upper signs in $\pm$ and $\mp$ refer to synchronisation in the positive direction, and the lower signs to synchronisation in the negative direction. On the left-hand sides of Eqs. (16a) and (16b) we have $J_3\ll J_1$, so the 2nd, 3rd and 4th terms may be ignored compared to the 1st term. Further, the first terms on the right-hand sides, indicating the energy transferred from the float to the gyro, are ignorable compared to the radiation damping terms $C_{h,1}\dot{\varphi}_1^1$ and $C_{h,3}\dot{\varphi}_3^1$. On the left-hand side of Eq. (16c) the 4th term is

ignorable compared to the 1st and 2nd terms. Then, Eq. (16) may be reduced to

$$(J_1+J_{h,1}(\omega))\ddot{\varphi}_1^1(t)+C_{h,1}(\omega)\dot{\varphi}_1^1(t)+k_1\varphi_1^1(t)=-J_3 2N\omega^2\cos(\omega t+\delta_0)-M_1(\omega)\sin(\omega t) \tag{22a}$$

$$(J_1+J_{h,3}(\omega))\ddot{\varphi}_3^1(t)+C_{h,3}(\omega)\dot{\varphi}_3^1(t)+k_3\varphi_3^1(t)=\pm J_3 2N\omega^2\sin(\omega t+\delta_0)-M_3(\omega)\cos(\omega t+\alpha) \tag{22b}$$

$$J_2\ddot{\psi}+J_3 2N\ \sin\ \psi\ \ddot{\varphi}_1^1+J_3 2N\ \cos\ \psi\ \ddot{\varphi}_3^1+NM_g(t)=0 \tag{22c}$$

Eqs. (22a) and (22b) represent the equations of motion of two uncoupled single-degree-of-freedom oscillators under harmonic excitation. The stationary solutions read [14]

$$\left.\begin{aligned}\varphi_1^1(t)&=-\Phi_1(\omega)\ \sin(\omega t+\beta_1(\omega))\\ \varphi_3^1(t)&=-\Phi_3(\omega)\ \cos(\omega t+\beta_3(\omega))\end{aligned}\right\} \tag{23}$$

where

$$\Phi_1(\omega)=\frac{\sqrt{M_1^2-4M_1J_3N\omega^2\ \sin\ \delta_0+(J_3 2N\omega^2)^2}}{\sqrt{(k_1-(J_1+J_{h,1})\omega^2)^2+C_{h,1}^2\omega^2}} \tag{24a}$$

$$\Phi_3(\omega)=\frac{\sqrt{M_3^2\pm 4M_3J_3N\omega^2\ \sin(\alpha-\delta_0)+(J_3 2N\omega^2)^2}}{\sqrt{(k_3-(J_1+J_{h,3})\omega^2)^2+C_{h,3}^2\omega^2}} \tag{24b}$$

$$\beta_1(\omega)=\arctan\left(\frac{J_3 2N\omega^2\ \cos\ \delta_0}{M_1-J_3 2N\omega^2\ \sin\ \delta_0}\right)-\arctan\left(\frac{\omega C_{h,1}}{k_1-(J_1+J_{h,1})\omega^2}\right) \tag{24c}$$

$$\beta_3(\omega)=\arctan\left(\frac{M_3\ \sin\ \alpha\pm J_3 2N\omega^2\ \cos\ \delta_0}{M_3\ \cos\ \alpha\mp J_3 2N\omega^2\ \sin\ \delta_0}\right)-\arctan\left(\frac{\omega C_{h,3}}{k_3-(J_1+J_{h,3})\omega^2}\right) \tag{24d}$$

The phases β_1, β_3 are arranged, so the amplitudes Φ_1, Φ_3 become positive. From Eqs. (24c) and (24d) follows that $\beta_1(\omega)\to 0$ and $\beta_3(\omega)\to\alpha$ for $\omega\to 0$, and $\beta_1(\omega)\to\delta_0$ and $\beta_3(\omega)\to\delta_0$ for $\omega\to\infty$. This means that $\varphi_1^1(t)$ and $\varphi_3^1(t)$ become increasingly in phase, as $\omega\to\infty$.

When the gyro is shut down ($\psi(t)=0$), the absolute value (modulus) of the frequency response function for the float (on both DOFs) with respect to the sea surface elevation can be obtained by modifying the first two equations in Eq. (24). The resulting expression are given by

$$\left.\begin{aligned}\frac{\Phi_1(\omega)}{\eta_0}&=\frac{H_1}{\sqrt{(k_1-(J_1+J_{h,1})\omega^2)^2+C_{h,1}^2\omega^2}}\\ \frac{\Phi_3(\omega)}{\eta_0}&=\frac{H_3}{\sqrt{(k_3-(J_1+J_{h,3})\omega^2)^2+C_{h,3}^2\omega^2}}\end{aligned}\right\} \tag{25}$$

The generator is assumed to be asynchronous with $M_{g,0}\equiv 0$ corresponding to the linear characteristic:

$$M_g(t)=M_{g,1}\dot{\theta}(t)=M_{g,1}N\dot{\psi}(t) \tag{26}$$

Insertion of Eqs. (23) and (26) into Eq. (22) provides

$$\ddot{\psi}+e\dot{\psi}+f(\Phi_1\ \sin\ \psi\ \sin(\omega t+\beta_1)+\Phi_3\ \cos\ \psi\ \cos(\omega t+\beta_3))=0 \tag{27}$$

where

$$e=\frac{2N^2}{1+2N^2}\frac{M_{g,1}}{J_3^3},\quad f=\frac{2N}{1+2N^2}\omega^2 \tag{28}$$

The following transformations are introduced:

$$\left.\begin{aligned}\Phi_1&=\Phi_0\ \sin\ \beta\\ \Phi_3&=\Phi_0\ \cos\ \beta\end{aligned}\right\}\quad\Rightarrow$$

$$\beta=\arctan\left(\frac{\Phi_1}{\Phi_3}\right),\quad \Phi_0=\sqrt{\Phi_1^2+\Phi_3^2} \tag{29}$$

So, Eq. (27) may be written as

$$\ddot{\psi}+e\dot{\psi}+\omega_0^2(\gamma_1\cos(\psi-\omega t)+\gamma_2\cos(\psi+\omega t)+\varepsilon_1\sin(\psi-\omega t)+\varepsilon_2\sin(\psi+\omega t))=0 \tag{30}$$

$$\left.\begin{array}{ll} \gamma_1 = \sin\beta\cos\beta_1 + \cos\beta\cos\beta_3, & \gamma_2 = -\sin\beta\cos\beta_1 + \cos\beta\cos\beta_3 \\ \varepsilon_1 = \sin\beta\sin\beta_1 + \cos\beta\sin\beta_3, & \varepsilon_2 = \sin\beta\sin\beta_1 - \cos\beta\sin\beta_3 \\ \omega_0 = \sqrt{\dfrac{1}{2} f\Phi_0} & \end{array}\right\} \tag{31}$$

Finally, the following transformations are introduced:

$$\left.\begin{array}{ll} \gamma_1 = \lambda_1\cos\mu_1, & \varepsilon_1 = \lambda_1\sin\mu_1 \\ \gamma_2 = \lambda_2\cos\mu_2, & \varepsilon_2 = \lambda_2\sin\mu_2 \end{array}\right\} \quad \Rightarrow$$

$$\left.\begin{array}{ll} \mu_1 = \arctan\left(\dfrac{\sin\beta\sin\beta_1 + \cos\beta\sin\beta_3}{\sin\beta\cos\beta_1 + \cos\beta\cos\beta_3}\right) + n\pi, & \lambda_1 = \sqrt{1+\sin(2\beta)\cos(\beta_1-\beta_3)} \\ \mu_2 = \arctan\left(\dfrac{\sin\beta\sin\beta_1 - \cos\beta\sin\beta_3}{-\sin\beta\cos\beta_1 + \cos\beta\cos\beta_3}\right) + n\pi, & \lambda_2 = \sqrt{1-\sin(2\beta)\cos(\beta_1-\beta_3)} \end{array}\right\} \tag{32}$$

where the integer n is chosen so $\mu_1, \mu_2 \in [0, 2\pi]$.

Then, Eq. (30) may be written as

$$\ddot{\psi} + e\dot{\psi} + \omega_0^2\left(\lambda_1\cos(\psi - \omega t - \mu_1) + \lambda_2\cos(\psi + \omega t - \mu_2)\right) = 0 \tag{33}$$

Eq. (33) indicates the motion of an autonomous nonlinear single-degree-of-freedom system with parametric excitation and linear viscous damping.

3. Stability analysis

At first, assume that $\Phi_1 = \Phi_3 \wedge \beta_1 = \beta_3 = 0$. Then, Eq. (27) may be written as

$$\ddot{\psi} + e\dot{\psi} + \omega_0^2\cos(\psi - \omega t) = 0 \tag{34}$$

where ω_0 has been redefined as

$$\omega_0 = \sqrt{f\Phi_1} \tag{35}$$

Eq. (34) may be rewritten in the form:

$$\ddot{\delta} + e\dot{\delta} + \omega_0^2\cos\delta + e\omega = 0 \tag{36}$$

where

$$\delta = \psi - \omega t \tag{37}$$

The equilibrium points of Eq. (36) are given as $(\delta, \dot{\delta}) = (\delta_1, 0)$ and $(\delta, \dot{\delta}) = (\delta_2, 0)$, where

$$\left.\begin{array}{l} \delta_1 = \pi + \arccos\left(\dfrac{e\omega}{\omega_0^2}\right) + 2n\pi \\ \delta_2 = \pi - \arccos\left(\dfrac{e\omega}{\omega_0^2}\right) + 2n\pi \end{array}\right\} \tag{38}$$

and n indicates an arbitrary integer. The actual value of this parameter depends on the initial values $\psi(0) = \psi_0$ and $\dot{\psi}(0) = \dot{\psi}_0$ of the ring motion. As follows from Eq. (38) equilibrium points representing synchronisation are only present for $e\omega \le \omega_0^2$. Further, $\delta_1 \to \delta_2$ as $e\omega \to \omega_0^2$.

In order to analyse the stability of the identified equilibrium points, the following perturbed motion is considered:

$$\delta(t) = \delta_{1,2} + \Delta\delta(t) \tag{39}$$

Upon insertion into Eq. (36) the following linearised equation is obtained, valid for motions of the perturbation in the proximity of the equilibrium points $\delta(t) = \delta_{1,2}$:

$$\Delta\ddot{\delta} + e\Delta\dot{\delta} - \omega_0^2\sin\delta_{1,2}\,\Delta\delta = 0 \tag{40}$$

where

$$\sin\delta_1 = -\sin\left(\arccos\left(\frac{e\omega}{\omega_0^2}\right)\right) < 0, \quad \sin\delta_2 = -\sin\delta_1 > 0 \tag{41}$$

Hence, the equilibrium points $\delta = \delta_2$ represent unstable saddle points, and the equilibrium points $\delta = \delta_1$ represent asymptotically stable focus. As $e\omega \to \omega_0^2$ a Hopf instability takes place of δ_1, and the synchronisation is lost. Instead, the system is attracted to a new stable state, where the ring performs small forced harmonic motions with the angular frequency ω around the point $\psi = \psi_1$, driven by the term $\omega_0^2\cos(\psi_2 + \omega t)$, where ψ_1 and ψ_2 are integration constants depending on the initial values ψ_0 and $\dot{\psi}_0$, respectively. These results were first given by Gulick and O'Reilly [7].

If $e\omega > \omega_0^2$ no synchronisation is possible. Using, Eqs. (28), (29) and (35) this provides the following stability condition for the synchronised motion:

$$M_{g,1} \le \frac{1}{N}\Phi_0 J_3^3 \omega \tag{42}$$

From Eq. (26) follows that the maximum electric power which can be extracted from the synchronised motion becomes

$$P_{e,\max} = N^2 M_{g,1}\omega^2 = \omega^3 J_3^3 N \Phi_0 \tag{43}$$

Next, assume $\Phi_1 \neq \Phi_3 \vee \beta_1 \neq 0 \vee \beta_3 \neq 0$. Let

$$\delta(t) = \psi(t) - \omega t - \mu_1 \tag{44}$$

Then, Eq. (36) may be written as

$$\ddot{\delta} + e\dot{\delta} + \lambda_1\omega_0^2 \cos\ \delta + \lambda_2\omega_0^2 \cos(\delta + 2\omega t + \mu_1 - \mu_2) + e\omega = 0 \tag{45}$$

The following equilibrium points are identified from Eq. (45), corresponding to possible synchronised motions:

$$\left.\begin{aligned} \delta_1 &= \pi + \arccos\left(\frac{e\omega}{\lambda_1\omega_0^2}\right) + 2n\pi \\ \delta_2 &= \pi - \arccos\left(\frac{e\omega}{\lambda_1\omega_0^2}\right) + 2n\pi \end{aligned}\right\} \tag{46}$$

As seen, $\delta_1 \downarrow (2n+1)\pi$ and $\delta_2 \uparrow (2n+1)\pi$ as $e\omega \uparrow \lambda_1\omega_0^2$.

At synchronisation to the equilibrium point δ_1 the rotation of the ring is given as

$$\psi(t) = \omega t + \mu_1 + \delta_1 \tag{47}$$

The assumed rotation at synchronisation in Eqs. (22)–(33) was $\psi(t) = \omega t + \delta_0$. Hence, we have the following relation for the unknown phase δ_0:

$$\delta_0 = \mu_1 + \delta_1 \tag{48}$$

$\mu_1 = \mu_1(\delta_0)$ and $\delta_1 = \delta_1(\delta_0)$ are nonlinear functions of δ_0, so Eq. (48) has to be solved by iteration. Since μ_1 is determined within an addend $2\pi n$, cyclic iteration and similar simple iteration algorithms will not work. In the present case the solution was found guided by the graphical representation of $\mu_1(\delta_0)$ and $\delta_1(\delta_0)$ for $\delta_0 \in]0, 2\pi]$.

The stability of Eq. (45) in the vicinity of the indicated equilibrium points is checked by a first-order Lyapunov analysis similar to the one performed Eqs. (39) and (40), resulting in

$$\Delta\ddot{\delta} + e\Delta\dot{\delta} - \omega_0^2(\lambda_1 \sin\ \delta_{1,2} + \lambda_2 \sin(\delta_{1,2} + 2\omega t + \mu_1 - \mu_2))\Delta\delta = -\lambda_2\omega_0^2 \cos(\delta_{1,2} + 2\omega t + \mu_1 - \mu_2) \tag{49}$$

Motions in the vicinity of $(\delta, \dot{\delta}) = (\delta_2, 0)$ are unstable, since $\sin\ \delta_2 > 0$. In the vicinity of $(\delta, \dot{\delta}) = (\delta_1, 0)$ forced harmonic vibrations with the angular frequency 2ω take place, which are partly caused by the parametric excitation $-\lambda_2\omega_0^2 \sin(\delta_1 + 2\omega t + \mu_1 - \mu_2)\Delta\delta$ and partly by the additive excitation $-\lambda_2\omega_0^2 \cos(\delta_1 + 2\omega t + \mu_1 - \mu_2)$. Generally, these vibrations are stable. Additionally, the parametric excitation may cause internal instability at the frequency ratios [15]:

$$\frac{\omega}{\sqrt{\lambda_1}\omega_0} = 1, \frac{1}{2}, \frac{1}{3}, \ldots \tag{50}$$

However, since $\omega > \omega_0$ for any realistic wave frequency and $\lambda_1 \le \sqrt{2}$, parametric instability is unlikely to happen. Hence, the condition for the existence of stable synchronisations essentially refers to the existence of the equilibrium point δ_1. Similar to Eq. (26) this implies

$$e\omega \le \lambda_1\omega_0^2 \quad \Rightarrow \quad M_{g,1} \le \frac{\omega J_3^3}{2N}\sqrt{\Phi_1^2 + \Phi_3^2}\sqrt{1 + \sin(2\beta)\cos(\beta_1 - \beta_3)} \tag{51}$$

where Eqs. (28), (29), (31) and (32) have been used.

The maximum electric power, which can be extracted from the synchronised motion becomes, cf. Eq. (26),

$$P_{e,\max} = \frac{\omega^3 J_3^3 N}{2}\sqrt{\Phi_1^2 + \Phi_3^2}\sqrt{1 + \sin(2\beta)\cos(\beta_1 - \beta_3)} \tag{52}$$

Eq. (52) reduces to Eq. (43) for $\Phi_1 = \Phi_3 = \Phi_0$ and $\beta_1 = \beta_3$.

Finally, consider synchronisation in the negative direction, corresponding to the following setting:

$$\delta(t) = \psi(t) + \omega t - \mu_2 \tag{53}$$

Then, Eq. (33) may be written as

$$\ddot{\delta} + e\dot{\delta} + \lambda_2\omega_0^2 \cos\ \delta + \lambda_1\omega_0^2 \cos(\delta - 2\omega t + \mu_2 - \mu_1) - e\omega = 0 \tag{54}$$

The following equilibrium points are identified from Eq. (54), corresponding to possible synchronised motions:

$$\left.\begin{aligned}\delta_1 &= -\arccos\left(\frac{e\omega}{\lambda_2\omega_0^2}\right)+2n\pi\\ \delta_2 &= \arccos\left(\frac{e\omega}{\lambda_2\omega_0^2}\right)+2n\pi\end{aligned}\right\} \tag{55}$$

As seen, $\delta_1\uparrow 2n\pi$ and $\delta_2\downarrow 2n\pi$ as $e\omega\uparrow\lambda_2\omega_0^2$.

At synchronisation to the equilibrium point δ_1 the rotation of the ring is given as

$$\psi(t) = -\omega t+\mu_2+\delta_1 \tag{56}$$

The assumed rotation at synchronisation was $\psi(t) = -\omega t-\delta_0$. Hence, we have the following nonlinear relation for the determination of the unknown phase δ_0:

$$\delta_0 = -\mu_2(\delta_0)-\delta_1(\delta_0) \tag{57}$$

Similar to Eq. (45), the stability of Eq. (54) in the vicinity of the indicated equilibrium points is checked by a first-order Lyapunov analysis, resulting in

$$\Delta\ddot{\delta}+e\Delta\dot{\delta}-\omega_0^2(\lambda_2\ \sin\delta_{1,2}+\lambda_1\ \sin(\delta_{1,2}-2\omega t+\mu_2-\mu_1))\Delta\delta = -\lambda_1\omega_0^2\ \cos(\delta_{1,2}-2\omega t+\mu_2-\mu_1) \tag{58}$$

Motions in the vicinity of $(\delta,\dot{\delta}) = (\delta_2,0)$ are unstable, since $\sin\delta_2 > 0$. In the vicinity of $(\delta,\dot{\delta}) = (\delta_1,0)$ stable forced harmonic vibrations with the angular frequency 2ω take place, partly caused by the parametric excitation $-\lambda_1\omega_0^2\sin(\delta_1-2\omega t+\mu_2-\mu_2)\Delta\delta$ and partly by the additive excitation $-\lambda_1\omega_0^2\cos(\delta_1-2\omega t+\mu_2-\mu_1)$. Since $\sqrt{\lambda_2}\omega_0$ normally is smaller than ω, parametric instability is unlikely to happen.

Then, the effective stability condition for synchronisation is related to the existence of the equilibrium point δ_1, which implies

$$e\omega \le \lambda_2\omega_0^2 \quad\Rightarrow\quad M_{g,1} \le \frac{\omega J_3^3}{2N}\sqrt{\Phi_1^2+\Phi_3^2}\sqrt{1-\sin(2\beta)\cos(\beta_1-\beta_3)} \tag{59}$$

where Eqs. (28), (29), (31) and (32) have been used.

The maximum electric power which can be extracted from the synchronised motion becomes

$$P_{e,\max} = \frac{\omega^3 J_3^3 N}{2}\sqrt{\Phi_1^2+\Phi_3^2}\sqrt{1-\sin(2\beta)\cos(\beta_1-\beta_3)} \tag{60}$$

Upon comparison of Eqs. (52) and (60) it follows that rotation in positive direction provides the largest power, if $\cos(\beta_1-\beta_3) > 0$, and rotation in the negative direction the largest power, if $\cos(\beta_1-\beta_3) < 0$. The orientation of the rotation of the ring should be adjusted accordingly.

Generally, we shall specify $M_{g,1}$ in the form:

$$M_{g,1} = \zeta M_{g,1,\max} \tag{61}$$

where $\zeta\in[0,1]$, and $M_{g,1,\max}$ indicate the right-hand sides of the inequalities in Eqs (52) or (60). Then, as seen from Eqs. (28), (32), (51) and (59) the following relations hold:

$$\left.\begin{aligned}\frac{e\omega}{\lambda_1\omega_0^2} &= \zeta\\ \frac{e\omega}{\lambda_2\omega_0^2} &= \zeta\end{aligned}\right\} \tag{62}$$

Hence, δ_1 and δ_2 in Eqs. (46) and (55) become independent of ω and δ_0. This facilitates the solution of Eqs. (48) and (57) somewhat.

4. Numerical example

The structural and hydrodynamic parameters of the scaled model of the GyroPTO shown in Fig. 6 have been indicated in Tables 1 and 2.

Fig. 7 shows the variation of the amplitude fraction Φ_1/Φ_3 and the quantity $\cos(\beta_1-\beta_3)$ as a function of the wave period T. Both quantities are independent of the wave amplitude η_0. As seen the vertical amplitude Φ_1 is larger than the horizontal amplitude Φ_3 for $T < 1$ s, whereas the opposite is the case for larger wave periods. Similarly, $\cos(\beta_1-\beta_3) < 0$ for $T > 0.8$ s. Consequently, the maximum energy harvest at these wave periods is given by Eq. (60), cf. the remarks following Eq. (60).

Fig. 8 shows the variation of Φ_0, $P_{e,\max}$ and the corresponding torque on the generator as a function of the wave period T and the wave amplitude η_0. $P_{e,\max}$ indicates the maximum of the absorbed powers determined by Eq. (52) or Eq. (60). $P_{e,\max}$ increase proportionally with the wave amplitude. This is because the power take off of the GyroPTO depends linearly on the vibration amplitudes of the float, which in turn depend linearly on the wave amplitude. This is in contrast to other wave

Fig. 6. Scaled model of the GyroPTO point absorber being tested in a wave tank.

Table 1
Structural parameters of the GyroPTO wave energy point absorber.

Parameter	Value	Unit	Parameter	Value	Unit
a	0.9891	m	J_1	72.808	kg m^2
b	0.0761	m	J_2	329.68	kg m^2
c	0.080	m	J_3	0.1830	kg m^2
d	0.550	m	e	0.0409	s^{-1}
r_1	0.009	m	f	1.7486	s^{-2}
r_2	0.203	m	k_1	146.7	N m/rad
m_1	20.27	kg	k_3	2925	N m/rad
m_2	5.270	kg	h	0.60	m
m_3	22.11	kg			
J_1	21.68	kg m^2			
J_2	0.0952	kg m^2			
J_3	0.366	kg m^2			

Table 2
Parameters in hydrodynamic load model as a function of the wave period.

T (s)	$C_{h,1}(\omega)$ (N m/(rad/s))	$C_{h,3}(\omega)$ (N m/(rad/s))	$J_{h,1}(\omega)$ (kg m^2)	$J_{h,3}(\omega)$ (kg m^2)	$H_1(\omega)$ (N)	$H_3(\omega)$ (N)	α (rad)
0.50	89.17	22.76	8.901	27.30	466.7	164.7	4.7997
1.00	123.3	101.6	26.81	25.42	1435	914.5	5.3966
1.50	29.01	103.2	33.05	33.58	1256	1651	5.9568
2.00	9.256	88.20	31.14	40.46	963.8	2074	6.1209
2.50	4.096	75.17	29.94	45.82	773.5	2308	6.1854
3.00	2.186	65.01	29.24	50.19	644.7	2449	6.2169

point absorbers, where the absorbed power increases proportionally with the square of the wave amplitude [10]. Further, the torque on the generator for the maximum absorbed power is calculated as $P_{e,\max}/(N\omega)$ and is illustrated in Fig. 8(c).

The time series for $\psi(t)$ and $\dot{\psi}(t)/\omega$ have been shown in Fig. 9 for the initial values $(\psi_0, \dot{\psi}_0) = (\pi/2, \omega)$ and the wave period $T=2$ s. Synchronisation takes place at the equilibrium point $\delta_1 = -\pi + \arccos(e\omega/(\lambda_1\omega_0^2))$, corresponding to $n=-1$ in Eq. (46). As shown in Fig. 9a, at synchronisation the quantity $\psi(t) - \omega t - \mu_1 - \delta_1$ and the fraction $\dot{\psi}(t)/\omega$ converge towards 0 and 1, respectively. The forced harmonic oscillations with the angular frequency 2ω around the equilibrium point in the stationary synchronised state is caused by the last term on the left-hand side of Eq. (33). The amplitude of these oscillations is proportional to the parameter λ_2. As seen, the relative magnitude of the amplitude amounts to $\simeq 0.25$ percent, which will cause a corresponding relative time variation of the generated electric power. Fig. 9b shows the corresponding results, when

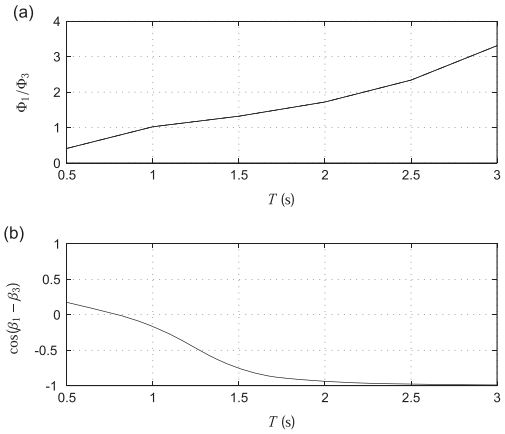

Fig. 7. Response quantities Φ_1/Φ_3 and $\cos(\beta_1-\beta_3)$ as a function of the wave period T.

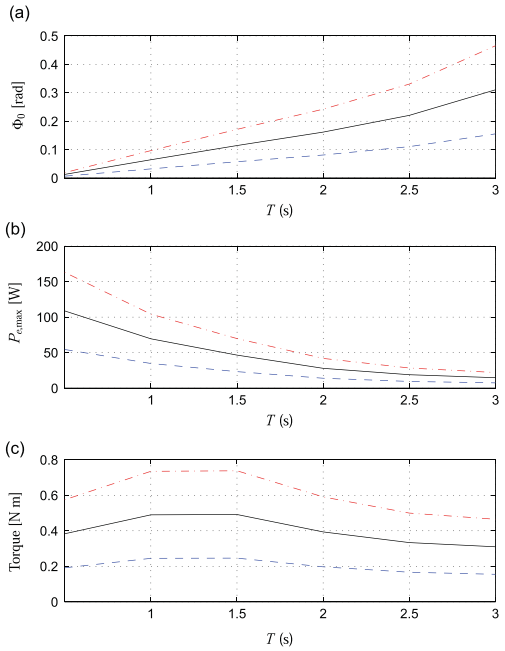

Fig. 8. Response quantities Φ_0 and $P_{e,\max}$ as a function of the wave period T and the amplitude η_0. - - -: $\eta_0 = 0.05$ m. —: $\eta_0 = 0.10$ m. -.-: $\eta_0 = 0.15$ m.

λ_2 is set to 0, equivalent to the system described in Eq. (34). In this case the oscillations around the equilibrium point cease completely.

In the present case the maximum value of the parameter ζ for which synchronisation with the selected initial values could be achieved was $\zeta = 0.8547$. The reason why the theoretical maximum cannot be achieved is due to the significant transient oscillations caused by the initial values, which brings the system out of the basin of attraction related to the considered equilibrium point.

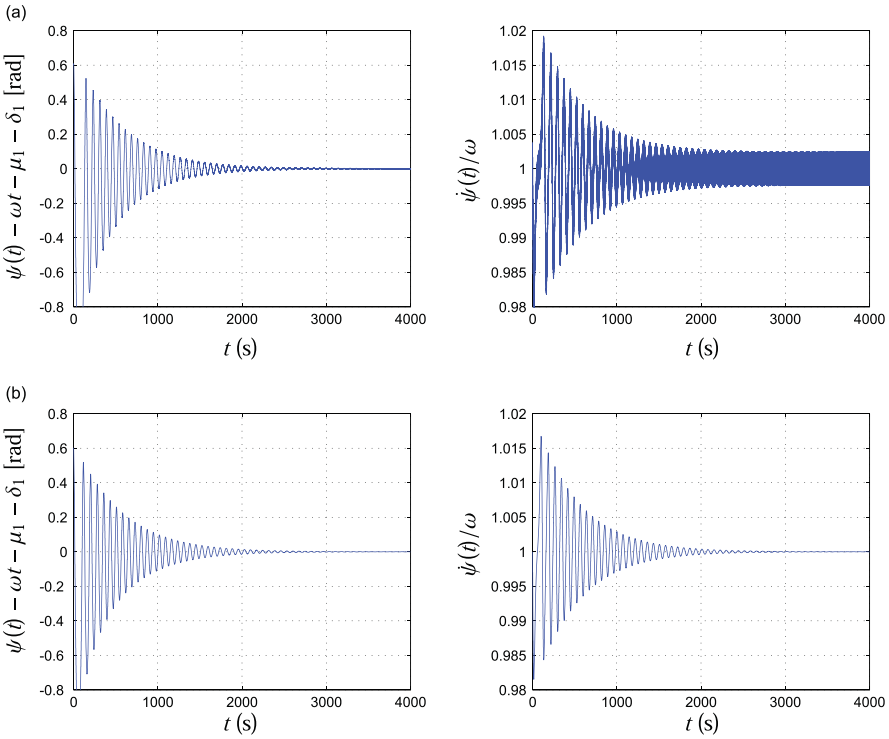

Fig. 9. Variation of $\psi(t)$ and $\dot{\psi}(t)$, $(\psi_0,\dot{\psi}_0)=(\frac{\pi}{2},\omega)$, T=2 s. (a) λ_2=1.3515. (b) λ_2=0.

Fig. 10a shows the corresponding results, when the initial conditions are changed to $(\psi_0,\dot{\psi}_0)=(-\pi/2,-\omega)$. In this case synchronisation takes place to the equilibrium point $\delta_1=-2\pi-\arccos(e\omega/(\lambda_1\omega_0^2))$, corresponding to $n=-1$ in Eq. (55). At synchronisation the quantity $\psi(t)+\omega t-\mu_2-\delta_1$ and the fraction $\dot{\psi}(t)/\omega$ converge towards 0 and -1, respectively. The forced harmonic oscillations with the angular frequency 2ω around the equilibrium point in the stationary synchronised state are caused by the second last term on the left-hand side of Eq. (33). The amplitude of these oscillations is proportional to the parameter λ_1. Since, $\lambda_1/\lambda_2=0.3079$, the relative amplitude and the relative variation of the generated power are reduced accordingly to $\simeq 0.075$ percent. The maximum value of the parameter ζ for which synchronisation with the selected initial values could be achieved was $\zeta=0.7290$.

Fig. 10b indicates the timeseries for the same system as shown in Fig. 10a, when the initial conditions are changed to $(\psi_0,\dot{\psi}_0)=(\pi/2,-\omega)$. No synchronisation to the angular wave frequency takes place. Instead, the system is attracted to the equilibrium point $\psi=\psi_1$, performing forced harmonic driven by the term $\omega_0^2(\lambda_1\cos(\psi_2-\omega t-\mu_1)+\lambda_1\cos(\psi_2+\omega t-\mu_2))$, where ψ_1 and ψ_2 are integration constants depending on the initial values ψ_0 and $\dot{\psi}_0$, respectively. In reality, these vibrations are more complex than indicated, determined by the full nonlinear equations of motion in Eq. (16).

As seen from the results in Figs. 9a, 10a and c the performance of the system depends strongly on the initial values $(\psi_0,\dot{\psi}_0)$. Next, in order to analyse this problem further the basins of attraction for synchronisation to $\dot{\psi}(t)=\omega$ and $\dot{\psi}(t)=-\omega$ are determined. The basin of attraction of an equilibrium point indicates the subset of initial values $(\psi_0,\dot{\psi}_0)$ in the phase space for which the trajectories tend to approach the equilibrium point, although persistent oscillations may occur. The basins of attraction are separated by the separatrix manifolds originating from the saddle points.

The basins of attraction at attraction related to Eq. (33) are determined from the separatrix manifolds of the following homogeneous differential equations, cf. Eqs. (45) and (54):

$$\left.\begin{aligned}&\ddot{\delta}+e\dot{\delta}+\omega_0^2\lambda_1\cos\delta+e\omega=0,\quad \delta(t)=\psi(t)-\omega t-\mu_1-\delta_1\\&\ddot{\delta}+e\dot{\delta}+\omega_0^2\lambda_2\cos\delta-e\omega=0,\quad \delta(t)=\psi(t)+\omega t-\mu_2-\delta_1\end{aligned}\right\}\tag{63}$$

where δ_1 are given by Eqs. (46) or (55).

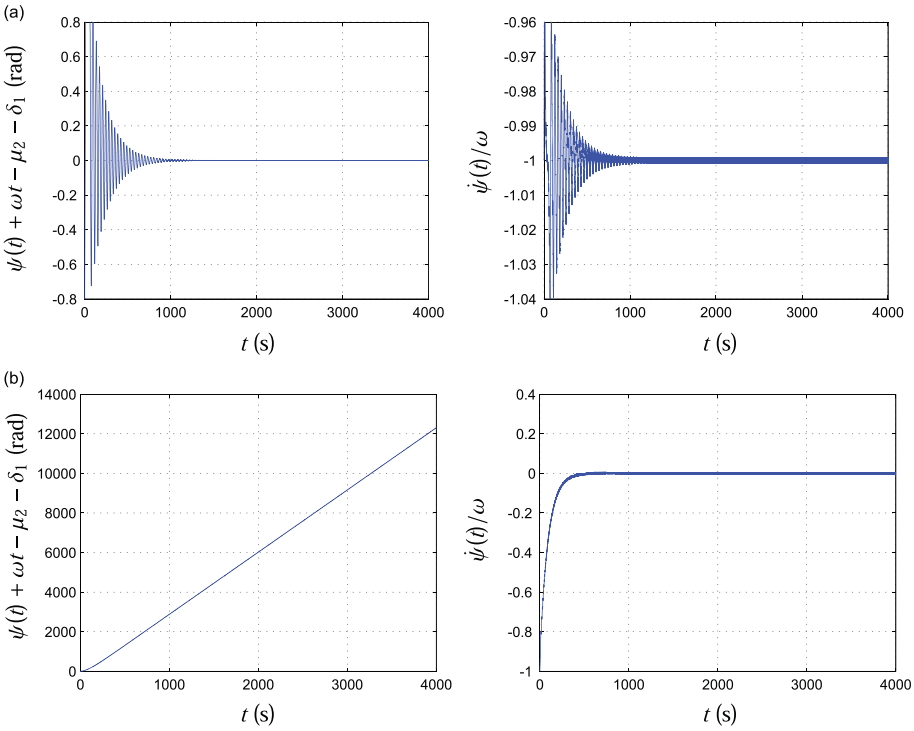

Fig. 10. Variation of $\psi(t)$ and $\dot{\psi}(t)$, T=2 s. (a) $(\psi_0,\dot{\psi}_0)=(-\frac{\pi}{2},-\omega)$. (b) $(\psi_0,\dot{\psi}_0)=(\frac{\pi}{2},-\omega)$.

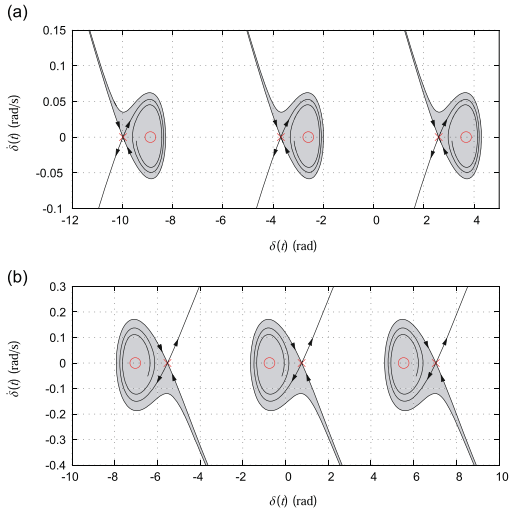

Fig. 11. Basins of attraction, T=2 s. (a) Synchronisation to $\dot{\psi}(t)=\omega$, $M_{1,g}=0.8547M_{1,g,\max}$. (b) Synchronisation to $\dot{\psi}(t)=-\omega$, $M_{1,g}=0.7290M_{1,g,\max}$. o: stable equilibrium points, δ_1, x: saddle points, δ_2.

In Fig. 11a and 11b the grey coloured areas show the basins of attraction in the $(\delta,\dot{\delta})$-plane for the same systems as considered in Figs. 9a and 10a corresponding to the equilibrium points for $n=-2$, $n=-1$ and $n=0$ in Eqs. (46) and (55). In the disjoint white part of the state space no synchronisation is possible, and the system is attracted to the point $\psi=\psi_1$. As seen stable synchronisation requires that $\delta(t)$ is confined to a finite interval centered around the equilibrium point δ_1. The width of the said interval depends on the magnitude of $M_{g,1}$. Actually, the basin of attraction reduces to the single point $(\delta,\dot{\delta})=(\delta_1,0)$ for $M_{g,1}=M_{g,1,\max}$, corresponding to $\zeta=1$. The indicated theory presumes a constant amplitude and phase of the impinging waves, resulting in constant amplitude and phase of the two response components of the float. In irregular sea-states, waves with different amplitudes and phases are exciting the structure, causing a broad-banded wave load. However, the response processes of the float turn out to be narrow-banded with slowly varying amplitude and phases. During operation, these phases and amplitudes need to be identified in real time in order to check whether the system remains within the basin of attraction guaranteeing synchronisation. If out-crossing of the domain of attraction is immanent, the magnitude of this domain must be increased by reducing the gain parameter $M_{g,1}$. Stochastic semi-active control of the stability in irregular sea-states has to be devised in the future work.

5. Conclusions

The equations of motion of the GyroPTO wave energy point absorbers have been derived based on a three degree-of-freedom rigid body model. The resulting equations are highly nonlinear for which reason subharmonic or chaotic response may occur for the float and the ring. The wave loading on the float is determined based on the first-order wave theory, where the related hydrodynamic coefficients are assumed to be calculated numerically. Next assuming synchronisation of the angular velocity of the ring to the angular wave frequency, it is demonstrated that the two equations of motion of the float may be linearised with no mutual coupling and no coupling to the ring equation. Hence, the motion of the float may be determined analytically. In turn, this means that the dynamics of the ring at synchronisation can be described by an autonomous, uncoupled, nonlinear differential equation with parametric excitation. The said equation is related with three types of point attractors. One where the ring vibrations are attracted to a state of rest indicating unstable synchronisation, and the other two point attractors where the ring is synchronised to the wave angular frequency, either rotating in one or the opposite direction. The stability of the synchronised points of attraction have been analysed by a first-order Lyapunov analysis, and the basins of attraction to these point attractors are determined.

Acknowledgements

The authors acknowledge the support from the Danish Energy Technological Development and Demonstration Program (EUDP) for financing the Project 64014-0129 Gyro electric energy converter unit for wave energy. The second author gratefully acknowledges the financial support from the Chinese Scholarship Council under the State Scholarship Fund.

References

[1] Oceantec Energas Marinas SL, ⟨http://tethyspnnlgov/annexivsites/oceantecwaveenergyconverter⟩.
[2] H. Kanki, S. Arii, T. Furusawa, T. Otoyo, Development of advanced wave power generation system by applying gyroscopic moment, *Proceedings of the Eighth European Wave and Tidal Energy Conference*, Uppsala, Sweden, 2009, pp. 280–283.
[3] H. Kanki, S. Arii, T. Hata, Gyro dynamics for new wave power generation system, *Proceedings of the Seventh IFToMM-Conference on Rotor Dynamics*, 25–28 September 2006, Vienna, Austria, 2006.
[4] G.M.G. Bracco, E. Giorcelli, Iswec: *a gyroscopic mechanism for wave power exploitation*, *Mechanism and Machine Theory* 46 (10) (2011) 1411–1424.
[5] G. Bracco, E. Giorcelli, G. Mattiazzo, D. Poggi, J. Taylor, Iswec: experimental tests on a small scale prototype model, *Proceedings of the Third International Conference on Ocean Energy (ICOE)*, Bilbao, Spain, 6 October 2010.
[6] N.C. Townsend, R.A. Shenoi, Modelling and analysis of a single gimbal gyroscopic energy harvester, *Nonlinear Dynamics* 72 (2013) 285–300.
[7] D.W. Gulick, O.M. O'Reilly, On the dynamics of the dynabee, *Journal of Applied Mechanics* 67(2) (2000) 321–325.
[8] T. Ishii, J. Iwasaki, H. Hosaka, Study on dynamic characteristics of gyroscopic power generator, *International Journal of Applied Electromagnetics and Mechanics* 36 (2011) 131–139.
[9] S. Yoshikawa, T. Ishii, J. Iwasaki, H. Hosaka, Stability analysis of gyroscopic power generator, *Proceedings of PowerMEMS*, Sendai, Japan, November 9–12, 2008, pp. 137–140.
[10] J. Falnes, *Ocean Waves and Oscillating Systems: Linear Interactions Including Wave–Energy Extraction*, Cambridge University Press, Cambridge, UK, 2002.
[11] L.A. Pars, *A Treatise on Analytical Dynamics*, Ox Bow Press, Woodbridge, Connecticut, 1979.
[12] M.G. Simoes, F. Farret, *Modeling and Analysis with Induction Generators*, Third Edition, CRC Press, Taylor and Francis Group, Boca Raton, Florida, 2015.
[13] WAMIT, Inc., Wamit User Manual, Version 7.0, ⟨http://www.wamit.com/⟩.
[14] S.R.K. Nielsen, *Vibration Theory, Vol. 1. Linear Vibration Theory*, Fourth edition, Aalborg University, Aalborg, Denmark, ISSN 1395-U2004-1, 2004.
[15] W.C. Xie, *Dynamic Stability of Structures*, Cambridge University Press, New York, USA, 2006.

APPENDIX J
More results from the real-time hybrid testing

J.1 General description

Considering the size of the manufactured TLD, the suitable ratings of wind turbine could be 2 MW and 3 MW, and both of them have been considered in establishing the Matlab/Simulink model.

Figure J.1 shows the Simulink model established in the present study, where the green block reads inputs (the measured reaction force and the actuator displacement and the) from the actuator through SCRAMNet, and the blue block sends outputs (the calculated displacement, the) to the actuator through SCRAMNet. The 13-DOF model is the key block, where all the terms are discretized and the backward Euler method has been used for solving the discrete equations of motion. The time-varying system matrices are handled by user-defined Matlab functions.

For each of the two wind turbine models, three different wind loads (time histories) have been considered. Table J.1 shows the six load cases in total, where V_0 is the mean wind speed and I is the turbulence intensity.

Further, for each wind turbine model. tests were undertaken for three different tuning ratios (ratio between the first sloshing frequency to the first lateral tower frequency) of the TLD, i.e. 0.95, 1.0, 1.05. Cases of the TLD with and without damping screens have been both evaluated. Therefore, in total 36 ($= 2 \times 3 \times 3 \times 2$) real-time hybrid tests were conducted, and the duration for each test was set to be 5 minutes.

J.2 Results of the 3 MW wind turbine

The performance of the TLD on damping lateral tower vibrations of the 3 MW wind turbine have been summarized in Table 3 in Appendix G. As an quantitative index of the damping effect of the TLD, the reduction ratio η is defined as

$$\eta = \frac{\sigma_{q,0} - \sigma_q}{\sigma_q} \tag{J.1}$$

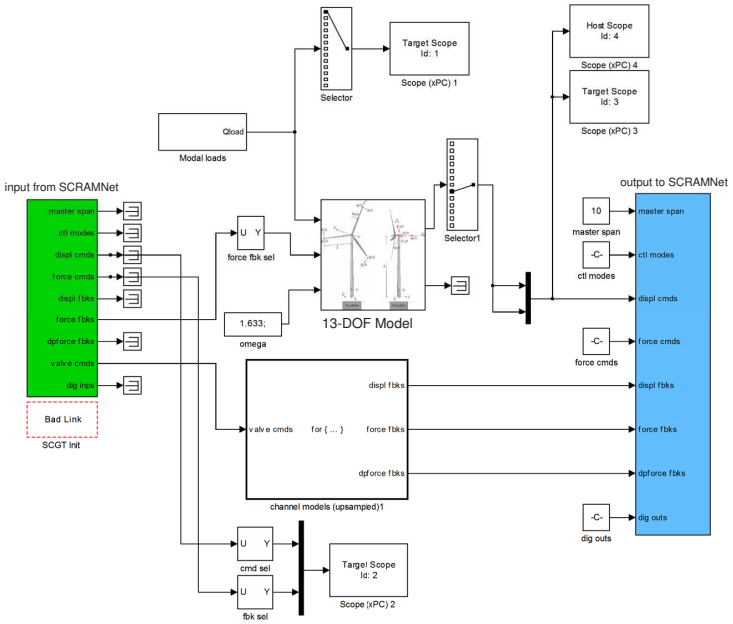

Figure J.1 Simulink model for the TLD-wind turbine system.

Table J.1 List of wind load cases in the test.

Load case	Rating	V_0	I	Load case	Rating	V_0	I
case 1	3 MW	12 m/s	0.08	case 4	2 MW	12 m/s	0.08
case 2	3 MW	12 m/s	0.1	case 5	2 MW	12 m/s	0.1
case 3	3 MW	8 m/s	0.1	case 6	2 MW	8 m/s	0.1

where $\sigma_{q,0}$ and σ_q are the standard deviations of the lateral tower vibration without and with TLD, respectively.

Time histories of the tower vibration for the 3 MW wind turbine during all 18 tests are presented in Figures J.2-J.10 below.

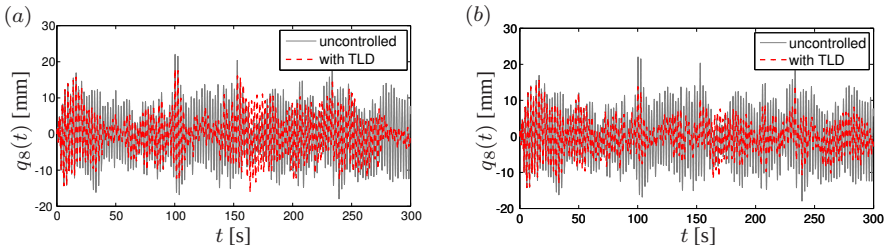

Figure J.2 Control effect of the TLD, **case 1**, tuning ratio = 1. (a) without damping screens, $\eta = 28.32\%$. (b) with damping screens, $\eta = 40.25\%$.

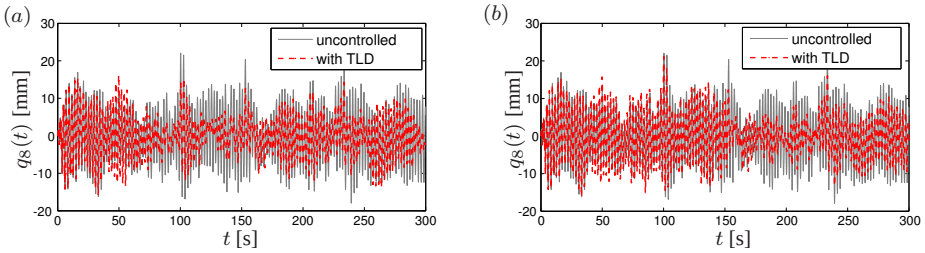

Figure J.3 Control effect of the TLD, **case 1**, tuning ratio = 0.95. (a) without damping screens, $\eta = 27.80\%$. (b) with damping screens, $\eta = 18.57\%$.

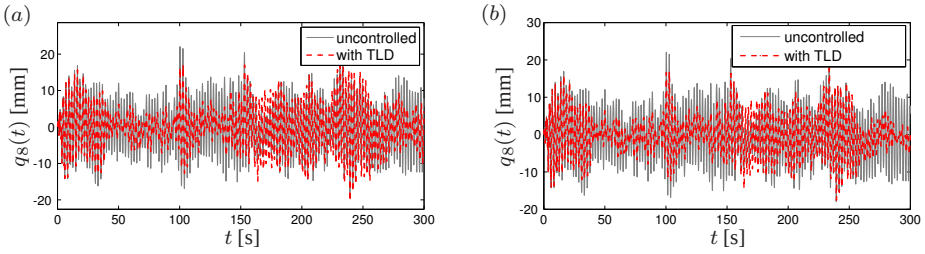

Figure J.4 Control effect of the TLD, **case 1**, tuning ratio = 1.05. (a) without damping screens, $\eta = 17.66\%$. (b) with damping screens, $\eta = 27.78\%$.

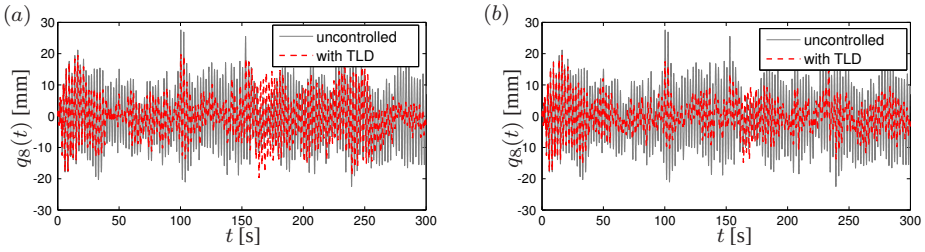

Figure J.5 Control effect of the TLD, **case 2**, tuning ratio = 1. (a) without damping screens, $\eta = 29.43\%$. (b) with damping screens, $\eta = 44.19\%$.

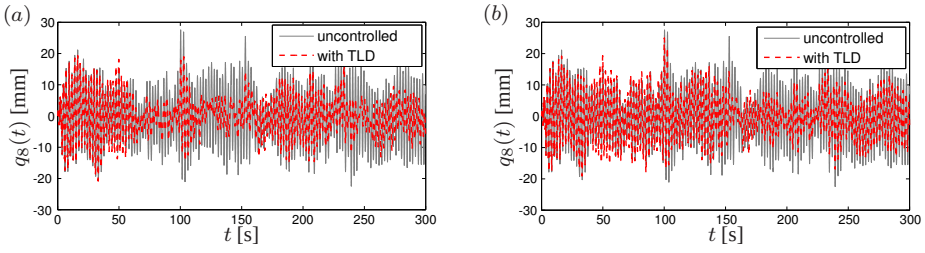

Figure J.6 Control effect of the TLD, **case 2**, tuning ratio = 0.95. (a) without damping screens, $\eta = 33.62\%$. (b) with damping screens, $\eta = 21.81\%$.

Both the uncontrolled and controlled tower vibrations are dominated by the first

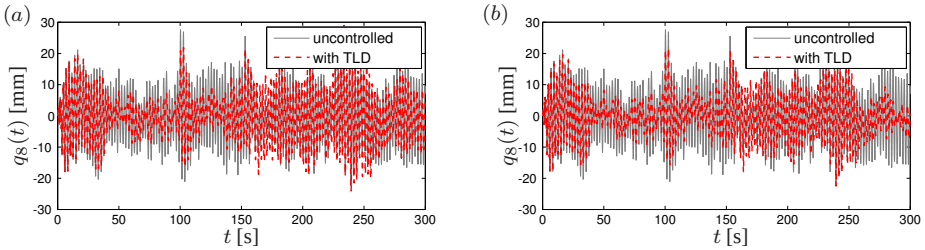

Figure J.7 Control effect of the TLD, **case 2**, tuning ratio = 1.05. (a) without damping screens, $\eta = 13.77\%$. (b) with damping screens, $\eta = 26.10\%$.

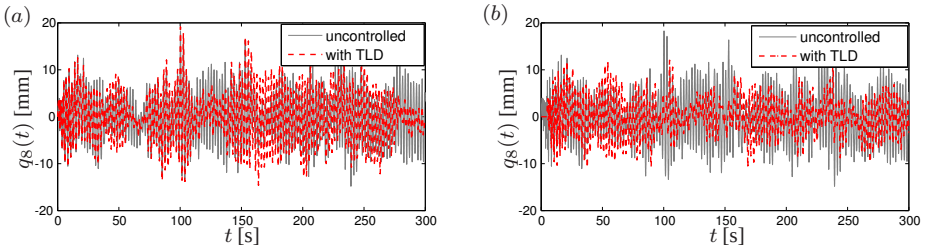

Figure J.8 Control effect of the TLD, **case 3**, tuning ratio = 1. (a) without damping screens, $\eta = 8.29\%$. (b) with damping screens, $\eta = 29.74\%$.

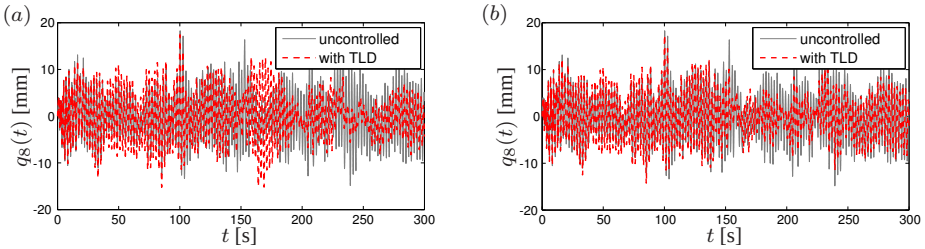

Figure J.9 Control effect of the TLD, **case 3**, tuning ratio = 0.95. (a) without damping screens, $\eta = 9.66\%$. (b) with damping screens, $\eta = 12.96\%$.

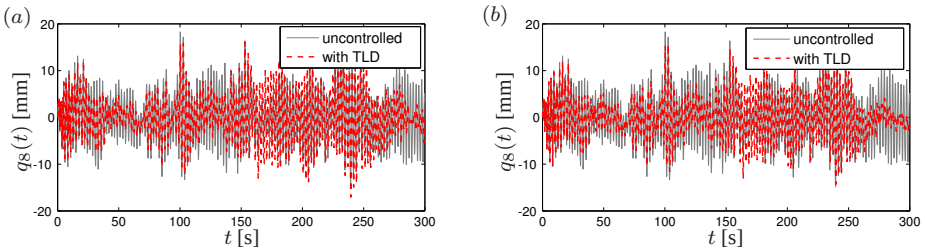

Figure J.10 Control effect of the TLD, **case 3**, tuning ratio = 1.05. (a) without damping screens, $\eta = 7.42\%$. (b) with damping screens, $\eta = 18.84\%$.

angular frequency of the lateral tower mode (2.74 rad/s), and the TLD reduces the peak around this frequency significantly. In contrast to this, as can be seen from Figures 11, 12, 13 and 14 in Appendix G, the measured interaction force and wave

height contain a lot of high frequency components, either from the higher sloshing modes or due to nonlinear coupling effect (multiples of the first sloshing frequency). Before summarizing the test results, Table J.2 gives the theoretical values of both the higher-order sloshing frequencies and the multiples of the first sloshing frequency, with the corresponding abbreviations. Based on these theoretical values, the frequency components of the interaction force and the wave height from measurements can be identified and classified accordingly.

Table J.2 Theoretical values of both the angular frequencies of the higher-order sloshing modes and the multiples of the first sloshing angular frequency, unit: [rad/s], TLD used in 3 MW wind turbine.

sloshing mode	value	abbrev.	multiples	value	abbrev.
1^{st} mode	2.7509	$\omega_{s,1}$	1 time	2.7509	$\omega_{s,1}$
2^{nd} mode	4.9718	$\omega_{s,2}$	2 times	5.5018	$2\omega_{s,1}$
3^{rd} mode	6.6134	$\omega_{s,3}$	3 times	8.2527	$3\omega_{s,1}$
4^{th} mode	7.8634	$\omega_{s,4}$	4 times	11.0036	$4\omega_{s,1}$
5^{th} mode	8.8838	$\omega_{s,5}$	5 times	13.7545	$5\omega_{s,1}$
6^{th} mode	9.7681	$\omega_{s,6}$	6 times	16.5054	$6\omega_{s,1}$

Next, Table J.3 summarizes the first four frequency components of the interaction force from Fourier amplitude of the measured time histories. The abbreviation inside the parenthesis indicates the source of this frequency component, either from the higher sloshing modes or from the multiples of the first sloshing frequency. "/" means no clear frequency peak can be observed.

Table J.3 First four frequency components of the measured interaction force, TLD for 3 MW wind turbine.

Load case	tuning	screens	1^{st} [rad/s]	2^{nd} [rad/s]	3^{rd} [rad/s]	4^{th} [rad/s]
case 1	1	no	2.723-2.827	$8.294(3\omega_{s,1})$	10.56	$14.1(5\omega_{s,1})$
		yes	2.744-2.827	$8.377(3\omega_{s,1})$	10.49	/
	0.95	no	2.681-2.827	$8.3(3\omega_{s,1})$	10.53	$14.05(5\omega_{s,1})$
		yes	2.597-2.744	$8.2(3\omega_{s,1})$	10.47	/
	1.05	no	2.744-2.932	$8.838(3\omega_{s,1})$	10.47	$13.66(5\omega_{s,1})$
		yes	2.744-2.974	$6.66(\omega_{s,3})$	10.53	/
case 2	1.0	no	2.744-2.869	$8.294(3\omega_{s,1})$	10.56	$14.12(5\omega_{s,1})$
		yes	2.744-2.827	$8.336(3\omega_{s,1})$	10.49	/
	0.95	no	2.744-2.806	$8.273(3\omega_{s,1})$	10.53	$14.1(5\omega_{s,1})$
		yes	2.597-2.744	$8.231(3\omega_{s,1})$	10.47	/
	1.05	no	2.744-2.974	$8.901(3\omega_{s,1})$	10.49	$13.66(5\omega_{s,1})$
		yes	2.744-2.974	10.53	/	/
case 3	1.0	no	2.723-2.827	$8.273(3\omega_{s,1})$	10.47	$14.1(5\omega_{s,1})$
		yes	2.744-2.786	$8.231(3\omega_{s,1})$	10.47	/
	0.95	no	2.618-2.786	$8.315(3\omega_{s,1})$	10.56	$13.93(5\omega_{s,1})$
		yes	2.597-2.744	10.56	/	/
	1.05	no	2.744-2.932	$6.639(\omega_{s,3})$	10.47	/
		yes	2.744-2.974	$6.66(\omega_{s,3})$	10.47	/

Similarly, Table J.4 summarizes the first four frequency components of the wave

height from Fourier amplitude of the measured time histories.

Table J.4 First four frequency components of the measured wave height, TLD for 3 MW wind turbine.

case	tuning	screens	1^{st} [rad/s]	2^{nd} [rad/s]	3^{rd} [rad/s]	4^{th} [rad/s]
case 1	1	no	2.728-2.822	$4.853(\omega_{s,2})$	$5.662(2\omega_{s,1})$	$6.49(\omega_{s,3})$
		yes	2.739-2.772	$5.595(2\omega_{s,1})$	$6.53(\omega_{s,3})$	$8.234(3\omega_{s,1})$
	0.95	no	2.685-2.83	$5.605(2\omega_{s,1})$	$8.384(3\omega_{s,1})$	$8.779(\omega_{s,5})$
		yes	2.606-2.776	$5.515(2\omega_{s,1})$	$6.44(\omega_{s,3})$	$8.14(3\omega_{s,1})$
	1.05	no	2.734-2.943	5.05-5.869	$6.635(\omega_{s,3})$	7.784-8.847
		yes	2.746-2.967	5.05-5.658	$6.654(\omega_{s,3})$	7.852-8.405
case 2	1.0	no	2.742-2.835	$4.849(\omega_{s,2})$	$5.614(2\omega_{s,1})$	$6.509(\omega_{s,3})$
		yes	2.77-2.824	$5.594(2\omega_{s,1})$	$6.535(\omega_{s,3})$	$8.382(3\omega_{s,1})$
	0.95	no	2.689-2.781	$4.734(\omega_{s,2})$	$5.581(2\omega_{s,1})$	$8.271(3\omega_{s,1})$
		yes	2.596-2.746	$5.547(2\omega_{s,1})$	$8.237(3\omega_{s,1})$	10.53
	1.05	no	2.745-2.97	5.05-5.941	$6.653(\omega_{s,3})$	7.8-8.946
		yes	2.746-2.975	5.072-5.797	$6.655(\omega_{s,3})$	7.837-8.409
case 3	1.0	no	2.713-2.831	$4.836(\omega_{s,2})$	$5.56(2\omega_{s,1})$	$6.487(\omega_{s,3})$
		yes	2.707-2.773	$5.481(2\omega_{s,1})$	$6.537(\omega_{s,3})$	$8.238(3\omega_{s,1})$
	0.95	no	2.621-2.775	$4.728(\omega_{s,2})$	$5.516(2\omega_{s,1})$	$6.389(\omega_{s,3})$
		yes	2.612-2.783	$4.714(\omega_{s,2})$	$5.375(2\omega_{s,1})$	$6.437(\omega_{s,3})$
	1.05	no	2.73-2.92	5.043-5.858	$6.655(\omega_{s,3})$	8.665
		yes	2.736-2.973	$5.453(2\omega_{s,1})$	$6.657(\omega_{s,3})$	10.54

It should be noted that the frequency component around 10.5 rad/s in Tables J.3 and J.4 is due to the coupling between the tower and the blade.

J.3 Results of the 2 MW wind turbine

The performance of the TLD on damping lateral tower vibrations of the 2 MW wind turbine have been summarized in Table 2 in Appendix G. Time histories of the tower vibration for the 2 MW wind turbine during all 18 tests are presented in Figures J.11-J.19 below.

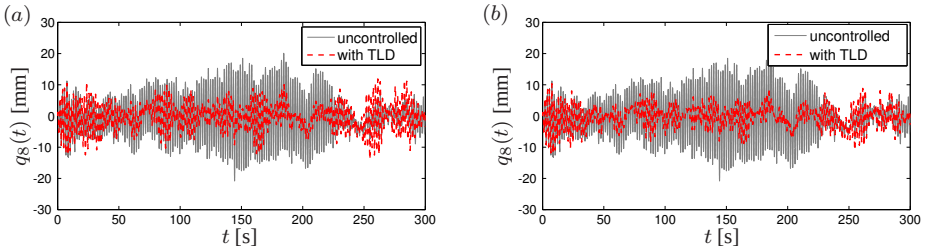

Figure J.11 Control effect of the TLD, **case 4**, tuning ratio = 1. (a) without damping screens, $\eta = 39.80\%$. (b) with damping screens, $\eta = 51.98\%$.

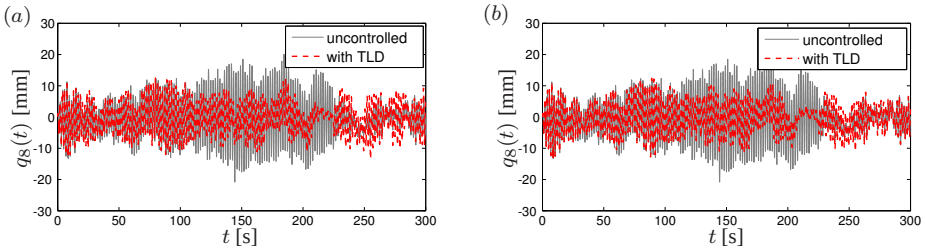

Figure J.12 Control effect of the TLD, **case 4**, tuning ratio = 0.95. (a) without damping screens, $\eta = 28.01\%$. (b) with damping screens, $\eta = 31.28\%$.

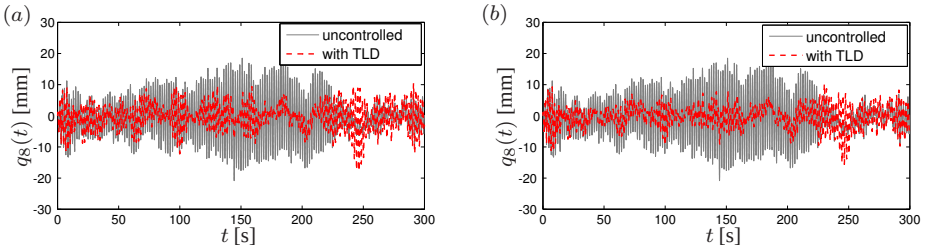

Figure J.13 Control effect of the TLD, **case 4**, tuning ratio = 1.05. (a) without damping screens, $\eta = 41.55\%$. (b) with damping screens, $\eta = 49.95\%$.

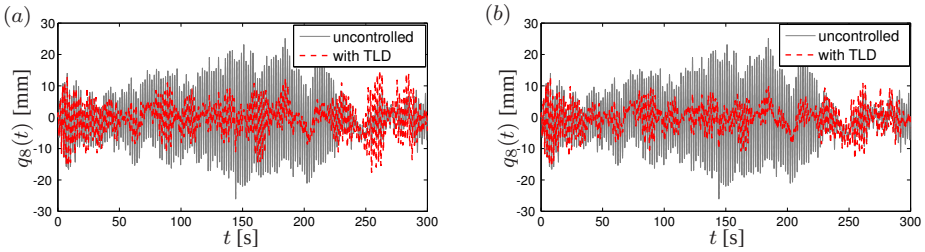

Figure J.14 Control effect of the TLD, **case 5**, tuning ratio = 1. (a) without damping screens, $\eta = 43.55\%$. (b) with damping screens, $\eta = 52.90\%$.

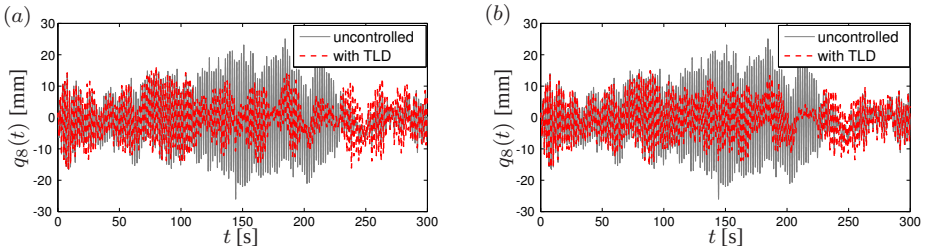

Figure J.15 Control effect of the TLD, **case 5**, tuning ratio = 0.95. (a) without damping screens, $\eta = 29.50\%$. (b) with damping screens, $\eta = 33.03\%$.

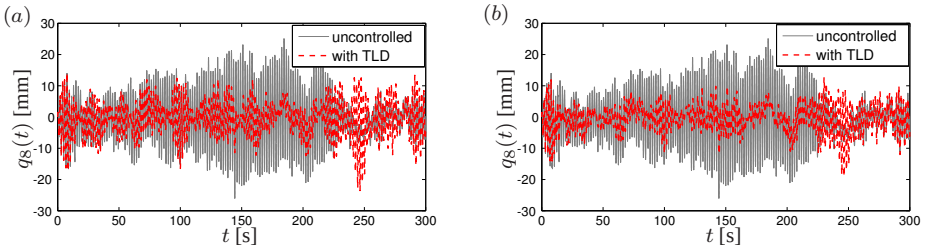

Figure J.16 Control effect of the TLD, **case 5**, tuning ratio = 1.05. (a) without damping screens, $\eta = 37.39\%$. (b) with damping screens, $\eta = 50.28\%$.

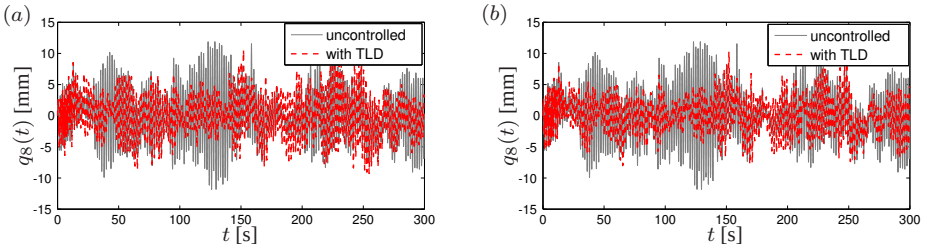

Figure J.17 Control effect of the TLD, **case 6**, tuning ratio = 1. (a) without damping screens, $\eta = 20.38\%$. (b) with damping screens, $\eta = 32.26\%$.

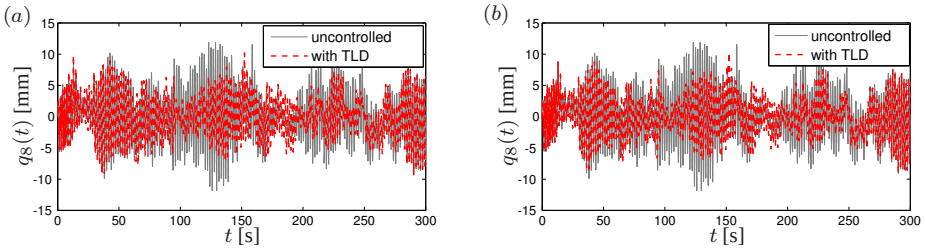

Figure J.18 Control effect of the TLD, **case 6**, tuning ratio = 0.95. (a) without damping screens, $\eta = 22.13\%$. (b) with damping screens, $\eta = 25.77\%$.

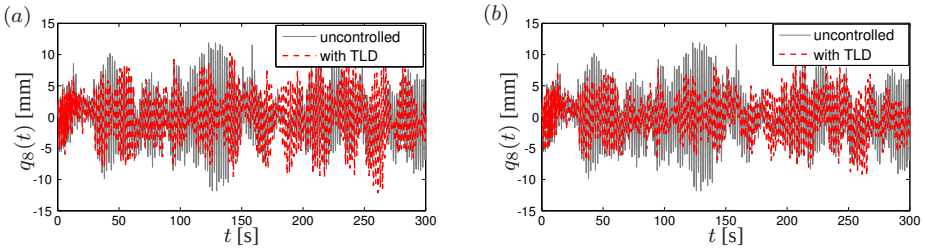

Figure J.19 Control effect of the TLD, **case 6**, tuning ratio = 1.05. (a) without damping screens, $\eta = 9.46\%$. (b) with damping screens, $\eta = 25.40\%$.

Table J.5 gives the theoretical values of both the higher-order sloshing frequencies and the multiples of the first sloshing frequency, for the TLD used in the 2 MW wind turbine.

Table J.5 Theoretical values of both the angular frequencies of the higher-order sloshing modes and the multiples of the first sloshing angular frequency, unit: [rad/s], TLD used in the 2 MW wind turbine.

sloshing mode	value	abbrev.	multiples	value	abbrev.
1^{st} mode	3.3691	$\omega_{s,1}$	1 time	3.3691	$\omega_{s,1}$
2^{nd} mode	5.4921	$\omega_{s,2}$	2 times	6.7382	$2\omega_{s,1}$
3^{rd} mode	6.8880	$\omega_{s,3}$	3 times	10.1073	$3\omega_{s,1}$
4^{th} mode	7.9856	$\omega_{s,4}$	4 times	13.4764	$4\omega_{s,1}$
5^{th} mode	8.9342	$\omega_{s,5}$	5 times	16.8455	$5\omega_{s,1}$
6^{th} mode	9.7881	$\omega_{s,6}$	6 times	20.2146	$6\omega_{s,1}$

Table J.6 summarizes the first four frequency components of the interaction force from Fourier amplitude of the measured time histories. The abbreviation inside the parenthesis indicates the source of this frequency component, either from the higher sloshing modes or from the multiples of the first sloshing frequency. "/" means no clear frequency peak can be observed.

Table J.6 First four frequency components of the measured interaction force, TLD for 2 MW wind turbine.

Load case	tuning	screens	1^{st} [rad/s]	2^{nd} [rad/s]	3^{rd} [rad/s]	4^{th} [rad/s]
case 4	1	no	3.246-3.456	$6.828(\omega_{s,3})$	$8.901(\omega_{s,5})$	13.01
		yes	3.246-3.456	$6.828(\omega_{s,3})$	13.01	/
	0.95	no	3.142-3.393	$6.786(\omega_{s,3})$	13.01	/
		yes	3.142-3.393	$6.786(\omega_{s,3})$	13.01	/
	1.05	no	3.372-3.56	$6.87(\omega_{s,3})$	$10.49(3\omega_{s,1})$	13.01
		yes	3.204-3.435	$6.849(\omega_{s,3})$	13.01	/
case 5	1.0	no	3.204-3.456	$6.828(\omega_{s,3})$	13.01	/
		yes	3.204-3.456	$6.849(\omega_{s,3})$	13.01	/
	0.95	no	3.142-3.393	$6.756(\omega_{s,3})$	$9.676(3\omega_{s,1})$	13.01
		yes	3.142-3.393	$6.723(\omega_{s,3})$	13.01	/
	1.05	no	3.33-3.56	$6.87(\omega_{s,3})$	$10.68(3\omega_{s,1})$	13.01
		yes	3.372-3.56	$6.87(\omega_{s,3})$	13.01	/
case 6	1.0	no	3.246-3.435	$6.849(\omega_{s,3})$	$8.88(\omega_{s,5})$	13.05
		yes	3.204-3.435	$6.849(\omega_{s,3})$	$8.88(\omega_{s,5})$	13.05
	0.95	no	3.142-3.435	$6.807(\omega_{s,3})$	$8.88(\omega_{s,5})$	13.15
		yes	3.142-3.435	$6.807(\omega_{s,3})$	$8.838(\omega_{s,5})$	13.15
	1.05	no	3.309-3.581	$6.87(\omega_{s,3})$	$8.901(\omega_{s,5})$	13.15
		yes	3.309-3.581	$6.87(\omega_{s,3})$	$8.838(\omega_{s,5})$	13.15

Similarly, Table J.7 summarizes the first four frequency components of the wave height from Fourier amplitude of the measured time histories.

It should be noted that the frequency component around 13.1 rad/s in Tables J.6 and J.7 is due to the coupling between the tower and the blade.

Table J.7 First four frequency components of the measured wave height, TLD for 2 MW wind turbine.

case	tuning	screens	1^{st} [rad/s]	2^{nd} [rad/s]	3^{rd} [rad/s]	4^{th} [rad/s]
case 1	1	no	3.247-3.465	$5.438(\omega_{s,2})$	$6.712(2\omega_{s,1})$	$6.93(\omega_{s,3})$
		yes	3.206-3.467	$6.656(2\omega_{s,1})$	$6.935(\omega_{s,3})$	$8.956(\omega_{s,5})$
	0.95	no	3.147-3.384	$5.331(\omega_{s,2})$	6.275-6.767	$8.892(\omega_{s,5})$
		yes	3.132-3.389	6.521-6.761	$8.883(\omega_{s,5})$	13.2
	1.05	no	3.307-3.559	$6.866(2\omega_{s,1})$	$7.118(\omega_{s,3})$	$8.897(\omega_{s,5})$
		yes	3.275-3.552	$6.901(2\omega_{s,1})$	$7.105(\omega_{s,3})$	$8.899(\omega_{s,5})$
case 2	1.0	no	3.212-3.471	$5.423(\omega_{s,2})$	$6.667(2\omega_{s,1})$	$6.926(\omega_{s,3})$
		yes	3.2-3.461	$6.661(2\omega_{s,1})$	$6.834(\omega_{s,3})$	$8.965(\omega_{s,5})$
	0.95	no	3.155-3.395	$5.296(\omega_{s,2})$	6.292-6.532	$6.754(\omega_{s,3})$
		yes	3.14-3.392	$6.531(2\omega_{s,1})$	$6.764(\omega_{s,3})$	$8.954(\omega_{s,5})$
	1.05	no	3.301-3.559	$6.86(2\omega_{s,1})$	$7.119(\omega_{s,3})$	$8.889(\omega_{s,5})$
		yes	3.3-3.559	$6.858(2\omega_{s,1})$	$7.118(\omega_{s,3})$	$8.897(\omega_{s,5})$
case 3	1.0	no	3.254-3.433	$5.454(\omega_{s,2})$	$6.687(2\omega_{s,1})$	$6.884(\omega_{s,3})$
		yes	3.216-3.434	$6.654(2\omega_{s,1})$	$6.843(\omega_{s,3})$	$8.893(\omega_{s,5})$
	0.95	no	3.145-3.441	$5.365(\omega_{s,2})$	$6.531(2\omega_{s,1})$	$6.79(\omega_{s,3})$
		yes	3.147-3.442	$5.32(\omega_{s,2})$	$6.45(2\omega_{s,1})$	$6.815(\omega_{s,3})$
	1.05	no	3.297-3.574	$5.526(\omega_{s,2})$	$6.871(2\omega_{s,1})$	$7.147(\omega_{s,3})$
		yes	3.308-3.57	$5.551(\omega_{s,2})$	$6.887(2\omega_{s,1})$	$7.158(\omega_{s,3})$

SUMMARY

The present thesis deals with fundamental researches on passive and active vibration control of renewable energy structures, and provides useful models for practical applications. Effective and robust vibration control methods have been explored for mitigating the lightly damped edgewise blade vibration and lateral tower vibration, with the main focus on structural control devices. Rigorous theoretical modeling of different dynamic system has been established, based on which detailed design and analysis of the proposed control devices can be carried out.

This thesis also explores technical solutions for wave energy point absorbers, in order to maximize the mean absorbed power and to deliver more smooth power to the grid. A novel suboptimal causal control law has been established for controlling the motion of the point absorber, and a new type of point absorber has also been proposed with detailed modeling and analysis.

ISSN (online): 2246-1248
ISBN (online):978-87-7112-361-6

AALBORG **UNIVERSITY PRESS**